Dredging Engineering

Special Topics

Miedema, Sape

DOI
10.5074/t.2019.004

Publication date
2019

Document Version
Final published version

Citation (APA)
Miedema, S. (2019). *Dredging Engineering: Special Topics*. TU Delft OPEN Publishing. https://doi.org/10.5074/t.2019.004

Dredging Engineering Special Topics

Sape A. Miedema

TU Delft open

Dredging Engineering
Special Topics

Entrainment of Particles
Cutter Head Spillage
Centrifugal Pumps
Pump/Pipeline Dynamics
Swing Winches
Trailing Suction Hopper Sedimentation
TSHD Water Jets
Clamshell Dredging

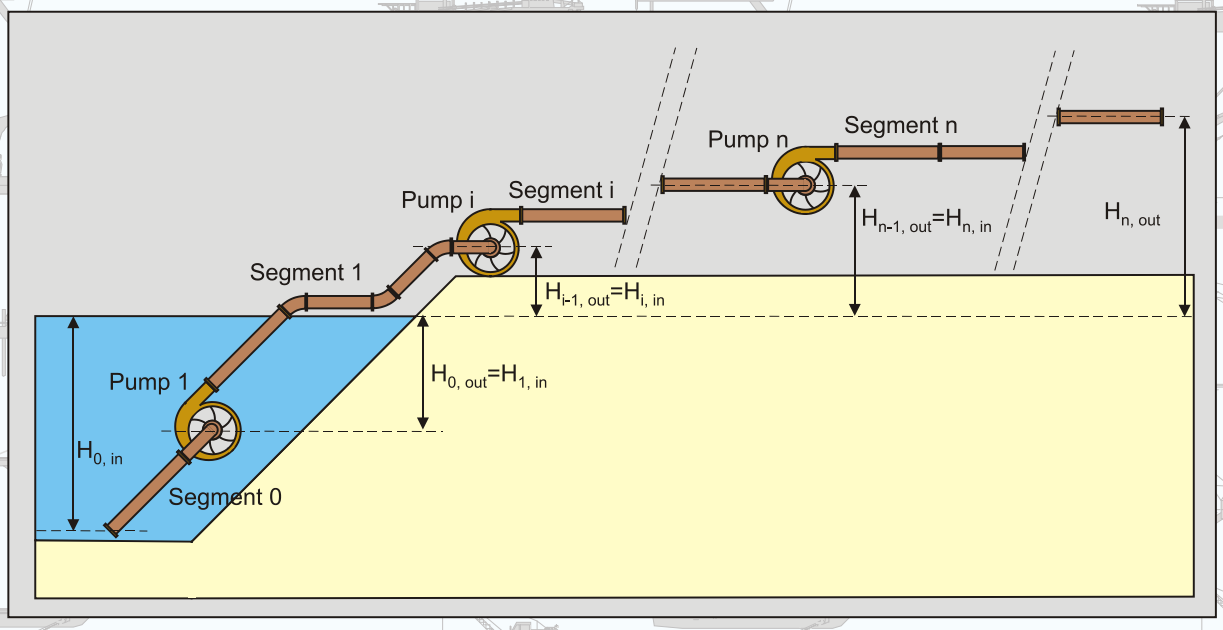

by
Dr.ir. Sape A. Miedema

Dredging Engineering Special Topics

Entrainment of Particles
Cutter Head Spillage
Centrifugal Pumps
Pump/Pipeline Dynamics
Swing Winches
Trailing Suction Hopper Sedimentation
TSHD Water Jets
Clamshell Dredging

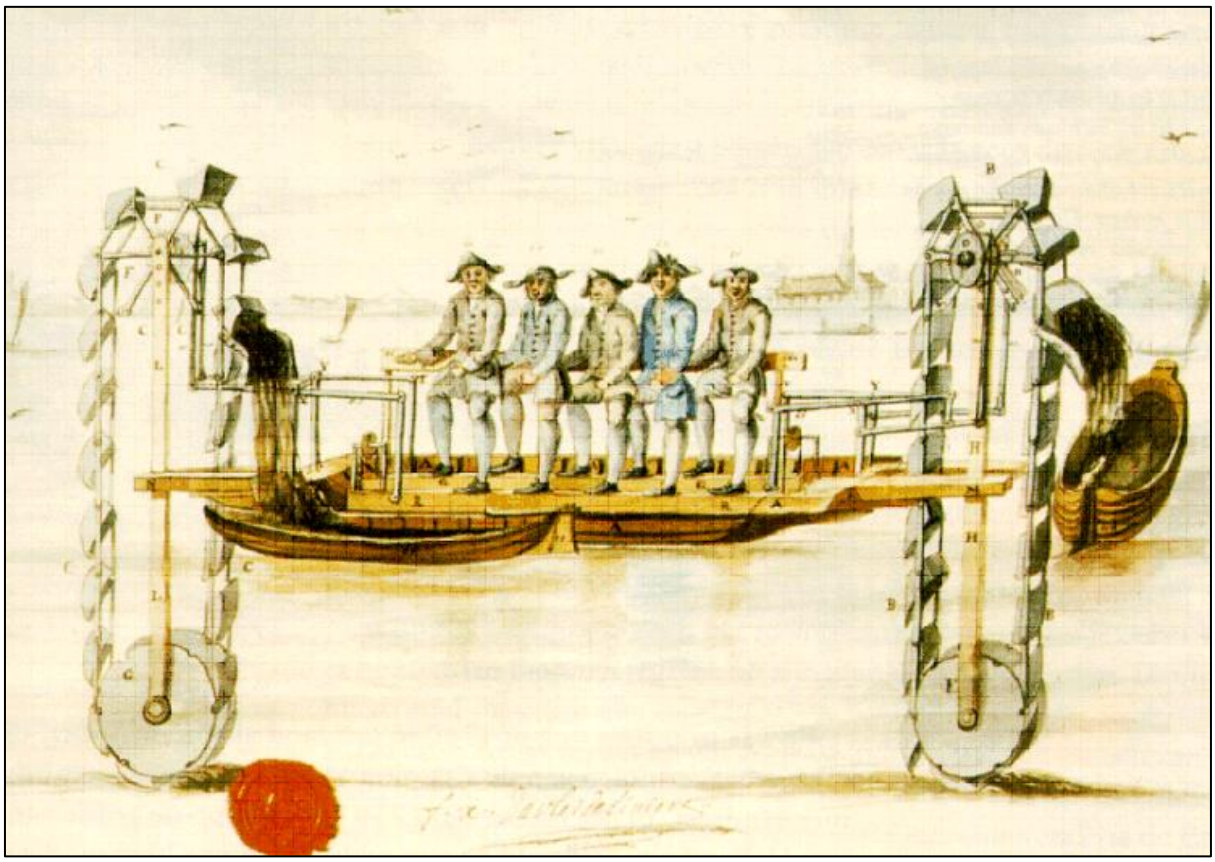

By

Dr.ir. Sape A. Miedema

Version: Thursday, June 27, 2019

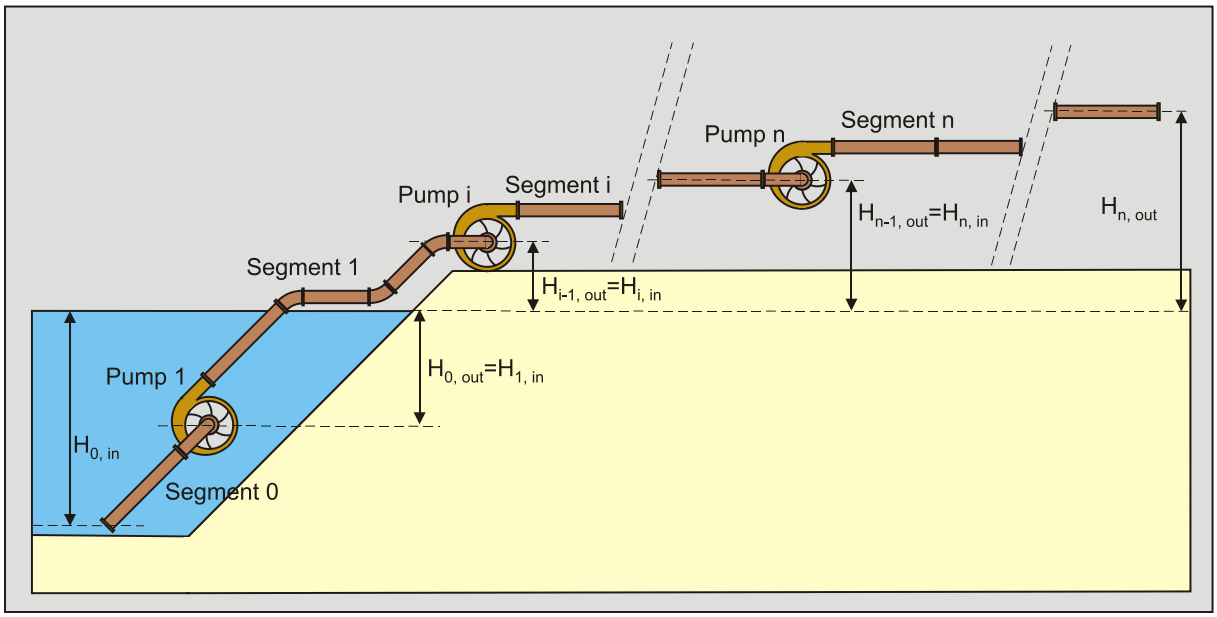

ISBN Paperback: 978-94-6366-173-7
ISBN EBook: 978-94-6366-174-4
DOI: https://doi.org/10.5074/t.2019.004

Preface

In dredging, trenching, (deep sea) mining, drilling, tunnel boring and many other applications, sand, clay or rock has to be excavated. The productions (and thus the dimensions) of the excavating equipment range from mm^3/sec - cm^3/sec to m^3/sec. In oil drilling layers with a thickness of a magnitude of 0.2 mm are cut, while in dredging this can be of a magnitude of 0.1 m with cutter suction dredges and meters for clamshells and backhoe's. Some equipment is designed for dry soil, while others operate under water saturated conditions. Installed cutting powers may range up to 10 MW. For both the design, the operation and production estimation of the excavating equipment it is important to be able to predict the cutting forces and powers. After the soil has been excavated it is usually transported hydraulically as a slurry over a short (TSHD's) or a long distance (CSD's) or mechanically. Estimating the pressure losses and determining whether or not a bed will occur in the pipeline is of great importance. Fundamental processes of sedimentation, initiation of motion and erosion of the soil particles determine the transport process and the flow regimes. In TSHD's the soil has to settle during the loading process, where also sedimentation and erosion will be in equilibrium. In all cases we have to deal with soil and high density soil water mixtures and its fundamental behavior.

The book: The Delft Sand, Clay & Rock Cutting Model, deals with everything related to the cutting processes.
The book: Slurry Transport: Fundamentals, A Historical Overview & The Delft Head Loss & Limit Deposit Velocity Framework deals with everything related to slurry transport.
Both books can be downloaded for free and/or printed on demand at Delft University of Technology Open Textbooks, , https://textbooks.open.tudelft.nl/index.php/textbooks/catalog .

Over the years the author has been carrying out research on many other topics like TSHD sedimentation, initiation of motion of particles, dynamics of slurry transport and so on. This book is a collection of the publications on these subjects, often with additional remarks.

This book is dedicated to my wife

Thuy K.T. Miedema Nguyen

About the Author.

Dr.ir. Sape A. Miedema (November 8th 1955) obtained his M.Sc. degree in Mechanical Engineering with honours at the Delft University of Technology (DUT) in 1983. He obtained his Ph.D. degree on research into the basics of soil cutting in relation with ship motions, in 1987. From 1987 to 1992 he was Assistant Professor at the chair of Dredging Technology. In 1992 and 1993 he was a member of the management board of Mechanical Engineering & Marine Technology of the DUT. In 1992 he became Associate Professor at the DUT with the chair of Dredging Technology. From 1996 to 2001 he was appointed Head of Studies of Mechanical Engineering and Marine Technology at the DUT, but still remaining Associate Professor of Dredging Engineering. In 2005 he was appointed Head of Studies of the MSc program of Offshore & Dredging Engineering and he is also still Associate Professor of Dredging Engineering. In 2013 he was also appointed as Head of Studies of the MSc program Marine Technology of the DUT.

Dr.ir. S.A. Miedema teaches (or has taught) courses on soil mechanics and soil cutting, pumps and slurry transport, hopper sedimentation and erosion, mechatronics, applied thermodynamics related to energy, drive system design principles, mooring systems, hydromechanics and mathematics. He is (or has been) also teaching at Hohai University, Changzhou, China, at Cantho University, Cantho Vietnam, at Petrovietnam University, Baria, Vietnam and different dredging companies in the Netherlands and the USA.

His research focuses on the mathematical modeling of dredging systems like, cutter suction dredges, hopper dredges, clamshell dredges, backhoe dredges and trenchers. The fundamental part of the research focuses on the cutting processes of sand, clay and rock, sedimentation processes in Trailing Suction Hopper Dredges and the associated erosion processes. Lately the research focuses on hyperbaric rock cutting in relation with deep sea mining and on hydraulic transport of solids/liquid settling slurries.

Table of Contents

Chapter 1: The Terminal Settling Velocity of Particles.

1.1. Introduction.

In many cases in hydraulic transport there will be equilibrium between erosion and deposition. In order to understand this, both deposition and erosion (initiation of motion) will be discussed. The settling velocity of grains depends on the grain size, shape and specific density. It also depends on the density and the viscosity of the carrier liquid the grains are settling in, it also depends upon whether the settling process is laminar or turbulent.
Most slurry transport models use the terminal settling velocity, the particle drag coefficient or the particle Froude number. So it is important to have a good unserstanding of these parameters.

1.2. The Equilibrium of Forces.

The settling velocity of grains depends on the grain size, shape and specific density. It also depends on the density and the viscosity of the liquid the grains are settling in, and it depends upon whether the settling process is laminar or turbulent. Discrete particles do not change their size, shape or weight during the settling process (and thus do not form aggregates). A discrete particle in a liquid will settle under the influence of gravity. The particle will accelerate until the frictional drag force of the liquid equals the value of the gravitational force, after which the vertical (settling) velocity of the particle will be constant (Figure 1-1), the so called terminal settling velocity.

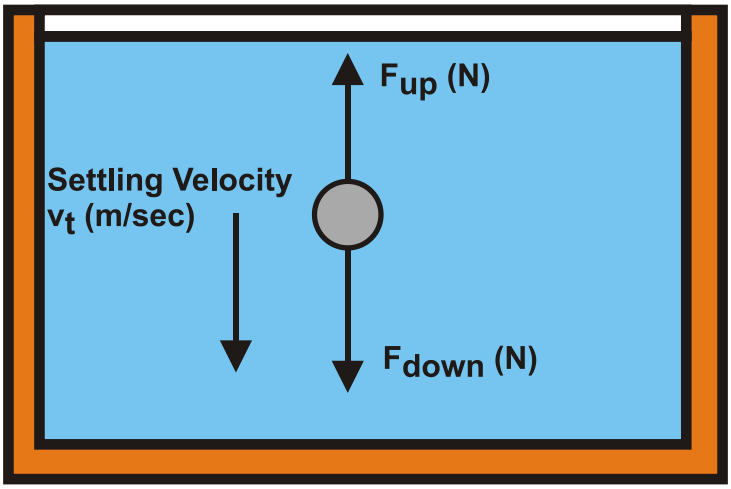

Figure 1-1: Forces on a settling particle.

The upward directed force on the particle, caused by the frictional drag of the liquid, can be calculated by:

$$F_{up} = C_D \cdot \frac{1}{2} \cdot \rho_l \cdot v_t^2 \cdot A \qquad (1\text{-}1)$$

The downward directed force, caused by the difference in density between the particle and the water can be calculated by:

$$F_{down} = (\rho_s - \rho_l) \cdot g \cdot V \cdot \psi \qquad (1\text{-}2)$$

In this equation a shape factor ψ is introduced to compensate for the shape of real sand grains. This shape factor is 1 for spheres and about 0.7 for real sand particles. The projected surface of the particle is:

$$A = \frac{\pi}{4} \cdot d^2 \qquad (1\text{-}3)$$

The volume of the particle is:

$$V = \frac{\pi}{6} \cdot d^3 \qquad (1\text{-}4)$$

In general, the terminal settling velocity $\mathbf{v_t}$ can be determined with the following equation:

$$\mathbf{v_t = \sqrt{\frac{4 \cdot g \cdot (\rho_s - \rho_l) \cdot d \cdot \psi}{3 \cdot \rho_l \cdot C_D}}} \qquad \textbf{(1-5)}$$

The Reynolds number of the settling process determines whether the process is laminar or turbulent. The Reynolds number can be determined by:

$$\mathbf{Re_p = \frac{v_t \cdot d}{\nu_l}} \qquad \textbf{(1-6)}$$

1.3. The Drag Coefficient.

In equation (1-5) all parameters are assumed to be known, except for the drag coefficient $\mathbf{C_D}$.

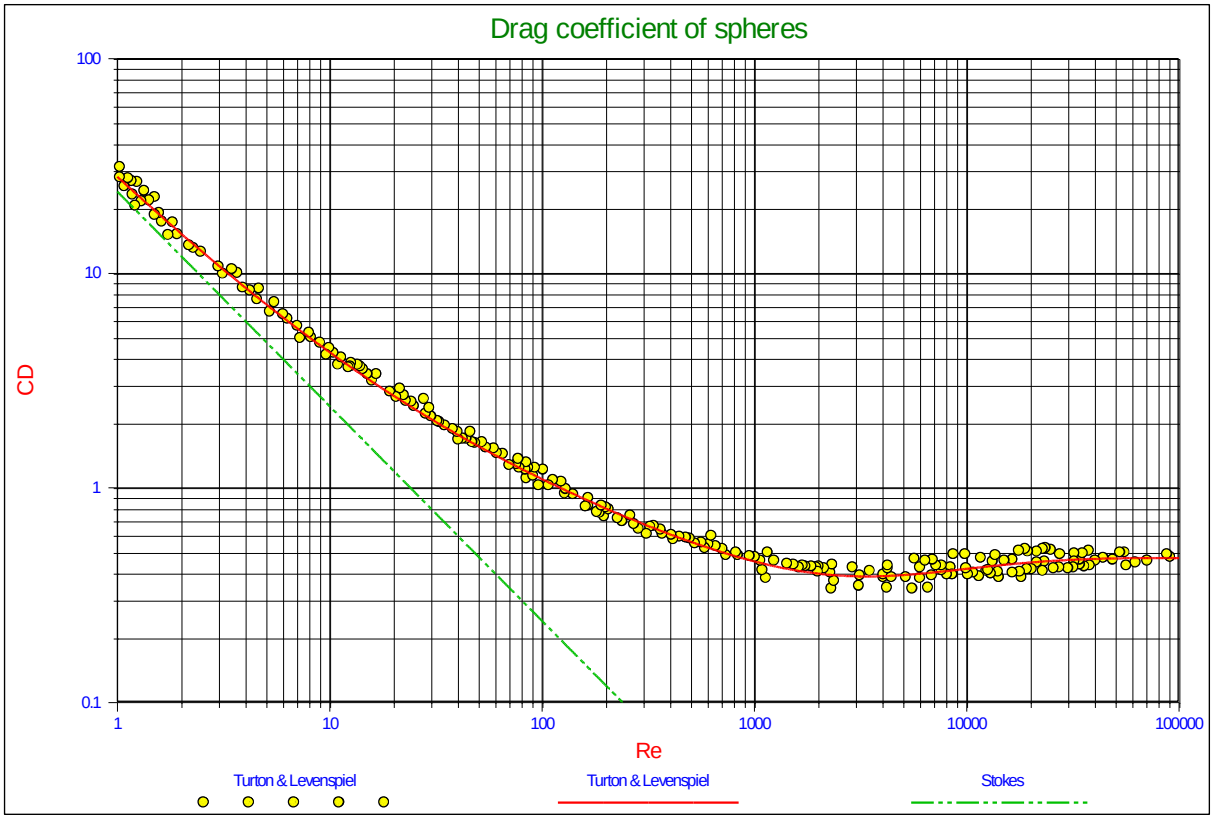

Figure 1-2: Experimental data for drag coefficients of spheres as a function of the Reynolds number (Turton & Levenspiel, 1986).

The drag coefficient $\mathbf{C_D}$ for spheres depends upon the Reynolds number according to:

The laminar region:

$$\mathbf{Re_p < 1} \quad \Rightarrow \quad \mathbf{C_D = \frac{24}{Re_p}} \qquad \textbf{(1-7)}$$

The transitional region:

$$\mathbf{1 < Re_p < 2000} \quad \Rightarrow \quad \mathbf{C_D = \frac{24}{Re_p} + \frac{3}{\sqrt{Re_p}} + 0.34} \qquad \textbf{(1-8)}$$

The turbulent region:

$$Re_p > 2000 \quad \Rightarrow \quad C_D = 0.445 \tag{1-9}$$

As can be seen from the above equations, the drag coefficient C_D is not continuous at the transition points of $Re_p=1$ and $Re_p=2000$. To get a smooth continuous curve the following equations can be applied:

The laminar region:

$$Re_p < 1 \quad \Rightarrow C_D = Re_p \cdot \left(\frac{24}{Re_p} + \frac{3}{\sqrt{Re_p}} + 0.34\right) + (1\text{-}Re_p) \cdot \frac{24}{Re_p} \tag{1-10}$$

The transitional region:

$$1 < Re_p < 2000 \quad \Rightarrow C_D = \frac{24}{Re_p} + \frac{3}{\sqrt{Re_p}} + 0.34 \tag{1-11}$$

The turbulent region:

$$Re_p > 10000 \quad \Rightarrow C_D = \frac{10000}{Re_p} \cdot \left(\frac{24}{Re_p} + \frac{3}{\sqrt{Re_p}} + 0.34\right) + \left(1 - \frac{10000}{Re_p}\right) \cdot 0.445 \tag{1-12}$$

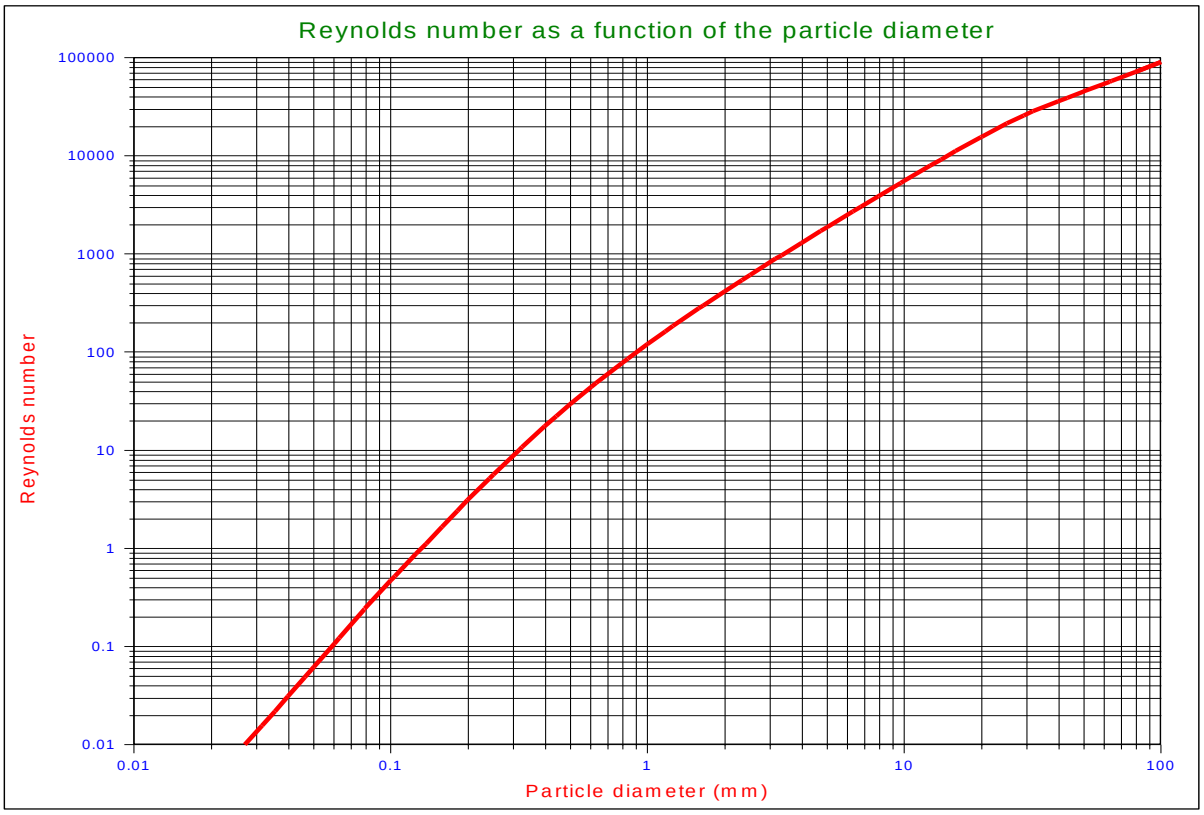

Figure 1-3: The particle Reynolds number as a function of the particle diameter.

Figure 1-3 shows the particle Reynolds number as a function of the particle diameter for sands and gravels, using the Ruby & Zanke (1977) equation.

Another equation for the transitional region has been derived by Turton & Levenspiel (1986):

$$C_D = \frac{24}{Re_p} \cdot \left(1 + 0.173 \cdot Re_p^{0.657}\right) + \frac{0.413}{1 + 16300 \cdot Re_p^{-1.09}} \tag{1-13}$$

The models derived to describe the Shields curve use the drag coefficient of spheres and hardly any discussion about this has been found in literature, although it is known that for sands and gravels the drag coefficients, especially at large Reynolds numbers, are larger than the drag coefficient for spheres. Engelund & Hansen (1967) found the following equation based on measurements and found it best suited for natural sands and gravels (Julien, 1995):

$$C_D = \frac{24}{Re_p} + 1.5 \qquad \textbf{(1-14)}$$

It must be noted here that in general the drag coefficients are determined based on the terminal settling velocity of the particles. Wu & Wang (2006) recently gave an overview of drag coefficients and terminal settling velocities for different particle Corey shape factors. The result of their research is reflected in Figure 1-4. Figure 1-4 shows the drag coefficients as a function of the Reynolds number and as a function of the Corey shape factor. Figure 1-5 shows the drag coefficient for natural sands and gravels. The asymptotic value for large Reynolds numbers is about 1, while equation (1-14) shows an asymptotic value of 1.5.
For shells lying flat on the bed, the drag coefficient will be similar to the drag coefficient of a streamlined half body (0.09), which is much much smaller than the drag coefficient for settling (3). So there is a large asymmetry between the settling process and the erosion process of shells, while for more or less spherical sand particles the drag coefficient is considered to be the same in each direction.
Figure 1-6 shows the C_D coefficient as a function of the Re_p number. In the transition area the equations are implicit. Iteration 1 shows the resulting C_D values based on equations (1-7), (1-8) and (1-9), while iteration 2 shows the results based on equations (1-10), (1-11) and (1-12). It is clear from this figure that iteration 2 matches the observed data better than iteration 1, but equation (1-13) of Turton & Levenspiel (1986) matches the best. This is however for spheres and not for real sand and gravel particles.

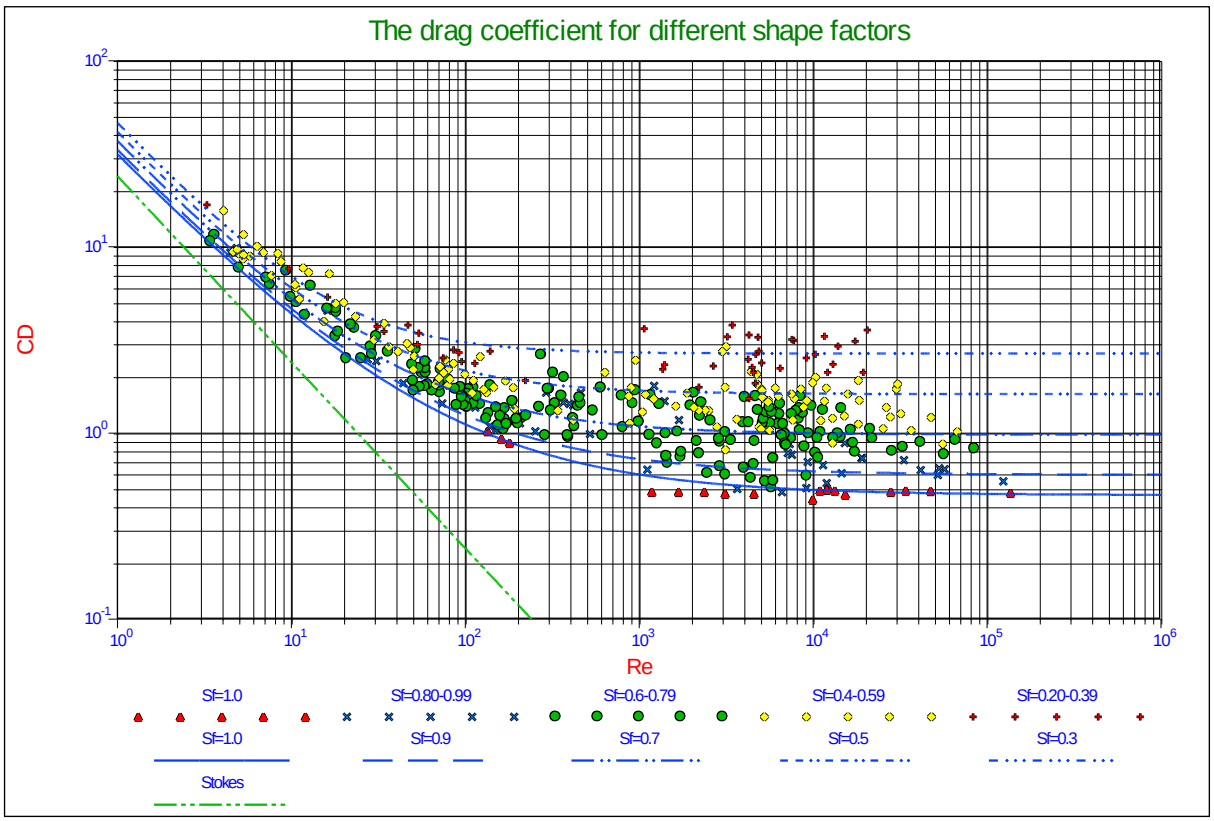

Figure 1-4: Drag coefficient as a function of the particle shape (Wu & Wang, 2006).

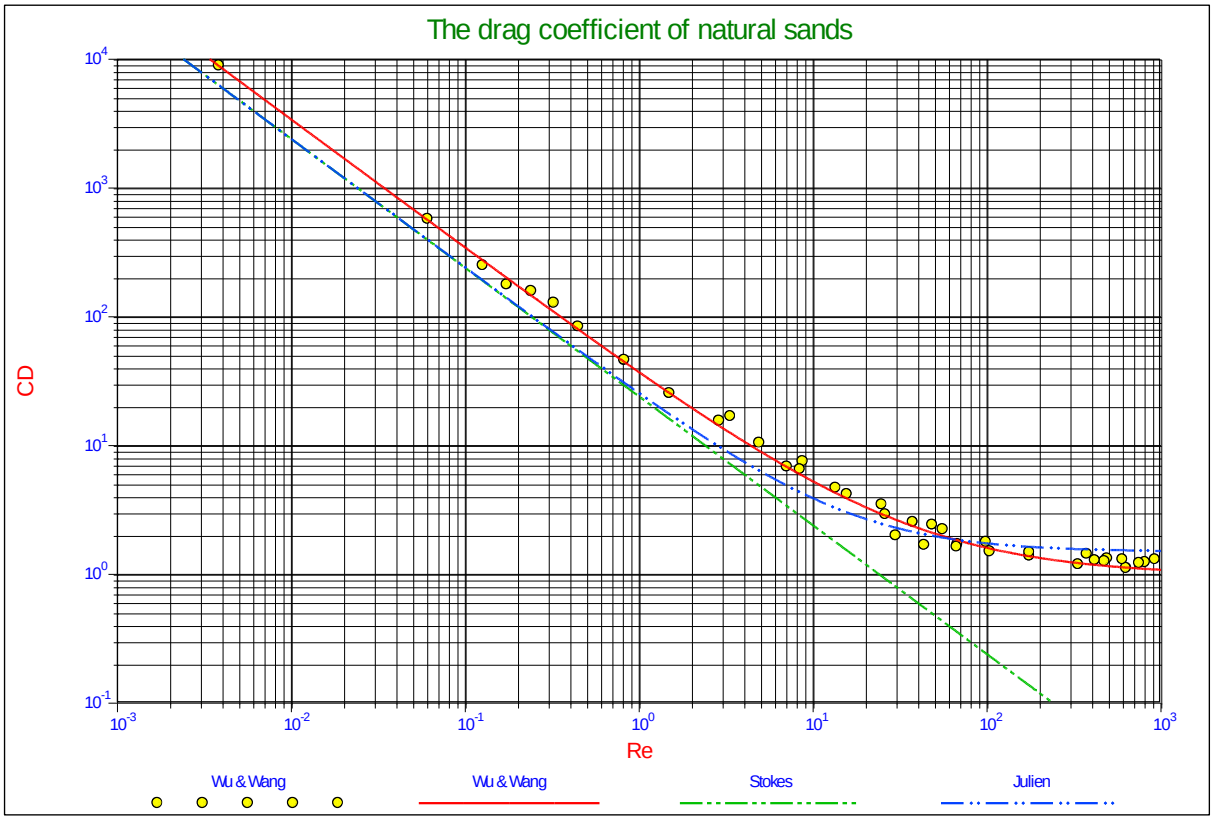

Figure 1-5: Drag coefficient for natural sediments (S_f=0.7) (Wu & Wang, 2006).

1.4. Terminal Settling Velocity Equations.

Stokes, Budryck and Rittinger used these drag coefficients to calculate settling velocities for laminar settling (Stokes), a transition zone (Budryck) and turbulent settling (Rittinger) of real sand grains. This gives the following equations for the settling velocity:

Laminar flow, **d<0.1 mm**, according to **Stokes**.

$$v_t = 424 \cdot R_{sd} \cdot d^2 \qquad \textbf{(1-15)}$$

Transition zone, **d>0.1 mm** and **d<1 mm**, according to **Budryck**.

$$v_t = 8.925 \cdot \frac{\left(\sqrt{(1+95 \cdot R_{sd} \cdot d^3)} - 1\right)}{d} \qquad \textbf{(1-16)}$$

Turbulent flow, **d>1 mm**, according to **Rittinger**.

$$v_t = 87 \cdot \sqrt{R_{sd} \cdot d} \qquad \textbf{(1-17)}$$

With the relative submerged density R_{sd} defined as:

$$R_{sd} = \frac{\rho_s - \rho_l}{\rho_l} \qquad \textbf{(1-18)}$$

In these equations the grain diameter is in mm and the settling velocity in mm/sec. Since the equations were derived for sand grains, the shape factor for sand grains is included for determining the constants in these equations.

Another equation for the transitional region (in m and m/sec) has been derived by Ruby & Zanke (1977):

$$v_t = \frac{10 \cdot \nu_l}{d} \cdot \left(\sqrt{1 + \frac{R_{sd} \cdot g \cdot d^3}{100 \cdot \nu_l^2}} - 1 \right) \qquad \textbf{(1-19)}$$

The effective drag coefficient can now be determined by:

$$C_D = \frac{4}{3} \cdot \frac{g \cdot R_{sd} \cdot d \cdot \psi}{{v_t}^2} \qquad \textbf{(1-20)}$$

Figure 1-7 shows the settling velocity as a function of the particle diameter for the Stokes, Budryck, Rittinger & Zanke equations.

In these equations the grain diameter is in mm and the settling velocity in mm/sec, except for the Zanke equation. Since the equations were derived for sand grains, the shape factor for sand grains is used for determining the constants in the equations. The shape factor can be introduced into the equations for the drag coefficient by dividing the drag coefficient by a shape factor ψ. For normal sands this shape factor has a value of 0.7. The viscosity of the water is temperature dependent. If a temperature of 10° is used as a reference, then the viscosity increases by 27% at 0° and it decreases by 30% at 20° centigrade. Since the viscosity influences the Reynolds number, the settling velocity for laminar settling is also influenced by the viscosity. For turbulent settling the drag coefficient does not depend on the Reynolds number, so this settling process is not influenced by the viscosity. Other researchers use slightly different constants in these equations but, these equations suffice to explain the basics of the Durand theory.

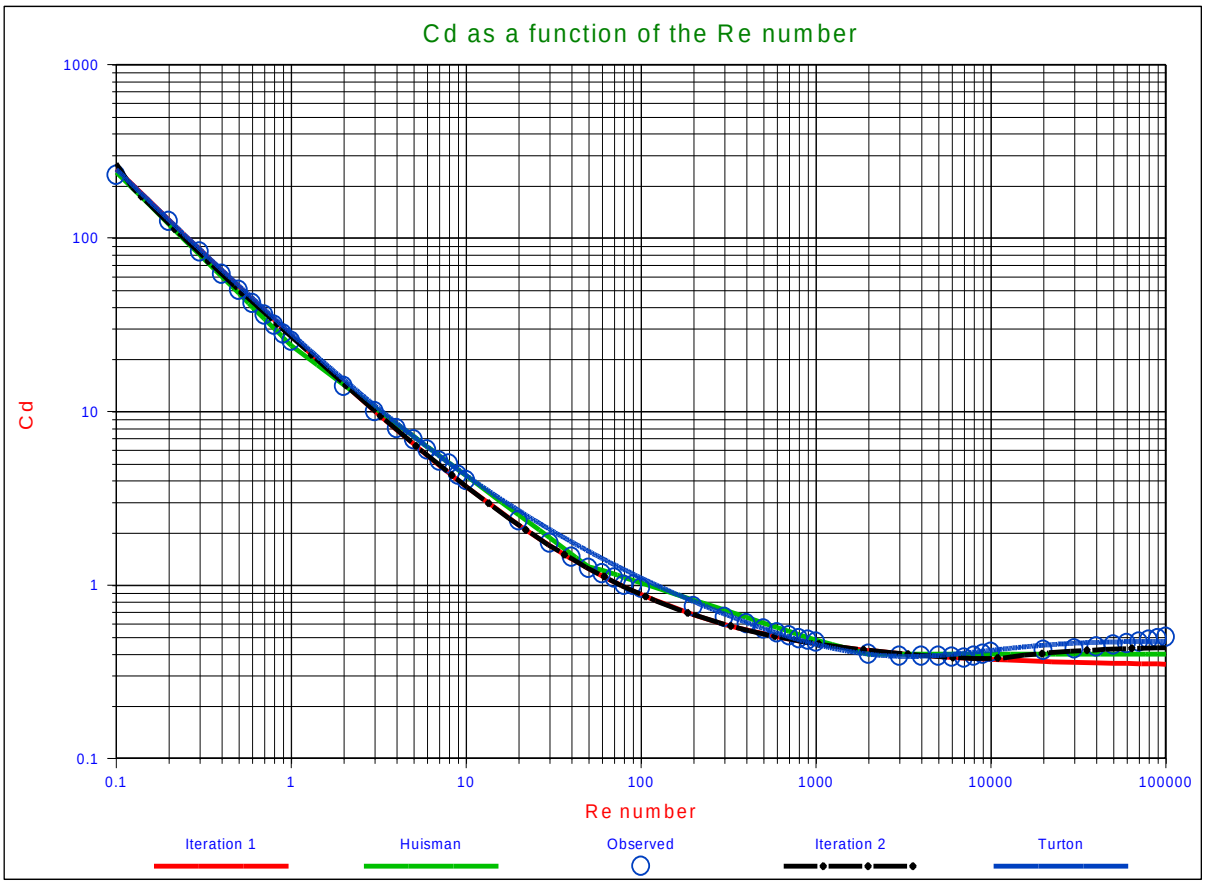

Figure 1-6: The drag coefficient as a function of the particle Reynolds number.

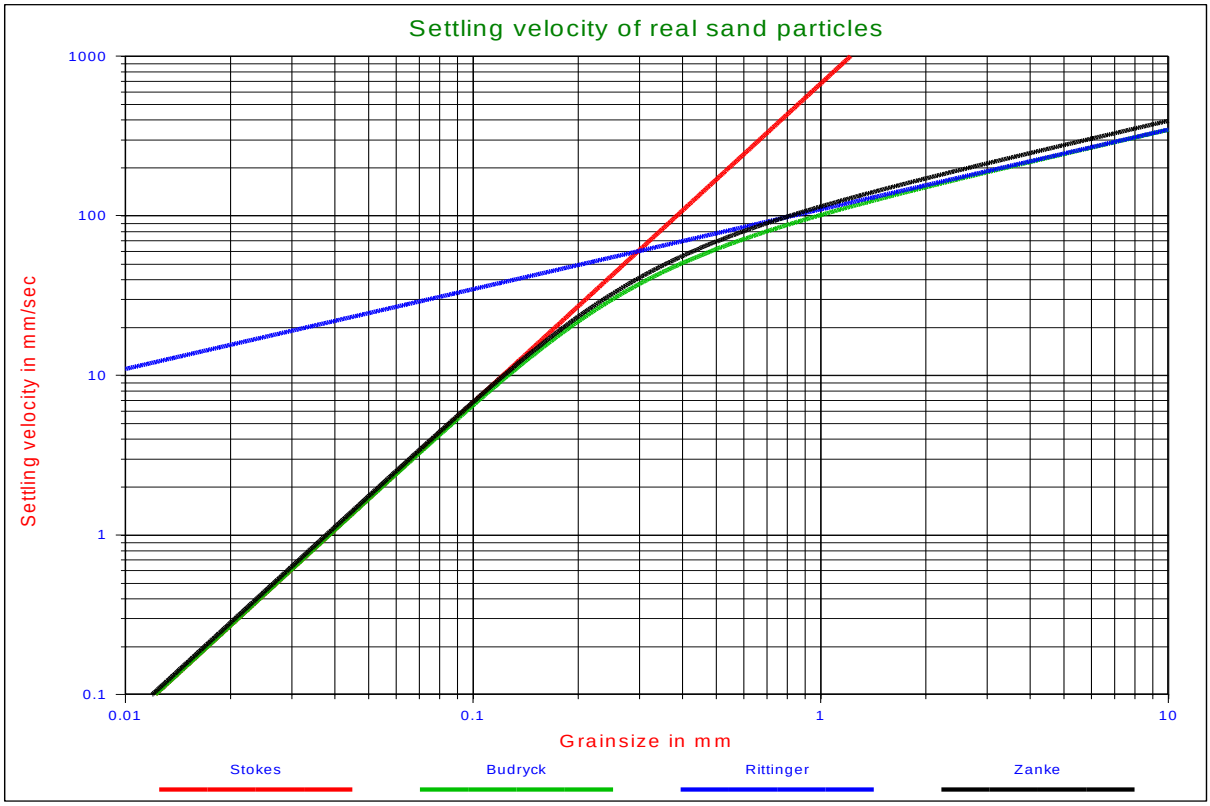

Figure 1-7: The settling velocity of individual particles.

The Huisman (1973-1995) Method.

A better approximation and more workable equations for the drag coefficient C_D may be obtained by subdividing the transition region, for instance:

$$Re_p < 1 \qquad C_D = \frac{24}{Re_p^1} \qquad (1\text{-}21)$$

$$1 < Re_p < 50 \qquad C_D = \frac{24}{Re_p^{3/4}} \qquad (1\text{-}22)$$

$$50 < Re_p < 1620 \qquad C_D = \frac{4.7}{Re_p^{1/3}} \qquad (1\text{-}23)$$

$$1620 < Re_p \qquad C_D = 0.4 \qquad (1\text{-}24)$$

This power approximation is also shown in Figure 1-6. Substitution of these equations in equation (1-19) gives:

$$Re_p < 1 \qquad v_t = \frac{1}{18} \cdot \frac{g^1}{\nu_l^1} \cdot R_{sd}^1 \cdot d^2 \qquad (1\text{-}25)$$

$$1 < Re_p < 50 \qquad v_t = \frac{1}{10} \cdot \frac{g^{0.8}}{\nu_l^{0.6}} \cdot R_{sd}^{0.8} \cdot d^{1.4} \qquad (1\text{-}26)$$

$$50 < Re_p < 1620 \qquad v_t = \frac{1}{2.13} \cdot \frac{g^{0.6}}{\nu_l^{0.2}} \cdot R_{sd}^{0.6} \cdot d^{0.8} \qquad (1\text{-}27)$$

$$1620 < Re_p \qquad v_t = 1.83 \cdot \frac{g^{0.5}}{\nu_l^{0}} \cdot R_{sd}^{0.5} \cdot d^{0.5} \qquad (1\text{-}28)$$

These equations are difficult to use in an actual case because the value of Re_p depends on the terminal settling velocity. The following method gives a more workable solution.

Equation (1-5) can be transformed into:

$$C_D \cdot Re_p^2 = \frac{4}{3} \cdot R_{sd} \cdot \frac{g}{\nu_l^2} \cdot d^3 \qquad (1\text{-}29)$$

This factor can be determined from the equations above:

$$Re_p < 1 \qquad C_D \cdot Re_p^2 = 24 \cdot Re_p \qquad (1\text{-}30)$$

$$1 < Re_p < 50 \qquad C_D \cdot Re_p^2 = 24 \cdot Re_p^{5/4} \qquad (1\text{-}31)$$

$$50 < Re_p < 1620 \qquad C_D \cdot Re_p^2 = 4.7 \cdot Re_p^{5/3} \qquad (1\text{-}32)$$

$$1620 < Re_p \qquad C_D \cdot Re_p^2 = 0.4 \cdot Re_p^2 \qquad (1\text{-}33)$$

From these equations the equation to be applied can be picked and the value of Re_p calculated. The settling velocity now follows from:

$$v_t = Re_p \cdot \frac{\nu_l}{d} \qquad (1\text{-}34)$$

The Grace Method (1986).

Following the suggestions of Grace (1986), it is found convenient to define a dimensionless particle diameter, which in fact is the Bonneville parameter (d in m and v_t in m/s):

$$D_* = d \cdot \left(\frac{R_{sd} \cdot g}{\nu_l^2} \right)^{1/3} \qquad (1\text{-}35)$$

And a dimensionless terminal settling velocity:

$$v_t^* = v_t \cdot \left(\frac{1}{\nu_l \cdot R_{sd} \cdot g} \right)^{1/3} \qquad (1\text{-}36)$$

Those are mutually related. Thus using the curve and rearranging gives directly the velocity v_t as a function of particle diameter d. No iteration is required. This described by analytic expressions appropriate for a computational determination of v_s according to Grace Method. Now v_t can be computed according to:

$$v_t = v_t^* \cdot \left(\frac{1}{\nu_l \cdot R_{sd} \cdot g} \right)^{-1/3} \qquad (1\text{-}37)$$

$$D^* < 3.8 \qquad v_t^* = \frac{\left(D^*\right)^2}{18} - 3.1234 \cdot 10^{-4} \cdot \left(D^*\right)^5 + 1.6415 \cdot 10^{-6} \cdot \left(D^*\right)^8 - 7.278 \cdot 10^{-10} \cdot \left(D^*\right)^{11} \qquad (1\text{-}38)$$

$$3.8 < D^* < 7.58 \qquad v_t^* = 10^{-1.5446 + 2.9162 \cdot \log(D^*) - 1.0432 \cdot \log(D^*)^2} \qquad (1\text{-}39)$$

$$7.58 < D^* < 227 \qquad v_t^* = 10^{-1.64758 + 2.94786 \cdot \log(D^*) - 1.09703 \cdot \log(D^*)^2 + 0.17129 \cdot \log(D^*)^3} \qquad (1\text{-}40)$$

$$227 < D^* < 3500 \qquad v_t^* = 10^{5.1837 - 4.51034 \cdot \log(D^*) + 1.687 \cdot \log(D^*)^2 - 0.189135 \cdot \log(D^*)^3} \qquad (1\text{-}41)$$

Figure 1-8 shows the terminal settling velocity for the iterative method according to equations (1-10), (1-11) and (1-12) and the methods of Huisman (1973-1995) and Grace (1986), using shape factors of 0.5 and 0.7. It can be seen that for small diameters these methods gives smaller velocities while for larger diameters larger velocities are predicted, compared with the other equations as shown in Figure 1-7. The iterative method gives larger velocities for the larger diameters, compared with the Huisman and Grace methods, but this is caused by the different way of implementing the shape factor. In the iterative method the shape factor is implemented according to equation 2, while with the Huisman and Grace methods the terminal settling velocity for spheres is multiplied by the shape factor according to equation (1-42). For the smaller grain diameters, smaller than 0.5 mm, which are of interest here, the 3 methods give the same results.

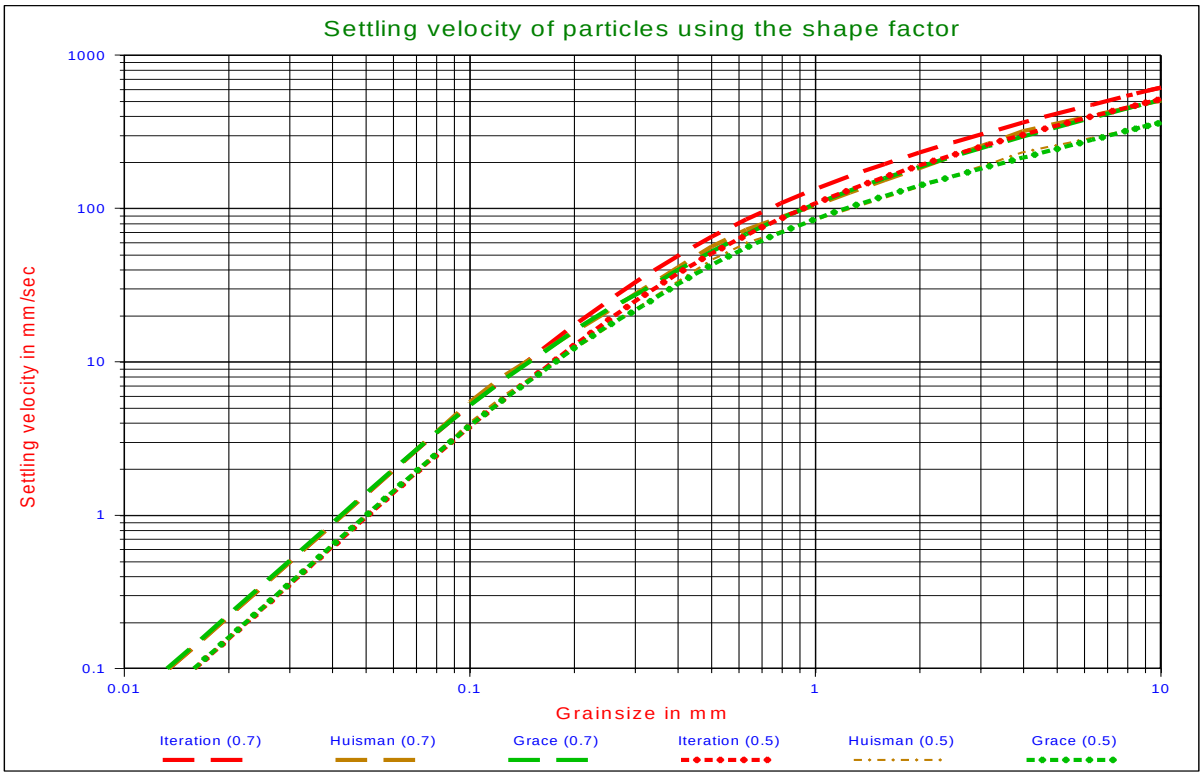

Figure 1-8: The settling velocity of individual particles using the shape factor.

1.5. The Shape Factor.

In the range of particle Reynolds numbers from roughly unity to about 100, which is the range of interest here, a particle orients itself during settling so as to maximize drag. Generally this means that an oblate or lenticular particle, i.e. a shape with one dimension smaller than the other two, will settle with its maximum area horizontal. The drag of fluid on the particle then depends most critically on this area. This is also the area seen if the particle lies in a stable position on a flat surface. Therefore, for estimation of drag, the non-spherical particle is

characterized by the 'area equivalent diameter', i.e. the diameter of the sphere with the same projected area. For particles whose sizes are determined by sieving rather than microscopic analysis, the diameter is slightly smaller than the mesh size. However, unless the particles are needle shaped, the difference between the diameter and the screen opening is relatively small, generally less than 20%.

Although equation (1-5) contains a shape factor, basically all the equations in this chapter are derived for spheres. The shape factor ψ in equation (1-5) is one way of introducing the effect of the shape of particles on the terminal settling velocity. In fact equation (1-5) uses a shape factor based on the weight ratio between a real sand particle and a sphere with the same diameter. Another way is introducing a factor ξ according to:

$$\xi = \frac{v_t}{v_{ts}} \tag{1-42}$$

Where ξ equals the ratio of the terminal settling velocity of a non-spherical particle v_t and the terminal velocity v_{ts} of a spherical particle with the same diameter. The shape of the particle can be described by the volumetric shape factor **K** which is defined as the ratio of the volume of a particle and a cube with sides equal to the particle diameter so that **K=0.524** for a sphere:

$$K = \frac{volume\ \ of\ \ particle}{d^3} \tag{1-43}$$

The shape factor ξ is a function of the volumetric form factor **K** and the dimensionless particle diameter **D*** according to equation (1-35).

$$\log(\xi) = -0.55 + K - 0.0015 \cdot K + 0.03 \cdot 1000^{K-0.524} + \frac{-0.045 + 0.05 \cdot K^{-0.6} - 0.0287 \cdot 55000^{K-0.524}}{\cosh(2.55 \cdot (\log(D^*) - 1.114)} \tag{1-44}$$

This equation takes a simpler form for sand shaped particles with **K=0.26**:

$$\log(\xi) = -0.3073 + \frac{0.0656}{\cosh(2.55 \cdot (\log(D^*) - 1.114)} \tag{1-45}$$

A value of **K=0.26** for sand grains would give a volume ratio of 0.26/0.524=0.496 and thus a factor ψ**=0.496** in equation (1-5), while often a factor ψ**=0.7** is used.

Figure 1-9 shows the shape factor ξ as a function of the dimensionless particle diameter **d***, according to equation (1-44).

Figure 1-8 also shows the terminal settling velocity according to the methods of Huisman (1973-1995) and Grace (1986) using the shape factor according to equation (1-45). It can be seen clearly that both methods give the same results. One can see that the choice of the shape factor strongly determines the outcome of the terminal settling velocity.

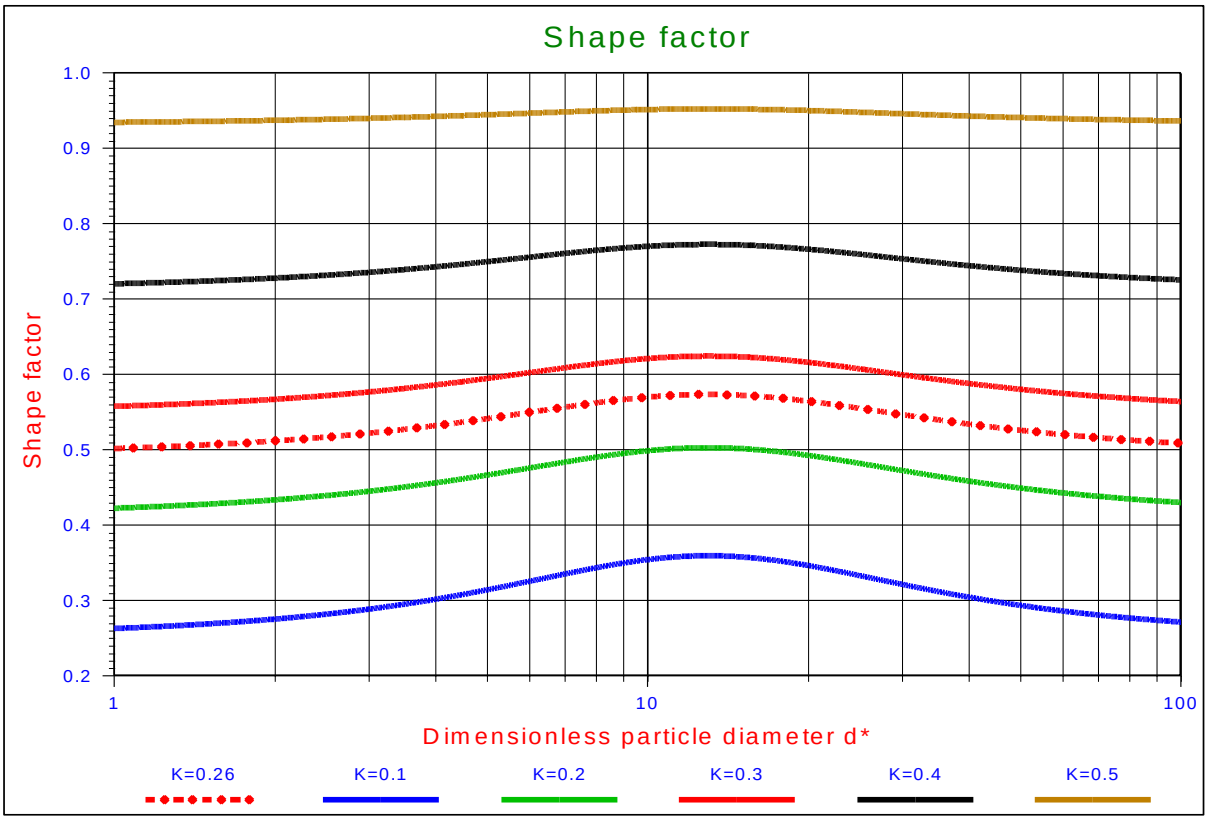

Figure 1-9: The shape factor ξ as a function of the dimensionless particle diameter D*.

1.6. Hindered Settling.

The above equations calculate the settling velocities for individual grains. The grain moves downwards and the same volume of water has to move upwards. In a mixture, this means that, when many grains are settling, an average upwards velocity of the water exists. This results in a decrease of the settling velocity, which is often referred to as hindered settling. However, at very low concentrations the settling velocity will increase because the grains settle in each other's shadow. Richardson and Zaki (1954) determined an equation to calculate the influence of hindered settling for volume concentrations C_{vs} between 0 and 0.3. The coefficient in this equation is dependent on the Reynolds number. The general equation yields:

$$\frac{v_{th}}{v_t} = \left(1 - C_{vs}\right)^{\beta} \qquad \textbf{(1-46)}$$

The following values for β should be used according to Richardson and Zaki (1954):

$Re_p<0.2$	$\beta=4.65$	**(1-47)**
$Re_p>0.2$ and $Re_p<1.0$	$\beta=4.35 \cdot Re_p^{-0.03}$	
$Re_p>1.0$ and $Re_p<200$	$\beta=4.45 \cdot Re_p^{-0.1}$	
$Re_p>200$	$\beta=2.39$	

However this does not give a smooth continuous curve. Using the following definition does give a continuous curve:

$Re_p<0.1$	$\beta=4.65$	**(1-48)**
$Re_p>0.1$ and $Re_p<1.0$	$\beta=4.35 \cdot Re_p^{-0.03}$	
$Re_p>1.0$ and $Re_p<400$	$\beta=4.45 \cdot Re_p^{-0.1}$	
$Re_p>400$	$\beta=2.39$	

Other researchers found the same trend but sometimes somewhat different values for the power **β**. These equations are summarized below and shown in Figure 1-10.

According to Rowe (1987) this can be approximated by:

$$\beta = \frac{4.7 + 0.41 \cdot Re_p^{0.75}}{1 + 0.175 \cdot Re_p^{0.75}} \qquad \textbf{(1-49)}$$

Wallis (1969) found an equation which matches Rowe (1987) for small Reynolds numbers and Garside & Al-Dibouni (1977) for the large Reynolds numbers:

$$\beta = \frac{4.7 \cdot (1 + 0.15 \cdot Re_p^{0.687})}{1 + 0.253 \cdot Re_p^{0.687}} \qquad \textbf{(1-50)}$$

Garside & Al-Dibouni (1977) give the same trend but somewhat higher values for the exponent **β**.

$$\beta = \frac{5.1 + 0.27 \cdot Re_p^{0.9}}{1 + 0.1 \cdot Re_p^{0.9}} \qquad \textbf{(1-51)}$$

Di Felici (1999) finds very high values for **β** but this relation is only valid for dilute mixtures (very low concentration, less than 5%).

$$\beta = \frac{6.5 + 0.3 \cdot Re_p^{0.74}}{1 + 0.1 \cdot Re_p^{0.74}} \qquad \textbf{(1-52)}$$

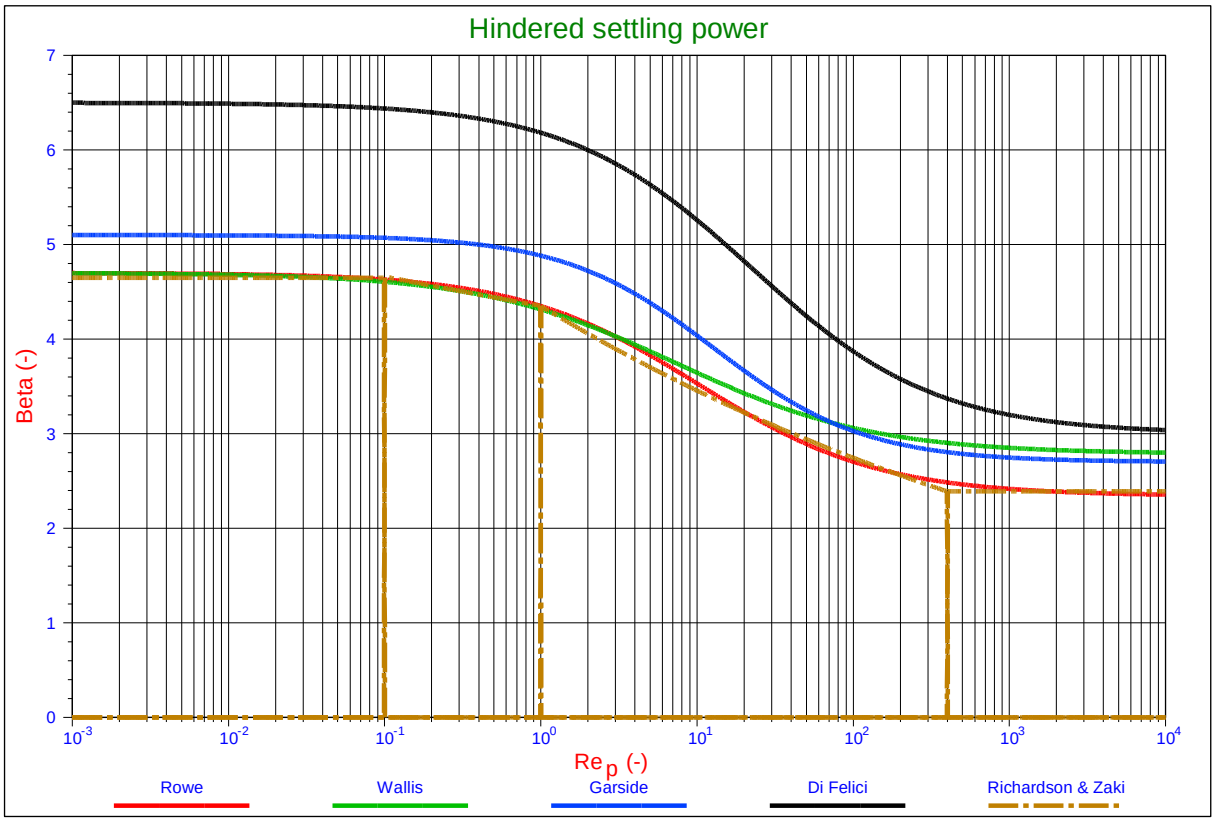

Figure 1-10: The hindered settling power according to several researchers.

1.7. Conclusions.

The equation of Ruby & Zanke (1977) will be used to determine the terminal settling velocity for sands and gravels. The equation of Richardson and Zaki (1954) will be used for hindered settling, with the equation of Rowe (1987) for the power **β** in the hindered settling equation. The DHLLDV framework is calibrated based on these equations.

Using different equations will result in slightly different hydraulic gradients and Limit Deposit Velocities, requiring the constants in the DHLLDV framework to be adjusted.

Particles with different shapes, like spheres or shells, and particles with different relative submerged densities may require different methods.

1.8. Nomenclature.

A	Cross section of particle	**m^2**
C_D	Drag coefficient	**-**
C_{vs}	Volumetric spatial concentration	**-**
d	Particle diameter	**m**
D_*	Bonneville parameter or dimensionless particle diameter	**-**
F_{down}	Downwards force on particle	**N**
F_{up}	Upwards force on particle	**N**
g	Gravitational constant 9.81 m/s^2	**m/s^2**
K	Volumetric form factor	**-**
Re_p	Particle Reynolds number	**-**
R_{sd}	Relative submerged density	**-**
v_t	Terminal settling velocity	**m/s**
v_t^*	Dimensionless terminal settling velocity	**-**
v_{th}	Hindered terminal settling velocity	**m/s**
v_{ts}	Terminal settling velocity sphere	**m/s**
V	Volume of particle	**m^3**
β	Hindered settling power	**-**
ρ_l	Density of carrier liquid	**ton/m^3**
ρ_s	Density of solid	**ton/m^3**
ψ	Shape factor	**-**
ξ	Shape factor	**-**
ν_l	Kinematic viscosity liquid	**m^2/s**

Chapter 2: Steady Uniform Flow in Open Channels.

This chapter is written with a view to bottom scour. The main outcome is the scour velocity as a function of the particle diameter. The coordinate system applied in this chapter is shown in Figure 2-1. This chapter is based on lecture notes of Liu (2001).

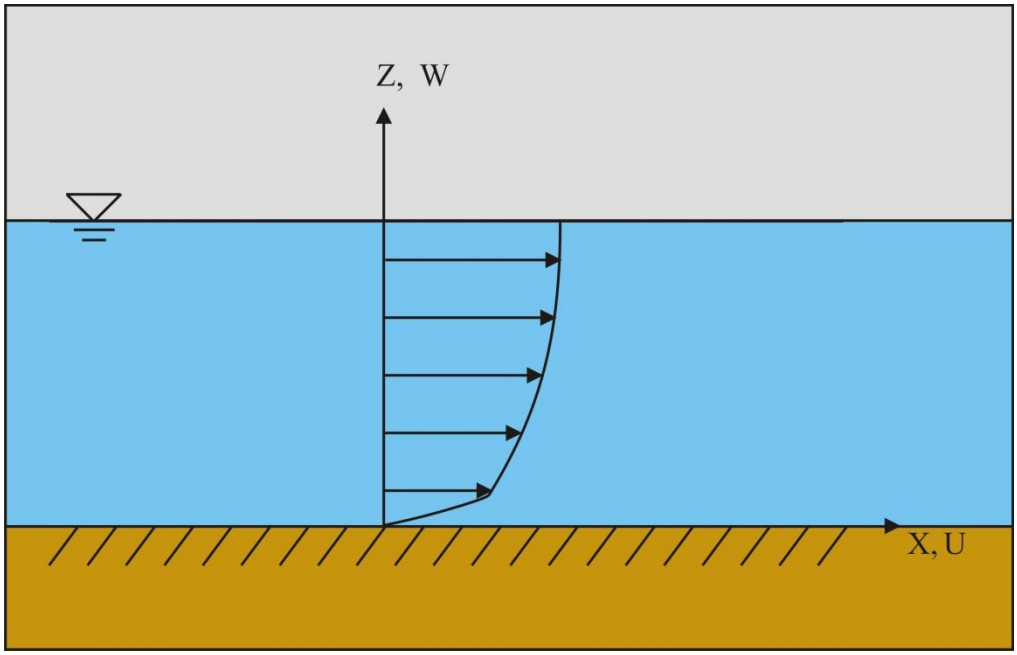

Figure 2-1: Coordinate system for the flow in open channels.

2.1. Types of Flow.

Description of various types of flow are given in the following.

Laminar versus turbulent

Laminar flow occurs at relatively low fluid velocity. The flow is visualized as layers which slide smoothly over each other without macroscopic mixing of fluid particles. The shear stress in laminar flow is given by Newton's law of viscosity:

$$\tau_\nu = \rho \cdot \nu \cdot \frac{du}{dz} \qquad (2\text{-}1)$$

Where **ρ** is density of water and **ν** kinematic viscosity (**ν** = 10−6 m^2/s at 200˚C). Most flows in nature are turbulent. Turbulence is generated by instability in the flow, which trigger vortices. However, a thin layer exists near the boundary where the fluid motion is still laminar. A typical phenomenon of turbulent flow is the fluctuation of velocity

$$U = u + u' \qquad W = w + w' \qquad (2\text{-}2)$$

Where: **U** and **W** are instantaneous velocities, in **x** and **z** directions respectively
u and **w** time-averaged velocities, in **x** and **z** directions respectively
u' and **w'** instantaneous velocity fluctuations, in **x** and **z** directions respectively
Turbulent flow is often given as the mean flow, described by **u** and **w**. In turbulent flow the water particles move in very irregular paths, causing an exchange of momentum from one portion of fluid to another, and hence, the turbulent shear stress (Reynolds stress). The turbulent shear stress, given by time-averaging of the Navier-Stokes equation, is:

$$\tau_t = -\rho \cdot \overline{u' \cdot w'} \qquad \textbf{(2-3)}$$

Note that $\overline{u' \cdot w'}$ is always negative. In turbulent flow both viscosity and turbulence contribute to shear stress. The total shear stress is:

$$\tau = \tau_\nu + \tau_t = \rho \cdot \nu \cdot \frac{du}{dz} + \rho \cdot \overline{u' \cdot w'} \qquad \textbf{(2-4)}$$

Steady versus unsteady

A flow is steady when the flow properties (e.g. density, velocity, pressure etc.) at any point are constant with respect to time. However, these properties may vary from point to point. In mathematical language:

$$\frac{\partial(\text{any flow property})}{\partial t} = 0 \qquad \textbf{(2-5)}$$

In the case of turbulent flow, steady flow means that the statistical parameters (mean and standard deviation) of the flow do not change with respect to time. If the flow is not steady, it is unsteady.

Uniform versus non-uniform

A flow is uniform when the flow velocity does not change along the flow direction, see Figure 2-2. Otherwise it is non-uniform flow.

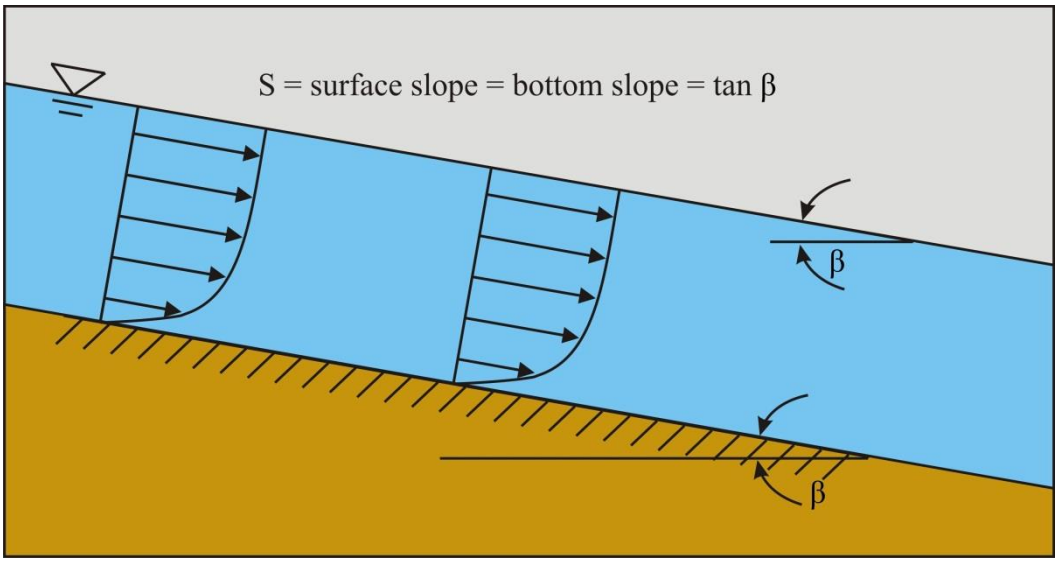

Figure 2-2: Steady uniform flow in a open channel.

Boundary layer flow

Prandtl developed the concept of the boundary layer. It provides an important link between ideal-fluid flow and real-fluid flow. Here is the original description.
For fluids having small viscosity, the effect of internal friction in the flow is appreciable only in a thin layer surrounding the flow boundaries.
However, we will demonstrate that the boundary layer fulfill the whole flow in open channels. The boundary layer thickness **δ** is defined as the distance from the boundary surface to the point where **u = 0.995·U**. The boundary layer development can be expressed as:

Laminar flow $\quad \frac{\delta}{x} = 5 \cdot \left(\frac{U \cdot x}{\nu} \right)^{-0.5} \quad$ when: $\quad Re_x = \frac{U \cdot x}{\nu} < 5 \cdot 10^5 \qquad \textbf{(2-6)}$

Turbulent flow $\frac{\delta}{x} = 0.4 \cdot \left(\frac{U \cdot x}{\nu}\right)^{-0.2}$ when: $Re_x = \frac{U \cdot x}{\nu} > 5 \cdot 10^5$ **(2-7)**

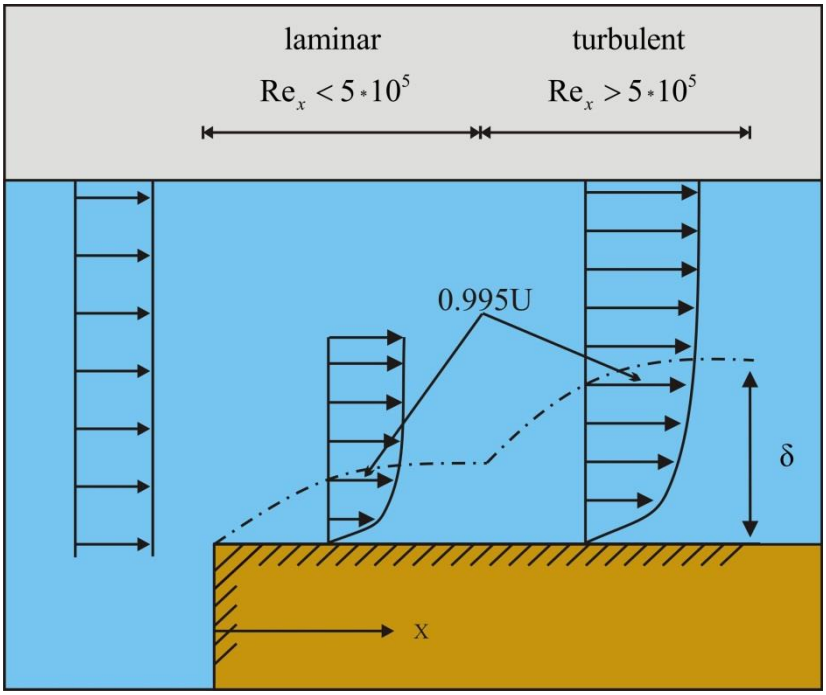

Figure 2-3: Development of the boundary layer.

2.2. Prandtl's Mixing Length Theory.

Prandtl introduced the mixing length concept in order to calculate the turbulent shear stress. He assumed that a fluid parcel travels over a length **ℓ** before its momentum is transferred.

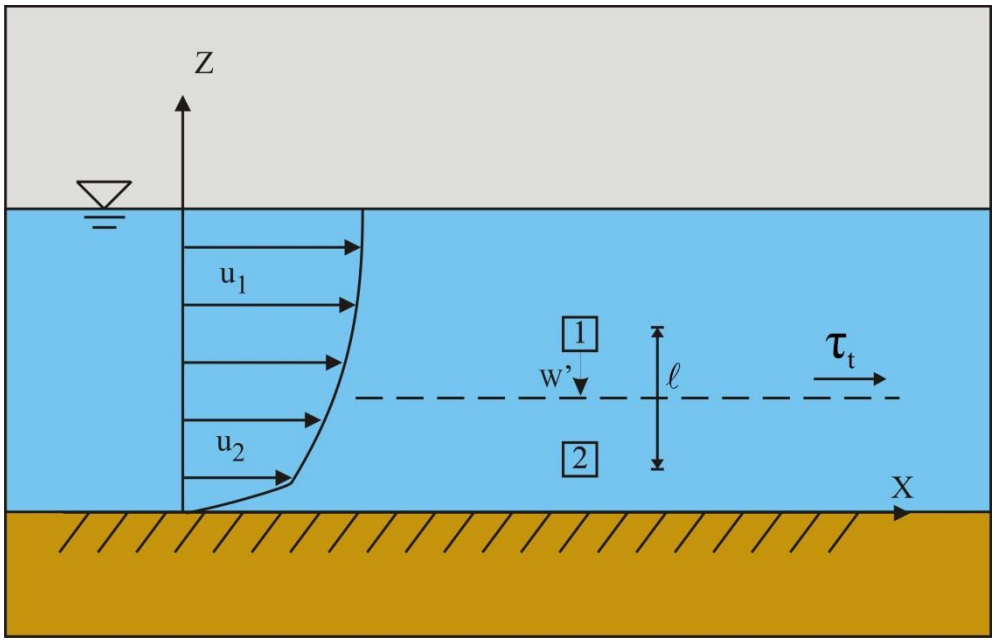

Figure 2-4: Prandtl's mixing length theory.

Figure 2-4 shows the time-averaged velocity profile. The fluid parcel, located in layer 1 and having the velocity $\mathbf{u_1}$, moves to layer 2 due to eddy motion. There is no momentum transfer during movement, i.e. the velocity of the fluid parcel is still $\mathbf{u_1}$ when it just arrives at layer 2, and decreases to $\mathbf{u_2}$ some time later by the momentum exchange with other fluid in layer 2. This action will speed up the fluid in layer 2, which can be seen as a turbulent shear

stress τ_t acting on layer 2 trying to accelerate layer 2. The horizontal instantaneous velocity fluctuation of the fluid parcel in layer 2 is:

$$u' = u_1 - u_2 = \ell \cdot \frac{du}{dz} \tag{2-8}$$

Assuming the vertical instantaneous velocity fluctuation having the same magnitude:

$$w' = -\ell \cdot \frac{du}{dz} \tag{2-9}$$

Where the negative sign is due to the downward movement of the fluid parcel, the turbulent shear stress now becomes:

$$\tau_t = -\rho \cdot u' \cdot w' = \rho \cdot \ell^2 \cdot \left(\frac{du}{dz}\right)^2 \tag{2-10}$$

If we define kinematic eddy viscosity as:

$$\varepsilon = \ell^2 \cdot \frac{du}{dz} \tag{2-11}$$

The turbulent shear stress can be expressed in a way similar to viscous shear stress:

$$\tau_t = \rho \cdot \varepsilon \cdot \frac{du}{dz} \tag{2-12}$$

2.3. Fluid Shear Stress and Friction Velocity.

Fluid shear stress

The forces on a fluid element with unit width are shown in Figure 2-5. Because the flow is uniform (no acceleration), the force equilibrium in x-direction reads:

$$\tau_z \cdot \Delta x = \rho \cdot g \cdot (h - z) \cdot \Delta x \cdot \sin(\beta) \tag{2-13}$$

For small slope we have $\sin(\beta) \approx \tan(\beta) = S$. Therefore:

$$\tau_z = \rho \cdot g \cdot (h - z) \cdot S \tag{2-14}$$

The bottom shear stress is:

$$\tau_b = \tau_{z=0} = \rho \cdot g \cdot h \cdot S \tag{2-15}$$

Bottom shear stress

In the case of arbitrary cross section, the shear stress acting on the boundary changes along the wetted perimeter, cf. Fig.5. Then the bottom shear stress means actually the average of the shear stress along the wetted perimeter. The force equilibrium reads:

$$\tau_b \cdot O \cdot \Delta x = \rho \cdot g \cdot A \cdot \Delta x \cdot \sin(\beta) \tag{2-16}$$

Where **O** is the wetted perimeter and **A** the area of the cross section. By applying the hydraulic radius ($R = A/O$) we get:

$$\tau_b = \rho \cdot g \cdot R \cdot S \tag{2-17}$$

In the case of wide and shallow channel, **R** is approximately equal to **h** and equation (2-15) is identical to equation (2-17).

Friction velocity

The bottom shear stress is often represented by friction velocity, defined by:

$$u_* = \sqrt{\frac{\tau_b}{\rho}} \qquad \textbf{(2-18)}$$

The term *friction velocity* comes from the fact that $\sqrt{\tau_b/\rho}$ has the same unit as velocity and it has something to do with friction force. Inserting equation (2-17) into equation (2-18), gives:

$$u_* = \sqrt{g \cdot R \cdot S} \qquad \textbf{(2-19)}$$

Viscous shear stress versus turbulent shear stress

Equation (2-15) states that the shear stress in flow increases linearly with water depth see Figure 2-6.

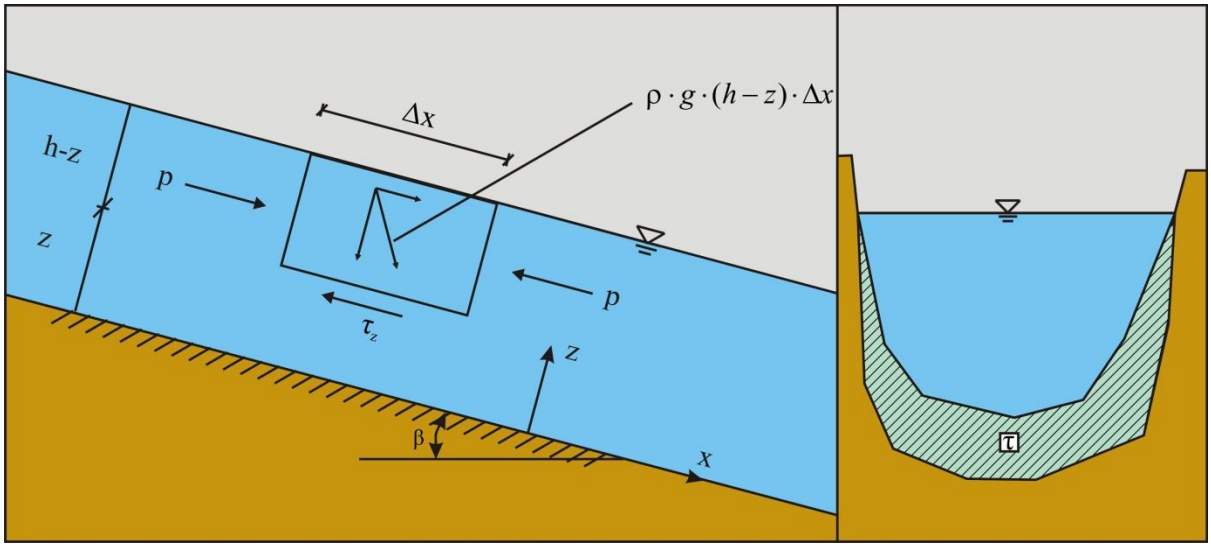

Figure 2-5: Fluid force and bottom shear stress.

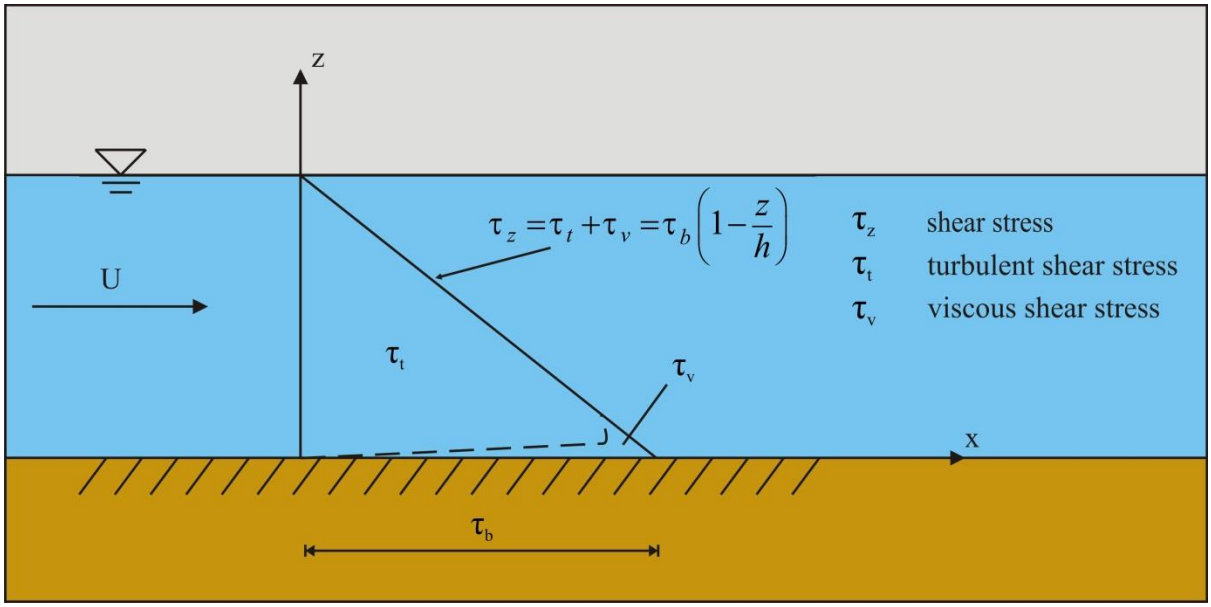

Figure 2-6: Shear stress components and distribution.

As the shear stress is consisted of viscosity and turbulence, we have:

$$\tau_z = \tau_v + \tau_t = \rho \cdot g \cdot (h - z) \cdot S \qquad \textbf{(2-20)}$$

On the bottom surface, there is no turbulence (**u=w=0**, **u'=w'=0**), the turbulent shear stress:

$$\tau_t = -\rho \cdot \overline{u' \cdot w'} = 0 \qquad \textbf{(2-21)}$$

Therefore, in a very thin layer above the bottom, viscous shear stress is dominant, and hence the flow is laminar. This thin layer is called viscous sub layer. Above the viscous sub layer, i.e. in the major part of flow, the turbulent shear stress dominates, see Figure 2-6. The measurement shows the shear stress in the viscous sub layer is constant and equal to the bottom shear stress, not increasing linearly with depth as indicated by Figure 2-6.

2.4. Classification of Flow Layers.

Scientific classification

Figure 2-7 shows the classification of flow layers. Starting from the bottom we have:

1. Viscous sub layer: a thin layer just above the bottom. In this layer there is almost no turbulence. Measurement shows that the viscous shear stress in this layer is constant. The flow is laminar. Above this layer the flow is turbulent.
2. Transition layer: also called buffer layer, viscosity and turbulence are equally important.
3. Turbulent logarithmic layer: viscous shear stress can be neglected in this layer. Based on measurement, it is assumed that the turbulent shear stress is constant and equal to bottom shear stress. It is in this layer where Prandtl introduced the mixing length concept and derived the logarithmic velocity profile.
4. Turbulent outer layer: velocities are almost constant because of the presence of large eddies which produce strong mixing of the flow.

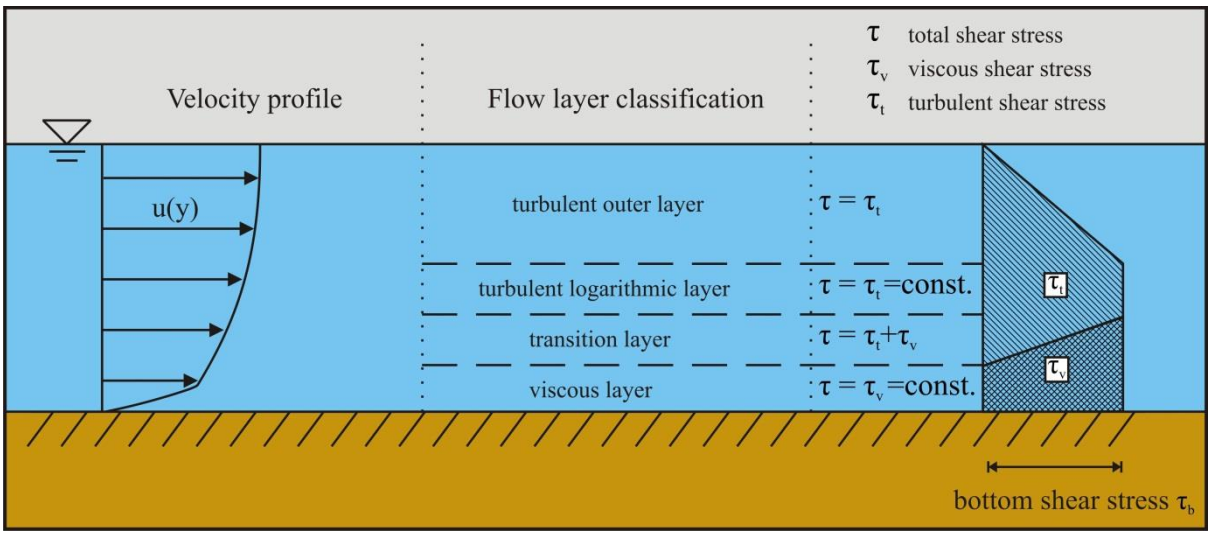

Figure 2-7: Scientific classification of flow region
(Layer thickness is not to scale, turbulent outer layer accounts for 80% - 90% of the region).

Engineering classification

In the turbulent logarithmic layer the measurements show that the turbulent shear stress is constant and equal to the bottom shear stress. By assuming that the mixing length is proportional to the distance to the bottom (**$\ell = \kappa \cdot z$**), Prandtl obtained the logarithmic velocity profile.
Various expressions have been proposed for the velocity distribution in the transitional layer and the turbulent outer layer. None of them are widely accepted. However, by the modification of the mixing length assumption, see next section, the logarithmic velocity profile applies also to the transitional layer and the turbulent outer layer. Measurement and computed velocities show reasonable agreement.

Therefore in engineering point of view, a turbulent layer with the logarithmic velocity profile covers the transitional layer, the turbulent logarithmic layer and the turbulent outer layer, see Figure 2-8.
As to the viscous sub layer, the effect of the bottom (or wall) roughness on the velocity distribution was first investigated for pipe flow by Nikuradse. He introduced the concept of equivalent grain roughness $\mathbf{k_s}$ (Nikuradse roughness, bed roughness). Based on experimental data, it was found

1. Hydraulically smooth flow for $\frac{u_* \cdot k_s}{\nu} \leq 5$, bed roughness is much smaller than the thickness of viscous sub layer. Therefore, the bed roughness will not affect the velocity distribution.
2. Hydraulically rough flow for $\frac{u_* \cdot k_s}{\nu} \geq 70$, bed roughness is so large that it produces eddies close to the bottom. A viscous sub layer does not exist and the flow velocity is not dependent on viscosity.
3. Hydraulically transitional flow for $5 \leq \frac{u_* \cdot k_s}{\nu} \leq 70$, the velocity distribution is affected by bed roughness and viscosity.

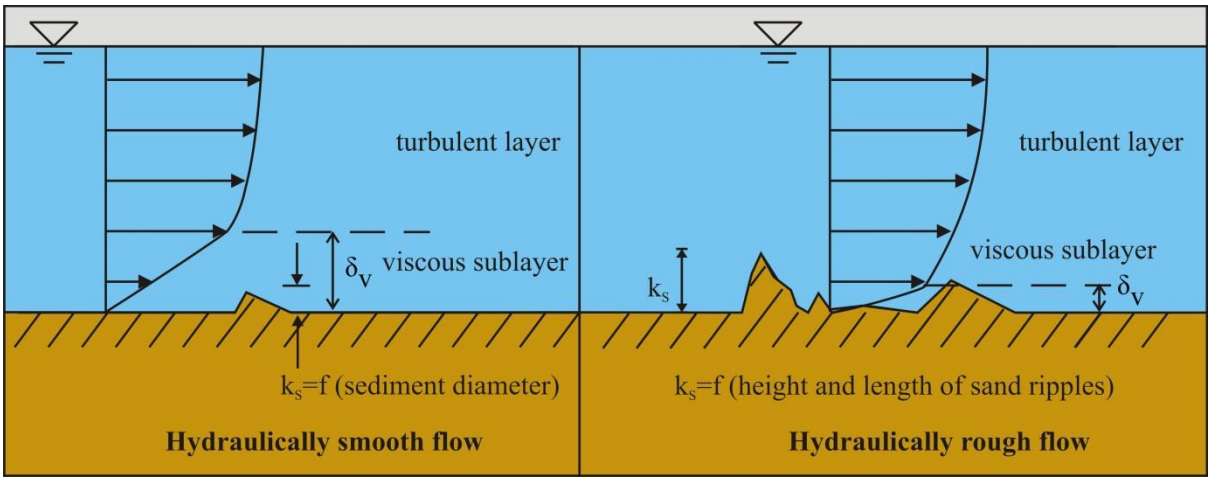

Figure 2-8: Engineering classification of flow region (Layer thickness is not to scale).

2.5. Velocity Distribution.

Turbulent layer

In the turbulent layer the total shear stress contains only the turbulent shear stress. The total shear stress increases linearly with depth (equation (2-15) or Figure 2-6), i.e.

$$\tau_t(z) = \tau_b \cdot \left(1 - \frac{z}{h}\right) \qquad \textbf{(2-22)}$$

By Prandtl's mixing length theory:

$$\tau_t = \rho \cdot \ell^2 \left(\frac{du}{dz}\right)^2 \qquad \textbf{(2-23)}$$

Now assuming the mixing length:

$$\ell = \kappa \cdot z \cdot \left(1 - \frac{z}{h}\right)^{0.5} \qquad \textbf{(2-24)}$$

With κ the Von Karman constant (κ**=0.4**) and **h>>z**, we get:

$$\frac{du}{dz} = \frac{1}{\kappa \cdot z} \cdot \sqrt{\frac{\tau_b}{\rho}} = \frac{u_*}{\kappa \cdot z} \qquad (2\text{-}25)$$

Integration of the equation gives the famous logarithmic velocity profile:

$$u(z) = \frac{u_*}{\kappa} \cdot \ln\left(\frac{z}{z_0}\right) \qquad (2\text{-}26)$$

Where the integration constant z_0 is the elevation corresponding to zero velocity ($u_{z=z0}=0$), given by Nikuradse by the study of the pipe flows.

$$z_0 = 0.11 \cdot \frac{\nu}{u_*} \quad \text{Hydraulically smooth flow} \quad \frac{u_* \cdot k_s}{\nu} \le 5 \qquad (2\text{-}27)$$

$$z_0 = 0.033 \cdot k_s \quad \text{Hydraulically rough flow} \quad \frac{u_* \cdot k_s}{\nu} \ge 70 \qquad (2\text{-}28)$$

$$z_0 = 0.11 \cdot \frac{\nu}{u_*} + 0.033 \cdot k_s \quad \text{Hydraulically transition flow} \quad 5 < \frac{u_* \cdot k_s}{\nu} < 70 \qquad (2\text{-}29)$$

It is interesting to note that the friction velocity u_*, which, by definition, has nothing to do with velocity, is the flow velocity at the elevation $z=z_0 \cdot e^{\kappa}$, thus:

$$u_{z=z_0 \cdot e^{\kappa}} = u_* \qquad (2\text{-}30)$$

In the study of sediment transport, it is important to know that the friction velocity is the fluid velocity very close to the bottom, see Figure 2-9.

Viscous sub layer

In the case of hydraulically smooth flow there is a viscous sub layer. Viscous shear stress is constant in this layer and equal to the bottom shear stress, i.e.

$$\tau_\nu = \rho \cdot \nu \cdot \frac{du}{dz} = \tau_b \qquad (2\text{-}31)$$

Integrating and applying $u_{z=0}=0$ gives:

$$u(z) = \frac{\tau_b}{\rho} \cdot \frac{z}{\nu} = \frac{u_*^2}{\nu} \cdot z \qquad (2\text{-}32)$$

Thus, there is a linear velocity distribution in the viscous sub layer. The linear velocity distribution intersects with the logarithmic velocity distribution at the elevation $z=11.6\nu/u_*$, yielding a theoretical viscous sub layer thickness:

$$\delta_\nu = 11.6 \cdot \frac{\nu}{u_*} \qquad (2\text{-}33)$$

The velocity profile is illustrated in Figure 2-9, with the detailed description of the fluid velocity near the bottom.

Bed roughness

The bed roughness k_s is also called the equivalent Nikuradse grain roughness, because it was originally introduced by Nikuradse in his pipe flow experiments, where grains are glued to the smooth wall of the pipes. The only situation where we can directly obtain the bed roughness is a flatbed consisting of uniform spheres, where k_s = diameter of sphere.

But in nature the bed is composed of grains with different size. Moreover, the bed is not flat, various bed forms, e.g. sand ripples or dunes, will appear depending on grain size and current. In that case the bed roughness can be obtained indirectly by the velocity measurement.

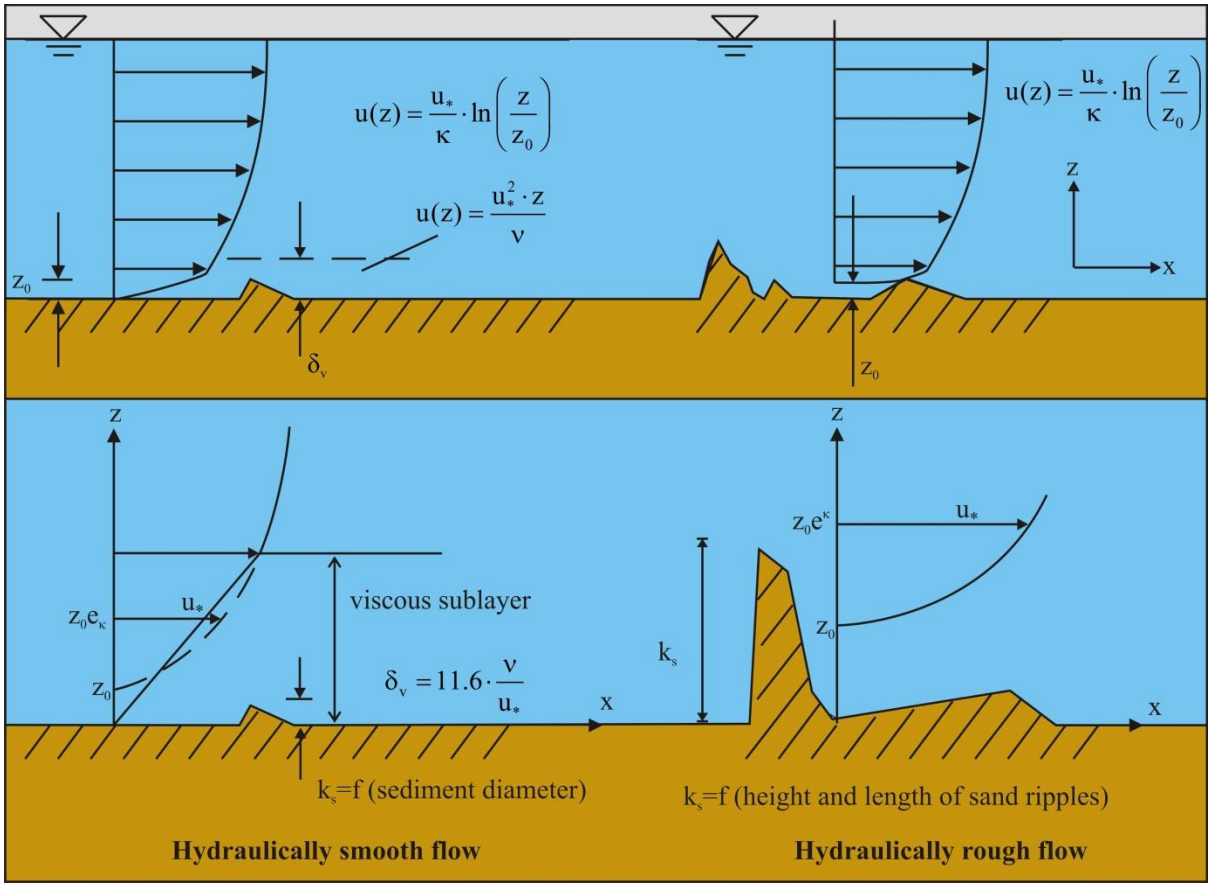

Figure 2-9: Illustration of the velocity profile in hydraulically smooth and rough flows.

2.6. Chézy Coefficient.

Chézy proposed an empirical formula for the average velocity of steady uniform channel flow:

$$\mathbf{U=C\cdot\sqrt{R\cdot S}} \tag{2-34}$$

Where: R - Hydraulic radius, i.e. area of cross section divided by wetted perimeter
S - Bed slope
C - Empirical coefficient called Chézy coefficient. **C** was originally thought to be constant. Various formulas for **C** have been proposed.

Here we will see that **C** can be theoretically determined by averaging the logarithmic velocity profile. Recalling that the friction velocity is (equation (2-19)) and applying it into equation (2-34), we get the expression of **C**:

$$\mathbf{C=\frac{U}{u_*}\cdot\sqrt{g}} \tag{2-35}$$

Averaging the logarithmic velocity profile gives:

$$\mathbf{U=\frac{1}{h}\cdot\int_{z_0}^{h}u(z)\cdot dz=\frac{u_*}{\kappa\cdot h}\cdot\int_{z_0}^{h}\ln\left(\frac{z}{z_0}\right)\cdot dz} \tag{2-36}$$

$$\mathbf{U=\frac{u_*}{\kappa}\cdot\left(\ln\left(\frac{h}{z_0}\right)-1+\frac{z_0}{h}\right)\approx\frac{u_*}{\kappa}\cdot\ln\left(\frac{h}{z_0\cdot e}\right)} \tag{2-37}$$

Inserting the above equation into equation 5.35 gives:

$$C = \frac{\sqrt{g}}{\kappa} \cdot \ln\left(\frac{h}{z_0 \cdot e}\right) = 2.3 \cdot \frac{\sqrt{g}}{\kappa} \cdot \log\left(\frac{h}{z_0 \cdot e}\right) \qquad \textbf{(2-38)}$$

$$C = 2.3 \cdot \frac{\sqrt{g}}{\kappa} \cdot \log\left(\frac{h}{\left(0.11 \cdot \frac{\nu}{u_*} + 0.033 \cdot k_s\right) \cdot e}\right) = 18 \cdot \log\left(\frac{11.14 \cdot h}{3.33 \cdot \frac{\nu}{u_*} + k_s}\right) \qquad \textbf{(2-39)}$$

This can be approximated by:

$$C \approx 18 \cdot \log\left(\frac{12 \cdot h \cdot u_*}{3.3 \cdot \nu}\right) \quad \text{Hydraulically smooth flow} \quad \frac{u_* \cdot k_s}{\nu} \le 5 \qquad \textbf{(2-40)}$$

$$C \approx 18 \cdot \log\left(\frac{12 \cdot h}{k_s}\right) \quad \text{Hydraulically rough flow} \quad \frac{u_* \cdot k_s}{\nu} \ge 70 \qquad \textbf{(2-41)}$$

Where the expression for z_0 has been used and **ln** has been converted to **log**. Moreover the inclusion of $g=9.8 m/s^2$ means that **C** has the unit $\sqrt{m/s}$.

Hydraulic roughness is expressed in terms of the Chézy (**C**), Manning-Strickler (**n**), Darcy-Weisbach (λ). The relation between **C** and λ is:

$$C^2 = \frac{8 \cdot g}{\lambda} \qquad \textbf{(2-42)}$$

Equation (2-39) is often written as a function of the theoretical viscous sub layer thickness δ_v (equation (2-33)) and the hydraulic radius (**R=A/O**):

$$C = 18 \cdot \log\left(\frac{12 \cdot R}{\delta_v / 3.5 + k_s}\right) \qquad \textbf{(2-43)}$$

Note that the hydraulic radius does not equal half the hydraulic diameter, but one fourth, since the hydraulic diameter **D=4·A/O**. The hydraulic diameter concept matches pipe flow, where the hydraulic diameter equals the pipe diameter for around pipe, where the hydraulic radius concept matches river flow, where for a wide river; the hydraulic radius equals the depth of the river.

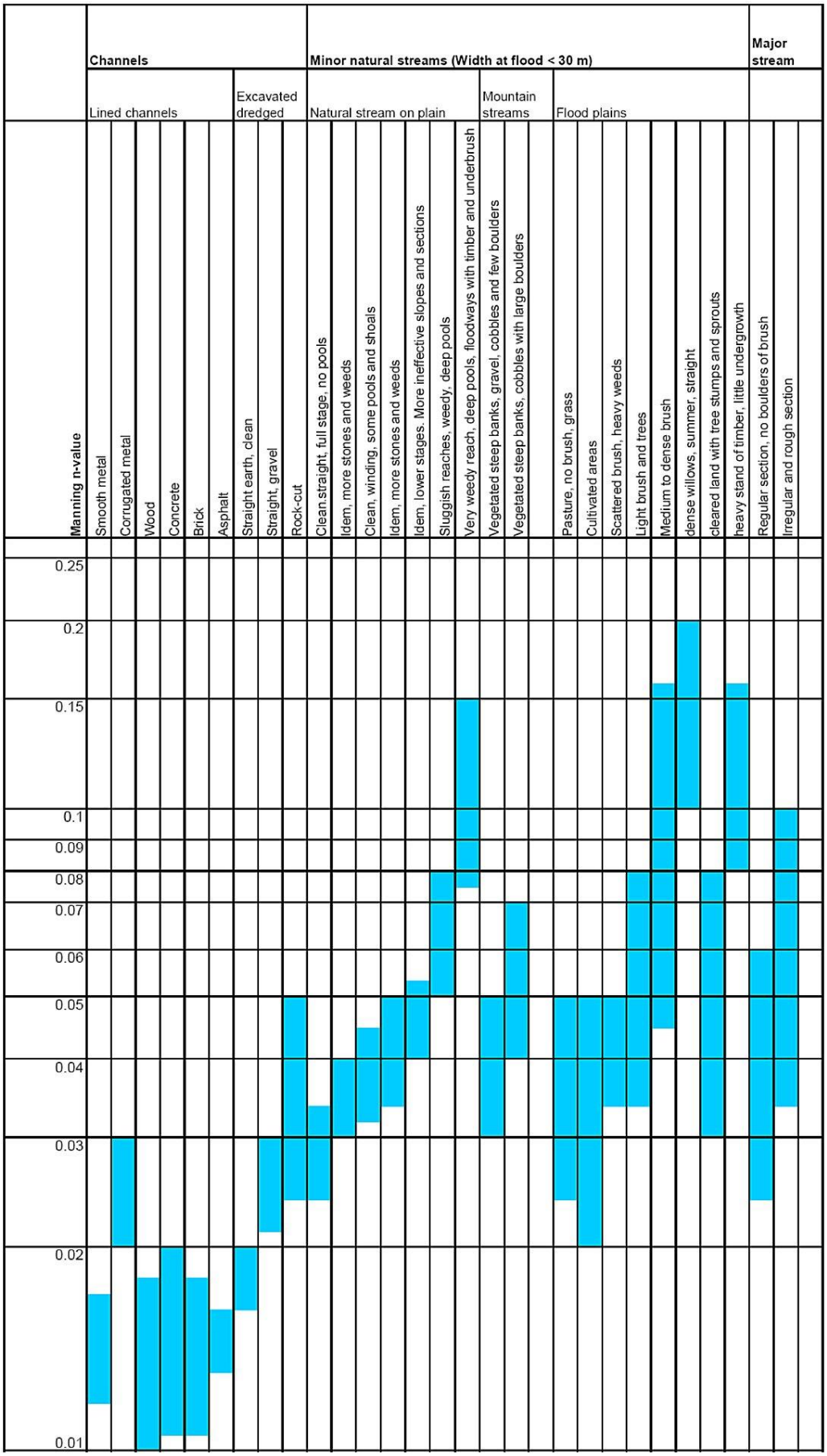

Figure 2-10: Range of values of the roughness coefficient n for different types of channels.

In these equations k_s is the equivalent sand roughness according to Nikuradse. For an alluvial bed the value of k_s varies strongly with the flow conditions. In rivers the flow regime will often be hydraulically rough ($k_s >> d$). According to Strickler the Chézy coefficient is:

$$C = \left(\frac{R}{k_s}\right)^{1/6} \qquad (2\text{-}44)$$

Most often used, and linked with Strickler's equation, is the Manning roughness formula (or Manning-Strickler roughness formula). The relation between Manning's roughness coefficient **n** and the Chézy coefficient **C** is (with **R** in meters):

$$C = \frac{R^{1/6}}{n} \qquad (2\text{-}45)$$

Figure 2-10 gives an overview of Manning's roughness coefficient **n** for different types of channels.

2.7. Drag Coefficient, Lift Coefficient and Friction Coefficient.

Drag and lift coefficients

A real fluid moving past a body will exert a drag force on the body, see Figure 2-11.

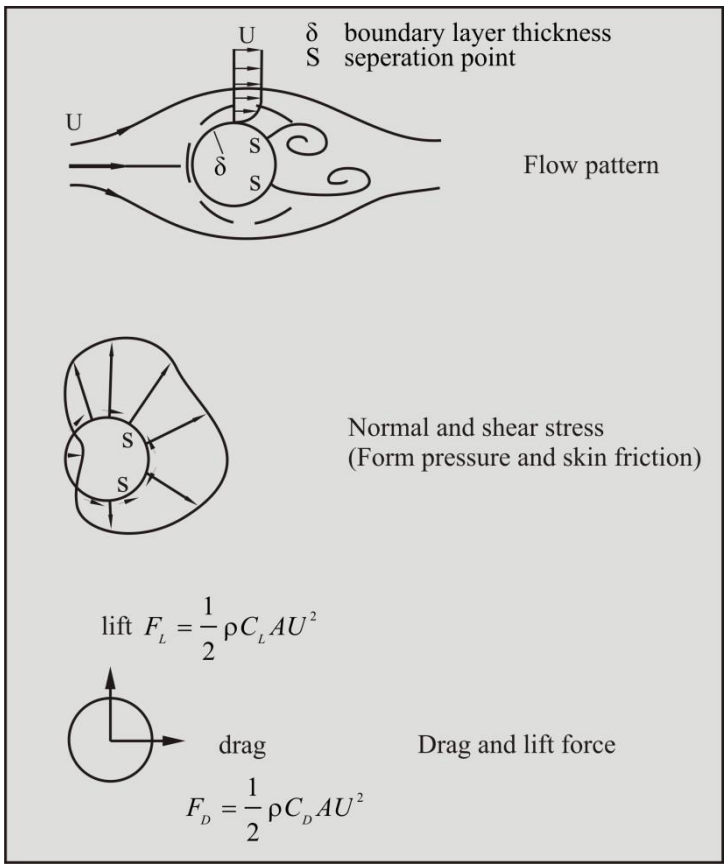

Figure 2-11: Drag force and lift force.

Drag force is consisted of friction drag and form drag, the former comes from the projection of skin friction force in the flow direction, and the latter from the projection of the form pressure force in the flow direction. The total drag is written as:

$$F_D = C_D \cdot \tfrac{1}{2} \cdot \rho \cdot U^2 \cdot A \qquad (2\text{-}46)$$

The lift force is written in the same way:

$$F_L = C_L \cdot \tfrac{1}{2} \cdot \rho \cdot U^2 \cdot A \qquad \textbf{(2-47)}$$

Where: **A -** Projected area of the body to the plane perpendicular to the flow direction.
C_D, C_L - Drag and lift coefficients, depend on the shape and surface roughness of the body and the Reynolds number. They are usually determined by experiments

Friction coefficient

Figure 2-12 illustrates fluid forces acting on a grain resting on the bed. The drag force:

$$F_D = C_D \cdot \tfrac{1}{2} \cdot \rho \cdot (\varsigma \cdot U)^2 \cdot A \qquad \textbf{(2-48)}$$

Where ζ is included because we do not know the fluid velocity past the grain, but we can reasonably assume that it is the function of the average velocity and other parameters.

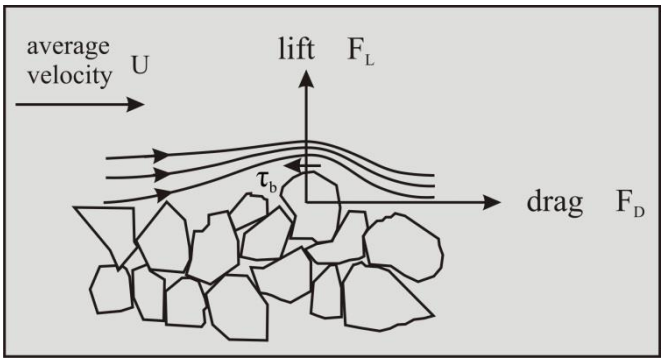

Figure 2-12: Fluid forces acting on a grain resting on the bed.

We can also say that the grain exerts a resistant force F_D on the flow. If **A'** is the projected area of the grain to the horizontal plane, the bottom shear stress is:

$$\tau_b = \frac{F_D}{A'} = \left(C_D \cdot \varsigma^2 \cdot \frac{A}{A'} \right) \cdot \tfrac{1}{2} \cdot \rho \cdot U^2 = f \cdot \tfrac{1}{2} \cdot \rho \cdot U^2 = \frac{\lambda}{4} \cdot \tfrac{1}{2} \cdot \rho \cdot U^2 \qquad \textbf{(2-49)}$$

Where: **f** is the Fanning friction ($4 \cdot f = \lambda$) coefficient of the bed, which is a dimensionless parameter. By applying the Chézy coefficient we get:

$$C^2 = \frac{2 \cdot g}{f} \qquad \textbf{(2-50)}$$

$$f \approx \frac{0.06}{\left(\log\left(\frac{12 \cdot h \cdot u_*}{3.3 \cdot \nu} \right) \right)^2} \quad \text{Hydraulically smooth flow} \quad \frac{u_* \cdot k_s}{\nu} \le 5 \qquad \textbf{(2-51)}$$

$$f \approx \frac{0.06}{\left(\log\left(\frac{12 \cdot h}{k_s} \right) \right)} \quad \text{Hydraulically rough flow} \quad \frac{u_* \cdot k_s}{\nu} \ge 70 \qquad \textbf{(2-52)}$$

2.8. Bed Roughness.

The bed roughness $\mathbf{k_s}$ is also called the equivalent Nikuradse grain roughness, because it was originally introduced by Nikuradse in his pipe flow experiments, where grains are glued to the smooth wall of the pipes. The only situation where we can directly obtain the bed roughness is a flat bed consisting of uniform spheres, where $\mathbf{k_s}$ = diameter of sphere. But in nature the bed is composed of grains with different size. Moreover, the bed is not flat, various bed forms, e.g. sand ripples or dunes, will appear depending on grain size and current. In that case the bed roughness can be obtained indirectly by the velocity measurement.

2.9. The Transition Laminar-Turbulent.

Reichardt (1951) derived an equation for the velocity that describes a laminar linear profile up to an $\mathbf{y^+}$ value of about 5, a turbulent logarithmic profile from an $\mathbf{y^+}$ value of about 40 and a transition velocity profile from 5 to 40 that is in excellent agreement with measurements made in that zone (see Schlichting (1968), p. 601). Equation (2-53) and Figure 2-13 show this velocity profile. Wiberg & Smith (1987A) and others also use this velocity profile.

$$\frac{u(y)}{u_*} = \frac{\ln(1+\kappa\cdot y^+)}{\kappa} - \frac{\ln(1/9)+\ln(\kappa)}{\kappa}\cdot\left(1-e^{-\frac{y^+}{11.6}} - \frac{y^+}{11.6}e^{-0.33\cdot y^+}\right) \qquad \textbf{(2-53)}$$

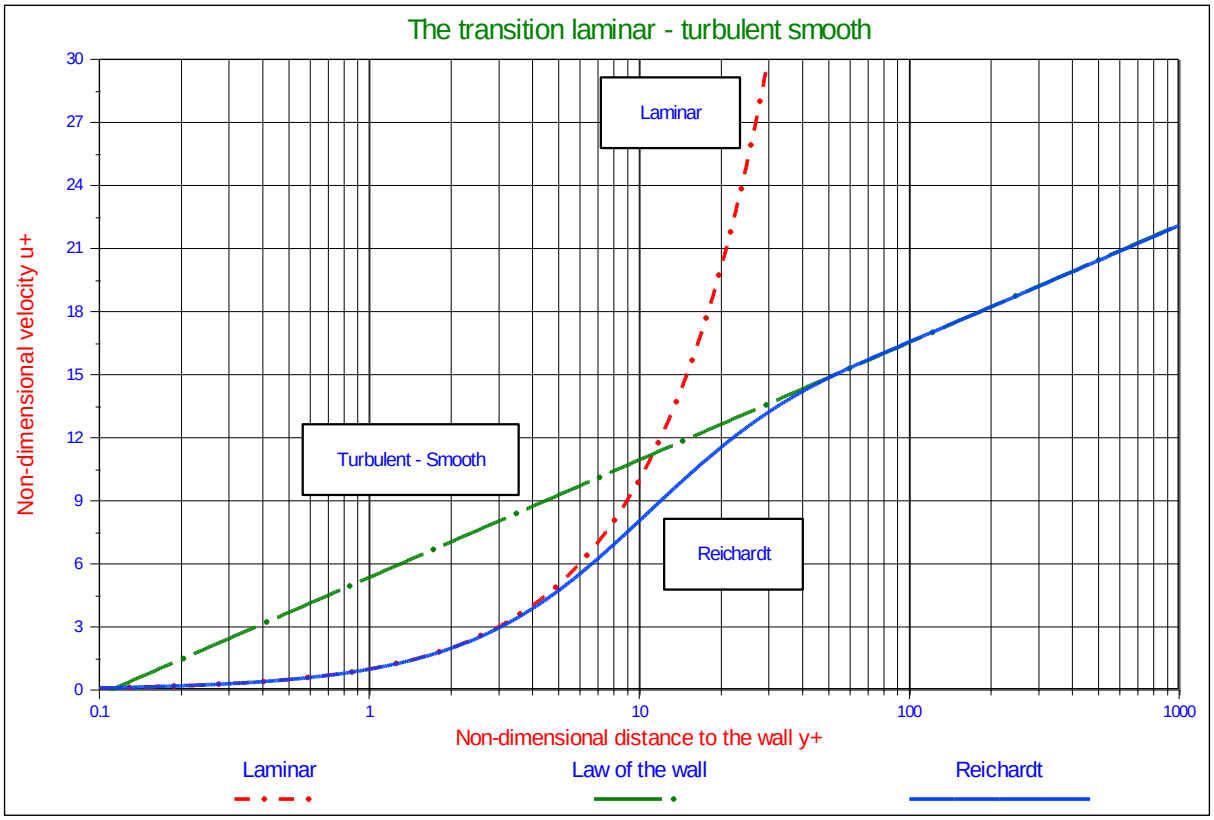

Figure 2-13: The velocity profile from laminar to smooth-turbulent.(lamturb.vwp)

2.10. The Transition Smooth-Rough.

The transition between hydraulic smooth and rough flow can be approximated in many ways, but the resulting equation should match measurements like shown in Garcia (2008) (fig. 2.3). The following equations (derived by the author), give a very good approximation of this transition, where the distance to the wall equals the roughness. Equation (2-54) gives the velocity as a function of the non-dimensional distance to the wall $\mathbf{y^+}$ and the non-dimensional roughness $\mathbf{k_s^+}$.

$$\frac{\bar{u}(y^+)}{u_*} = \frac{1}{\kappa}\cdot\ln\left(\frac{y^+}{0.11}\right)\cdot e^{-0.95\cdot\frac{k_s^+}{11.6}} + \frac{1}{\kappa}\cdot\ln\left(\frac{y^+}{0.033\cdot k_s^+}\right)\cdot\left(1-e^{-0.95\cdot\frac{k_s^+}{11.6}}\right) \qquad \textbf{(2-54)}$$

Since $11.6 = \delta_v\cdot u_*/\nu = \delta_v^+$ and $0.11 = 0.11\cdot\delta_v\cdot u_*/\nu/11.6 = 0.0095\cdot\delta_v^+$ and the influence of the second right hand term (giving 95 instead of 105), equation (2-54) can be written as:

$$\frac{\bar{u}(y^+)}{u_*} = \frac{1}{\kappa}\cdot\ln\left(95\cdot\frac{y^+}{\delta_v^+}\right)\cdot e^{-0.95\cdot\frac{k_s^+}{\delta_v^+}} + \frac{1}{\kappa}\cdot\ln\left(30\cdot\frac{y^+}{k_s^+}\right)\cdot\left(1-e^{-0.95\cdot\frac{k_s^+}{\delta_v^+}}\right) \qquad \textbf{(2-55)}$$

In terms of the dimensional parameters for the distance to the wall **y**, the roughness $\mathbf{k_s}$ and thickness of the laminar layer $\boldsymbol{\delta_v}$ this gives:

$$\frac{\bar{u}(y)}{u_*} = \frac{1}{\kappa}\cdot\ln\left(95\cdot\frac{y}{\delta_v}\right)\cdot e^{-0.95\cdot\frac{k_s}{\delta_v}} + \frac{1}{\kappa}\cdot\ln\left(30\cdot\frac{y}{k_s}\right)\cdot\left(1-e^{-0.95\cdot\frac{k_s}{\delta_v}}\right) \qquad \textbf{(2-56)}$$

Figure 2-14 shows the non dimensional velocity $\mathbf{u^+}$ at distances $\mathbf{y=k_s}$, $\mathbf{y=0.9k_s}$, $\mathbf{y=0.8k_s}$, $\mathbf{y=0.7k_s}$, $\mathbf{y=0.6k_s}$, $\mathbf{y=0.5k_s}$ and, $\mathbf{y=0.4k_s}$ from the wall. Up to a Reynolds number of 20 and above a Reynolds number of 70 equation (2-55) matches the measurements very well, between 20 and 70 the equation underestimates the measured values, but overall the resemblance is very good.

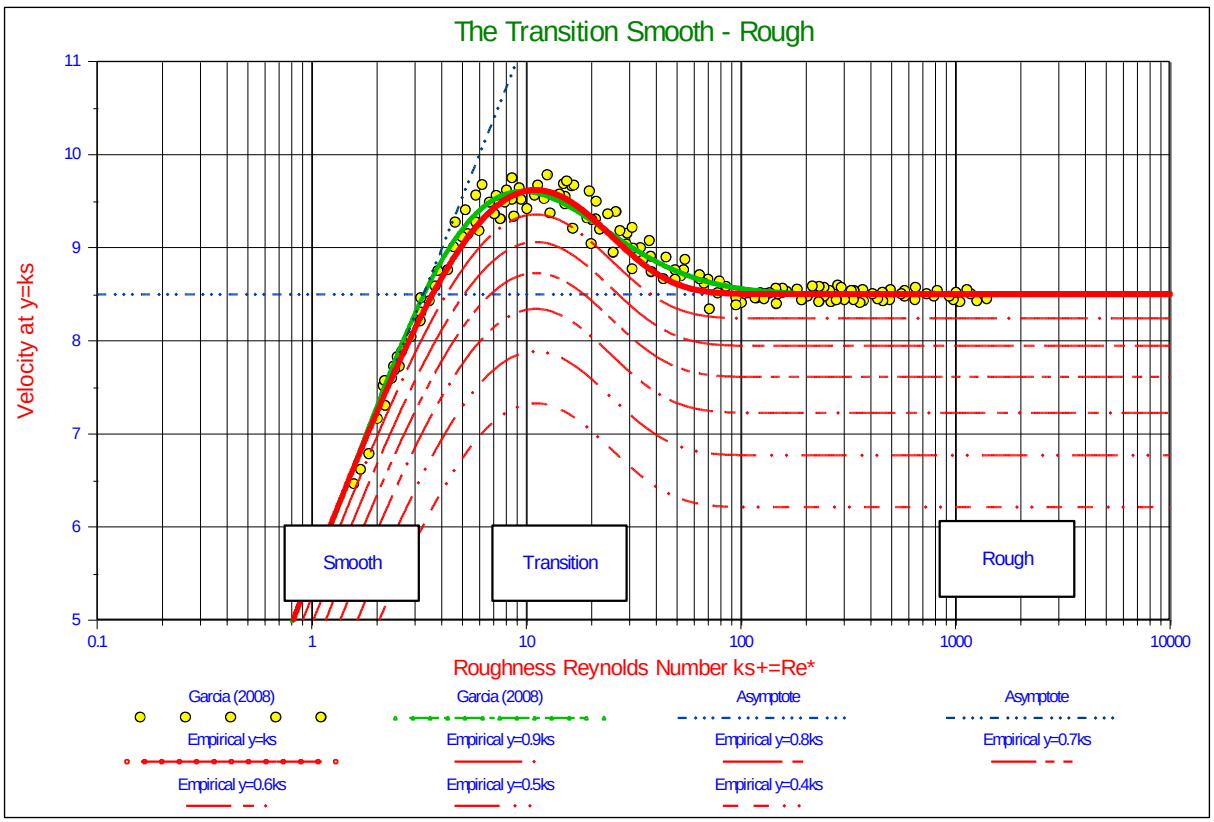

Figure 2-14: The transition smooth-rough for a number of distances to the wall.

2.11. The Angle of Internal Friction/The Friction Coefficient.

When the mechanism for the initiation of motion is sliding, friction is involved. The angle of repose of granular material is often referred to as the angle of internal friction of the material in a loose condition. By rotating a bed until the top layer of particles starts to move (slide or roll) the angle of repose is determined, which is the slope angle at that point. Another way of determining this angle is to poor the particles on a surface and measure the slope angle of the cone shaped heap of particles that is formed. In literature a value between $30° - 35°$ is mentioned for natural sands. Naden (1987) distinguishes between the friction angle ϕ, the dilatation angle ψ and the friction angle at zero dilatation ϕ_0. Where $\phi = \psi + \phi_0$, with values of $\phi = 35°$, $\psi = 30°$ and $\phi_0 = 5°$ (Kirkby & Statham, 1975). The value of ϕ_0 deals with the sliding of a quarts sphere on a quarts surface, so Coulomb friction, and could be related to rolling resistance. Figure 2-15 shows the angle of repose for different materials and grain sizes. The relation between the friction coefficient and the angle of repose is:

$$\mu = \tan(\phi) \qquad (2\text{-}57)$$

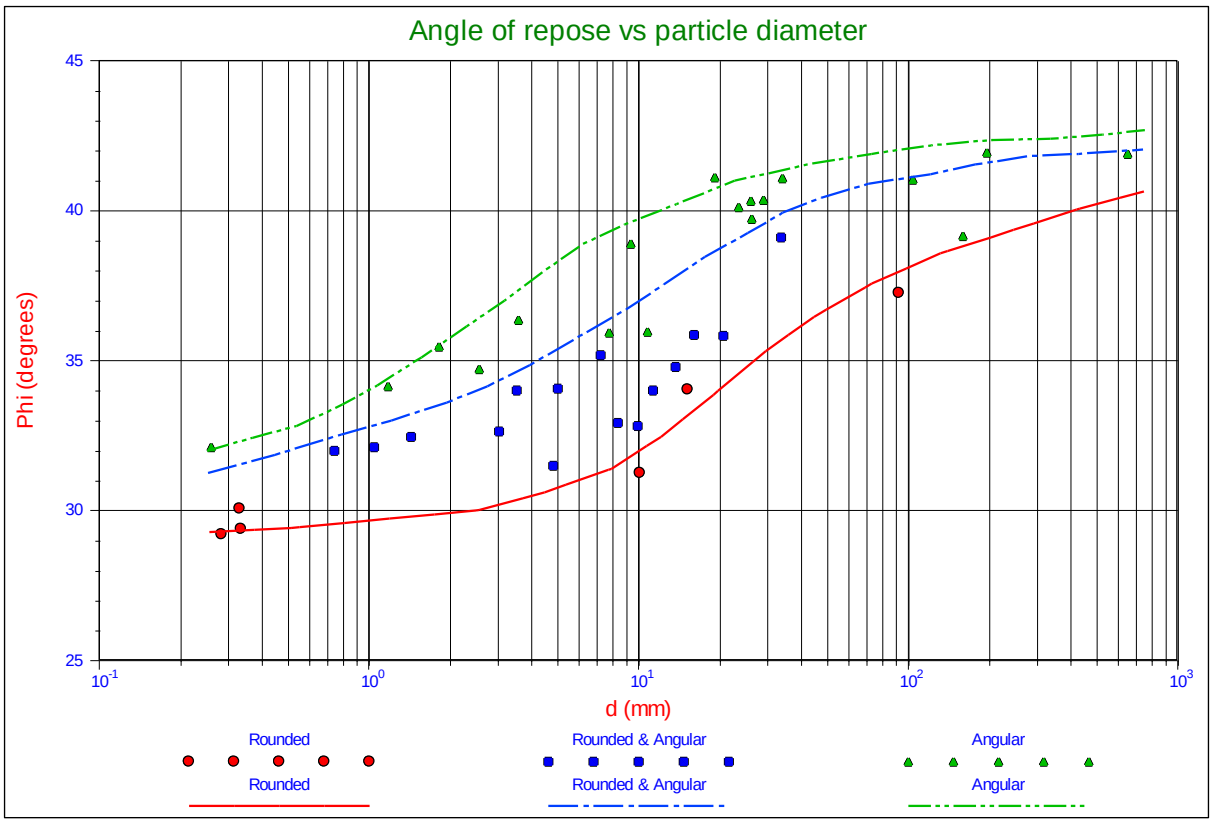

Figure 2-15: Angle of repose for granular material (Simons, 1957).

It should be noted that the angle of repose, in this context, is a global soil mechanical parameter, which can be used as an average value when the whole top layer starts to move. Individual particles may encounter a different value. It should also be noted that the angle of repose is related to friction, which always has to do with the dissipation of energy, so it should not be mixed up with the pivot or dilatation angle which is related to resistance but not to the dissipation of energy.

2.12. The Pivot Angle/The Dilatation Angle.

When the mechanism for the initiation of motion is rolling, a pivot angle is involved. For spheres there is a geometrical relation between the pivot angle and the protrusion level. The pivot angle is sometimes referred to as the dilatation angle, which however is a global soil mechanical parameter and it is preferred not to use it as a local parameter, so we will use the term pivot angle. Luckner (2002) (page 18) determined the pivot angle for 3D sphere configurations, from protrusion levels ranging from 0% to 82%. In fact the maximum protrusion level of a sphere on top of other spheres in a 3D configuration is 82%. At a protrusion level of 0%, meaning the sphere is in between and at the same level as the surrounding spheres, the pivot angle is $\psi = 90°$. At a protrusion level of 30% the pivot angle is $\psi = 59°$, at 80% about $\psi = 20°$, at 90% about $\psi = 12°$ and of course at 100% $\psi = 0°$. In between these values a linear interpolation can be carried out. It is obvious that one is not free to choose the pivot angle, since it is related to the protrusion level.

2.13. Nomenclature.

$\mathbf{A}$	Surface or cross section	m^2
$\mathbf{A_{Lam}}$	Interpolation constant for the laminar region	-
$\mathbf{A_{Turb}}$	Interpolation constant for the turbulent region	-
$\mathbf{C_D}$	Drag coefficient	-
$\mathbf{C_L}$	Lift coefficient	-
$\mathbf{d}$	Sphere, particle or grain diameter	m
$\mathbf{D_*}$	The Bonneville parameter or non dimensional grain diameter	-
$\mathbf{E}$	Exposure level	-
$\mathbf{f_D}, \mathbf{f_{Drag}}$	Fraction of cross section exposed to drag	-
$\mathbf{f_L}, \mathbf{f_{Lift}}$	Fraction of top surface exposed to lift	-
$\mathbf{F_D}$	Drag force	N
$\mathbf{F_L}$	Lift force	N
$\mathbf{F_w}$	Weight of a particle	N
$\mathbf{g}$	Gravitational constant	9.81 m/sec^2
$\mathbf{h}$	Thickness of the layer of water	m
$\mathbf{k_s}$	Roughness often chosen equal to the particle diameter	m
$\mathbf{k_s^+}$	The non dimensional roughness or roughness Reynolds number	-
ℓ	The point of action of the drag force	-
ℓ	Mixing length	m
$\ell_{\mathbf{Drag}}$	Drag point of action	-
$\ell_{\mathbf{Lift}}$	Lift point of action	-
$\ell_{\mathbf{Lever-D}}$	Additional lever arm for drag	-
$\ell_{\mathbf{Lever-L}}$	Additional lever arm for lift	-
$\mathbf{n}$	Turbulence intensity factor	-
$\mathbf{P}$	Probability used in interpolation	-
$\mathbf{p/d}$	Relative protrusion level	-
$\mathbf{Q}$	Factor used in interpolation	-
$\mathbf{R}$	Radius of sphere, particle or grain	m
$\mathbf{R_d}$	The relative submerged specific density	-
$\mathbf{Re_D}$	The particle drag Reynolds number	-
$\mathbf{Re_*}$	Boundary Reynolds number	-
$\mathbf{Re_p}$	The particle Reynolds number	-
$\mathbf{S_*}$	The Grant & Madsen parameter	-
$\mathbf{u}$	Time and surface averaged velocity	m/sec

u_*	Friction velocity	m/sec
u^+	Non dimensional time and surface averaged velocity	-
$u_{r.m.s.}$	Turbulence intensity	m/sec
$u'_{r.m.s.}$	Modified turbulence intensity	m/sec
$u'_{n\cdot r.m.s.}$	The n^{th} moment of the modified turbulence intensity	m/sec
$u_{eff.}$	The effective modified turbulence intensity	m/sec
$u^+_{r.m.s.}$	Non dimensional turbulence intensity	-
u^+_{total}	Non dimensional total velocity	-
V	Volume	m^3
y	Distance to the wall or virtual bed level	m
y_0	Integration constant	m
y^+	Non dimensional distance to the wall (Reynolds number)	-
α	The velocity factor at a certain exposure level	-
δ_v	Thickness of the viscous sub layer	m
δ_v^+	The non dimensional thickness of the viscous sub layer	11.6
κ	Von Karman constant	0.412
ρ	Fluid density	kg/m^3
ρ_f	Fluid density	kg/m^3
ρ_s	Solids density	kg/m^3
ρ_w	The density of water or fluids	kg/m^3
ρ_q	The density of quarts or solids	kg/m^3
ϕ	Internal friction angle/angle of repose	°
ϕ_0	The Coulomb friction angle quarts-quarts	°
ϕ_0	Pivot angle in Wiberg & Smith (1987A)	°
ϕ_{Roll}	Friction angle for rolling resistance	°
Ψ	The dilatation angle	°
ψ	The pivot angle	°
θ	The Shields parameter or non dimensional shear stress	-
θ_5	The Shields parameter for $\xi = 5$	-
θ_{70}	The Shields parameter for $\xi = 70$	-
τ	Total shear stress	Pa
τ_t	Turbulent shear stress	Pa
τ_v	Viscous shear stress	Pa
τ_b	Bed shear stress	Pa
ν	Kinematic viscosity	m^2/sec
μ	Friction coefficient usually the tangent of the internal friction angle	-
μ_{Roll}	Equivalent friction coefficient for rolling	-
ξ	The non dimensional distance of the top of the sphere to the virtual bed level	-

Chapter 3: Constructing the Shields Curve, Part A.

3.1. Fundamentals of the Sliding, Rolling and Lifting Mechanisms for the Entrainment of Particles.

Prediction of the entrainment of particles is an essential issue for the study of erosion phenomena in many applications. The original Shields curve describes the entrainment of many particles at many locations and is thought critical to general transport. The mechanisms involved in general are sliding, rolling and lifting, new models of which have been developed. I will introduce new concepts for the determination of the effective velocity and the acting point of the drag force, based on integration of the drag force over the cross section of the exposed particle (where earlier models were based on integration of the velocity), the behavior of turbulence intensity very close to the virtual bed level and the factor of simultaneous occurrence of the small turbulent eddies. The resulting values of the Shields parameter, based on practical and reasonable properties, are compared with data, resulting in the best correlation for the sliding mechanism with the data of many researchers. The Shields parameter found for rolling and lifting overestimates the measurements from literature. Sliding seems to be the mechanism moving the top layer of the particles, while rolling and lifting are much more mechanisms of individual particles. In the new model it is considered that in the laminar region entrainment is dominated by drag and the influence of small turbulent eddies, while in the turbulent region this is dominated by drag and lift. The transition region is modeled based on sophisticated interpolation. The model correlates very well with the original data of Shields (1936) and data of others and also matches the empirical relation of Soulsby & Whitehouse (1997) well. The model is suitable for incorporating exposure and protrusion levels and laminar main flow.
Part B of this publication gives a sensitivity analysis, describes the influence of exposure and protrusion levels and compares the model with data from different points of view like terminal settling velocity, shear stress, friction velocity, erosion flux and laminar main flow.

3.2. Introduction.

Erosion is displacement of solids (soil, mud, rock and other particles) usually by the agents of currents such as, wind, water, or ice by downward or down-slope movement in response to gravity (Wikipedia). Erosion can be induced by natural currents or by human intervention.
The purpose of this research is to find a mechanistic, transparent mathematical formulation for the initiation of motion of particles in a flow field. This phenomena is often referred to as erosion or scour, while also terms like threshold velocity, incipient motion and entrainment are used. A sub-goal of the research is to use as few as possible empirical coefficients (not proven by either fundamental science or scientific research) and to use practical and reasonable values for the different properties. To understand the influence of the physical phenomena involved, such as gravity, drag, lift and turbulence, a step by step approach is applied, each step adding an influence factor to the model, starting with gravity and drag, then adding lift and finally turbulence. This research is initiated out of scientific curiosity into the mechanistic background of the Shields curve.

3.3. Previous Research.

3.3.1. Introduction.

Erosion exists as long as the planet earth exists and it is one of the natural processes that has shaped or planet. In modern ages man tries to control nature and to be able to do so, man has to understand the physics behind these natural processes. Although there may have been others before, Shields (1936) was one of the first who managed to give some physical explanation to the erosion phenomena and to found this with experiments. The results of his research are shown in Figure 3-1 together with the resulting theoretical curve from the current research. The original research as carried out by Shields in 1936 was based on a limited number of experiments and should be looked at in the context of the technology in that period. So it was and is a big achievement of Shields to find a relation for the initiation of motion of (spherical) particles that still holds today, although many have carried out additional research and tried to find a physical and mathematical explanation. These explanations usually incorporate phenomena such as gravity, drag, lift and turbulence and are based on sliding, rolling or lifting. Aspects such as, which velocity to use for the drag and the lift, where is the point of action of the drag force, the choice of the angle of repose and the pivoting angle are not always consistent. Especially the definition of incipient motion, is it when one particle starts moving, or many and then how many, is interpreted differently by different researchers. Some use sliding as the main mechanism, others rolling and a few lifting. Almost everybody uses the drag coefficient for spheres because many experiments are carried out for spheres, but real quarts grains have a

larger drag coefficient especially at high Reynolds numbers. In general each of these models lacks one of these phenomena and/or aspects. The modeling usually stops, if a model has sufficient correlation with the data of many researchers (Buffington & Montgomery, 1997) and with the original Shields diagram (Shields, 1936).

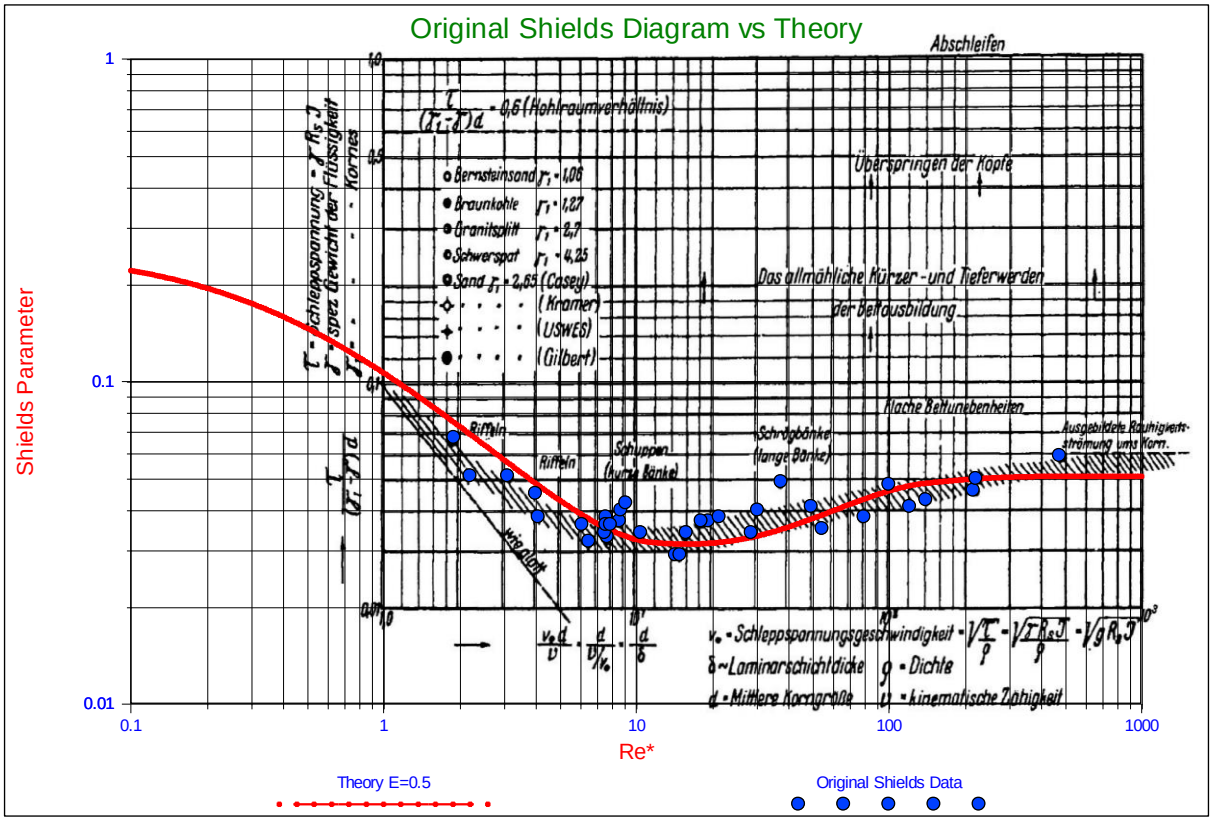

Figure 3-1: The original Shields diagram (Shields, 1936) and the resulting theoretical curve from the current research.

3.3.2. Concept of Initiation of Motion.

Dey distinguished 3 types of concepts for the definition of initiation of motion (Dey, 1999).
The first type of concept is based on bed particle motion through visual observations. Kramer (1935) defined 4 different bed shear conditions, (1) no transport, (2) weak transport, (3) medium transport and (4) general transport. Although clear limits between these 4 levels do not exist, Kramer defined threshold shear stress to be the stress initiating general transport. Vanoni (1975) distinguished 5 levels, (1) no transport, (2) negligible transport, (3) small transport, (4) critical transport and (5) general transport. The Delft Hydraulics Laboratory carried out research in the sixties and seventies (DHL, 1972) and distinguished 7 levels of erosion, (1) occasional particle movement at some locations, (2) frequent particle movement at some locations, (3) frequent particle movement at many locations, (4) frequent particle movement at nearly all locations, (5) frequent particle movement at all locations, (6) permanent particle movement at all locations and (7) general transport. Graf and Pazis also distinguishes 4 levels of erosion but based it on the number of particles per unit area being entrained (Graf & Pazis, 1977), (1) N=1, (2) N=10, (3) N=100 and (4) N=1000. All the measurements show that the highest level (general transport) gives values in the Shields diagram slightly above the Shields curve. The Shields curve matches measurements between critical and general transport (Vanoni, 1975), between N=100 and N=1000 (Graf & Pazis, 1977) and between frequent particle movement at all locations and general transport (DHL, 1972).

The second type of concept is based on sediment flux in such a way that sediment threshold is the shear stress at which the extrapolated sediment flux becomes zero (Shields, 1936). USWES however set a concept of sediment threshold that tractive force results in a general motion of bed particles (USWES, 1936). Later this was changed to sediment threshold as a minimum flux.

The third type of concept is based on field measurements in marine environments.

Dey (and many others) concludes that the inconsistencies of these concepts lead to widely varying results (Dey, 1999), although the results of Vanoni (1975), Delft Hydraulics (1972) and Graf & Pazis (1977) show consistency.

Maybe part of the scatter is caused by not understanding the physics of erosion completely. Figure 3-2 gives an impression of the scatter of a collection of measurements found in Yalin & Karahan (1979) and used in publications of Julien (1995) and Zanke (2003), complemented with measurements from different sources.

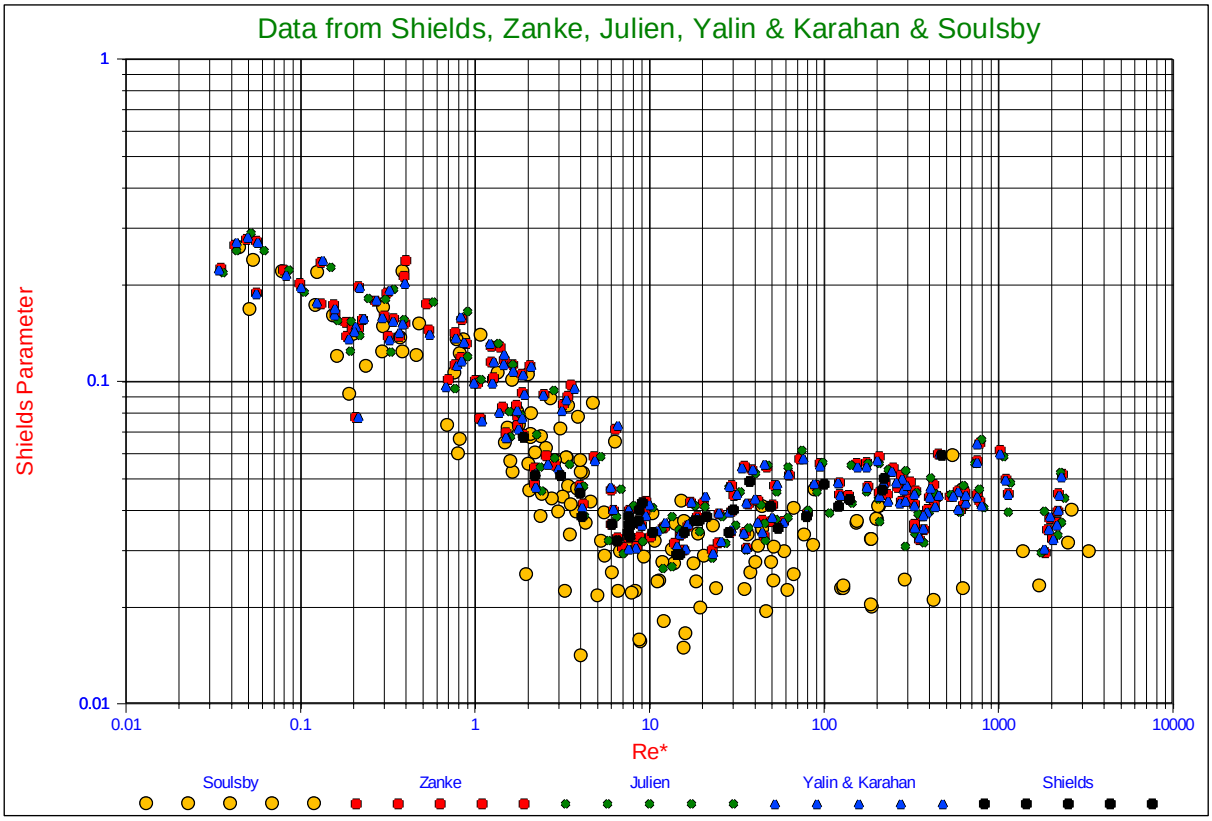

Figure 3-2: Data digitized and copied from Zanke (2003), Julien (1995), Yalin & Karahan (1979), Shields (1936) and others.

3.3.3. Models on Sediment Threshold.

Since there are many models available, only the most relevant ones, in the context of this paper, will be discussed. Shields (1936) introduced the fundamental concepts for initiation of motion and made a set of observations (see Figure 3-1) that have become legendary. From dimensional analysis and fluid mechanics considerations he deduced the relation between the ratio of the bed shear stress $\tau_b = \rho_f \cdot u_*^2$ and the gravitational force on a particle $(\rho_s - \rho_f) \cdot g \cdot d$ as a function of the boundary Reynolds number $Re_* = u_* \cdot d / \nu$. Based on curve fitting on his observations, the famous Shields curve was born. Later many experiments were carried out by numerous scientists of which Buffington & Montgomery give a nice summary (Buffington & Montgomery, 1997). Buffington also gives a critical analyses of the developments since Shields did his first findings (Buffington, 1999). In fact Shields did not derive a model or an equation, but published his findings as a graph (Figure 3-1). It is inconvenient that the Shields diagram is implicit, the friction velocity u_* appears in both the horizontal and the vertical axis. However with modern computers this should not be any problem.

Although less famous, Hjulstrom also carried out his research in the thirties (Hjulstrøm, 1935) and (Hjulstrøm, 1939). He presented his work in a graph showing the relation between the erosion velocity (average velocity above the bed) and the grain diameter. The graph, although explicit, depends on the water height, standard a height of 100 cm is used. For a certain water height, the Shields diagram can be converted to the Hjulstrom diagram. A mathematical description of the Hjulstrom diagram could not be found.

The equilibrium of a single particle resting on a granular bed was studied by White (1940). He obtained an expression for the threshold shear stress, but neglected the lift force. Later Kurihara (1948) extended the model and proposed some empirical equations for the estimation of threshold shear stress.

Egiazaroff (1965) found a relation between the threshold shear stress and the particle Reynolds number. He assumed that at the moment of incipient motion the velocity at a height of $0.63 \cdot d$ is equal to the terminal settling velocity of the particle. His results did not match the original Shields data quantitatively, although some relation will exist.

An extended Shields diagram was developed by Mantz (1977) followed by a graphical representation of a large volume of data by Yalin & Karahan (1979) (see also Figure 3-2)
The Ikeda-Coleman-Iwagaki model was presented by Ikeda (1982) and is based on the work of Iwagaki (1956) and Coleman (1967). The model is based on the assumption that the initiation of motion mechanism is sliding. Gravity, drag and lift are taken into account, but turbulence and grain placement are neglected. The zero level for the velocity profile is taken at the base of the grain exposed to the flow and the velocity used is at the center of the grain, so at $y = d/2$. This means that the grain is exposed to drag over the full height of the grain. For $d/\delta_v < 0.5$ the velocity profile of the viscous sub-layer is applied giving $F(Re_*) = u/u_* = u_* \cdot d/(2 \cdot \nu) = Re_*/2$, while for $d/\delta_v > 2$ the logarithmic velocity profile for rough boundaries is applied giving $F(Re_*) = u/u_* = 6.77$. In the transition area, $0.5 < d/\delta_v < 2$ the fit for the velocity profile proposed by Swamee (1993) or Reichardt (1951) can be used by setting $y = d/2$ and $k_s = d$. This leads to the following equation for the Shields parameter:

$$\theta = \frac{4}{3} \cdot \frac{\mu}{C_D + \mu \cdot C_L} \cdot \frac{1}{F(Re_*)^2} \qquad \textbf{(3-1)}$$

This equation is valid for horizontal beds, but the effect of a slope can easily be incorporated. Considering two angles of internal friction (repose), $\phi = 40^\circ$, ($\mu = 0.84$) and $\phi = 60^\circ$, ($\mu = 1.73$) and further assuming that $k_s = 2 \cdot d$, $C_L = 0.85 \cdot C_D$ and using the standard relations for the drag coefficient for spheres, Garcia (2008) shows the resulting curves, compared with the original Shields (1936) data (fig. 2-17). The $\phi = 40^\circ$ curve underestimates the values of the Shields parameter compared with the original Shields data, while the $\phi = 60^\circ$ curve gets close, but still gives to small values. A $\phi = 60^\circ$ friction angle however is unreasonably high. The curve predicted follows the trend of Shields data, but is about a factor 1.6 smaller for the $\phi = 40^\circ$ case. A predecessor of this model was advanced by Egiazaroff (1965)
The Wiberg & Smith (1987A) model is based on the assumption that the initiation of motion mechanism is rolling. Gravity, drag and lift are taken into account and to some extend also turbulence. The equilibrium of moments around a pivot point is taken, where the location of the pivot point is defined as the contact point with an underlying particle under an angle ϕ_0 with the vertical. This angle is named the particle angle of repose or the dilatation angle. This angle differs from the internal friction angle, as used in the Ikeda-Coleman-Iwagaki model, because the internal friction angle (angle of natural repose) is a global soil mechanical parameter, where local variations are averaged out, while the pivot angle is a local angle matching a specific configuration of the grains. The resulting Wiberg-Smith equation is almost equal to the Ikeda-Coleman-Iwagaki equation apart from the difference between the internal friction angle (using the friction coefficient) in equation (3-1) and the pivot angle in equation (3-2)

$$\theta = \frac{4}{3} \cdot \frac{\tan(\phi_0)}{C_D + \tan(\phi_0) \cdot C_L} \cdot \frac{1}{F(Re_*)^2} \qquad \textbf{(3-2)}$$

Wiberg & Smith (1987A) use the velocity profile as proposed by Reichardt (1951) providing a smooth transition between the viscous sub layer and the logarithmic profile. A lift coefficient of $C_L = 0.2$ is applied in the turbulent region, while it is assumed that particles residing completely in the viscous sub layer are not subject to lift. The calculations are carried out using $\phi_0 = 50^\circ$ and $\phi_0 = 60^\circ$ with $k_s = d$. In Wiberg & Smith (1987B) the average velocity on the particle is applied, giving $F(Re_*) = 6.0$ for the hydraulic rough region. The model matches the original Shields data well for the turbulent rough region for $\phi_0 = 60^\circ$, but overestimates the Shields data for the laminar flow in the viscous sub layer. The first conclusion does not come as a surprise, since $\phi_0 = 60^\circ$ is equal to $\mu = 1.73$ in the Ikeda-Coleman-Iwagaki model and Wiberg & Smith use a smaller lift coefficient, resulting in a slightly higher curve. For the small Reynolds numbers the resulting curve overestimates the original Shields data. Wiberg & Smith (1987A) solve this by introducing turbulence. They state that periodic intrusions of high momentum fluid erode the viscous sub layer and produce locally higher boundary stresses. When the instantaneous boundary shear stress is sufficiently large, movement is more likely. To implement this the thickness of the viscous sub layer is reduced to 60%, maintaining the momentum of the flow, resulting in higher instantaneous velocities by a factor 1.66. This lowers the curve in the lower Reynolds area and gives a good match with the Shields data.

This effect of turbulence however is the same for the whole lower Reynolds area and influences the asymptotic value of the Shields curve going to a Reynolds number of zero.
Dey (1999) developed a detailed model based on rolling as the mechanism for incipient motion. The model includes gravity, drag and lift and even Magnus lift forces, but no turbulence. The Morsi & Alexander (1972) relation for the drag coefficient is used, while the Saffman (1965) approach for the lift force is followed. Additionally the lift due to the Magnus effect is used for large Reynolds numbers. Based on detailed mathematics the lever arms for the equilibrium of moments are derived. The average velocity acting on the sphere is determined by integration of the velocity over the actual surface of the sphere, depending on the virtual bed level. The Reichardt (1951) velocity profile is used. The resulting equation for the Shields parameter is similar to equation (3-2), but much more detailed. There is an excellent agreement between the model developed by Dey and the experimental data used for a pivot angle of $\phi_0 = 32^\circ$. For the particle considered, a particle resting on top of 3 other particles in a dense 3D configuration, the exposure level would be near 1.0 and the protrusion level near 0.8. According to a detailed study of Luckner (2002) this would result in a pivot angle of about $\phi_0 = 20^\circ$.
Zanke (2001) and (2003) follows an approach different from all other researchers. Starting with a non dimensional shear stress based on tilting a bed of particles and assuming that the shear stress exerted at the moment the top layer of the particles starts to move, he deducts the influences of turbulence and lift and finds a curve that is in good correlation with experimental data. The base non dimensional shear stress is set to $\theta = (1-n)\cdot\tan(\phi/1.5)$, where the porosity n is set to 0.3 and the friction angle to $\phi = 30^\circ$. This starting point can be disputed since the driving force when tilting a bed until the grains start to move is gravity, while the main influence in initiation of motion is flow. The way turbulence is incorporated, both in drag and in lift is very interesting. The basis of the turbulence influences is the equation formulated by Nezu & Nakagawa (1993) for the turbulence intensity parallel to the wall as a function to the distance to the wall. Close to the wall in the viscous sub layer the turbulence intensity is about $u^+_{r.m.s.} = 0.3\cdot y^+$, where the time averaged velocity profile is known to be $u^+ = 1\cdot y^+$. Taking $u^+_{total} = u^+ + 2.2\cdot u^+_{r.m.s.} = 1.66\cdot u^+$, should give the same result as Wiberg & Smith (1987A) found by reducing the thickness of the viscous sub layer to 60%. Zanke (2001) uses a factor of 1.8 instead of 2.2, but then his approach is completely different. Zanke (2001) must also have noticed that the asymptotic value of the curve for very low Reynolds numbers decreases when adding the influence of turbulence as stated above. Now it can be discussed whether the virtual bed level for the time averaged velocity and the turbulence intensity are exactly the same. By choosing a lower virtual bed level for the time averaged velocity, the ratio between the turbulence intensity and the time averaged velocity is zero at the virtual bed level for the turbulence intensity, resulting in an asymptotic value that is not influenced by the turbulence. Another interesting addition in the model of Zanke (2001) is the influence of cohesion, although it is the question which fundamental forces are taken into account.
Stevenson, Thorpe & Davidson (2002) and Stevenson, Cabrejos & Thorpe (2002) look at the process of incipient motion from the perspective of chemical engineering and also incorporated the rolling resistance. For small Reynolds numbers (viscous sub layer) the lift force is neglected.
It should be noted that a number of fit equations to the Shields data exist in order to be able to calculate the Shields parameter. A well know equation is the equation of Brownlie (1981) based on the Bonneville (1963) parameter.

$$\theta = \frac{0.22}{D_*^{0.9}} + 0.06\cdot e^{-17.77\cdot D_*^{-0.9}} \qquad \textbf{(3-3)}$$

Soulsby & Whitehouse (1997) defined another fit equation, based on the Bonneville (1963) parameter. The two fit equations differ in the asymptotic values. Brownlie uses 0.06 for very large Reynolds numbers, while Soulsby & Whitehouse use 0.055. As we will see later, this difference is not very relevant. The asymptote for very small Reynolds values for the Brownlie equation is proportional to $Re^{-0.9}$, while Shields (1936) proposed $0.1\cdot Re^{-1}$, but Soulsby & Whitehouse found a value of 0.3, matching the mechanistic models as shown in the equations (3-1) and (3-2).

$$\theta = \frac{0.30}{(1+1.2\cdot D_*)} + 0.055\cdot\left(1-e^{-0.02\cdot D_*}\right) \qquad \textbf{(3-4)}$$

Often it is found that for real sands and gravels the values found for initiation of motion (depending on the definition of course) are smaller than the ones found with the models and with the above equations. For this reason it is proposed to divide these equations by 2 for engineering purposes. Later we will see that this matches using the C_D values for sands and gravels for large Reynolds numbers, but not for small Reynolds numbers.

3.3.4. Shortcomings of the Existing Models.

The existing models have developed during the years and have become more and more detailed. Still some shortcoming have been found and there is space for improvement.

1. In general the exposure and protrusion levels used have not been well defined.
2. When rolling is chosen as the mechanism for the initiation of motion, there is a relation between the protrusion level and the pivot angle and this cannot be chosen freely.
3. The choice of rolling, sliding or lifting as the main mechanism for the initiation of motion has not been motivated well. It is very well possible that at high protrusion levels rolling will occur, while at low protrusion levels the mechanism is sliding and at protrusion levels around zero the mechanism is lifting. Looking at nature this does not sound unreasonable, since nature will choose the mechanism with the least resistance.
4. All models use the relations for the drag coefficient for spheres, which is reasonable realizing that many experiments are carried out for spheres, but in reality we have to deal with natural sands and gravel, so the drag coefficient for sand should be used.
5. The models do not incorporate rolling resistance which is reasonable since quarts is very hard and thus the rolling resistance is very low. Still it is interesting to investigate the influence of rolling resistance at very high protrusion levels.
6. The models are not based on lifting, which is also reasonable, since it can be proven mathematically that initiation of motion by lifting requires a higher shear stress than rolling or sliding, so sliding or rolling will already occur before lifting could occur. Unless the bed is fixed and one single grain is subjected to the flow at a very low protrusion level.
7. It is difficult to distinguish between the influence of drag and lift, since both are in the denominator of equations (3-1) and (3-2). Considering full turbulent flow resulting in drag and lift, while turbulence is phased out due to the size of the particles in relation with the size of the small turbulent eddies and considering laminar flow resulting in drag and the influence of small turbulent eddies, enables us to tune the model on the different physical phenomena.
8. The models use the velocity at the centre of the sphere, the average velocity on the sphere or the surface averaged velocity on the sphere. Also the lever arms for rolling are sometimes chosen at the centre of the sphere or are determined by the surface averaged velocity. Since the forces on the sphere are determined by the square of the velocity in a linear or logarithmic velocity profile, the effective velocity should be determined by the surface averaged square of the velocity. This will give the actual acting point and lever arm.
9. The models are based on velocity profiles and not on the effect of the velocity on the forces on the sphere. Turbulence is a stochastic process and turbulence intensity should not be treated as a velocity profile.
10. The cross section for dragging and lifting is often chosen as the cross section of the sphere and thus chosen equal. The cross section for dragging sand lifting should depend on the protrusion and exposure levels and be different for dragging and lifting.
11. Using a velocity profile in the transition between laminar and turbulent flow is dangerous, since it is not only the velocity that changes, but also the contributions of lift and turbulence and for example the position of the acting point of the drag force.

3.3.5. Known's and Unknowns.

The models identified with equations (3-1) and (3-2) contain a number of known's and unknowns. The velocity profile and the drag coefficient can be determined theoretically or with semi-empirical equations. The viscosity (at a fixed temperature) and the Karman constant are known constants. The friction coefficient and the pivot angle can be found from many experiments or calculated geometrically. The main unknowns are the influence of turbulence and the influence of the lift coefficient. It is only useful to have different unknowns in a model if they can be isolated and measured independently. Looking at equations (3-1) and (3-2) we can see that both drag and lift are in the denominator and both drag and lift can be subject to the influence of turbulence, but then these influences cannot be isolated and measured separately. In general it can be assumed that lift does not occur in a laminar viscous flow, while the influence of small eddies is phased out for larger particles in a turbulent flow. So we will consider drag and turbulence for laminar viscous flow occurring at boundary Reynolds numbers below 5 and we will consider drag and lift for turbulent flow for boundary Reynolds numbers above 70. Since the drag based on the time averaged velocity profile is deterministic, this means that in the laminar viscous flow the only influence to make the model match the measurements is the turbulence, while in the turbulent flow the only influence to make the model match the measurements is the lift force. If there would be some lift force in the laminar viscous flow, the influence will be incorporated in the turbulence modelling, while a possible influence of turbulence in the turbulent region will be incorporated in the lift force modelling.

3.3.6. Definitions.

Before starting with the model it is convenient to define a number of parameters as they are often used in literature.

The relative submerged specific density $\mathbf{R_d}$ is defined as:

$$\mathbf{R_d} = \frac{\rho_q - \rho_w}{\rho_w} \qquad \textbf{(3-5)}$$

The term ***friction velocity*** comes from the fact that $\sqrt{\tau_b / \rho_w}$ has the same unit as velocity and it has something to do with the friction force. The bottom shear stress is often represented by friction velocity $\mathbf{u_*}$, defined by:

$$\mathbf{u_*} = \sqrt{\frac{\tau_b}{\rho_w}} \qquad \textbf{(3-6)}$$

The Shields parameter θ is the ratio between the force resulting from the bottom shear stress and the force resulting from gravity:

$$\theta = \frac{\mathbf{u_*^2}}{\mathbf{R_d \cdot g \cdot d}} \qquad \textbf{(3-7)}$$

The boundary Reynolds number:

$$\mathbf{Re_*} = \frac{\mathbf{u_* \cdot d}}{\nu} \qquad \textbf{(3-8)}$$

The roughness Reynolds number:

$$\mathbf{k_s^+} = \frac{\mathbf{u_* \cdot k_s}}{\nu} \qquad \textbf{(3-9)}$$

The distance to the wall Reynolds number:

$$\mathbf{y^+} = \frac{\mathbf{u_* \cdot y}}{\nu} \qquad \textbf{(3-10)}$$

The original Shields graph is not convenient to use, because both axis contain the shear velocity $\mathbf{u_*}$ and this is usually an unknown, this makes the graph an implicit graph. To make the graph explicit, the graph has to be transformed to another axis system. In literature often the dimensionless grain diameter $\mathbf{D_*}$ is used, also called the Bonneville (1963) parameter:

$$\mathbf{D_*} = \mathbf{d} \cdot \sqrt[3]{\frac{\mathbf{R_d \cdot g}}{\nu^2}} \qquad \textbf{(3-11)}$$

The relation between the Shields parameter and the Bonneville parameter is:

$$\mathbf{Re_*} = \sqrt{\theta} \cdot \mathbf{D_*^{1.5}} \qquad \textbf{(3-12)}$$

So the Bonneville parameter is a function of the Shields number and the boundary Reynolds number according to:

$$\mathbf{D_*} = \left(\frac{\mathbf{Re_*}}{\sqrt{\theta}} \right)^{2/3} \qquad \textbf{(3-13)}$$

Another parameter that is often used for the horizontal axis is the so called Grant and Madsen (1976) parameter or sediment fluid parameter:

$$\mathbf{S_*} = \frac{\mathbf{D_*^{1.5}}}{4} = \frac{\mathbf{Re_*}}{4 \cdot \sqrt{\theta}} \qquad \textbf{(3-14)}$$

The particle Reynolds number, which differs a factor 4 from the Grant and Madsen parameter:

$$\mathbf{Re_p} = \mathbf{D_*^{1.5}} = \frac{\mathbf{Re_*}}{\sqrt{\theta}} \qquad \textbf{(3-15)}$$

The non-dimensional velocity

$$\mathbf{u^+} = \frac{\overline{\mathbf{u(y)}}}{\mathbf{u_*}} \qquad \textbf{(3-16)}$$

The non-dimensional laminar sub-layer thickness

$$\delta_v^+ = \frac{\delta_v \cdot \mathbf{u_*}}{\nu} = 11.6 \qquad \textbf{(3-17)}$$

The particle drag Reynolds number is the Reynolds number used to calculate the drag coefficient $\mathbf{C_D}$. This Reynolds number differs from the particle Reynolds number, using the effective velocity used to calculate the drag force on a particle.

$$\mathbf{Re_D} = \ell \cdot \alpha \cdot \mathbf{Re_*} \qquad \textbf{(3-18)}$$

3.4. The Model.

Before developing the model a number of assumptions have to be made in order to have starting points for the modeling to match the Shields curve and the measurements from literature . These assumptions have to be reasonable, matching literature and practice. These assumptions are:

1. The bed consists of spheres with one diameter **d**.
2. The virtual bed level is chosen at $\mathbf{0.2 \cdot d}$ below the top of the bed.
3. The criterion for initiation of motion is chosen to be between critical transport and general transport according to Vanoni (1975), Delft Hydraulics (1972) and Graf & Pazis (1977).
4. The exposure level **E** is chosen as $\mathbf{0.5 \cdot d}$, resulting in a protrusion level of $\mathbf{0.3 \cdot d}$, meaning that the standard sphere is exposed to the flow for 50% and reaches above the other spheres in the bed for 30%, based on Fenton & Abbot (1977) and Chin & Chiew (1993).
5. For the model an internal friction angle (angle of natural repose) of $\phi = 30°$ is chosen (for the sliding mechanism), which matches spheres and rounded particles of natural sands and gravel (see Figure 2-15).
6. For the model a pivot angle of $\psi = 59°$ is chosen (for the rolling mechanism), which matches a protrusion level of $\mathbf{0.3 \cdot d}$, based on Luckner (2002).
7. First full laminar flow will be considered up to a boundary/roughness Reynolds number of 11.6 and full turbulent flow above 11.6. The laminar flow is described with equation (2-53) and the turbulent flow with equation (2-55).
8. Later a transition area is introduced with full laminar flow up to a boundary/roughness Reynolds number of 5, a transition zone from 5 to 70 and a full turbulent flow above 70, with logarithmic interpolation in the transition zone.
9. For the laminar flow, the velocity at the top of the sphere is $\mathbf{0.5 \cdot Re_* \cdot u_*}$, resulting in an acting point at $\ell_{\mathbf{Drag}} = \mathbf{0.5}$, meaning at 50% of the flow field (see equation (2-53)). This also means the acting point is at $\mathbf{0.25 \cdot d}$ above the centre of the sphere (based on a surface averaged square of the velocity).
10. For the turbulent flow, the velocity at the top of the sphere is $\frac{\ln(\frac{0.5}{0.033})}{\kappa} \cdot \mathbf{u_*} = \mathbf{6.6 \cdot u_*}$, resulting in an acting point at $\ell_{\mathbf{Drag}} = \mathbf{0.655}$, meaning at 65.5% of the flow field (see equation (2-55)). This also means the acting point is at $\mathbf{0.327 \cdot d}$ above the centre of the sphere (based on a surface averaged square of the velocity).

3.4.1. Drag Induced Sliding and Rolling.

To analyze the initiation of motion, the different physical phenomena will be taken into account one by one, starting with the drag force. Figure 3-3 shows the different forces (A) and moments (B) that play a role in drag induced motions.

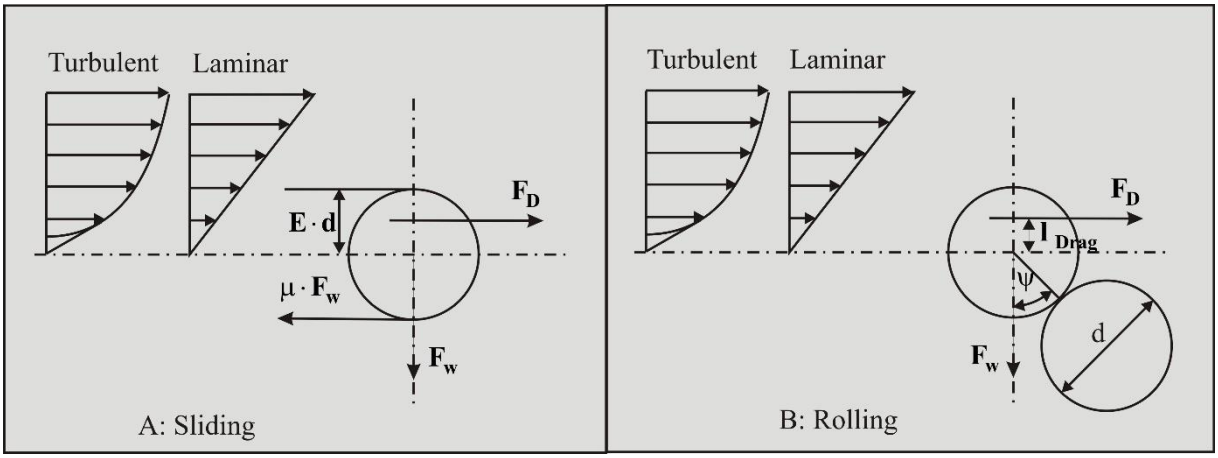

Figure 3-3: Drag induced sliding (A) and rolling (B).

3.4.2. Drag Induced Sliding.

Let us consider a steady flow over a bed composed of cohesion less grains. The driving force is the flow drag force on the grain, assuming that part of the surface of the particle is hiding behind other particles and only a fraction E (the exposure level) is subject to drag:

$$F_D = C_D \cdot \tfrac{1}{2} \cdot \rho_w \cdot \left(\ell_{Drag} \cdot \alpha \cdot u_*\right)^2 \cdot f_D \cdot \frac{\pi \cdot d^2}{4} \qquad (3\text{-}19)$$

The velocity $\alpha \cdot u_*$ is the actual velocity at the top of the sphere, so for an exposure level of 0.5 in a laminar flow, this would be equal to $0.5 \cdot Re_* \cdot u_*$, assuming the roughness is equal to the sphere diameter. In a turbulent flow this gives $\ln(0.5/0.033)/\kappa \cdot u_* = 6.6 \cdot u_*$ (see equation (2-55)). The velocity $\ell_{Drag} \cdot \alpha \cdot u_*$ is the effective velocity resulting from integration of the velocity squared over the part of the sphere that is subject to flow. For an exposure level of 0.5 in a laminar flow the factor $\ell_{Drag} = 0.5$. In a turbulent flow $\ell_{Drag} = 0.655$. In fact the factor ℓ_{Drag} gives the point of action of the drag force related to the exposure level **E**. The factor f_D is the fraction of the cross section being subject to drag and this factor is 0.5 for an exposure level of 0.5.

The submerged weight of the particle is:

$$F_w = (\rho_q - \rho_w) \cdot g \cdot \frac{\pi \cdot d^3}{6} \qquad (3\text{-}20)$$

At equilibrium the drag force is equal to the friction force:

$$F_D = \mu \cdot F_w \qquad (3\text{-}21)$$

By substituting equation (3-19) and equation (3-20) in equation (3-21),this can be written as:

$$C_D \cdot \tfrac{1}{2} \cdot \rho_w \cdot (\ell_{Drag} \cdot \alpha \cdot u_*)^2 \cdot f_D \cdot \frac{\pi \cdot d^2}{4} = \mu \cdot (\rho_q - \rho_w) \cdot g \cdot \frac{\pi \cdot d^3}{6} \qquad (3\text{-}22)$$

Which can be re-arranged into (showing the Shields parameter):

$$\theta = \frac{u_*^2}{R_d \cdot g \cdot d} = \frac{4}{3} \cdot \frac{1}{\alpha^2} \cdot \frac{\mu}{\ell_{Drag}^2 \cdot f_D \cdot C_D} \qquad (3\text{-}23)$$

3.4.3. Drag Induced Rolling.

In the case of rolling the sphere will pivot around the contact point with a sphere below, which has an angle with the vertical named the pivot angle ψ. There may be some rolling resistance which can be taken into account by introducing the friction angle for rolling ϕ_{Roll}. This friction will be very small for quarts-quarts rolling and is taken $1°$ in the calculations. The equilibrium equation for rolling is:

$$F_D \cdot (\ell_{Lever} + \cos(\psi + \phi_{Roll})) \cdot R = F_w \cdot \sin(\psi + \phi_{Roll}) \cdot R \qquad (3\text{-}24)$$

With ℓ_{Lever} the distance of the acting point of the drag force above the centre of the sphere. This distance is $\ell_{Lever} = 0.5$ for laminar flow and $\ell_{Lever} = 0.655$ for turbulent flow. Substituting equations (3-19) and (3-20) in equation (**3-24**) gives the following equilibrium equation.

$$C_D \cdot \tfrac{1}{2} \cdot \rho_w \cdot (\ell_{Drag} \cdot \alpha \cdot u_*)^2 \cdot f_D \cdot \frac{\pi \cdot d^2}{4} \cdot (\ell_{Lever} + \cos(\psi + \phi_{Roll})) \cdot R = (\rho_q - \rho_w) \cdot g \cdot \frac{\pi \cdot d^3}{6} \cdot \sin(\psi + \phi_{Roll}) \cdot R \qquad (3\text{-}25)$$

$$\ell_{Lever} = 1 - 2 \cdot E \cdot (1 - \ell_{Drag}) \tag{3-26}$$

Which can be re-arranged into (showing the Shields parameter):

$$\theta = \frac{u_*^2}{R \cdot g \cdot d} = \frac{4}{3} \cdot \frac{1}{\alpha^2} \cdot \frac{\sin(\psi + \phi_{Roll})}{\ell_{Drag}^2 \cdot f_D \cdot C_D \cdot (\ell_{Lever} + \cos(\psi + \phi_{Roll}))} \tag{3-27}$$

3.4.4. The Drag Coefficient.

Equations (3-23) and (3-27) contain the drag coefficient, which is one of the mainly experimental determined coefficients influencing the value of the Shields parameter. In 1851 Stokes theoretically derived the drag coefficient for spherical particles in a laminar flow and found that (for $Re_p < 0.5$):

$$C_D = \frac{24}{Re_p} \tag{3-28}$$

For large Reynolds numbers the drag coefficient of spheres is a fixed number for which often the value of 0.445 is used. In the intermediate range of Reynolds numbers many fit functions are known. A good fit function for the transitional region has been derived by Turton & Levenspiel (1986), which is a 5 parameter fit function to the data as shown in Figure 1-2:

$$C_D = \frac{24}{Re_D} \cdot (1 + 0.173 \cdot Re_D^{0.657}) + \frac{0.413}{1 + 16300 \cdot Re_D^{-1.09}} \tag{3-29}$$

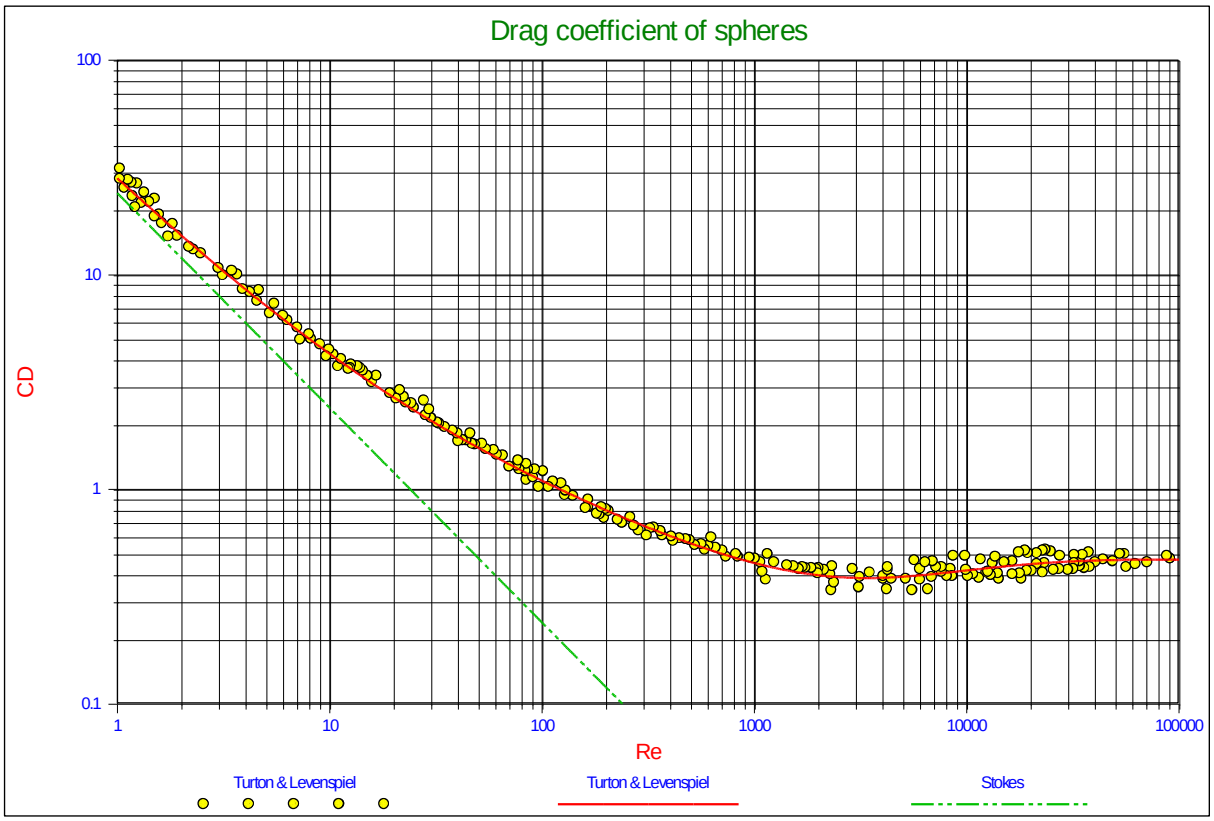

Figure 3-4: Experimental data for drag coefficients of spheres as a function of the Reynolds number (Turton & Levenspiel, 1986).

The models derived to describe the Shields curve use the drag coefficient of spheres and hardly any discussion about this has been found in literature, although it is known that for sands and gravels the drag coefficients, especially at large Reynolds numbers, are larger than the drag coefficient for spheres. Engelund & Hansen (1967)

found the following equation based on measurements and found it best suited for natural sands and gravels (Julien, 1995):

$$C_D = \frac{24}{Re_D} + 1.5 \qquad \textbf{(3-30)}$$

It must be noted here that in general the drag coefficients are determined based on the terminal settling velocity of the particles. Wu & Wang (2006) recently gave an overview of drag coefficients and terminal settling velocities for different particle Corey shape factors. The result of their research is reflected in Figure 1-4 and Figure 1-5. Figure 1-4 shows the drag coefficients as a function of the Reynolds number and as a function of the Corey shape factor. Figure 1-5 shows the drag coefficient for natural sands and gravels. The asymptotic value for large Reynolds numbers is about 1, while equation (1-14) shows an asymptotic value of 1.5. To emphasise the effect of the natural sands and gravels, equation (1-14) will be used in the model for natural sands and gravels, while equation (3-29) is used for spheres.
The Reynolds number used to calculate the drag coefficient is based on the velocity determined by the actual surface averaged velocity squared, according to equation (3-18).

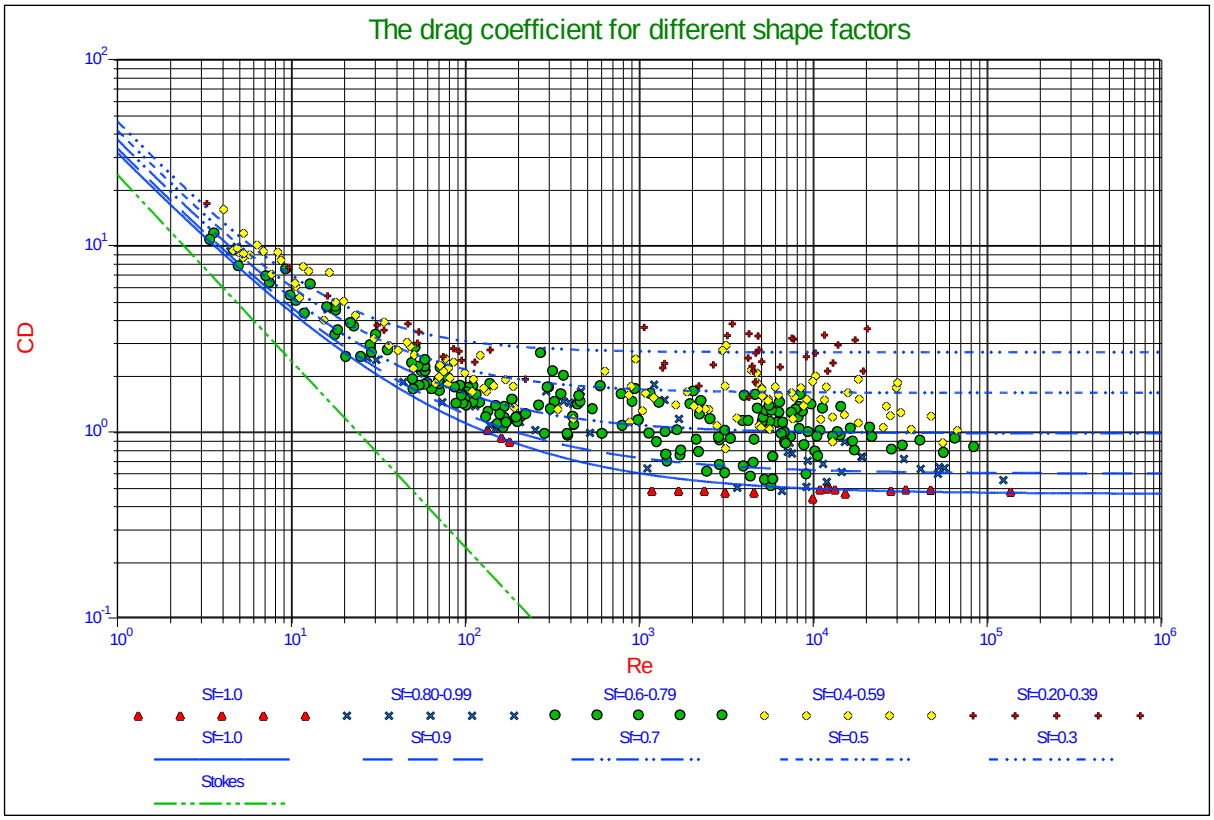

Figure 3-5: Drag coefficient as a function of the particle shape (Wu & Wang, 2006).

Figure 3-7 shows the results of equation (3-23) for sliding and equation (3-27) for rolling. It is obvious from this figure that the Shields parameter found as a function of the boundary Reynolds number overestimates with regards to the measurements, except for very small Reynolds numbers, so there must be other phenomena that have to be taken into account, like lift forces and turbulence. It is also clear from this figure that the curve for rolling is higher than the curve for sliding, out of which the conclusion can be drawn that the general mechanism of initiation of motion for critical to general transport is sliding and not rolling. The asymptotic value of the curve for sliding at very small Reynolds numbers is about 0.26, matching the asymptotic value of Soulsby & Whitehouse of 0.3 given in equation (3-4). The minimum at a Reynolds number of 23.2 is caused by the fact that, at that Reynolds number, the top of the sphere reaches the top of the viscous sub layer, so at lower Reynolds numbers laminar viscous flow is considered and at higher Reynolds numbers turbulent flow.

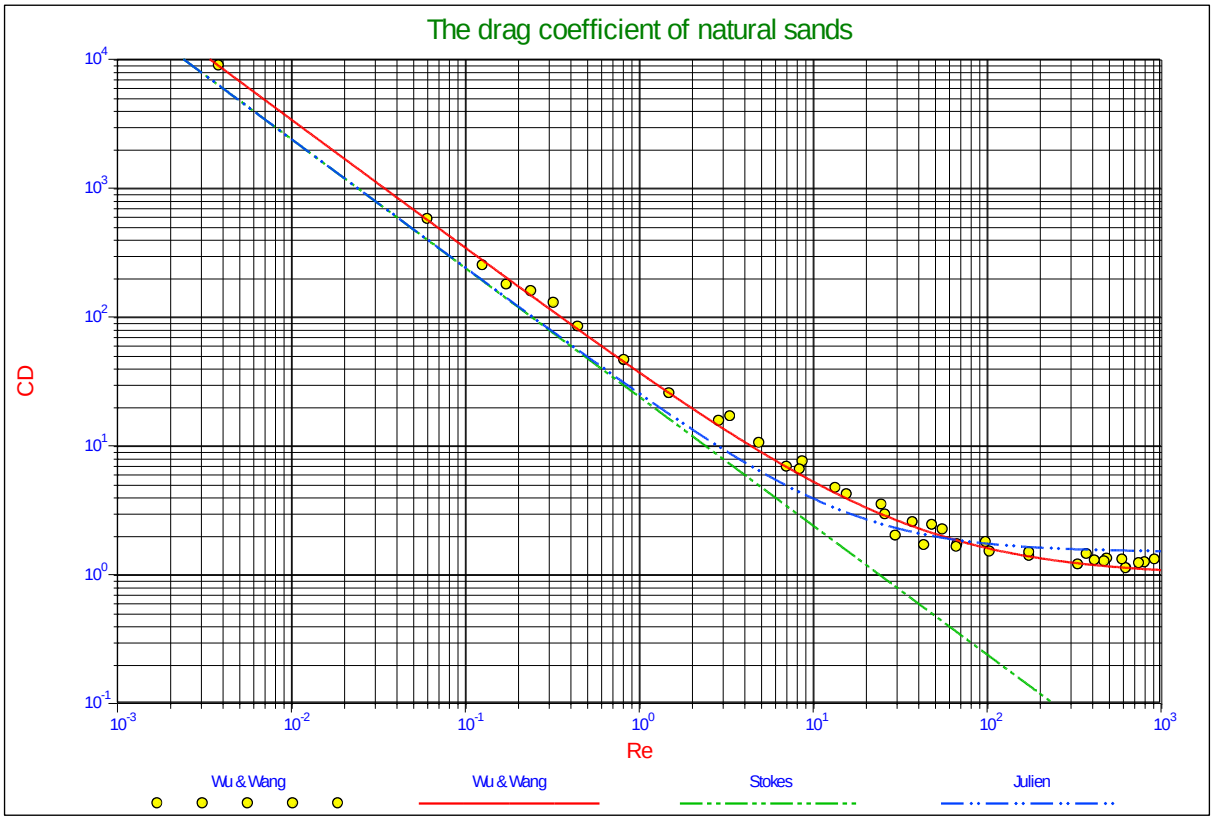

Figure 3-6: Drag coefficient for natural sediments (S_f=0.7) (Wu & Wang, 2006).

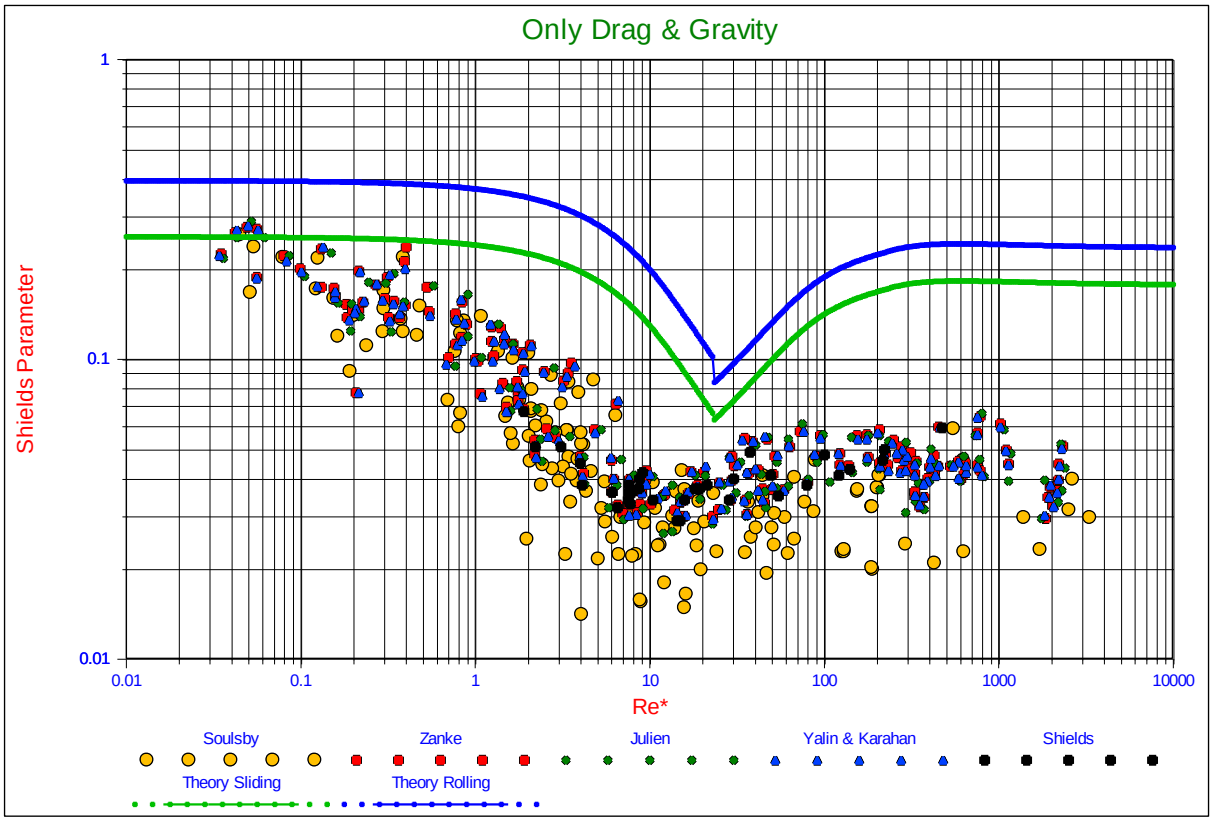

Figure 3-7: Drag induced initiation of motion.

Pilotti & Menduni (2001) also derived a model based on drag and gravity only, for laminar main flow up to boundary Reynolds numbers of about 100. They assume that the sphericity of the grains is such that the drag coefficient of spheres can be applied. Using almost uniform grains in the range of 0.08 to 3 mm, the boundary

Reynolds number was also varied by using a water glucose mixture with different densities, resulting in viscosities varying from $\mathbf{1.01 \cdot 10^{-6}}$ to $\mathbf{2.81 \cdot 10^{-4}}$ in m^2/sec. Turbulence is not taken into account in the model. The mechanism for initiation of motion was rolling of individual particles with pivot angles of $\mathbf{35°}$, $\mathbf{40°}$ and $\mathbf{45°}$. The resulting curves (only for the laminar region) have the same shape as the curves in Figure 3-7 with asymptotic values of 0.13, 0.19 and 0.27 for the 3 pivot angles. The measured values of the Shields parameter are comparable with the data in Figure 3-7 for the very low Reynolds numbers ($\mathbf{Re_* < 1}$), but higher in the intermediate range ($\mathbf{1 < Re_* < 100}$), matching the curve for sliding. It is difficult to compare the results exactly with Figure 3-7, since the exposure level of the model of Pilotti & Menduni (2001) is not known. In Part B of this publication these measurements are analyzed in relation with laminar (turbulence free) main flow.

3.4.5. Drag and Lift Induced Sliding, Rolling and Lifting.

Drag induced sliding and rolling overestimates the Shields parameter compared with the measurements, so there must be other influences. The first influence considered is lift as is shown in Figure 3-8. The lift force is assumed to be upwards directed. Based on literature and theory, lift is assumed to occur in the turbulent region only.

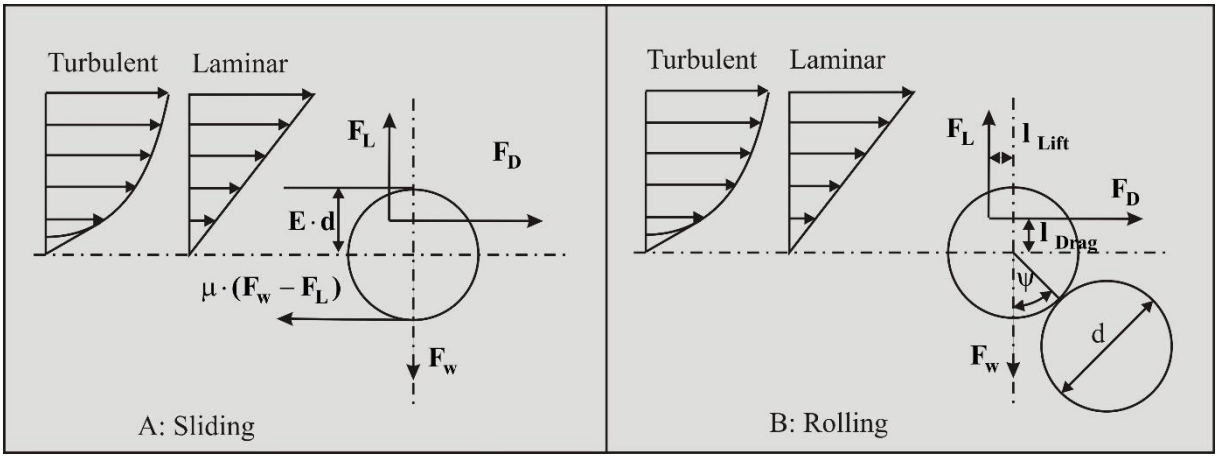

Figure 3-8: Drag and lift induced sliding (A) and rolling (B).

3.4.6. Drag and Lift Induced Sliding.

Let us consider the steady flow over a bed composed of cohesion less grains. The driving forces are the flow drag and lift forces on the grain, assuming that part of the surface of the particle is hiding behind other particles and only a fraction E (the exposure level) is subject to drag and lift. This gives the following equation for the drag force:

$$\mathbf{F_D = C_D \cdot \tfrac{1}{2} \cdot \rho_w \cdot \left(\ell_{Drag} \cdot \alpha \cdot u_*\right)^2 \cdot f_D \cdot \frac{\pi \cdot d^2}{4}} \qquad \textbf{(3-31)}$$

The lift force is written in the same way, but it is assumed that the lift force is determined by the velocity difference between the top and the bottom of the particle and the surface that is subject to lift is the projected horizontal cross section subject to the flow, this factor $\mathbf{f_L = 1}$ for an exposure level $\mathbf{E = 0.5}$, while the factor for drag $\mathbf{f_D = 0.5}$ in this case:

$$\mathbf{F_L = C_L \cdot \tfrac{1}{2} \cdot \rho_w \cdot (\alpha \cdot u_*)^2 \cdot f_L \cdot \frac{\pi \cdot d^2}{4}} \qquad \textbf{(3-32)}$$

The submerged weight of the particle is:

$$\mathbf{F_w = (\rho_q - \rho_w) \cdot g \cdot \frac{\pi \cdot d^3}{6}} \qquad \textbf{(3-33)}$$

At equilibrium the drag force and the friction force are equal (note that the friction force is reduced by the lift):

$$F_D = \mu \cdot (F_w - F_L) \tag{3-34}$$

Substituting the equations (3-31), (3-32) and (3-33) into (3-34) results in the following equation:

$$C_D \cdot \tfrac{1}{2} \cdot \rho_w \cdot (\ell_{Drag} \cdot \alpha \cdot u_*)^2 \cdot f_D \cdot \frac{\pi \cdot d^2}{4} = \mu \cdot \left((\rho_q - \rho_w) \cdot g \cdot \frac{\pi \cdot d^3}{6} - C_L \cdot \tfrac{1}{2} \cdot \rho_w \cdot (\alpha \cdot u_*)^2 \cdot f_L \cdot \frac{\pi \cdot d^2}{4} \right) \tag{3-35}$$

Which can be re-arranged into (showing the Shields parameter):

$$\theta = \frac{u_*^2}{R_d \cdot g \cdot d} = \frac{4}{3} \cdot \frac{1}{\alpha^2} \cdot \frac{\mu}{\ell_{Drag}^2 \cdot f_D \cdot C_D + \mu \cdot f_L \cdot C_L} \tag{3-36}$$

3.4.7. Drag and Lift Induced Rolling.

The equilibrium equation for rolling is:

$$F_D \cdot (\ell_{Lever-D} + \cos(\psi + \phi_{Roll})) \cdot R + F_L \cdot (\ell_{Lever-L} + \sin(\psi + \phi_{Roll})) \cdot R = F_w \cdot \sin(\psi + \phi_{Roll}) \cdot R \tag{3-37}$$

Substituting the equations (3-31), (3-32) and (3-33) into (3-37) gives:

$$\begin{aligned} &C_D \cdot \tfrac{1}{2} \cdot \rho_w \cdot (\ell_{Drag} \cdot \alpha \cdot u_*)^2 \cdot f_D \cdot \frac{\pi \cdot d^2}{4} \cdot (\ell_{Lever-D} + \cos(\psi + \phi_{Roll})) \cdot R \\ &+ C_L \cdot \tfrac{1}{2} \cdot \rho_w \cdot (\alpha \cdot u_*)^2 \cdot f_L \cdot \frac{\pi \cdot d^2}{4} \cdot (\ell_{Lever-L} + \sin(\psi + \phi_{Roll})) \cdot R \\ &= (\rho_q - \rho_w) \cdot g \cdot \frac{\pi \cdot d^3}{6} \cdot \sin(\psi + \phi_{Roll}) \cdot R \end{aligned} \tag{3-38}$$

With the additional lever arms for drag and lift :

$$\begin{aligned} \ell_{Lever-D} &= 1 - 2 \cdot E \cdot (1 - \ell_{Drag}) \\ \ell_{Lever-L} &= 0 \end{aligned} \tag{3-39}$$

Which can be re-arranged into the Shields parameter:

$$\theta = \frac{u_*^2}{R_d \cdot g \cdot d} = \frac{4}{3} \cdot \frac{1}{\alpha^2} \cdot \frac{\sin(\psi + \phi_{Roll})}{\ell_{Drag}^2 \cdot f_D \cdot C_D \cdot (\ell_{Lever-D} + \cos(\psi + \phi_{Roll})) + f_L \cdot C_L \cdot (\ell_{Lever-L} + \sin(\psi + \phi_{Roll}))} \tag{3-40}$$

3.4.8. Lift Induced Lifting.

A third possible mechanism for the initiation of motion is pure lifting. This will occur if the lift force is equal to the gravity force according to:

$$F_w = F_L \tag{3-41}$$

Substituting the equations (3-31) and (3-33) into equation (3-41) gives:

$$(\rho_q - \rho_w) \cdot g \cdot \frac{\pi \cdot d^3}{6} = C_L \cdot \tfrac{1}{2} \cdot \rho_w \cdot (\alpha \cdot u_*)^2 \cdot f_L \cdot \frac{\pi \cdot d^2}{4} \tag{3-42}$$

Which can be re-arranged into the Shields parameter:

$$\theta = \frac{u_*^2}{R_d \cdot g \cdot d} = \frac{4}{3}\frac{1}{\alpha^2 \cdot C_L \cdot f_L} \qquad \textbf{(3-43)}$$

Since it is assumed that lift only occurs in turbulent flow and not in laminar flow, this mechanism only applies for boundary Reynolds numbers higher than 70. For an exposure level of 0.5, the factor $\alpha = 6.6$, the surface coefficient $f_L = 1$ and a lift coefficient of $C_L = 0.423$ is applied, which will be explained in the next paragraph. This results in a Shields parameter of 0.0726 for large boundary Reynolds numbers. How this relates to rolling and sliding will be discussed in the next paragraph.

3.4.9. The Lift Coefficient.

The choice of the lift coefficient is a discussion in many of the models and many different values are found. Sometimes the lift coefficient is expressed as a fraction of the drag coefficient and sometimes as a constant. In most models however lift is present in the turbulent flow, but not in the laminar viscous sub layer. In this model also the choice is made to neglect lift in the laminar region, so for boundary Reynolds numbers below 5. Wiberg & Smith (1987A), Dey (1999), Pilotti & Menduni (2001), Stevenson, Thorpe & Davidson (2002) and others support this assumption. For the turbulent region different values are used for the lift coefficient.

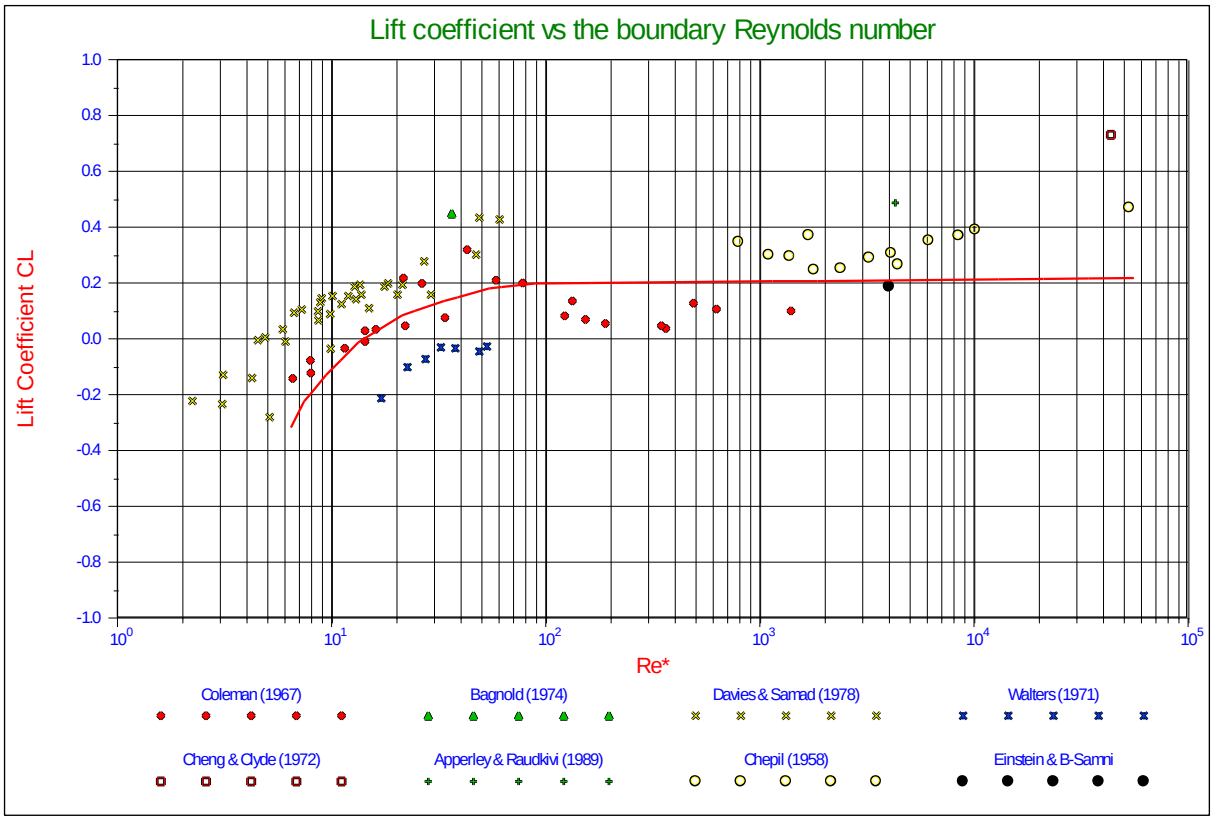

Figure 3-9: The lift coefficient as a function of the particle Reynolds number.

Wiberg & Smith (1987A) use a value of 0.2, while using $0.85 \cdot C_D$ in (Wiberg & Smith, 1987B) inspired by the work of Chepil (1958). Marsh, Western & Grayson (2004) compared 4 models, but also evaluated the lift coefficient as found by a number of researchers as is shown in Figure 3-9. For large Reynolds numbers an average value of 0.2 is found, while for small Reynolds numbers the lift coefficient can even become negative. Luckner (2002) found a relation where the lift coefficient is about $1.9 \cdot E \cdot C_D$ (including the effect of turbulence), which matches the findings of Dittrich, Nestmann & Ergenzinger (1996). For an exposure level of 0.5 this gives $0.95 \cdot C_D$, which is close to the findings of Chepil (1958). Using a lift coefficient of $0.95 \cdot C_D = 0.423$ for boundary Reynolds numbers above 70, results in Shields curves as shown in Figure 3-10.

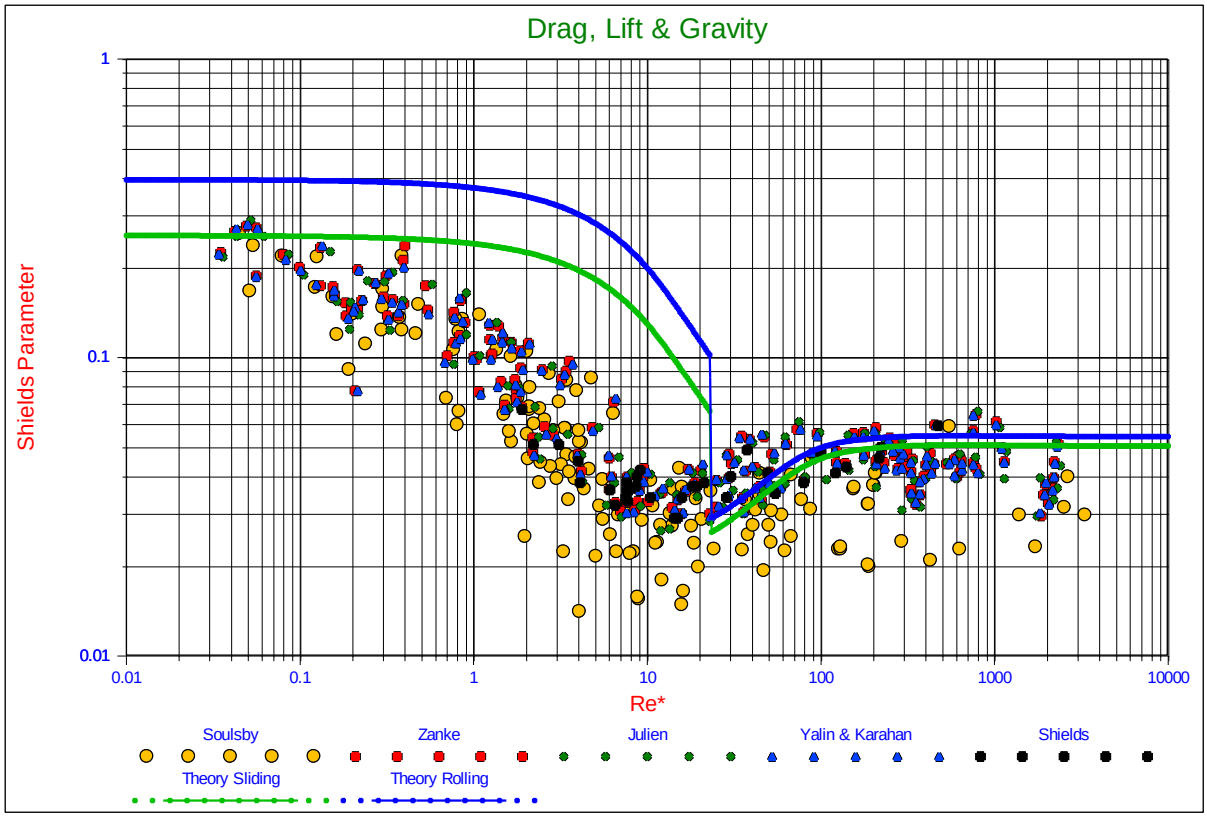

Figure 3-10: Drag and lift induced initiation of motion.

The resulting curves for boundary Reynolds numbers below 23.2 have not changed, but the curves for boundary Reynolds numbers above 23.2 have lowered to a level of about 0.058 for rolling and 0.052 for sliding for very large boundary Reynolds numbers. This implies that sliding will also be the main mechanism for the initiation of motion when lift is included in the model. Comparing the values of 0.052 for sliding and 0.058 for rolling with the value of 0.0726 for pure lift, gives the conclusion that pure lift will not play an important role in the initiation of motion for an exposure level of 0.5, independent of the choice of the lift coefficient, since the lift coefficient is involved in all 3 mechanisms. The curve found for sliding matches the data, although it is high for large boundary Reynolds numbers, but then some of the experiments were carried out in sand where a different drag coefficient should be used as will be shown later. Compared with Shields (1936) and many other researchers, a value of 0.052 for large boundary Reynolds numbers is in the range of what should be expected.

3.4.10. Turbulence.

Turbulence describes the stochastic non-deterministic velocity fluctuations in a flow and although coherent structures exist in the occurrence of turbulence, turbulence has no long term memory. The implication of this is that turbulence cannot be described by a velocity profile, but instead it can be described by statistical properties. In general it is described by the turbulence intensity of the horizontal and vertical velocity and the intensity of the Reynolds stress. These intensities reflect the so called r.m.s. (root mean square) values of the velocity fluctuations. Assuming the velocity fluctuations are according to a normal or Gaussian distribution, the time and surface averaged velocity profiles represent the mean value of the distribution, as used in equations (2-53) and (2-55), while the standard deviation is represented by the r.m.s. value, also called the first moment of the distribution. The second moment and third moment correspond to two times and three times the r.m.s. value. The probability of having an instantaneous velocity higher than the standard deviation in the direction of the mean velocity is 14.9%, for the second moment this is 2.3% and for the third moment 0.13%. Wiberg & Smith (1987A) reduce the height of the viscous sub layer to 60%, resulting in an increase of 1/0.6=1.66 of the velocity in the viscous sub layer. Assuming a turbulence intensity of $\mathbf{0.3 \cdot y^+ \cdot u_*}$ (Nezu & Nakagawa, 1993) and a mean velocity of $\mathbf{y^+ \cdot u_*}$, implicitly this means adding 2.2 times the turbulence intensity to the mean velocity. Since Wiberg & Smith only apply this for low boundary Reynolds numbers where the particles are small with regard to the height of the viscous sub layer, implicitly this means adding a turbulence effect to small boundary Reynolds numbers (smooth boundaries) and not to large boundary Reynolds numbers (rough boundaries). Hofland (2005) in his PhD thesis states that fluctuations created by smaller eddies are negligible for larger particles due to phase cancellations when

integrated over the surface of a stone. Zanke (2001) and later Luckner (2002) apply turbulent velocity fluctuations both for small and large boundary Reynolds numbers and add 1.8 times the turbulence intensity to the mean velocity. Nezu & Nakagawa (1977) and (1993) and Nezu & Rodi (1986) found the following relation for the turbulence intensity parallel to the wall.

$$\frac{u_{r.m.s.}}{u_*} = 0.3 \cdot y^+ \cdot e^{-\frac{y^+}{10}} + 2.26 \cdot e^{-\frac{y}{h}} \cdot \left(1 - e^{-\frac{y^+}{10}}\right) \qquad \textbf{(3-44)}$$

The asymptotic value of the ratio between the turbulence intensity and the time and surface averaged velocity is 0.3. Measurements of this ratio, carried out by Eckelman (Hinze, 1975) on smooth walls as a function of the distance to the wall y^+, show a small increase near the wall to a value of 0.38 at $y^+ = 4$. Approaching the wall further shows a decrease to a value of 0.24, but the measurements do not contradict the assumption of having a ratio at the wall of zero. Kim, Moin and Moser (1987) confirm these findings, but state that additional measurements show a finite value at the wall, although the measurements in their paper do not contradict a value of zero. Zanke (2003) assumes a ratio of zero at the wall and achieves this by shifting the time averaged velocity with respect to the distance to the wall. In fact implicitly this means that the virtual bed level for the time averaged velocity (which is chosen at $0.2 \cdot d$ below the top of the spheres in this paper) is located lower than the virtual bed level for the turbulence intensity. Considering that the measurements of Eckelman and later Kim, Moin & Moser were carried out on a smooth wall where the wall is the virtual bed level, while here we consider a bed of grains or spheres where a virtual bed level has to be defined, resulting in a correct drag force on the spheres, there is no reason why the two virtual bed levels should be the same. The solution of Zanke, choosing two different virtual bed levels is one way of solving this problem. One can also choose one virtual bed level for both, the time averaged velocity and the turbulence intensity, but consider that below the top of the spheres, the turbulence intensity is decreased, due to the shadow effect of the spheres. Assuming the turbulence intensity to be zero at the virtual bed level and increasing proportional to the square of the distance to the wall, very close to the wall between the grains, and proportional to the distance to the wall above the grains, this can be represented with the following equation:

$$\frac{u'_{r.m.s.}}{u_*} = \frac{u_{r.m.s.}}{u_*} \cdot \left(1 - e^{-y^+}\right) \qquad \textbf{(3-45)}$$

Another reason for assuming a ratio of zero at the virtual bed level is the fact that the asymptotic value found for the Shields curve for the boundary Reynolds number approaching zero matches the measurements (see Figure 3-7 and Figure 3-10). Any ratio larger than zero would lower the curves found. Figure 3-11C shows the turbulence intensity according to equation (3-44), while Figure 3-11A shows the turbulence intensity very close to the wall. Figure 3-11B shows the difference between equation (3-44) and applying damping on the turbulence intensity very close to the wall according to equation (3-45). The turbulence intensity profile according to equation (3-45) does not contradict the findings of Nezu and Nakagawa (1993), Eckelman (Hinze, 1975) and Kim, Moin & Moser (1987) and matches the findings of Zanke (2003). Now it is the question how many times the standard deviation of the turbulence intensity should be used. Wiberg & Smith (1987A) implicitly used a factor 2.2 and Zanke (2003) used a factor 1.8 explicitly. Since we consider the initiation of motion, particles or spheres will start to entrain if there is one moment when the condition for entrainment is satisfied. On the other hand the Shields curve falls somewhere between critical and general transport, meaning that already many particles at many locations entrain. A factor of 3 will be chosen here, meaning that the probability of having a higher instantaneous velocity is only 0.13%, so about 1 out of 1000 occurrences of turbulent eddies. The factor n in equation (3-46), the turbulence intensity factor, is chosen 3.

$$\frac{u'_{n \cdot r.m.s.}}{u_*} = n \cdot \frac{u'_{r.m.s.}}{u_*} \qquad \textbf{(3-46)}$$

The resulting turbulence intensity profile should not be interpreted as a velocity distribution, since it describes the intensity of stochastic turbulent velocity fluctuations. This means that the influence of these fluctuations on the drag force can be derived by integrating the fluctuations over the height of a particle and in fact this should be added to the mean velocity and then the surface averaged value of the square of the total velocity should be determined. Taking the square root of this velocity and deducting the time averaged velocity gives the contribution of the turbulence. Since at one location the turbulent velocity fluctuations will be positive, while at the same time at other locations they will be negative, the probability that at one moment in time the turbulent velocity fluctuations over the height of the particle are unidirectional in the direction of the time averaged velocity, is almost

zero. For very small particles having a diameter smaller than or equal to the size of the small turbulent eddies, this may still be the case, but with increasing diameter the influence of the eddies will decrease due to the fact that they cancel each other out. For very large particles the influence of this turbulence will reduce to zero. It is proposed to name this effect the probability of simultaneous occurrence effect and the factor determining the turbulent velocity that should be added to the time averaged velocity, the factor of simultaneous occurrence. The point of action of the resulting surface averaged square of the velocity is assumed not to change, although there is no reason for that. With the height $\mathbf{y^+ = E \cdot Re_*}$ at the top of a particle with exposure level **E,** equation (3-47) is proposed for the factor of simultaneous occurrence and this is shown in Figure 3-11D. The resulting effective velocity profile is shown in Figure 3-11C and Figure 3-11A and used to calculate the resulting Shields curve as shown in Figure 3-12.

$$\frac{u_{eff}}{u_*} = \frac{u'_{n\cdot r.m.s.}}{u_*} \cdot e^{-\left(\frac{y^+}{10}\right)^2} \qquad \textbf{(3-47)}$$

From Figure 3-12 it can be concluded that the resulting curve matches the measurements very well for sliding, while the curve for rolling still overestimates the values of the Shields parameter. The transition point for the boundary Reynolds number is at 23.2, because the laminar regime extends to the point where the top of a grain reaches the thickness of the viscous sub layer. The two regions, laminar and turbulent do not connect very well, due to different physics and different conditions. In the laminar region drag and turbulence determine the values and the shape of the curves, while drag and lift determine this in the turbulent region. It should be noted here that having a smooth or a rough wall, is not the same as having laminar or turbulent flow around a particle. Smooth or rough depends on the relative roughness of the wall and this is represented by the boundary Reynolds number, which is equal to the roughness Reynolds number if the roughness is represented by the particle diameter, while laminar or turbulent flow is determined by the height of the particle exposed to the flow in relation to the height of the viscous sub layer.

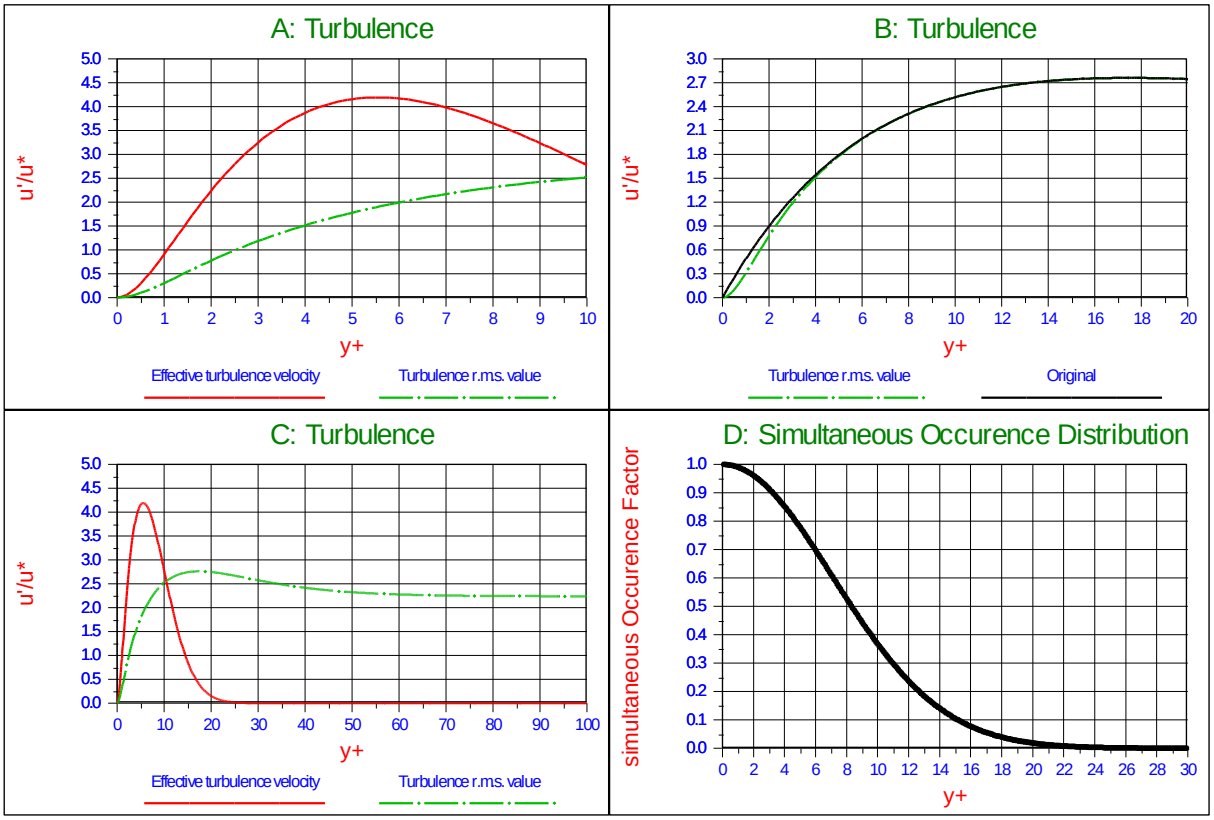

Figure 3-11: The contribution of turbulence to the velocity.

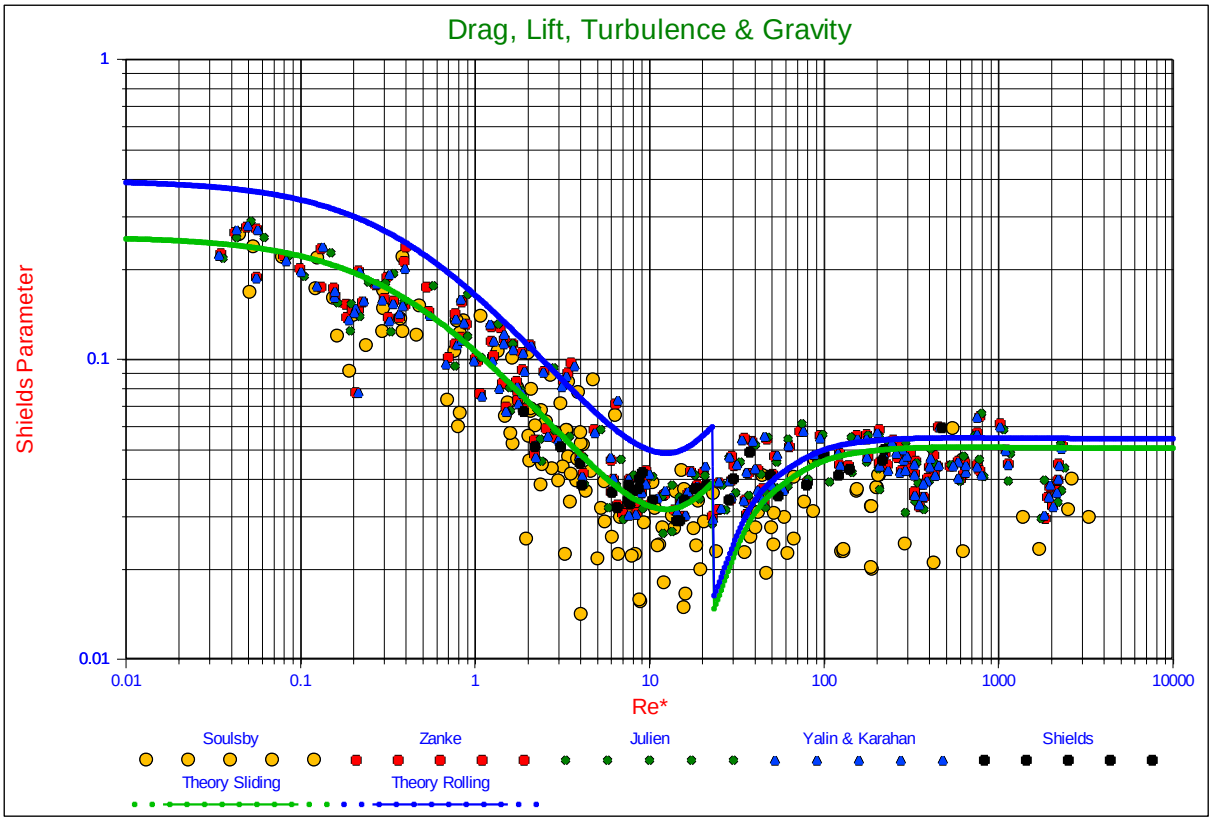

Figure 3-12: Drag, lift and turbulence induced initiation of motion.

3.4.11. The Transition Zone.

The transition zone covers the transition from a laminar regime to a turbulent regime. This does not just involve the velocity profile. In the laminar regime, $y^+ < 5$, the velocity profile is considered to be linear, but also the influence of small turbulent eddies is considerable, while in the turbulent regime, $y^+ > 70$, the velocity profile is logaritmic and the lift force has a considerable influence. If we would carry out an interpolation between the linear and logaritmic velocity profiles only, like Wiberg & Smith (1987) and others did, we would neglect the fact that in the laminar regime we have the influence of snall turbulent eddies, while in the turbulent regime they are phased out, and in the turbulent regime we have the lift force, while in the laminar regime this can be neglected. Also the point of action of the drag force changes considerably going from laminar to turbulent. So the interpolation has to be carried out on the Shields parameter itself, in order to take into account all the parameters that play a role. Since the Shields diagram is drawn in double logaritmic coordinates, the interpolation is carried out the following way. First the distance to the wall as a function of the coordinate on the horizontal axis is determined according to:

$$\xi = y^+ = \frac{u_* \cdot E \cdot d}{\nu} = E \cdot Re_* \qquad \textbf{(3-48)}$$

A straight line in the double logarithmic diagram can be represented by:

$$\ln(\theta) = A + \ln(\xi) \cdot \left[\frac{\partial \ln(\theta)}{\partial \ln(\xi)}\right] \qquad \textbf{(3-49)}$$

A non dimensional distance of 5 is chosen as the limit of pure laminar flow in the viscous sub layer. At higher values there is a deviation of the linear velocity profile. The derevative of the Shields parameter with respect to the distance to the wall in the laminar region is:

$$\left[\frac{\partial \ln(\theta)}{\partial \ln(\xi)}\right]_{Lam} = \frac{\ln(\theta_5) - \ln(\theta_{5-\Delta\xi})}{\ln(5) - \ln(5-\Delta\xi)} \qquad \textbf{(3-50)}$$

Now the constant A can be determined according to:

$$A_{Lam} = \ln(\theta_5) - \left[\frac{\partial \ln(\theta)}{\partial \ln(\xi)}\right]_{Lam} \cdot \ln(5) \qquad (3\text{-}51)$$

This results in the equation for the Shields parameter given by a straight line going to the right at a non dimensional distance from the wall above 5.

$$\ln(\theta_{Lam}) = A_{Lam} + \ln(\xi) \cdot \left[\frac{\partial \ln(\theta)}{\partial \ln(\xi)}\right]_{Lam} \qquad (3\text{-}52)$$

For the turbulent region the same procedure is applied, but at a non dimensional distance from the wall of 70. The derevative of the Shields parameter with respect to the distance to the wall in the laminar region is:

$$\left[\frac{\partial \ln(\theta)}{\partial \ln(\xi)}\right]_{Turb} = \frac{\ln(\theta_{70}) - \ln(\theta_{70+\Delta\xi})}{\ln(70) - \ln(70+\Delta\xi)} \qquad (3\text{-}53)$$

Now the constant A can be determined according to:

$$A_{Turb} = \ln(\theta_{70}) - \left[\frac{\partial \ln(\theta)}{\partial \ln(\xi)}\right]_{Turb} \cdot \ln(70) \qquad (3\text{-}54)$$

This results in the equation for the Shields parameter according to a straight line going to the right at a non dimensional distance to the wall below 70.

$$\ln(\theta_{Turb}) = A_{Turb} + \ln(\xi) \cdot \left[\frac{\partial \ln(\theta)}{\partial \ln(\xi)}\right]_{Turb} \qquad (3\text{-}55)$$

The location in between the non dimensional distances to the wall of 5 and 70 is determined logaritmically according to:

$$Q = \frac{\ln(\xi) - \ln(5)}{\ln(70) - \ln(5)} \qquad (3\text{-}56)$$

So at 5 the value of **Q** is zero and at 70 the value is one. To ensure a smooth transition between the laminar and turbulent region, a sine shaped probability is introduced, giving a probability of one for Q at a non dimensional distance of 5 and zero at 70, according to:

$$P = 1 - \frac{\left(1 + \sin\left(\frac{\pi}{2} \cdot (2 * Q - 1)\right)\right)}{2} \qquad (3\text{-}57)$$

Now the values of the Shields parameter can be determined in the transition zone, based on the values and the direction of the curves found in the transition points at the non dimensional distances to the wall of 5 and 70. It should be noted that for an exposure level of 0.5, this is at values of the boundary Reynolds number of 10 and 140.

$$\theta(\xi) = Exp\left(\left(A_{Lam} + \ln(\xi) \cdot \left[\frac{\partial \ln(\theta)}{\partial \ln(\xi)}\right]_{Lam}\right) \cdot P + \left(A_{Turb} + \ln(\xi) \cdot \left[\frac{\partial \ln(\theta)}{\partial \ln(\xi)}\right]_{Turb}\right) \cdot (1 - P)\right) \qquad (3\text{-}58)$$

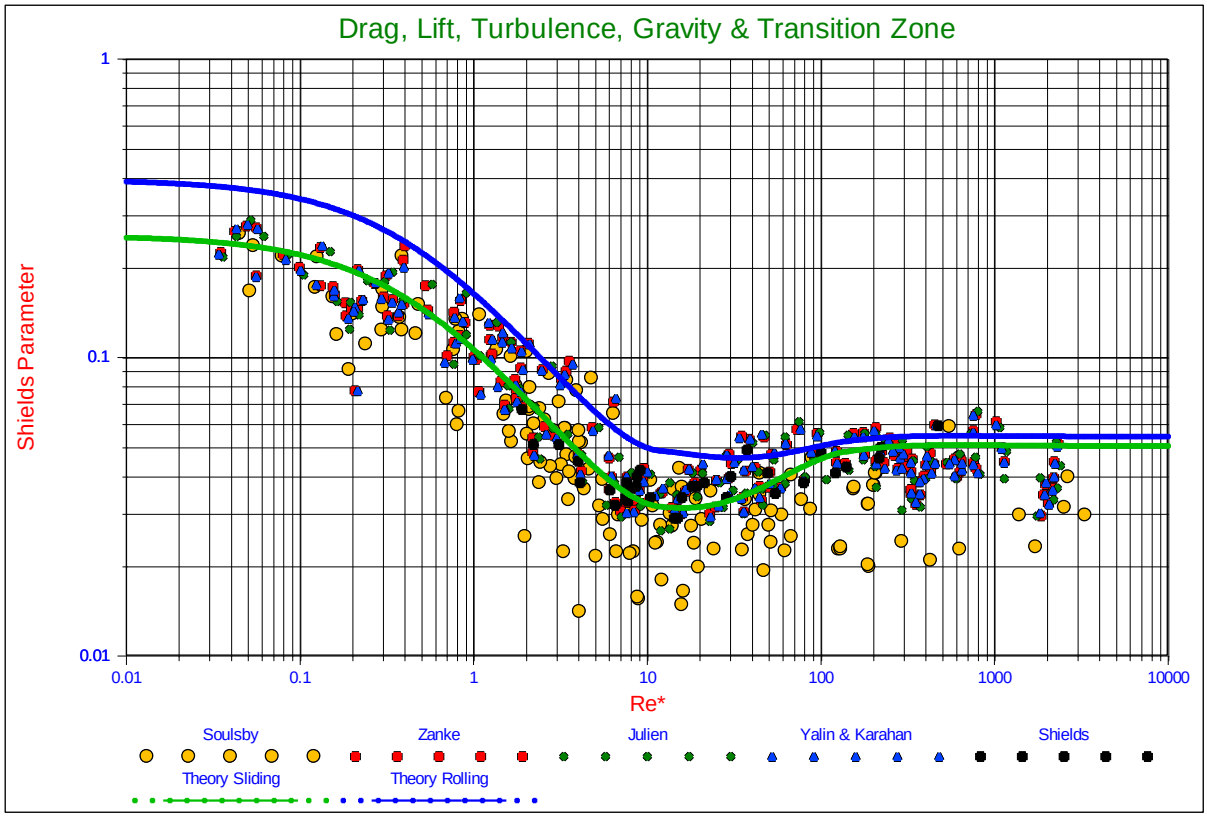

Figure 3-13: Drag, lift and turbulence induced initiation of motion with transition interpolation.

The resulting curves for sliding and rolling are shown in Figure 3-13. The curve for sliding is still the lowest of the two curves and matches the data very well. The difference between sliding and rolling is small in the turbulent region and bigger in the laminar region. The main mode of entrainment is sliding, which makes sense, since many particles at many locations are entrained. Sliding seems to be the mechanism for making the whole top layer starting to move, while rolling is much more the mechanism of individual particles.

3.5. Conclusions and Discussion.

A model to explain the Shields curve has been developed, based on realistic values of the properties involved. The model correlates well with the original data of Shields (1936) (see Figure 3-1), the data collected by Yalin & Karahan (1979) and the data of others. Sliding, rolling and lifting are considered as the mechanism for entrainment, where sliding correlated the best with the data. Rolling gives higher values than sliding for the Shields parameter, while pure lift only occurs in the turbulent region at even higher values of the Shields parameter than rolling. Since sliding correlates the best and the fact that the original Shields data match critical to general transport, meaning that many particles at many locations are entrained, the main mechanism is sliding. Rolling and lifting are much more mechanisms of individual particles, while sliding may mobilize the whole top layer of the particles. Rolling by pivoting can only occur if a pivot point exists, but when most particles in the top layer start to move, there often is no next particle, creating a pivot point. It can be expected however that particles having a higher exposure level than the 0.5 considered, will start to roll at lower values of the Shields parameter then predicted with the model.
Some new concepts have been introduced, comparing the model developed with already existing models. First of all the definition of the exposure and protrusion level in relation with the flow field and the use of the acting velocity and lever arm. The acting velocity and lever arm are not estimated, but determined based on taking the square root of the surface averaged square of the velocity integrated over the cross section of the particle exposed to the flow. It is surprising that previous researchers choose an average velocity or surface averaged velocity, since we are dealing with forces. To find the acting point of a stress or pressure, the stress or pressure has to be integrated over the cross section exposed to the flow in order to determine the acting point and the effective value. The introduction of the influence of turbulence is not new, but the introduction of the effective turbulence influence, based on the factor of simultaneous occurrence is. Also here, it is not about a velocity distribution or turbulence intensity distribution, but it is about the probability of the resulting force on a particle taking into account the phase cancellations of the small eddies. The original turbulence intensity profile as proposed by Nezu & Nakagawa (1993) has been modified slightly, so not only the turbulence intensity at the virtual bed is zero, but also the derivative with respect to the distance to the wall. The laminar region is dominated by drag and small eddy turbulence, while the turbulent region is dominated by drag and lift. A transition zone is chosen for non dimensional particle exposure heights from 5 to 70 and a sophisticated interpolation method is used.
Finally, the virtual bed level is chosen at $\mathbf{0.2 \cdot d}$ below to top of the bed. In literature different values are used for the virtual bed level. Van Rijn (1984) and later Dey (1999) for example used $\mathbf{0.25 \cdot d}$. To interpret the value of the virtual bed level we have to consider that it is a value used to justify the velocity profile above the bed. Most probably, the velocity profile between the top of the grains will not follow the theoretical velocity profile, but most probably there will already be velocity at lower levels than the assumed virtual bed level. This implies that at very low exposure levels, resulting in negative protrusion levels, the velocity distribution should be corrected with respect to the theoretical profile. This also implies that the virtual bed levels for the time averaged velocities and the turbulence intensity do not necessarily have to be the same, justifying the modified turbulence intensity, but also the assumptions made by Zanke (2003). The fact that the model developed correlates very well with the data for very common values for the different properties, including the virtual bed level, proves that the model gives a good description of reality, without having the presumption of being reality.

3.6. Nomenclature.

A	Surface or cross section	m^2
$\mathbf{A_{Lam}}$	Interpolation constant for the laminar region	-
$\mathbf{A_{Turb}}$	Interpolation constant for the turbulent region	-
$\mathbf{C_D}$	Drag coefficient	-
$\mathbf{C_L}$	Lift coefficient	-
d	Sphere, particle or grain diameter	m
$\mathbf{D_*}$	The Bonneville parameter or non dimensional grain diameter	-
E	Exposure level	-
$\mathbf{f_D}$,$\mathbf{f_{Drag}}$	Fraction of cross section exposed to drag	-
$\mathbf{f_L}$,$\mathbf{f_{Lift}}$	Fraction of top surface exposed to lift	-
$\mathbf{F_D}$	Drag force	N
$\mathbf{F_L}$	Lift force	N
$\mathbf{F_w}$	Weight of a particle	N
g	Gravitational constant	9.81 m/sec^2
h	Thickness of the layer of water	m
$\mathbf{k_s}$	Roughness often chosen equal to the particle diameter	m
$\mathbf{k_s^+}$	The non dimensional roughness or roughness Reynolds number	-
ℓ	The point of action of the drag force	-
ℓ	Mixing length	m
$\ell_{\mathbf{Drag}}$	Drag point of action	-
$\ell_{\mathbf{Lift}}$	Lift point of action	-
$\ell_{\mathbf{Lever-D}}$	Additional lever arm for drag	-
$\ell_{\mathbf{Lever-L}}$	Additional lever arm for lift	-
n	Turbulence intensity factor	-
P	Probability used in interpolation	-
p/d	Relative protrusion level	-
Q	Factor used in interpolation	-
R	Radius of sphere, particle or grain	m
$\mathbf{R_d}$	The relative submerged specific density	-
$\mathbf{Re_D}$	The particle drag Reynolds number	-
$\mathbf{Re_*}$	Boundary Reynolds number	-
$\mathbf{Re_p}$	The particle Reynolds number	-
$\mathbf{S_*}$	The Grant & Madsen parameter	-
u	Time and surface averaged velocity	m/sec
$\mathbf{u_*}$	Friction velocity	m/sec
$\mathbf{u^+}$	Non dimensional time and surface averaged velocity	-
$\mathbf{u_{r.m.s.}}$	Turbulence intensity	m/sec
$\mathbf{u'_{r.m.s.}}$	Modified turbulence intensity	m/sec
$\mathbf{u'_{n\cdot r.m.s.}}$	The n^{th} moment of the modified turbulence intensity	m/sec
$\mathbf{u_{eff.}}$	The effective modified turbulence intensity	m/sec
$\mathbf{u^+_{r.m.s.}}$	Non dimensional turbulence intensity	-
$\mathbf{u^+_{total}}$	Non dimensional total velocity	-
V	Volume	m^3
y	Distance to the wall or virtual bed level	m

y_0	Integration constant	m
y^+	Non dimensional distance to the wall (Reynolds number)	-
α	The velocity factor at a certain exposure level	-
δ_v	Thickness of the viscous sub layer	m
δ_v^+	The non dimensional thickness of the viscous sub layer	11.6
κ	Von Karman constant	0.412
ρ	Fluid density	kg/m^3
ρ_f	Fluid density	kg/m^3
ρ_s	Solids density	kg/m^3
ρ_w	The density of water or fluids	kg/m^3
ρ_q	The density of quarts or solids	kg/m^3
ϕ	Internal friction angle/angle of repose	°
ϕ_0	The Coulomb friction angle quarts-quarts	°
ϕ_0	Pivot angle in Wiberg & Smith (1987A)	°
ϕ_{Roll}	Friction angle for rolling resistance	°
Ψ	The dilatation angle	°
Ψ	The pivot angle	°
θ	The Shields parameter or non dimensional shear stress	-
θ_5	The Shields parameter for $\xi = 5$	-
θ_{70}	The Shields parameter for $\xi = 70$	-
τ	Total shear stress	Pa
τ_t	Turbulent shear stress	Pa
τ_v	Viscous shear stress	Pa
τ_b	Bed shear stress	Pa
ν	Kinematic viscosity	m^2/sec
μ	Friction coefficient usually the tangent of the internal friction angle	-
μ_{Roll}	Equivalent friction coefficient for rolling	-
ξ	The non dimensional distance of the top of the sphere to the virtual bed level	-

Chapter 4: Constructing the Shields Curve, Part B.

4.1. Sensitivity Analysis, Exposure & Protrusion Levels, Settling Velocity, Shear Stress & Friction Velocity, Erosion Flux and Laminar Main Flow.

The model developed in Part A is verified and validated from 6 points of view.
1. The traditional Shields diagram, a sensitivity analysis
2. Exposure and protrusion levels
3. Shear velocity and shear stress
4. The ratio between the friction velocity and the terminal settling velocity
5. Stages of entrainment
6. Laminar main flow

It is proposed to distinguish 4 different Shields curves:
1. The Shields curve based on spheres in a turbulent main flow.
2. The Shields curve based on natural sands and gravels in a turbulent main flow.
3. The Shields curve in a laminar main flow for spheres.
4. The Shields curve in a laminar main flow for natural sand and gravels.

The general conclusions of this research are:
- The basic Shields curve can be determined by applying the sliding entrainment mechanism, with a friction angle of 30°, an exposure level of 0.5 (protrusion level of 0.3), a turbulence intensity factor of n=3, a lift coefficient of 0.415 and the drag coefficient of spheres.
- Using a reasonable bandwidth for the properties, like friction angle, lift coefficient and turbulence intensity, most of the scatter in the data found, can be explained.
- For natural sands and gravels a modified drag coefficient should be applied, based on the angularity of the particles.
- In the laminar region entrainment is dominated by drag and turbulence, while in the turbulent region this is dominated by drag and lift.
- Up to an exposure level of 0.6 sliding is the main entrainment mechanism, while for higher exposure levels rolling will occur.
- Laminar and turbulent main flow result in two different entrainment curves, based on the presence of turbulence. For laminar main flow a turbulence intensity factor of 0.5 has been found to correlate well with the measurements.
- The model developed correlates well with datasets of many independent researchers.

In Part A, a model for the entrainment of particles as a result of fluid (or air) flow over a bed of particles has been developed. The model distinguishes sliding, rolling and lifting as the mechanisms of entrainment. Sliding is a mechanism that occurs when many particles are starting to move and it is based on the global soil mechanical parameter of internal friction. Both rolling and lifting are mechanisms of individual particles and they are based on local parameters such as the pivot angle and the exposure and protrusion rate. Equations (4-1), (4-2) and (4-3) give the Shields parameter for these 3 mechanisms.

4.1.1. Sliding.

$$\theta_{sliding} = \frac{u_*^2}{R_d \cdot g \cdot d} = \frac{4}{3} \cdot \frac{1}{\alpha^2} \cdot \frac{\mu}{\ell_{Drag}^2 \cdot f_D \cdot C_D + \mu \cdot f_L \cdot C_L} \qquad (4\text{-}1)$$

4.1.2. Rolling

$$\theta_{rolling} = \frac{u_*^2}{R_d \cdot g \cdot d} = \frac{4}{3} \cdot \frac{1}{\alpha^2} \cdot \frac{\sin(\psi + \phi_{Roll})}{\ell_{Drag}^2 \cdot f_D \cdot C_D \cdot (\ell_{Lever-D} + \cos(\psi + \phi_{Roll})) + f_L \cdot C_L \cdot (\ell_{Lever-L} + \sin(\psi + \phi_{Roll}))} \qquad (4\text{-}2)$$

4.1.3. Lifting.

$$\theta_{lifting} = \frac{u_*^2}{R_d \cdot g \cdot d} = \frac{4}{3}\frac{1}{\alpha^2 \cdot C_L \cdot f_L} \tag{4-3}$$

4.1.4. Analysis.

The additional lever arm for lifting $\ell_{Lever-L} = 0$, since there is no reason to assume that the lift force does not go through the center of the particle. Now an effective friction coefficient for rolling, μ_{Roll}, can be introduced:

$$\mu_{Roll} = \frac{\sin(\psi + \phi_{Roll})}{\ell_{Lever-D} + \cos(\psi + \phi_{Roll})} \tag{4-4}$$

Substituting equation (4-4) in to equation (4-2), gives an equation for the Shields parameter for rolling, very similar to the equation for sliding. For very small values of the surface coefficient f_D at low exposure and protrusion levels, both equations (4-1) and (4-5) reduce to equation (4-3), meaning that at very low exposure and protrusion levels, the three mechanisms give the same Shields parameter. Using $\phi = 30°$ for sliding and $\psi + \phi_{Roll} = 60°$ for rolling, an exposure level of $E = 0.5$ and an additional lever arm for the drag force of $\ell_{Lever-D} = 0.5$ for laminar flow and $\ell_{Lever-D} = 0.655$ for turbulent flow, results in a friction coefficient for sliding of $\mu = 0.577$, for laminar rolling of $\mu_{Roll-Lam} = 0.866$ and for turbulent rolling of $\mu_{Roll-Turb} = 0.75$. This explains why the Shields parameter found for rolling is higher than the one for sliding, where the difference is bigger in the laminar region than in the turbulent region.

$$\theta_{rolling} = \frac{u_*^2}{R_d \cdot g \cdot d} = \frac{4}{3} \cdot \frac{1}{\alpha^2} \cdot \frac{\mu_{Roll}}{\ell_{Drag}^2 \cdot f_D \cdot C_D + \mu_{Roll} \cdot f_L \cdot C_L} \tag{4-5}$$

4.1.5. Laminar Region.

For the laminar region (the viscous sub layer) the velocity profile of Reichardt (1951) is chosen. This velocity profile gives a smooth transition going from the viscous sub layer to the smooth turbulent layer.

$$u_{top}^+ = \frac{u(y_{top})}{u_*} = \frac{\ln(1 + \kappa \cdot y_{top}^+)}{\kappa} - \frac{\ln(1/9) + \ln(\kappa)}{\kappa} \cdot \left(1 - e^{-\frac{y_{top}^+}{11.6}} - \frac{y_{top}^+}{11.6} e^{-0.33 \cdot y_{top}^+} \right) \approx y_{top}^+ \tag{4-6}$$

For small values of the boundary Reynolds number and thus the height of a particle, the velocity profile can be made linear to:

$$y_{top}^+ = E \cdot Re_* = E \cdot k_s^+ \tag{4-7}$$

Adding the effective turbulent velocity to the time averaged velocity gives for the velocity function α_{Lam}:

$$\alpha_{Lam} = y_{top}^+ + u_{eff}^+(y_{top}^+) \tag{4-8}$$

4.1.6. Turbulent Region.

Particles that extend much higher into the flow will be subject to the turbulent velocity profile. This turbulent velocity profile can be the result of either a smooth boundary or a rough boundary. Normally it is assumed that for boundary Reynolds numbers less than 5 a smooth boundary exists, while for boundary Reynolds numbers larger than 70 a rough boundary exists. In between in the transition zone the probability of having a smooth boundary is:

$$P = e^{-0.95\cdot\frac{Re_*}{11.6}} = e^{-0.95\cdot\frac{k_s^+}{11.6}} \qquad (4\text{-}9)$$

This gives for the velocity function α_{Turb}:

$$\alpha_{Turb} = \frac{1}{\kappa}\cdot\ln\left(\frac{E\cdot d}{0.11\cdot\frac{\nu}{u_*}}+1\right)\cdot P + \frac{1}{\kappa}\cdot\ln\left(\frac{E\cdot d}{0.033\cdot k_s}+1\right)\cdot(1-P) \qquad (4\text{-}10)$$

The velocity profile function has been modified slightly by adding 1 to the argument of the logarithm. Effectively this means that the velocity profile starts y_0 lower, meaning that the virtual bed level is chosen y_0 lower for the turbulent region. This does not have much effect on large exposure levels (just a few percent), but it does on exposure levels of 0.1 and 0.2. Not applying this would result in to high (not realistic) shear stresses at very low exposure levels.

4.2. Sensitivity Analysis.

In the previous paragraphs a model for the determination of the Shields curve was developed, based on a number of assumptions. The exposure level was chosen as 0.5, giving a protrusion level of 0.3, assuming a virtual bed level at $0.2\cdot d$ below the top of the bed of uniform spheres. For sliding a friction angle of $\phi = 30°$ and for rolling a pivot angle of $\psi = 59°$ were chosen. The drag coefficient for spheres is applied and the lift coefficient according to $C_L = 0.423$ for the turbulent region. Finally the influence of turbulence is modelled, using 3 times the r.m.s. value of the turbulence intensity. The resulting curve, matching the data the best, is the curve for sliding. Now the question is, how sensitive this model for variations in these assumptions is.

4.2.1. The Angle of Natural Repose/The Angle of Internal Friction.

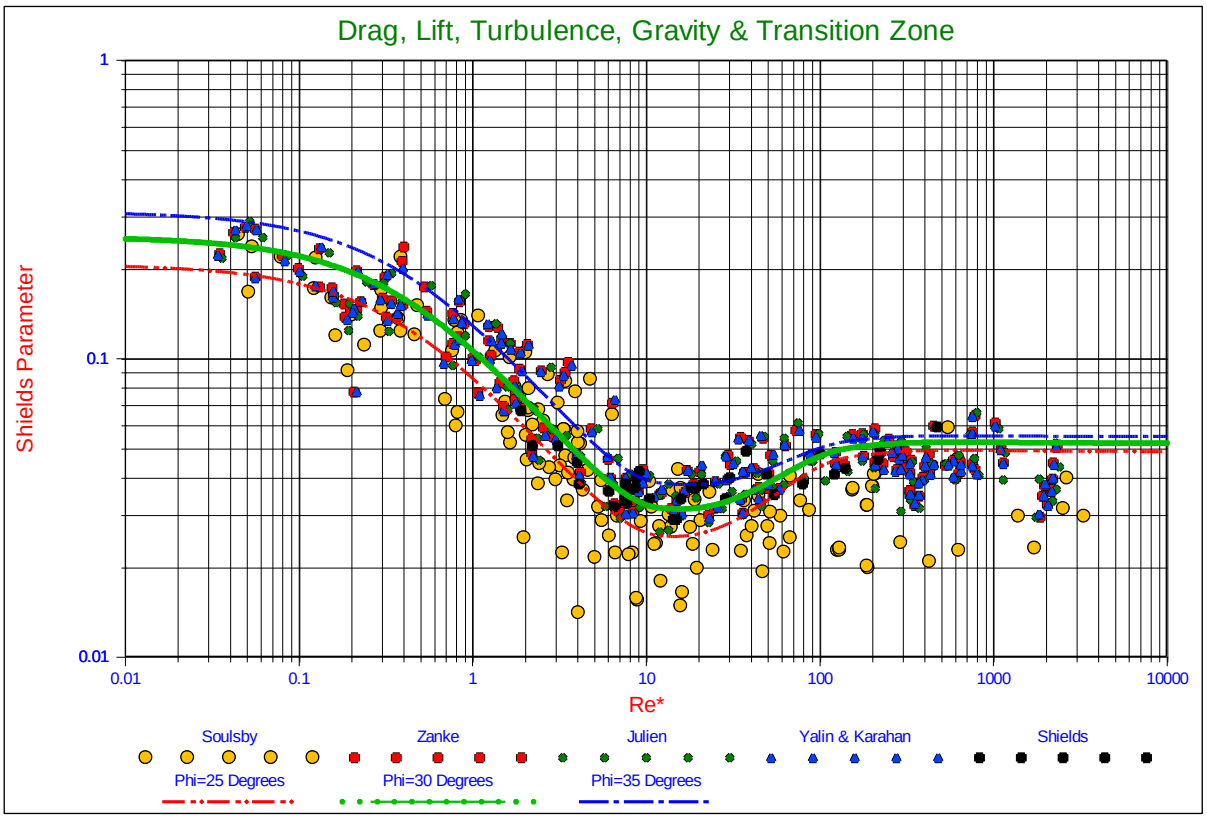

Figure 4-1: The Shields curve for sliding with friction angles of 25°, 30° and 35°.

The angle of repose/the angle of internal friction has been chosen at $\phi = 30°$, but could be a bit smaller or bigger according to Miedema (2010A), so also values of $\phi = 25°$ and $\phi = 35°$ will be applied. Figure 4-1 shows the resulting curves. From this figure it is obvious that the variation of the friction angle might explain some of the scatter in the laminar region, while the influence of this variation is very limited in the turbulent region.

4.2.2. Turbulence.

In the model an influence of 3 times the r.m.s. value of the turbulence intensity was used. The question is, if this is the best option and how sensitive is the model for the influence of turbulence. To test this also turbulence intensity factors of 0, 1, 2 and 4 times the r.m.s. value of the turbulence intensity are applied. A factor of 0 means no turbulence, so laminar main flow. The results are shown in Figure 4-2 and show that part of the scatter for boundary Reynolds numbers in the range between 1 and 20 can be explained. The relatively high values for the Shields parameter as found by Pilotti & Menduni (2001), could be explained by a different behavior of the turbulence intensity, due to the laminar flow used.

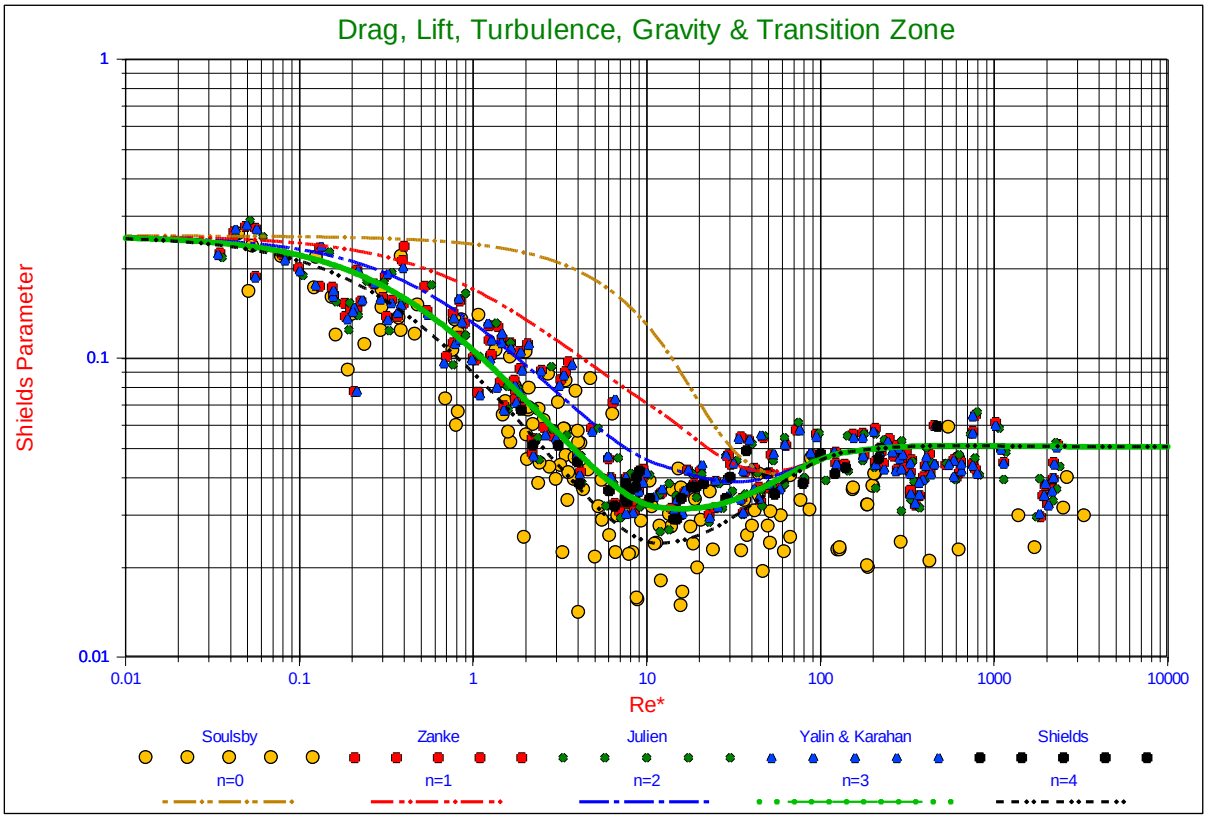

Figure 4-2: The Shields curve for sliding with different levels of turbulence.

4.2.3. The Drag and the Lift Coefficient.

The drag coefficient as known for spherical particles is used, like in the models found in literature, but it is known that non spherical particles encounter a higher drag coefficient, especially in the turbulent region. The lift coefficient is chosen at $C_L = 0.423$, but what is the influence of a smaller lift coefficient, like the factor 0.2 as used by Wiberg & Smith (1987A). To investigate this calculations are carried out with the drag coefficient for sand, according to Miedema (2010A) and a lift coefficient of $C_L = 0.3$. The results of these calculations are shown in Figure 4-3. Reduced lift may explain some scatter above the regular curve in the turbulent region, while using the drag coefficient for natural sand grains, explains a lot of the scatter below the regular curve in the turbulent region, especially since some of these data are achieved from experiments with natural sands. In the laminar region both lift and the drag coefficient have no effect, since lift is supposed to occur in the turbulent region only and the drag coefficient for spheres and natural sand grains does not differ much for very small particles.

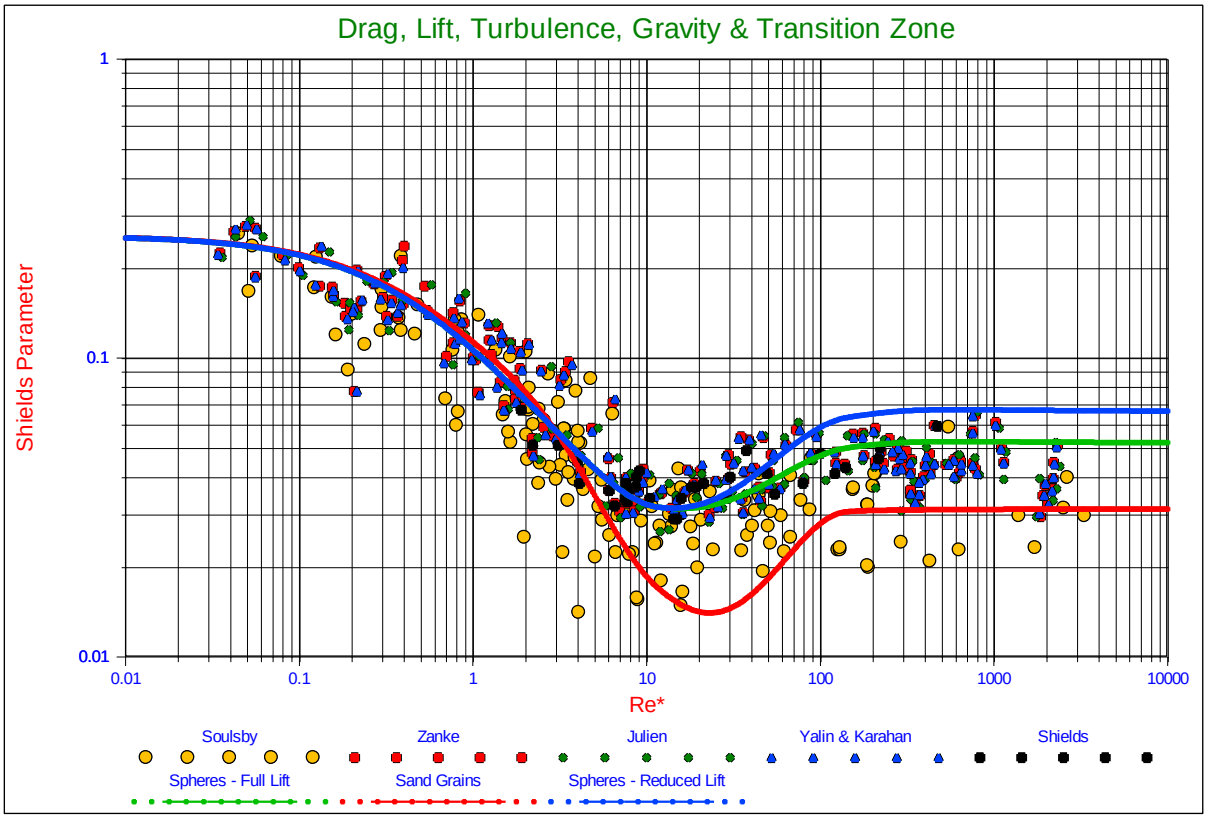

Figure 4-3: The Shields curve for spheres, sand grains and with reduced lift.

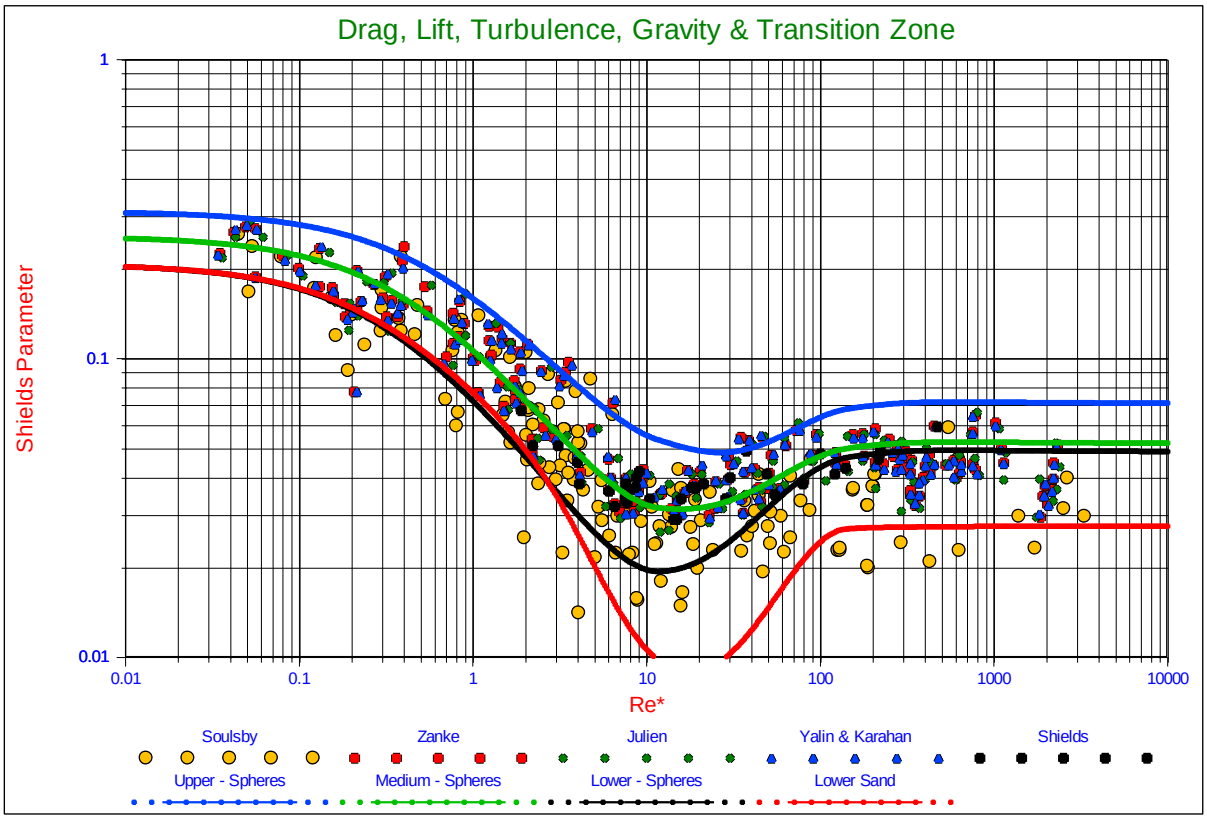

Figure 4-4: The medium (regular), lower and upper Shields curves for spheres and natural sand.

4.2.4. Lower, Medium and Upper Levels and Real Sand Particles.

From this sensitivity analysis a lower, medium (regular) and upper level for the Shields curve can be constructed. The lower level has a friction angle of $\phi = 25°$, a turbulence intensity factor of 4 and a $C_L = 0.423$. The medium or regular level has a friction angle of $\phi = 30°$, a turbulence intensity factor of 3 and a $C_L = 0.423$. The upper level has a friction angle of $\phi = 35°$, a turbulence intensity factor of 2 and a $C_L = 0.3$. As a special case the lower level is also calculated with the drag coefficient for natural sands and gravels.

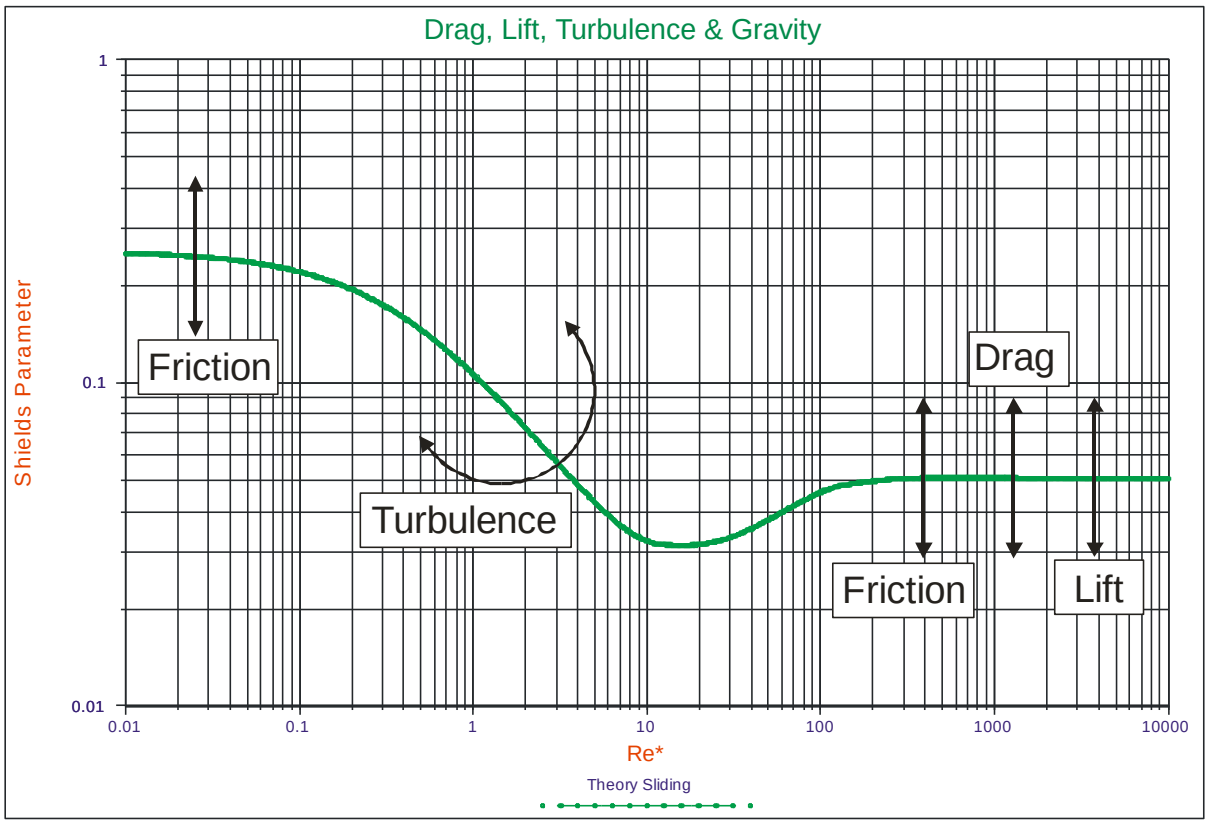

Figure 4-5: The influence of friction, drag, lift and turbulence on the shape of the Shields curve.

Figure 4-4 shows the results of these calculations. The upper level explains most of the scatter of the data above the regular or medium curve. The lower level explains most of the scatter in the laminar and transition region below the regular curve, but not in the turbulent region. However, applying the drag coefficient for natural sand grains also explains for the scatter below the regular curve in the turbulent region. Also the observation that in reality entrainment often occurs at values for the Shields parameter much lower than the original Shields curve and the proposal to take 50% for engineering purposes (Brownlie, 1981), can be explained by using the drag coefficient for natural sands and gravels. In the laminar region however the regular curve should be used up to boundary Reynolds numbers of about 5. In fact there should be two different Shields curves, one for spheres matching most of the experiments and one for natural sands and gravels using the appropriate drag coefficient.
Figure 4-5 explains for the influence of friction (or pivot angle), drag, lift and turbulence on the shape of the Shields curve. Increasing the friction coefficient will move the whole curve up, but more in the laminar region. Increasing the drag by using the drag coefficient for natural sands and gravels will move the turbulent and the transition region down. Increasing the lift will move the turbulent region down. Increasing the influence of turbulence will rotate the laminar region clockwise, while the asymptotic value for very small boundary Reynolds numbers will not change.

4.3. Exposure and Protrusion Levels.

To determine the influence of exposure and protrusion levels, exposure levels from 0.2 up to 1.2 will be investigated as is shown in Figure 4-6 and Figure 4-7. In the laminar region the virtual bed level is chosen at $\mathbf{0.2 \cdot d}$ below the top of the bed, while in the turbulent region this is corrected with $\mathbf{0.2 \cdot d + y_0 = 0.233 \cdot d}$, still giving an exposure level starting at $\mathbf{0.2 \cdot d}$ below the top of the bed, assuming the roughness $\mathbf{k_s = d}$.

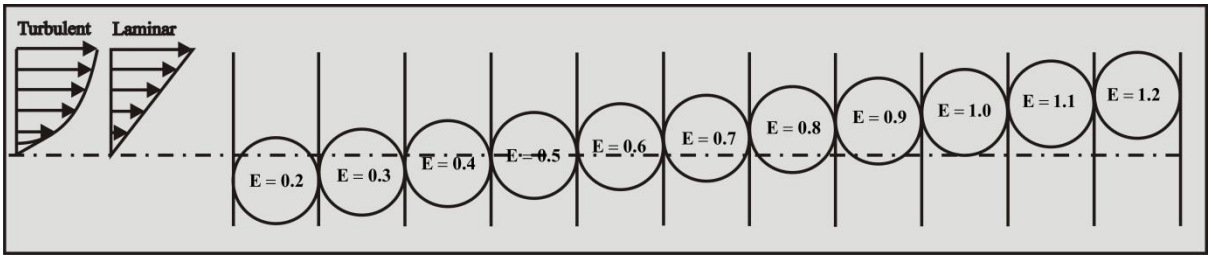

Figure 4-6: The exposure levels from 0.2 to 1.2.

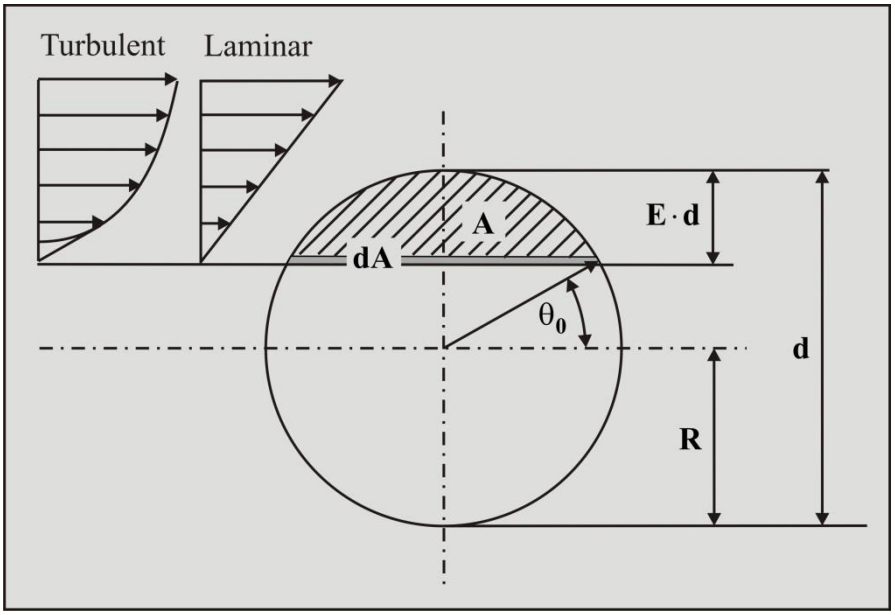

Figure 4-7: The area subjected to the flow.

To determine the cross section subjected to the flow and the effective velocity on the cross section subjected to the flow, first the relation between the exposure level and the initial angle θ_0 for integration has to be determined, this relation is:

$$\sin(\theta_0) = 1 - 2 \cdot E$$

$$\theta_0 = \arcsin(1 - 2 \cdot E) \qquad \textbf{(4-11)}$$

To determine the cross section subjected to the flow we must integrate from the initial angle θ_0 for integration to an angle of $\pi/2$ according to:

$$dA = 2 \cdot R \cdot \cos(\theta) \cdot R \cdot d\theta \cdot \cos(\theta)$$

$$A = \int_{\theta_0}^{\pi/2} 2 \cdot R^2 \cdot \cos(\theta) \cdot \cos(\theta) \cdot d\theta \qquad \textbf{(4-12)}$$

4.3.1. The Drag Surface Factor.

To determine the fraction f_{Drag} of this cross section with respect to the cross section of the whole sphere, equation (4-12) must be divided by $\pi \cdot R^2$ as is shown in equation (4-13).

$$f_{Drag} = \frac{2 \cdot R^2 \cdot \int_{\theta_0}^{\pi/2} \cos^2(\theta) \cdot d\theta}{\pi \cdot R^2} \qquad (4\text{-}13)$$

4.3.2. The Lift Surface Factor.

The lift surface factor is an empirical factor. One can imagine that the lift coefficient depends on the exposure level. At very low exposure levels, only the top of a sphere is affected by the flow and a smaller lift coefficient should be applied. At an exposure level of 0.5 the top half of the sphere is affected by the flow, but the bottom half is not. At an exposure level of 1.0 the whole sphere is surrounded by flow. Inspired by the work of Luckner (2002) the following empirical equation has been derived for the relation between the lift surface factor and the exposure level. The lift coefficient itself is chosen to be equal to the drag coefficient at high Reynolds numbers being $C_L = 0.445$.

$$f_{Lift} = 0.7125 + 0.4375 \cdot E \qquad (4\text{-}14)$$

Table 4-1: Protrusion level, surface factors and pivot angle as a function of the exposure level

E	p/d	f_{Drag}	f_{Lift}	ψ	Θ_0
0.2	0.0	0.133	0.800	90	36.89
0.3	0.1	0.252	0.844	80	23.59
0.4	0.2	0.373	0.888	68	11.54
0.5	0.3	0.500	0.932	59	00.00
0.6	0.4	0.632	0.975	49	-11.54
0.7	0.5	0.759	1.019	40	-23.59
0.8	0.6	0.867	1.062	34	-36.89
0.9	0.7	0.954	1.106	27	-53.16
1.0	0.8	1.000	1.150	20	-90.00
1.1	0.9	1.000	1.150	12	-90.00
1.2	1.0	1.000	1.150	00	-90.00

4.3.3. The Pivot Angle.

The pivot angles chosen are also inspired by the work of Luckner (2002) and corrected for the difference between exposure level and protrusion level.
The resulting values for the protrusion level (laminar), the drag surface factor, the lift surface factor, the pivot angle and the integration starting angle can be found in Table 4-1 as a function of the exposure level. For exposure levels above 1.0, the surface factors and the integration angles are chosen to be equal to the ones at an exposure level of 1.0.

4.3.4. The Drag Point of Action.

To determine exactly which velocity to use for calculating the drag force, the surface averaged drag force has to be calculated. Since the drag force depends on the square of the local velocity, the surface averaged square of the velocity has to be determined. To find the drag point of action, the square of the local velocity has to be integrated over the surface exposed to the flow, the result has to be divided by the square of the velocity at the top of the sphere and divided by the surface. Taking the square root of this gives the drag point of action as a fraction of the exposure level. Equation (4-15) gives the general equation for this, while equation (4-16) and equation (4-17) show this for laminar flow in the viscous sub layer and turbulent flow in the turbulent region.

$$\ell_{Drag} = \sqrt{\frac{\int_{\theta_0}^{\pi/2} \overline{u(y)}^2 \cdot dA}{\overline{u(y)}_{top}^2 \cdot A}} \tag{4-15}$$

$$\ell_{Drag-Lam} = \sqrt{\frac{2 \cdot R^2 \int_{\theta_0}^{\pi/2} \left(\frac{2 \cdot E - 1 + \sin(\theta)}{2}\right)^2 \cdot \cos(\theta)^2 \cdot d\theta}{E^2 \cdot 2 \cdot R^2 \cdot \int_{\theta_0}^{\pi/2} \cos^2(\theta) \cdot d\theta}} \tag{4-16}$$

$$\ell_{Drag-Turb} = \sqrt{\frac{2 \cdot R^2 \int_{\theta_0}^{\pi/2} \left(\ln\left(\frac{\left(\frac{2 \cdot E - 1 + \sin(\theta)}{2}\right)}{0.033} + 1\right)\right)^2 \cdot \cos^2(\theta) \cdot d\theta}{\left(\ln\left(\frac{E}{0.033} + 1\right)\right)^2 \cdot 2 \cdot R^2 \cdot \int_{\theta_0}^{\pi/2} \cos^2(\theta) \cdot d\theta}} \tag{4-17}$$

4.4. The Additional Lever Arms.

The additional lever arms, necessary for the pivoting mechanism, are related to the drag point of action according to equation (4-18) for laminar flow and equation (4-19) for turbulent flow. It is obvious that these additional lever arms for laminar and turbulent flow are not equal.

$$\ell_{Lever-Lam} = 1 - 2 \cdot E \cdot (1 - \ell_{Drag-Lam}) \tag{4-18}$$

$$\ell_{Lever-Turb} = 1 - 2 \cdot E \cdot (1 - \ell_{Drag-Turb}) \tag{4-19}$$

Table 4-2 gives the values of the drag point of action and the additional lever arms for laminar and turbulent flow as a function of the exposure and the protrusion level. In general, the drag point of action is located higher for turbulent flow than for laminar flow, also resulting in a larger additional lever arm.

Table 4-2: The drag point of action and the additional lever arms.

E	p/d	$\ell_{Drag-Lam}$	$\ell_{Lever-Lam}$	$\ell_{Drag-Turb}$	$\ell_{Lever-Turb}$
0.2	0.0	0.485	0.794	0.541	0.816
0.3	0.1	0.490	0.694	0.586	0.752
0.4	0.2	0.494	0.596	0.623	0.698
0.5	0.3	0.500	0.500	0.655	0.655
0.6	0.4	0.505	0.405	0.682	0.618
0.7	0.5	0.511	0.315	0.706	0.588
0.8	0.6	0.522	0.235	0.730	0.568
0.9	0.7	0.537	0.166	0.754	0.557
1.0	0.8	0.559	0.118	0.784	0.568
1.1	0.9	0.591	0.100	0.788	0.533
1.2	1.0	0.619	0.086	0.792	0.501

Table 4-3: Shields values for 3 mechanisms at different exposure levels.

E	p/d	Sliding Laminar	Sliding Turbulent	Sliding Minimum	Rolling Laminar	Rolling Turbulent	Rolling Minimum	Lift
0.1	-0.1	9.5117	0.3344	0.3344	20.4147	0.3399	0.3399	0.3462
0.2	0.0	2.4783	0.1535	0.1340	5.0364	0.1596	0.1561	0.1664
0.3	0.1	0.8634	0.0958	0.0727	1.6287	0.1025	0.0988	0.1128
0.4	0.2	0.4327	0.0674	0.0458	0.7440	0.0731	0.0677	0.0865
0.5	0.3	0.2551	0.0505	0.0314	0.3926	0.0543	0.0461	0.0706
0.6	0.4	0.1665	0.0393	0.0228	0.2253	0.0408	0.0306	0.0598
0.7	0.5	0.1172	0.0316	0.0174	0.1359	0.0305	0.0202	0.0519
0.8	0.6	0.0878	0.0262	0.0140	0.0836	0.0225	0.0133	0.0459
0.9	0.7	0.0690	0.0226	0.0117	0.0507	0.0159	0.0086	0.0412
1.0	0.8	0.0568	0.0194	0.0103	0.0287	0.0103	0.0052	0.0373
1.1	0.9	0.0488	0.0179	0.0094	0.0127	0.0058	0.0024	0.0341
1.15	0.95	0.0456	0.0173	0.0090	0.0065	0.0034	0.0013	0.0327
1.2	1.0	0.0427	0.0167	0.0086	0.0012	0.0007	0.0002	0.0313

4.5. Calculations

4.5.1. Spheres.

Based on the basic equations for sliding, rolling and lifting, the surface factors, pivot angle, the calculated values for the drag point of action, the additional lever arms and the assumptions of an angle of repose of $\phi = 30°$ and a lift coefficient $C_L = 0.445$, the values of the Shields parameter can be calculated as a function of the exposure level and the mechanism.

Table 4-3 gives these values for the laminar region, the turbulent region and the minimum in the transition region and for pure lift in the turbulent region.

In the laminar region, the Shields values for sliding are smaller than the Shields values for rolling for exposure levels smaller than 0.6. Above an exposure level of 0.6 the Shields values for rolling are smaller. In the turbulent region this transition occurs at an exposure level somewhere between 0.6 and 0.7. The Shields values for pure lifting are always bigger than sliding and rolling, but at the smallest exposure level considered of 0.1, the value is almost equal to sliding and rolling. The conclusion can be drawn here that for exposure levels up to 0.6 the main mechanism for entrainment is sliding, which will occur for many particles at many locations simultaneously, while at higher exposure levels rolling will be the main mechanism, which will occur for single particles. Figure 4-8 and Figure 4-9 show the resulting curves for exposure levels from 0.2 up to 1.2 for sliding and rolling for spheres.

Figure 4-10 shows the Shields curves for sliding for an exposure level of 0.2 up to an exposure level of 0.6 and rolling from an exposure level of 0.7 up to 1.2. Figure 4-11 shows the same set of curves, but now as a function of the non-dimensional particle diameter (the Bonneville parameter). The advantage of using the Bonneville parameter is that this diagram is explicit. There is an explicit relation between the Shields parameter and the particle diameter, while this relation is implicit in the original Shields diagram where the friction velocity is part of both the boundary Reynolds number on the horizontal axis and the Shields parameter on the vertical axis. Dividing the Bonneville parameter by about 20 will give the particle diameter in mm for quarts with a density of 2650 kg/m^3 in a fluid with a viscosity of about 10^{-6} m^2/sec.

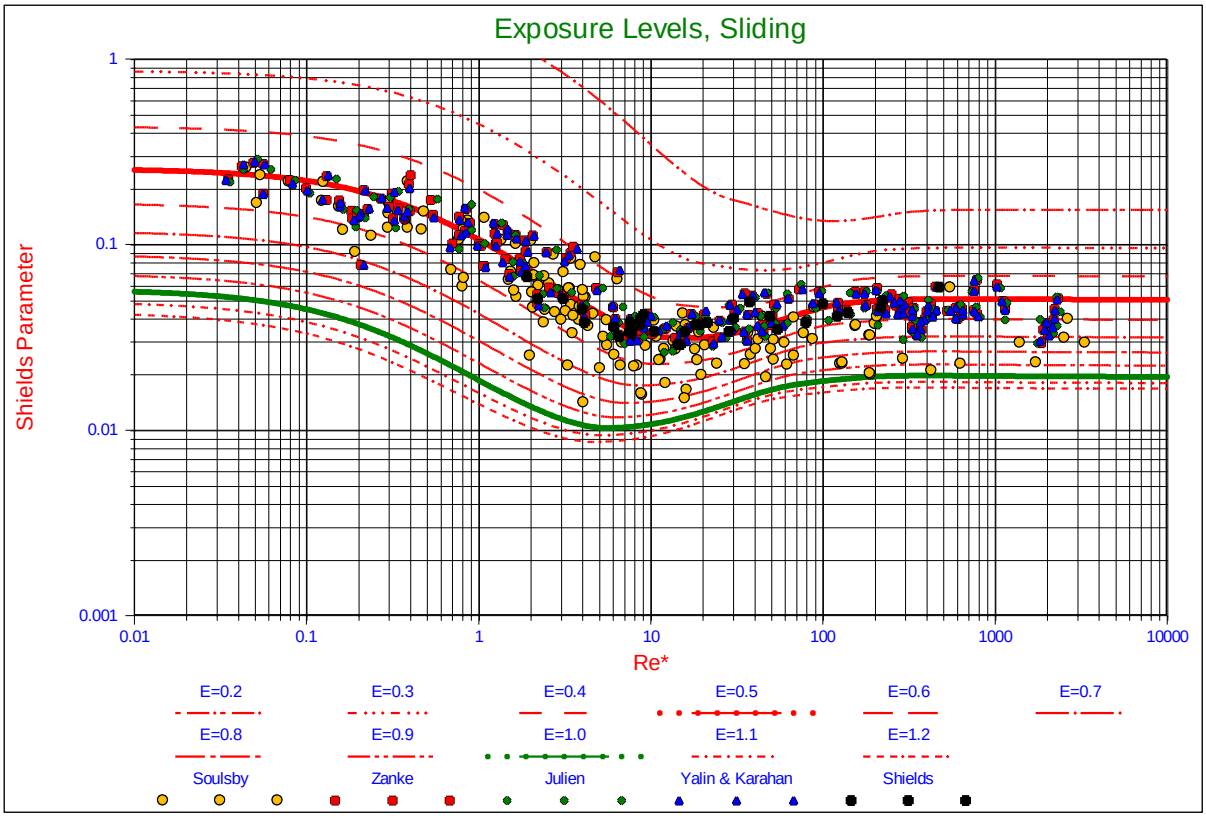

Figure 4-8: The Shields curves for the sliding mechanism.

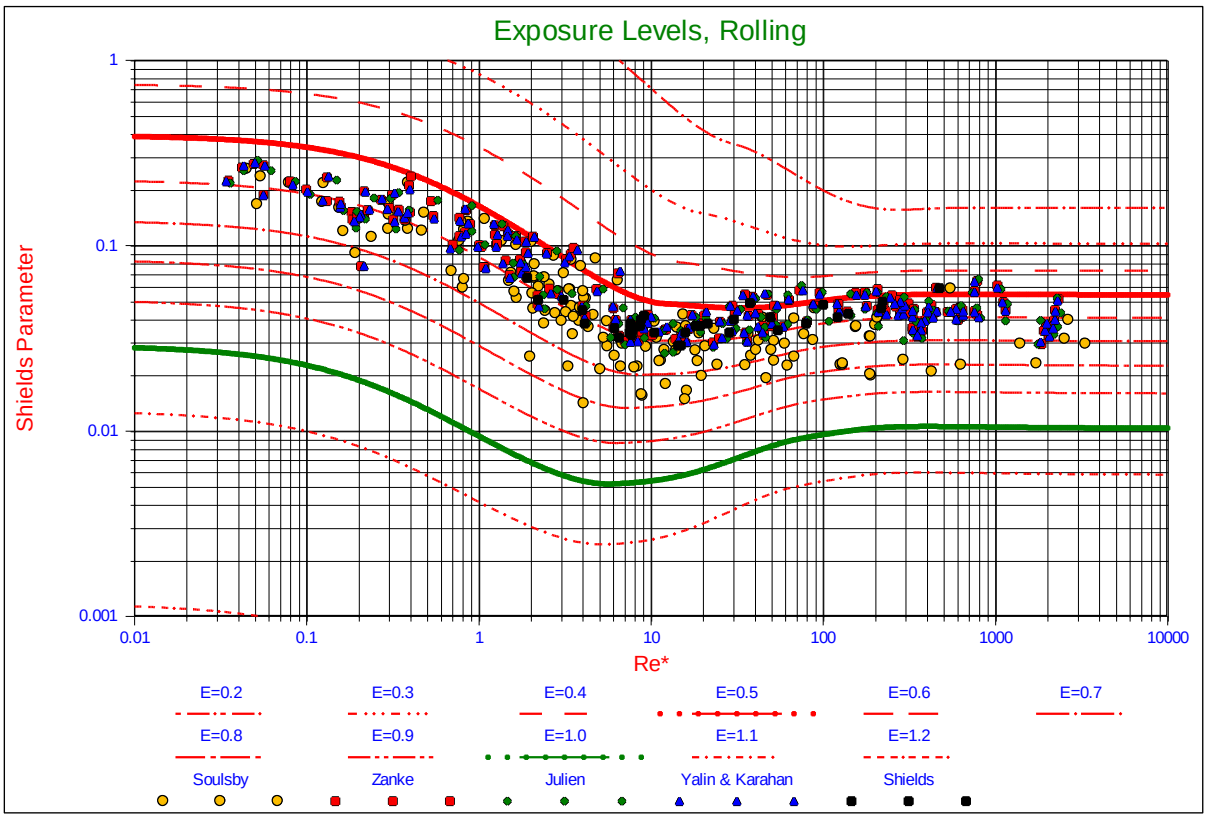

Figure 4-9: The Shields curves for the rolling mechanism.

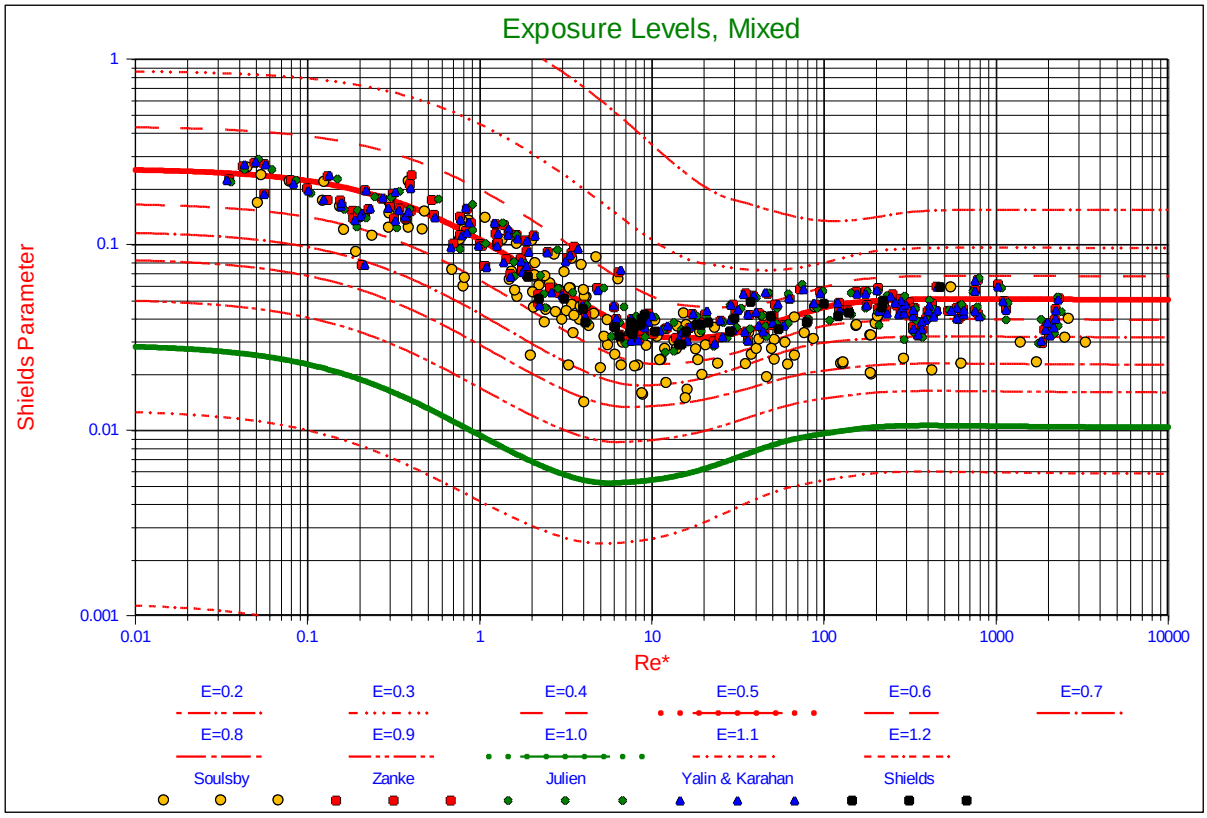

Figure 4-10: The Shields curves for sliding and rolling.

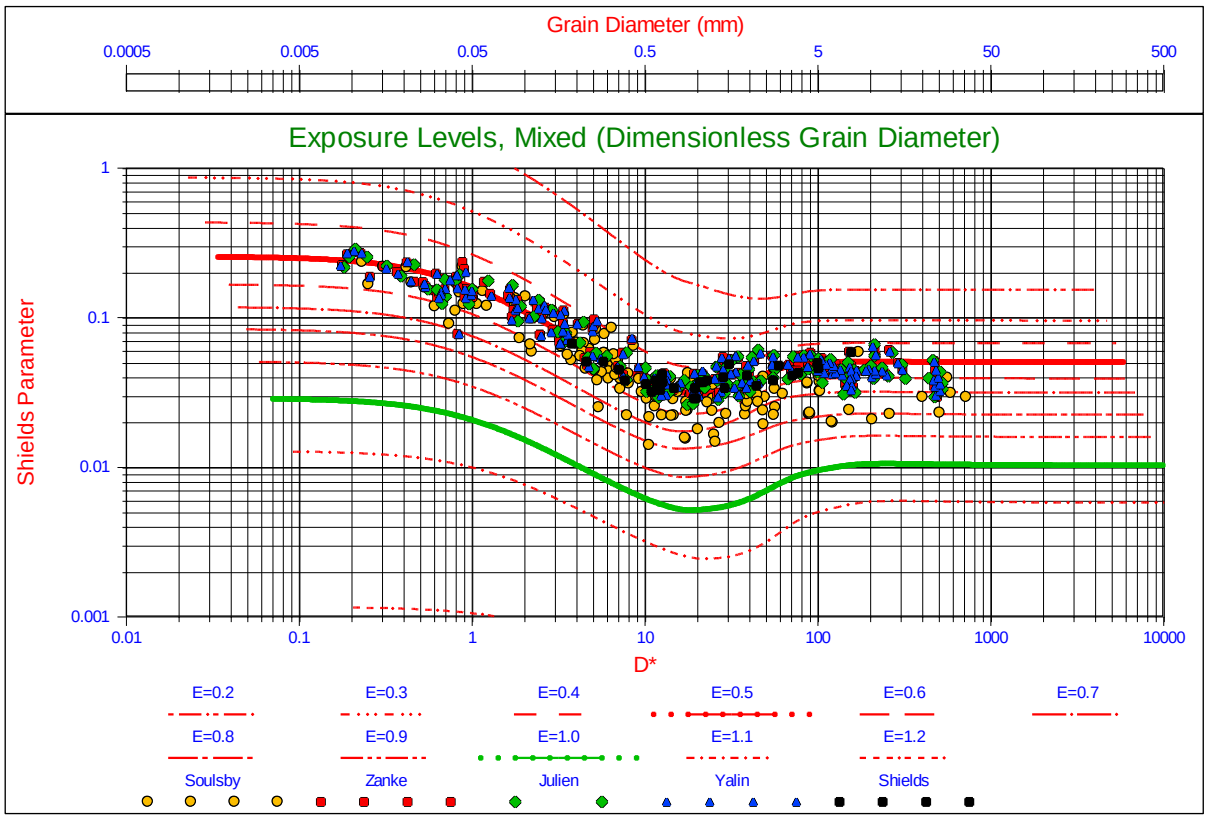

Figure 4-11: The Shields curves as a function of the Bonneville parameter.

4.5.2. Natural Sands and Gravels.

As has been described in Part A of this publication, the drag coefficient of natural sands and gravels differs from the drag coefficient of spheres. For rounded grains this difference is probably not too big, but for angular grains it is. In the laminar region at low Reynolds numbers both spheres and natural particles follow (or almost follow) the Stokes law, giving a drag coefficient of $C_D = 24/Re$, while some researchers use $C_D = 32/Re$ for natural sands. In the turbulent region however the difference is much larger. At large Reynolds numbers the drag coefficient for spheres is about $C_D = 0.445$, while for natural sands and gravels values of $C_D = 1-2$ are used. Using the equation as mentioned in Julien (1995) gives Shields curves as shown in Figure 4-12. In the laminar region the curves are almost identical to the curves for spheres, but in the turbulent region the curves gives values of 50% to 60% of the curves for spheres. The curves in Figure 4-12 are for the sliding mechanism for exposure levels up to 0.6 and the rolling mechanism for larger exposure levels.

$$C_D = \frac{24}{Re_D} + 1.5 \qquad \textbf{(4-20)}$$

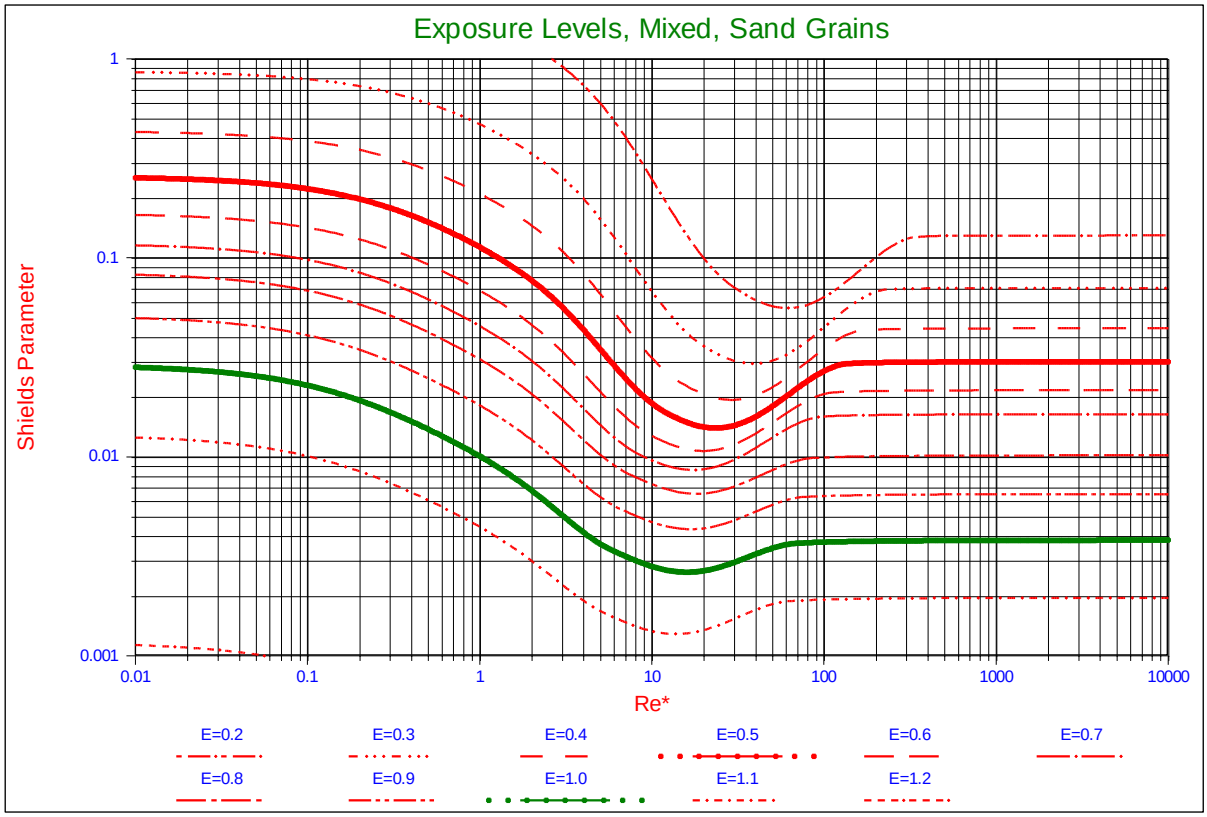

Figure 4-12: The Shields curves for natural sands and gravels.

4.6. Exposure & Protrusion Levels.

The model developed here is now capable of predicting the non-dimensional shear stress or Shields parameter as a function of the exposure and protrusion level, so it is interesting to see how this correlates with experiments. The most cited experiments are those from Fenton & Abbot (1977) and Chin & Chiew (1993), who performed their experiments with spheres, where the bed consisted of fixed spheres, having a single loose sphere at a certain protrusion level. The only possible entrainment mechanism is rolling (pivoting), so their results will be compared with the curves calculated for rolling. Fenton & Abbot (1977) also re-analyzed the tests carried out by Coleman (1967) but the Shields values found should only be used as an indication of the magnitude of the Shields parameter. Figure 4-13 shows all the measurements as a function of the boundary Reynolds number, grouped by protrusion level according to Table 4-4. The measurements of Coleman (1967) were carried out with spheres on top of the bed having a protrusion level of about 0.8 and an exposure level of 1.0, assuming a virtual bed level of 0.2 times the diameter below the actual bed level.

It is clear from Figure 4-13 that the magnitude of the Shields values of the Coleman (1967) experiments match the Shields curve for an exposure level of 1.0 very well, although the minimum for these experiments tends to occur at a higher boundary Reynolds number than in the calculated curve. It should be mentioned that the experimental results of Coleman (1967) were calculated by Fenton & Abbot (1977) assuming full turbulent flow, while a number of these experiments are inside the transition region. Using the assumption of laminar flow for these experiments would increase the value of the Shields parameter to values between 0.005 and 0.01, still being close to the calculated curve. For large boundary Reynolds numbers, the Coleman (1967) experiments gives value between 0.01 and 0.015, on average a bit higher than the theoretical curve.

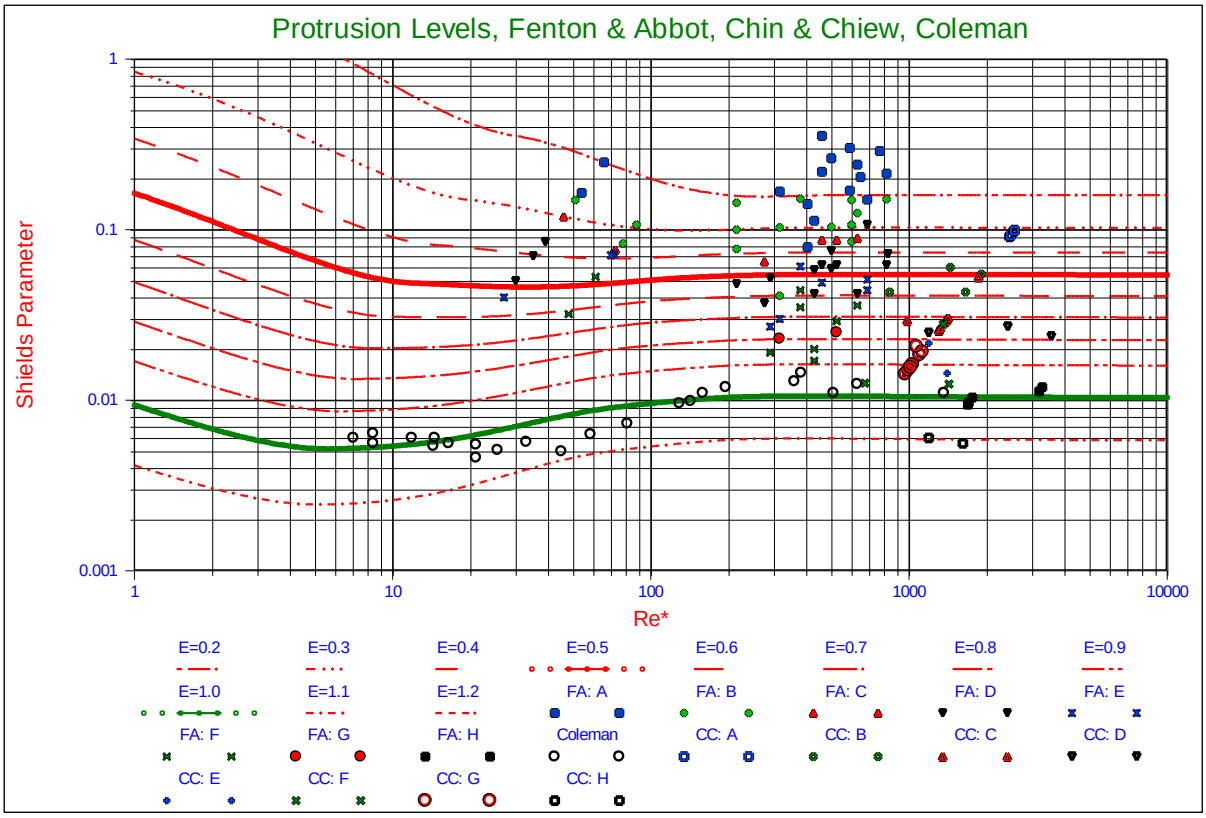

Figure 4-13: The measurements of Fenton & Abbot, Chin & Chiew and Coleman.

Table 4-4: Explanation of the legend of Figure 4-13.

Fenton & Abbot	p/d	Chin & Chiew	p/d
FA: A	-0.3 – 0.0	CC: A	-0.3 – 0.1
FA: B	0.0 – 0.1	CC: B	0.1 – 0.3
FA: C	0.1 – 0.2	CC: C	0.3 – 0.5
FA: D	0.2 – 0.3	CC: D	0.5 – 0.6
FA: E	0.3 – 0.4	CC: E	0.6 – 0.7
FA: F	0.4 – 0.5	CC: F	0.7 – 0.8
FA: G	0.5 – 0.6	CC: G	0.8 – 0.9
FA: H	0.6 – 1.0	CC: H	0.9 – 1.0

Figure 4-14 and Figure 4-15 show the measurements of Fenton & Abbot (1977) and Chin & Chiew (1993) in a linear-linear graph and a logarithmic-linear graph. Both graphs also show the calculated values for rolling at very high boundary Reynolds numbers, the minimum for rolling in the transition zone and the values for lifting. Most of the experiments of Fenton & Abbot (1977) were carried out at protrusion levels below 0.5 (exposure levels below 0.7), while Chin & Chiew (1993) wanted to observe what would happen at higher protrusion levels. Figure 4-14 shows that the theoretical values for protrusion levels from 0.1 up to 0.7 match very well with the experiments. At protrusion levels below 0.1 the theoretical values still match, but also many experiments have values below the theoretical ones. In general, the theory overestimates the Shields values compared with the experiments in this region. For protrusion levels above 0.7 its better to use the logarithmic-linear graph of Figure 4-15. The measurements carried out at a protrusion level of 0.82, which is the maximum protrusion level of a sphere resting on other spheres, show Shields values between 0.01 and 0.02, where Fenton & Abbot (1977) give values close to

0.01 and Chin & Chiew (1993) give the higher values. The theoretical value is about 0.01. Chin & Chiew (1993) also carried out experiments at protrusion levels of 0.90 and 0.94 and the theoretical value matches the measurement at the protrusion level of 0.90, but underestimates the protrusion level of 0.94. Still in general it can be concluded that the theoretical values match the measurements well enough, being evidence for the way the lift coefficient is used in the theoretical model. At the very low protrusion levels, -0.3 to -0.1, most probably another mechanism is occurring, since these protrusion levels are near the virtual bed level and without having enough velocity, entrainment can never be explained.

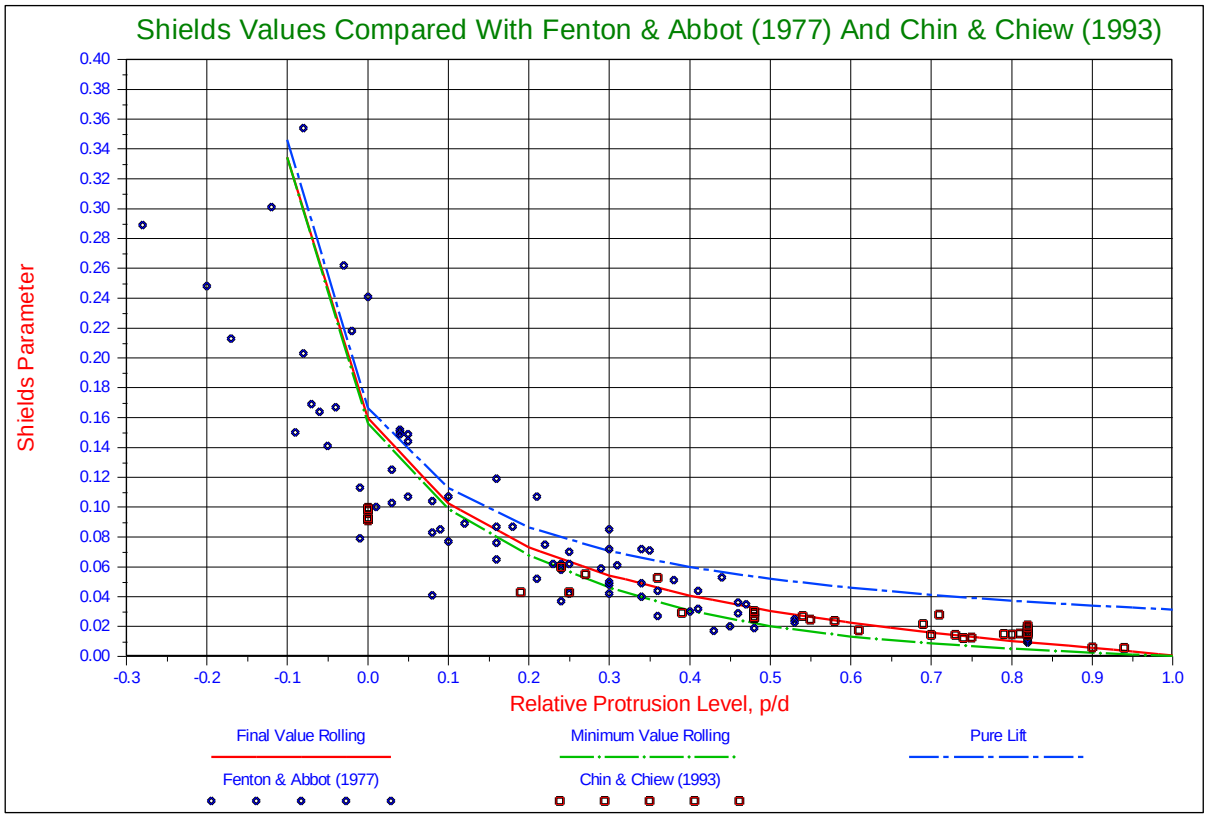

Figure 4-14: The experimental results of Fenton & Abbot (1977) and Chin & Chiew (1993) compared with the theory for rolling.

4.7. Shear Velocity and Shear Stress.

For the verification of the model to predict the initiation of motion, it is good to look at this physical phenomenon from different points of view. The first point of view is comparing the calculated Shields curve with the available data with the boundary Reynolds number at the horizontal axis and the non-dimensional shear stress on the vertical axis. A second point of view is to compare the theory with measurements of the Shields parameter for different protrusion levels. A third point of view is to compare the theory with measurements of the critical shear velocity (friction velocity) or with the critical shear stress. Wiberg & Smith (1987A) used the data selected by Miller, McCave & Comar (1977) that employed a consistent definition of critical motion. In addition, they required that the measurements were made in parallel sided flumes with an initially flat bed, using rounded, non-cohesive particles of nearly uniform size. The data satisfying these criteria are given by Casey (Tison, 1953), Neil (1967), Grass (1970), White (1970), Everts (1973) and Paintal (1971), complemented with data from Julien (1995). Sundborg (1956) also used these data. The data are shown as the friction velocity as a function of the grain diameter in Figure 4-16 and as the shear stress as a function of the grain diameter in Figure 4-17. In both figures the calculated Shields curves are plotted for exposure levels ranging from 0.2 up to 1.2 (protrusion levels from 0.0 up to 1.0). The calculated curve for an exposure level of 0.5 matches very well with the measurements, while most measurements lie in the range of exposure levels ranging from 0.4 to 0.6. Some of the scatter is caused by the fact that, although each researcher used a consistent definition of initial motion in their own experiments, some discrepancy exists among the different researchers regarding this definition. Wiberg & Smith (1987A) go more in to detail regarding this definition.

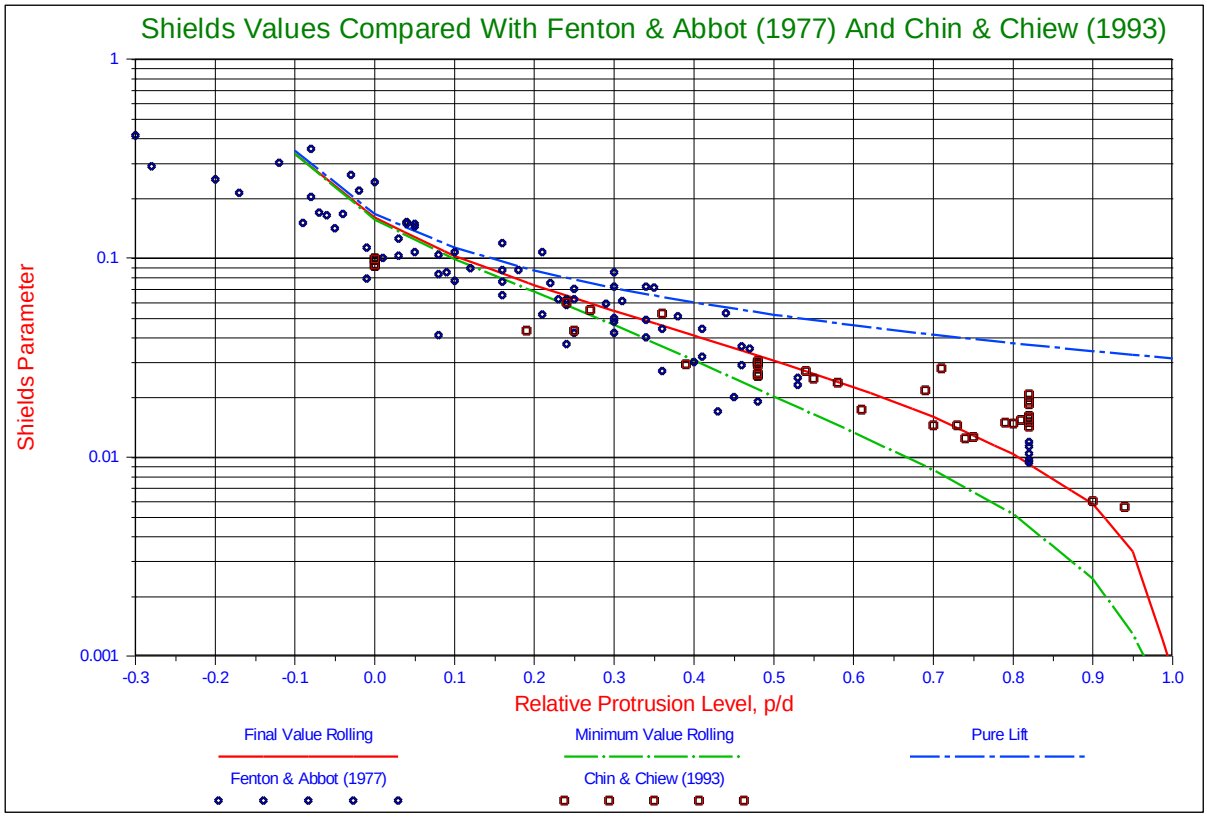

Figure 4-15: The experimental results of Fenton & Abbot and Chin & Chiew compared with the theory for rolling.

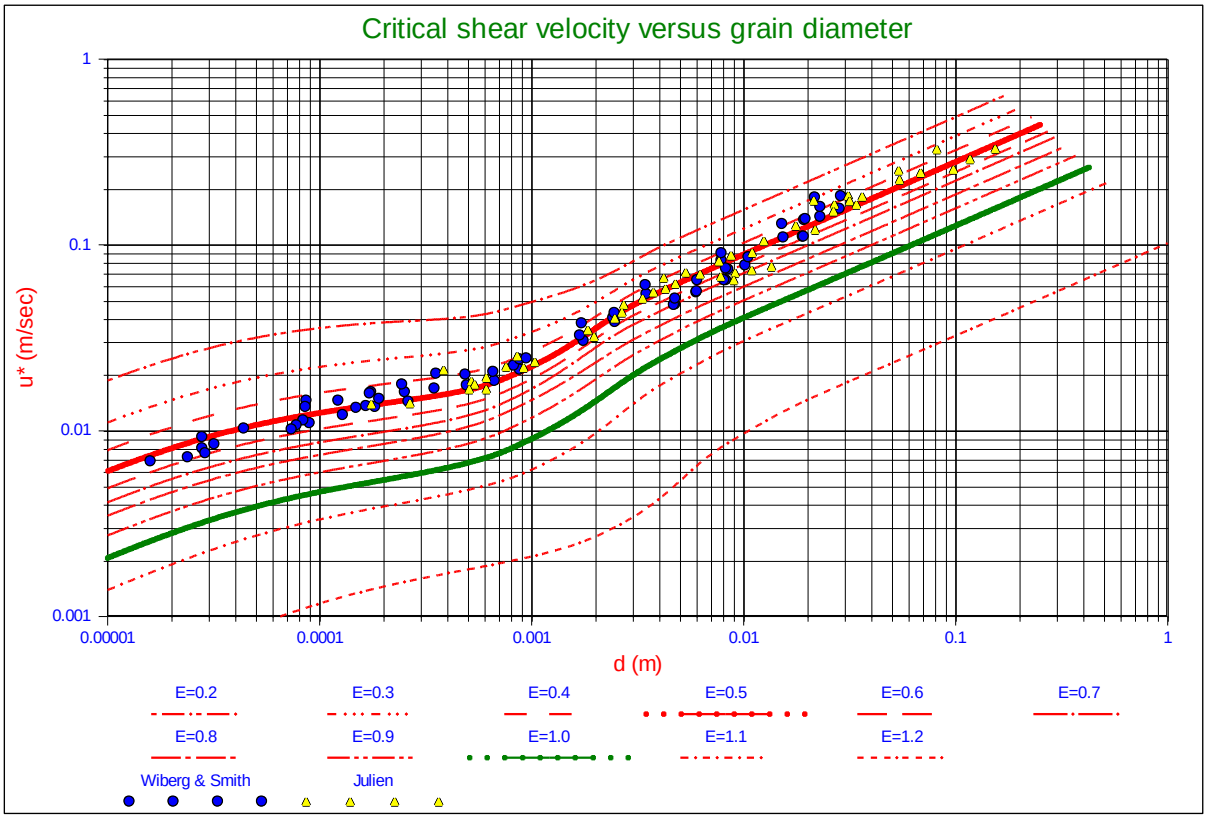

Figure 4-16: The critical shear velocity (friction velocity) as a function of the grain diameter.

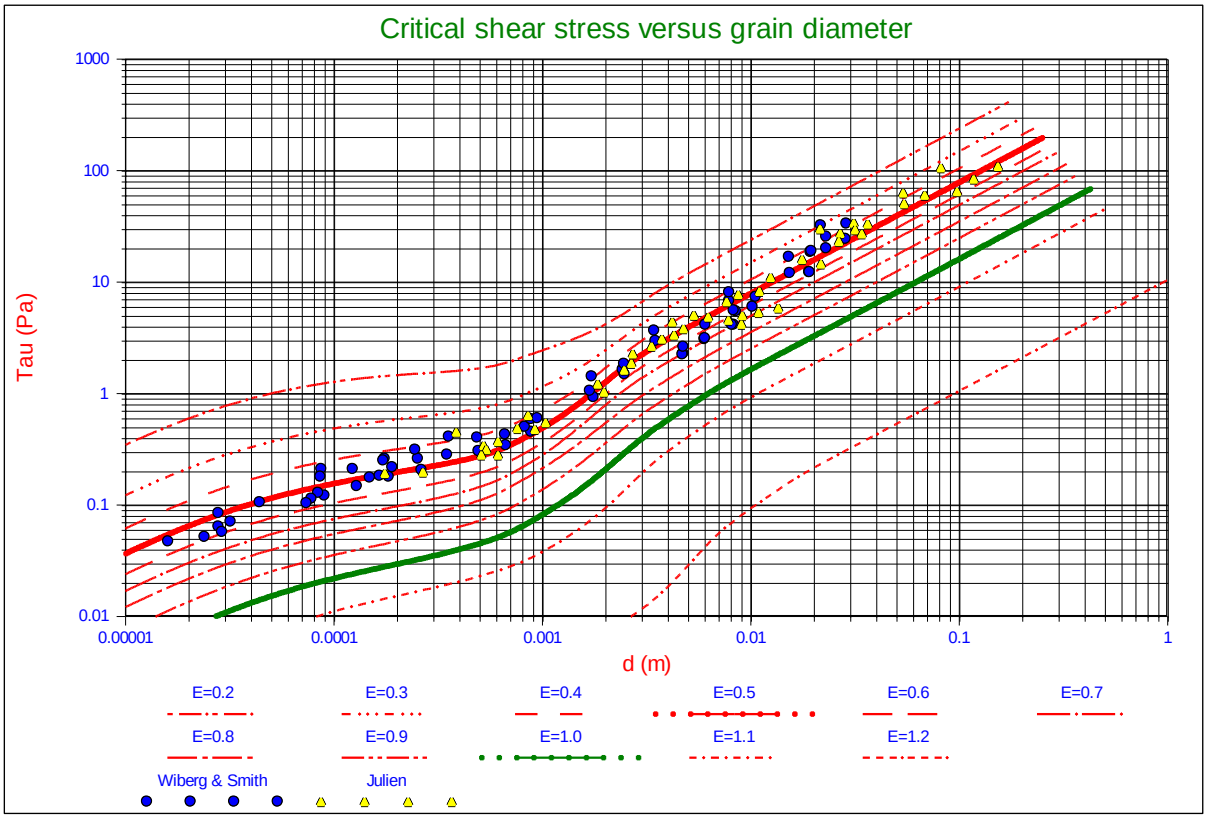

Figure 4-17: The critical shear stress as a function of the grain diameter.

4.8. Stages of Entrainment.

A fifth point of view is the stage of entrainment. Several researchers investigated different stages of entrainment, usually starting with a single particle being entrained and ending with general transport. Vanoni (1975) investigated small particles (0.037 mm, 0.102 mm) in the laminar sub layer with boundary Reynolds numbers ranging from 0.2 to 2. Delft Hydraulics (1976), see van Rijn (1993), carried out tests on particles of 7 diameters with boundary Reynolds numbers ranging from 1 to 150. Graf & Pazis (Rijn L. v., 1993) carried out tests in the boundary Reynolds range of 50 to 150, while more recently experiments were carried out by Dey & Raikar (2007) in the turbulent region with boundary Reynolds numbers ranging from 200 to 2000. Ziervogel (2003) carried out experiments on sediments in the Baltic Sea. Figure 4-18 shows the results of these researchers as a function of the boundary Reynolds number. Figure 4-19 shows the same measurements, but now as a function of the Bonneville parameter.

The Delft Hydraulics (1972) defined 7 levels of erosion according to:

1. Occasional particle movement at some locations (DHL7).
2. Frequent particle movement at some locations (DHL6).
3. Frequent particle movement at many locations (DHL5).
4. Frequent particle movement at nearly all locations (DHL4).
5. Frequent particle movement at all locations (DHL3).
6. Permanent particle movement at all locations (DHL2).
7. General transport (initiation of ripples) (DHL1).

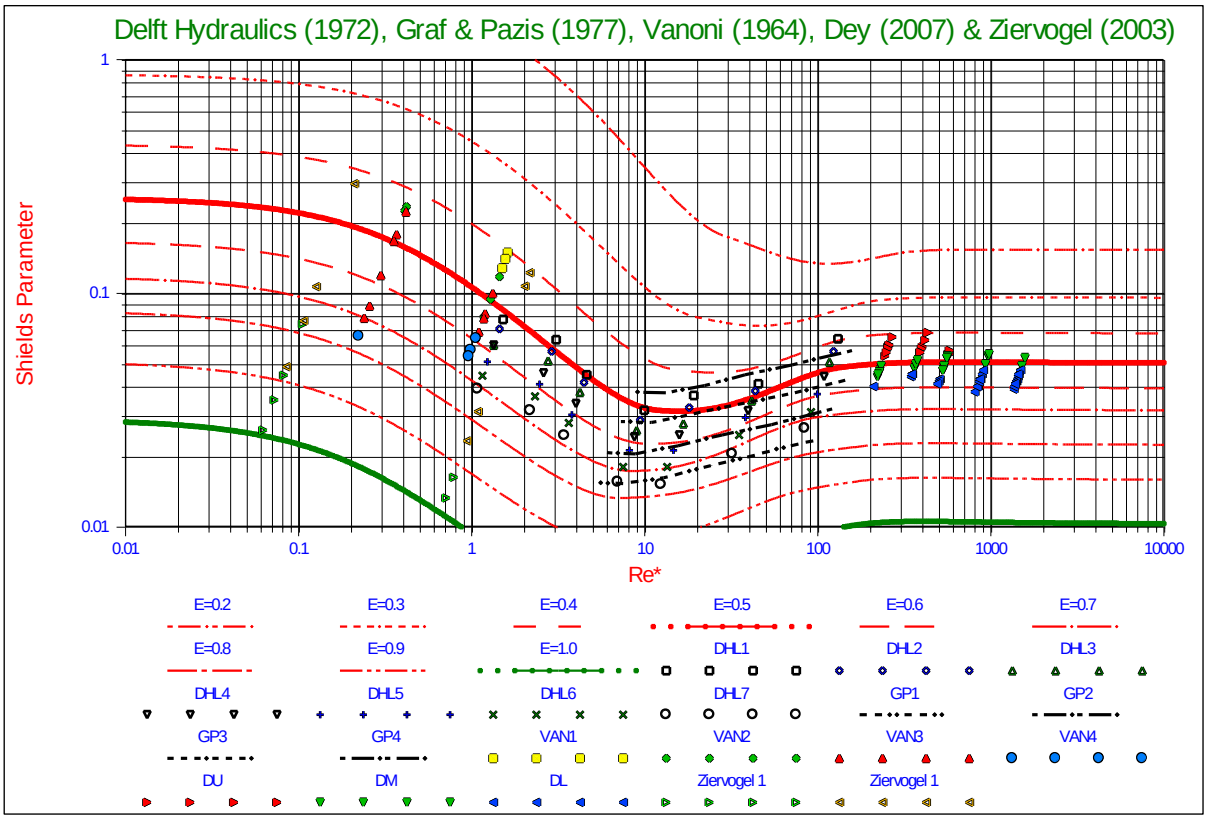

Figure 4-18: Stages of entrainment.

Graf & Pazis (1977) defined 4 levels for the threshold of motion, based on experiments with 6 particle sizes ($0.5<=d_{50}<=3.0$ mm). They calculated the average number, N, of particles in motion per unit area as a function of bed stress.

1. GP1: N=1.
2. GP2: N=10.
3. GP3: N=100.
4. GP4: N=1000.

Vanoni (1964) distinguishes 4 levels for the threshold of motion, for runs with two sediments in a turbulent shear flow (0.0037 mm, 0.102 mm).

1. General
2. Critical
3. Small
4. Negligible

Originally all the measurements with the 0.037 mm sand were below the original Shields curve, which would continue to increase with a decreasing boundary Reynolds number. From Figure 4-18 and Figure 4-19 it is clear that the Vanoni (1975) measurements also match very well with the new calculated curve for an exposure level of 0.5.

Dey & Raikar (2007) investigated the entrainment of gravel and distinguished 3 levels.

1. Lower threshold level (DL: a few surface particles are disturbed)
2. Medium threshold level (DM: many surface particles are disturbed)
3. Upper threshold level (DU: almost all the surface particles are disturbed, a weakly mobile boundary)

It should be mentioned that the angle of repose (friction angle) is increasing slightly with increasing grain diameter (from 32.5° to 39°), which probably is the reason for a higher transition between the three threshold levels for bigger particles as is also shown in the sensitivity analysis.

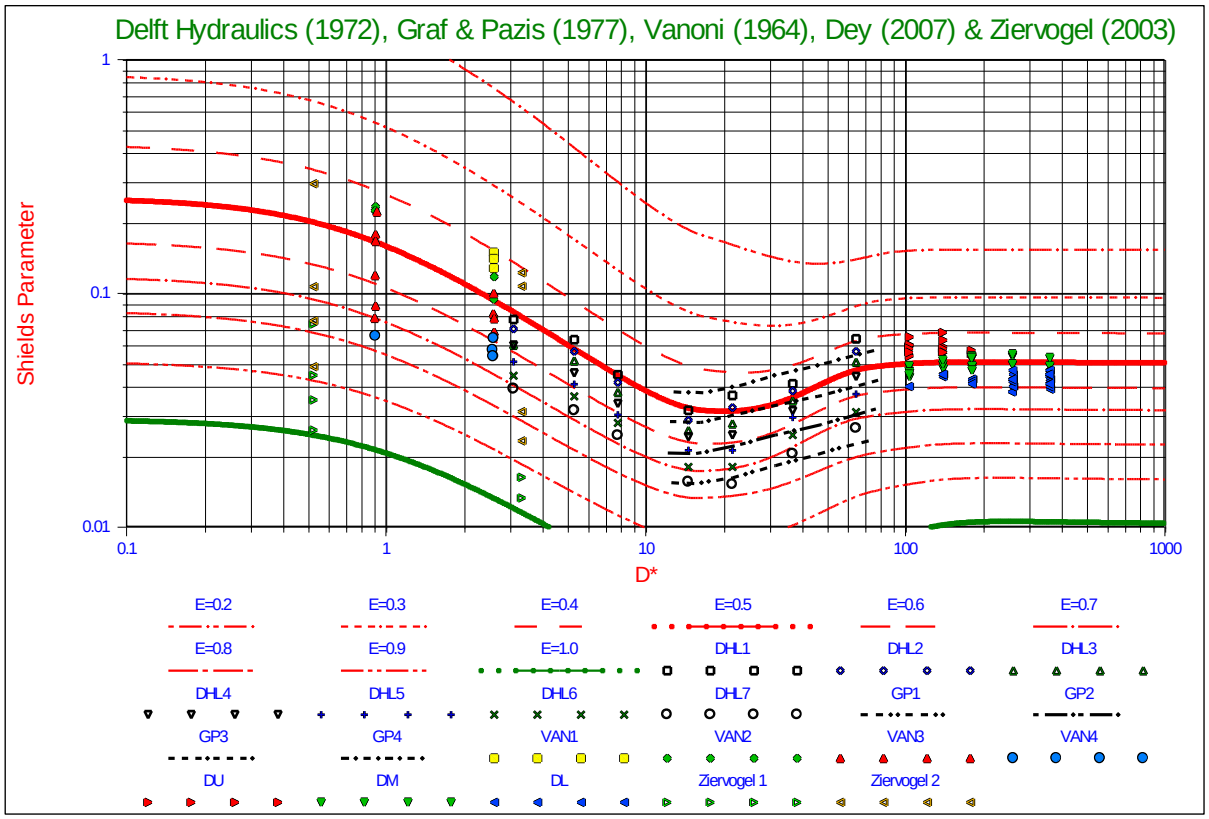

Figure 4-19: Stages of entrainment as a function of the Bonneville parameter.

Ziervogel (2003) only distinguished no-erosion (Ziervogel 1) or erosion (Ziervogel 2), his experiments were carried out on sediments with a d_{50} of 20 µm and 130 µm.
From Figure 4-19 the conclusion can be drawn that incipient motion starts incidentally for exposure levels between 0.65 and 0.85 (protrusion levels between 0.45 and 0.55). Although it would be expected to find incidental incipient motion at higher exposure levels sooner. However these exposure levels will occur much less frequent in a bed of natural grains and may not have been present in the beds used, since often the bed is prepared by a flow over the bed at a low flow rate, until no particles move anymore, moving the grains with the highest protrusion levels to spots in the bed where they will have a lower protrusion rate and thus more resistance to the flow. General transport occurs at exposure levels between 0.4 and 0.5 (protrusion levels between 0.2 and 0.3). On average the general transport occurs at an exposure level of 0.45 which is lower than the 0.5 on which the theoretical Shields curve is based, the resulting Shields parameter values are thus higher. Combining the data of Delft Hydraulics (1972), Graf & Pazis (1977), Vanoni (1964), Dey & Raikar (2007) and Ziervogel (2003) gives information over a broad range of boundary Reynolds numbers (0.06 to 2000) or as a function of the Bonneville parameter (0.5 to 400).

4.9. Laminar Main Flow.

A sixth point of view is laminar main flow. In the previous paragraphs the words laminar flow and laminar region have always been used for the flow around the top of a particle causing drag, lift and local eddies. The words turbulent flow and turbulent region have been used in the same way. The main flow has always been considered to be turbulent with either a smooth or a rough wall. But the main flow could also be laminar, implying that a viscous sub layer does not exist, since the whole main flow is viscous. This means that theoretically turbulence does not exist. The fact whether the flow is laminar or turbulent depends on the Reynolds number of the main flow. For Reynolds numbers below 2000 (literature also often mentions 2300) the flow is considered laminar, above 2000 it is considered turbulent. Around 2000 a transition zone exists having some turbulence, but not fully developed. The velocity profile in a laminar flow can be determined with:

$$u^+ = \frac{u(y)}{u_*} = \frac{u_* \cdot y}{\nu} \cdot \left(1 - \frac{y}{2 \cdot h}\right) \qquad \textbf{(4-21)}$$

The average flow velocity can be derived from the friction velocity according to:

$$\overline{u(y)} = \frac{1}{3} \cdot \frac{u_*^2 \cdot h}{\nu} \qquad \textbf{(4-22)}$$

Thus, the friction velocity can also be determined from the average flow velocity:

$$u_* = \sqrt{\frac{3 \cdot \overline{u(y)} \cdot \nu}{h}} \qquad \textbf{(4-23)}$$

For small values of **y**, the distance to the wall, equation (4-21) gives the same velocity profile as the one found in the viscous sub layer. This means that the same equations can be applied for calculating the drag forces, while turbulence should be almost absent. Almost, because many of the measurements found in literature are in the transition zone between laminar and turbulent main flow, so some turbulent eddies might exist. The measurements found in literature are those of White (1940), Mantz (1977), Yalin & Karahan (1979), Pilotti & Menduni (2001), Charru et al. (2004), Loiseleux et al. (2005) and Ourimi et al. (2007).
Most measurements were carried out in the 'laminar' region with natural sands, while Pilotti & Menduni (2001) also carried out some tests in the 'turbulent' region with Reynolds numbers of the main flow up to about 3500. Figure 4-20 shows the measurements and a number of calculated Shields curves for natural sands, while Figure 4-21 shows the results for spheres. The calculated Shields curves are for 0, 1, 2, 3 and 4 times the effect of turbulence intensity (the turbulence intensity factor) based on Nezu & Rodi (1986) for natural sands and one curve for an exposure level of 0.6 and 0.5 times the turbulence intensity for spheres. Analyzing the data points shows that the data points can be grouped in 3 sub-groups. The first sub group are the data points of Pilotti & Menduni (2001) for boundary Reynolds numbers below 1. On average, these data points are below the calculated curves and below the asymptotic value of 0.255 for very small boundary Reynolds numbers. It is difficult to draw any reasonable conclusion from these data points, except that they are not too far from the theoretical curves. The second sub group also consists of data points from Pilotti & Menduni (2001) for boundary Reynolds numbers above 1. These data points are mainly located between the theoretical Shields curves with a turbulence intensity factor of 0 and 1, with a best fit at a turbulence intensity factor of 0.5 to 0.6. The Shields curve for full turbulent main flow has a turbulence intensity factor of 3. There is no real difference between the data points of laminar and turbulent main flow of Pilotti & Menduni (2001) in this region. The third sub group of data points are the data points measured by White (1940), Mantz (1977), Yalin & Karahan (1979) and Loiseleux et al. (2005). Loiseleux et al. (2005) used spherical particles and observed rolling of many particles at many locations, matching an exposure level of 0.6 (see stages of entrainment) as is shown in Figure 4-21.

For the small boundary Reynolds numbers these measurements tend to have an asymptotic value of about 0.17 which matches the exposure level of 0.6. With a turbulence intensity factor of 0.5 a good fit of the theoretical Shields curve for spheres and the data points is achieved. In general it can be concluded that the measurement of the Shields parameter in a laminar main flow match the calculated curves with a turbulence intensity factor of 0.5 well, while a turbulence intensity factor of 3 should be used for turbulent main flow. Again a good fit has been found between measurements and the calculated Shields curves, but laminar and turbulent main flow should never be mixed in one graph, just like spheres and natural sands and gravels should not be mixed. To show this, the measurements of Prager et al. (1996) in turbulent flow, using angular carbonate sands, are shown in Figure 4-20 as well. These measurements range for boundary Reynolds numbers from 7 to 20 and Shields numbers from 0.018 to 0.028, matching the Shields curve for natural sands with a turbulence intensity factor of 3. Govers (1987) carried out experiments in both laminar and turbulent main flow. The data can be found in Figure 4-21. The data points for laminar flow tend to give slightly higher Shields values than the data points of White (1940), Mantz (1977), Yalin & Karahan (1979) and Loiseleux et al. (2005). The data fit very well using an exposure level of 0.53 and a turbulence intensity of 0.50. The data points for turbulent flow match very well with the Shields curve using an exposure level of 0.53 and a turbulence intensity of 2.3. The latter can be explained by the fact that the Reynolds numbers of the main flow were not high and turbulence might not have been fully developed.
For large boundary Reynolds numbers (above 30), still the model for turbulent main flow is applied for calculating the Shields curves, since the main flow Reynolds numbers of the measurements in this range were above 2300.

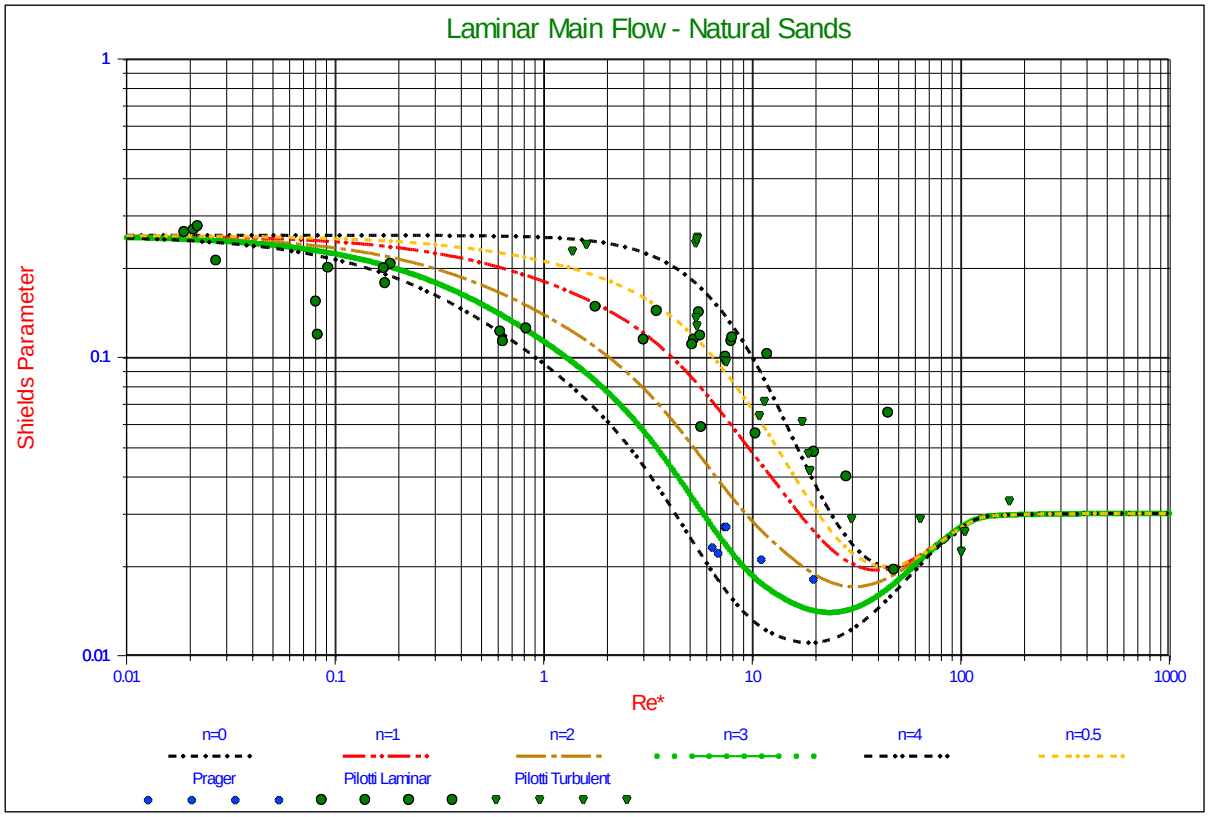

Figure 4-20: Measurements and calculation in a laminar main flow.

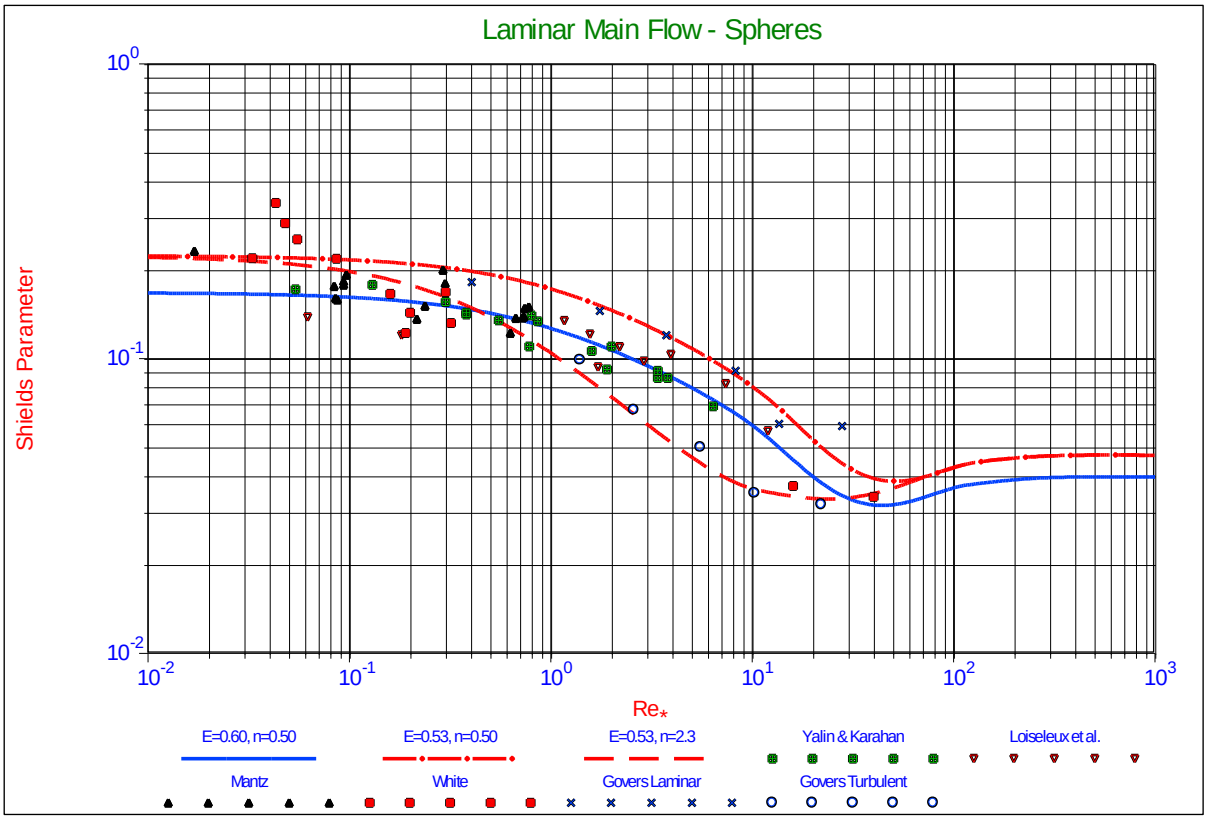

Figure 4-21: Spheres in a laminar main flow.

4.10. The Shields-Parker Diagram.

A well-known application of the Shields curve is the so called Shields-Parker diagram, showing erosion versus no erosion, suspension versus no suspension and ripples versus dunes. This diagram is shown in Figure 4-22 with the boundary Reynolds number on the abscissa and Figure 4-23 with the particle Reynolds number on the abscissa.

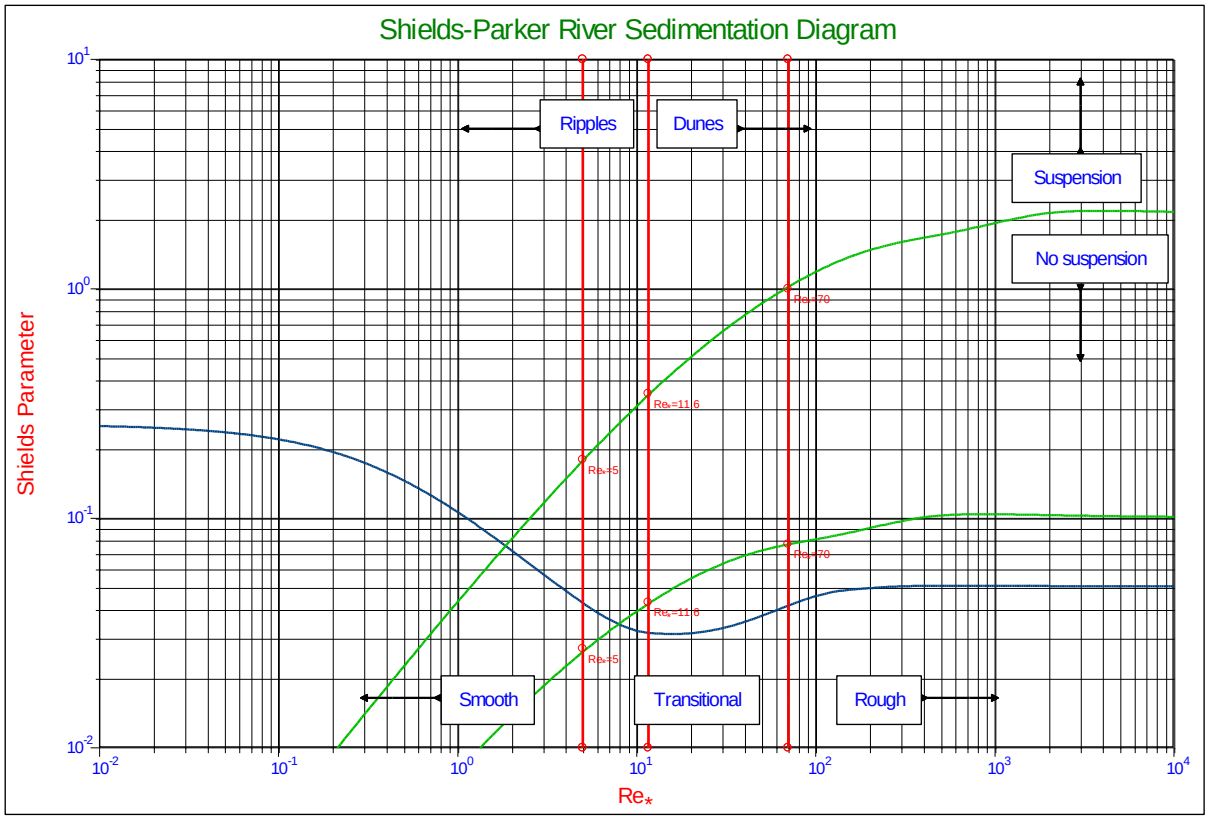

Figure 4-22: The Shields-Parker diagram as a function of the roughness Reynolds number.

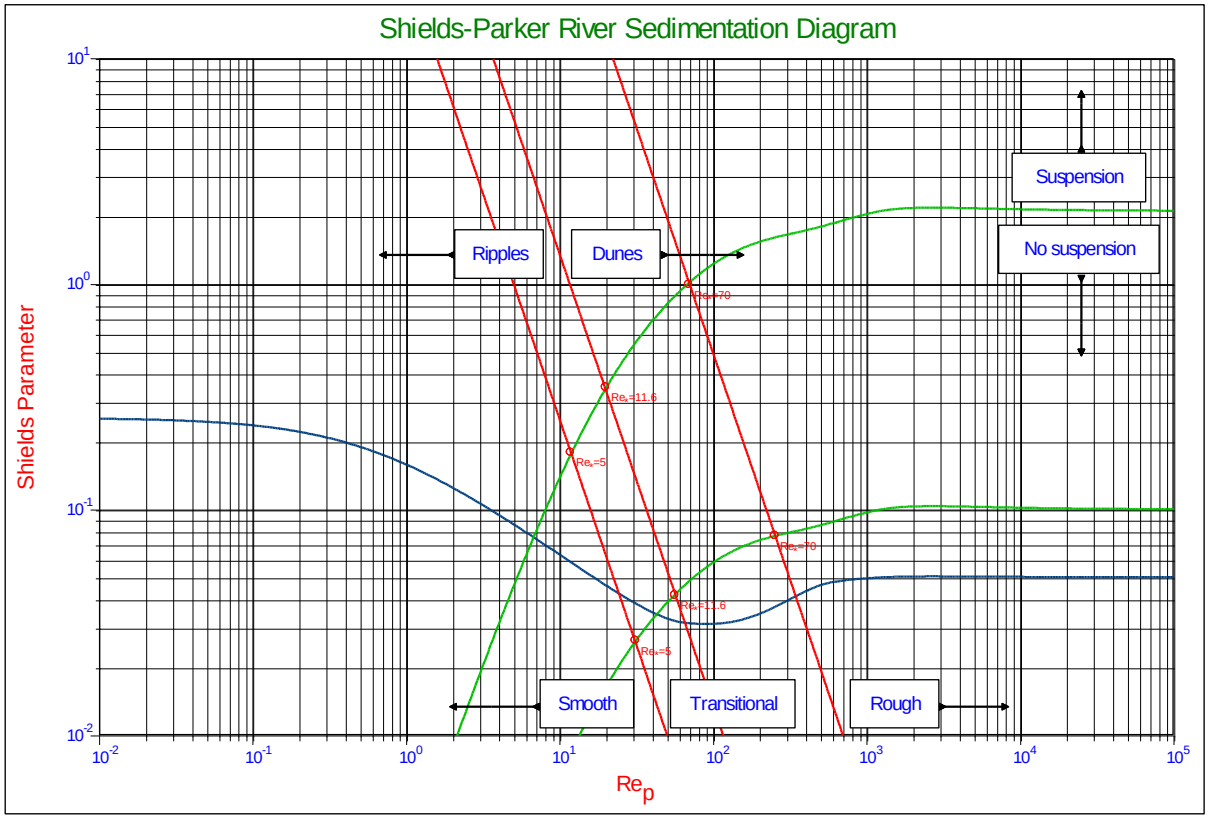

Figure 4-23: The Shields-Parker diagram as a function of the particle Reynolds number.

4.11. Conclusions and Discussion.

The model developed in Part A has been verified and validated from 6 points of view.
1. The traditional Shields diagram, a sensitivity analysis
2. Exposure and protrusion levels
3. Shear velocity and shear stress
4. The ratio between the friction velocity and the terminal settling velocity
5. Stages of entrainment
6. Laminar main flow

The 3 possible mechanisms for the entrainment of particles, sliding, rolling and lifting, are considered, based on a set of equations where the exposure level and the surface averaged drag force acting point are an integral part of these equations.
The sensitivity analysis shows that most of the scatter of the measured data points in the Shields diagrams can be explained by applying a range of the friction angle from 25° to 35°, a turbulence intensity factor from n=2 to n=4 for the laminar region (particles in the viscous sub layer), a lift coefficient from $\mathbf{C_L = 0.7 \cdot 0.445}$ to $\mathbf{C_L = 0.445}$ in the turbulent region and applying a drag coefficient for spheres and natural sands and gravels. It must be mentioned here that some of the measured Shields values used in the sensitivity analysis were the result of laminar main flow, resulting in more scatter. Applying the drag coefficient of natural sands and gravels may reduce the value of the Shields parameter to about 50%-60% in the transition and the turbulent region, explaining for the statement found in literature that for engineering purposes in real sands and gravels the Shields parameter should be divided by 2. In the laminar region however this is not the case, since the drag coefficient follows or almost follows the Stokes law for very small boundary Reynolds numbers.
The Shields curves calculated for different exposure and protrusion levels match the findings of Fenton & Abbot (1977), Chin & Chiew (1993) and Coleman (1967) well, assuming a sliding mechanism of entrainment for exposure levels up to 0.6 and a rolling mechanism for larger exposure levels. The lifting mechanism might occur for single particles in a bed where all the other particles are fixed (glued) and the rolling mechanism cannot occur. The surface factor used for the dependency of the lift coefficient in relation to the exposure level has proven to give correct results in the turbulent region.
Additional measured data, as also being used by Wiberg & Smith (1987A) and Julien (1995) , of the shear velocity (friction velocity) and the bottom shear stress, give a high correlation with the calculated curve for an exposure level of 0.5 and the sliding entrainment mechanism for spheres.
Other additional measurements, as carried out by Liu (1957), of the ratio between the friction velocity and the terminal settling velocity give an almost perfect match with the Shields curve as calculated with an exposure level of 0.5 and the sliding entrainment mechanism.
There has always been discussion amongst the different researchers about the definition of the stage of entrainment related to the Shields curve. In the past, when the extrapolated curve based on the original data of Shields was used, the measured data did not always match with this curve, because this extrapolated curve did not have an asymptotic value for very small boundary Reynolds numbers. Especially the measurements of Vanoni (1975) with the 0.037 mm grains fell below the extrapolated Shields curve. The new model as explained in this paper has an asymptotic value of about 0.25 for very small boundary Reynolds numbers, resulting in a different shape of the Shields curve. The different measurements all give the same conclusion, the Shields curve describes critical to general transport, with general transport at an exposure level of about 0.45, whilst a measurable incipient motion starts at an exposure level of about 0.7.
Most experiments on the entrainment of particles have been carried out in a turbulent main flow, however some experiment were carried out in a laminar main flow. Buffington & Montgomery (1997) give a nice overview of most of the experiments carried out until 1997 and show the data of White (1940) and Yalin & Karahan (1979) of experiments carried out in a laminar main flow. Later Pilotti & Menduni (2001) carried out experiments in a laminar main flow and in the transition region between laminar and turbulent main flow. From these data it is clear that entrainment in a laminar main flow differs from entrainment in a turbulent main flow. Although for very small boundary Reynolds numbers there is not much difference theoretically, in the region of boundary Reynolds numbers from 0.1 to around 70 there is a big difference and the two regimes should not be mixed. Yalin & Karahan (1979) already proposed a separate equation for laminar main flow, but their measurements were limited to boundary Reynolds numbers of about 7. The Pilotti & Menduni (2001) experiments extended to boundary Reynolds numbers of about 70 and show the difference between the laminar and turbulent regimes clearly. Comparing the measured data with the theory developed results in a good correlation between the theory and the data if a turbulence intensity factor of 0.5 is applied for an exposure level of 0.5 and the sliding entrainment mechanism.

Using the data from laminar main flow experiments to validate a turbulence based theory like Luckner & Zanke (2007) did in their fig. 1 (the laminar experiments of Pilotti & Menduni and Yalin & Karahan are used), gives a lot of scatter and a low correlation, which is obvious.
It is proposed to distinguish 4 different Shields curves:

1. The Shields curve based on spheres in a turbulent main flow.
2. The Shields curve based on natural sands and gravels in a turbulent main flow.
3. The Shields curve in a laminar main flow for spheres (n=0.5).
4. The Shields curve in a laminar main flow for natural sands and gravels (n=0.5).

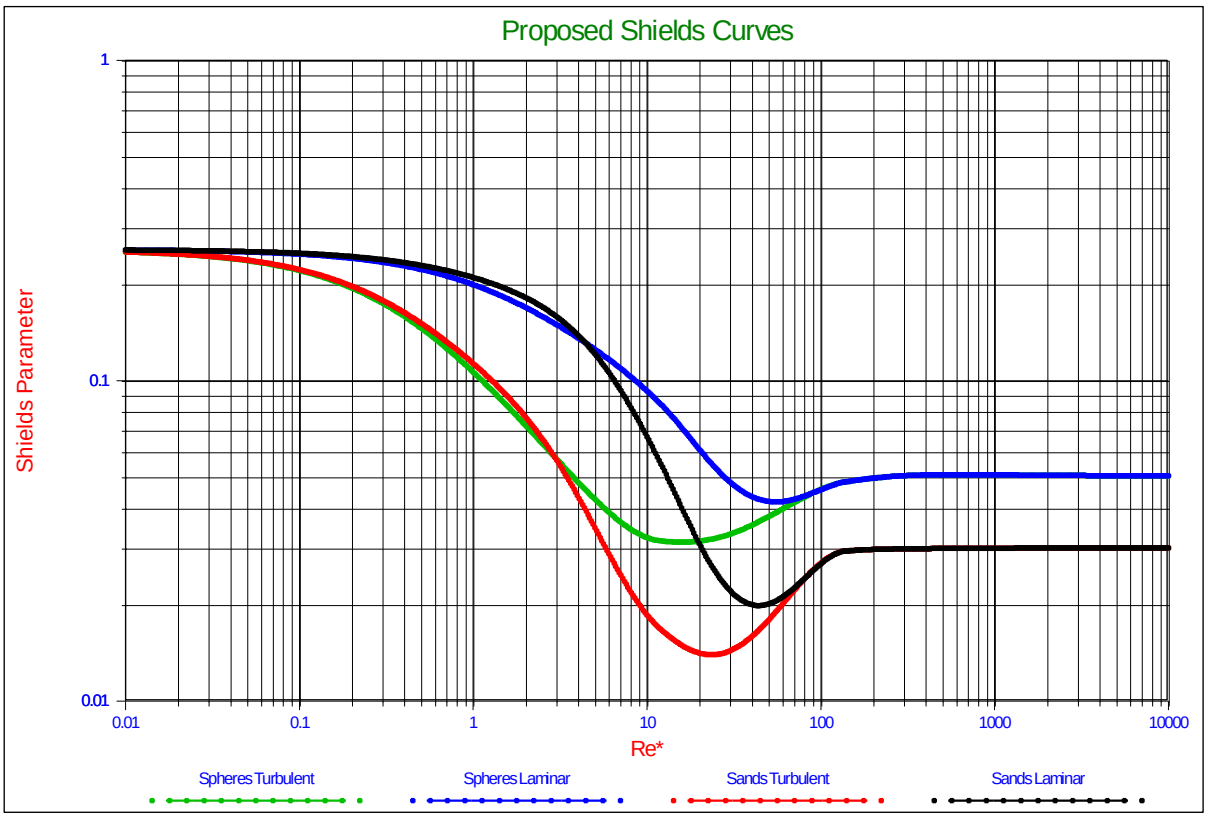

Figure 4-24: The proposed Shields curves.

The two curves for laminar flow exist for boundary Reynolds numbers of about 70, for Reynolds numbers above 70 a normal turbulent rough flow is assumed, since the Reynolds numbers of the main flow will be far above 2300.
The general conclusions of this research are:

- The basic Shields curve can be determined by applying the sliding entrainment mechanism, with a friction angle of 30°, an exposure level of 0.5 (protrusion level of 0.3), a turbulence intensity factor of n=3, a lift coefficient of 0.415 and the drag coefficient of spheres.
- Using a reasonable bandwidth for the different properties, a lower, medium and upper level for the Shields curve have been formed, explaining for most of the scatter of the data used.
- For natural sands and gravels a modified drag coefficient should be applied, based on the angularity of the particles.
- In the laminar region entrainment is dominated by drag and turbulence, while in the turbulent region this is dominated by drag and lift.
- Up to an exposure level of 0.6 sliding is the main entrainment mechanism, while for higher exposure levels rolling will occur.
- Laminar and turbulent main flow result in two different entrainment curves, based on the presence of turbulence. For laminar main flow a turbulence intensity factor of 0.5 has been found to correlate with the measurements.
- The new model developed correlates well with datasets of many independent researchers.

4.12. Nomenclature.

A	Surface or cross section	m^2
$\mathbf{A_{Lam}}$	Interpolation constant for the laminar region	-
$\mathbf{A_{Turb}}$	Interpolation constant for the turbulent region	-
$\mathbf{C_D}$	Drag coefficient	-
$\mathbf{C_L}$	Lift coefficient	-
d	Sphere, particle or grain diameter	m
$\mathbf{D_*}$	The Bonneville parameter or non-dimensional grain diameter	-
E	Exposure level	-
$\mathbf{f_D}$,$\mathbf{f_{Drag}}$	Fraction of cross section exposed to drag	-
$\mathbf{f_L}$,$\mathbf{f_{Lift}}$	Fraction of top surface exposed to lift	-
$\mathbf{F_D}$	Drag force	N
$\mathbf{F_L}$	Lift force	N
$\mathbf{F_w}$	Weight of a particle	N
g	Gravitational constant	9.81 m/sec^2
h	Thickness of the layer of water	m
$\mathbf{k_s}$	Roughness often chosen equal to the particle diameter	m
$\mathbf{k_s^+}$	The non-dimensional roughness or roughness Reynolds number	-
ℓ	The point of action of the drag force	-
ℓ	Mixing length	m
$\ell_{\mathbf{Drag}}$	Drag point of action	-
$\ell_{\mathbf{Lift}}$	Lift point of action	-
$\ell_{\mathbf{Lever-D}}$	Additional lever arm for drag	-
$\ell_{\mathbf{Lever-L}}$	Additional lever arm for lift	-
n	Turbulence intensity factor	-
P	Probability used in interpolation	-
p/d	Relative protrusion level	-
Q	Factor used in interpolation	-
R	Radius of sphere, particle or grain	m
$\mathbf{R_d}$	The relative submerged specific density	-
$\mathbf{Re_D}$	The particle drag Reynolds number	-
$\mathbf{Re_*}$	Boundary Reynolds number	-
$\mathbf{Re_p}$	The particle Reynolds number	-
$\mathbf{S_*}$	The Grant & Madsen parameter	-
u	Time and surface averaged velocity	m/sec
$\mathbf{u_*}$	Friction velocity	m/sec
$\mathbf{u^+}$	Non dimensional time and surface averaged velocity	-
$\mathbf{u_{r.m.s.}}$	Turbulence intensity	m/sec
$\mathbf{u'_{r.m.s.}}$	Modified turbulence intensity	m/sec
$\mathbf{u'_{n\cdot r.m.s.}}$	The n^{th} moment of the modified turbulence intensity	m/sec
$\mathbf{u_{eff.}}$	The effective modified turbulence intensity	m/sec
$\mathbf{u^+_{r.m.s.}}$	Non dimensional turbulence intensity	-
$\mathbf{u^+_{total}}$	Non dimensional total velocity	-
V	Volume	m^3
y	Distance to the wall or virtual bed level	m

y_0	Integration constant	m
y^+	Non dimensional distance to the wall (Reynolds number)	-
α	The velocity factor at a certain exposure level	-
δ_v	Thickness of the viscous sub layer	m
δ_v^+	The non-dimensional thickness of the viscous sub layer	11.6
κ	Von Karman constant	0.412
ρ	Fluid density	kg/m^3
ρ_f	Fluid density	kg/m^3
ρ_s	Solids density	kg/m^3
ρ_w	The density of water or fluids	kg/m^3
ρ_q	The density of quarts or solids	kg/m^3
ϕ	Internal friction angle/angle of repose	°
ϕ_0	The Coulomb friction angle quarts-quarts	°
ϕ_0	Pivot angle in Wiberg & Smith (1987A)	°
ϕ_{Roll}	Friction angle for rolling resistance	°
Ψ	The dilatation angle	°
Ψ	The pivot angle	°
θ	The Shields parameter or non-dimensional shear stress	-
θ_5	The Shields parameter for $\xi = 5$	-
θ_{70}	The Shields parameter for $\xi = 70$	-
τ	Total shear stress	Pa
τ_t	Turbulent shear stress	Pa
τ_v	Viscous shear stress	Pa
τ_b	Bed shear stress	Pa
ν	Kinematic viscosity	m^2/sec
μ	Friction coefficient usually the tangent of the internal friction angle	-
μ_{Roll}	Equivalent friction coefficient for rolling	-
ξ	The non-dimensional distance of the top of the sphere to the virtual bed level	-

Chapter 5: Constructing the Shields Curve, Part C.

5.1. Cohesion by Silt & Clay, Hjulstrom, Sundborg.

The 'standard' Shields curve is intended for determining an erosion criterion for non-cohesive particles. Non-cohesive in this respect means that the particles are subject to drag and lift forces and subject to turbulent instantaneous velocities. The particles are not subject to inter-particle attraction or repulsion forces such as van der Waals forces and electro-chemical forces. The bed also is not subject to shear strength or yield stress. A cohesive sediment however is subject to these phenomena, resulting in higher critical shear stresses and higher Shields values. The cohesive effect can result from the presence of a silt (quartz) fraction or the presence of a clay fraction in the sediment. Here only the presence of a silt fraction will be considered. The silt particles in general are small enough to be subject to van der Waals forces. These attraction forces are strong enough to act like glue between the larger sand particles. In order to determine these attraction forces a Virtual Attraction Particle Diameter (VAPD) is introduced. The VAPD is the diameter of a virtual silt particle that can explain for the attraction forces in combination with the d_{50} of the sand. The VAPD will be in the range of the d_1-d_5. The van der Waals forces (if strong enough) increase the critical shear stress and thus the Shields parameter with a factor, which is inversely proportional with the d_{50} and inversely proportional with the VAPD (the diameter of the smallest fraction of the silt particles) to the third power. The relation often found in literature for this factor, inversely proportional with the d_{50} to the second power, can be explained by the fact that there is often a relation between the d_{50} and the VAPD. The smaller the d_{50}, the smaller the VAPD. This however can lead to inverse proportionalities with different powers between the first power and the third power, depending on the coincidental choice of the diameter of the silt fraction. The model developed also shows that there does not exist a single Shields curve for sands with a cohesive silt fraction, but for a given set of the sediment density, the maximum sediment density (minimum porosity) and the VAPD, a Shields curve can be constructed. Using a density of 1.95 ton/m^3, a minimum porosity of 0.32 (a rather uniform PSD) and a VAPD of 3 µm, the Brownlie equation can be approximated very closely. If the silt does not contain particles with a diameter smaller than 10 µm, there is hardly any cohesive effect. If the silt however contains a fraction of particles with a diameter around 1 µm, the cohesive effect is huge and already influences sand particles with a diameter of 1 mm. The model developed has been verified and validated with experiments from literature and gives a very good match, both quantitatively and qualitatively. The model developed also gives a good explanation of the famous Hjulström and Sundborg diagrams and gives these diagrams a more fundamental basis.

5.2. Introduction.

In Part A & B (Miedema (2012A) & (2012B)), a model for the entrainment of particles as a result of fluid (or air) flow over a bed of particles has been developed. The model distinguishes sliding, rolling and lifting as the mechanisms of entrainment. Sliding is a mechanism that occurs when many particles are starting to move and it is based on the global soil mechanical parameter of internal friction. Both rolling and lifting are mechanisms of individual particles and they are based on local parameters such as the pivot angle and the exposure and protrusion rate. Equations (5-1), (5-2) and (5-4) give the Shields parameter for these 3 mechanisms.

Sliding

$$\theta_{sliding} = \frac{u_*^2}{R_d \cdot g \cdot d} = \frac{4}{3} \cdot \frac{1}{\alpha^2} \cdot \frac{\mu_{sliding}}{\ell_{Drag}^2 \cdot f_D \cdot C_D + \mu_{sliding} \cdot f_L \cdot C_L} \qquad (5\text{-}1)$$

Rolling

$$\theta_{rolling} = \frac{u_*^2}{R_d \cdot g \cdot d} = \frac{4}{3} \cdot \frac{1}{\alpha^2} \cdot \frac{\mu_{rolling}}{\ell_{Drag}^2 \cdot f_D \cdot C_D + \mu_{rolling} \cdot f_L \cdot C_L} \qquad (5\text{-}2)$$

With the effective rolling friction coefficient $\mu_{rolling}$:

$$\mu_{rolling} = \frac{\sin(\psi + \phi_{Roll})}{\ell_{Lever-D} + \cos(\psi + \phi_{Roll})} \qquad (5\text{-}3)$$

Lifting

$$\theta_{lifting} = \frac{u_*^2}{R_d \cdot g \cdot d} = \frac{4}{3}\frac{1}{\alpha^2 \cdot C_L \cdot f_L} \quad \textbf{(5-4)}$$

This model does not yet include additional attraction forces between the particles, such as van der Waals forces or the effects of yield stress. Already in 1935 Hjulström (1935) developed the famous Hjulström diagram, incorporating cohesive effects for very small particles. In many other studies like Shields (1936) carried out, the cohesive effects were not taken into account, maybe because they were negligible.
In order to use the correct naming conventions for cohesion and adhesion, a definition will be given. Cohesion or cohesive attraction or cohesive force is a physical property of a substance, caused by intermolecular attraction between like-molecules within a body or substance that acts to unite them.
Adhesion or adhesive attraction or adhesive force is a physical property of two substances, caused by intermolecular attraction between dissimilar molecules within a substance that acts to unite them. Mechanical, chemical, dispersive, electrostatic and diffusive adhesion can be distinguished. The forces involved may find their origin in Coulomb forces (ionic or covalent bonding) or van der Waals forces (Keesom forces or London forces). The attraction between like-materials, such as the attraction between sand and silt particles, both consisting of quartz, will be considered to be a cohesive attraction, while the attraction between sand and clay particles will be considered to be an adhesive attraction. The shear strength or yield stress of clay is considered to be a cohesive attraction between clay particles. Sand and silt particles are considered not to have an electrical charge at the surface and thus not to have an electrical diffusive repulsive double layer, resulting in only being subjected to van der Waals attraction forces, besides the forces resulting from drag, lift and turbulence.
Some other definitions those are important in interpreting the findings from literature. Sand is considered to consist of quartz with particle diameters above 62 µm, above 2 mm this is considered to be gravel and above 64 mm it is called cobbles.
Silt is also considered to consist of quartz particles with diameters between 2 µm and 62 µm. Smaller particles consisting of quartz will also be considered to be silt here. Silt is considered to be inert and only subject to long range van der Waals forces. Clay consists of clay minerals (other than quartz) like kaolinite, montmorillonite, smectite, illite and chlorite, also named phyllosilicates minerals. Clay is often classified as consisting of particles smaller than 2 µm, but since the mineral composition is completely different from quartz, it is better to distinguish based on mineral composition. Clay is considered to be subject to all sorts of electro-chemical interactions as well as to the long range van der Waals forces. Mud is considered to be a mixture of silt and clay, with possibly other additions like organic matter.
To explain for the cohesive effect of very small particles as shown in the famous Hjulström diagram, only the long range van der Waals forces will be considered here, as a result of silt-sand interactions. The effect of other attraction (or repulsion) forces, resulting in for example yield stress, will be discussed later.

5.3. Previous Research.

5.3.1. Hjulström (1935), Sundborg (1956) and Postma (1967).

Hjulström (1935) & (1939) published the famous Hjulström diagram, showing the threshold flow velocity as a function of the particle diameter for a 100 cm water level flow. For large particles the threshold flow velocity increases with an increasing particle diameter, but for small particles the threshold flow velocity increases with a decreasing particle diameter. For particles near 0.5 mm a minimum threshold flow velocity is found. Figure 5-1 shows the Hjulström diagram. The increase of the threshold flow velocity with a decreasing particle diameter is explained with the phenomenon of cohesion. The research of Shields (1936) which was carried out in the same period of time did not contain such small particle diameters, thus cohesive effects were not included in this research. The Hjulström diagram can be well approximated with the following 2 empirical equations for the threshold flow velocity and the deposition velocity.

$$U_c = 1.5 \cdot \left(\frac{\nu}{d}\right)^{0.80} + 0.85 \cdot \left(\frac{\nu}{d}\right)^{0.35} + 9.5 \cdot \frac{R_d \cdot g \cdot d}{\left(1 + 2.25 \cdot R_d \cdot g \cdot d\right)} \quad \textbf{(5-5)}$$

$$U_d = 77 \cdot \frac{d}{\left(1 + 24 \cdot d\right)} \quad \textbf{(5-6)}$$

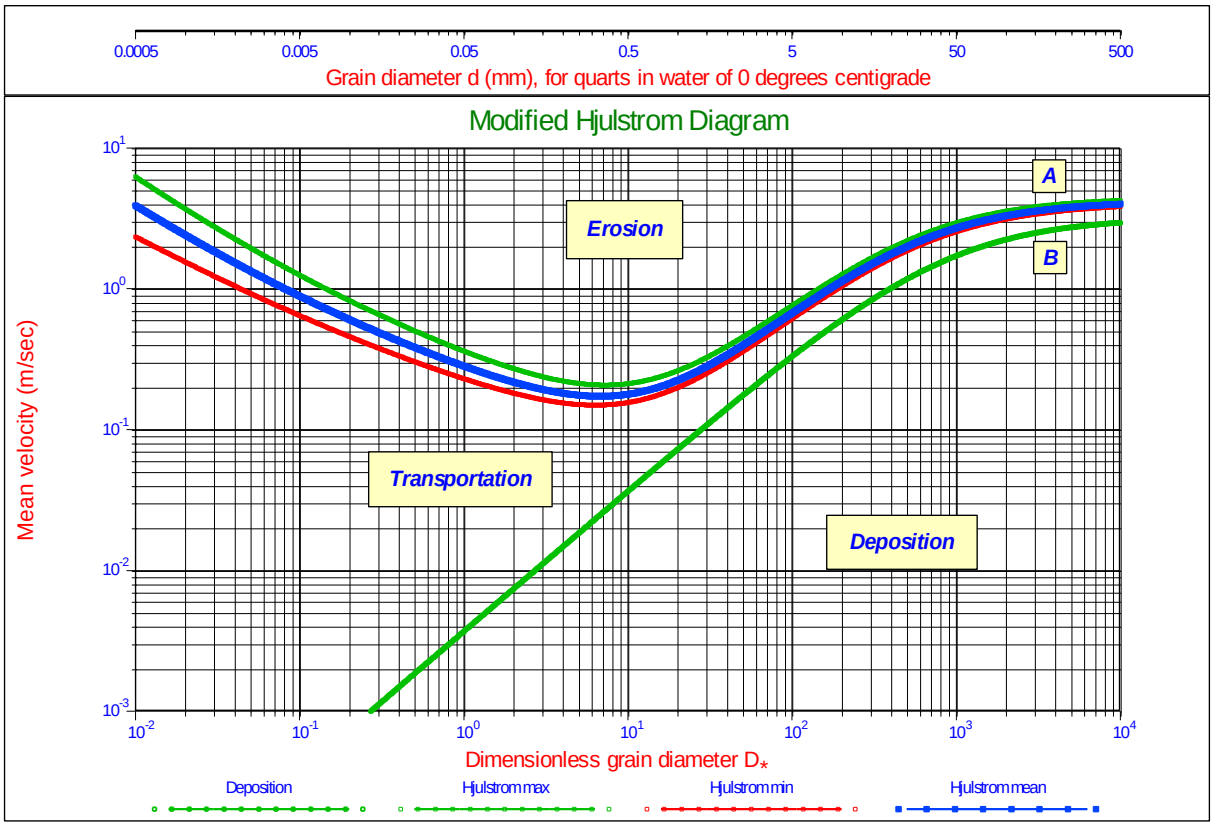

Figure 5-1: The modified Hjulström diagram.

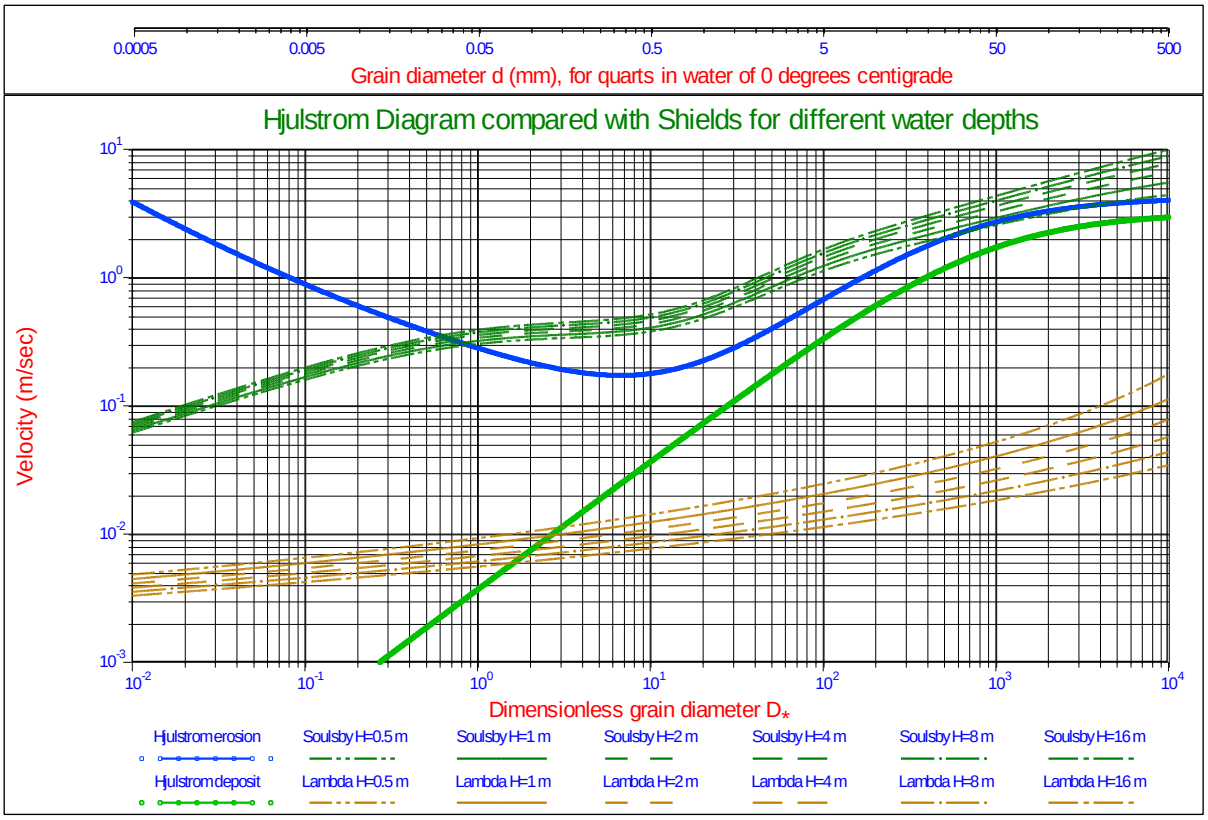

Figure 5-2: Hjulström compared with Shields for different water depths, according to Soulsby & Whitehouse (1997).

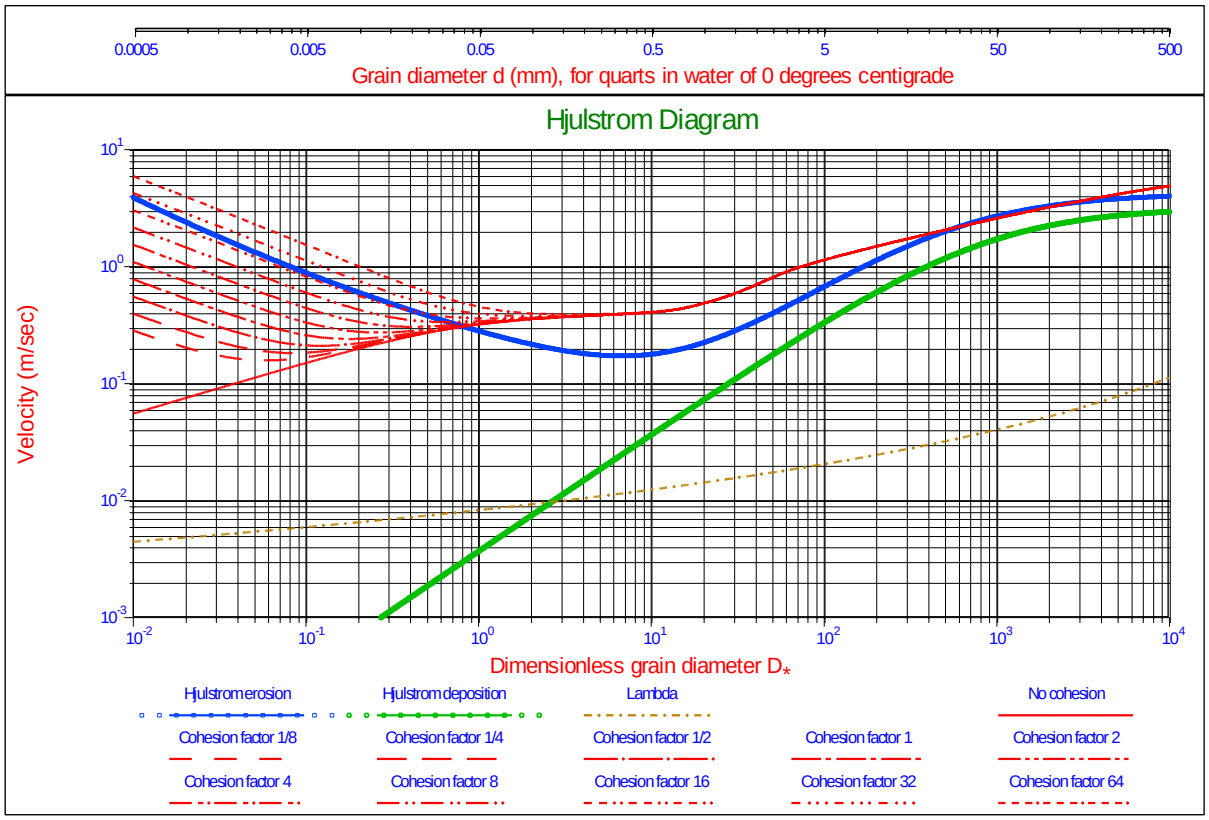

Figure 5-3: The Hjulström diagram compared with Shields curves with cohesion.

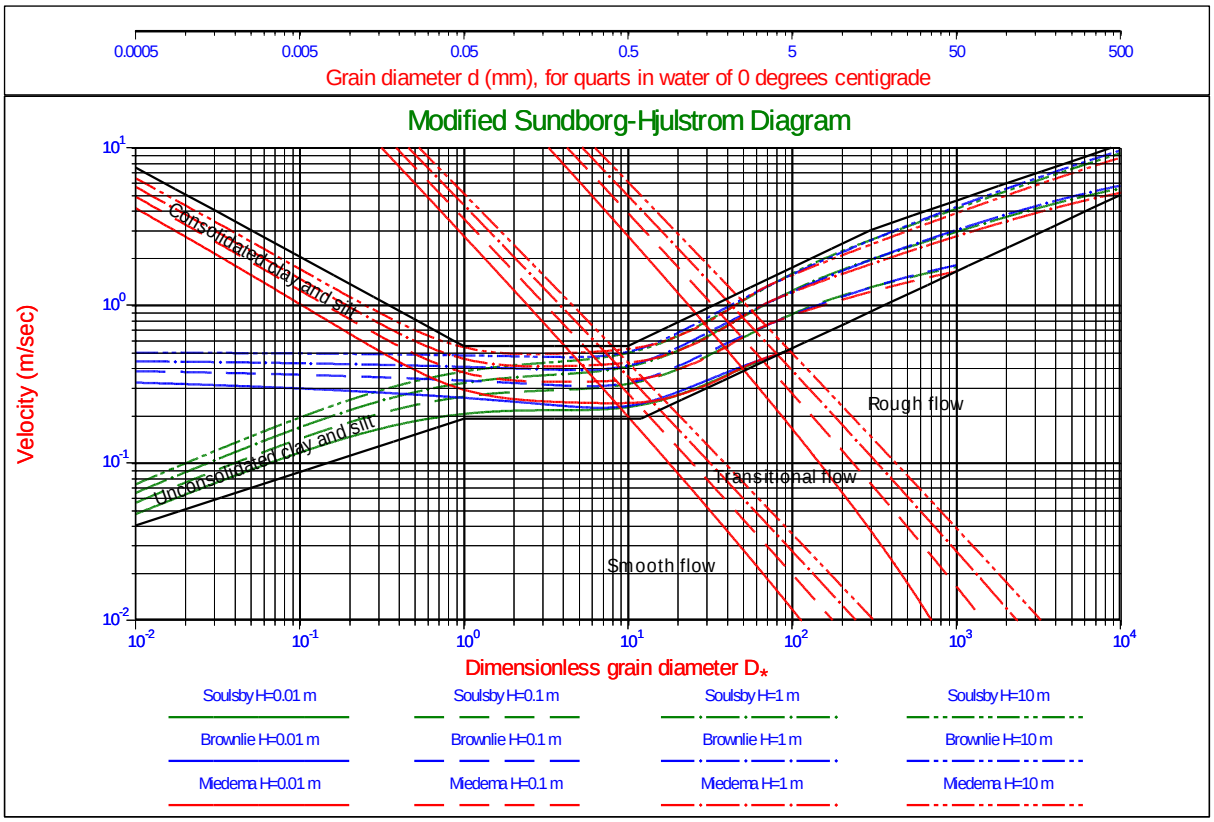

Figure 5-4: The modified Sundborg-Hjulström diagram.

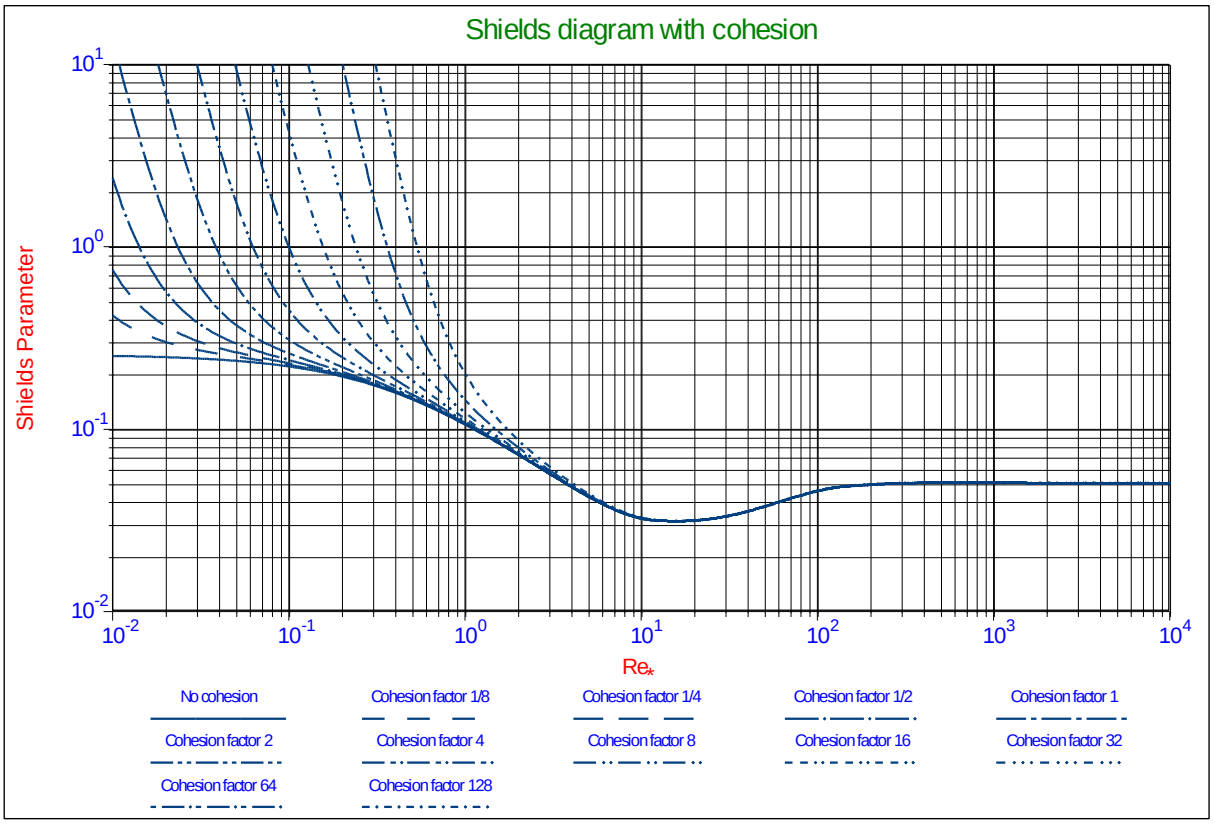

Figure 5-5: The Shields diagram with cohesion.

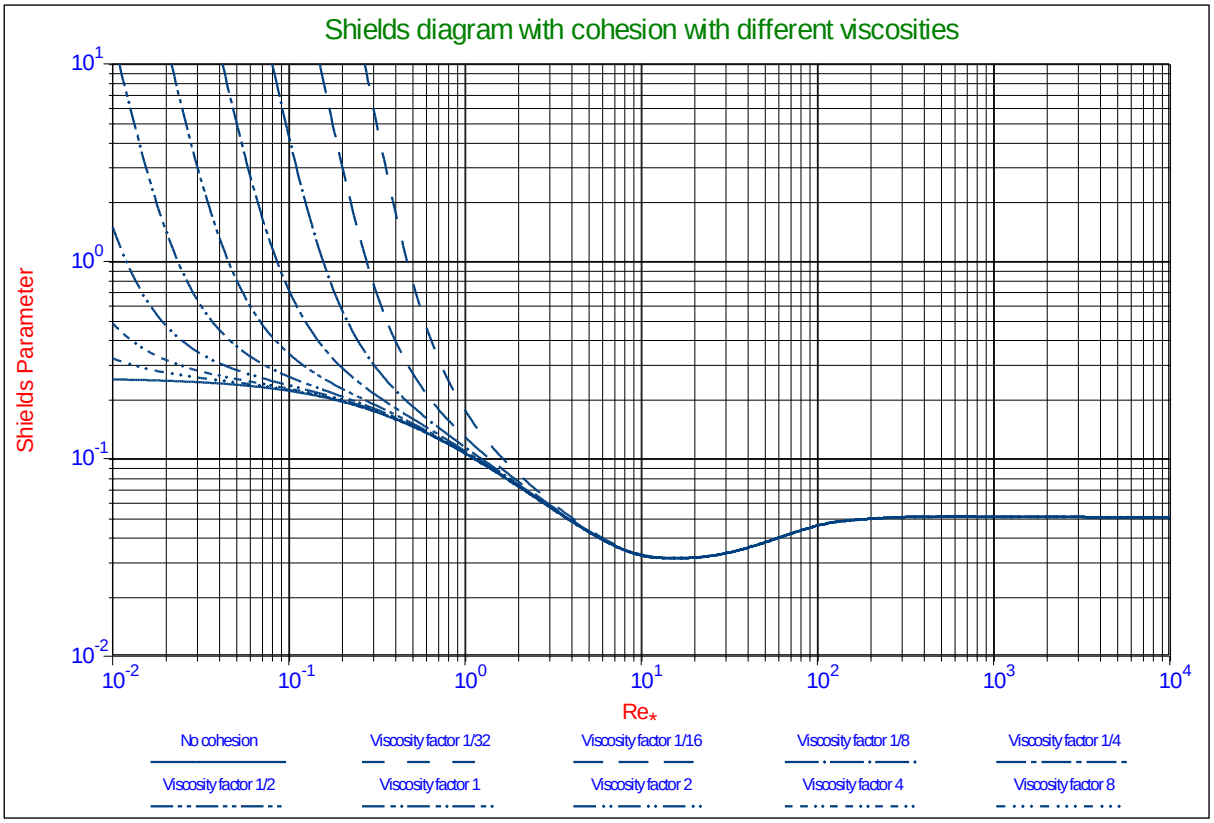

Figure 5-6: The Shields curve with cohesion with different viscosities.

Sundborg (1956) modified the Hjulström diagram and included different levels of cohesion, resulting in a more or less constant threshold flow velocity in the absence of cohesive effects for small particle diameters and a similar behavior for cohesive soils. Postma (1967) further improved the diagram and talks about consolidated and unconsolidated soils. Figure 5-4 shows a modified Sundborg-Hjulström diagram. Later the research focused more on improving the modeling of the Shields diagram and finding experimental proof for this, resulting in a number of mechanistic models, as summarized by Buffington & Montgomery (1997) and Paphitis (2001), and a number of empirical equations of which the Brownlie (1981) equation and the Soulsby & Whitehouse (1997) equation should be mentioned.

The Brownlie (1981) equation results in an increasing Shields value for a decreasing boundary Reynolds number with a power of almost -1. Translated into critical shear stress or shear velocity, this would result in an almost constant critical shear stress and shear velocity for a decreasing particle diameter. The Soulsby & Whitehouse (1997) equation results in an increasing shear stress and shear velocity for an increasing particle diameter for small particles. The shear stress increases almost linear with the particle diameter and thus the shear velocity with the square root. Figure 5-4 shows the behavior of both the Brownlie (1981) equation and the Soulsby & Whitehouse (1997) equation in the Sundborg-Hjulström diagram for 4 water depths. The third set of curves in this diagram are curves based on the Miedema (2012A) & (2012B) model, extended with the Zanke (2001) model for cohesion, as will be discussed later. From Figure 5-4 it is clear that unconsolidated soils (no cohesion) do not result in a horizontal line, but follow the Soulsby & Whitehouse (1997) equation, resulting in proportionality between the threshold flow velocity and the particle diameter with a power of 0.5 for very small particles. The Brownlie (1981) equation gives a power of 0 and the Miedema (2012A) & (2012B) & Zanke (2001) model a power of -0.5 for cohesive soils. So the concept of a horizontal curve for unconsolidated/non-cohesive soils according to Sundborg (1956) and Postma (1967) is rejected here, instead the Soulsby & Whitehouse (1997) equation or the Miedema (2012A) & (2012B) model without cohesion should be used.
To understand the physics behind the phenomena of cohesion and adhesion, a number of models will be analyzed and a new model will be developed.

5.3.2. Dou Go-Ren (1962).

Dou Go-Ren (1962), (1964), (2000) and (2001) derived the following equation for the friction velocity $\mathbf{u_{*c}}$ with the water depth as a parameter.

$$\mathbf{u_{*c} = k \cdot \left(\frac{d'}{d_*}\right)^{1/6} \cdot \left(3.6 \cdot R_d \cdot g \cdot d + \left(\frac{\gamma_0}{\gamma_{0*}}\right)^{5/2} \cdot \frac{\varepsilon_0}{d} + \left(\frac{\gamma_0}{\gamma_{0*}}\right)^{5/2} \cdot g \cdot H \cdot \left(\frac{\delta}{d}\right)^{3/2} \right)^{0.5}} \qquad \textbf{(5-7)}$$

For water depths greater than $\mathbf{70 \cdot d}$, Dou Go-Ren (1962) gives $\mathbf{k = 0.128}$, $\mathbf{\varepsilon_0 = 1.75 \cdot 10^{-6}\ m^3/sec^2}$ for normal sands, $\mathbf{\delta = 2.31 \cdot 10^{-7}\ m}$ and $\mathbf{R_d = 1.65}$. Further Dou uses:

$$\mathbf{d' = \begin{cases} 0.5\ mm & \rightarrow \quad d \le 0.5\ mm \\ d & \rightarrow \quad 0.5\ mm < d < 10\ mm \\ 10\ mm & \rightarrow \quad d \ge 10\ mm \end{cases}} \qquad \textbf{(5-8)}$$

$$\mathbf{d_* = 10\ mm}$$

And $\mathbf{\gamma_0 / \gamma_{0*} = 1}$ the effect of the degree of compaction, where the value of 1 gives a normal compacted sand. $\mathbf{\gamma_0}$ is the dry bulk density of the sand, while $\mathbf{\gamma_{0*}}$ gives the dry bulk density of a stable compacted sand.
Equation (5-8) can easily be transformed into the critical shear stress or the Shields parameter by:

$$\mathbf{\tau_{cr} = \rho_w \cdot u_{*c}^2 \ \ and \ \ \theta_{cr} = \frac{\rho_w \cdot u_{*c}^2}{\left(\rho_q - \rho_w\right) \cdot g \cdot d}} \qquad \textbf{(5-9)}$$

For direct use in the Hjulström diagram, Dou (1962) gives, based on the velocity distribution:

$$\mathbf{u_c = k \cdot 2.5 \cdot \ln\left(11 \cdot \frac{H}{k_s}\right) \cdot \left(\frac{d'}{d_*}\right)^{1/6} \cdot \left(3.6 \cdot R_d \cdot g \cdot d + \left(\frac{\gamma_0}{\gamma_{0*}}\right)^{5/2} \cdot \frac{\varepsilon_0}{d} + \left(\frac{\gamma_0}{\gamma_{0*}}\right)^{5/2} \cdot g \cdot H \cdot \left(\frac{\delta}{d}\right)^{3/2} \right)^{0.5}} \qquad \textbf{(5-10)}$$

With the bed roughness $\mathbf{k_s}$ according to:

$$\mathbf{k_s = \begin{cases} 1.0\ mm & \rightarrow \quad d \le 0.5\ mm \\ 2 \cdot d & \rightarrow \quad 0.5\ mm < d < 10\ mm \\ 20\ mm & \rightarrow \quad d \ge 10\ mm \end{cases}} \qquad \textbf{(5-11)}$$

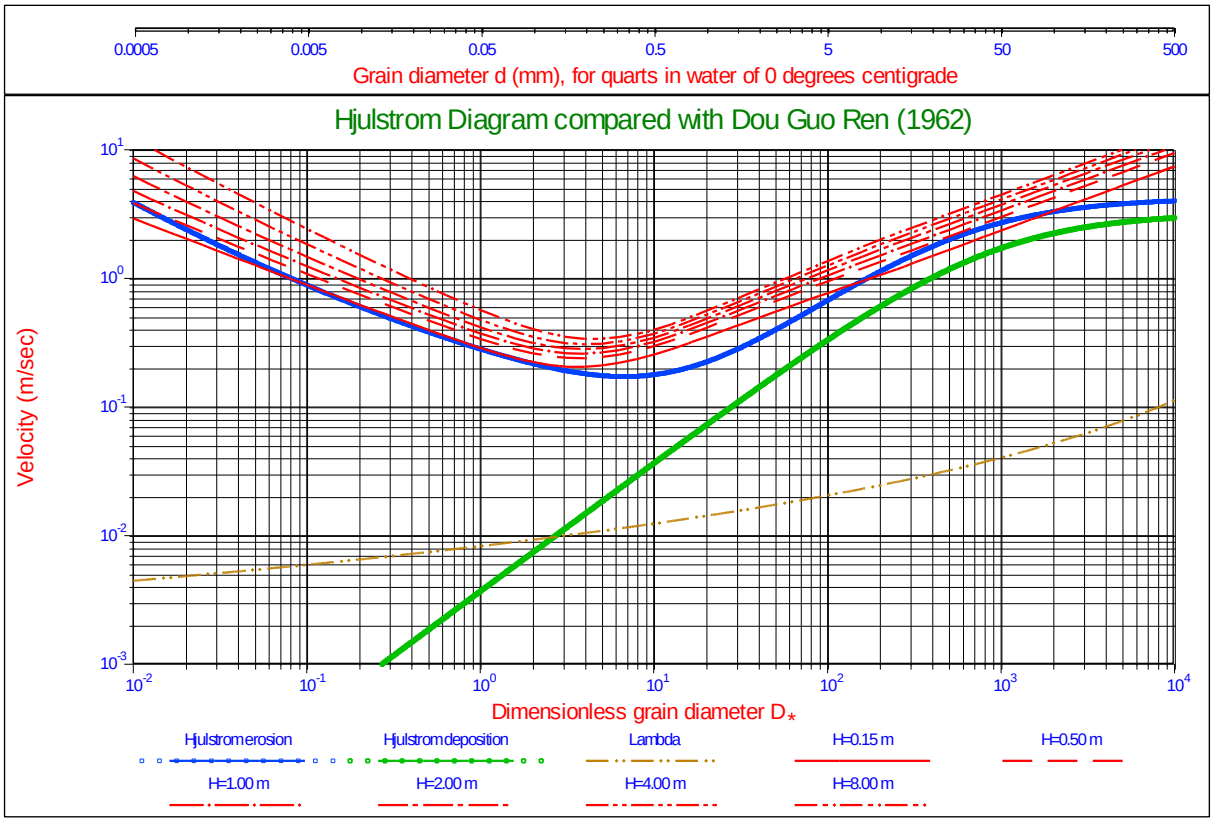

Figure 5-7: The Hjulström diagram compared with the equation of Dou Guo Ren (1962).

Figure 5-7 shows the results of the equation of Dou for different water depths and compared with the Hjulström diagram. The Dou equation overestimates the Hjulström curve for the water depth of 1 m on which the standard Hjulström curve is based.

Analysing the Dou equation results in the following conclusions: The first term of the Dou equation matches the Shields curve for large particles, giving $\tau_{cr} = 955 \cdot d$ and $\theta_{cr} = 0.06$ (Miedema (2012A) found $\tau_{cr} = 836 \cdot d$ and $\theta_{cr} = 0.05$). For very small particles the Dou equation gives smaller values, $\tau_{cr} = 344 \cdot d$ and $\theta_{cr} = 0.022$, which contradicts with the Shields curve (Miedema (2012A) found $\tau_{cr} = 4264 \cdot d$ and $\theta_{cr} = 0.255$) giving higher value for the Shields parameter for small particles, also according to the Soulsby & Whitehouse (1997) equation. The second term in the Dou equation is the term representing cohesion. Compared to the first (Shields) term, the cohesion is inversely proportional to the particle diameter to the second power, proportional to the cohesion coefficient ε_0 and proportional to the dry bulk density to the power 2.5. The explanation of this term should be found in physical properties and mineral and chemical factors resulting in bonds between particles, according to Dou (2001). The third term deals with the hydrostatic (over)pressure, a term that does not contribute a lot and should be included in the influence of the water depth on the relative roughness. The roughness term in equation (5-11) matches a friction coefficient of about 0.01 in the relation $u_{*c} = \sqrt{\lambda / 8} \cdot u_c$. Resuming it can be stated that according to Dou (1962), for very fine particles when the first term (gravity term) and the third term are neglected, the critical velocity u_c and the critical friction velocity u_{*c} are inversely proportional to the square root of the particle diameter and the critical shear stress τ_{cr} is inversely proportional to the particle diameter. Dou (1962) does not distinguish between quartz and clay particles.

5.3.3. Zanke (1982) & (2003).

Zanke (1982) & (2003) and Luckner (2002) state that in the range of very fine grains, cohesive action occurs in the quarts-water system. According to Zanke (1982) the cohesive force originates from surface tension and from the fact that there will always be a small fraction of very fine particles available. A small film with a thickness of just a few molecules will surround the particles and is bonded to the particles (hygroscopic). In the contact point between particles this thin film results in an attraction force due to the phenomenon of surface tension. For particles inside the bed, these attraction forces are phased out because they act from every direction, but for particles at the surface these attraction forces result in a downwards directed resulting force. This cohesive action or attractive force increases the apparent weight of the particles with a factor **K** and thus also increases the friction coefficient in the case of a sliding mechanism or the effective friction coefficient the in case of the rolling mechanism. This gives for the factor **K**:

$$K = \frac{F_{w,eff}}{F_w} = \frac{\mu_{sliding,eff}}{\mu_{sliding}} = \frac{\mu_{rolling,eff}}{\mu_{rolling}} = \left(1 + c \cdot \frac{3 \cdot 10^{-8}}{\left(\rho_q - \rho_w\right) \cdot d^2}\right) \tag{5-12}$$

The factor c is introduced here to be able to experiment with the strength of the cohesive effect. Zanke (2003) validated equation (5-12) based on measurements of Unsold (1984). Incorporating the cohesive effect in equations (5-1) & (5-2) gives:

Sliding

$$\theta_{sliding} = \frac{u_*^2}{R_d \cdot g \cdot d} = \frac{4}{3} \cdot \frac{1}{\alpha^2} \cdot \frac{\mu_{sliding} \cdot K}{\ell_{Drag}^2 \cdot f_D \cdot C_D + \mu_{sliding} \cdot K \cdot f_L \cdot C_L} \tag{5-13}$$

Rolling

$$\theta_{rolling} = \frac{u_*^2}{R_d \cdot g \cdot d} = \frac{4}{3} \cdot \frac{1}{\alpha^2} \cdot \frac{\mu_{rolling} \cdot K}{\ell_{Drag}^2 \cdot f_D \cdot C_D + \mu_{rolling} \cdot K \cdot f_L \cdot C_L} \tag{5-14}$$

For very fine grains the factor K becomes very large leading to:

$$\theta = \frac{u_*^2}{R_d \cdot g \cdot d} = \frac{4}{3} \cdot \frac{1}{\alpha^2} \cdot \frac{1}{f_L \cdot C_L} \tag{5-15}$$

Which in fact means that the Shields value becomes independent of the drag coefficient, but also independent of the factor **K**. Based on later reasoning one can assume that the factor **K** should only be used in the nominator and not in the denominator. The factor **K** is a multiplication factor for the critical Shields parameter or the critical shear stress, but not for the weight or the friction coefficient. In the current model, this does not really matter, since lift is considered not to be present at small boundary Reynolds numbers, eliminating **K** from the denominator. To understand the reasoning of Zanke (1982), the phenomenon of surface tension will be analysed further.

Surface Tension of a Bubble.

The pressure inside an ideal (one surface) bubble can be derived from thermodynamic free energy considerations. At constant temperature, the differential Helmholtz free energy is given by:

$$dF = -p_{st} \cdot dV + \gamma \cdot dA \tag{5-16}$$

Where p is, the pressure difference between inside and outside of the bubble and γ is the surface tension. In equilibrium $dF = 0$ and so:

$$p_{st} \cdot dV = \gamma \cdot dA \tag{5-17}$$

For a spherical bubble, the volume and the surface area are given by:

$$V = \frac{4}{3} \cdot \pi \cdot R^3 \rightarrow dV = 4 \cdot \pi \cdot R^2 \cdot dR \tag{5-18}$$

And

$$A = 4 \cdot \pi \cdot R^2 \rightarrow dA = 8 \cdot \pi \cdot R \cdot dR \tag{5-19}$$

Substituting these relations into equation (5-17) gives:

$$p_{st} = \frac{2}{R} \cdot \gamma = \frac{4}{d} \cdot \gamma \tag{5-20}$$

For real bubbles the pressure is doubled due to the presence of two interfaces, one inside and one outside. Now consider a small bridge between two particles at the contact point, with a cross-section α times the cross-section of the particle A. The pressure inside the bridge will be smaller than the surrounding pressure due to the surface tension, resulting in an attraction force between the two particles. When the density of the sand is smaller, the contact areas will be smaller, resulting in a smaller cross-section of the bridge and thus a smaller attraction force. This could be an explanation for the attraction force between very small particles and also for the fact that this attraction force decreases with decreasing density (increasing particle-particle distance) of the solids-water mixture. Adding the surface tension force to the weight of the particle would give an effective weight of:

$$\begin{aligned} &F_{w,eff} = F_w + F_{st} = F_w \cdot \left(1 + \frac{F_{st}}{F_w}\right) \\ &\left(\rho_q - \rho_w\right) \cdot g \cdot \frac{\pi}{6} \cdot d^3 + p_{st} \cdot \alpha \cdot A = \left(\rho_q - \rho_w\right) \cdot g \cdot \frac{\pi}{6} \cdot d^3 + \frac{4}{d} \cdot \gamma \cdot \alpha \cdot \frac{\pi}{4} \cdot d^2 \end{aligned} \tag{5-21}$$

Writing this in the form of equation (5-12) gives:

$$F_{w,eff} = \left(\rho_q - \rho_w\right) \cdot g \cdot \frac{\pi}{6} \cdot d^3 \cdot \left(1 + \frac{6 \cdot \alpha \cdot \gamma}{\left(\rho_q - \rho_w\right) \cdot g \cdot d^2}\right) = F_w \cdot \left(1 + \frac{6 \cdot \alpha \cdot \gamma}{\left(\rho_q - \rho_w\right) \cdot g \cdot d^2}\right) \tag{5-22}$$

Combining equations (5-12) and (5-22) gives:

$$\left(1 + c \cdot \frac{3 \cdot 10^{-8}}{\left(\rho_q - \rho_w\right) \cdot d^2}\right) = \left(1 + \frac{6 \cdot \alpha \cdot \gamma}{\left(\rho_q - \rho_w\right) \cdot g \cdot d^2}\right) \tag{5-23}$$

This way the coefficient as used by Zanke (1982) can be related to the surface tension, according to:

$$c \cdot 3 \cdot 10^{-8} = \frac{6 \cdot \alpha \cdot \gamma}{g} \rightarrow \alpha = \frac{3 \cdot 10^{-8} \cdot c \cdot g}{6 \cdot \gamma} = 6.54 \cdot 10^{-7} \cdot c \tag{5-24}$$

$$\text{With : } \gamma = 75 \cdot 10^{-3}\ N/m$$

Figure 5-8 shows the cohesive effect according to Zanke (1982) for an exposure level of 0.6 and laminar main flow. The data in this figure originate from White (1940), Mantz (1977), Yalin & Karahan (1979) and Loiseleux et al. (2005). It is clear from this figure that for very small boundary Reynolds numbers and thus particle diameters, the Shields value does not always have asymptotic behavior towards a constant value, but especially the data of White (1940) suggest that the Shields value might increase with decreasing particle diameter. Applying the Zanke (1982) cohesion model shows such behavior. Figure 5-8 also shows how to apply the cohesion model. Just multiplying the Shields value with the factor from equation (5-12) does not suffice. A higher Shields value implies a higher critical shear stress, which in turn means a higher friction velocity. A higher friction velocity implies a higher boundary Reynolds number. Applying the cohesive effect thus gives an even steeper curve than the ones found in the publications of Zanke (2001) and (2003), Luckner (2002) and Luckner & Zanke (2007). The bridge

surface factor **α** and thus the cohesion strength factor **c**, will depend on the shape of the particles, the amount of fines, the bulk density and probably on factors like salinity and pH of the water.
Analyzing the trends of the Zanke (1982) equations with respect to the critical velocity, critical friction velocity, critical shear stress and the Shields parameter, results in the following conclusions:

1. The factor **K** should not be applied to the gravity force, resulting in an influence in nominator and denominator, but this factor should be used as a multiplication factor for the critical shear stress τ_{cr} of the Shields parameter θ_{cr} .
2. Neglecting the **1** in the factor **K** makes the critical shear stress inversely proportional to the particle diameter, the Shields parameter inversely proportional to the particle diameter squared and the critical velocity or critical friction velocity inversely proportional to the square root of the particle diameter.
3. This behavior matches the Hjulström curve (Figure 5-1) for small particles and also matches the equation (5-7) of Dou (1962).
4. Just like with the Dou (1962) equation, the proportionalities are fixed, while literature also shows other proportionalities. So there must be physical phenomena that are not taken into account yet.
5. Zanke (1982) clearly states that the cohesive effect in equation (5-12) is the result of the silt fraction (quartz).

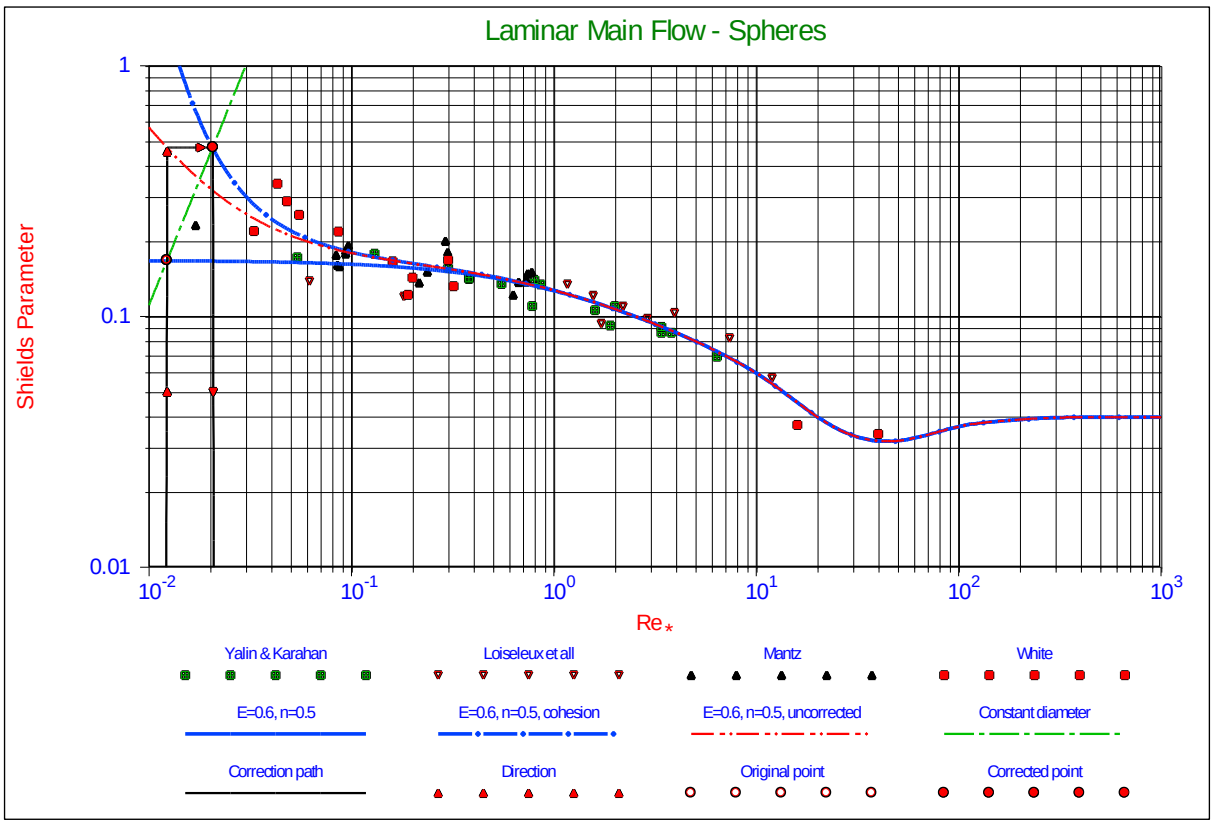

Figure 5-8: The cohesive effect according to Zanke (1982).

Zanke (1977) also gives an approximation equation for the Hjulström curve, based on the average flow velocity, according to:

$$u_{cm} = 2.8 \cdot \sqrt{R_d \cdot g \cdot d} + 14.7 \cdot c \cdot \frac{\nu}{d} \qquad \textbf{(5-25)}$$

The factor **c** determines the strength of the attraction forces between the particles. Zanke (1982) states that the value of **c=1.0** for natural sands. Figure 5-9 shows the above relation for different values of the factor **c**, compared with the original Hjulström curve. For small particles, this critical velocity is inversely proportional with the particle diameter, where equation (5-12) results in an inverse proportionality with the square root of the particle diameter. The proportionality of equation (5-25) results in an inverse proportionality of the critical shear stress with the second power of the particle diameter and an inverse proportionality of the Shields parameter with the third power of the particle diameter. Ziervogel (2003), Ziervogel & Bohling (2003), Bohling (2009) and Bobertz et al. (2009) use equation (5-25) in relation with the Hjulström diagram with the critical velocity or the critical

friction velocity or the critical shear stress on the vertical axis. They state, citing Whitehouse et al. (2000), that for muddy cohesive sediments, the critical friction velocity $\mathbf{u_{*cr}}$ is limited to 3 cm/sec.

5.3.4. Dade et al. (1992).

Dade et al. (1992) added an adhesive/cohesive force to the equilibrium of moments for the rolling action of individual particles. They assumed this adhesive/cohesive force originated from the van der Waals forces, similar to equation (5-36). Dade et al. (1992) do not distinguish between small and big particles, resulting in an inverse proportionality with the fourth power of the particle diameter. They also did not distinguish between silt and clay particles. However, most of the examples shown are based on mud and clay and will be discussed by Miedema (2013D).

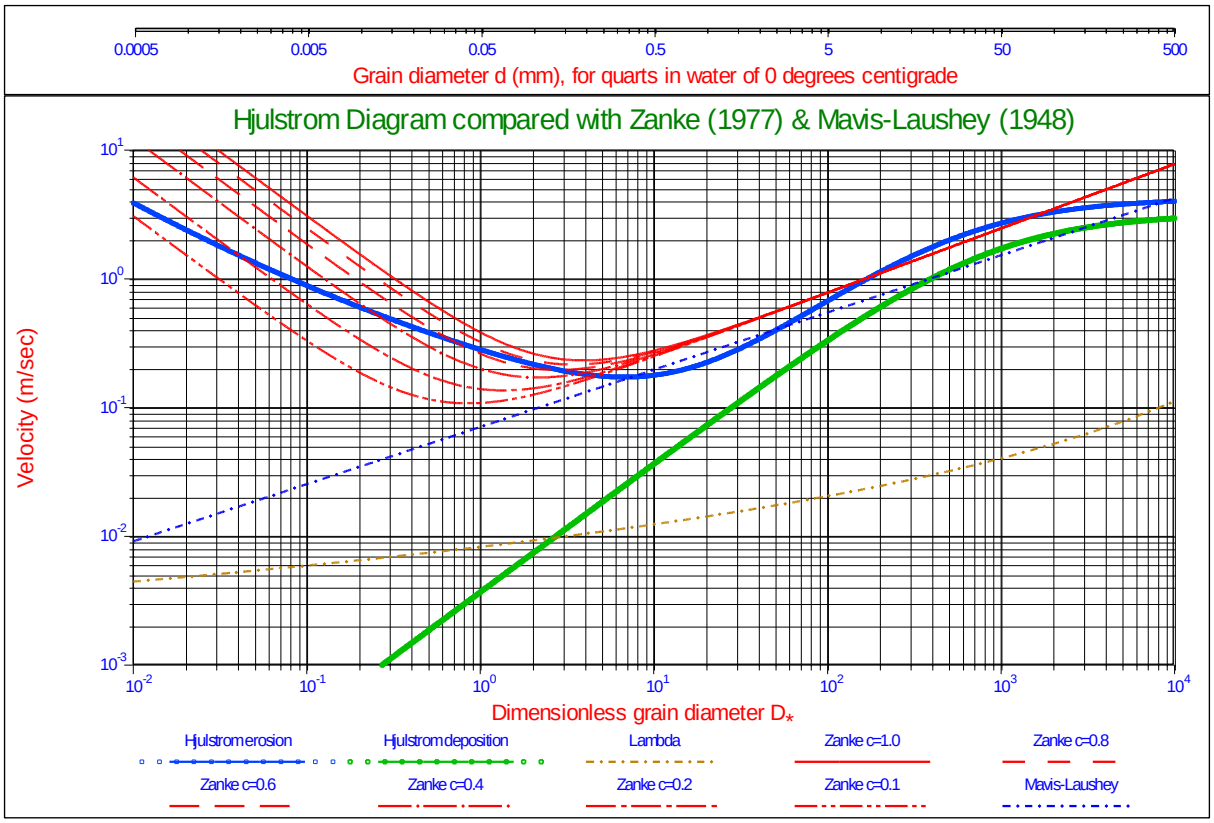

Figure 5-9: The Hjulström diagram compared with Zanke (1977) & Mavis-Laushey (1948).

5.3.5. Roberts et al. (1998) and later Lick et al. (2004).

Roberts et al. (1998) and later Lick et al. (2004) used the following basic equations for the modeling of cohesive effects. First the equation (d in m) for the critical shear stress for coarse particles from Chepil (1959), without any cohesive effect (see the data of Miller et al. (1977)) was given.

$$\tau_{cr,no-cohesion} = 414 \cdot d \qquad \textbf{(5-26)}$$

Second the equation for the critical shear stress for fine particles, derived from the data of White (1970), was given.

$$\tau_{cr,no-cohesion} = 0.275 \cdot \left(1000 \cdot d\right)^{0.4} \qquad \textbf{(5-27)}$$

Based on experiments carried out by WIHEE (1960), Dou (1964), Tang (1964), Sha (1965), Mehta & Lee (1994) and Chien & Wan (1999) a general relation for cohesive effects was derived by Lick et al. (2004):

$$\tau_{cr,cohesion} = a_0 \cdot d + \frac{b_0}{d} = a_0 \cdot d \cdot \left(1 + \frac{b_0}{a_0 \cdot d^2}\right) = \tau_{cr,no-cohesion} \cdot \left(1 + \frac{b_0}{a_0 \cdot d^2}\right) \qquad \textbf{(5-28)}$$

This general equation matches the equations of Zanke (1982) and Dou (1962) and thus also has an inversely proportional relation between the critical shear stress and the particle diameter for small particles, if the first term in equation (5-28) can be neglected. This can be explained by adding a cohesive force $\mathbf{F_c}$ and dividing it by the gravity force $\mathbf{F_w}$ (weight).

$$\tau_{cr,cohesion} = \tau_{cr,no-cohesion} \cdot \left(\frac{F_w + F_c}{F_w} \right) = \tau_{cr,no-cohesion} \cdot \left(1 + \frac{F_c}{F_w} \right) \tag{5-29}$$

Lick et al. (2004) assume that the cohesive force is proportional to the particle diameter and the gravity force is proportional to the third power of the particle diameter, resulting in a multiplication factor for the critical shear stress, which is inversely proportional to the second power of the particle diameter, for very small particles, according to:

$$\tau_{cr,cohesion} = \tau_{cr,no-cohesion} \cdot \left(1 + \frac{c_4}{c_3 \cdot d^2} \right) = 414 \cdot d \cdot \left(1 + \frac{c_4}{c_3 \cdot d^2} \right)$$

$$c_3 = \frac{\pi}{6} \cdot \left(\rho_q - \rho_w \right) \cdot g \approx 8.21 \cdot 10^3 \ \ N/m^3 \tag{5-30}$$

$$c_4 = 1.33 \cdot 10^{-4} \ \ N/m$$

The influence of the density of the sediment is taken into account by using an empirical exponential function, which is fitted on the data of Roberts et al. (1998).

$$\frac{c_4(\rho_s)}{c_4(1.85)} = \frac{a_1 \cdot e^{b_1 \cdot \rho_s}}{a_1 \cdot e^{b_1 \cdot 1.85}} = e^{b_1 \cdot (\rho_s - 1.85)} \tag{5-31}$$

$$a_1 = 7 \cdot 10^{-8} \quad N/m^2 : b_1 = 9.07 \quad L/kg$$

This leads to the following equation for the critical shear stress for a cohesive (based on a silt fraction) sediment.

$$\tau_{cr,cohesion} = 414 \cdot d \cdot \left(1 + \frac{1.33 \cdot 10^{-4} \cdot e^{9.07 \cdot (\rho_s - 1.85)}}{8.21 \cdot 10^3 \cdot d^2} \right) = 414 \cdot d \cdot \left(1 + \frac{1.62 \cdot 10^{-8} \cdot e^{9.07 \cdot (\rho_s - 1.85)}}{d^2} \right) \tag{5-32}$$

The graphical representation of this equation is shown in Figure 5-10, together with the data of Roberts et al. (1998) and Jin et al. (2002).
Using the model derived by Miedema (2012A) & (2012B), results in slightly different equations. You (2006) already commented on the equations used by Lick et al. (2004). First the equation for the critical shear stress for coarse particles, $\mathbf{d > 0.6mm}$, can be derived from the asymptotic value of the Shields curve for large boundary Reynolds numbers according to (d in m):

$$\theta_{cr} = \frac{\tau_{cr}}{\rho_w \cdot R_d \cdot g \cdot d} = 0.05$$

$$\tau_{cr} = \theta_{cr} \cdot \rho_w \cdot R_d \cdot g \cdot d = 0.05 \cdot 1025 \cdot 1.65 \cdot 9.81 \cdot d = 836 \cdot d \tag{5-33}$$

Which is roughly double the value as used by Roberts et al. (1998) and later Lick et al. (2004). For the intermediate particle sizes, from $\mathbf{0.02mm < d < 0.6mm}$, the following equation can be used (d in m):

$$\tau_{cr} = 0.38 \cdot (1000 \cdot d)^{0.4} \tag{5-34}$$

For the very fine particles, $\mathbf{d < 0.02mm}$, the following equation can be applied, based on the asymptotic value of the Shields curve according to Miedema (2012A) & (2012B), see also Figure 5-11 (d in m).

$$\theta_{cr} = \frac{\tau_{cr}}{\rho_w \cdot R_d \cdot g \cdot d} = 0.255 \qquad (5\text{-}35)$$

$$\tau_{cr} = \theta_{cr} \cdot \rho_w \cdot R_d \cdot g \cdot d = 0.255 \cdot 1025 \cdot 1.65 \cdot 9.81 \cdot d = 4264 \cdot d$$

The last 3 equations also match the data of Miller et al. (1977). The most probable reason for the difference between the equations (5-26) and (5-27) of Lick et al. (2004) and equations (5-33), (5-34) and (5-35) lies in the shape of the critical shear stress curve in figure 7 of Miller et al. (1977). Looking at a particle diameter of 1 mm, a critical shear stress of about 0.4 Pa is found, matching equation (5-26). At a particle diameter of 30 mm however, a critical shear stress of about 23 Pa is found, matching equation (5-33) closely. The shape of the critical shear stress curve in Figure 5-11 explains this difference. The critical shear stress of 0.4 Pa for a particle diameter of 1 mm almost matches equation (5-34) but not equation (5-27) of Roberts et al. (1998). The fit curves in Figure 5-11 are based on the Zanke (2001) model (equation (5-12)) with different values for the cohesion strength, combined with the Miedema (2012A) & (2012B) model. It is obvious that using the correct Shield curve as a basis, leads to a better fit with the data of Roberts et al. (1998). Jin et al. (2002) carried out measurements without and with a 2% bentonite addition. From Figure 5-11 it is clear that the data points without bentonite addition are already far above the Shields curve, probably due to the presence of a very fine silt fraction. Lick et al. (2004) conclude that these data points match equation(5-27), but this conclusion is rejected here. The data points of the experiments with the 2% bentonite addition are even more far above the Shields curve, which is explained by Lick et al. (2004) by introducing an additional binding force $F_b = B \cdot d^2$. The addition of clay particles, like bentonite, will be discussed in Miedema (2013D).
Resuming it can be concluded that the measurements of Roberts et al. (1998) and Jin et al. (2002) are valuable and will be used in the verification and validation paragraph. The trends, as described by the model of Lick et al. (2004) are also valuable, but the equations are based on an incorrect Shields curve as already noted by You (2006).

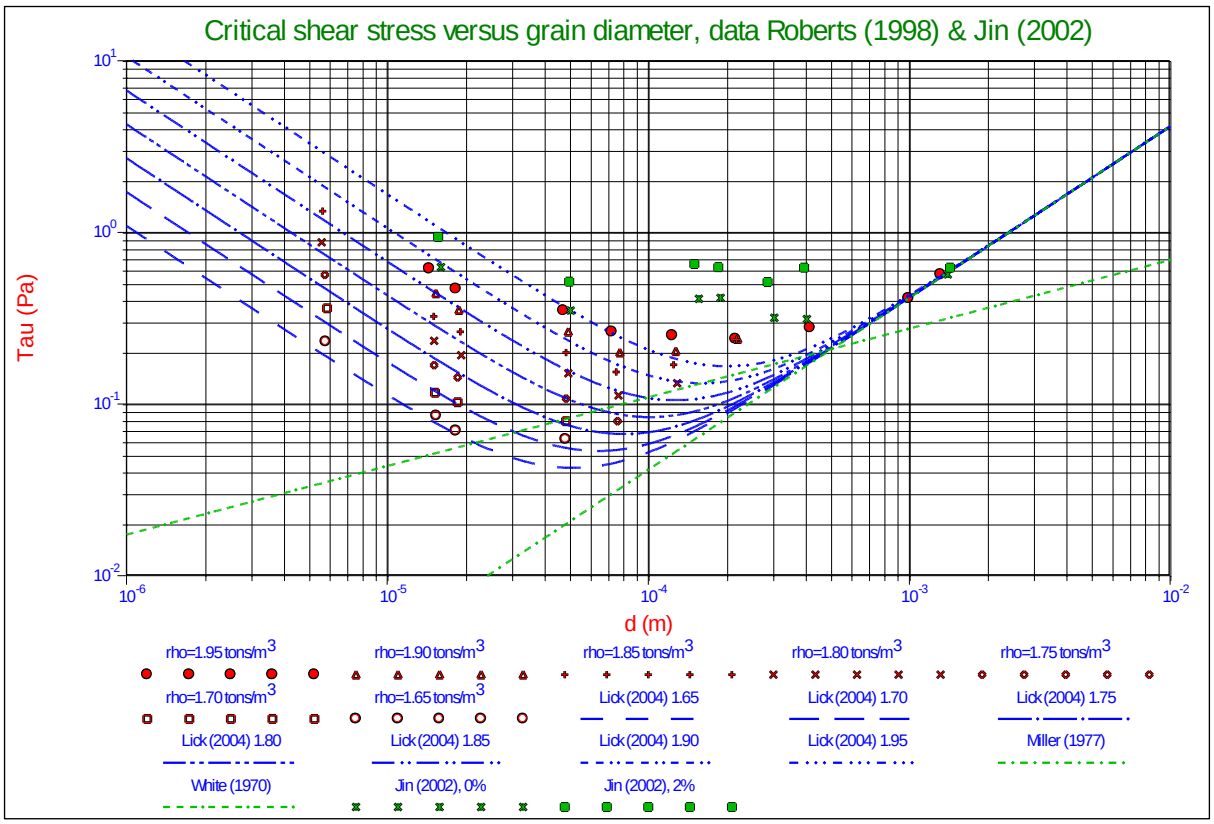

Figure 5-10: The shear stress as measured by Roberts et al (1998) and Jin (2002), modeled by Lick (2004).

5.3.6. Ternat (2007) & Ternat et al. (2008).

Ternat (2007) & Ternat et al. (2008) based his model for the attractive force between two particles on the van der Waals forces, according to Israelachvili (1985), just like Dade et al. (1992):

$$F_c = \frac{A_H \cdot d_1 \cdot d_2}{12 \cdot (d_1 + d_2) \cdot d_i^2} \qquad \textbf{(5-36)}$$

The coefficient A_H is the so called Hamaker constant, d_1 and d_2 are the particle diameters and d_i is the distance between the two particles. The main difficulty is to provide a good physical model for the inter-particle distance d_i, which appears to be a function of the porosity of the sediment. Ternat (2007) assumes a simple cubic packing arrangement and derives the following equation for the inter-particle distance d_i:

$$d_i = \left(\left(\frac{n_{max} - n_{min}}{n_{max} - n} \right)^{1/3} - 1 \right) \cdot d \qquad \textbf{(5-37)}$$

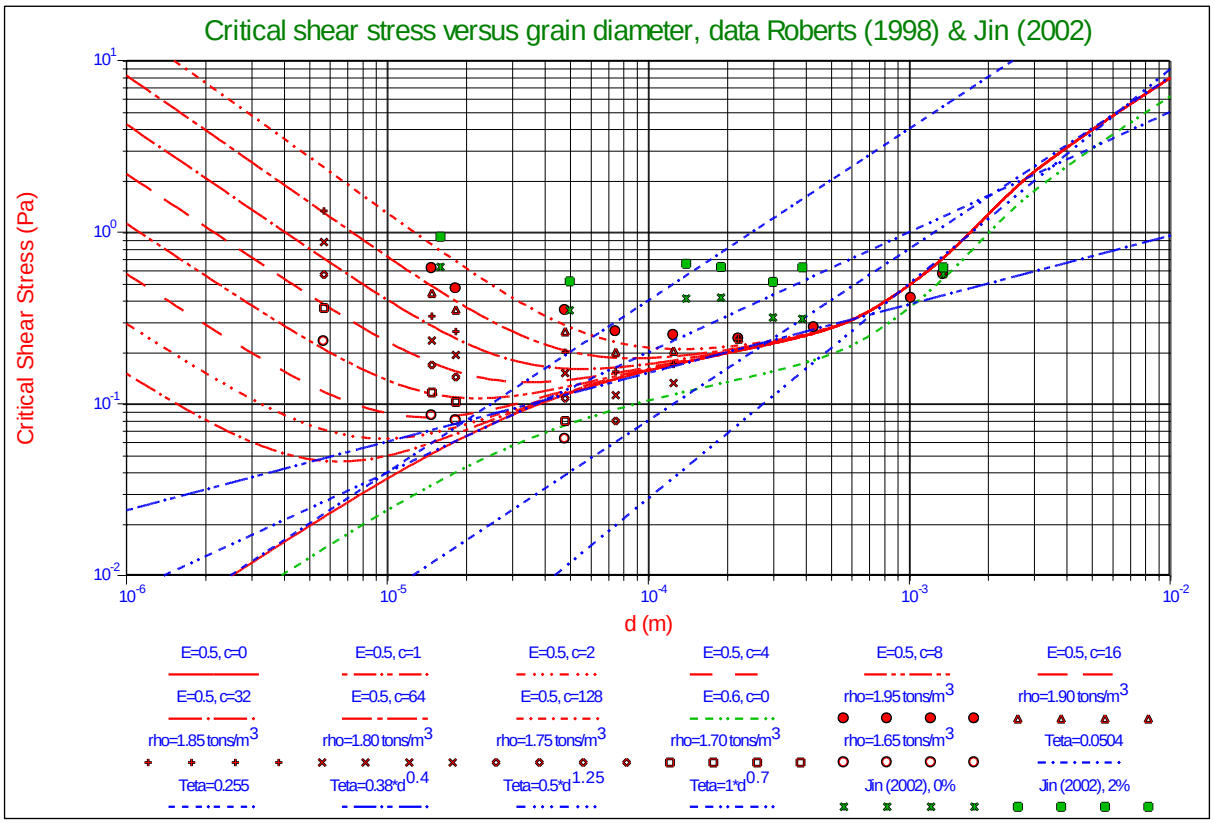

Figure 5-11: The shear stress as measured by Roberts et al. (1998) and Jin et al. (2002), modeled by Miedema (2012A).

The maximum porosity n_{max} is chosen 1, meaning, no solids, only fluid. The minimum porosity n_{min} depends on the packing arrangement and is $1-\pi/6$ for a cubic packing arrangement and 0.26 for a compact hexagonal structure. However, equation (5-37) is based on the cubic packing and should be adapted for other packing arrangements. It would be convenient to find a more general relation for the inter-particle distance. By assuming bi-modal sediment, consisting of small and big particles, the number of small particles surrounding one big particle can be determined. Further assuming that big particles at the surface are only covered with small particles over an angle ψ with the vertical and applying equation (5-36) for the force between one small particle and the big particle, gives:

$$F_{c,tot} = \frac{A_H \cdot d_b \cdot d_s}{12 \cdot (d_b + d_s) \cdot d_i^2} \cdot \left(\frac{1 - \cos(\psi)}{2} \right) \cdot \left(\frac{d_b}{d_s + 2 \cdot d_i} \right) \cdot \left(\left(1 + 2 \cdot \frac{d_s + 2 \cdot d_i}{d_b} \right)^3 - 1 \right) \quad \textbf{(5-38)}$$

This model, however promising, has a number of shortcomings. The relation for the inter-particle distance is based on a cubic packing and the maximum porosity. In soil mechanics it is more convenient to base such an equation on the minimum porosity according to Youd (1973) and the sediment porosity. The calculation of the number of small particles surrounding one big particle does not take into account the pores between the small particles, but assumes a solid layer of small particles. The calculation of the total attraction force for big particles at the surface is based on a summation or integration of all the attraction forces surrounding the surface particle, but not on the vertical components of these attraction forces. As a last point of criticism, Ternat (2007) assumes that all the additional pore volume of the sediment compared with the sediment having a minimum porosity, is part of the layer of water surrounding the small particles, resulting in a much too big inter-particle distance. The concept of this model is however very useful, although Ternat (2007) did not put it in an easily applicable form.

5.4. The Theoretical Model.

5.4.1. Equilibrium of Forces.

If sliding is considered to be the mechanism for the initiation of motion at the level of the Shields curve, the equilibrium of forces in the horizontal direction has to be valid, as derived in Miedema (2012A) & (2012B). However, in the case of the occurrence of cohesion and/or adhesion two additional forces may act on the particles considered. The first force is a tensile force F_{cv}, acting downwards, due to the attraction between particles and the second force is a shear force F_{ch}, acting horizontally, due to adhesion between the particles. This adhesion is be caused by the presence of clay particles between the sand particles, but in fact the real physical background of both forces is not yet fully understood, so an attempt is made to find an explanation for these forces. Now the horizontal equilibrium of forces yields:

$$F_D = F_{ch} + \mu \cdot (F_w + F_{cv} - F_L) \quad \textbf{(5-39)}$$

Assuming that there is no lift force in the region of the boundary Reynolds number, where cohesive effects are expected, the very small boundary Reynolds numbers, this gives:

$$\frac{F_D}{F_w} = \frac{F_{ch}}{F_w} + \mu \cdot \left(1 + \frac{F_{cv}}{F_w} \right) \quad \textbf{(5-40)}$$

With:

$$\frac{F_D}{F_w} = \frac{\mu \cdot F_{ch}}{\mu \cdot F_w} + \mu \cdot \left(1 + \frac{F_{cv}}{F_w} \right) = \mu \cdot \left(1 + \frac{F_{cv}}{F_w} + \frac{F_{ch}}{\mu \cdot F_w} \right) \quad \textbf{(5-41)}$$

This gives for the Shields parameter and for the critical shear stress:

$$\theta_{cr,cohesion} = \theta_{cr,no-cohesion} \cdot \left(1 + \frac{F_{cv}}{F_w} + \frac{F_{ch}}{\mu \cdot F_w} \right)$$
$$\tau_{cr,cohesion} = \tau_{cr,no-cohesion} \cdot \left(1 + \frac{F_{cv}}{F_w} + \frac{F_{ch}}{\mu \cdot F_w} \right) \quad \textbf{(5-42)}$$

Similar equations have been found by Dou Go-Ren (1962), Zanke (1982), Dade et al. (1992), Roberts et al. (1998), Lick et al. (2004) and Ternat et al. (2008). The origin of these forces could be the surface tension (Zanke (1982)) and/or the van der Waals forces (Dade et al. (1992), Roberts et al. (1998), Lick et al. (2004) and Ternat et al. (2008)). It is assumed that the vertical attraction forces find their origin in van der Waals forces (inert quartz particles like silt) or a combination of van der Waals forces and electro chemical forces (clay particles). The horizontal force is assumed to find its origin in the shear strength or yield stress of the material (clay). Surface tension finds its origin in van der Waals forces and its possible presence is considered under van der Waals forces.

5.4.2. Van der Waals Forces.

Van der Waals forces (Israelachvili (1985)) exist between atoms and molecules. The attractive van der Waals force between atoms is proportional to $1/r^7$, where r is the distance between the atoms. The empirical potential often used is the Lennard-Jones potential (LJ):

$$\phi(r) = 4\cdot\varepsilon\cdot\left(\left(\frac{\sigma}{r}\right)^{12} - \left(\frac{\sigma}{r}\right)^{6}\right);\ \ \sigma = \left(\frac{C}{A}\right)^{1/6};\ \ \varepsilon = \frac{C^2}{4\cdot B} \tag{5-43}$$

The $(\sigma/r)^{12}$ term represents the repulsive interaction, while the $(\sigma/r)^{6}$ term represents the attractive interaction. The empirical constant ε represents the characteristic energy of interaction between molecules (the maximum energy of attraction between a pair of molecules), while σ is a characteristic diameter of the molecule (also called the collision diameter) where the LJ potential equals zero. The diameter of atoms roughly ranges from 0.5 to 3 Ångström (10^{-10} m). The value of the collision diameter σ roughly ranges from 2.9 Ångström for H_2 to 6 Ångström for large molecules. Above a few Ångström to hundreds of Ångströms, van der Waals forces are significant, particularly between macroscopic bodies. The interaction between different geometries can be calculated by integration or summation of the LJ potential on the basis of pair wise additivity (Hamaker Summation Method). For example, the attractive force between two spheres with two different diameters is (in fact the two radii of curvature matter), according to Israelachvili (1985):

$$F(\delta) = \frac{A_H}{6\cdot\delta_{p,n}^2\cdot d_s^2}\cdot\frac{R_1\cdot R_2}{(R_1+R_2)} \tag{5-44}$$

If the two spheres have the same radius this results in:

$$F(\delta) = \frac{A_H}{6\cdot\delta_{p,n}^2\cdot d_s^2}\cdot\frac{R\cdot R}{(R+R)} = \frac{A_H}{6\cdot\delta_{p,n}^2\cdot d_s^2}\cdot\frac{R}{2} = \frac{A_H}{24\cdot\delta_{p,n}^2\cdot d_s} \tag{5-45}$$

If one of the two spheres is much smaller than the other one this results in the attractive force between a sphere and a plane, where R is the radius of the small sphere.

$$F(\delta) = \frac{A_H\cdot R}{6\cdot\delta_{p,n}^2\cdot d_s^2} = \frac{A_H\cdot d_s}{12\cdot\delta_{p,n}^2\cdot d_s^2} = \frac{A_H}{12\cdot\delta_{p,n}^2\cdot d_s} \tag{5-46}$$

The interaction constant A_H is called the Hamaker constant and depends on the type of molecules the spheres consist of and it depends on whether there is vacuum or water between the spheres. The distance $\delta_{p,n}\cdot d_s$ is the distance between the two spheres or the sphere and the plane. One notices that the very short ranged atom-atom interactions depend on $1/r^6$, while the macroscopic long ranged van der Waals sphere-sphere or sphere-plane interactions depend on $1/\left(\delta_{p,n}^2\cdot d_s\right)$. For two atoms or molecules in contact, the distance $\delta_{p,n}\cdot d_s$ has to be replaced by 40% of the so called interaction or collision distance σ, resulting in a surface tension force according to:

$$F(\sigma) = \frac{A_H}{6\cdot(0.4\cdot\sigma)^2}\cdot\frac{R_1\cdot R_2}{(R_1+R_2)} = 4\cdot\pi\cdot\gamma\cdot\frac{R_1\cdot R_2}{(R_1+R_2)} \tag{5-47}$$

This gives for the surface tension:

$$\gamma = \frac{A_H}{24\cdot\pi\cdot D_0^2} = \frac{A_H}{24\cdot\pi\cdot(0.4\cdot\sigma)^2} \tag{5-48}$$

$$D_0 = 0.4\cdot\sigma$$

For $\sigma = 0.4$ nm it follows $D_0 = 0.16$ nm. $D_0 = 0.16$ nm is a remarkable "universal constant" yielding values for surface energies that are in good agreement with experiments, except for strongly H-bonding liquids like water with a Hamaker constant of $3.7 \cdot 10^{-20}$ J and a surface tension of $73 \cdot 10^{-3}$ N/m at 20°C. Fused quartz has a Hamaker constant of $6.5 \cdot 10^{-20}$ J and crystalline quartz of $8.8 \cdot 10^{-20}$ J, both in vacuum. With a medium, like water, between the particles the Hamaker constant can be evaluated according to:

$$A_{H,particle-medium} = \left(\sqrt{A_{H,particle}} - \sqrt{A_{H,medium}}\right)^2 \quad \text{(5-49)}$$

If the two particles consist of two different materials and are separated by a medium, the Hamaker constant can be evaluated according to:

$$A_{H,particle1-medium-particle2} = \left(\sqrt{A_{H,particle1}} - \sqrt{A_{H,medium}}\right) \cdot \left(\sqrt{A_{H,particle2}} - \sqrt{A_{H,medium}}\right) \quad \text{(5-50)}$$

According to equation (5-49), the Hamaker constant of two crystalline quartz particles in water equals $1.088 \cdot 10^{-20}$ J. This value will be used in the calculations that follow. Table 5-1 gives Hamaker constant for some relevant materials, but it should be mentioned here that literature in general may give slightly different values. It should also be mentioned that salinity may influence the value of the Hamaker constant of the solution and in general it will reduce the value of the Hamaker constant. According to equations (5-49) and (5-50), the Hamaker constant of two similar particles separated by a layer of medium will always be positive, resulting in an attractive force. The Hamaker constant of two dissimilar particles separated by a medium, may however become negative if the Hamaker constant of one of the two particles is smaller than the Hamaker constant of the medium. A negative Hamaker constant implies that there is a repulsive force between the particles. Feiler et al. (2008) use this phenomenon to create super lubricity and explain that an increasing Hamaker constant increases the friction coefficient between bodies, but a negative Hamaker constant switches the divergent repulsive force on, preventing solid-solid contact. This way, a gold sphere interacting with a smooth Teflon surface in cyclohexane had a friction coefficient of just 0.0003.

Table 5-1: Hamaker constants for some relevant materials.

Material	Vacuum	Water
Water	$3.7 \cdot 10^{-20}$ J	-
Quartz (Crystalline)	$8.83 \cdot 10^{-20}$ J	$1.70 \cdot 10^{-20}$ J
Quartz (Fused)	$5 - 6.5 \cdot 10^{-20}$ J	$0.833 \cdot 10^{-20}$ J
Silica (Fused)	$6.55 \cdot 10^{-20}$ J	$0.849 \cdot 10^{-20}$ J
Calcite	$10.1 \cdot 10^{-20}$ J	$2.23 \cdot 10^{-20}$ J
Mica	$10 - 13.5 \cdot 10^{-20}$ J	$2.20 \cdot 10^{-20}$ J
Kaolinite	$6.8 \cdot 10^{-20}$ J	$3.10 \cdot 10^{-20}$ J
Montmorillonite	$7.8 \cdot 10^{-20}$ J	$2.20 \cdot 10^{-20}$ J
Illite	$8.6 \cdot 10^{-20}$ J	$2.50 \cdot 10^{-20}$ J

5.5. Theoretical Model for Cohesive/Adhesive Forces.

5.5.1. Number of Bonds.

Consider a two particle system with big particles with a diameter d_b and small particles with a diameter d_s. The small particles form a thin layer around the big particle as is shown in Figure 5-12. The small particles are surrounded with a thin layer of water with a thickness $\delta_{p,n} \cdot d_s$. The volume of a big particle with diameter d_b surrounded with small particles with a diameter d_s, where each small particle is surrounded by a layer of water with a layer thickness $\delta_{p,n} \cdot d_s$, minus the volume of the big particle, gives the volume containing all the small particles including the surrounding layer of water (see Figure 5-12):

$$V_v = \frac{4}{3}\cdot\pi\cdot\left(\left(\frac{d_b}{2}+d_s+2\cdot\delta_{p,n}\cdot d_s\right)^3-\left(\frac{d_b}{2}\right)^3\right) \quad (5\text{-}51)$$

The volume occupied by a small particle, including the layer thickness and the pore volume, is the volume of a cube, considering the small particle is much smaller than the big particle.

$$V_s = \left(d_s+2\cdot\delta_{p,n}\cdot d_s\right)^3 \quad (5\text{-}52)$$

The number of small particles having a bond (van der Waals attraction force) with one big particle is now, which is different from the equation as derived by Ternat et al. (2008), since they did not take into account the pore volume:

$$N_b = \frac{V_v}{V_s} = \frac{\pi}{6}\cdot\left(\frac{1}{\left(1+2\cdot\delta_{p,n}\right)}\cdot\frac{d_b}{d_s}\right)^3\cdot\left(\left(1+2\cdot\left(1+2\cdot\delta_{p,n}\right)\cdot\frac{d_s}{d_b}\right)^3-1\right)\approx\frac{\pi\cdot d_b^2}{d_s^2\cdot\left(1+2\cdot\delta_{p,n}\right)^2} \quad (5\text{-}53)$$

The total amount of small particles required is equal to the number of small particles per big particle, times the number of big particles, if there is no overlap of small particles between big particles, as is shown in Figure 5-13. In general there will be overlap, resulting in a reduction of the required number of small particles. This amount can be reduced to 20%-25%. The ratio between the weight of the small particles surrounding one big particle and the weight of the one big particle $r_{s,b}$ without overlap is now:

$$r_{s,b} = \frac{\rho_q\cdot N_b\cdot V_s}{\rho_q\cdot V_b} = \frac{\pi}{6}\cdot\left(\frac{1}{\left(1+2\cdot\delta_{p,n}\right)}\cdot\frac{d_b}{d_s}\right)^3\cdot\left(\left(1+2\cdot\left(1+2\cdot\delta_{p,n}\right)\cdot\frac{d_s}{d_b}\right)^3-1\right)\cdot\frac{V_s}{V_b} \quad (5\text{-}54)$$

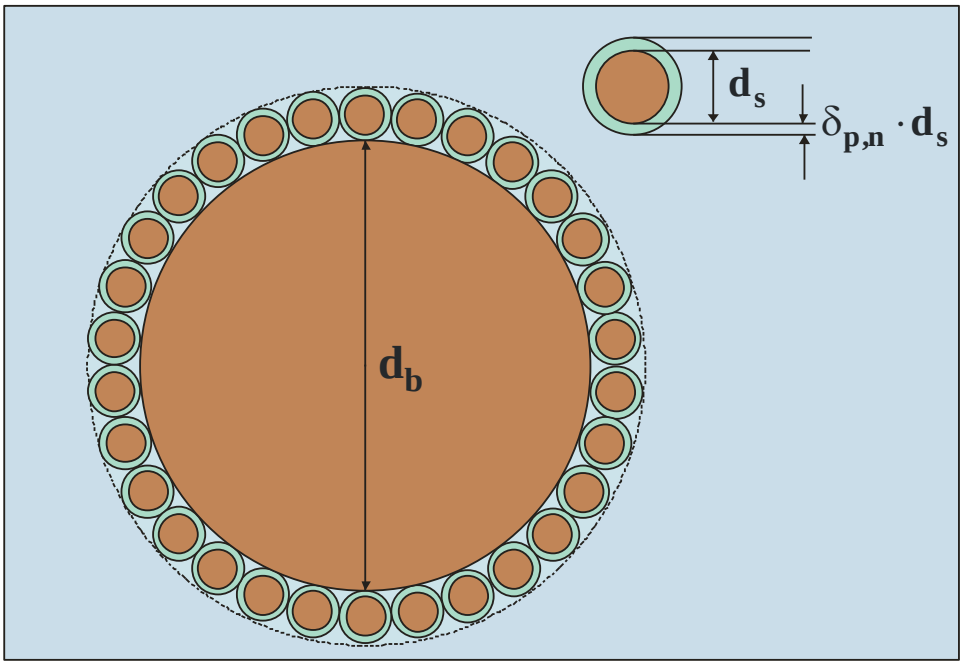

Figure 5-12: The two particle system.

This ratio is an upper limit to the weight percentage of small particles, as is required, in the cumulative PSD as is shown in Figure 5-16.

Particles at the surface are only partially buried (see Figure 5-14), resulting in only a part of the surface in contact with the bed. The number of small particles in contact with the one big particle can be determined by integration according to:

$$N_{b,s} = \frac{\pi}{6} \cdot \left(\frac{1-\cos(\psi)}{2} \right) \cdot \left(\frac{1}{\left(1+2\cdot\delta_{p,n}\right)} \cdot \frac{d_b}{d_s} \right)^3 \cdot \left(\left(1+2\cdot\left(1+2\cdot\delta_{p,n}\right)\cdot\frac{d_s}{d_b} \right)^3 - 1 \right) \quad \textbf{(5-55)}$$

Of this part of the surface, only the vertical component of the van der Waals force should be taken into account, resulting in the following equation, which is different from the equation as derived by Ternat et al. (2008), since they integrated the radial force and not the vertical component of the force.

$$N_{F,b,s} = \frac{\pi}{6} \cdot \left(\frac{1-\cos(2\cdot\psi)}{8} \right) \cdot \left(\frac{1}{\left(1+2\cdot\delta_{p,n}\right)} \cdot \frac{d_b}{d_s} \right)^3 \cdot \left(\left(1+2\cdot\left(1+2\cdot\delta_{p,n}\right)\cdot\frac{d_s}{d_b} \right)^3 - 1 \right) \quad \textbf{(5-56)}$$

Combining the approximation of equation (5-53) for the force factor and equation (5-46) for the attractive force per small particle gives for the total vertical attractive force on the big particle:

$$F_{cv} = \frac{\pi \cdot A_H \cdot d_b^2}{12 \cdot \delta_{p,n}^2 \cdot d_s^3 \cdot \left(1+2\cdot\delta_{p,n}\right)^2} \cdot \left(\frac{1-\cos(2\cdot\psi)}{8} \right) \quad \textbf{(5-57)}$$

Substituting this in equation (5-42) gives for the multiplication factor:

$$\frac{\tau_{cr,cohesion}}{\tau_{cr,no-cohesion}} = \frac{\theta_{cr,cohesion}}{\theta_{cr,no-cohesion}} = \left(1 + \frac{A_H \cdot \left(1-\cos(2\cdot\psi)\right)}{16 \cdot \left(\rho_q - \rho_w\right) \cdot g \cdot \delta_{p,n}^2 \cdot d_s^3 \cdot d_b \cdot \left(1+2\cdot\delta_{p,n}\right)^2} + \frac{F_{ch}}{\mu \cdot F_w} \right) \quad \textbf{(5-58)}$$

This factor is inversely proportional with; the third power of the diameter of the small particle d_s, the first power of the diameter of the big particle d_b and the second power of the layer thickness factor of the water surrounding the small particles $\delta_{p,n}$. Now the main unknown that remains is the factor $\delta_{p,n}$, giving the thickness of the layer of water surrounding the small particle as a fraction of the diameter of the small particle d_s, depending on the porosity n.

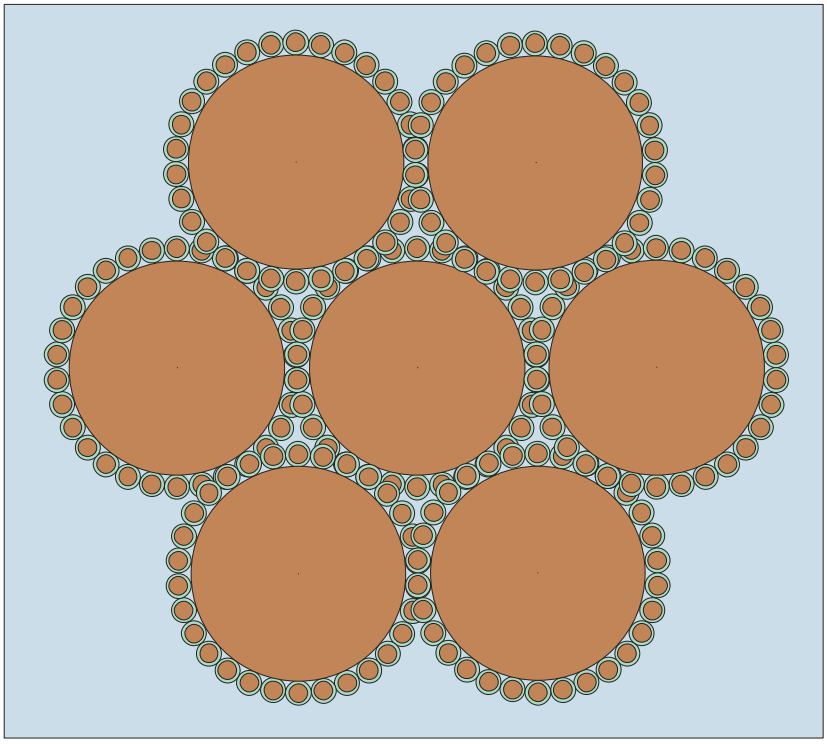

Figure 5-13: Overlap of the small particles.

5.5.2. The Layer Thickness.

The porosity $\mathbf{n}$ of a soil with density ρ_s, consisting of particles with a density ρ_q and pores filled with a fluid with density ρ_w can be calculated with:

$$n = \frac{\rho_q - \rho_s}{\rho_q - \rho_w} \rightarrow n_{min} = \frac{\rho_q - \rho_{s,max}}{\rho_q - \rho_w} \tag{5-59}$$

The minimum porosity n_{min} is reached at the maximum soil density $\rho_{s,max}$. Now suppose 1 m^3 is filled with particles with a diameter d_p and water in the pores. The number of particles in this 1 m^3 is the volume occupied by the particles $1-n$ divided by the particle volume, according to:

$$N_{p,n} = \frac{1-n}{\frac{\pi}{6}\cdot d_p^3} \tag{5-60}$$

Suppose at maximum density, each particle is surrounded by a thin layer of water with a thickness δ_{min} and suppose at lower densities a fraction f_δ of the additional pore volume $n-n_{min}$ is occupied by an increase of the thickness of this thin layer of water by δ_n, as is shown in Figure 5-15.
The relation between the fraction of the additional pore volume and the thickness of this thin layer of water is now (assuming this layer thickness is small compared with the particle diameter, allowing the use of some simplifications):

$$\begin{aligned} V_{\delta,n} &= f_\delta \cdot (n - n_{min}) = N_{p,n} \cdot \frac{\pi}{6} \cdot d_p^3 \left[(1+\delta_{min}+\delta_n)^3 - (1+\delta_{min})^3 \right] \\ &= N_{p,n} \cdot \frac{\pi}{2} \cdot d_p^3 \cdot (1+\delta_{min})^2 \cdot \delta_n = \frac{1-n}{\frac{\pi}{6}\cdot d_p^3} \cdot \frac{\pi}{2} \cdot d_p^3 \cdot (1+\delta_{min})^2 \cdot \delta_n \\ \Rightarrow f_\delta \cdot (n - n_{min}) &= 3 \cdot (1-n) \cdot (1+\delta_{min})^2 \cdot \delta_n \end{aligned} \tag{5-61}$$

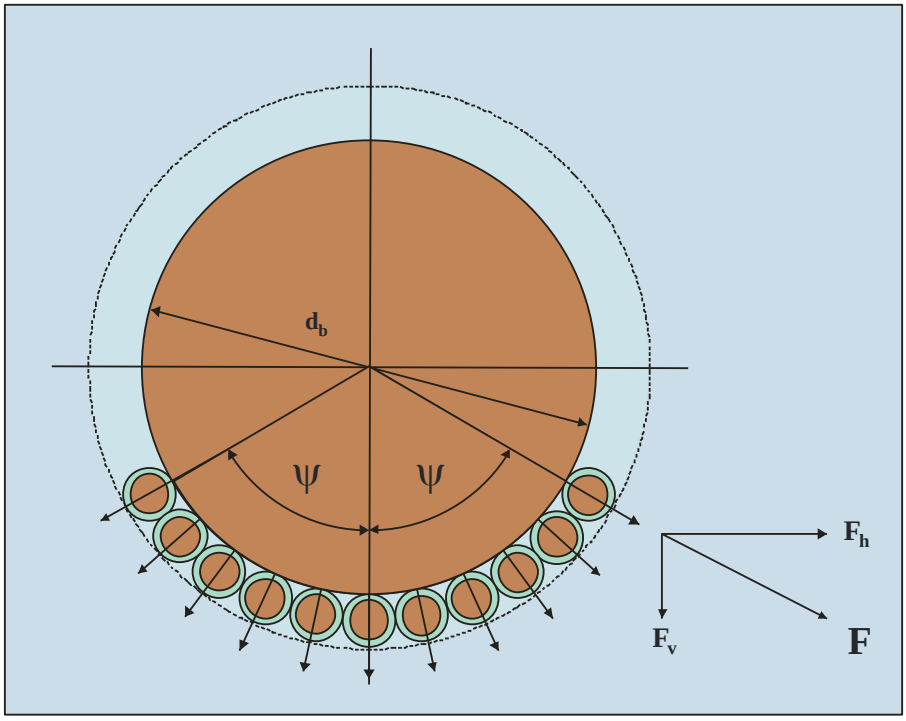

Figure 5-14: The forces on a surface particle.

This gives for the increase of the thickness of the thin layer of water surrounding the particle:

$$\delta_n = \frac{f_\delta}{3} \cdot \frac{(n - n_{min})}{(1-n)} \cdot \frac{1}{(1+\delta_{min})^2} \qquad \textbf{(5-62)}$$

The total thickness factor of the layer of water surrounding the particle $\delta_{p,n}$ is now:

$$\delta_{p,n} = \delta_{min} + \delta_n = \delta_{min} + \frac{f_\delta}{3} \cdot \frac{(n - n_{min})}{(1-n)} \cdot \frac{1}{(1+\delta_{min})^2} \qquad \textbf{(5-63)}$$

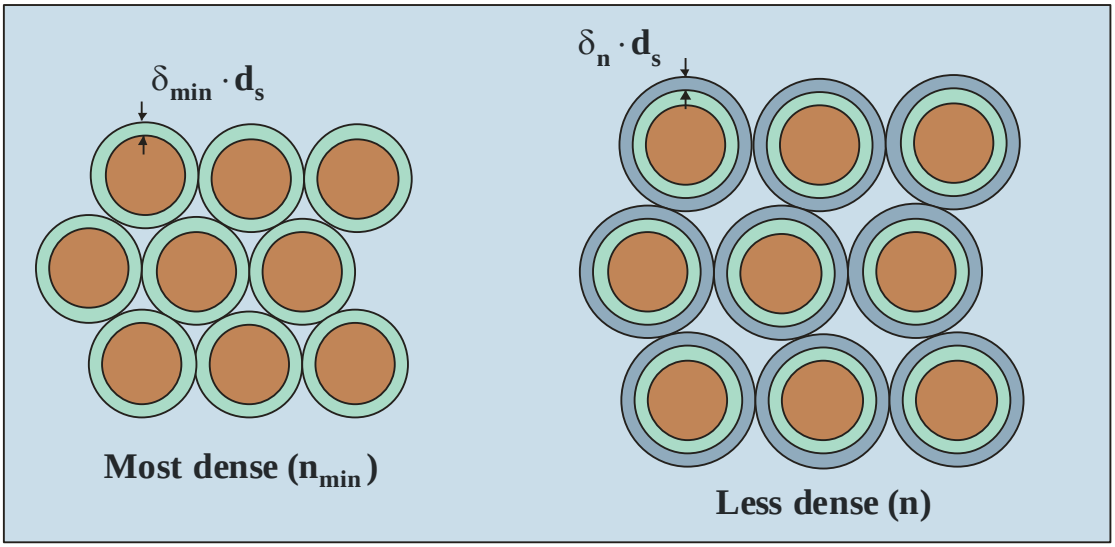

Figure 5-15: The increase of the thickness of the layer of water.

5.5.3. Virtual Attraction Particle Diameter (VAPD).

In a natural silt or sand, there are not just two particle diameters, the big particle with diameter d_b and the small particle with diameter d_s. The PSD (particle size distribution) will consist of particles ranging from the smallest particle to the biggest particle, as is shown in Figure 5-16 for the silts and sands used by Roberts et al. (1998). For the big particle some characteristic diameter has to be chosen, representing the whole PSD, for example the $d_b = d_{50}$. Considering that a silt or a sand with a certain PSD and density will have a certain fixed critical shear stress resulting from the attractive van der Waals forces and gravity, irrespective of the choice of the diameters of the big and the small particle, the bigger the big particle, the smaller the small particle in order to find the same total attractive force and thus critical shear stress. This implies that for each choice of the diameter of the big particle, a diameter for the small particle can be found, representing the total system of attractive forces between the particles of the entire PSD. In the model presented here, the $d_b = d_{50}$ is chosen for the diameter of the big particle. The diameter of the small particle will be named VAPD (Virtual Attraction Particle Diameter). Since the VAPD is the result of the summation of the attraction forces of all the particles in the PSD, one can expect that the VAPD exists in the PSD. The exact location of the VAPD within the PSD depends on the ratio between the d_{50} and the VAPD and on the shape (especially the steepness) of the PSD. In general, one would expect the VAPD to be in the range of the d_3 to the d_{10}, depending on the PSD. A very large ratio between the d_{50} and the VAPD requires just a very small weight percentage of the VAPD in order to create enough "glue" to establish the necessary attraction force. A small ratio would require a high weight percentage, but with a small ratio, both the small and the big particle contribute to the attraction forces if both are small enough, otherwise there is no attraction at all. So the PSD will be characterized by the d_{50} for the big particle and the VAPD for the small particle.

5.6. Validation & Verification.

The model developed is validated and verified with the data measured by Roberts et al. (1998) and Jin et al. (2002). Basically the model developed has 4 unknowns that have to be solved in order to be able to predict the critical shear stress and the Shields parameter. These unknowns are the fraction of the additional pore volume surrounding the particles $\mathbf{f_\delta}$, the minimum layer thickness of the water layer surrounding the particles at maximum density $\mathbf{\delta_{min}}$, the minimum porosity (at maximum density) depending on the PSD $\mathbf{n_{min}}$ and the VAPD. The $\mathbf{d_{50}}$ is supposed to be a known variable, given a certain PSD.
The values found for $\mathbf{f_\delta}$ and $\mathbf{\delta_{min}}$ are **0.09** and **0.001**, based on the experiments of Roberts et al. (1998), which means that 9% of the volume change due to density differences is part of the water layer around the particles, while a water layer with a thickness of 0.1% of the particle diameter is surrounding the particles at maximum density. For the minimum porosity $\mathbf{n_{min}}$ a value of 32% is chosen, based on a smallest porosity in the experiments of Roberts et al. (1998) of about 42% (density $\mathbf{1.95\ ton/m^3}$), the shear stresses at the different densities and the shape of the PSD's according to Youd (1973), Lambe & Whitman (1969) and Winterwerp & van Kesteren (2004). The sands used by Roberts et al. (1998) have a uniformity coefficient ranging from 2 to 3. Equation (5-64) gives an empirical relation between the uniformity coefficient $\mathbf{d_{60}/d_{10}}$ and the minimum porosity $\mathbf{n_{min}}$ based on Youd (1973). The values for $\mathbf{f_\delta}$ and $\mathbf{\delta_{min}}$ follow from a best fit on the data of Roberts et al. (1998).

$$\mathbf{n_{min} = 0.3858 \cdot \left(\frac{d_{60}}{d_{10}} \right)^{-0.19}} \qquad \textbf{(5-64)}$$

5.6.1. Roberts et al. (1998) and Lick et al. (2004).

Based on the PSD's of the sands used by Roberts et al. (1998) as shown in Figure 5-16, the sands can be divided into 3 groups. First of all the 3 finest sands with a rather steep PSD (high uniformity so low uniformity coefficient) with d_{50}'s of 5.7 µm, 14.8 µm and 18.3 µm. For these 3 sands it is expected that the whole PSD will participate in the attractive forces. The second group is the group of 4 sands with relatively high d_{50}'s, but still with a fraction of fines creating the glue effect. These are the sands with d_{50}'s of 48 µm, 75 µm, 125 µm and 222 µm. The third group is the group of 3 sands with large d_{50}'s without fines. These are the sands with d50's of 432 µm, 1020 µm and 1350 µm. It is expected that in these sands no attractive forces will occur.

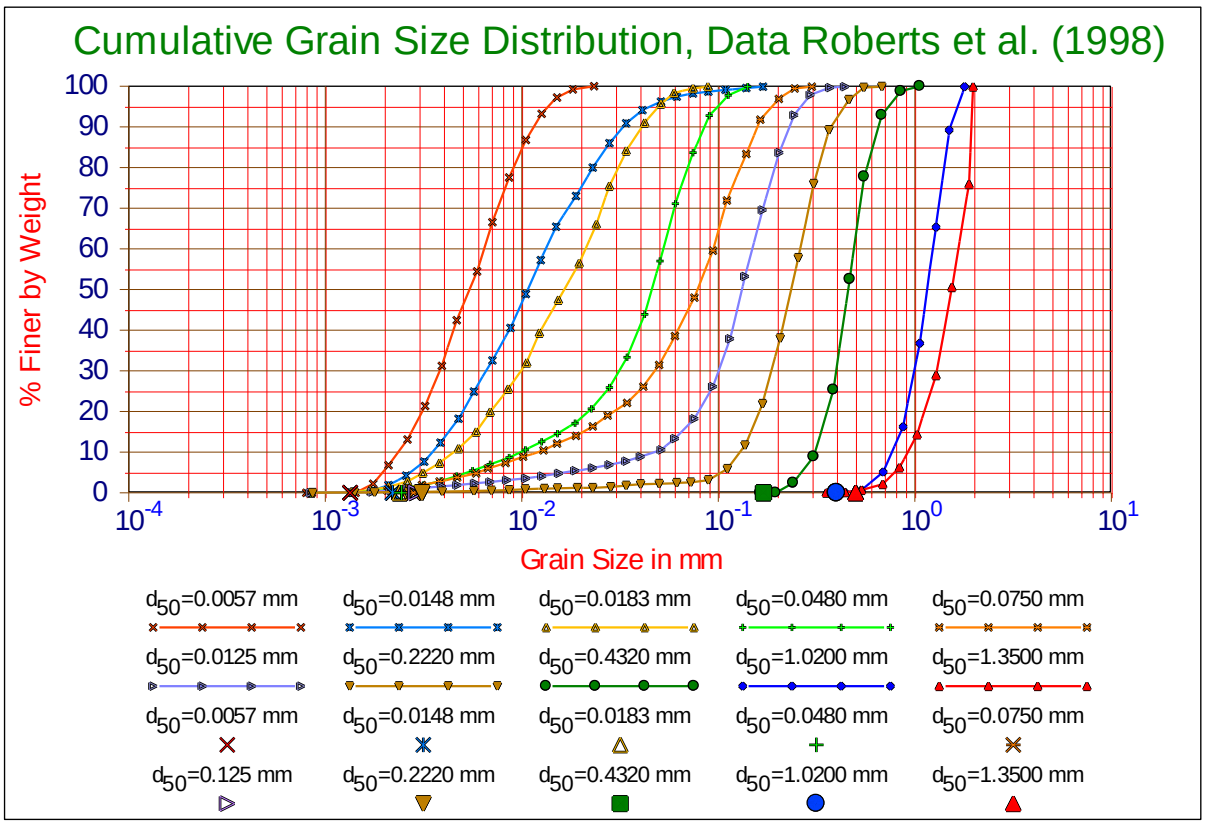

Figure 5-16: The particle size distributions of the sands used by Roberts et al. (1998).

According to equation (5-58) the additional shear stress is inversely proportional to the diameter of the big particle, in our case, the $\mathbf{d_{50}}$ of the sands. Lick et al. (2004) assume that the shear stress is inversely proportional with the $\mathbf{d_{50}}$ to the second power, as is also assumed by Zanke (1982), Dade et al. (1992) and Ternat et al. (2008). Equation (5-58) also shows that the excess shear stress is inversely proportional to the third power of the diameter of the small particle or VAPD. First analysing the relation between the $\mathbf{d_5}$ and the $\mathbf{d_{10}}$ with the $\mathbf{d_{50}}$ gives for the 5.7 μm, 14.8 μm and the 18.3 μm PSD's (these dominate the trend of the critical shear stresses):

$$\mathbf{d_5 = 5.364 \cdot 10^{-4} \cdot d_{50}^{0.4724}}$$
$$\mathbf{d_{10} = 1.089 \cdot 10^{-3} \cdot d_{50}^{0.5114}} \qquad \textbf{(5-65)}$$

The power found is about 0.5, leading to an overall power of 2.5. Analysing the PSD's in Figure 5-16, shows that the VAPD (the large symbols on the horizontal axis) is also decreasing with a decreasing $\mathbf{d_b = d_{50}}$. Further analysis shows the following relation between the $\mathbf{d_s = VAPD}$ and $\mathbf{d_b = d_{50}}$, for the sands ranging from:

$\mathbf{5.7 \cdot 10^{-6} \rightarrow 1.25 \cdot 10^{-4}\ m}$.

$$\mathbf{d_s = 5 \cdot 10^{-5} \cdot d_b^{0.2859}} \qquad \textbf{(5-66)}$$

Using the third power for the diameter of the VAPD, according to equation (5-58), gives a total power of 1.8577 for the diameter of the big particle, which is close to the second power as found by the other researchers. Observing the data of Roberts et al. (1998) in Figure 5-18 more accurately, shows that for the 3 smallest $\mathbf{d_{50}}$ sands a higher power would be expected. Analysing these data gives the following relation between the diameter of the VAPD and the $\mathbf{d_{50}}$.

$$\mathbf{d_s = 6.028 \cdot 10^{-4} \cdot d_b^{0.5057}} \qquad \textbf{(5-67)}$$

This relation results in a total power of the diameter of the $\mathbf{d_{50}}$ of 2.52, which matches the data of Roberts et al. (1998) for the critical shear stresses very well and also the trend found with equation (5-65). So equation (5-58) gives the correct trends. Now it is not necessary to know the VAPD's exactly in order to find the correct power. Knowing the $\mathbf{d_5}$ **or** $\mathbf{d_{10}}$ of each sand (see equation (5-65)), is already sufficient to find a good estimate for the power similar to the powers in equations (5-66) and (5-67). It is a very important conclusion that the trend (power) of the VAPD's follows the trends of the $\mathbf{d_5}$ and the $\mathbf{d_{10}}$. Figure 5-17 shows the relations for the d_5, d_{10} and VAPD, while Figure 5-18 shows data of Roberts et al. (1998) and the theoretical curves for the different densities.

For the second groups of sands, the following equation has been derived for the relation between the VAPD and the $\mathbf{d_{50}}$. The power of 0.1453 results in a total power of 1.4359.

$$\mathbf{d_s = 1 \cdot 10^{-5} \cdot d_b^{0.1453}} \qquad \textbf{(5-68)}$$

Figure 5-18 also shows the theoretical curves for these sands for the highest 4 densities as used by Roberts et al. (1998).
For the third group of sands, no attractive forces are expected and this is confirmed with the theory. No fines, means no glue in the PSD, so no attractive effects.
It is clear that using the correct relations between the VAPD and the $\mathbf{d_{50}}$, gives very high correlations between the measurements and the theory. But it is also clear from this analysis that each sand should be analysed individually. The correlations found between the VAPD and the $\mathbf{d_{50}}$ are coincidental, just based on the choice of the sands by the researchers.

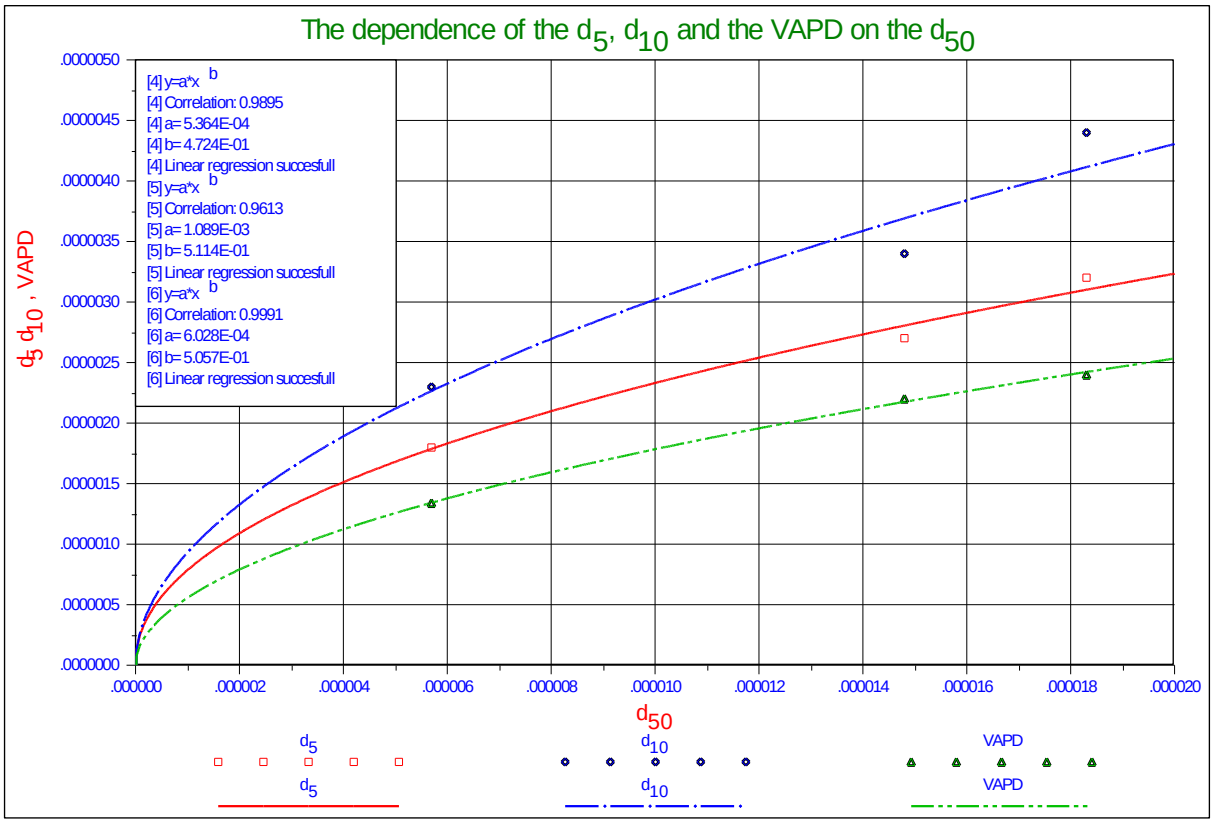

Figure 5-17: The dependence of the d_5, d_{10} and the VAPD on the d_{50} for the sands of Roberts et al. (1998).

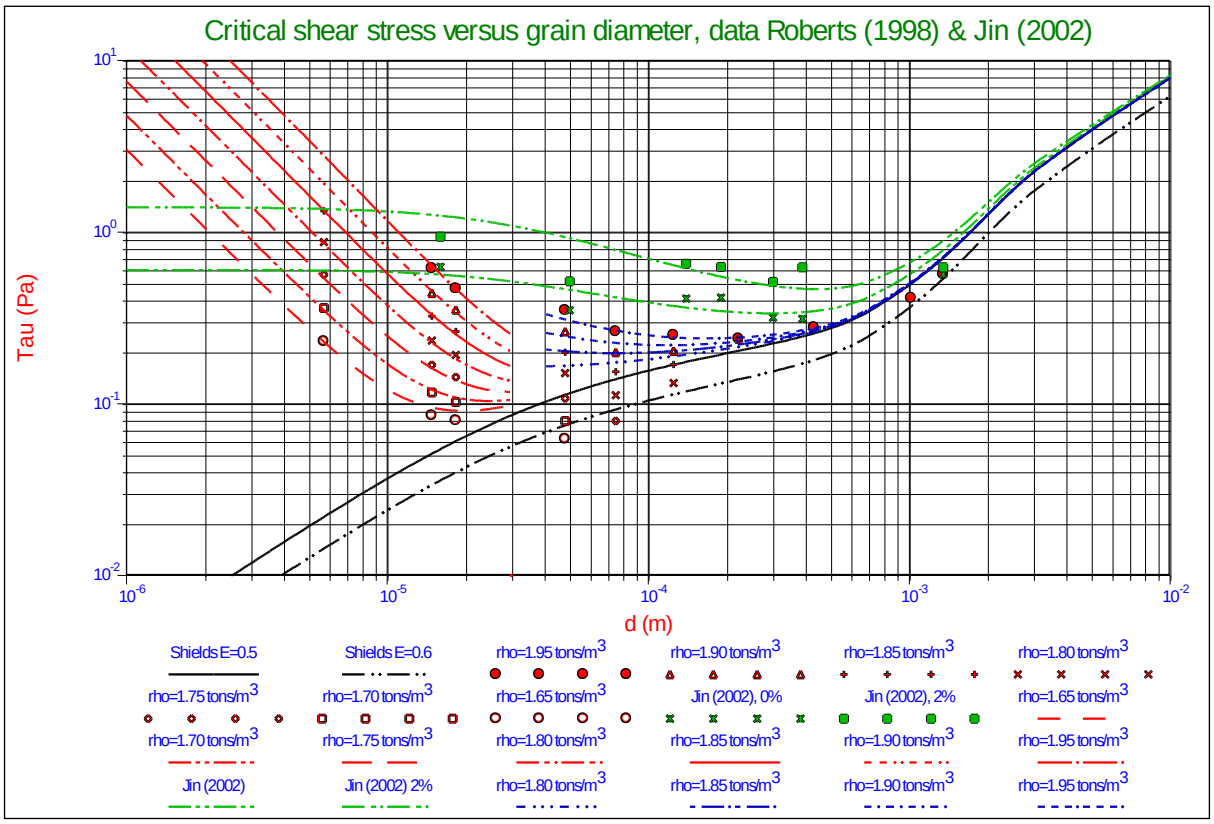

Figure 5-18: The data of Roberts et al. (1998) and Jin et al. (2002) versus the theoretical curves.

5.6.2. Jin et al. (2002).

Lick et al. (2004) also showed some data of Jin et al. (2002) regarding experiments with and without the addition of 2% of bentonite in order to investigate the effect of yield stress. These experiments were carried out with sands/silts with d_{50}'s of 15 µm, 48 µm, 160 µm, 190 µm, 280 µm, 400 µm and 1350 µm. The measured critical shear stresses are clearly higher than the critical shear stresses measured by Roberts et al. (1998) and much higher than the critical shear stresses that would be expected based on the Shields curve, as is shown in Figure 5-18, although Lick et al. state that the results are similar to the results of Roberts et al. (1998). The PSD's of these sands and silts are not given by Lick et al. (2004), but with the theory developed an average VAPD of about 1.6 µm is predicted to explain the higher critical shear stresses. In other words, there has to be enough glue available in order to explain these critical shear stresses. The VAPD's predicted do not differ much for the 7 sands used by Jin et al. (2002), resulting in a power of 1, meaning that the additional critical shear stress factor is inversely proportional to the d_{50} to the power 1, which results in a constant critical shear stress for very small particles. The resulting critical shear stress curve is shown in Figure 5-9 and matches the measurements very well. Only the sand with a d_{50} of 48 µm gives a lower critical shear stress, caused by a VAPD of 2.5 µm. Now the question is, do these sands contain fines with a diameter near 1.6 µm. Lodge (2006), an MSc student of Wilbert Lick, carried out erosion tests in the same laboratory as Jin et al. (2002) and Lick et al. (2004) and shows the PSD's in his MSc report. These PSD's of sands with the same d_{50}'s clearly show the existence of fines, even for the larger d_{50}'s. For the 160 µm sand, the PSD shows particles in the range from 50 µm to 400 µm, but also a few % fines from 1 µm to 5 µm, enough to explain the VAPD of 1.6 µm. Figure 5-19 shows the resulting Shields curves together with the data of Jin et al. (2002).

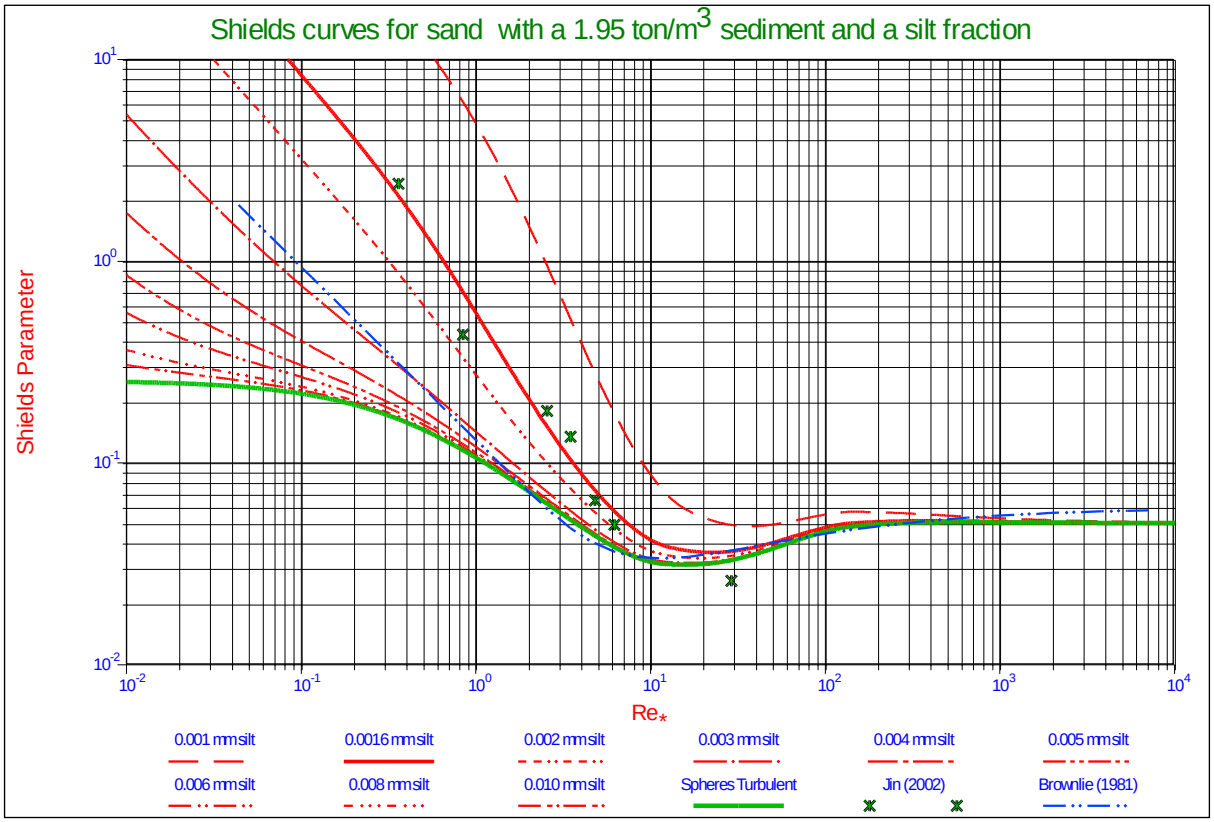

Figure 5-19: Shields curves with silt fraction.

The effect of adding bentonite can be explained with the effect of yield stress, according to equation (5-70). Since the bentonite consisted of particles with a diameter around 5 µm, according to Lick et al. (2004), it is not expected that these particles have a big influence on the attractive force, since the VAPD of 2 µm is much smaller and the influence of the VAPD is to the third power. Lick et al. (2004) do not give a value for the yield stress, but derive a value based on the critical shear stresses as measured by Jin et al. (2002). Assuming a yield stress of $\tau_y = 3.72$ **Pa and** $\eta_c = 0.45$ would, based on equation (5-70), explain for the increase of the critical shear stresses.

Figure 5-18 also shows the theoretical critical shear stress curve for the sands and silts with a VAPD of 2 µm and

a yields stress of $\tau_y = 3.72$ Pa and $\eta_c = 0.45$. The correlation between the measurements and the theory is good enough, to explain for the behaviour of the critical shear stresses.

5.7. Shear Strength or Yield Stress.

5.7.1. Theoretical Model.

Adding a small amount of clay particles to the sand or silt will change the erosion behaviour. Since the clay particles are considered to be small, they will have a diameter in the range of the VAPD or even smaller, replacing part of the small particles surrounding the big particles. The clay particles are considered to be responsible for van der Waals forces, like the quartz particles, but also for some shear strength, often called yield stress. If a volume fraction p_{clay} of clay particles is added, a fraction $\alpha_c(p_{clay})$ of the small particles will be replaced by clay particles (see Figure 5-20). This fraction depends on the fraction of small particles that was already in the sand or silt. The horizontal shear force can now be taken into account by integrating the horizontal component of the shear stress over the surface of the particle (considered a sphere) in contact with the small particles, according to (5-42). This gives the same result as using the projected surface. Equation (5-69) gives the horizontal shear force on a single particle:

$$F_{ch} = \eta_c \cdot \tau_y \cdot \frac{\pi}{4} \cdot \left(d_b \cdot \sin(\psi)\right)^2 = \eta_c \cdot \alpha_c(p_{clay}) \cdot \tau_y(p_{clay}) \cdot \frac{\pi}{4} \cdot d_b^2 \cdot \left(\frac{1-\cos(2\cdot\psi)}{2}\right) \qquad (5\text{-}69)$$

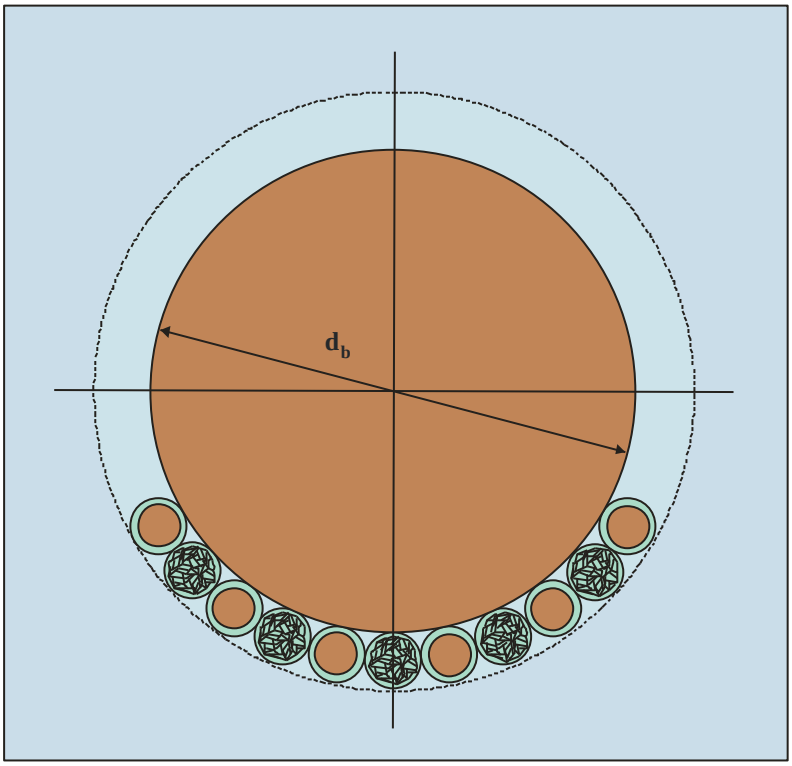

Figure 5-20: Replacement of silt particles by clay particles.

The yield stress efficiency η_c is introduced, because the clay structure is not continuous, but it is interrupted by sand and silt particles, reducing the effect of the yield stress on the critical shear stress. The yield stress $\tau_y(p_{clay})$ will also be a function of the weight fraction of clay particles added. Substituting equation (5-69) in equation (5-42) gives:

$$\frac{\tau_{cr,cohesion}}{\tau_{cr,no-cohesion}} = \frac{\theta_{cr,cohesion}}{\theta_{cr,no-cohesion}}$$

$$= \left(\begin{array}{l} 1+(1-\alpha_c)\cdot \dfrac{A_{H,qwq}\cdot(1-\cos(2\cdot\psi))}{16\cdot(\rho_q-\rho_w)\cdot g\cdot\delta_{p,n}^2\cdot d_{s,q}^3\cdot d_b\cdot(1+2\cdot\delta_{p,n})^2} \\ \\ +\alpha_c\cdot \dfrac{A_{H,qwc}\cdot(1-\cos(2\cdot\psi))}{16\cdot(\rho_q-\rho_w)\cdot g\cdot\delta_{p,n}^2\cdot d_{s,c}^3\cdot d_b\cdot(1+2\cdot\delta_{p,n})^2} + \eta_c\cdot\alpha_c\cdot\frac{3}{4}\cdot\frac{\tau_y\cdot(1-\cos(2\cdot\psi))}{\mu\cdot(\rho_q-\rho_w)\cdot g\cdot d_b} \end{array} \right) \qquad \textbf{(5-70)}$$

Since the multiplication factor, equation (5-70), depends on the particle diameter d_b, which also occurs in the boundary Reynolds number, the boundary Reynolds number will also change according to:

$$\frac{Re_{*,cohesion}}{Re_{*,no-cohesion}} = \frac{u_{*,cohesion}}{u_{*,no-cohesion}} = \left(\frac{\tau_{cr,cohesion}}{\tau_{cr,no-cohesion}}\right)^{0.5} = \left(\frac{\theta_{cr,cohesion}}{\theta_{cr,no-cohesion}}\right)^{0.5}$$

$$= \left(\begin{array}{l} 1+(1-\alpha_c)\cdot \dfrac{A_{H,qwq}\cdot(1-\cos(2\cdot\psi))}{16\cdot(\rho_q-\rho_w)\cdot g\cdot\delta_{p,n}^2\cdot d_{s,q}^3\cdot d_b\cdot(1+2\cdot\delta_{p,n})^2} \\ \\ +\alpha_c\cdot \dfrac{A_{H,qwc}\cdot(1-\cos(2\cdot\psi))}{16\cdot(\rho_q-\rho_w)\cdot g\cdot\delta_{p,n}^2\cdot d_{s,c}^3\cdot d_b\cdot(1+2\cdot\delta_{p,n})^2} + \eta_c\cdot\alpha_c\cdot\frac{3}{4}\cdot\frac{\tau_y\cdot(1-\cos(2\cdot\psi))}{\mu\cdot(\rho_q-\rho_w)\cdot g\cdot d_b} \end{array} \right)^{0.5} \qquad \textbf{(5-71)}$$

It should be noted here that in both equations (5-70) and (5-71), the approximation of the number of bonds is used according to equation (5-53), in order to make the trends clearer. For an exact solution, the full equation for the number of bonds should be used (equation (5-53)).
Luckner (2002) determined the relation between the protrusion level and the pivot angle by using an ideal tetrahedral arrangement of spheres in a three-dimensional approach. With the transformation from protrusion to exposure level and some curve fitting on the calculations of Luckner (2002), the following relation is found between the pivot angle ψ (in degrees) and the exposure level E, assuming the pivot angle equals the angle of contact as used here.

$$\psi = -144.12\cdot E^4 + 342.7\cdot E^3 - 245.05\cdot E^2 - 37.184\cdot E + 104.28 \qquad \textbf{(5-72)}$$

Now 3 basic cases may occur (qwq=quartz-water-quartz, qwc=quartz-water-clay):

1. $\frac{A_{H,qwq}}{d_{s,q}^3} < \frac{A_{H,qwc}}{d_{s,c}^3}$, the attraction force of the original quartz VAPD is smaller than the attraction force of the clay particles they are replaced with. The total resulting attraction force will increase with an increasing fraction of clay particles, in fact the clay particles take over the glue function. The yield stress will be very small at small clay fractions and be negligible, but at bigger clay fractions it will start to dominate.
2. $\frac{A_{H,qwq}}{d_{s,q}^3} \approx \frac{A_{H,qwc}}{d_{s,c}^3}$, although clay particles take over the glue function, their glue strength is about the same as the quarts particles, so increasing the clay fraction will not noticeably increase or decrease the critical shear stress. At higher clay fractions the yield stress will dominate the critical shear stress.
3. $\frac{A_{H,qwq}}{d_{s,q}^3} > \frac{A_{H,qwc}}{d_{s,c}^3}$, the attraction force of the original quartz VAPD is bigger than the attraction force of the clay particles they are replaced with. The total resulting attraction force will decrease with an

increasing fraction of clay particles, in fact part of the glue function of the quartz particles is removed. The yield stress will increase with an increasing clay fraction and neutralize this decrease at a certain clay fraction. Increasing the clay fraction further will increase the critical shear stress further.

The replacement fraction $\alpha_c(p_{clay})$ is a function of the clay fraction p_{clay} and the fraction of fines in the original sand or silt p_s. The replacement fraction $\alpha_c(p_{clay})$ has a value between 0 and 1. Now suppose there is an clay fraction p_{clay} and a corresponding replacement fraction $\alpha_c(p_{clay})$, increasing the clay fraction with dp_{clay} will increase the replacement fraction with $d\alpha_c$. The increase of the replacement fraction will be proportional to the increase of the clay fraction, but also proportional to the fraction of large particle surface that has not yet been replaced and inversely proportional to the fraction of fines originally in the sand. This gives the following equation for the replacement fraction, where λ is a proportionality constant.

$$\frac{d\alpha_c}{dp_{clay}} = \frac{\lambda}{p_s}\cdot\left(1-\alpha_c\right)$$

$$\alpha_c(p_{clay}) = \left(1-e^{-\frac{\lambda\cdot p_{clay}}{p_s}}\right) \qquad \textbf{(5-73)}$$

In a bi-modal sand, consisting of large particles with diameter d_b and a large fraction p_b and small particles with diameter d_s and small fraction p_s, using equation (5-73) is clear. For more heterogeneous sands, determining p_s is more complicated. Figure 5-21 illustrates the 3 cases as mentioned above for different initial silt fractions. It is clear from this figure that a very small (0.25%) initial silt fraction already increases the critical shear stress of the 0% clay sand noticeably. According to the calculations, a 1.4 mm sand only requires about 0.25% 1 µm silt to establish such a glue effect. Equation (5-70) contains 4 terms. The first term (1) represents the critical shear stress of sand without any cohesive effect. The second term represents the cohesive effect due to very fine silt particles caused by van der Waals forces. This term will decrease with an increasing replacement fraction $\alpha_c(p_{clay})$, causing a possible decrease of the critical shear stress at low clay fractions p_{clay}. The third term represents the adhesive effect due to very fine clay particles caused by van der Waals forces. This term will increase with an increasing replacement fraction $\alpha_c(p_{clay})$, causing a possible direct increase of the critical shear stress at low clay fractions p_{clay}. The latter depends on the ratio of the attraction forces between the silt and the clay particles. The fourth term represents the effect of the yield stress τ_y on the critical shear velocity. The yield stress will increase with an increasing clay fraction p_{clay}, but not linear. All these effects are shown in Figure 5-21.

5.7.2. The Relation between Yield Stress and Clay Fraction.

The relation between the yield stress τ_y and the clay concentration (by weight) p_{clay} can be found in literature. Garcia (2008) gives an overview of relations found in literature (table 4-10). In general the yield stress is proportional with the solids (clay) content to a certain power, where this power varies between 0.9 and 4.0. Laribi et al. (2005) found that the yield stress is proportional to the clay fraction to a power between 2.5 and 3. To be more specific, they found powers of 2.54 and 2.76 for two smectite clays. Migniot (1968) found a power of 2.5 for the proportionality between the critical shear stress and the clay concentration, and assumed that the critical shear stress is proportional to the yield stress (see also Figure 5-22) for higher yield stresses. Krone (1986) also found a power of 2.5 between the critical shear stress and the clay concentration and assumed that the critical shear stress and the yield stress are proportional. Talmon & Huisman (2005) show the relation between the yield stress and the mass concentration of bentonite and a mix of bentonite and polymer. Although they do not mention a power, from their data powers in the range of 2.5-4.0 can be deduced.
The following relation is proposed between the yield stress τ_y and the clay fraction p_{clay}, with the presumption that the power could be in a range from 1 to 4:

$$\tau_y = c_{clay} \cdot p_{clay}^{2.5} \qquad \textbf{(5-74)}$$

The value of the proportionality coefficient c_{clay} depends on the type of clay. Laribi et al. found coefficients of **10000 Pa** and **5000 Pa** for the two types of smectite clay. Combining equations (5-73) and (5-74) gives the relation between the replacement fraction $\alpha_c(\tau_y)$ and the yield stress τ_y of the clay:

$$\alpha(\tau_y) = \left(1 - e^{-\frac{\lambda \cdot (\tau_y / c_{clay})^{0.4}}{p_s}} \right) \qquad \textbf{(5-75)}$$

5.7.3. Salinity.

Parchure & Mehta (1985) found that the mean bed shear strength increases with the salinity. An increase of the salinity up to 2 ppt almost doubles the shear strength, at 10 ppt the increase is with a factor 3.5, but above 10 ppt there is hardly any increase.
Korreman & Posselt (2001) state that the Hamaker constant of the solution is decreased by the addition of all salts, owing to Debye screening. What causes this surprising behavior? The Debye screening length 1/κ, which defines the distance over which charges interact decreases with salinity. In effect, then, 1/κ defines the (average) preferred distance between a charge and its dissociated counter-ion. Increasing the salt concentration in the system reduces the screening length, and thus, the confinement of the dissociated counter-ions. The result of a decreasing Hamaker constant for the water/salt solution is an increasing Hamaker constant for the quartz-water-quartz interaction, resulting in higher attractive van der Waals forces.
Petrache et al. (2006) derived an equation for the Hamaker parameter as a function of the salt concentration, based on the static (low frequency), H_0 and optical (high frequency) H' contributions. At high salt concentrations only the high frequency contributions are left.

$$H = H_0 \cdot (1 + 2 \cdot \chi \cdot p) \cdot e^{-2 \cdot \chi \cdot p} + H' \qquad \textbf{(5-76)}$$

In which, $\chi = 0.2$ an empirical constant and p the salt concentration in Mol/liter. The resulting increase of the quartz-water-quartz Hamaker constant will result in stronger attractive forces between sand particles and the much smaller silt particles and thus increase the critical shear stress.
Barry et al. (2006) also measured the influence of salinity on the critical shear stress as a function of the clay fraction for an 0.83 mm sand. Based on the above, a higher critical shear stress is expected, which was also the case. At all clay fractions the critical shear stress is higher with 3 ppt salt than without, except for the reference situation with 0% clay. Now it is assumed that the reference measurement has only been carried out once with fresh water, because no influence of salinity was expected. This means that the reference situation has to be corrected for the effect of salinity.

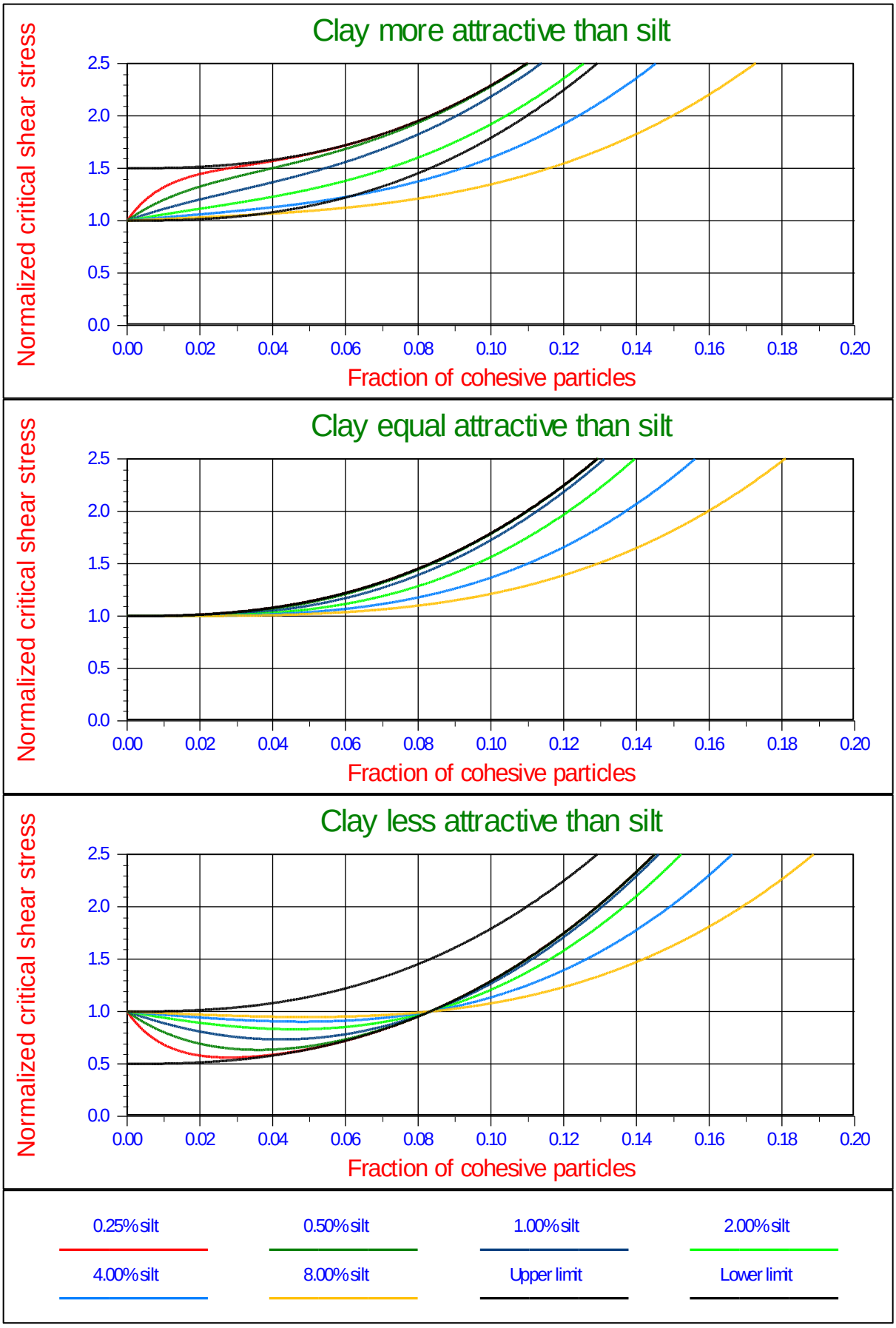

Figure 5-21: The normalized critical bed shear stress as a function of the fraction of cohesive (clay) particles for different silt fractions, for case 1 (top), case 2 (middle) and case 3 (bottom).

5.7.4. Validation & Verification.

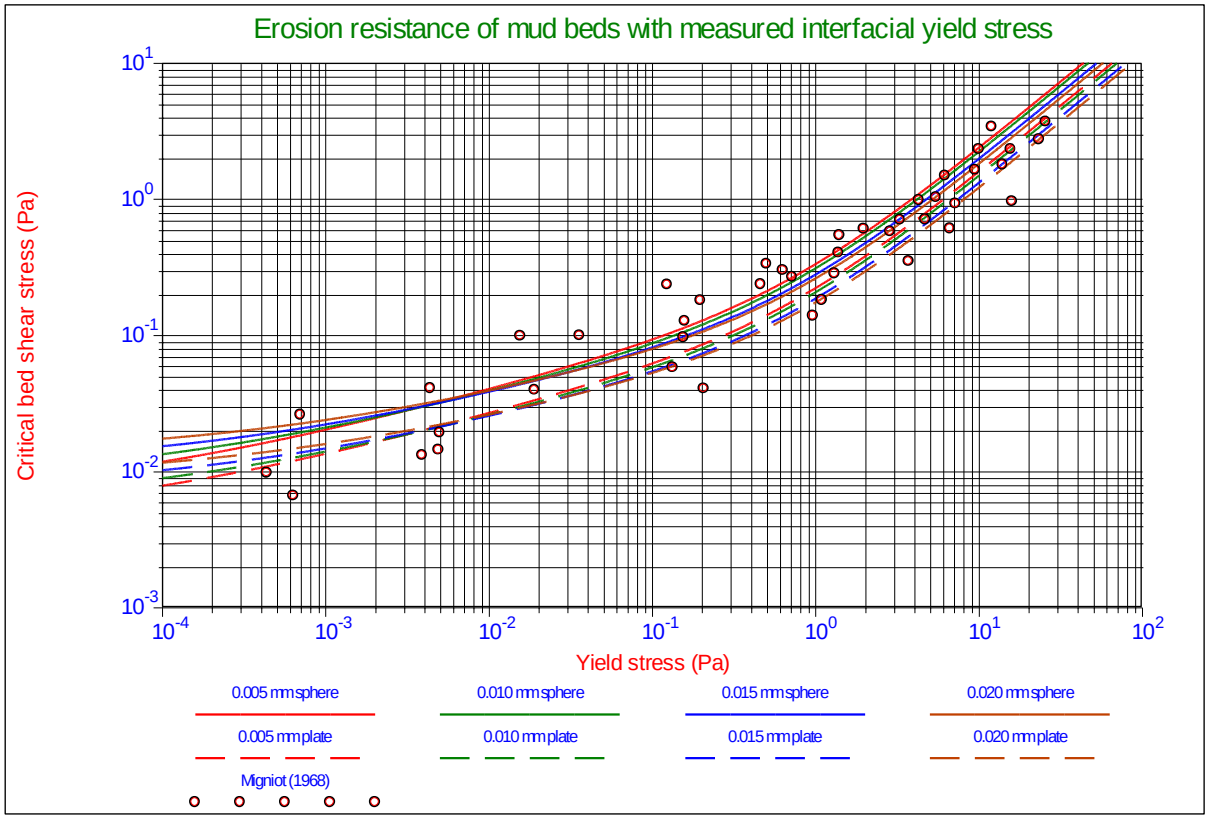

Figure 5-22: Data of Migniot (1968) and Dade (1992).

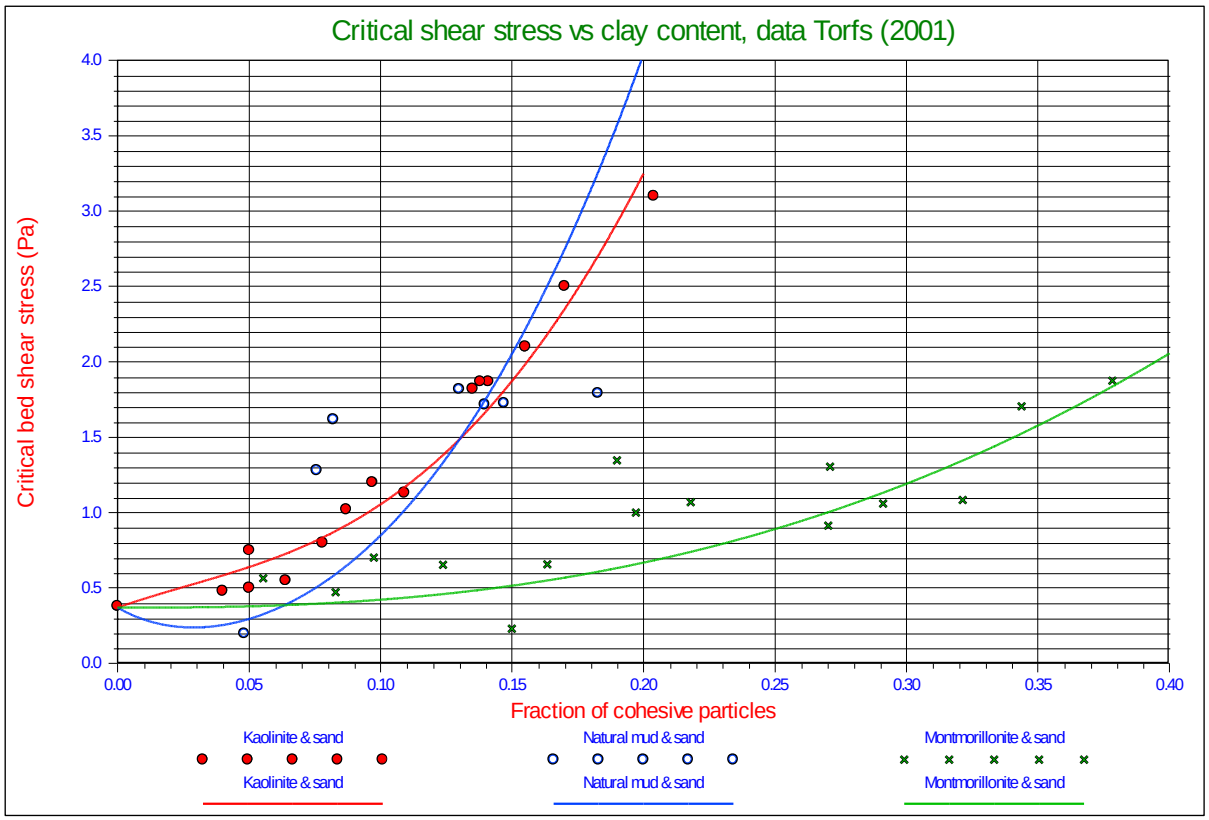

Figure 5-23: Torfs (1995), Mitchener & Torfs (1996) & Torfs et al. (2001).

5.7.5. Barry (2003) & Barry et al. (2006)

Barry (2003) collected data of Sharif (2002), Torfs (1995), Huygens & Verhofen (1996) & Panagiotopoulos et al. (1997) on the critical shear stress, with and without the addition of clay. The resulting data are shown in Figure 5-24, together with the data points of Barry (2003) and the Shields curves for spheres and sands according to Miedema (2010A) & (2010B). The figure shows that almost all the data points of sand without clay addition, lie above the Shields curve for spheres. Only the data points of Huygens & Verhofen (1996) and Sharif (2002) lie very close to this Shields curve. Most of the data points with clay addition (showing the minimum critical shear stress) lie close, but below, the data points of sand without clay addition. Except for the data points of Barry (2003) for the 0.41 mm and the 0.83 mm sands. There are a number of possible explanations for the position of the data points with respect to the Shields curves.

1. The lift coefficient could be smaller resulting in a higher critical shear stress.
2. The friction coefficient could be higher resulting in a higher critical shear stress.
3. The main flow could be laminar resulting in a higher critical shear stress.
4. There could be a percentage of very fines resulting in cohesion and thus a higher critical shear stress.
5. The drag coefficient could be smaller resulting in a higher critical shear stress.

There is no reason to assume a smaller drag or lift coefficient, in fact there could be a reason for assuming a higher drag coefficient, because of the shape of the particles, but this would only decrease the critical shear stress and not increase it. There is also no reason to assume a higher friction coefficient than the one used to determine the Shields curve, since the densities of the sand used by Barry (2003) were 1830 kg/m^3 for the 1.4 mm sand, 1700 kg/m^3 for the 0.83 mm sand and 1680 kg/m^3 for the 0.41 mm sand. The density of the 1.4 mm sand is not high, but could still have a friction angle of 30°, but the densities of the 0.83 mm sand and the 0.41 mm sand are low and would normally result in lower friction angles, decreasing the critical shear stresses. Since there is no plausible reason for higher critical shear stresses, but there are plausible reasons for lower critical shear stresses, it is assumed that the sands used by Barry (2003) contained a small fraction of very fine silt, resulting in enough cohesive effect in order to explain for the position of the data points of the sands without clay addition. Barry (2003) shows the PSD's, but they were measured using sieves, which cannot detect less than 1% of very fines. For the 0.83 mm sand and the 0.41 mm sand, a friction angle of 16° is assumed, giving the same sort of effect as a higher exposure or protrusion level. Further it is assumed that the tests of Barry (2003) with clay 1, clay 2 and saline kaolinite have a critical shear stress without the addition of clay of 1 Pa instead of 0.7 Pa, due to the salinity of the pore water as discussed before. A higher salinity will increase the effective Hamaker constant, resulting in an increase of the van der Waals forces and thus an increase of the critical shear stress. An increase in salinity also means an increase in cation concentration and therefore a decrease of the diffusive double layer thickness and thus an increase in attraction. With the above assumptions the theory developed here is compared with the data of Barry (2003). First the power of 2.5 in equation (5-74) is verified, as is show in Figure 5-25. This figure shows the results of equation (5-70) for powers in equation (5-74) ranging from 1.0 to 4.0 together with the data of Barry (2003) of the 0.83 mm sand with the addition of clay 2 in saline (3 ppt) water. All the curves are forced through the lowest data point in order to be able to compare. The curve with a power of 2.5 gives the best fit, which is also the case for the other sands as used by Barry (2003).

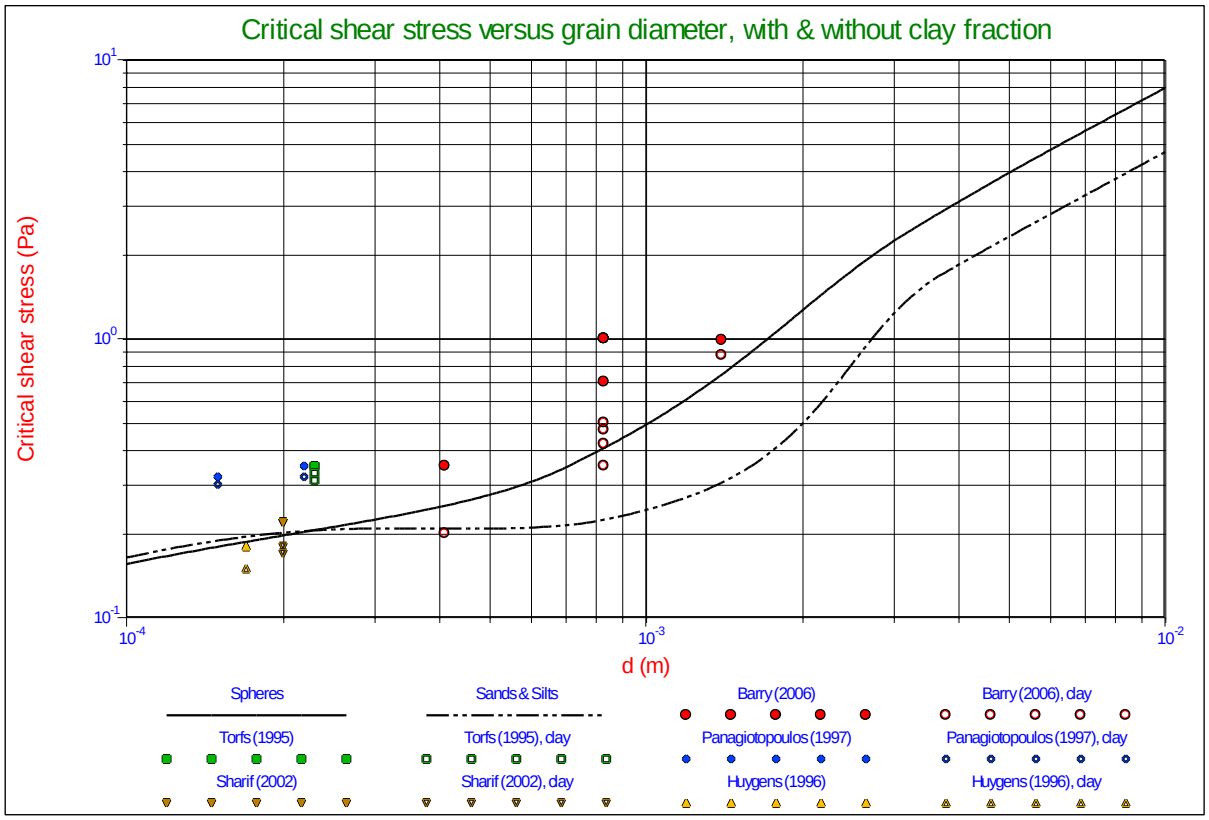

Figure 5-24: Critical shear stresses as measured by several authors compared with the Shields curves.

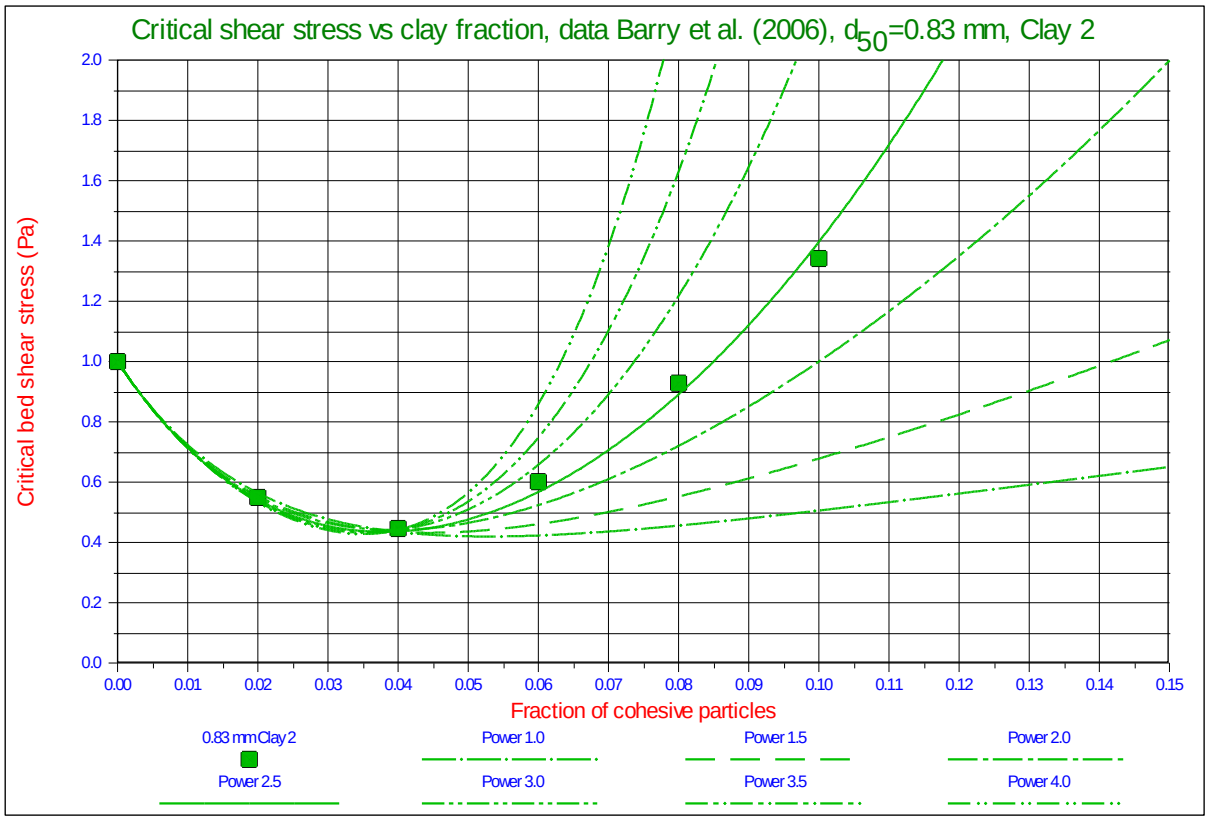

Figure 5-25: The critical shear stress as a function of the clay fraction for different powers for the clay fraction yield stress relation.

Figure 5-26 shows the theoretical critical shear stress curves versus the data of Barry (2003), using the above assumptions with VAPD's near 1 µm for the silt fraction (less than 1%) and assuming clay aggregates of 20 µm as mentioned by Barry (2003). All the curves match good to very good with the measurements. It should be mentioned here that the measurements with the 1.4 mm sand, the 0.83 mm sand fresh and the 0.41 mm sand were carried out with the addition of kaolinite in fresh water, while the measurements of 0.83 mm sand with clay 1, clay 2 and kaolinite saline were carried out in 3 ppt saline water. It should also be mentioned that some discrepancies were found between the data as found in Barry (2003) and Barry et al. (2006) regarding the values of critical shear stresses and grain diameters.

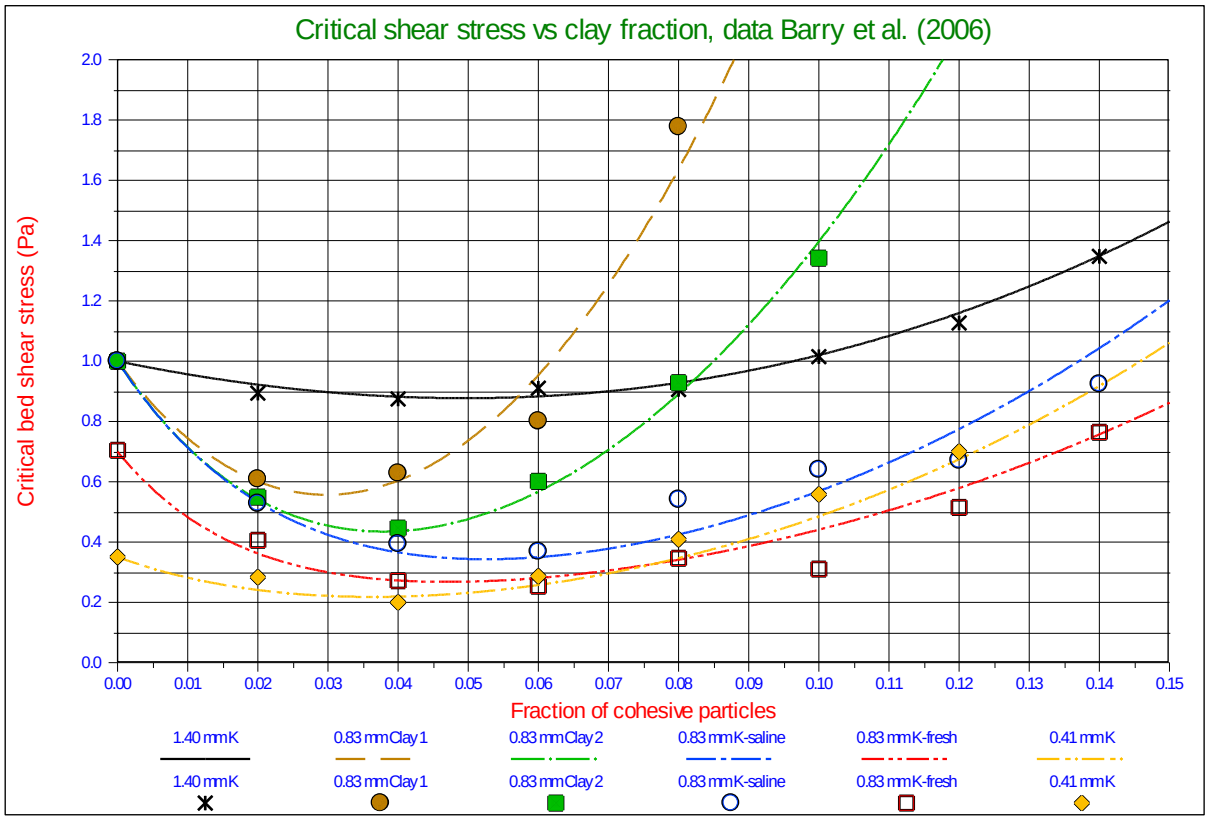

Figure 5-26: The critical shear stress vs the clay fraction for the sands used by Barry (2003).

The yield stresses used are shown in Figure 5-27. It can be seen that the yield stress curves of the 1.4 mm sand, the 0.83 mm sand and the 0.41 mm sand, all with kaolinite in fresh water, are the same. The yield stress curve for the 0.83 mm sand with kaolinite in saline water is a bit higher as was expected, since salinity increases both the van der Waals forces and the yield stress. For the 0.83 mm sand with clay 1 and clay 2, both in saline water, the yield stresses are even higher which could be expected based on the composition of both clay mixtures. Clay 1 is composed of 50% kaolinite, 45% attapulgite and 5% bentonite. Clay 2 is composed of 50% kaolinite, 35% attapulgite and 15% bentonite. Bentonite (sodium montmorillonite) with the same solids fraction will have a much higher yield stress than kaolinite, while attapulgite (palygorskite) has a higher yield stress than bentonite. The value for $\mathbf{c_{clay}}$ is **3000 Pa** for the 1.4 mm sand, 0.83 mm sand and 0.41 mm sand, all 3 with kaolinite in fresh water. For the 0.83 mm sand with kaolinite in saline water a value of **4500 Pa** is found. The experiments with clay 1 and clay 2 in saline water give **30000 Pa** and **15000 Pa**.

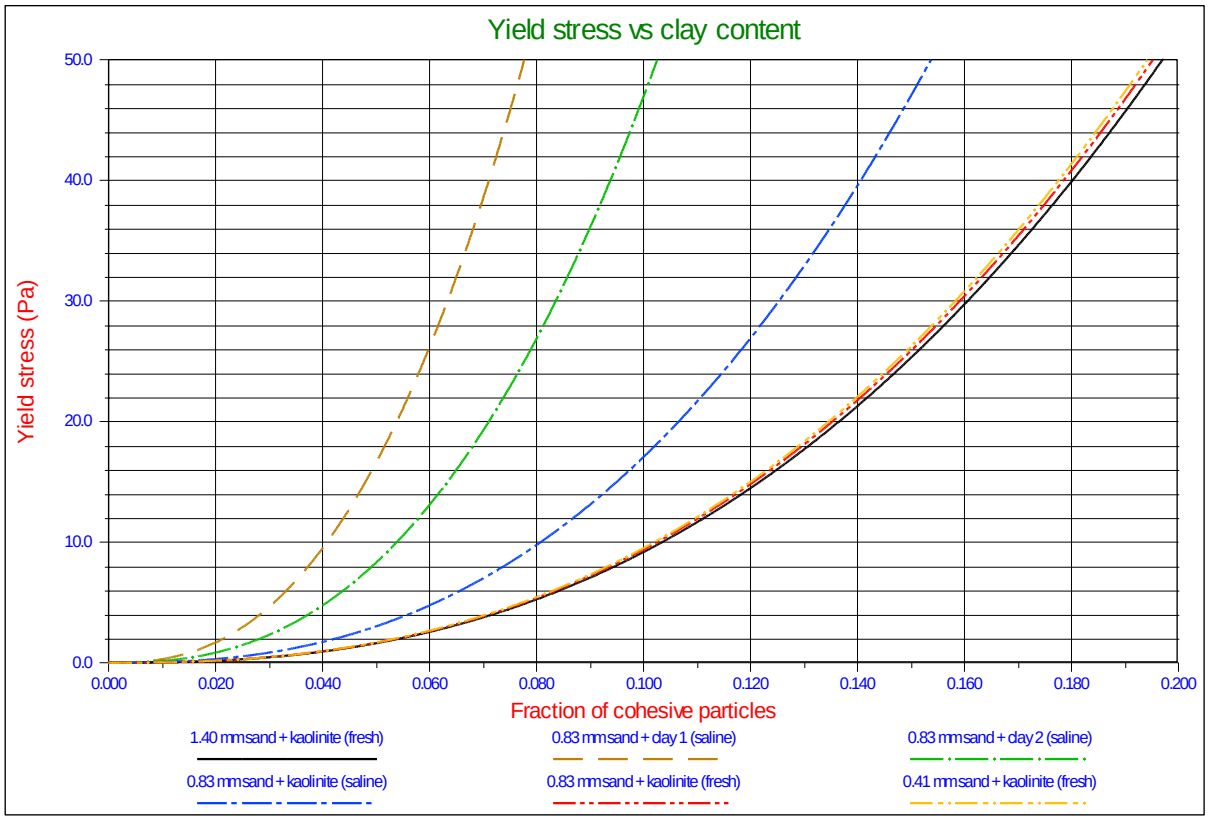

Figure 5-27: The yield stress vs the clay content.

5.8. Discussion & Conclusions.

One of the questions of this study is, does the Shields curve really exist? Now one can argue that this is a matter of definition, which of course is true. In the previous studies (Miedema (2012A) & (2012B)) it appeared that a definition exists, leading to one single Shields curve for non-cohesive sands and gravels. If initiation of motion is defined as frequent particle movement at all locations, matching an erosion rate of 10^{-4} cm/sec, then for spheres in a turbulent main flow the Shields curve can be determined as is shown in Figure 5-19. Adding fine silt will increase the critical shear stress and thus modify the Shields curve. Figure 5-19 shows the influence of fine silt on the resulting Shields curve for a 1.95 ton/m^3 sand with a minimum porosity of 32%, for silt fractions with VAPD's of 1 µm, 2 µm, 3 µm, 4 µm, 5 µm, 6 µm, 7 µm, 8 µm and 10 µm. The conclusion of this is, that there does not exist a single Shields curve representing the cohesive effects resulting from the van der Waals forces. The curves found in Figure 5-19 depend on the density and the minimum porosity of the sand and depend strongly to the size of the particles in the silt fraction. Lower densities decrease the cohesive effect, a smaller minimum porosity also decreases the cohesive effect, while an increasing VAPD decreases the cohesive effect. Silt fractions with a VAPD bigger than 10 µm hardly encounter a cohesive effect as can be seen in Figure 5-19. It should be mentioned here that the 3 µm curve, closely matches the Brownlie (1981) approximation equation.

The cohesive attraction forces are inversely proportional to the d_{50} and inversely proportional to the VAPD (the size of the silt particles) to the third power. Relations given in literature where the cohesive attraction forces, due to a silt fraction, are inversely proportional to the d_{50} to the second or any other power are based on a coincidental relation between the VAPD and the d_{50} of the silts and sands used in the research. The influence of the bed density can be taken into account by using 9% of the additional pore volume for the increase of the water layer thickness of the layer of water surrounding the particles.
The model developed fits very well with the data used and does not contradict with previous models from literature. In fact it explains the variety of the relations used.
The model is intended for use of a silt (quartz) fraction and not of a clay fraction. Equations for the addition of a clay fraction might be correct as will be discussed in Miedema (2010D).
The model developed seems to depend on the choice of the Hamaker constant, but this is only partially true. The model is tuned with the combination of the Hamaker constant and the percentage of additional pore volume of 9% that is taken into account for the calculation of the water layer thickness of the layer of water surrounding the particles. A bigger Hamaker constant would result in a larger percentage, although this is not a linear relation, but more or less inversely proportional to the second power. In other words, the factor $\mathbf{A_H / f_\delta^2}$ is a constant with a value of $\mathbf{1.088 \cdot 10^{-20} / 0.09^2 = 1.343 \cdot 10^{-18}}$ for quartz particles in fresh water.

5.9. Nomenclature.

a_0	Shear stress coefficient (Lick)	N/m^3
a_1	Shear stress/density coefficient (Lick)	N/m^2
A	Surface or cross section	m^2
A_H	Hamaker constant for van der Waals long range forces	J
b_0	Shear stress coefficient (Lick)	N/m
b_1	Shear stress/density coefficient (Lick)	L/kg
C_D	Drag coefficient	-
C_L	Lift coefficient	-
c	Cohesion strength factor	-
c_3	Shear stress coefficient (Lick)	N/m^3
c_4	Shear stress coefficient (Lick)	N/m
d, d_p	Sphere, particle or grain diameter	m
d_1, d_2	Diameters of two spheres in relation with van der Waals forces	m
d_{50}, d_5, d_{10}	Diameter fractions of a PSD	m
d_i	Inter-particle distance in relation with van der Waals forces	m
d_b	Diameter of big particle (van der Waals forces)	m
d_s	Diameter of small particle (van der Waals forces)	m
d'	Roughness diameter according to Dou Guo Ren	m
d_*	Maximum roughness diameter according to Dou Guo Ren	m
D_0	Inter atom distance	-
f_D,f_{Drag}	Fraction of cross section exposed to drag	-
f_L,f_{Lift}	Fraction of top surface exposed to lift	-
f_δ	Volume fraction occupied by water film	-
F	Helmholz free energy	J
F(δ)	Van der Waals force between two bodies	N
F_c	Cohesive force between two particles	N
$F_{c,tot}$	Total cohesive force between 1 big particle and many small particles	N
F_{ch}	Horizontal cohesive/adhesive force	N
F_{cv}	Vertical cohesive/adhesive force	N
F_D	Drag force	N
F_L	Lift force	N
F_w	Weight of a particle	N
F_{st}	Surface tension force	N
g	Gravitational constant	$9.81\ m/sec^2$
H	Water depth	m
k_s	Roughness often chosen equal to the particle diameter	m
k	Constant (Dou Guo Ren)	-
K	Cohesion coefficient (Zanke)	-
ℓ_{Drag}	Drag point of action	-
$\ell_{Lever-D}$	Additional lever arm for drag	-
n	Porosity	-
n_{max}	Maximum porosity (Ternat, value=1)	-
n_{min}	Minimum porosity (Ternat, value=0.47)	-
N_b, $N_{b,s}$	Number of small particles having a bond with one big particle	-

$N_{F,b,s}$	Multiplication factor to determine the total vertical van der Waals force on one big particle at the surface	-
p_{st}	Surface tension pressure	Pa
r	Distance between atoms	m
$r_{s,b}$	Ratio of weight of small particles and one big particle	-
R, R_1, R_2	Radius of curvature of sphere, particle, grain or bubble	m
R_d	The relative submerged specific density	-
U_c, u_c, u_{cm}	Critical erosion velocity according to Hjulström	m/sec
U_d	Critical deposition velocity according to Hjulström	m/sec
V, V_v, V_s	Volume	m^3
α	The velocity factor at a certain exposure level	-
α	Surface fraction	-
ε	Interaction energy between atoms	J
ε_0	Cohesion strength	m^3/sec^2
δ	Water film thickness (Dou Guo Ren)	m
$\delta_n, \delta_{p,n}, \delta_{min}$	Water film thickness factor small particle	-
ρ	Fluid density	kg/m^3
ρ_f	Fluid density	kg/m^3
ρ_s	Solids density	kg/m^3
ρ_s	Sediment density	kg/m^3
ρ_w	The density of water or fluids	kg/m^3
ρ_q	The density of quarts or solids	kg/m^3
γ	Surface tension	N/m
γ_0	Sediment specific gravity (Dou Guo Ren)	N/m^3
γ_{0*}	Maximum specific gravity (Dou Guo Ren)	N/m^3
ϕ_{Roll}	Friction angle for rolling resistance	°
$\phi(r)$	Lennart-Jones potential	J
ψ	The pivot angle	°
θ, θ_{cr}	The Shields parameter or non-dimensional (critical) shear stress	-
$\theta_{sliding}$	The Shields parameter for the sliding mechanism	-
$\theta_{lifting}$	The Shields parameter for the lifting mechanism	-
$\theta_{rolling}$	The Shields parameter for the rolling mechanism	-
τ	Total shear stress	Pa
τ_b	Bed shear stress	Pa
τ_{cr}	Critical bed shear stress	Pa
ν	Kinematic viscosity	m^2/sec
σ	Molecule diameter	m
μ	Friction coefficient usually the tangent of the internal friction angle	-
$\mu_{rolling}$	Equivalent friction coefficient for rolling	-
$\mu_{sliding}$	Friction coefficient for sliding	-

Chapter 6: Hydraulic Transport of Sand/Shell Mixtures in Relation with the LDV.

6.1. Introduction.

This chapter is based on Ramsdell & Miedema (2010), Ramsdell et al. (2011) and Miedema & Ramsdell (2011). When considering pumping shells through a pipeline we have to consider that the shells are not spherical, but more disc shaped. When shells settle they will settle like leaves where the biggest cross section is exposed to the drag. But when they settle, they will settle in the same orientation, flat on the sediment, so the side of the shells is exposed to the horizontal flow in the pipeline. Since the side cross section is much smaller than the horizontal cross section, a much higher velocity is required to make them erode and go back into suspension. The settling velocity is much smaller because of the large area of the cross section.

Now normally pipeline resistance is calculated based on the settling velocity, where the resistance is proportional to the settling velocity of the grains. The Limit Deposit Velocity (LDV) is also proportional to the settling velocity. Since shells have a much lower settling velocity than sand grains with the same weight and much lower than sand grains with the same sieve diameter, one would expect a much lower resistance and a much lower critical velocity, matching the lower settling velocity. Now this is only partly true. As long as the shells are in suspension, on average they want to stay in suspension because of the low settling velocity. But as stated before, settling and erosion are stochastic processes because of the turbulent character of the flow in the pipeline. Since we operate at Reynolds numbers above 1 million the flow is always turbulent, meaning that eddies and vortices occur stochastically making the particles in the flow move up and down, resulting in some particles hitting the bottom of the pipe. Normally these particles will be picked up in the flow because of erosion, so there exists equilibrium between sedimentation and erosion, resulting in not having a bed at the bottom of the pipeline. In fact the capacity of the flow to erode is bigger than the sedimentation. If the line speed decreases, the shear velocity at the bottom of the pipe also decreases and less particles will be eroded, so the erosion capacity is decreasing. Now this does not matter as long as the erosion capacity is bigger than the sedimentation there will not be sediment at the bottom of the pipeline. As soon as the line speed decreases so much that the erosion capacity (erosion flux) is smaller than the sedimentation flux, not all the particles will be eroded, resulting in a bed to be formed at the bottom of the pipe. Having a bed at the bottom of the pipe also means that the cross section of the pipe decreases and the actual flow velocity above the bed increases. This will result in a new equilibrium between sedimentation flux and erosion flux for each bed height.

So from the moment there is a bed, decreasing the flow will result in an almost constant flow velocity above the bed, resulting in equilibrium between erosion and sedimentation. This equilibrium however is sensitive for changes in the line speed and in the mixture density. Increasing the line speed will reduce the bed height; a decrease will increase the bed height. Having a small bed does not really matter, but a thick bed makes the system vulnerable for plugging the pipeline. The LDV in most models is chosen in such a way that a thin bed is allowed. Now for the shells, as said before, there will always be some shells that will reach the bottom of the pipe due to the combination of settling velocity and turbulence. Once these shells are on top of the sediment they are hard to remove by erosion, because they lay flat on the surface and have a small cross section that is exposed to the flow compared with the weight of the shell. So although their settling velocity is much lower than equivalent sand particles, the erosion velocity is much higher. If we look at the beach in an area with many shells, we can always see the shells on top of the sand, covering the sand. In fact the shells are shielding the sand from erosion, because they are hard to erode. The bigger shells will also shield the smaller pieces, because the smaller pieces settle faster.

Compare this with leaves falling from a tree, the bigger leaves, although heavier, will fall slower, because they are exposed to higher drag. The same process will happen in the pipeline. Shells settle slower than sand grains, so they will be on top of the bed (if there is a bed), just like on the beach. Since they are hard to erode, in fact they protect the bed from being eroded, even if the line speed is increased. But there will always be velocities above the bed that will make the shells erode. Now the question is how we can quantify this behavior in order to get control over it. We have to distinguish between sedimentation and erosion. First of all assume shells are disc shaped with a diameter d and a thickness of $\boldsymbol{\alpha \cdot d}$ and let's take $\boldsymbol{\alpha=0.1}$ this gives a cross section for the terminal settling velocity of $\boldsymbol{\pi/4 \cdot d^2}$, a volume of $\boldsymbol{\pi/40 \cdot d^3}$ and a cross section for erosion of $\boldsymbol{d^2/10}$. Two processes have to be analyzed to determine the effect of shells on the critical velocity, the sedimentation process and the erosion process.

6.2. The Drag Coefficient.

The drag coefficient C_D depends upon the Reynolds number according to Turton & Levenspiel (1986), which is a 5 parameter fit function to the data:

$$C_D = \frac{24}{Re_p} \cdot (1 + 0.173 \cdot Re_p^{0.657}) + \frac{0.413}{1 + 16300 \cdot Re_p^{-1.09}} \qquad (6\text{-}1)$$

It must be noted here that in general the drag coefficients are determined based on the terminal settling velocity of the particles. Wu & Wang (2006) recently gave an overview of drag coefficients and terminal settling velocities for different particle Corey shape factors. The result of their research is reflected in Figure 6-1. Figure 6-1 shows the drag coefficients as a function of the Reynolds number and as a function of the Corey shape factor.

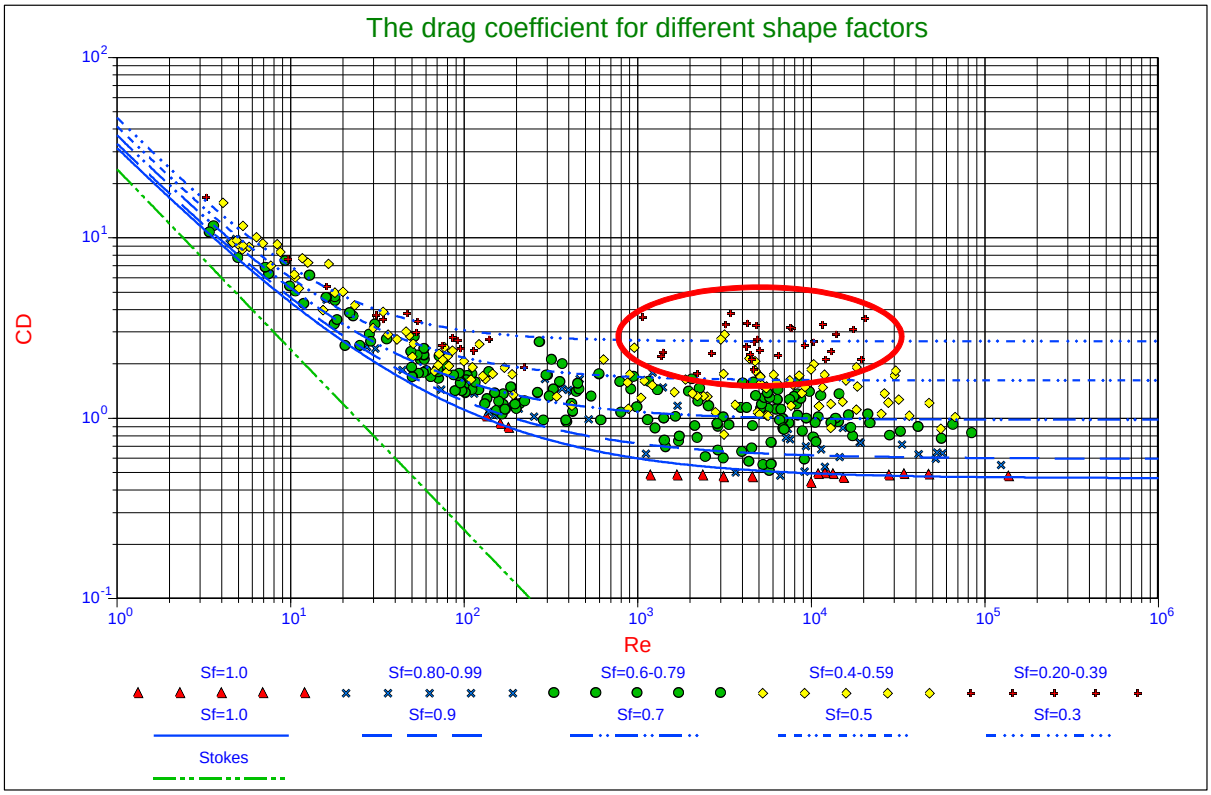

Figure 6-1: Drag coefficient as a function of the particle shape (Wu & Wang, 2006).

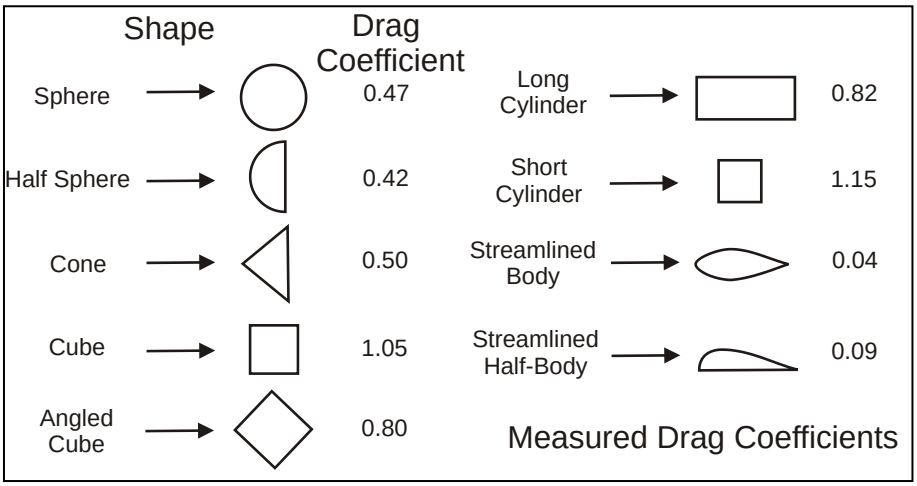

Figure 6-2: Some drag coefficients (source Wikipedia).

For shells settling the Corey shape factor is very small, like 0.1, resulting in high drag coefficients. According to Figure 6-1 the drag coefficient should be like:

$$C_D = \frac{32}{Re_p} + 2 \text{ up to } C_D = \frac{36}{Re_p} + 3 \qquad (6\text{-}2)$$

For shells lying flat on the bed, the drag coefficient will be similar to the drag coefficient of a streamlined half body (0.09), which is much smaller than the drag coefficient for settling (3). So there is a large asymmetry between the settling process and the erosion process of shells, while for more or less spherical sand particles the drag coefficient is considered to be the same in each direction.

6.3. Non-Uniform Particle Size Distributions.

In the model for uniform particle distributions, the roughness k_s was chosen equal to the particle diameter d, but in the case of non-uniform particle distributions, the particle diameter d is a factor d^+ times the roughness k_s, according to:

$$d^+ = \frac{d}{k_s} \qquad (6\text{-}3)$$

The roughness k_s should be chosen equal to some characteristic diameter related to the non-uniform particle distribution, for example the d_{50}.

6.4. Laminar Region.

For the laminar region (the viscous sub layer) the velocity profile of Reichardt (1951) is chosen. This velocity profile gives a smooth transition going from the viscous sub layer to the smooth turbulent layer.

$$u^+_{top} = \frac{u(y_{top})}{u_*} = \frac{\ln(1+\kappa \cdot y^+_{top})}{\kappa} - \frac{\ln(1/9)+\ln(\kappa)}{\kappa} \cdot \left(1 - e^{-\frac{y^+_{top}}{11.6}} - \frac{y^+_{top}}{11.6} e^{-0.33 \cdot y^+_{top}} \right) \approx y^+_{top} \qquad (6\text{-}4)$$

For small values of the boundary Reynolds number and thus the height of a particle, the velocity profile can be made linear to:

6-5

$$u^+_{top} = y^+_{top} = d^+ \cdot E \cdot Re_* = d^+ \cdot E \cdot k^+_s \qquad (6\text{-}6)$$

Adding the effective turbulent velocity to the time averaged velocity, gives for the velocity function α_{Lam}:

$$\alpha_{Lam} = y^+_{top} + u^+_{eff}(y^+_{top}) \qquad (6\text{-}7)$$

6.5. Turbulent Region.

Particles that extend much higher into the flow will be subject to the turbulent velocity profile. This turbulent velocity profile can be the result of either a smooth boundary or a rough boundary. Normally it is assumed that for boundary Reynolds numbers less than 5 a smooth boundary exists, while for boundary Reynolds numbers larger than 70 a rough boundary exists. In between in the transition zone the probability of having a smooth boundary is:

$$P = e^{-0.95 \cdot \frac{Re_*}{11.6}} = e^{-0.95 \cdot \frac{k^+_s}{11.6}} \qquad (6\text{-}8)$$

This probability is not influenced by the diameter of individual particles, only by the roughness k_s which is determined by the non-uniform particle distribution as a whole. This gives for the velocity function α_{Turb}:

$$\alpha_{Turb} = \frac{1}{\kappa}\cdot\ln\left(95\cdot\frac{y_{top}^{+}}{\delta_{v}^{+}}+1\right)\cdot P+\frac{1}{\kappa}\cdot\ln\left(30\cdot\frac{y_{top}^{+}}{k_{s}^{+}}+1\right)\cdot(1-P) \qquad (6\text{-}9)$$

The velocity profile function has been modified slightly by adding 1 to the argument of the logarithm. Effectively this means that the velocity profile starts y_0 lower, meaning that the virtual bed level is chosen y_0 lower for the turbulent region. This does not have much effect on large exposure levels (just a few percent), but it does on exposure levels of 0.1 and 0.2. Not applying this would result in to high (not realistic) shear stresses at very low exposure levels.

6.6. The Exposure Level.

Effectively, the exposure level **E** is represented in the equations (5-1), (5-2) and (5-3) for the Shields parameter by means of the velocity distribution according to equations (6-7) and (6-9) and the sliding friction coefficient μ_{sf} or the pivot angle ψ. A particle with a diameter bigger than the roughness k_s will be exposed to higher velocities, while a smaller particle will be exposed to lower velocities. So it is important to find a relation between the non-dimensional particle diameter d^+ and the exposure level **E**.

6.7. The Angle of Repose & the Friction Coefficient.

Miller & Byrne (1966) found the following relation between the pivot angle ψ and the non-dimensional particle diameter d^+, with c_0=**61.5°** for natural sand, c_0=**70°** for crushed quartzite and c_0=**50°** for glass spheres, see Figure 6-3.

$$\psi = c_o\cdot(d^+)^{-0.3} \qquad (6\text{-}10)$$

Wiberg & Smith (1987A) re-analyzed the data of Miller & Byrne (1966) and fitted the following equation:

$$\psi = \cos^{-1}\left(\frac{d^+ + z_*}{d^+ + 1}\right) \qquad (6\text{-}11)$$

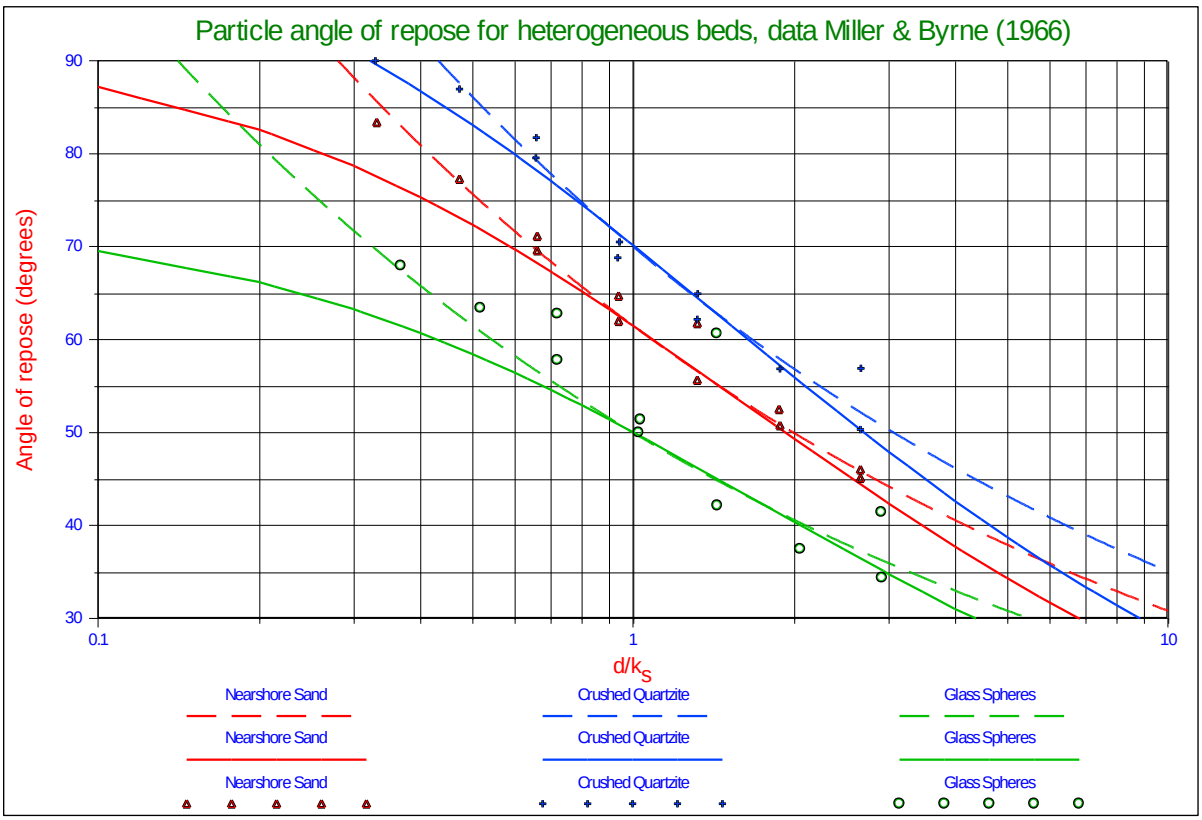

Figure 6-3: Particle angle of repose as a function of the ratio particle size/roughness.

The average level of the bottom of the almost moving grain z_* depends on the particle sphericity and roundness. The best agreement is found for natural sand with z_***=-0.045**, for crushed quartzite with z_***=-0.320** and for glass spheres with z_***=-0.285**. Wiberg & Smith (1987A) used for natural sand with z_***=-0.020**, for crushed quartzite with z_***=-0.160** and for glass spheres with z_***=14**. The values found here are roughly 2 times the values as published by Wiberg & Smith (1987A). It is obvious that equation (6-11) underestimates the angle of repose for d^+ values smaller than 1.

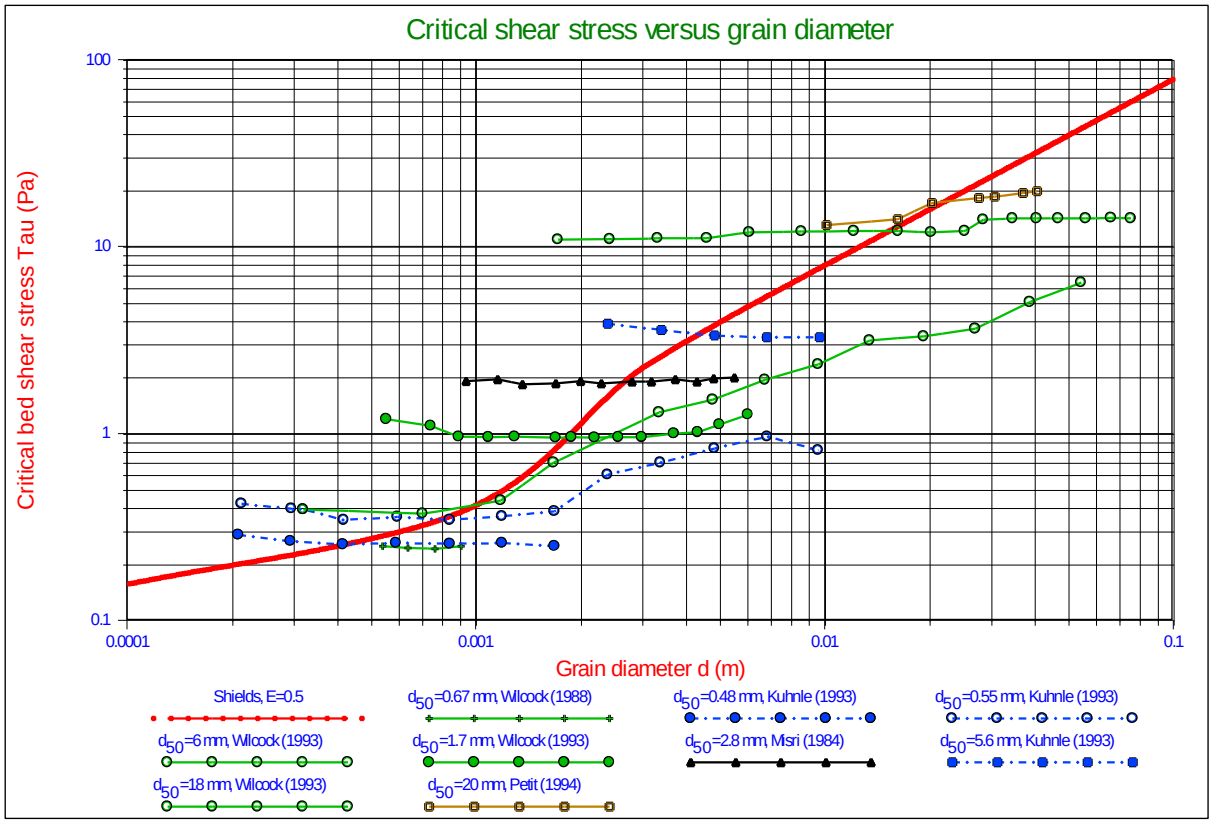

Figure 6-4: Critical bed shear stress of individual size fractions in a mixture as a function of grain diameter (modified after van Rijn (2006) and Wilcock (1993)).

6.8. The Equal Mobility Criterion.

Now two different cases have to be distinguished. Particles with a certain diameter can lie on a bed with a different roughness diameter. The bed roughness diameter may be larger or smaller than the particle diameter. Figure 6-5 shows the Shields curves for this case (which are different from the graph as published by Wiberg & Smith (1987A)), combined with the data of Fisher et al. (1983), and based on the velocity distributions for non-uniform particle size distributions. Fisher et al. carried out experiments used to extend the application of the Shields entrainment function to both organic and inorganic sediments over passing a bed composed of particles of different size. Figure 6-5 shows a good correlation between the theoretical curves and the data, especially for the cases where the particles considered are bigger than the roughness diameter (**d/k_s>1**). It should be noted that most of the experiments were carried out in the transition zone and in the turbulent regime. Figure 6-5 is very important for determining the effect of shells on a bed, because with this figure we can determine the critical Shields parameter of a particle with a certain diameter, lying on a bed with a roughness of a different diameter. In the case of the shells the bed roughness diameter will be much smaller than the shell diameter (dimensions). To interpret Figure 6-5 one should first determine the bed roughness diameter and the roughness Reynolds number and take the vertical through this roughness Reynolds number (also called the boundary Reynolds number). Now determine the ratio **d/k_s** and read the Shields parameter from the graph. From this it appears that the bigger this ratio, the smaller the Shields value found. This is caused by the fact that the Shields parameter contains a division by the particle diameter, while the boundary shear stress is only influenced slightly by the changed velocity distribution. Egiazaroff (1965) was one of the first to investigate non-uniform particle size distributions with respect to initiation of motion. He defined a hiding factor or exposure factor as a multiplication factor according to:

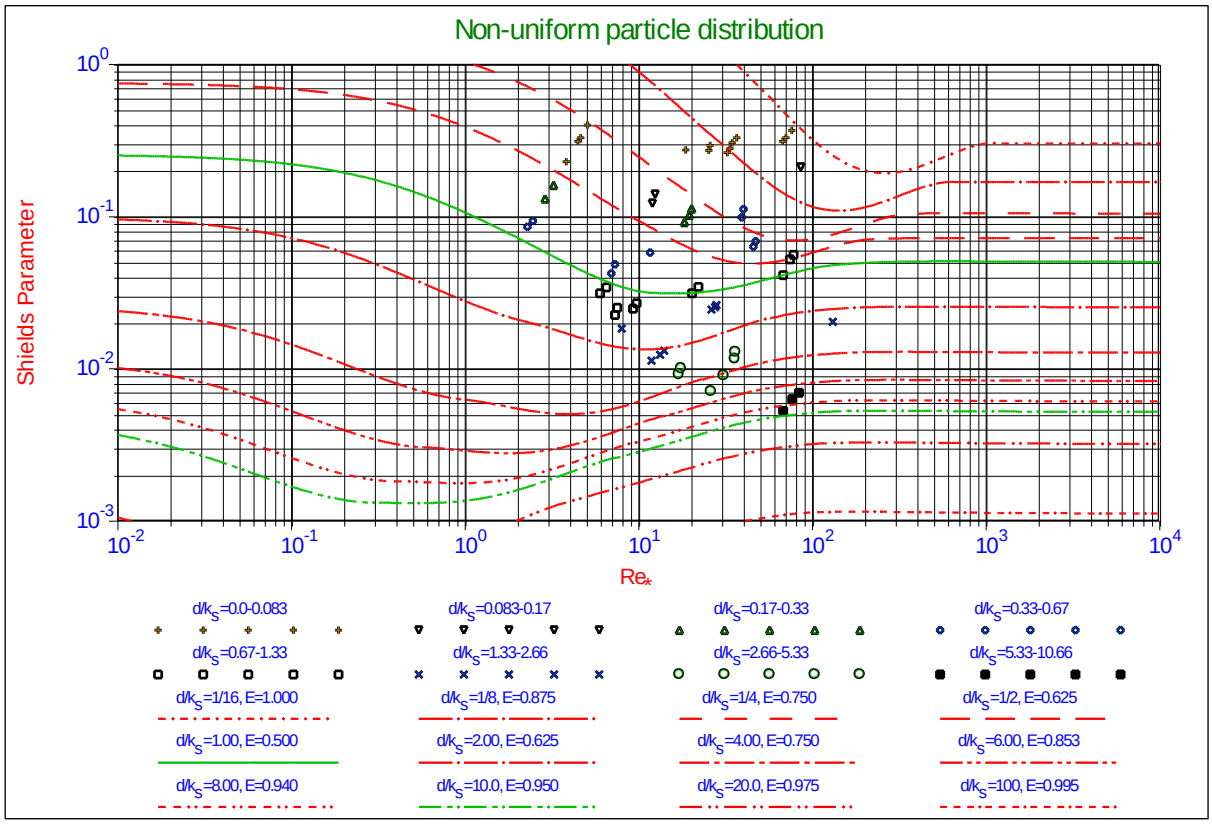

Figure 6-5: Non-uniform particle distributions.

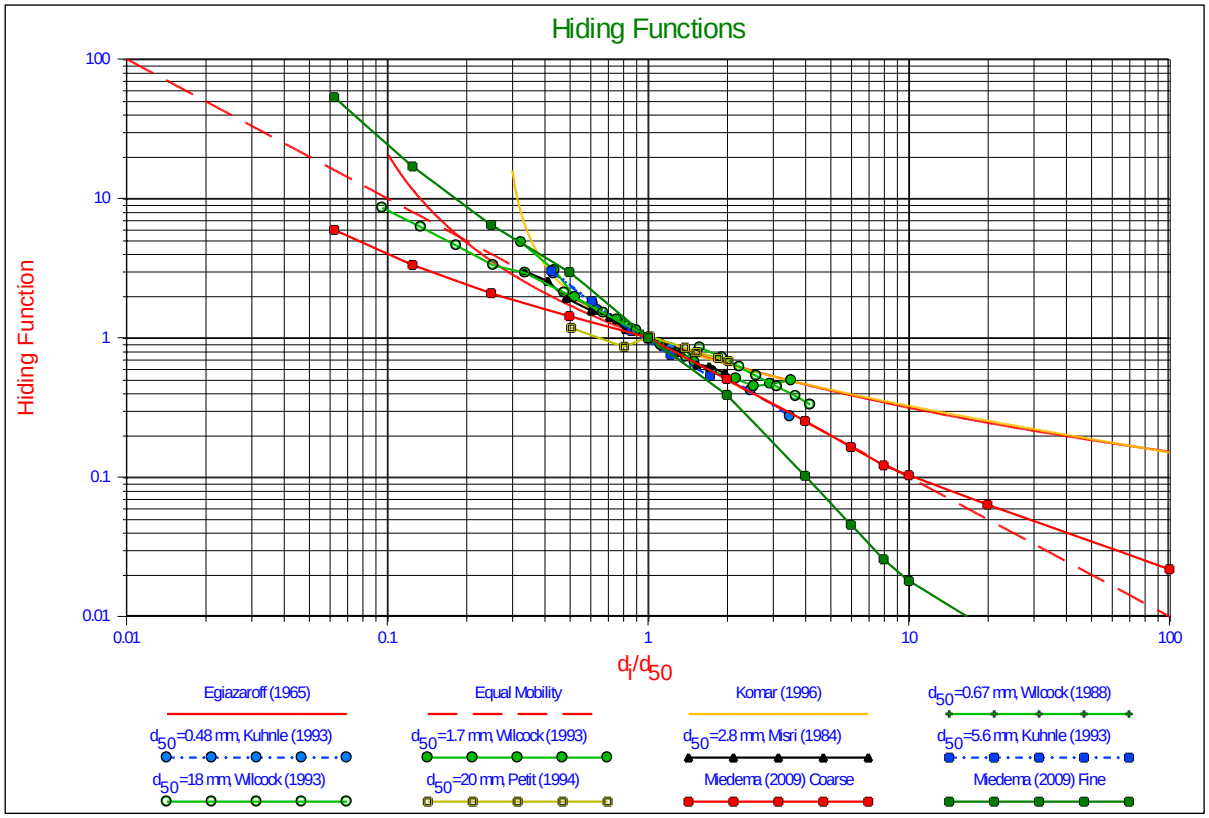

Figure 6-6: Hiding functions.

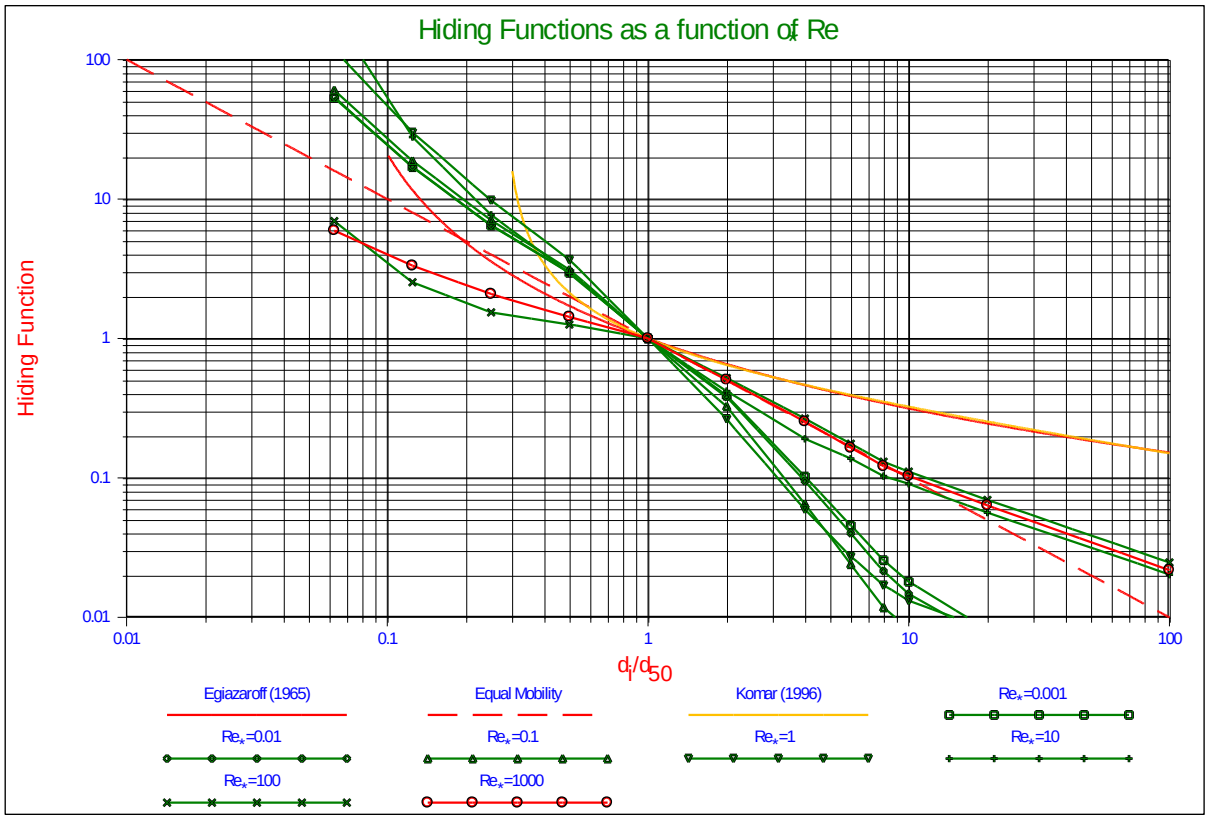

Figure 6-7: Hiding Functions as a function of Re*.

$$\theta_{cr,i} = \theta_{cr,d50} \cdot \left(\frac{\log(19)}{\log\left(19 \cdot \frac{d_i}{d_{50}}\right)} \right)^2 \qquad \textbf{(6-12)}$$

The tendency following from this equation is the same as in Figure 6-5, the bigger the particle, the smaller the Shields value, while in equation (6-12) the $\mathbf{d_{50}}$ is taken equation to the roughness diameter $\mathbf{k_s}$. The equal mobility criterion is the criterion stating that all the particles in the top layer of the bed start moving at the same bed shear stress, which matches the conclusion of Miedema (2010) that sliding is the main mechanism of entrainment of particles. Figure 6-4 shows that the results of the experiments are close to the equal mobility criterion, although not 100%, and the results from coarse sand from the theory as shown in Figure 6-5, matches the equal mobility criterion up to a ratio of around 10. Since shells on sand have a $\mathbf{d/k_s}$ ratio bigger than 1, the equal mobility criterion will be used for the interpretation of the shell experiments as also shown in Figure 6-5.

6.9. Shells.

Dey (2003) has presented a model to determine the critical shear stress for the incipient motion of bivalve shells on a horizontal sand bed, under a unidirectional flow of water. Hydrodynamic forces on a solitary bivalve shell, resting over a sand bed, are analyzed for the condition of incipient motion including the effect of turbulent fluctuations. Three types of bivalve shells, namely Coquina Clam, Cross-barred Chione and Ponderous Ark, were tested experimentally for the condition of incipient motion. The shape parameter of bivalve shells is defined appropriately.

Although the model for determining the Shields parameter of shells is given, the experiments of Dey (2003) were not translated into Shields parameters. It is interesting however to quantify these experiments into Shields parameters and to see how this relates to the corresponding Shields parameters of sand grains. In fact, if the average drag coefficient of the shells is known, the shear stress and thus the friction velocity, required for incipient motion, is known, the flow velocity required to erode the shells can be determined. Figure 6-8 and Figure 6-9 give an impression of the shells used in the experiments of Dey (2003). From Figure 6-8 it is clear that the shape of the shells match the shape of a streamlined half body lying on a surface and thus a drag coefficient is expected of

about 0.1, while sand grains have a drag coefficient of about 0.45 at very high Reynolds numbers in a full turbulent flow. The case considered here is the case of a full turbulent flow, since we try to relate the incipient motion of shells to the critical velocity.

Equation (5-1) shows the importance of the drag coefficient in the calculation of the incipient motion, while the lift coefficient is often related to the drag coefficient. Whether the latter is true for shells is the question. For sand grains at high Reynolds numbers of then the lift coefficient is chosen to be 0.85 times the drag coefficient or at least a factor between 0.5 and 1, shells are aerodynamically shaped and also asymmetrical. There will be a big difference in the lift coefficient of shells lying on the bed, between convex upwards and convex downwards. A convex upwards shell is like the streamlined half body with a small drag coefficient. A convex downwards shell obviously is easy to catch the flow and start to move, because the drag coefficient is larger and most probably, the lift coefficient is much larger. So it will be the convex upwards shells that armor the bed or the beach.

Now the question is, what the drag coefficient would be, based on the experiments of Dey (2003). Figure 6-10 shows the Shields parameters for the three types of shells lying convex upwards on the bed with two types of sand, a d50=0.8 mm and a d50=0.3 mm, also the average values are shown. For the determination of the Shields values, the definition of the Shields parameter has to be used more strictly. Often a definition is used where the Shields parameter equals the ratio between the shear force and the normal force on the grain, resulting in a denominator with the particles diameter.

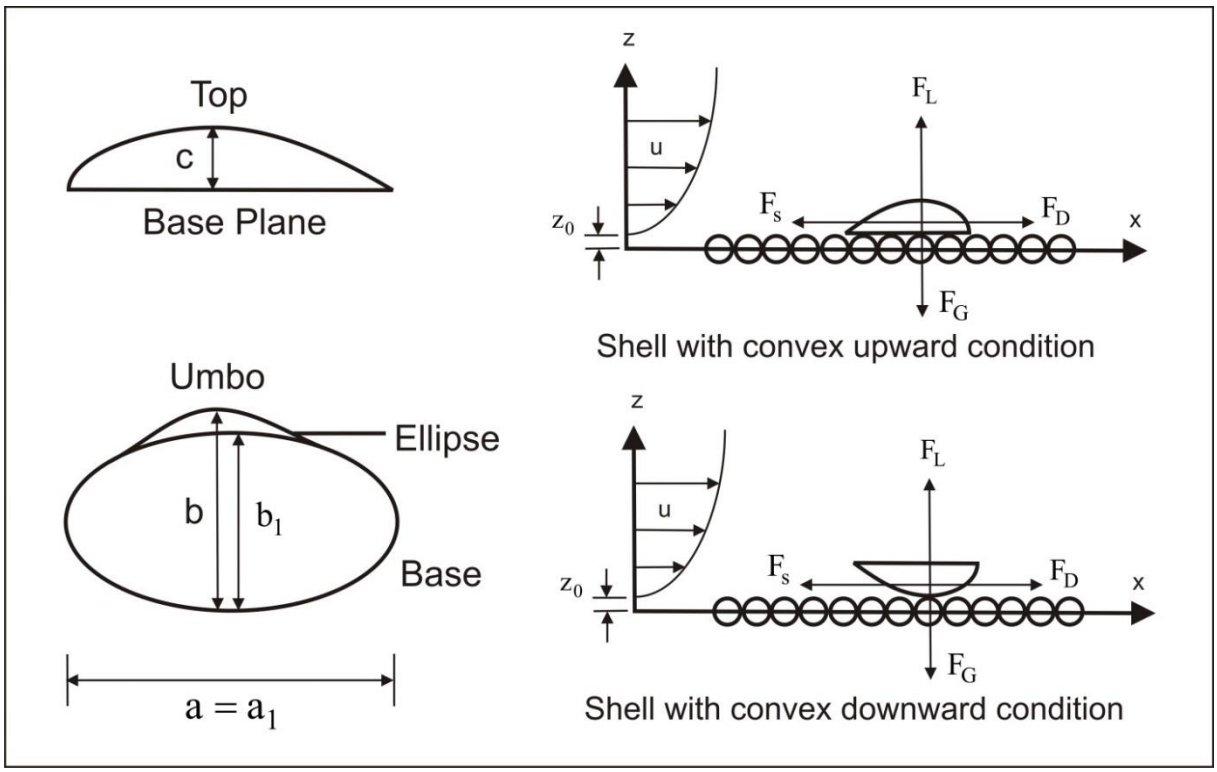

Figure 6-8: Shape of bivalve shell (Dey (2003)).

More strictly, the Shields parameter is the shear stress divided by the normal stress and in the case of shells; the normal stress depends on the average thickness of the shell and not the size of the shell. Using this definition, results in useful Shields values. Since convex upwards is important for the critical velocity analysis, this case will be analyzed and discussed. It is clear however from these figures that the convex downwards case results in much smaller Shields values than the convex upwards case as was expected. Smaller Shields values in this respect means smaller shear stresses and thus smaller velocities above the bed causing erosion. In other words, convex downwards shells erode much easier than convex upwards.

Although the resulting Shields values seem to be rather stochastic, it is clear that the mean values of the Chione and the Coquina are close to the Shields curve for $\mathbf{d/k_s=1}$. The values for the Ponderous Ark are close to the Shields curve for $\mathbf{d/k_s=3}$. In other words, the Ponderous Ark shells are easier to erode than the Chione and the Coquina shells. Looking at the shells in Figure 6-9 we can see that the Ponderous Ark shells have ripples on the outside and will thus be subject to a higher drag. On the other hand, the Ponderous Ark shells have an average thickness of 2.69 mm (1.95-3.98 mm) as used in the equation of the Shields parameter, while the Coquina clam has a thickness

of 1.6 mm (0.73-3.57 mm) and the Chione 1.13 mm (0.53-2.09 mm). This also explains part of the smaller Shields values of the Ponderous Ark. The average results of the tests are shown in the following table.

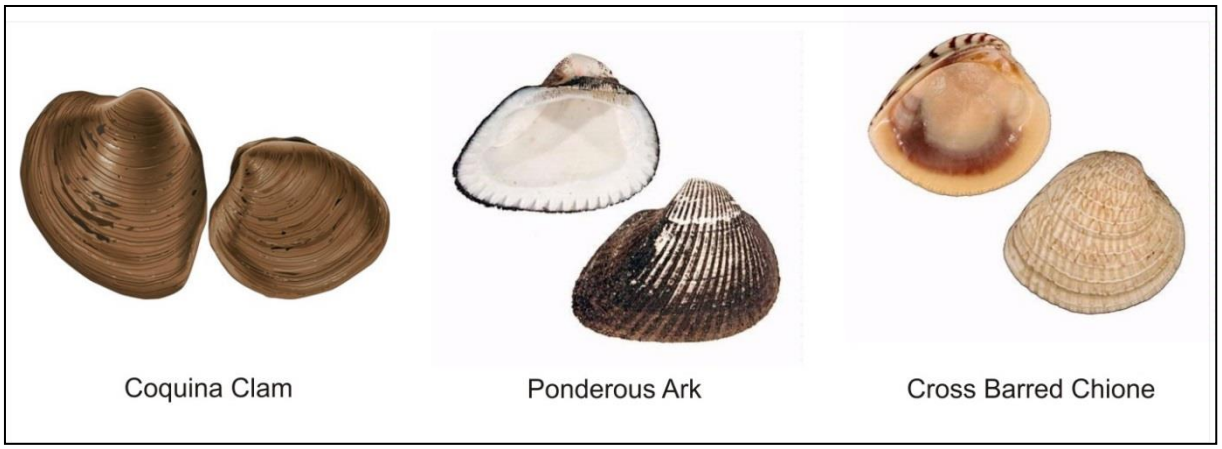

Figure 6-9: Selected samples of bivalve shells (Dey (2003)).

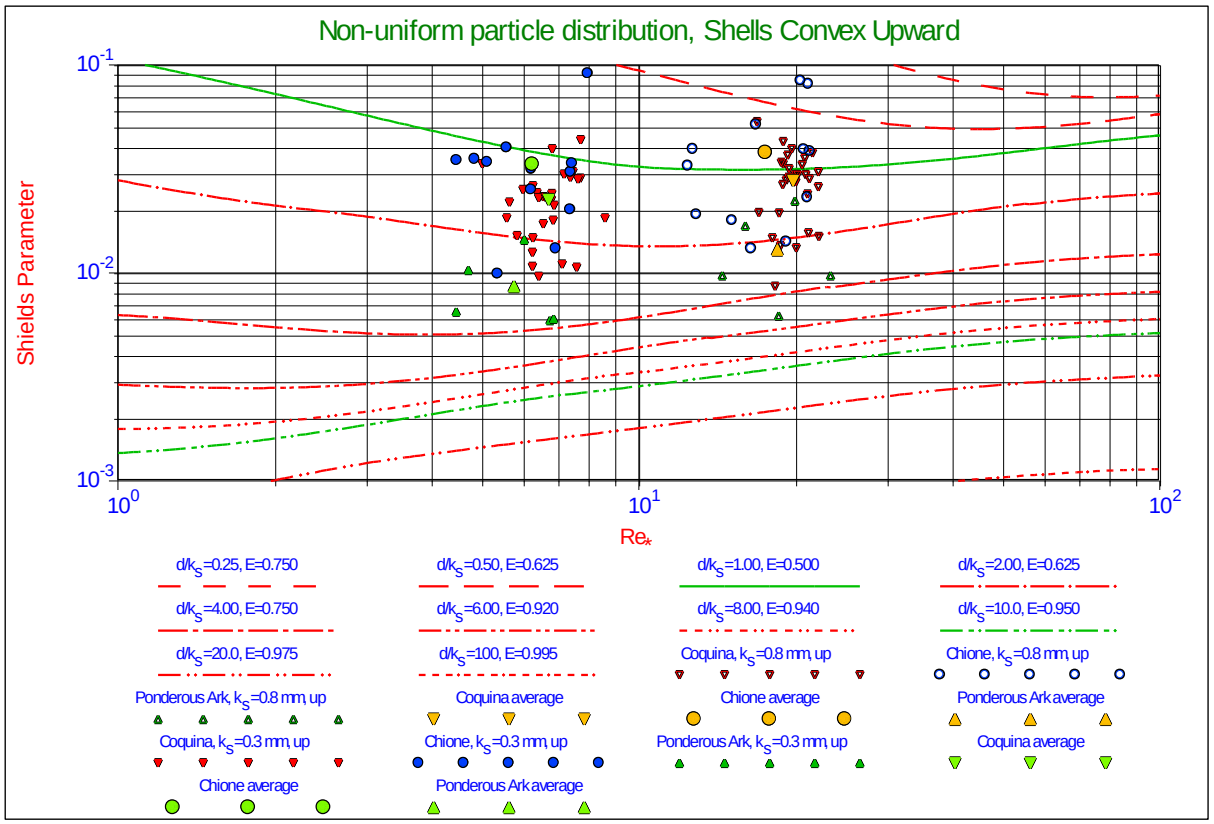

Figure 6-10: Shells convex upward.

A closer look at the data, based on this table, shows the following. For the shells on the 0.8 mm sand the $\mathbf{d/k_s}$ values vary from 1.41-3.36. The average Shields values found do not match the corresponding curves, but lead to slightly lower $\mathbf{d/k_s}$ values. For example, the Cross Barred Chione had a Shields value of 0.0378, but based on the $\mathbf{d/k_s}$ value of 1.41, a Shields value of about 0.02 would be expected, a ratio of 1.89. The Coquina Clam had an average Shields value of 0.0277, but based on the $\mathbf{d/k_s}$ value of 2.00 a Shields value of about 0.015 would be expected, a ratio of 1.84. The Ponderous Ark had an average Shields value of 0.0129, but based on the $\mathbf{d/k_s}$ value of 3.36 a Shields value of about 0.008 would be expected, a ratio of 1.61. For the 0.3 mm sand the average ratio is about 5.5. In other words, the shells require larger Shields values than corresponding sand grains. This effect is larger in the case of shells on a bed with finer sand particles. The exact ratios depend on the type of shells.

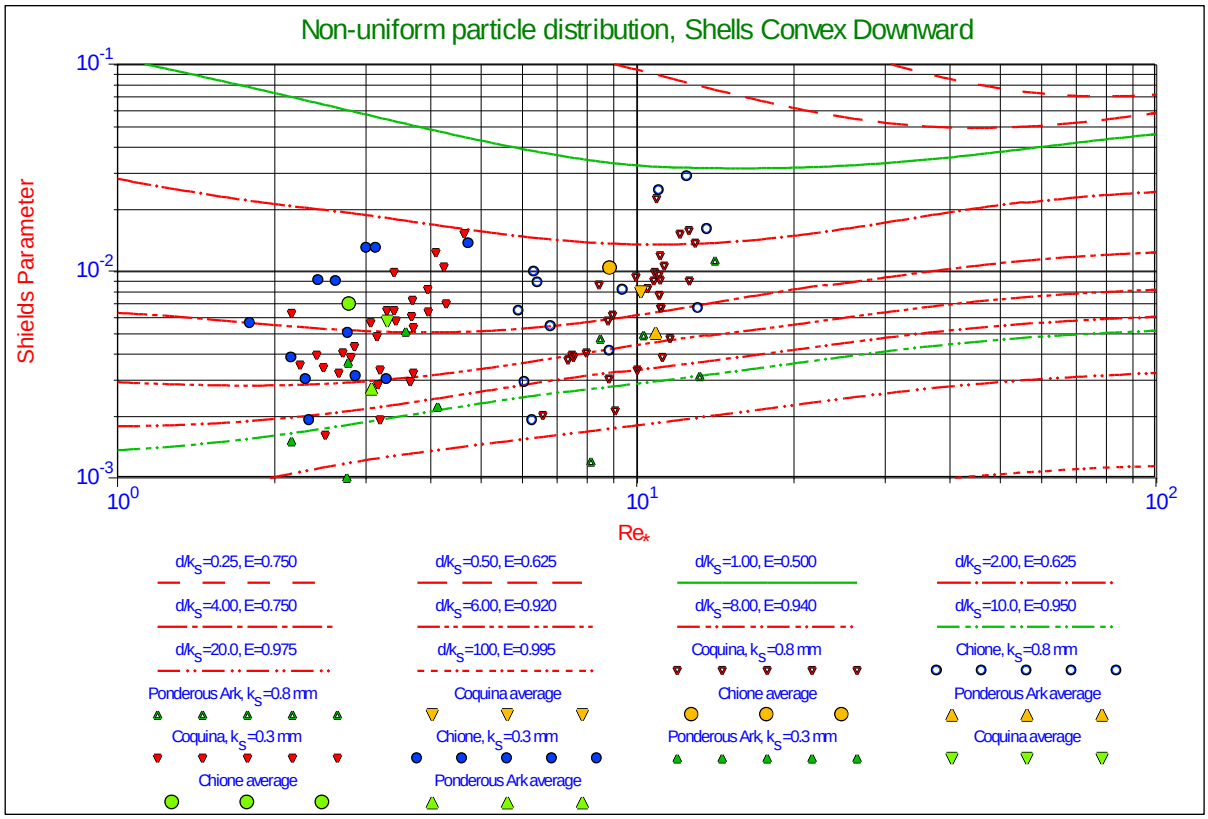

Figure 6-11: Shells convex downward.

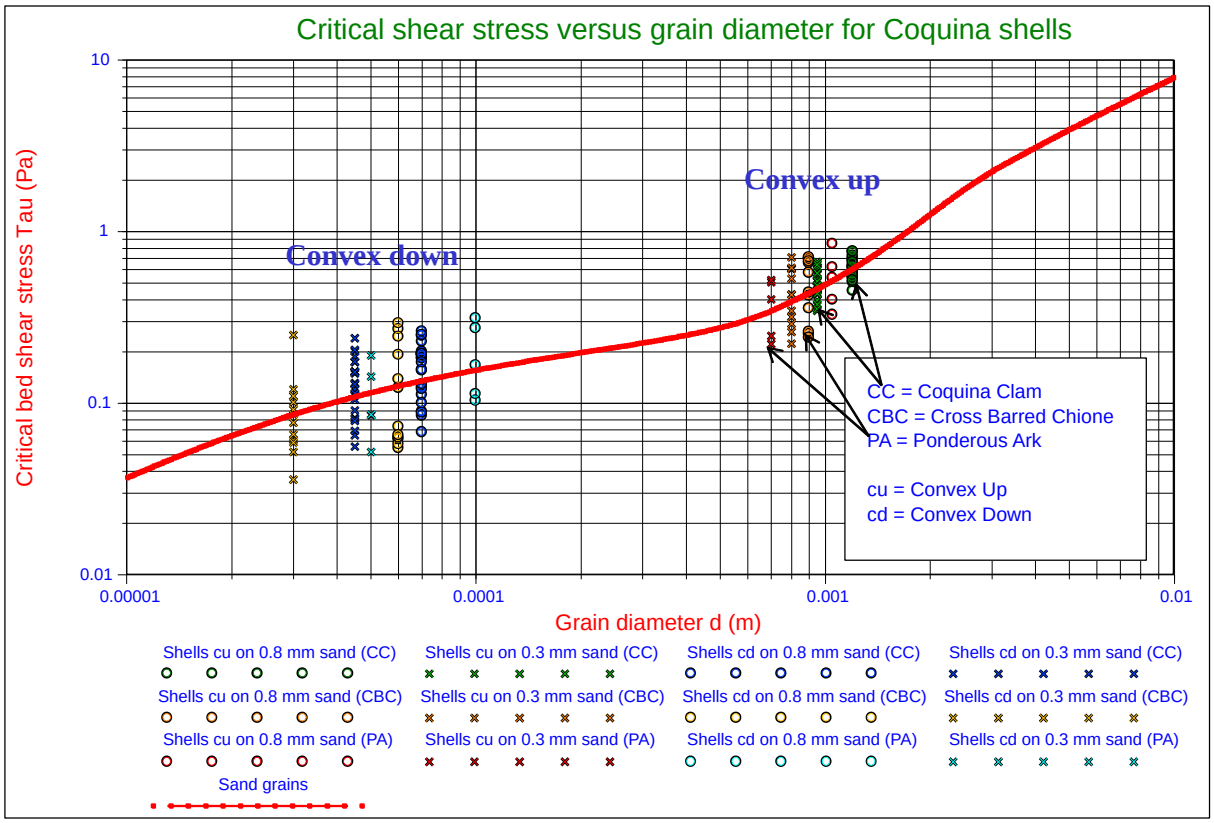

Figure 6-12: The critical shear stresses of the shells compared with sand.

Table 6-1: Average Shields values.

	d_{50}=0.8 mm		d_{50}=0.3 mm			d_{50}=0.8 mm	d_{50}=0.3 mm
	Re_*	θ	Re_*	θ	d	d/k_s	d/k_s
Coquina Clam	19.78	0.0277	6.71	0.0225	1.60	2.00	5.33
Cross Barred Chione	17.51	0.0378	6.24	0.0333	1.13	1.41	3.76
Ponderous Ark	18.46	0.0129	5.76	0.0086	2.69	3.36	8.97

6.10. The Limit Deposit Velocity.

A familiar phenomenon in the transport of sand slurries is the LSDV (Limit of Stationary Deposit Velocity), the velocity at which the mixture forms a stationary bed in the pipeline. As the velocity increases from the LSDV, the bed starts to slide along the bottom of the pipe. As the velocity increases further the bed begins to erode with the particles either rolling or saltating along the top of the bed, or fully suspended in the fluid, the LDV where all particles are in suspension.

A related concept is that of the minimum friction velocity, $\mathbf{V_{imin}}$, at which the friction in the pipeline is minimized. At low concentrations the $\mathbf{V_{imin}}$ may be equal to or just above the LDV, but as concentration increases the LDV starts to decrease while the $\mathbf{V_{imin}}$ continues to rise. In operational terms, the $\mathbf{V_{imin}}$ represents a point of instability, so we generally try to design our pumping systems to maintain sufficiently high velocities that the system velocity never falls below (or close to) $\mathbf{V_{imin}}$ during the operational cycle.

Implicit in most models of slurry transport is the idea that the system can transition smoothly in both directions along the system resistance curves. So if the dredge operator inadvertently feeds too high of a concentration, dropping the velocity close to the minimum friction or even the LDV, he can recover by slowly lowering the mixture concentration, which in turn lowers the density in the pipeline and allows the velocity to recover. Alternatively the operator can increase the pressure by turning up the pumps to raise the velocity. In a sand-sized material this works because the critical and minimum friction velocities are fairly stable, so raising the pumping velocity or lowering the concentration will be enough to start the bed sliding, then erode the bed and return to stable operation.

With a sand-shell mixture, as described above, the LDV and minimum friction velocities become time-dependent parameters. The stochastic nature of the process means that some fraction of the shells will fall to the bottom of the pipe. The asymmetry between deposition and erosion velocity means that these shells will stay on the bottom, forming a bed that grows over time, increasing the critical velocity and minimum friction velocity. Unless the system is operated with very high margins of velocity, the new LDV and $\mathbf{V_{imin}}$ eventually fall within the operating range of the system, leading to flow instability and possible plugging.

Now, how to combine this LDV with the erosion behavior of shells. As mentioned above, there are different models in literature for the LDV and there is also a difference between the LDV and the minimum friction velocity. However, whatever model is chosen, the real LDV is the result of an equilibrium of erosion and deposition resulting in a stationary bed. This equilibrium depends on the particle size distribution, the slurry density and the flow velocity. At very low concentrations it is often assumed that the LDV is zero, but based on the theory of incipient motion, there is always a certain minimum velocity required to erode an existing bed.

There are two ways to look at this problem, we can compare the Shields values of the shells with the Shields values of sand particles with a diameter equal to the thickness of the shells, resulting in the factors as mentioned in the previous paragraph or we compare the shear stresses occurring to erode the shells with the shear stresses required for the sand beds used. The latter seems more appropriate because the shear stresses are directly related to the average velocity above the bed with the following relation:

$$\rho_l \cdot u_*^2 = \frac{\lambda_l}{8} \cdot \rho_l \cdot U^2 \qquad \textbf{(6-13)}$$

Where the left hand side equals the bed shear stress, λ_l the friction coefficient following from the Moody diagram and **U** the average flow velocity above the bed. The average shear stresses are shown in the next table.

.

Table 6-2: Average shear stresses.

	d_{50}=0.8 mm				d_{50}=0.3 mm			
	Re_*	**θ**	**$\rho_l \cdot u_*^2$**	**ratio**	**Re_***	**θ**	**$\rho_l \cdot u_*^2$**	**ratio**
Coquina Clam	19.78	0.0277	0.72	1.60	6.71	0.0225	0.58	3.41
Cross Barred Chione	17.51	0.0378	0.69	1.53	6.24	0.0333	0.61	3.59
Ponderous Ark	18.46	0.0129	0.56	1.24	5.76	0.0086	0.37	2.18

The Shields values for both sands are about 0.035, resulting in shear stresses of 0.45 Pa for the 0.8 mm sand and 0.17 Pa for the 0.3 mm sand. The ratios between the shear stresses required eroding the shells and the shear stresses required to erode the beds are also shown in the table. For the shells laying convex upwards on the 0.8 mm sand bed these ratio's vary from 1.24-1.60, while this is a range from 2.18-3.41 for the 0.3 mm sand bed. These results make sense, the shear stress required for incipient motion of the shells does not change much because of the sand bed, although there will be some reduction for sand beds of smaller particles due to the influence of the bed roughness on the velocity profile according to equation (6-4). Smaller sand particles with a smaller roughness allow a faster development of the velocity profile and thus a bigger drag force on the shells at the same shear stress.

The main influence on the ratios is the size of the sand particles, because smaller particles require a smaller shear stress for the initiation of motion. This is also known from the different models for the LDV, the finer the sand grains, the smaller the critical velocity. In order words, the smaller the velocity to bring the particles in a bed back into suspension. It also makes sense that the ratio between shell erosion shear stress and sand erosion shear stress will approach 1 if the sand particles will have a size matching the thickness of the shells and even may become smaller than 1 if the sand particles are bigger than the shells.

Since the velocities are squared in the shear stress equation, the square root of the ratios has to be taken to get the ratios between velocities. This leads to velocity ratio's from 1.11-1.26 for the 0.8 mm sand and ratio's from 1.48-1.89 for the 0.3 mm sand. Translating this to the LDV, can be carried out under the assumption that the LDV is proportional to the average flow velocity resulting in incipient motion. Although the LDV results from an equilibrium between erosion and deposition of particles and thus is more complicated, the here derived ratios can be used as a first attempt to determine the critical velocities for a sand bed covered with convex upwards shells.

For the coarser sands (around 0.8 mm) this will increase the critical velocity by 11%-26%, while this increase is 48%-89% for the finer 0.3 mm sand. Even finer sands will have a bigger increase, while coarser sands will have a smaller increase. As stated, the shear stress required to erode the shells is almost constant, but decreasing a little bit with decreasing sand particle diameters, an almost constant critical velocity for the shells is expected. From the measurements it is also clear, that very smooth shells (Coquina Clam and Cross Barred Chione) are harder to erode and will have a higher critical velocity than the rough shells (Ponderous Ark).

6.11. Conclusions and Discussion.

The LDV for the hydraulic transport of a sand-water mixture depends on a number of physical processes and material properties. The LDV is the result of equilibrium between the deposition of sand particles and the erosion of sand particles. The deposition of sand particles depends on the settling velocity, including the phenomenon of hindered settling as described in this paper. The erosion or incipient motion of particles depends on equilibrium of driving forces, like the drag force, and frictional forces on the particles at the top of the bed. This results in the so called friction velocity and bottom shear stress. Particles are also subject to lift forces and so called Magnus forces, due to the rotation of the particles. So particles that are subject to rotation may stay in suspension due to the Magnus forces and do not contribute to the deposition. From this it is clear that an increasing flow velocity will result in more erosion, finally resulting in hydraulic transport without a bed. A decreasing flow velocity will result in less erosion and an increasing bed thickness, resulting in the danger of plugging the pipeline.

Shells lying convex upwards on the bed in general are more difficult to erode than sand particles, as long as the sand particles are much smaller than the thickness of the shells. The shells used in the research had a thickness varying from 1.13 to 2.69 mm. So the shells armor the bed and require a higher flow velocity than the original sand bed. Now as long as the bed thickness is not increasing, there is no problem, but since hydraulic transport is not a simple stationary process, there will be moments where the flow may decrease and moments where the density may increase, resulting in an increase of the bed thickness. Since the shells are armoring the bed, there will not be a decrease of the bed thickness at moments where the flow is higher or the density is lower, which would be the case if the bed consists of just sand particles. So there is a danger of a bed thickness increasing all the time and finally plugging the pipeline. The question arises, how much we have to increase the flow or flow velocity in order to erode the top layer of the bed where the shells are armoring the bed.

From the research of Dey (2003) it appears that the bottom shear stress to erode the shells varies from 0.56-0.72 Pa for a bed with 0.8 mm sand and from 0.37-0.61 Pa for a bed with 0.3 mm sand. It should be noted that these are shear stresses averaged over a large number of observations and that individual experiments have led to smaller and bigger shear stresses. So the average shear stresses decrease slightly with a decreasing sand particle size due to the change in velocity distribution. These shear stresses require average flow velocities that are 11%-26% higher than the flow velocities required to erode the 0.8 mm sand bed and 48%-89% higher to erode the 0.3 mm sand bed.

From these numbers it can be expected that the shear stresses required to erode the shells, match the shear stresses required to erode a bed with sand grains of 1-1.5 mm and it is thus advised to apply the LDV of 1-1.5 mm sand grains in the case of dredging a sand containing a high percentage of shells, in the case the shells are not too much fragmented.

6.12. Nomenclature.

c_0	Pivot angle at $d^+=1$	°
C_D	Drag coefficient	-
d	Diameter of particle or sphere	**m**
d^+	Dimensionless particle diameter	-
E	Exposure level	-
k_s	Bed roughness	**m**
k_s^+	Dimensionless bed roughness	**m**
LDV	Limit Deposit Velocity	**m/s**
P	Probability related to transition smooth/rough	-
Re_p	Particle Reynolds number	-
Re_*	Boundary Reynolds number	-
T	Temperature	**K**
u_*	Friction velocity	**m/s**
u	Velocity	**m/s**
u_{top}^+	Dimensionless velocity at top of particle	-
u_{eff}^+	Dimensionless effective turbulent added velocity	-
U	Average velocity above the bed.	**m/s**
V_{imin}	Minimum friction velocity	**m/s**
y_{top}	Height of particle	**m**
y_{top}^+	Dimensionless height of particle	-
z_*	Coefficient	-
α	Shell shape factor	-
α_{Lam}	Laminar velocity function	-
α_{Turb}	Turbulent velocity function	-
δ_v	Thickness of the viscous sub-layer	**m**
δ_v^+	Dimensionless thickness of the viscous sub-layer	-
κ	Von Karman constant	**0.412**
λ_l	Friction coefficient (see Moody diagram)	-
ρ_l	Liquid density	**ton/m^3**
ψ	Shape factor particle	-
ψ	Pivot angle	°
θ	Shields parameter	-
θ_{cr}	Critical Shield parameter, initiation of motion	-
μ_{sf}	Sliding friction coefficient	-

Chapter 7: Cutter Head Spillage

7.1. Introduction.

In dredging soils is excavated with dredging equipment. One of the main types of equipment is the cutter suction dredge (CSD). Figure 7-1 shows a large CSD, the Mashour, build in the 90's for the Suez Canal Port Authorities for maintenance of the Suez Canal. The CSD consists of a floating pontoon, with in the back a spud pole penetrating the soil. In the front there is a ladder, which can rotate around a horizontal bearing. By means of this rotation the cutter head (see Figure 7-2 for rock cutter heads), mounted at the end of the ladder, can be positioned in the soil (the bank). Also, at the end of the ladder two swing wires are connected (port and starboard wires) enabling the CSD to rotate around the spud pole and thus letting the cutter head make a circular movement through the bank. During this rotation, with a circumferential swing velocity $\mathbf{v_s}$ at the center of the cutter head, the cutter head (also rotating around its axis with a certain rpm) is excavating (cutting) the soil. The theoretical soil production $\mathbf{Q_c}$ equals the cross section of the cutter head in the bank cutting, perpendicular to the swing velocity $\mathbf{v_s}$ times the swing velocity $\mathbf{v_s}$. The cutter head consists of the cutter axis connected to the hub (top of the cutter head), 5 or 6 arms on one side connected to the hub and on the other side connected to the ring and a suction pipe to catch the soil cut and transport the soil to its destination. This is shown in Figure 7-3. If the theoretical soil production is 100%, usually less than 100% will enter the suction pipe. The real production. The difference between the theoretical production and the real production is the spillage. So, this is the percentage of the theoretical production not entering the suction pipe.

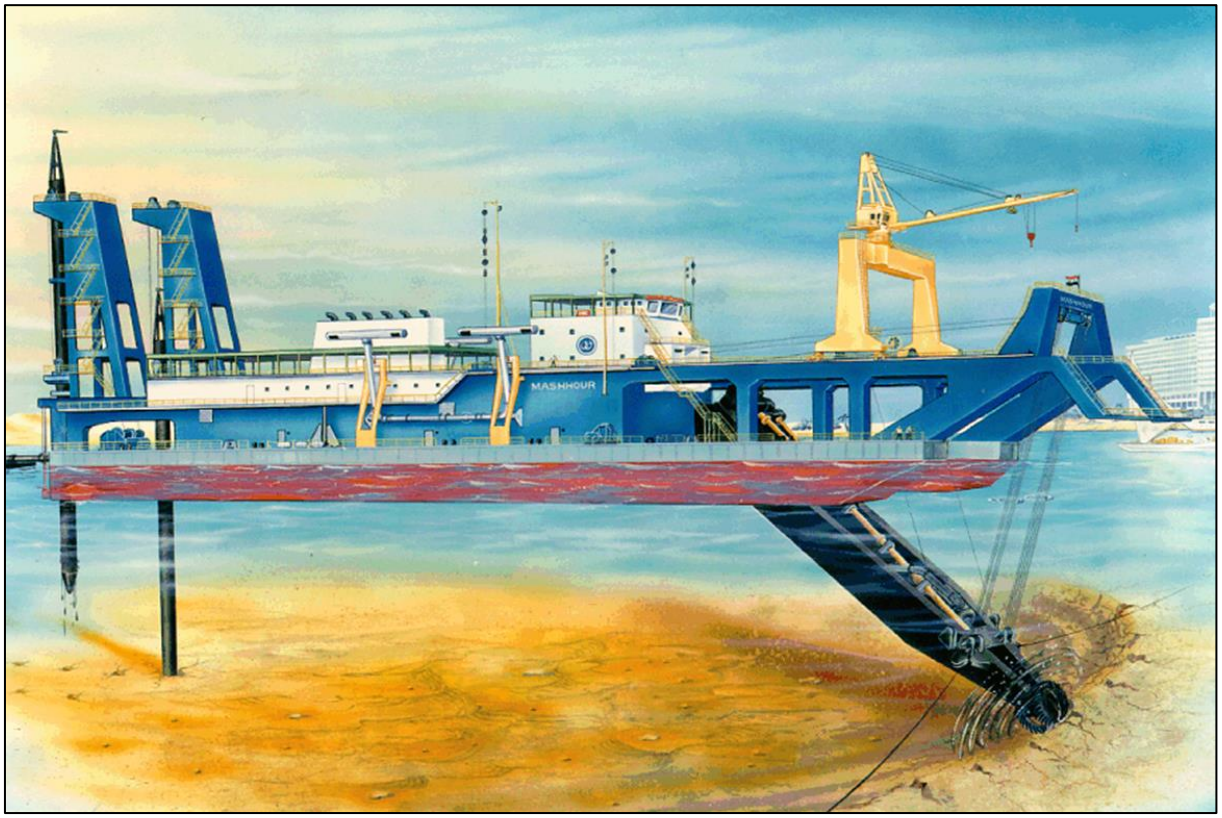

Figure 7-1: The Mashour (Suez Canal Port Authorities).

Now in practice it is more difficult to define the spillage, because often a number of swings at different levels is necessary to excavate a bank. The spillage of a previous swing may be cut a second time during the current swing and thus enter the suction pipe in the current swing. So, the spillage of one swing does not have to be spillage overall. In this report however just one swing is considered, assuming a fresh bank, where all the soil that does not enter the suction pipe is considered spillage.

The modelling consists of two phases. In the first phase a model is derived based on the affinity laws for centrifugal pumps. This model only uses the outside radii of the cutter head, the revolutions of the cutter head and the suction velocity. In the second phase a model is derived based on the Euler equation for centrifugal pumps, including inner and outer radii and blade angles. Both models are calibrated on the experimental data mentioned in den Burger

(2003). Because of this both models give almost exactly the same production/spillage curves. Using different radii and blade angles will give a slightly different production curve.

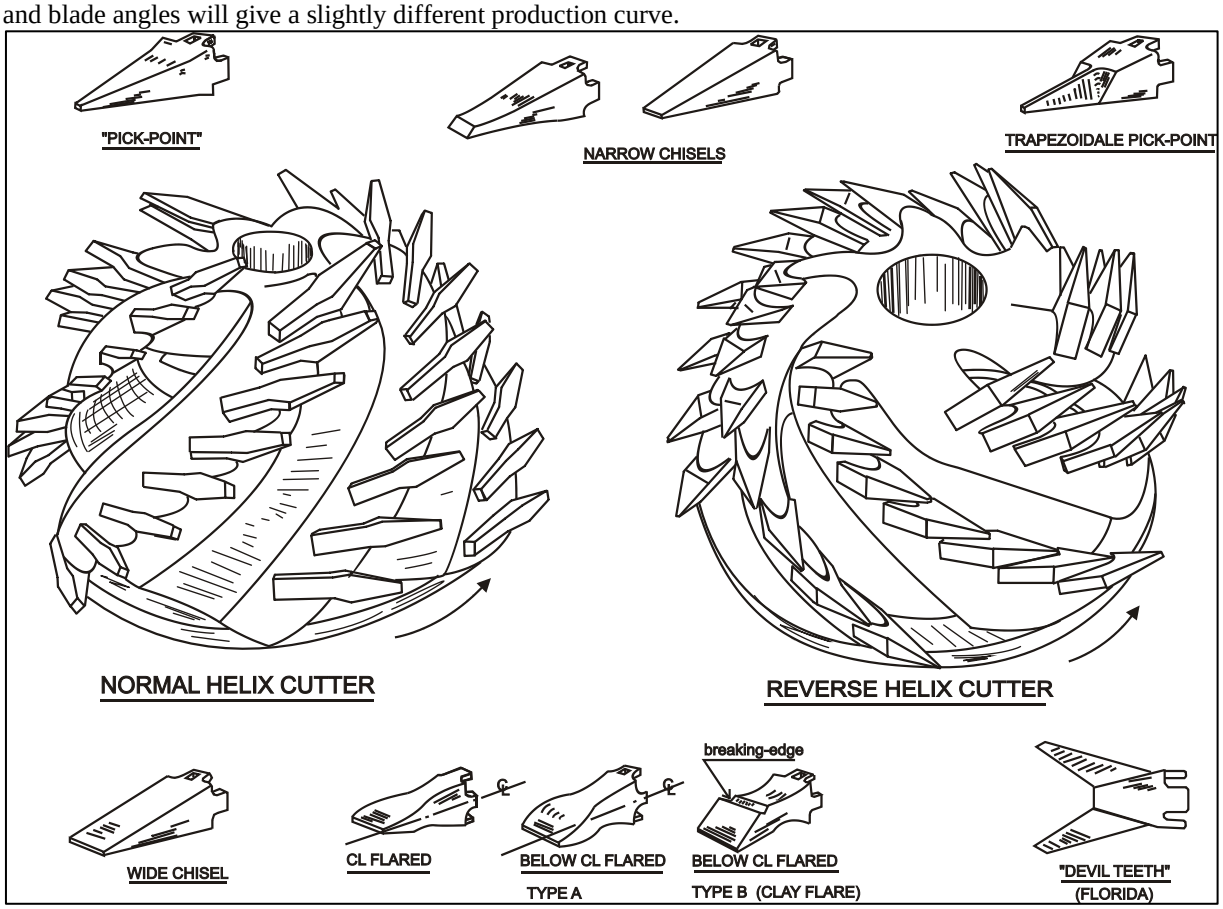

Figure 7-2: Cutter heads and pick points.

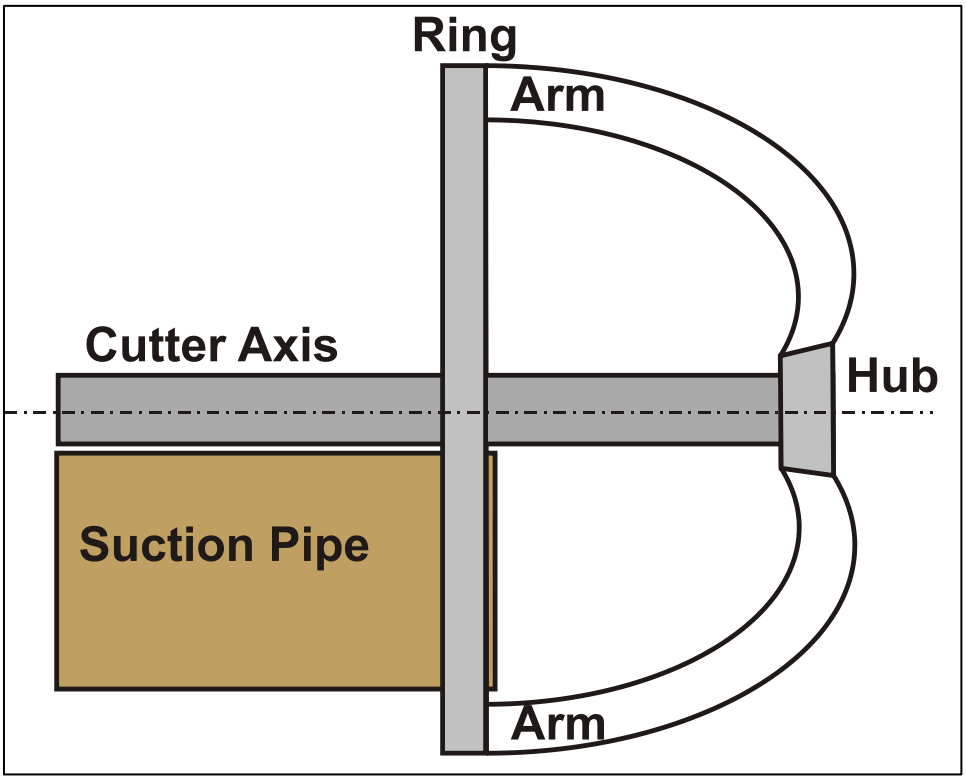

Figure 7-3: The simplified cutter head.

7.2. Scale Laws.

1. The ladder angle must be the same in prototype and model.

$$\theta_p = \theta_m \tag{7-1}$$

2. The part of the cross section of the cutter head cutting must have the same shape in prototype and model.

3. The volumetric concentration in cutter head and suction mouth must be the same in prototype and model. This relates the swing velocity times the cross section cutting (the cut production) to the mixture flow through the suction mouth.

$$\frac{Q_c \cdot (1-n)}{Q_m} = constant \tag{7-2}$$

4. The ratio of the rotating mixture flow to the mixture flow through the suction mouth must be constant.

$$Bu = \frac{\omega \cdot r_r^3}{Q_m} = constant \tag{7-3}$$

5. The ratio of the settling flux through a cutter head cross section to the mixture flow through the suction mouth must be constant.

$$\frac{v_t \cdot r_r^2}{Q_m} = constant \tag{7-4}$$

The dimensionless number based on the filling degree must be constant:

$$\frac{\omega \cdot r_r}{v_t} = constant \tag{7-5}$$

If the conditions of equations **(7-3)** and **(7-4)** are met, automatically equation **(7-5)** is valid. So, basically there are 5 independent scaling rules that have to be met.

Table 6.1: Properties on prototype and model scale

	prototype scale	model scale
Diameter suction pipe: D_{sp}	0.95 [m]	0.1 [m]
Diameter ring cutter head: D_c	3.12 [m]	0.4 [m]
Density rock: ρ_r	2200 [kg/m^3]	
Density gravel bank: ρ_b		1700 [kg/m^3]
Density gravel grain: ρ_g		2650 [kg/m^3]
Suction flow: Q_s	3.0 [m^3/s]	0.021 [m^3/s]
(mixture velocity: v_m)	(4.2 m/s)	(2.6 m/s)
Rotational velocity: n_c	30 [RPM]	90 [RPM]
Haul velocity: v_h	0.2 [m/s]	0.1 [m/s]
Cut off area: A_{cut}	1.4 [m^2]	0.023 [m^2]
Cutter inclination angle: λ	45 [°]	45 [°]

Figure 7-4: The prototype cutter head data, source den Burger (2003).

Now how to use the scale laws? Where to start? Let's assume the model cutter head has exactly the same shape as the prototype cutter head and there is a length scale λ_l. The same shape also means that the cross section of the suction mouth scales with the length scale squared. The mixture velocity scales roughly with the length scale to the power 0.4 (see Miedema (June 2016) the Limit Deposit Velocity). So, the mixture flow scales according to:

$$\frac{Q_{m,p}}{Q_{m,m}} = \frac{A_{p,p}}{A_{p,m}} \cdot \frac{v_{m,p}}{v_{m,m}} = \lambda_l^2 \cdot \lambda_l^{0.4} = \lambda_l^{2.4} \tag{7-6}$$

This means, with equation **(7-2)** that the cut production has to scale in the same way, so:

$$\frac{Q_{c,p}}{Q_{c,m}} = \frac{A_{c,p} \cdot v_{s,p}}{A_{c,m} \cdot v_{s,m}} = \lambda_l^2 \cdot \lambda_l^{0.4} = \lambda_l^{2.4} \quad \Rightarrow \quad \frac{v_{s,p}}{v_{s,m}} = \lambda_l^{0.4} \tag{7-7}$$

This results in a swing speed that scales in the same manner as the mixture velocity, because the mixture flow scales the same way as the cut production, assuming the porosity of the sand or gravel is constant. For the dimensionless den Burger number this gives:

$$\frac{Bu_p}{Bu_m} = \frac{\dfrac{\omega_p \cdot r_{r,p}^3}{Q_{m,p}}}{\dfrac{\omega_m \cdot r_{r,m}^3}{Q_{m,m}}} = \frac{\omega_p}{\omega_m} \cdot \frac{r_{r,p}^3}{r_{r,m}^3} \cdot \frac{Q_{m,m}}{Q_{m,p}} = \frac{\omega_p}{\omega_m} \cdot \lambda_l^3 \cdot \lambda_l^{-2.4} = 1 \quad \Rightarrow \quad \frac{\omega_p}{\omega_m} = \lambda_l^{-0.6} \tag{7-8}$$

Using the settling flux to mixture flow ratio the following is found:

$$\frac{\dfrac{v_{t,p} \cdot r_{r,p}^2}{Q_{m,p}}}{\dfrac{v_{t,m} \cdot r_{r,m}^2}{Q_{m,m}}} = \frac{v_{t,p}}{v_{t,m}} \cdot \frac{r_{r,p}^2}{r_{r,m}^2} \cdot \frac{Q_{m,m}}{Q_{m,p}} = \frac{v_{t,p}}{v_{t,m}} \cdot \lambda_l^2 \cdot \lambda_l^{-2.4} = 1 \quad \Rightarrow \quad \frac{v_{t,p}}{v_{t,m}} = \lambda_l^{0.4} \tag{7-9}$$

Checking the latter with the filling degree parameter gives:

$$\frac{\dfrac{\omega_p \cdot r_{r,p}}{v_{t,p}}}{\dfrac{\omega_m \cdot r_{r,m}}{v_{t,m}}} = \frac{\omega_p}{\omega_m} \cdot \frac{r_{r,p}}{r_{r,m}} \cdot \frac{v_{t,m}}{v_{t,p}} = \lambda_l^{-0.6} \cdot \lambda_l^1 \cdot \lambda_l^{-0.4} = 1 \tag{7-10}$$

The latter shows that the scale laws are consistent. All 3 velocities, the mixture velocity, the swing velocity and the terminal settling velocity, scale with the length scale to a power of 0.4. This also implies that in prototype larger particles are required than in model. The cutter head revolutions scale with the length scale to a power of minus 0.6, meaning the revolutions of the model are higher than the revolutions of the prototype.

Comparing this with Figure 7-4, the model rules as applied by den Burger (2003), a length scale of about 7.8 was used. This should result in a mixture flow ratio of 138.4, while 143 was used. So almost the same. The revolutions of the model should be 3.43 times the revolutions of the prototype, this was a factor 3, so also close. The swing velocity in prototype should be 2.27 times the swing velocity in the model, which was a factor 2, so again close. For the terminal settling velocity no scaling was reported. However, according to the above this should be a factor 2.27, similar to the swing speed ratio.

So, the conclusion is that the den Burger (2003) scale laws were close to the scale laws derived here, with the exception for the scale law for the terminal settling velocity, which was not present in den Burger (2003).

7.3. Preliminary Spillage Model based on Affinity Laws.

7.3.1. The Affinity Laws.

The affinity law for pressure of a centrifugal pump yields:

$$\Delta p = \varepsilon \cdot \rho_m \cdot \omega^2 \cdot r_o^2 = \varepsilon \cdot \rho_m \cdot u_o^2 \qquad \textbf{(7-11)}$$

The flow through the impeller blades can be considered to be, based on the affinity laws:

$$Q = \alpha \cdot (2 \cdot \pi \cdot r_o) \cdot u_o \cdot w = \alpha \cdot (2 \cdot \pi \cdot r_o) \cdot (\omega \cdot r_o) \cdot w = \alpha \cdot 2 \cdot \pi \cdot r_o^2 \cdot \omega \cdot w \qquad \textbf{(7-12)}$$

The specific flow, flow per unit of width is now:

$$q = \frac{Q}{w} = \alpha \cdot 2 \cdot \pi \cdot \omega \cdot r_o^2 = \frac{2 \cdot \pi \cdot \alpha}{\varepsilon \cdot \rho_m \cdot \omega} \cdot \Delta p \qquad \textbf{(7-13)}$$

Figure 7-5 shows a cross section of a cutter head with main dimensions and velocities.

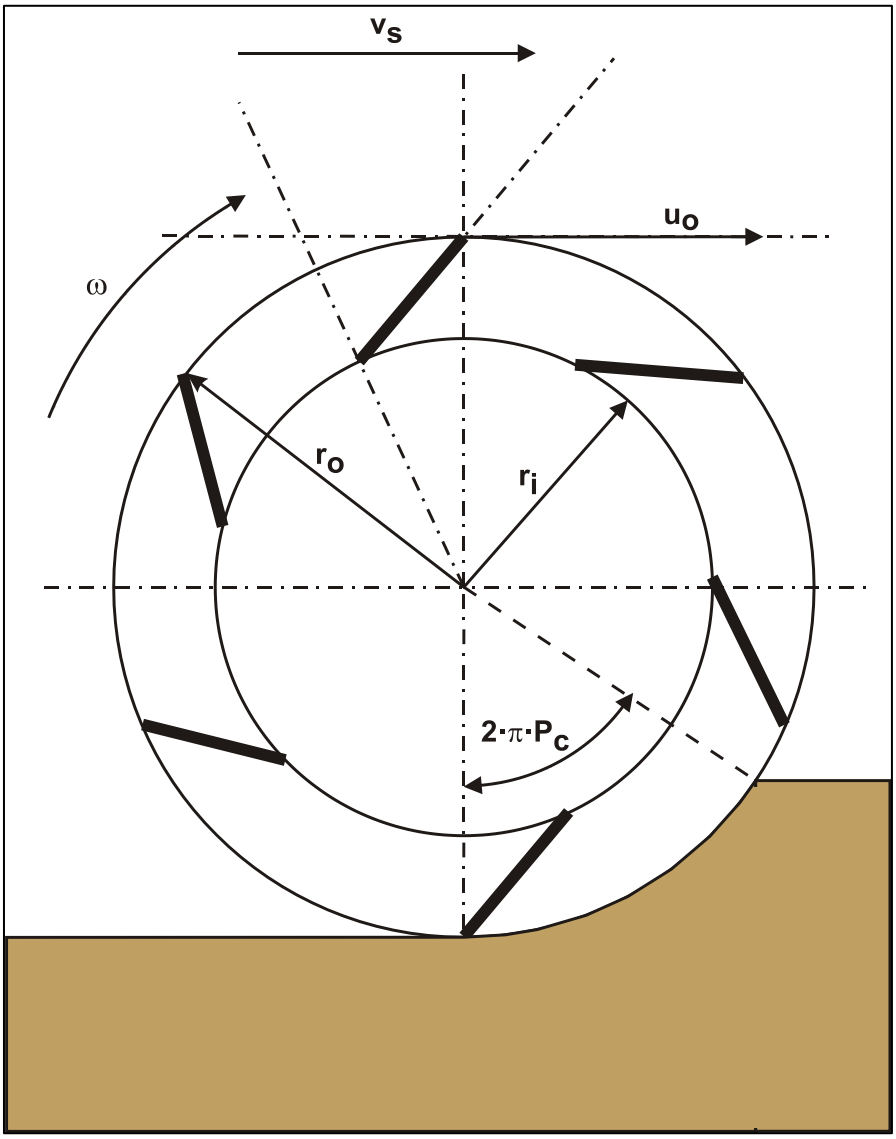

Figure 7-5: The cutter head and the bank.

7.3.2. The Cutter Head.

The cutter head is considered to behave as a centrifugal pump, so it is assumed that the affinity laws also apply on a cutter head. Now suppose the cutter head can be divided into two segments. Segment 1 near the ring of the cutter head, where there is outflow of mixture, because of the centrifugal pump behavior of the cutter head (see Figure 7-6). Segment 2 near the top of the cutter head, where there is inflow of water, because the outside pressure (the pressure generated in segment 1) is higher than the pressure generated in segment 2. There are three other flows, the mixture flow $\mathbf{Q_m}$ in the suction mouth, the axial flow $\mathbf{Q_a}$ and the cut production $\mathbf{Q_c}$ as a result of the cutting process in the bank, see Figure 7-7.

The mixture flow is the suction pipe cross section times the mixture velocity (line speed):

$$\mathbf{Q_m = \frac{\pi}{4} \cdot D_{p,s}^2 \cdot v_m} \tag{7-14}$$

The cut production is, based on a fraction $\mathbf{P_c}$ of the circumference cutting, an average cutter radius $\mathbf{r_{c,a}}$ and a swing velocity $\mathbf{v_s}$, given a certain total width $\mathbf{w}$:

$$\mathbf{Q_c = r_{c,a} \cdot \left(1 - \cos\left(2 \cdot \pi \cdot P_c\right)\right) \cdot w \cdot v_s} \tag{7-15}$$

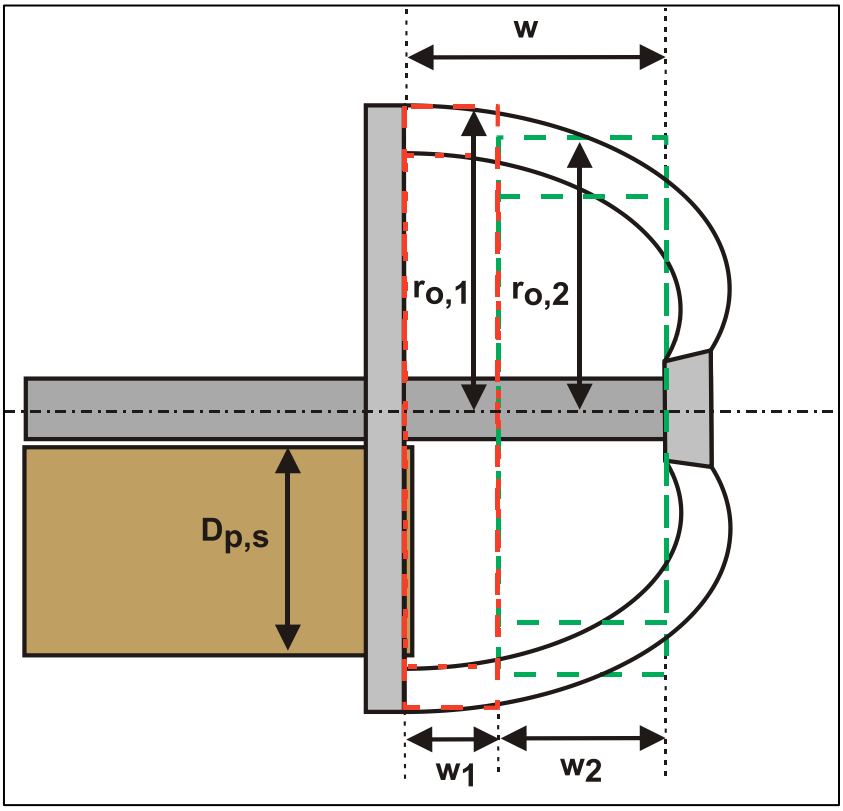

Figure 7-6: Cutter head geometry & segments.

The axial flow is added to the model as a variable, however there is not yet a model to determine this axial flow. Adding it to the model however, enables us to investigate the importance of the axial flow. So, how much does it influence the spillage.

In order to derive the model, the pressure and flow equations for the two segments are derived.

7.3.3. Segment 1.

Based on the affinity laws, for segment 1 the following equations are valid (see Figure 7-6):

$$\Delta p_1 = \varepsilon \cdot \rho_{m,1} \cdot \omega^2 \cdot r_{o,1}^2$$

$$Q_{1,out} = \alpha \cdot 2 \cdot \pi \cdot r_{o,1}^2 \cdot \omega \cdot w_1$$

$$Q_{1,out} = \frac{2 \cdot \pi \cdot \alpha}{\varepsilon \cdot \rho_{m,1} \cdot \omega} \cdot \Delta p_1 \cdot w_1 \qquad (7\text{-}16)$$

$$q_{1,out} = \frac{2 \cdot \pi \cdot \alpha}{\varepsilon \cdot \rho_{m,1} \cdot \omega} \cdot \Delta p_1$$

1.1 Segment 2.

Based on the affinity laws, for segment 2 the following equations are valid (see Figure 7-6):

$$\Delta p_2 = \varepsilon \cdot \rho_{m,2} \cdot \omega^2 \cdot r_{o,2}^2$$

$$Q_{2,out} = \alpha \cdot 2 \cdot \pi \cdot r_{o,2}^2 \cdot \omega \cdot w_2$$

$$Q_{2,out} = \frac{2 \cdot \pi \cdot \alpha}{\varepsilon \cdot \rho_{m,2} \cdot \omega} \cdot \Delta p_2 \cdot w_2 \qquad (7\text{-}17)$$

$$q_{2,out} = \frac{2 \cdot \pi \cdot \alpha}{\varepsilon \cdot \rho_{m,2} \cdot \omega} \cdot \Delta p_2$$

Now suppose the pressure difference on segment 2 equals:

$$\Delta p_1 - \Delta p_2 = \left(q_{1,out} \cdot \frac{\varepsilon \cdot \rho_{m,1} \cdot \omega}{2 \cdot \pi \cdot \alpha} - q_{2,out} \cdot \frac{\varepsilon \cdot \rho_{m,2} \cdot \omega}{2 \cdot \pi \cdot \alpha} \right) = \left(q_{1,out} \cdot \rho_{m,1} - q_{2,out} \cdot \rho_{m,2} \right) \cdot \frac{\varepsilon \cdot \omega}{2 \cdot \pi \cdot \alpha} \qquad (7\text{-}18)$$

The inflow in segment 2 is the difference of the specific outflow of segment 1 and the specific outflow of segment 2 multiplied with the width of segment 2, assuming the mixture densities are equal to the water density:

$$Q_{2,in} = \left(q_{1,out} - q_{2,out} \right) \cdot w_2 = \left(\Delta p_1 - \Delta p_2 \right) \cdot \frac{2 \cdot \pi \cdot \alpha}{\varepsilon \cdot \rho_l \cdot \omega} \cdot w_2 \qquad (7\text{-}19)$$

7.3.4. Volume Flow Balance.

There are 5 main volume flows in the cutter head, see Figure 7-7. Although one can always use a different definition of the volume flows. These 5 volume flows are:

1. The mixture flow through the suction mouth, $\mathbf{Q_m}$.
2. The flow of sand, gravel or rock being cut by the cutter head, $\mathbf{Q_c}$.
3. The outflow of mixture through segment 1 due to the centrifugal pump effect of the cutter head, $\mathbf{Q_{1,out}}$.
4. The inflow of water through segment 2 due to the pressure difference as generated in segments 1 and 2, $\mathbf{Q_{2,in}}$.
5. Axial flow through the top of the cutter head, $\mathbf{Q_a}$.

Although the axial flow is not yet modelled, for completeness this flow is already added to the equations.

The volume flow balance is:

$$\mathbf{Q_{1,out} - Q_{2,in} + Q_m - Q_c - Q_a = 0} \qquad \textbf{(7-20)}$$

In this equation the outflow terms are positive (have a plus sign), while the inflow terms are negative (have a minus sign). Substituting equations **(7-16)** and **(7-17)** gives:

$$\mathbf{\frac{2\cdot\pi\cdot\alpha}{\varepsilon\cdot\rho_l\cdot\omega}\cdot\Delta p_1\cdot w_1\cdot(1-P_c)-\frac{2\cdot\pi\cdot\alpha}{\varepsilon\cdot\rho_l\cdot\omega}\cdot(\Delta p_1-\Delta p_2)\cdot w_2\cdot(1-P_c)+Q_m-Q_c-Q_a=0} \qquad \textbf{(7-21)}$$

It is assumed that $\mathbf{Q_m}$ and $\mathbf{Q_c}$ do not depend on cutter revolutions or diameter, while the axial flow $\mathbf{Q_a}$ is considered a constant here.

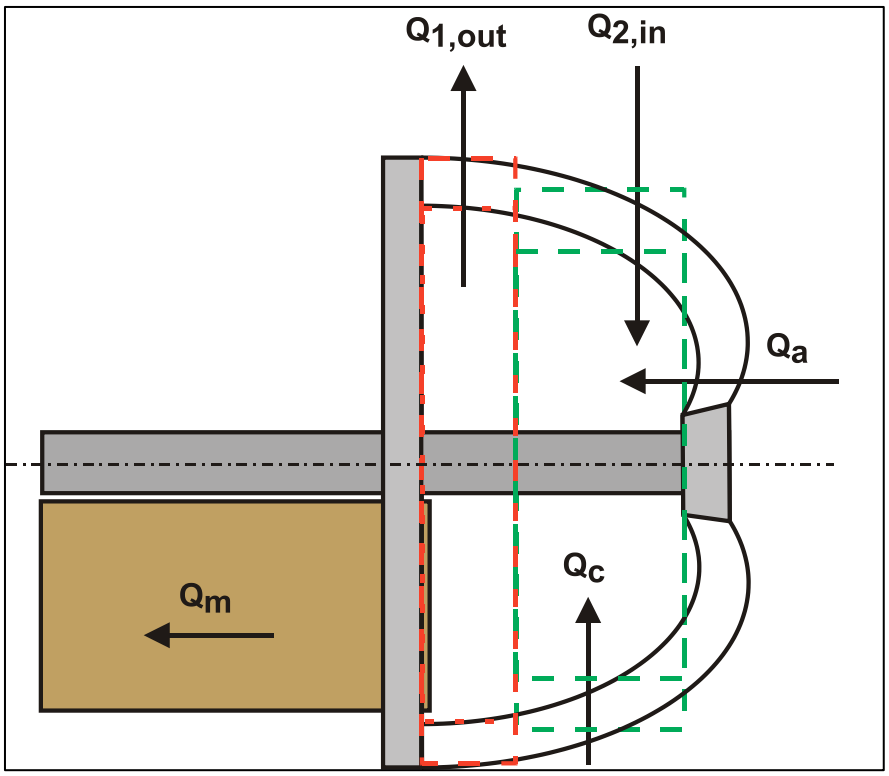

Figure 7-7: The flows in and out of the cutter head.

7.3.5. Determining w_1 and w_2.

Equation **(7-21)** can be written as:

$$\Delta p_1 \cdot w_1 - (\Delta p_1 - \Delta p_2) \cdot w_2 + \frac{\varepsilon \cdot \rho_l \cdot \omega}{2 \cdot \pi \cdot \alpha \cdot (1 - P_c)} \cdot (Q_m - Q_c - Q_a) = 0 \qquad \textbf{(7-22)}$$

So, for the width of segment 1:

$$w_1 = \left(\frac{\Delta p_1 - \Delta p_2}{\Delta p_1} \right) \cdot w_2 - \frac{\varepsilon \cdot \rho_l \cdot \omega}{2 \cdot \pi \cdot \alpha \cdot (1 - P_c)} \cdot \left(\frac{Q_m - Q_c - Q_a}{\Delta p_1} \right) \qquad \textbf{(7-23)}$$

With:

$$\Delta p_1 = \varepsilon \cdot \rho_l \cdot \omega^2 \cdot r_{o,1}^2$$

$$\Delta p_2 = \varepsilon \cdot \rho_l \cdot \omega^2 \cdot r_{o,2}^2 \qquad \textbf{(7-24)}$$

$$w = w_1 + w_2$$

This gives for the width of segment 1:

$$w_1 = \left(\frac{r_{o,1}^2 - r_{o,2}^2}{r_{o,1}^2} \right) \cdot w_2 - \frac{\varepsilon \cdot \rho_l \cdot \omega}{2 \cdot \pi \cdot \alpha \cdot (1 - P_c)} \cdot \left(\frac{Q_m - Q_c - Q_a}{\varepsilon \cdot \rho_l \cdot \omega^2 \cdot r_{o,1}^2} \right)$$

$$w_1 = \left(\frac{r_{o,1}^2 - r_{o,2}^2}{r_{o,1}^2} \right) \cdot w_2 - \frac{1}{2 \cdot \pi \cdot \alpha \cdot \omega} \cdot \left(\frac{Q_m - Q_c - Q_a}{r_{o,1}^2 \cdot (1 - P_c)} \right) \qquad \textbf{(7-25)}$$

With:

$$f = \left(\frac{r_{o,1}^2 - r_{o,2}^2}{r_{o,1}^2} \right) \quad \textbf{and} \quad 1+f = \left(\frac{2 \cdot r_{o,1}^2 - r_{o,2}^2}{r_{o,1}^2} \right) \qquad \textbf{(7-26)}$$

This can be written as:

$$w_1 = f \cdot w_2 - \frac{1}{2 \cdot \pi \cdot \alpha \cdot \omega} \cdot \left(\frac{Q_m - Q_c - Q_a}{r_{o,1}^2 \cdot (1 - P_c)} \right) \qquad \textbf{(7-27)}$$

Now the width of segment 2 equals the total width **w** minus the width of segment 1 w_1, giving:

$$w_1 = f \cdot (w - w_1) - \frac{1}{2 \cdot \pi \cdot \alpha \cdot \omega} \cdot \left(\frac{Q_m - Q_c - Q_a}{r_{o,1}^2 \cdot (1 - P_c)} \right)$$

$$w_1 \cdot (1 + f) = f \cdot w - \frac{1}{2 \cdot \pi \cdot \alpha \cdot \omega} \cdot \left(\frac{Q_m - Q_c - Q_a}{r_{o,1}^2 \cdot (1 - P_c)} \right) \qquad \textbf{(7-28)}$$

So, the width of segment 1 equals:

$$w_1 = \frac{f}{(1+f)} \cdot w - \frac{1}{(1+f)} \cdot \frac{1}{2 \cdot \pi \cdot \alpha \cdot \omega} \cdot \left(\frac{Q_m - Q_c - Q_a}{r_{o,1}^2 \cdot (1 - P_c)} \right) \tag{7-29}$$

The width of segment 2 can now be determined as (see equation **(7-27)**:

$$w_2 = \frac{1}{f} \cdot w_1 + \frac{1}{f} \cdot \frac{1}{2 \cdot \pi \cdot \alpha \cdot \omega} \cdot \left(\frac{Q_m - Q_c - Q_a}{r_{o,1}^2 \cdot (1 - P_c)} \right) \tag{7-30}$$

Substituting equation **(7-29)** gives:

$$w_2 = \frac{1}{f} \cdot \left(\frac{f}{(1+f)} \cdot w - \frac{1}{(1+f)} \cdot \frac{1}{2 \cdot \pi \cdot \alpha \cdot \omega} \cdot \left(\frac{Q_m - Q_c - Q_a}{r_{o,1}^2 \cdot (1 - P_c)} \right) \right) + \frac{1}{f} \cdot \frac{1}{2 \cdot \pi \cdot \alpha \cdot \omega} \cdot \left(\frac{Q_m - Q_c - Q_a}{r_{o,1}^2 \cdot (1 - P_c)} \right) \tag{7-31}$$

Giving:

$$w_2 = \frac{1}{(1+f)} \cdot w + \frac{1}{(1+f)} \cdot \frac{1}{2 \cdot \pi \cdot \alpha \cdot \omega} \cdot \left(\frac{Q_m - Q_c - Q_a}{r_{o,1}^2 \cdot (1 - P_c)} \right) \tag{7-32}$$

To test the correctness, the width of segment 1 w_1 plus the width of segment 2 w_2 has the be the total width w, giving:

$$w = w_1 + w_2$$

$$w = \frac{f}{(1+f)} \cdot w - \frac{1}{(1+f)} \cdot \frac{1}{2 \cdot \pi \cdot \alpha \cdot \omega} \cdot \left(\frac{Q_m - Q_c - Q_a}{r_{o,1}^2 \cdot (1 - P_c)} \right) + \frac{1}{(1+f)} \cdot w + \frac{1}{(1+f)} \cdot \frac{1}{2 \cdot \pi \cdot \alpha \cdot \omega} \cdot \left(\frac{Q_m - Q_c - Q_a}{r_{o,1}^2 \cdot (1 - P_c)} \right) \tag{7-33}$$

$$w = \frac{f}{(1+f)} \cdot w + \frac{1}{(1+f)} \cdot w = w$$

So, the equations are correct.

7.3.6. The Resulting Flows.

The two flows out of segments 1 and 2 are now:

$$Q_{1,out} = \alpha \cdot 2 \cdot \pi \cdot \omega \cdot r_{o,1}^2 \cdot \left(\frac{f}{(1+f)} \cdot w - \frac{1}{(1+f)} \cdot \frac{1}{2 \cdot \pi \cdot \alpha \cdot \omega} \cdot \left(\frac{Q_m - Q_c - Q_a}{r_{o,1}^2 \cdot (1-P_c)} \right) \right) \cdot (1-P_c) \quad \textbf{(7-34)}$$

$$Q_{2,out} = \alpha \cdot 2 \cdot \pi \cdot \omega \cdot r_{o,2}^2 \cdot \left(\frac{1}{(1+f)} \cdot w + \frac{1}{(1+f)} \cdot \frac{1}{2 \cdot \pi \cdot \alpha \cdot \omega} \cdot \left(\frac{Q_m - Q_c - Q_a}{r_{o,1}^2 \cdot (1-P_c)} \right) \right) \cdot (1-P_c)$$

The flow into segment 2 is:

$$Q_{2,in} = 2 \cdot \pi \cdot \alpha \cdot \omega \cdot \left(r_{o,1}^2 - r_{o,2}^2 \right) \cdot \left(\frac{1}{(1+f)} \cdot w + \frac{1}{(1+f)} \cdot \frac{1}{2 \cdot \pi \cdot \alpha \cdot \omega} \cdot \left(\frac{Q_m - Q_c - Q_a}{r_{o,1}^2 \cdot (1-P_c)} \right) \right) \cdot (1-P_c) \quad \textbf{(7-35)}$$

7.3.7. Concentrations and Spillage.

Now, with a porosity **n** of the soil (sand will have about 40% while for rock it depends strongly on the type of rock), the flow of solids into the cutter head Q_s is:

$$Q_s = Q_c \cdot (1-n) \quad \textbf{(7-36)}$$

The spatial concentration of solids, assuming the concentration in the suction mouth and the concentration in the outflow of segment 1 are the same, gives:

$$C_{vs} = \frac{Q_s}{Q_m + Q_{1,out}} \quad \textbf{(7-37)}$$

The density of the outflow in segment 1 is:

$$\rho_m = C_{vs} \cdot \rho_q + (1-C_{vs}) \cdot \rho_l \quad \textbf{(7-38)}$$

The spillage is now the outflow in segment 1 divided by the total outflow, giving:

$$\textbf{Spillage} = \frac{Q_{1,out}}{Q_m + Q_{1,out}} = \frac{Q_{1,out} \cdot C_{vs}}{Q_s} \quad \textbf{(7-39)}$$

The spillage is also the solids outflow in segment 1 divided by the total inflow of solids.

7.3.8. Validation, Conclusions and Discussion CHSDSG 1 Model.

The preliminary model is based on the affinity laws of centrifugal pumps and does not yet incorporate mixture densities. The purpose of this preliminary model is to see if spillage can be determined using some operational parameters. The result is a model that actually calculates spillage with swing speed, cutter revolutions and cutter geometry as parameters. This model is developed by Miedema in March/April 2017 and used by Louis (2017). The model is further published by Werkhoven et al. (2018).

Den Burger (2003) defined a dimensionless number based on the ratio of the cutter volume times the revolutions to the mixture flow, giving (with $\mathbf{r_r}$ the cutter head radius near the ring):

$$\mathbf{Bu} = \frac{\omega \cdot r_r^3}{Q_m} \tag{7-40}$$

So, basically this is a measure for ratio of the rotating volumetric flow to the mixture flow. It is interesting that den Burger (2003) also mentioned another ratio, the ratio of the circumferential velocity near the ring of the cutter head to the mixture velocity (see Mol (1977A)and (1977B), Moret (1977A) (1977B)):

$$\mathbf{Bu} \cdot \frac{\frac{\pi}{4} \cdot D_{p,s}^2}{r_r^2} = \frac{\omega \cdot r_r}{v_m} = 0.42 - 0.6 \tag{7-41}$$

For every mixture velocity there appeared to be a transition value for the rotational velocity of the cutter head. Below this transition value there is an inward flow along the entire contour of the cutter head. Above this transition value an outward flow is present near the cutter ring. This outward flow increases with increasing rotational velocity or decreasing mixture velocity. The transition ratio was found to be fairly constant at 0.42 for a cutter head with a diameter of 0.6 m. When a swing velocity was present, the transition value increased to 0.5 for under cutting and 0.6 for over cutting. In both cases the cutter was freely rotating (not cutting). Now assuming that the diameter of the suction pipe is about 45%-55% of the radius of the cutter ring, we find:

$$\mathbf{Bu} = \frac{\omega \cdot r_r}{v_m} \cdot \frac{r_r^2}{\frac{\pi}{4} \cdot D_{p,s}^2} = 0.42/0.6 \cdot \frac{r_r^2}{\frac{\pi}{4} \cdot D_{p,s}^2} = 0.42/0.6 \cdot \frac{r_r^2}{\frac{\pi}{4} \cdot 0.55^2 \cdot r_r^2} = \frac{4}{0.55^2 \cdot \pi} \cdot 0.42/0.6 \tag{7-42}$$

$$= 1.76 \text{ to } 2.53 \ (55\%) \quad \text{or} \quad 2.71\text{-}3.86 \ (45\%)$$

The values found in Figure 7-9 and Figure 7-10, for sand cutting with an 0.6 m cutter head, match this very well. The values found in Figure 7-11 and Figure 7-12 of about 2 for the **Bu** number are a bit low, but this can be explained by the suction pipe diameter to cutter ring radius ratio, which was slightly larger than 50% and the fact that the cutter head was not freely rotating but cutting.

Based on equation **(7-29)** this ratio can also be determined analytically, starting with:

$$w_1 \cdot (1+f) = f \cdot w - \frac{1}{2 \cdot \pi \cdot \alpha \cdot \omega} \cdot \left(\frac{Q_m - Q_c - Q_a}{r_{o,1}^2 \cdot (1 - P_c)} \right) \tag{7-43}$$

Now for a freely rotating cutter head, the cut production is zero. It is also assumed that there is no axial flow. This gives for the transition:

$$f \cdot w - \frac{1}{2 \cdot \pi \cdot \alpha \cdot \omega} \cdot \left(\frac{Q_m}{r_r^2} \right) = 0 \tag{7-44}$$

This can be written as:

$$\mathbf{Bu = \frac{\omega \cdot r_r^2}{Q_m} \cdot r_r = \frac{r_r}{2 \cdot \pi \cdot \alpha \cdot f \cdot w}} \qquad \textbf{(7-45)}$$

For sand cutting this way a number of 2.42 is found, while rock cutting gives a number of 1.66. The latter is a bit lower than the 1.76 in equation **(7-42)**, but still acceptable given a slightly different suction pipe diameter. Applying some axial flow will also change these numbers. To match the experiments of den Burger, the factor **α** is about 0.157 for sand and 0.205 for rock. This can be described by:

$$\mathbf{\alpha = 0.155 + \left(0.205 - 0.155\right) \cdot \frac{v_t}{0.45} \cdot \lambda^{-0.4}} \qquad \textbf{(7-46)}$$

The main conclusion here is that the transition Bu number can be determined theoretically with a set of reasonable inputs. So, it seems the model describes the physics occurring, both qualitatively and quantitatively.

The model is based on a 100% mixing in the cutter head where the particles follow the flow, so the concentration and mixture density are the same everywhere. Particles following $\mathbf{Q_m}$ result in production, while particles following $\mathbf{Q_{1,out}}$ result in spillage. For fine particles this 100% mixing is always assumed, resulting in a homogeneous mixture as mentioned. For coarser particles however, the mixture may not be homogeneous. For very large particles there may also be additional spillage due to gravity. The maximum spillage is 100%, so the maximum concentration of the spillage is:

$$\mathbf{Spillage = \frac{Q_{1,out} \cdot C_{vs}}{Q_s} \quad \Rightarrow \quad Spillage=1 \quad \Rightarrow \quad C_{vs,max} = \frac{Q_s}{Q_{1,out}}} \qquad \textbf{(7-47)}$$

Where the maximum concentration should be limited to a value near 50%, otherwise there are solids leaving segment 1, which is not physically possible. This 100% spillage can be achieved with the following equation:

$$\mathbf{Spillage = \frac{Q_{1,out} \cdot \left(C_{vs} + \left(C_{vs,max} - C_{vs}\right) \cdot Factor\right)}{Q_s}} \qquad \textbf{(7-48)}$$

$$\mathbf{With: \quad C_{vs,max} = \frac{Q_s}{Q_{1,out}} \quad and \quad C_{vs,max} < 0.5}$$

To incorporate the gravity and the mixing effects, the following equation is found for the preliminary model and will also be used in the advanced model:

$$\mathbf{Factor = 0.1 \cdot \left(\frac{v_t \cdot \sin(\theta) \cdot \pi \cdot r_r^2}{Q_m} \right)^2 + \left(\frac{Bu}{10.8} \right)^3} \qquad \textbf{(7-49)}$$

$$\mathbf{Factor \le 1}$$

This factor of course is limited to 1. If the terminal settling velocity $\mathbf{v_t}$ is very small compared to the mixture velocity $\mathbf{v_m}$, the gravity effect can be ignored, however for rock (large particles) it plays an important role. Substituting this factor in the spillage equation gives:

$$\mathbf{Spillage = \frac{Q_{1,out} \cdot \left(C_{vs} + \left(C_{vs,max} - C_{vs}\right) \cdot \left(0.1 \cdot \left(\frac{v_t \cdot \sin(\theta) \cdot \pi \cdot r_r^2}{Q_m} \right)^2 + \left(\frac{Bu}{10.8} \right)^3 \right) \right)}{Q_s}} \qquad \textbf{(7-50)}$$

The equations **(7-46)** and **(7-49)** are calibrated on the den Burger (2003) experiments and should most probably be more advanced if more experiments are available.

Figure 7-4 shows the data of the prototype and model cutter head as used by den Burger (2003). Figure 7-9 and Figure 7-11 show production data for sands/plastic and gravels/rock both experimental from den Burger (2003) and according to the preliminary model as described here, where coefficients are calibrated based on the experimental data. Figure 7-10 and Figure 7-12 show the production data for sands and gravels/rock both for the prototype cutter head. For sands the graphs of the model cutter head and the prototype cutter head do not differ too much, but for gravels the graphs differ significantly. The reason is the gravity effect based on the terminal settling velocity, which is scale dependent. The mixing effect is implemented depending on the Bu number. Because of this scaling does not have influence on this effect.

In general, the preliminary model matches well with the experimental data for the model cutter heads in sand and rock.

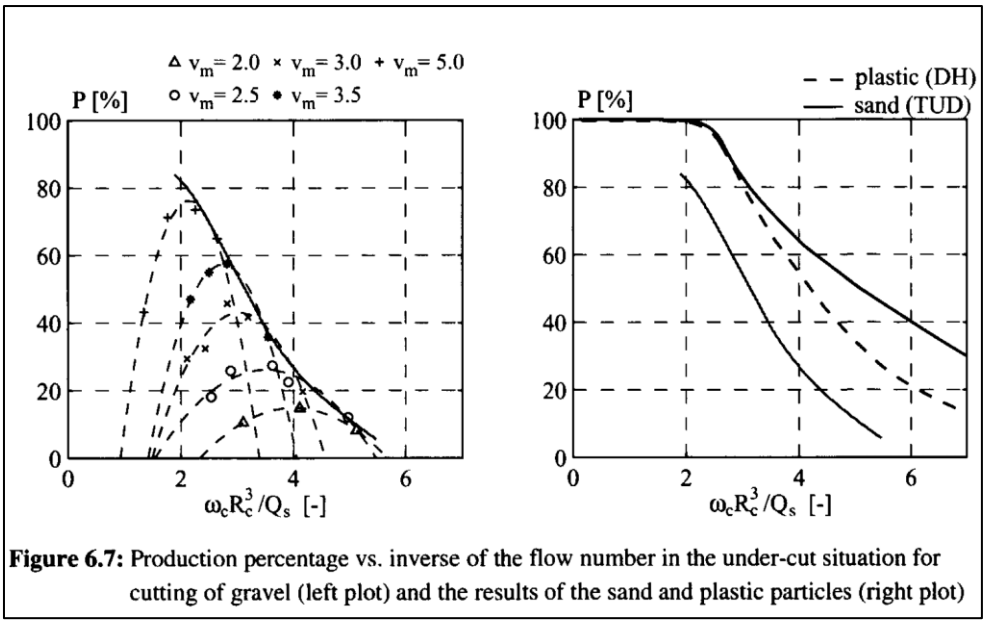

Figure 6.7: Production percentage vs. inverse of the flow number in the under-cut situation for cutting of gravel (left plot) and the results of the sand and plastic particles (right plot)

Figure 7-8: Production curves as a function of revolutions and mixture velocity, source den Burger (2003).

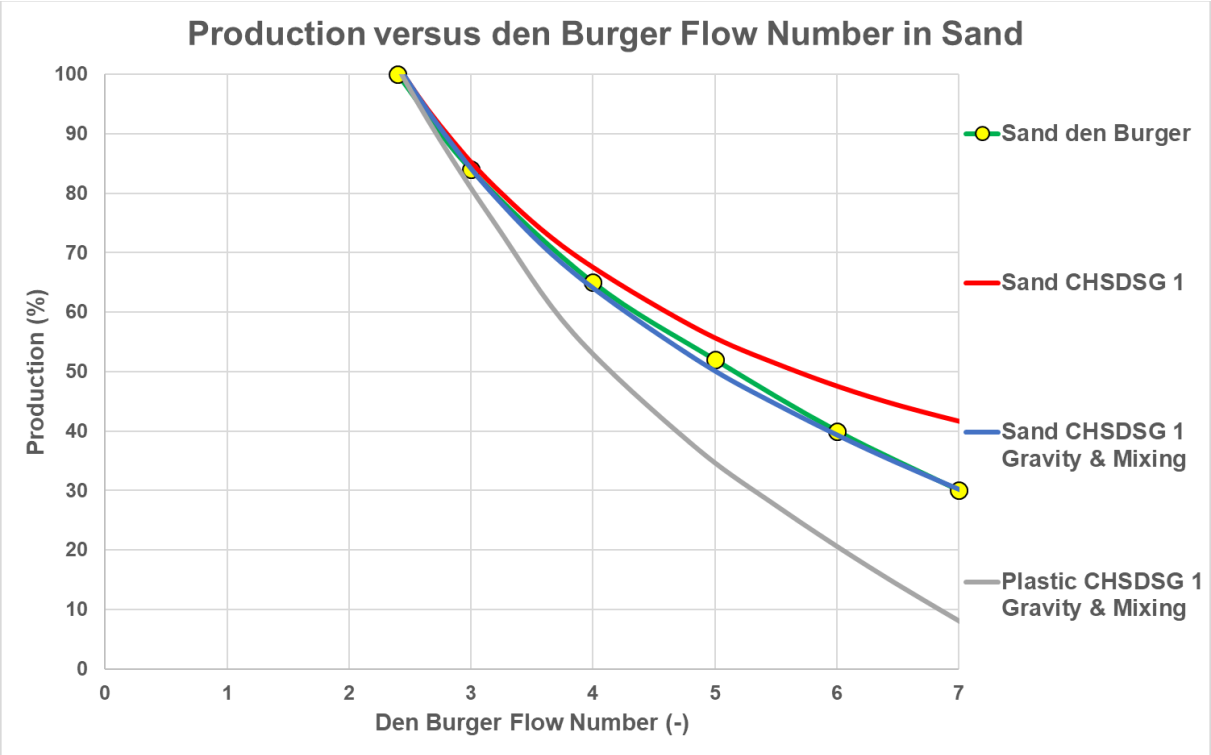

Figure 7-9: Production in sand, the preliminary model, model cutter head.

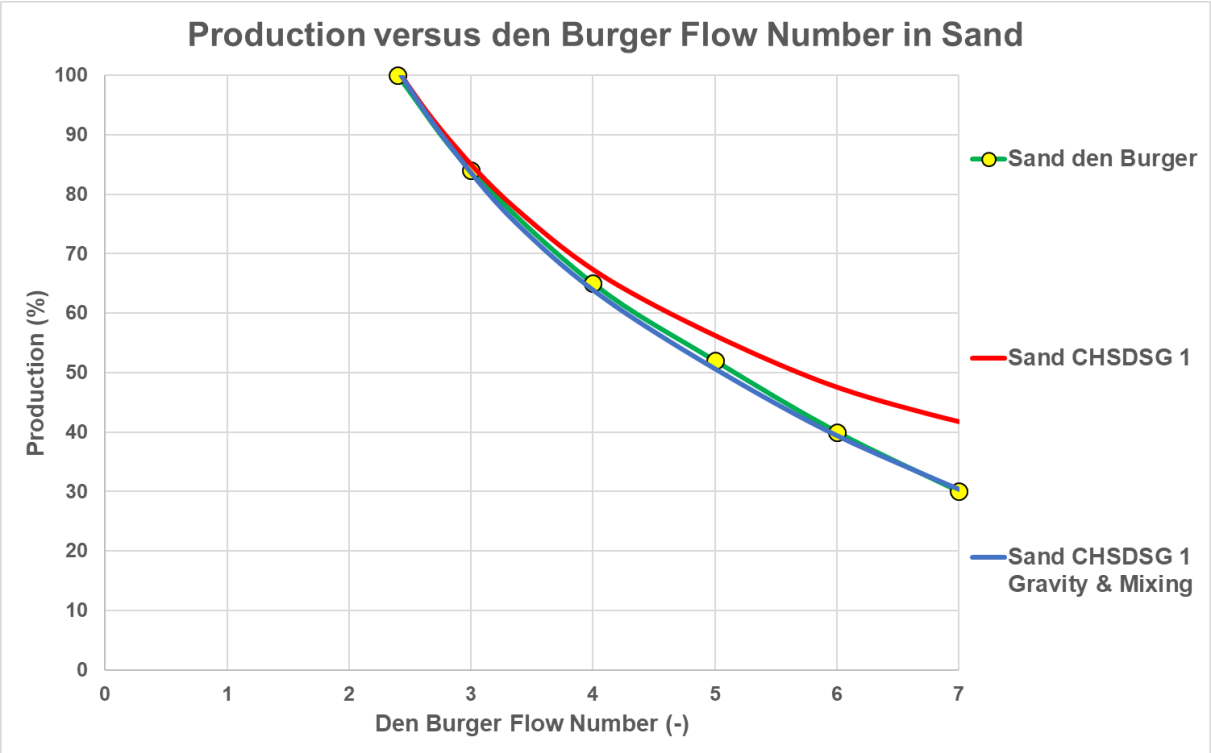

Figure 7-10: Production in sand, the preliminary model, prototype cutter head.

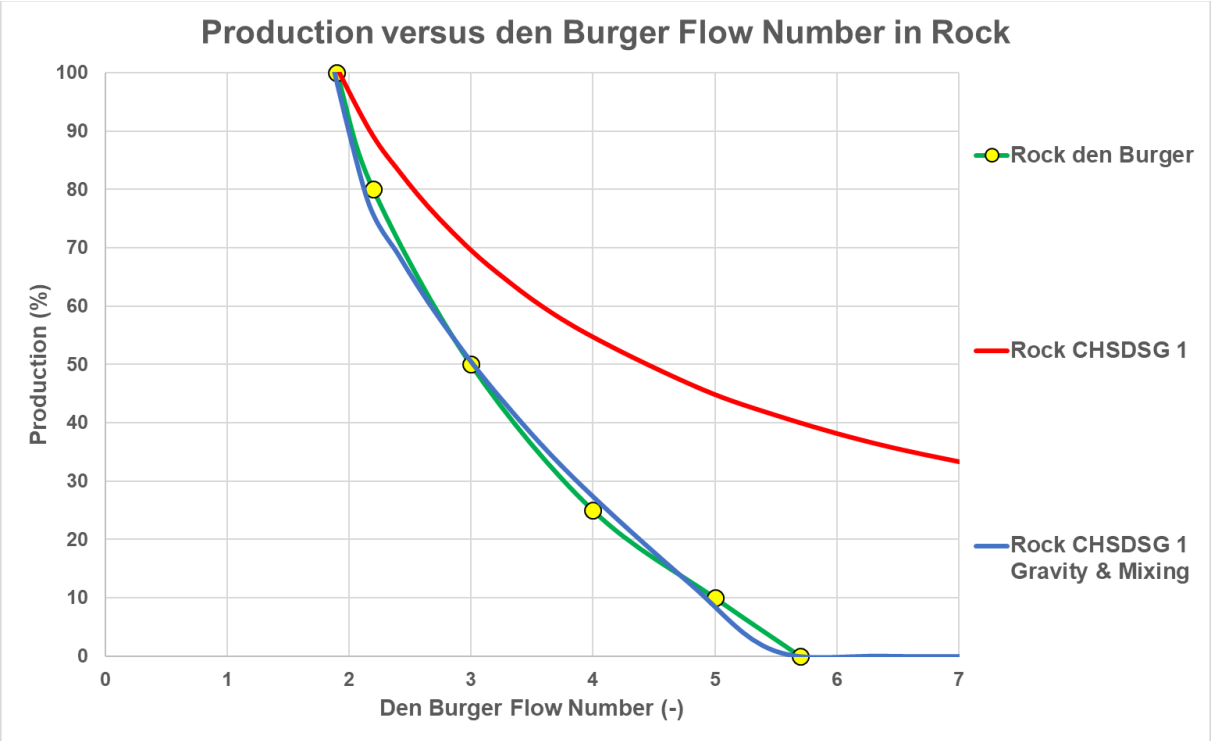

Figure 7-11: Production in rock, the preliminary model, model cutter head.

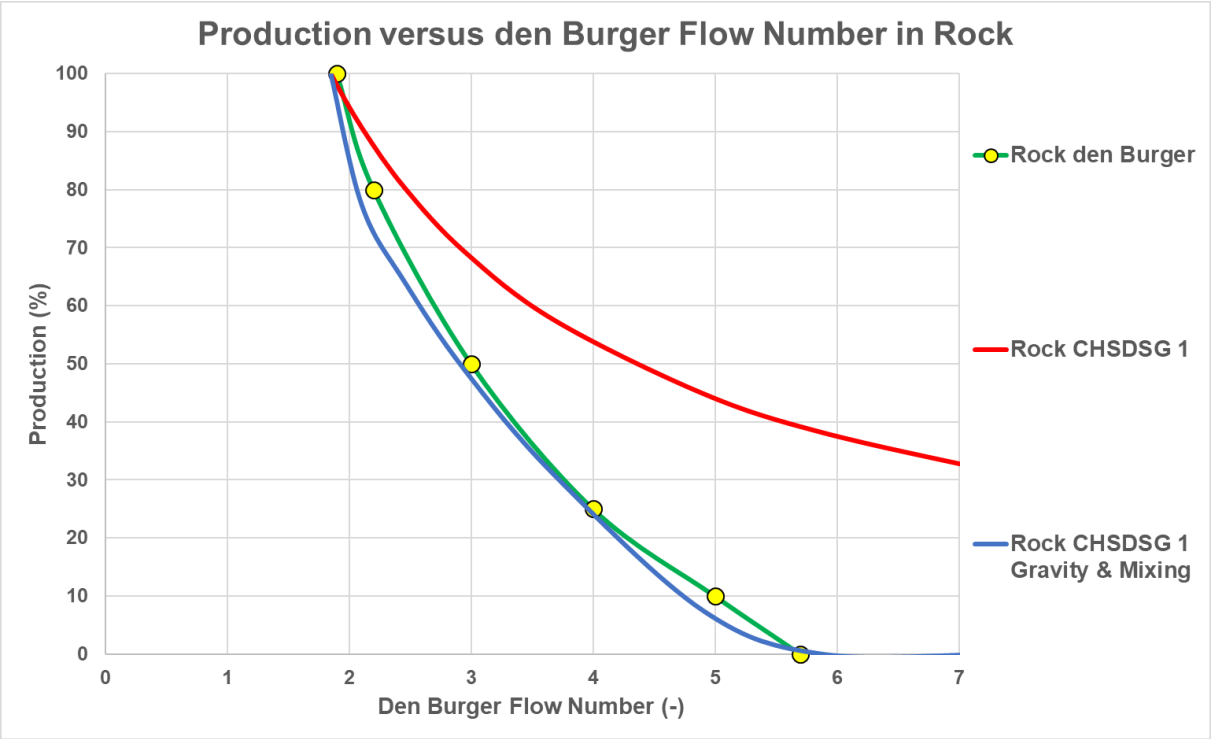

Figure 7-12: Production in rock, the preliminary model, prototype cutter head.

Both model and prototype match if the scale laws from chapter 2 are applied. With a length scale of 7.8 and the model as a starting point, the mixture flow ratio is taken 138.4, the revolutions ratio 1/3.43, the swing velocity ratio 2.27 and the terminal settling velocity ratio also 2.27.

7.4. Advanced Spillage Model based on the Euler Equation.

7.4.1. The Euler Equation.

The basic Euler equation for centrifugal pumps yields (see Figure 7-13):

$$\Delta p_E = \rho_m \cdot u_o \cdot \left(u_o - \frac{Q \cdot \cot(\beta_o)}{2 \cdot \pi \cdot r_o \cdot w} \right) - \rho_m \cdot u_i \cdot \left(u_i - \frac{Q \cdot \cot(\beta_i)}{2 \cdot \pi \cdot r_i \cdot w} \right) \quad \textbf{(7-51)}$$

In terms of radial frequency (like rpm) and radii this gives:

$$\Delta p_E = \rho_m \cdot \omega^2 \cdot \left(r_o^2 - r_i^2 \right) - \frac{\rho_m \cdot \omega \cdot Q}{2 \cdot \pi \cdot w} \cdot \left(\cot(\beta_o) - \cot(\beta_i) \right) \quad \textbf{(7-52)}$$

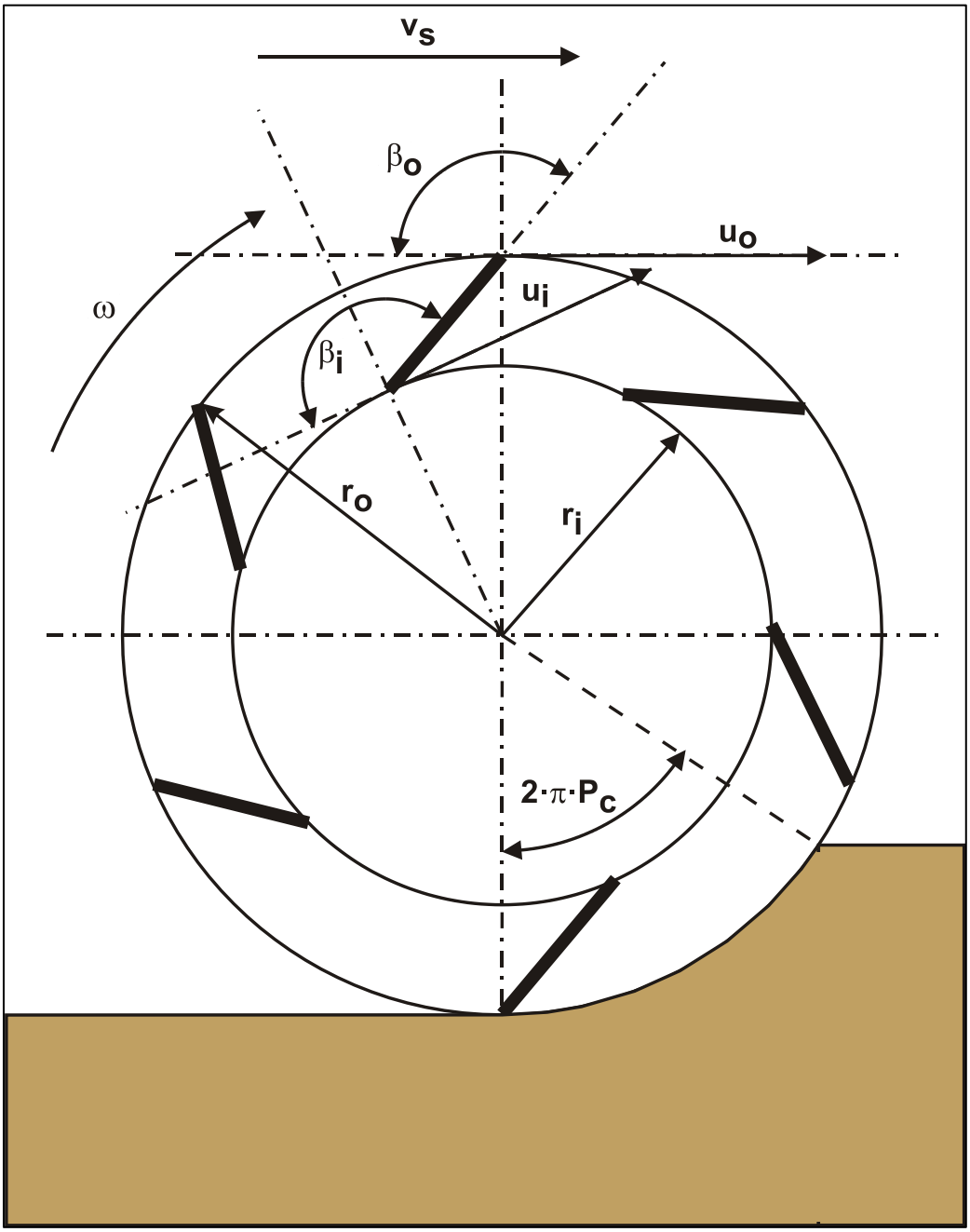

Figure 7-13: The definitions of the Euler equation for a cutter head.

The flow through the impeller blades can be considered to be:

$$Q = \alpha \cdot 2 \cdot \pi \cdot \omega \cdot r_o^2 \cdot w \tag{7-53}$$

The factor α is a variable that can still be anything. Substituting equation **(7-53)** in equation **(7-52)** gives:

$$\Delta p_E = \rho_m \cdot \omega^2 \cdot \left(r_o^2 - r_i^2\right) - \alpha \cdot \rho_m \cdot \omega^2 \cdot r_o^2 \cdot \left(\cot(\beta_o) - \cot(\beta_i)\right) \tag{7-54}$$

This can be simplified to:

$$\Delta p_E = \rho_m \cdot \omega^2 \cdot \left(\left(r_o^2 - r_i^2\right) - \alpha \cdot r_o^2 \cdot \left(\cot(\beta_o) - \cot(\beta_i)\right)\right) \tag{7-55}$$

7.4.2. The Cutter Head.

The cutter head is assumed to consist of two segments. Segment 1, near the ring of the cutter head, where mixture flows out of the cutter head and segment 2, near the top of the cutter head, where water flows in to the cutter head and where also axial flow flows into the cutter head. It is also assumed that for both segments a percentage of the circumference is cutting sand or rock, so this percentage P_c does not participate in the circular flow causing the spillage, see Figure 7-14 and Figure 7-15.

The pressure generated by segment 1, the driving pressure is now, assuming mixture:

$$\Delta p_{E,1} = \rho_{m,1} \cdot \omega^2 \cdot \left(\left(r_{o,1}^2 - r_{i,1}^2\right) - \alpha_1 \cdot r_{o,1}^2 \cdot \left(\cot(\beta_{o,1}) - \cot(\beta_{i,1})\right)\right) \tag{7-56}$$

The outflow through segment 1 is:

$$Q_{1,out} = \alpha_1 \cdot 2 \cdot \pi \cdot \omega \cdot r_{o,1}^2 \cdot w_1 \cdot \left(1 - P_c\right) \tag{7-57}$$

The pressure generated by segment 2 is now, assuming water:

$$\Delta p_{E,2} = \rho_{m,2} \cdot \omega^2 \cdot \left(\left(r_{o,2}^2 - r_{i,2}^2\right) - \alpha_2 \cdot r_{o,2}^2 \cdot \left(\cot(\beta_{o,2}) - \cot(\beta_{i,2})\right)\right) \tag{7-58}$$

The outflow through segment 2 without outside pressure from segment 1 is:

$$Q_{2,out} = \alpha_2 \cdot 2 \cdot \pi \cdot \omega \cdot r_{o,2}^2 \cdot w_2 \cdot \left(1 - P_c\right) \tag{7-59}$$

Now suppose the inflow in segment 2 equals the specific flow of segment 1 minus the specific flow of segment 2 times the width of segment 2, this gives:

$$Q_{2,in} = \left(\alpha_1 \cdot 2 \cdot \pi \cdot \omega \cdot r_{o,1}^2 - \alpha_2 \cdot 2 \cdot \pi \cdot \omega \cdot r_{o,2}^2\right) \cdot w_2 \cdot \left(1 - P_c\right) \tag{7-60}$$

If it is also assumed that the inflow in segment 2 is proportional to the pressure difference between segments 1 and 2, this gives:

$$\begin{aligned} Q_{2,in} &= \varepsilon \cdot \left(\Delta p_{E,1} - \Delta p_{E,2}\right) \cdot \frac{w_2}{\rho_{m,2} \cdot \omega} \cdot \left(1 - P_c\right) \\ &= \varepsilon \cdot \omega \cdot w_2 \begin{pmatrix} \frac{\rho_{m,1}}{\rho_{m,2}} \cdot \left(\left(r_{o,1}^2 - r_{i,1}^2\right) - \alpha_1 \cdot r_{o,1}^2 \cdot \left(\cot(\beta_{o,1}) - \cot(\beta_{i,1})\right)\right) \\ -\left(\left(r_{o,2}^2 - r_{i,2}^2\right) - \alpha_2 \cdot r_{o,2}^2 \cdot \left(\cot(\beta_{o,2}) - \cot(\beta_{i,2})\right)\right) \end{pmatrix} \cdot \left(1 - P_c\right) \end{aligned} \tag{7-61}$$

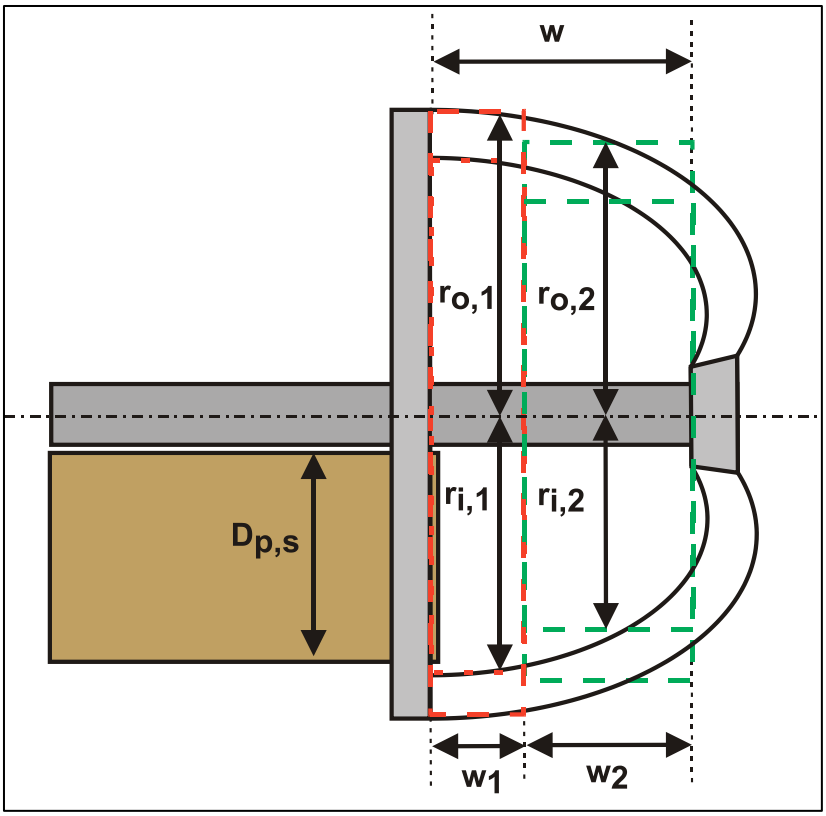

Figure 7-14: The dimensions of the cutter head.

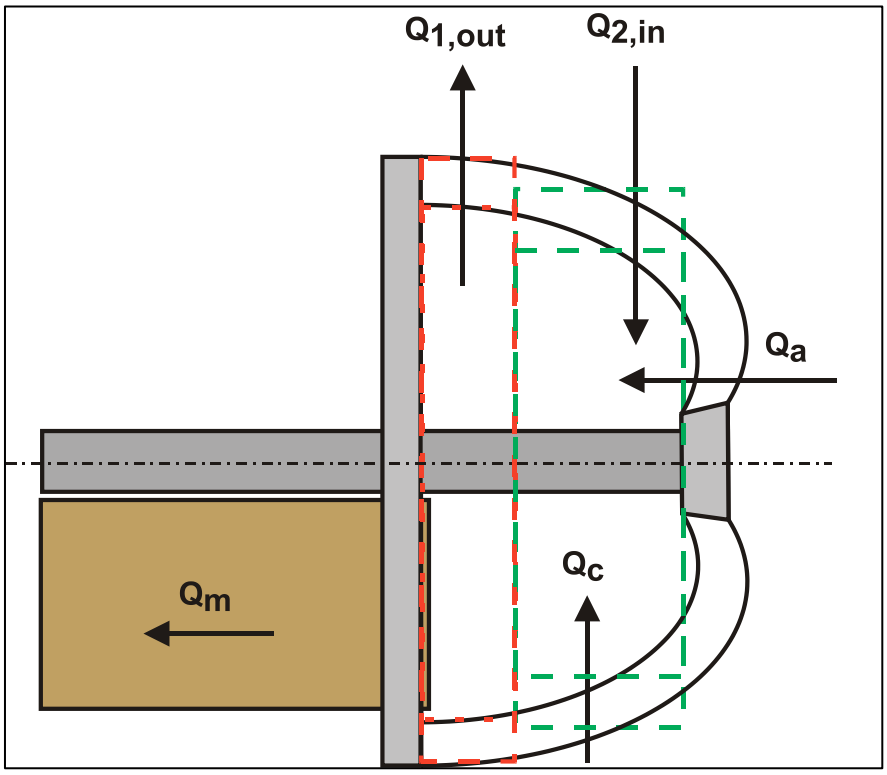

Figure 7-15: The flows in the cutter head.

7.4.3. The Volume Balance.

The volume balance is:

$$Q_{1,out} - Q_{2,in} + Q_m - Q_c - Q_a = 0$$

$$\alpha_1 \cdot 2 \cdot \pi \cdot \omega \cdot r_{o,1}^2 \cdot w_1 \cdot (1 - P_c) - \left(\alpha_1 \cdot 2 \cdot \pi \cdot \omega \cdot r_{o,1}^2 - \alpha_2 \cdot 2 \cdot \pi \cdot \omega \cdot r_{o,2}^2\right) \cdot w_2 \cdot (1 - P_c) + Q_m - Q_c - Q_a = 0 \quad \textbf{(7-62)}$$

The total width (height) of the cutter head is the width of segment 1 plus the width of segment 2:

$$w = w_1 + w_2 \quad \textbf{(7-63)}$$

Equations **(7-60)**, **(7-61)**, **(7-62)** and **(7-63)** form a system of 4 equations with 5 unknowns α_1, α_2, ε, w_1 and w_2. Such a system requires a fifth equation or condition. If the unknown ε is chosen based on calibration with the den Burger data, 4 unknowns remain, and the system can be solved. If ε is known the following is valid and α_1 and α_2 can be solved:

$$\left(\alpha_1 \cdot 2 \cdot \pi \cdot r_{o,1}^2 - \alpha_2 \cdot 2 \cdot \pi \cdot r_{o,2}^2\right) = \varepsilon \cdot \begin{pmatrix} \frac{\rho_{m,1}}{\rho_{m,2}} \cdot \left(\left(r_{o,1}^2 - r_{i,1}^2\right) - \alpha_1 \cdot r_{o,1}^2 \cdot \left(\cot\left(\beta_{o,1}\right) - \cot\left(\beta_{i,1}\right)\right)\right) \\ -\left(\left(r_{o,2}^2 - r_{i,2}^2\right) - \alpha_2 \cdot r_{o,2}^2 \cdot \left(\cot\left(\beta_{o,2}\right) - \cot\left(\beta_{i,2}\right)\right)\right) \end{pmatrix} \quad \textbf{(7-64)}$$

This equation can be written as:

$$\left(\alpha_1 \cdot A - \alpha_2 \cdot B\right) = \varepsilon \cdot \left(C - \alpha_1 \cdot D - E + \alpha_2 F\right)$$

$$\begin{aligned} A &= 2 \cdot \pi \cdot r_{o,1}^2 \\ B &= 2 \cdot \pi \cdot r_{o,2}^2 \\ C &= \frac{\rho_{m,1}}{\rho_{m,2}} \cdot \left(r_{o,1}^2 - r_{i,1}^2\right) \\ D &= \frac{\rho_{m,1}}{\rho_{m,2}} \cdot r_{o,1}^2 \cdot \left(\cot\left(\beta_{o,1}\right) - \cot\left(\beta_{i,1}\right)\right) \\ E &= \frac{\rho_{m,2}}{\rho_{m,2}} \cdot \left(r_{o,2}^2 - r_{i,2}^2\right) \\ F &= \frac{\rho_{m,2}}{\rho_{m,2}} \cdot r_{o,2}^2 \cdot \left(\cot\left(\beta_{o,2}\right) - \cot\left(\beta_{i,2}\right)\right) \end{aligned} \quad \textbf{(7-65)}$$

So:

$$\alpha_1 = \frac{\varepsilon \cdot (C - E) + \alpha_2 \cdot (B + \varepsilon \cdot F)}{(A + \varepsilon \cdot D)} \quad \textbf{(7-66)}$$

Now suppose α_1 and α_2 are equal because of similarity, then:

$$\alpha_1 \cdot (A + \varepsilon \cdot D) - \alpha_1 \cdot (B + \varepsilon \cdot F) = \varepsilon \cdot (C - E)$$

$$\alpha = \alpha_1 = \alpha_2 = \frac{\varepsilon \cdot (C - E)}{(A + \varepsilon \cdot D) - (B + \varepsilon \cdot F)} \quad \textbf{(7-67)}$$

7.4.4. Determining w_1 and w_2.

Substituting equation **(7-67)** in equation **(7-60)** gives:

$$Q_{2,in} = \frac{\varepsilon\cdot(C-E)}{(A+\varepsilon\cdot D)-(B+\varepsilon\cdot F)}\cdot 2\cdot\pi\cdot\omega\cdot\left(r_{o,1}^2-r_{o,2}^2\right)\cdot w_2\cdot(1-P_c) \qquad (7\text{-}68)$$

Substituting equation **(7-67)** in equation **(7-57)** gives:

$$Q_{1,out} = \frac{\varepsilon\cdot(C-E)}{(A+\varepsilon\cdot D)-(B+\varepsilon\cdot F)}\cdot 2\cdot\pi\cdot\omega\cdot r_{o,1}^2\cdot w_1\cdot(1-P_c) \qquad (7\text{-}69)$$

The volume balance gives now:

$$\alpha\cdot 2\cdot\pi\cdot\omega\cdot r_{o,1}^2\cdot(w-w_2)\cdot(1-P_c)-\left(\alpha\cdot 2\cdot\pi\cdot\omega\cdot r_{o,1}^2-\alpha\cdot 2\cdot\pi\cdot\omega\cdot r_{o,2}^2\right)\cdot w_2\cdot(1-P_c)+Q_m-Q_c-Q_a=0 \qquad (7\text{-}70)$$

This equals:

$$\alpha\cdot 2\cdot\pi\cdot\omega\cdot r_{o,1}^2\cdot w\cdot(1-P_c)-\left(\alpha\cdot 4\cdot\pi\cdot\omega\cdot r_{o,1}^2-\alpha\cdot 2\cdot\pi\cdot\omega\cdot r_{o,2}^2\right)\cdot w_2\cdot(1-P_c)+Q_m-Q_c-Q_a=0 \qquad (7\text{-}71)$$

So, for the width of segment 2 this gives:

$$w_2 = \frac{Q_m-Q_c-Q_a+\alpha\ \cdot 2\cdot\pi\cdot\omega\cdot r_{o,1}^2\cdot w\cdot(1-P_c)}{\left(\alpha\cdot 4\cdot\pi\cdot\omega\cdot r_{o,1}^2-\alpha\cdot 2\cdot\pi\cdot\omega\cdot r_{o,2}^2\right)\cdot(1-P_c)} \qquad (7\text{-}72)$$

The width of segment 1 is now:

$$w_1 = w-\frac{Q_m-Q_c-Q_a+\alpha\cdot 2\cdot\pi\cdot\omega\cdot r_{o,1}^2\cdot w\cdot(1-P_c)}{\left(\alpha\cdot 4\cdot\pi\cdot\omega\cdot r_{o,1}^2-\alpha\cdot 2\cdot\pi\cdot\omega\cdot r_{o,2}^2\right)\cdot(1-P_c)} \qquad (7\text{-}73)$$

With:

$$f=\left(\frac{r_{o,1}^2-r_{o,2}^2}{r_{o,1}^2}\right) \quad \text{and} \quad 1+f=\left(\frac{2\cdot r_{o,1}^2-r_{o,2}^2}{r_{o,1}^2}\right) \qquad (7\text{-}74)$$

So, the width of segment 1 equals:

$$w_1 = \frac{f}{(1+f)}\cdot w-\frac{1}{(1+f)}\cdot\frac{1}{2\cdot\pi\cdot\alpha\cdot\omega}\cdot\left(\frac{Q_m-Q_c-Q_a}{r_{o,1}^2\cdot(1-P_c)}\right) \qquad (7\text{-}75)$$

The width of segment 2 can now be determined as:

$$w_2 = \frac{1}{(1+f)}\cdot w+\frac{1}{(1+f)}\cdot\frac{1}{2\cdot\pi\cdot\alpha\cdot\omega}\cdot\left(\frac{Q_m-Q_c-Q_a}{r_{o,1}^2\cdot(1-P_c)}\right) \qquad (7\text{-}76)$$

7.4.5. Determining the Outflow and Inflow.

So, it seems the equations are correct. The two flows out of segments 1 and 2 are now:

$$Q_{1,out} = \alpha \cdot 2 \cdot \pi \cdot \omega \cdot r_{o,1}^2 \cdot \left(\frac{f}{(1+f)} \cdot w - \frac{1}{(1+f)} \cdot \frac{1}{2 \cdot \pi \cdot \alpha \cdot \omega} \cdot \left(\frac{Q_m - Q_c - Q_a}{r_{o,1}^2 \cdot (1-P_c)} \right) \right) \cdot (1-P_c)$$

$$Q_{2,out} = \alpha \cdot 2 \cdot \pi \cdot \omega \cdot r_{o,2}^2 \cdot \left(\frac{1}{(1+f)} \cdot w + \frac{1}{(1+f)} \cdot \frac{1}{2 \cdot \pi \cdot \alpha \cdot \omega} \cdot \left(\frac{Q_m - Q_c - Q_a}{r_{o,1}^2 \cdot (1-P_c)} \right) \right) \cdot (1-P_c) \quad \textbf{(7-77)}$$

The flow into segment 2 is:

$$Q_{2,in} = 2 \cdot \pi \cdot \alpha \cdot \omega \cdot \left(r_{o,1}^2 - r_{o,2}^2 \right) \cdot \left(\frac{1}{(1+f)} \cdot w + \frac{1}{(1+f)} \cdot \frac{1}{2 \cdot \pi \cdot \alpha \cdot \omega} \cdot \left(\frac{Q_m - Q_c - Q_a}{r_{o,1}^2 \cdot (1-P_c)} \right) \right) \cdot (1-P_c) \quad \textbf{(7-78)}$$

The last two equations are equal to equations **(7-34)** and **(7-35)**. So apparently the preliminary model and the advanced model give the same spillage is the factor **α** is the same. The factor **α** for sand was 0.134 and for gravel 0.216 in the preliminary model. For the advanced model the following equation is valid (see equation **(7-67)**).

$$\alpha = \frac{\varepsilon \cdot (C - E)}{(A + \varepsilon \cdot D) - (B + \varepsilon \cdot F)} \quad \textbf{(7-79)}$$

So, the parameter ε has to be calibrated in such a way that the factor **α** for sand gives 0.134 and for gravel 0.216. Since the resulting spillage should be the same if calibrated with the same experimental data.

7.4.6. Flows and Spillage.

The flow of soil cut into the cutter head equals the projected cross section in the direction of the swing speed and is equals to:

$$Q_c = \left(r_{o,1} \cdot \left(1 - \cos\left(2 \cdot \pi \cdot P_c\right)\right) \cdot w_1 + r_{o,2} \cdot \left(1 - \cos\left(2 \cdot \pi \cdot P_c\right)\right) \cdot w_2\right) \cdot v_s \qquad (7\text{-}80)$$

To avoid an implicit model, this can also be written in terms of an average radius r_o and the full width w of the cutter head, giving:

$$Q_c = r_o \cdot \left(1 - \cos\left(2 \cdot \pi \cdot P_c\right)\right) \cdot w \cdot v_s \qquad (7\text{-}81)$$

Now, with a porosity n of the soil (sand will have about 40% while for rock it depends strongly on the type of rock), the flow of solids into the cutter head is:

$$Q_s = Q_c \cdot \left(1 - n\right) \qquad (7\text{-}82)$$

The concentration of solids, assuming the concentration in the suction mouth and the concentration in the outflow of segment 1 are the same, gives:

$$C_{vs} = \frac{Q_s}{Q_m + Q_{1,out}} \qquad (7\text{-}83)$$

The density of the outflow is:

$$\rho_m = C_{vs} \cdot \rho_q + \left(1 - C_{vs}\right) \cdot \rho_l \qquad (7\text{-}84)$$

This is the soil flow divided by the total outflow. The spillage is now the outflow in segment 1 divided by the total outflow, giving:

$$\text{Spillage} = \frac{Q_{1,out}}{Q_m + Q_{1,out}} = \frac{Q_{1,out} \cdot C_{vs}}{Q_s} \qquad (7\text{-}85)$$

The spillage is also the solids outflow in segment 1 divided by the total inflow of solids.

To incorporate the gravity and mixing effect the following equation is found for the advanced and preliminary models:

$$\text{Spillage} = \frac{Q_{1,out} \cdot \left(C_{vs} + \left(C_{vs,max} - C_{vs}\right) \cdot \left(0.1 \cdot \left(\frac{v_t \cdot \sin(\theta) \cdot \pi \cdot r_r^2}{Q_m} \right)^2 + \left(\frac{Bu}{10.8} \right)^3 \right) \right)}{Q_s} \qquad (7\text{-}86)$$

$$\text{With:} \quad C_{vs,max} = \frac{Q_s}{Q_{1,out}}$$

Where the maximum concentration should be limited to a value near 50%, otherwise there are solids leaving segment 1, which is not physically possible. If the terminal settling velocity v_t is very small compared to the mixture velocity v_m, the gravity effect can be ignored, however for rock it plays an important role.

7.4.7. Comparing with the Affinity Law Model.

If the blade angles in and out are equal, then terms D and F are zero and equations **(7-67)**, **(7-68)** and **(7-69)** are more simple.

$$\alpha = \alpha_1 = \alpha_2 = \frac{\varepsilon \cdot (C - E)}{(A - B)} \tag{7-87}$$

If the inner radii and density differences are omitted the following is valid:

$$\alpha = \frac{\varepsilon}{2 \cdot \pi} \tag{7-88}$$

The width of segment 1 is:

$$w_1 = w - \frac{r_{o,1}^2 \cdot w}{\left(2 \cdot r_{o,1}^2 - r_{o,2}^2\right)} - \frac{Q_m - Q_c - Q_a}{\alpha \cdot 2 \cdot \pi \cdot \omega \cdot \left(2 \cdot r_{o,1}^2 - r_{o,2}^2\right) \cdot (1 - P_c)} \tag{7-89}$$

This can be written as:

$$w_1 = w \cdot \left(\frac{\left(r_{o,1}^2 - r_{o,2}^2\right)}{\left(2 \cdot r_{o,1}^2 - r_{o,2}^2\right)} \right) - \frac{Q_m - Q_c - Q_a}{\alpha \cdot 2 \cdot \pi \cdot \omega \cdot \left(2 \cdot r_{o,1}^2 - r_{o,2}^2\right) \cdot (1 - P_c)} \tag{7-90}$$

With:

$$f = \left(\frac{r_{o,1}^2 - r_{o,2}^2}{r_{o,1}^2} \right) \quad \text{and} \quad 1+f = \left(\frac{2 \cdot r_{o,1}^2 - r_{o,2}^2}{r_{o,1}^2} \right) \tag{7-91}$$

This gives:

$$w_1 = \frac{f}{(1+f)} \cdot w - \frac{1}{(1+f)} \cdot \frac{1}{2 \cdot \pi \cdot \alpha \cdot \omega} \cdot \left(\frac{Q_m - Q_c - Q_a}{r_{o,1}^2 \cdot (1 - P_c)} \right) \tag{7-92}$$

This is exactly the equation from the preliminary model. So, the model is consistent with the old model as published at WEDA 2018.

7.5. Advanced Spillage Model with Advanced Cutting.

7.5.1. The Cutter Head.

The cutter head is assumed to consist of two segments. Segment 1, near the ring of the cutter head, where mixture flows out of the cutter head and segment 2, near the top of the cutter head, where water flows in to the cutter head and where also axial flow flows into the cutter head. It is also assumed that for both segments a percentage of the circumference is cutting sand or rock, so this percentage $\mathbf{P_c}$ does not participate in the circular flow causing the spillage. Here this percentage is different for the two segments, which will be the case in reality.

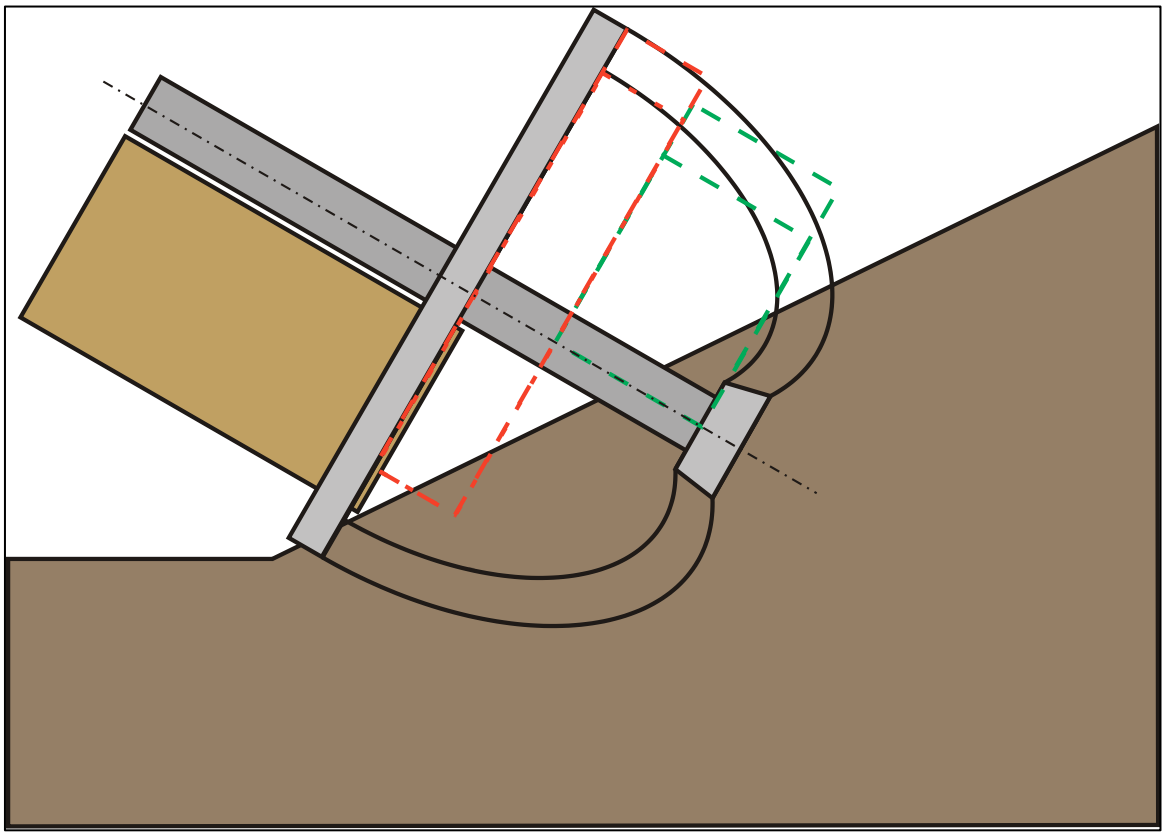

Figure 7-16: The cutter head in the bank.

The pressure generated by segment 1, the driving pressure is now, assuming mixture:

$$\Delta p_{E,1} = \rho_{m,1} \cdot \omega^2 \cdot \left(\left(r_{o,1}^2 - r_{i,1}^2 \right) - \alpha_1 \cdot r_{o,1}^2 \cdot \left(\cot\left(\beta_{o,1}\right) - \cot\left(\beta_{i,1}\right) \right) \right) \tag{7-93}$$

The outflow through segment 1 is:

$$Q_{1,out} = \alpha_1 \cdot 2 \cdot \pi \cdot \omega \cdot r_{o,1}^2 \cdot w_1 \cdot \left(1 - P_{c,1}\right) \tag{7-94}$$

The pressure generated by segment 2 is now, assuming another mixture density:

$$\Delta p_{E,2} = \rho_{m,2} \cdot \omega^2 \cdot \left(\left(r_{o,2}^2 - r_{i,2}^2 \right) - \alpha_2 \cdot r_{o,2}^2 \cdot \left(\cot\left(\beta_{o,2}\right) - \cot\left(\beta_{i,2}\right) \right) \right) \tag{7-95}$$

The outflow through segment 2 without outside pressure from segment 1 is:

$$Q_{2,out} = \alpha_2 \cdot 2 \cdot \pi \cdot \omega \cdot r_{o,2}^2 \cdot w_2 \cdot \left(1 - P_{c,2}\right) \tag{7-96}$$

Now suppose the inflow in segment 2 equals the specific flow of segment 1 minus the specific flow of segment 2 times the width of segment 2, this gives:

$$Q_{2,in} = \left(\alpha_1 \cdot 2 \cdot \pi \cdot \omega \cdot r_{o,1}^2 - \alpha_2 \cdot 2 \cdot \pi \cdot \omega \cdot r_{o,2}^2\right) \cdot w_2 \cdot \left(1 - P_{c,2}\right) \tag{7-97}$$

If it is also assumed that the inflow in segment 2 is proportional to the pressure difference between segments 1 and 2, this gives:

$$\begin{aligned} Q_{2,in} &= \varepsilon \cdot \left(\Delta p_{E,1} - \Delta p_{E,2}\right) \cdot \frac{w_2}{\rho_{m,2} \cdot \omega} \cdot \left(1 - P_{c,2}\right) \\ &= \varepsilon \cdot \omega \cdot w_2 \begin{pmatrix} \frac{\rho_{m,1}}{\rho_{m,2}} \cdot \left(\left(r_{o,1}^2 - r_{i,1}^2\right) - \alpha_1 \cdot r_{o,1}^2 \cdot \left(\cot\left(\beta_{o,1}\right) - \cot\left(\beta_{i,1}\right)\right)\right) \\ -\left(\left(r_{o,2}^2 - r_{i,2}^2\right) - \alpha_2 \cdot r_{o,2}^2 \cdot \left(\cot\left(\beta_{o,2}\right) - \cot\left(\beta_{i,2}\right)\right)\right) \end{pmatrix} \cdot \left(1 - P_{c,2}\right) \end{aligned} \tag{7-98}$$

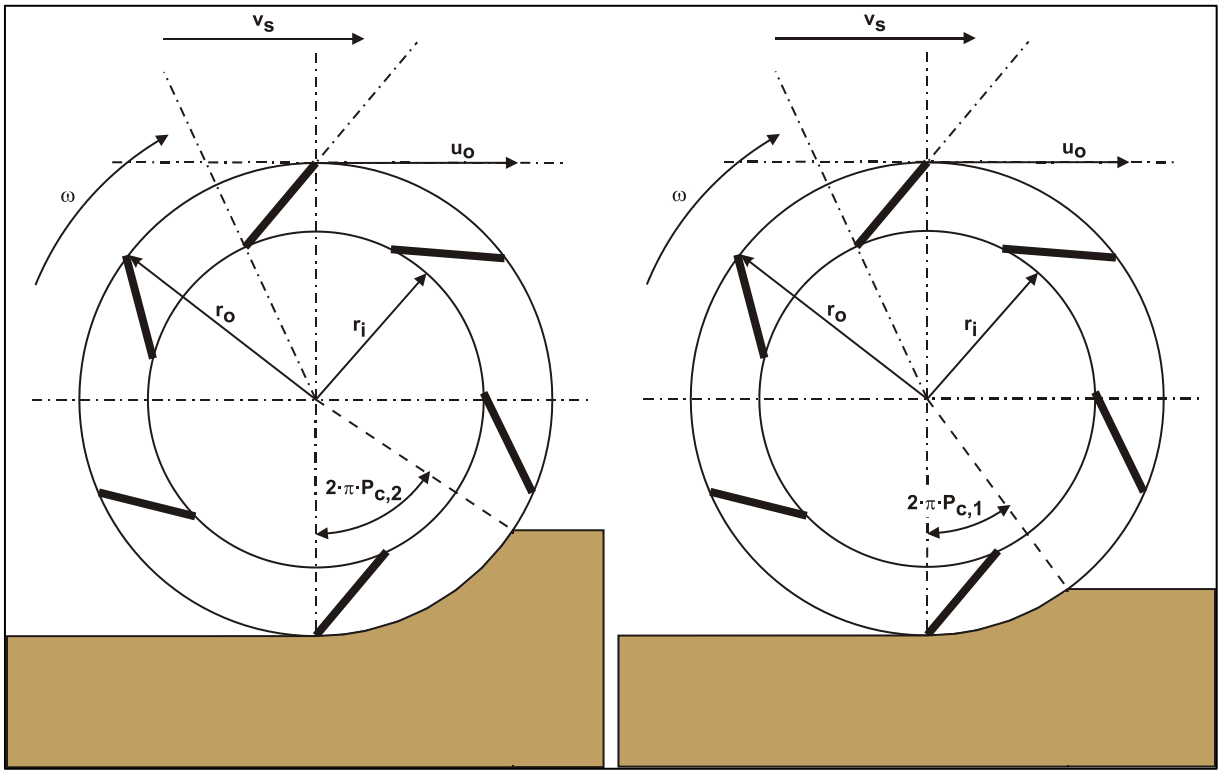

Figure 7-17: The percentages cut in segments 1 and 2.

7.5.2. The Volume Balance.

The volume balance is:

$$Q_{1,out} - Q_{2,in} + Q_m - Q_c - Q_a = 0$$

$$\alpha_1 \cdot 2 \cdot \pi \cdot \omega \cdot r_{o,1}^2 \cdot w_1 \cdot \left(1 - P_{c,1}\right) - \left(\alpha_1 \cdot 2 \cdot \pi \cdot \omega \cdot r_{o,1}^2 - \alpha_2 \cdot 2 \cdot \pi \cdot \omega \cdot r_{o,2}^2\right) \cdot w_2 \cdot \left(1 - P_{c,2}\right) \quad \textbf{(7-99)}$$

$$+Q_m - Q_c - Q_a = 0$$

The total width (height) of the cutter head is the width of segment 1 plus the width of segment 2:

$$w = w_1 + w_2 \quad \textbf{(7-100)}$$

Equations **(7-60)**, **(7-61)**, **(7-62)** and **(7-63)** form a system of 4 equations with 5 unknowns α_1, α_2, ε, w_1 and w_2. Such a system requires a fifth equation or condition. If the unknown ε is chosen based on calibration with the den Burger data, 4 unknowns remain, and the system can be solved. If ε is known the following is valid and α_1 and α_2 can be solved:

$$\left(\alpha_1 \cdot 2 \cdot \pi \cdot r_{o,1}^2 - \alpha_2 \cdot 2 \cdot \pi \cdot r_{o,2}^2\right) \cdot \left(1 - P_{c,2}\right)$$

$$= \varepsilon \cdot \begin{pmatrix} \frac{\rho_{m,1}}{\rho_{m,2}} \cdot \left(\left(r_{o,1}^2 - r_{i,1}^2\right) - \alpha_1 \cdot r_{o,1}^2 \cdot \left(\cot\left(\beta_{o,1}\right) - \cot\left(\beta_{i,1}\right)\right)\right) \\ -\left(\left(r_{o,2}^2 - r_{i,2}^2\right) - \alpha_2 \cdot r_{o,2}^2 \cdot \left(\cot\left(\beta_{o,2}\right) - \cot\left(\beta_{i,2}\right)\right)\right) \end{pmatrix} \cdot \left(1 - P_{c,2}\right) \quad \textbf{(7-101)}$$

This equation can be written as:

$$\left(\alpha_1 \cdot A - \alpha_2 \cdot B\right) = \varepsilon \cdot \left(C - \alpha_1 \cdot D - E + \alpha_2 F\right)$$

$$\begin{aligned} A &= 2 \cdot \pi \cdot r_{o,1}^2 \\ B &= 2 \cdot \pi \cdot r_{o,2}^2 \\ C &= \frac{\rho_{m,1}}{\rho_{m,2}} \cdot \left(r_{o,1}^2 - r_{i,1}^2\right) \\ D &= \frac{\rho_{m,1}}{\rho_{m,2}} \cdot r_{o,1}^2 \cdot \left(\cot\left(\beta_{o,1}\right) - \cot\left(\beta_{i,1}\right)\right) \\ E &= \frac{\rho_{m,2}}{\rho_{m,2}} \cdot \left(r_{o,2}^2 - r_{i,2}^2\right) \\ F &= \frac{\rho_{m,2}}{\rho_{m,2}} \cdot r_{o,2}^2 \cdot \left(\cot\left(\beta_{o,2}\right) - \cot\left(\beta_{i,2}\right)\right) \end{aligned} \quad \textbf{(7-102)}$$

So:

$$\alpha_1 = \frac{\varepsilon \cdot \left(C - E\right) + \alpha_2 \cdot \left(B + \varepsilon \cdot F\right)}{\left(A + \varepsilon \cdot D\right)} \quad \textbf{(7-103)}$$

Now suppose α_1 and α_2 are equal because of similarity arguments, then:

$$\alpha_1 \cdot (A + \varepsilon \cdot D) - \alpha_1 \cdot (B + \varepsilon \cdot F) = \varepsilon \cdot (C - E)$$

$$\alpha = \alpha_1 = \alpha_2 = \frac{\varepsilon \cdot (C - E)}{(A + \varepsilon \cdot D) - (B + \varepsilon \cdot F)} \quad \textbf{(7-104)}$$

The factor α does not depend on the percentages cut, only on the geometry of the cutter head.

7.5.3. Determining w_1 and w_2.

Substituting equation **(7-67)** in equation **(7-60)** gives:

$$Q_{2,in} = \frac{\varepsilon \cdot (C - E)}{(A + \varepsilon \cdot D) - (B + \varepsilon \cdot F)} \cdot 2 \cdot \pi \cdot \omega \cdot (r_{o,1}^2 - r_{o,2}^2) \cdot w_2 \cdot (1 - P_{c,2}) \quad \textbf{(7-105)}$$

Substituting equation **(7-67)** in equation **(7-57)** gives:

$$Q_{1,out} = \frac{\varepsilon \cdot (C - E)}{(A + \varepsilon \cdot D) - (B + \varepsilon \cdot F)} \cdot 2 \cdot \pi \cdot \omega \cdot r_{o,1}^2 \cdot w_1 \cdot (1 - P_{c,1}) \quad \textbf{(7-106)}$$

The volume balance gives now:

$$\alpha \cdot 2 \cdot \pi \cdot \omega \cdot r_{o,1}^2 \cdot (w - w_2) \cdot (1 - P_{c,1}) - (\alpha \cdot 2 \cdot \pi \cdot \omega \cdot r_{o,1}^2 - \alpha \cdot 2 \cdot \pi \cdot \omega \cdot r_{o,2}^2) \cdot w_2 \cdot (1 - P_{c,2})$$

$$+ Q_m - Q_c - Q_a = 0 \quad \textbf{(7-107)}$$

This equals:

$$\alpha \cdot 2 \cdot \pi \cdot \omega \cdot r_{o,1}^2 \cdot w \cdot (1 - P_{c,1})$$

$$- \left(\alpha \cdot 2 \cdot \pi \cdot \omega \cdot r_{o,1}^2 \cdot (1 - P_{c,1}) + \alpha \cdot 2 \cdot \pi \cdot \omega \cdot r_{o,1}^2 \cdot (1 - P_{c,2}) - \alpha \cdot 2 \cdot \pi \cdot \omega \cdot r_{o,2}^2 \cdot (1 - P_{c,2})\right) \cdot w_2 \quad \textbf{(7-108)}$$

$$+ Q_m - Q_c - Q_a = 0$$

So, for the width of segment 2 this gives:

$$w_2 = \frac{Q_m - Q_c - Q_a + \alpha \cdot 2 \cdot \pi \cdot \omega \cdot r_{o,1}^2 \cdot w \cdot (1 - P_{c,1})}{\left(\alpha \cdot 2 \cdot \pi \cdot \omega \cdot r_{o,1}^2 \cdot (1 - P_{c,1}) + \alpha \cdot 2 \cdot \pi \cdot \omega \cdot r_{o,1}^2 \cdot (1 - P_{c,2}) - \alpha \cdot 2 \cdot \pi \cdot \omega \cdot r_{o,2}^2 \cdot (1 - P_{c,2})\right)} \quad \textbf{(7-109)}$$

The width of segment 1 is now:

$$w_1 = w - \frac{Q_m - Q_c - Q_a + \alpha \cdot 2 \cdot \pi \cdot \omega \cdot r_{o,1}^2 \cdot w \cdot (1 - P_{c,1})}{\left(\alpha \cdot 2 \cdot \pi \cdot \omega \cdot r_{o,1}^2 \cdot (1 - P_{c,1}) + \alpha \cdot 2 \cdot \pi \cdot \omega \cdot r_{o,1}^2 \cdot (1 - P_{c,2}) - \alpha \cdot 2 \cdot \pi \cdot \omega \cdot r_{o,2}^2 \cdot (1 - P_{c,2})\right)} \quad \textbf{(7-110)}$$

With:

$$f = \left(\frac{r_{o,1}^2 \cdot (1 - P_{c,2}) - r_{o,2}^2 \cdot (1 - P_{c,2})}{r_{o,1}^2 \cdot (1 - P_{c,1})}\right) \quad \textbf{and} \quad 1 + f = \left(\frac{r_{o,1}^2 \cdot (1 - P_{c,1}) + r_{o,1}^2 \cdot (1 - P_{c,2}) - r_{o,2}^2 \cdot (1 - P_{c,2})}{r_{o,1}^2 \cdot (1 - P_{c,1})}\right) \quad \textbf{(7-111)}$$

So, the width of segment 1 equals:

$$w_1 = \frac{f}{(1+f)} \cdot w - \frac{1}{(1+f)} \cdot \frac{1}{2 \cdot \pi \cdot \alpha \cdot \omega} \cdot \left(\frac{Q_m - Q_c - Q_a}{r_{o,1}^2 \cdot (1 - P_{c,1})} \right) \quad \textbf{(7-112)}$$

The width of segment 2 can now be determined as:

$$w_2 = \frac{1}{(1+f)} \cdot w + \frac{1}{(1+f)} \cdot \frac{1}{2 \cdot \pi \cdot \alpha \cdot \omega} \cdot \left(\frac{Q_m - Q_c - Q_a}{r_{o,1}^2 \cdot (1 - P_{c,1})} \right) \quad \textbf{(7-113)}$$

7.5.4. Determining the Flows.

The two flows out of segments 1 and 2 are now:

$$Q_{1,out} = \alpha \cdot 2 \cdot \pi \cdot \omega \cdot r_{o,1}^2 \cdot \left(\frac{f}{(1+f)} \cdot w - \frac{1}{(1+f)} \cdot \frac{1}{2 \cdot \pi \cdot \alpha \cdot \omega} \cdot \left(\frac{Q_m - Q_c - Q_a}{r_{o,1}^2 \cdot (1 - P_{c,1})} \right) \right) \cdot (1 - P_{c,1})$$

$$Q_{2,out} = \alpha \cdot 2 \cdot \pi \cdot \omega \cdot r_{o,2}^2 \cdot \left(\frac{1}{(1+f)} \cdot w + \frac{1}{(1+f)} \cdot \frac{1}{2 \cdot \pi \cdot \alpha \cdot \omega} \cdot \left(\frac{Q_m - Q_c - Q_a}{r_{o,1}^2 \cdot (1 - P_{c,1})} \right) \right) \cdot (1 - P_{c,2}) \quad \textbf{(7-114)}$$

The flow into segment 2 is:

$$Q_{2,in} = 2 \cdot \pi \cdot \alpha \cdot \omega \cdot \left(r_{o,1}^2 - r_{o,2}^2 \right) \cdot \left(\frac{1}{(1+f)} \cdot w + \frac{1}{(1+f)} \cdot \frac{1}{2 \cdot \pi \cdot \alpha \cdot \omega} \cdot \left(\frac{Q_m - Q_c - Q_a}{r_{o,1}^2 \cdot (1 - P_{c,1})} \right) \right) \cdot (1 - P_{c,2}) \quad \textbf{(7-115)}$$

7.5.5. Spillage.

The flow of soil cut into the cutter head equals the projected cross section in the direction of the swing speed and is equals to:

$$Q_c = \left(r_{o,1} \cdot \left(1 - \cos\left(2 \cdot \pi \cdot P_{c,1}\right)\right) \cdot w_1 + r_{o,2} \cdot \left(1 - \cos\left(2 \cdot \pi \cdot P_{c,2}\right)\right) \cdot w_2\right) \cdot v_s \quad \textbf{(7-116)}$$

To avoid an implicit model, this can also be written in terms of an average radius $r_{c,a}$ and the full width w of the cutter head, giving:

$$Q_c = r_{c,a} \cdot \left(1 - \cos\left(2 \cdot \pi \cdot P_c\right)\right) \cdot w \cdot v_s \quad \textbf{(7-117)}$$

Now, with a porosity n of the soil (sand will have about 40% while for rock it depends strongly on the type of rock), the flow of solids into the cutter head is:

$$Q_s = Q_c \cdot (1 - n) \quad \textbf{(7-118)}$$

The concentration of solids, assuming the concentration in the suction mouth and the concentration in the outflow of segment 1 are the same, gives:

$$C_{vs} = \frac{Q_s}{Q_m + Q_{1,out}} \quad \textbf{(7-119)}$$

The density of the outflow is:

$$\rho_m = C_{vs} \cdot \rho_q + (1 - C_{vs}) \cdot \rho_l \quad \textbf{(7-120)}$$

This is the soil flow divided by the total outflow. The spillage is now the outflow in segment 1 divided by the total outflow, giving:

$$\text{Spillage} = \frac{Q_{1,out}}{Q_m + Q_{1,out}} = \frac{Q_{1,out} \cdot C_{vs}}{Q_s} \quad \textbf{(7-121)}$$

The spillage is also the solids outflow in segment 1 divided by the total inflow of solids.

To incorporate the gravity and mixing effect the following equation is found for the advanced and preliminary models:

$$\text{Spillage} = \frac{Q_{1,out} \cdot \left(C_{vs} + \left(C_{vs,max} - C_{vs}\right) \cdot \left(0.1 \cdot \left(\frac{v_t \cdot \sin(\theta) \cdot \pi \cdot r_r^2}{Q_m}\right)^2 + \left(\frac{Bu}{10.8}\right)^3\right)\right)}{Q_s} \quad \textbf{(7-122)}$$

$$\text{With:} \quad C_{vs,max} = \frac{Q_s}{Q_{1,out}}$$

Where the maximum concentration should be limited to a value near 50%, otherwise there are solids leaving segment 1, which is not physically possible. If the terminal settling velocity v_t is very small compared to the mixture velocity v_m, the gravity effect can be ignored, however for rock it plays an important role.

7.5.6. Validation & Sensitivity Analysis, both Models: CHSDSG 1 & CHSDSG 2.

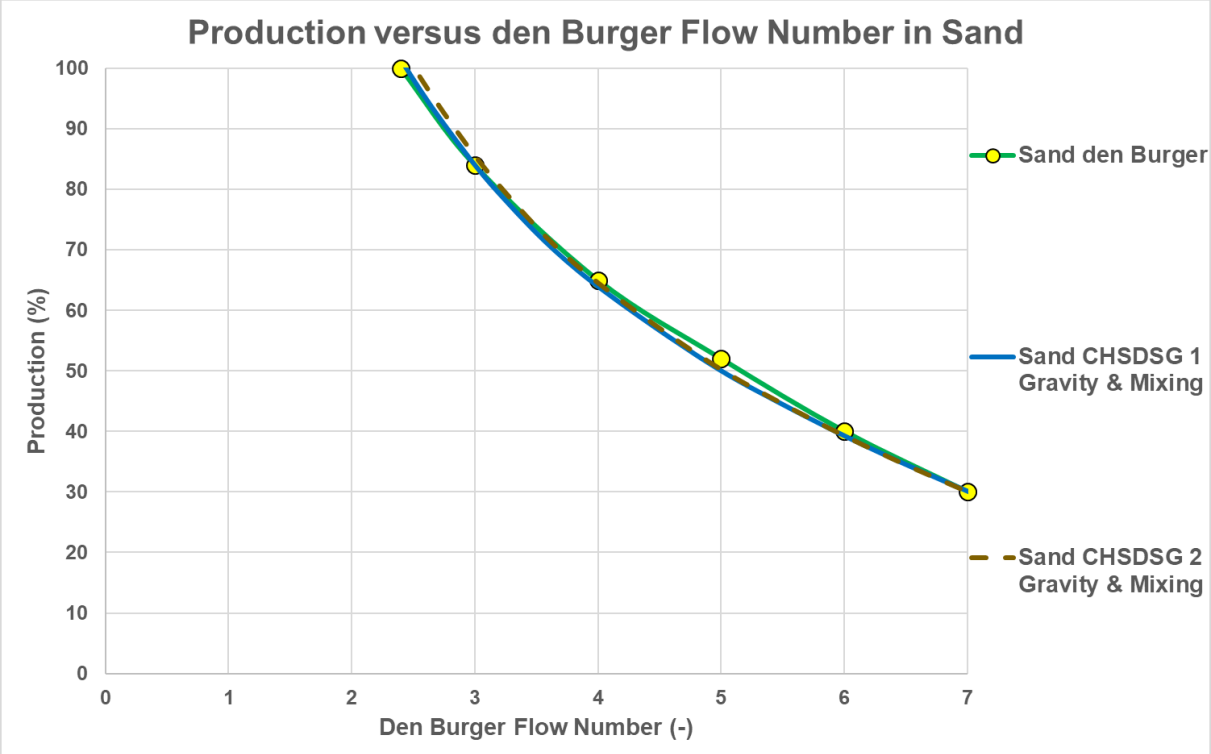

Figure 7-18: Production in sand, CHSDSG 1 & 2, model cutter head.

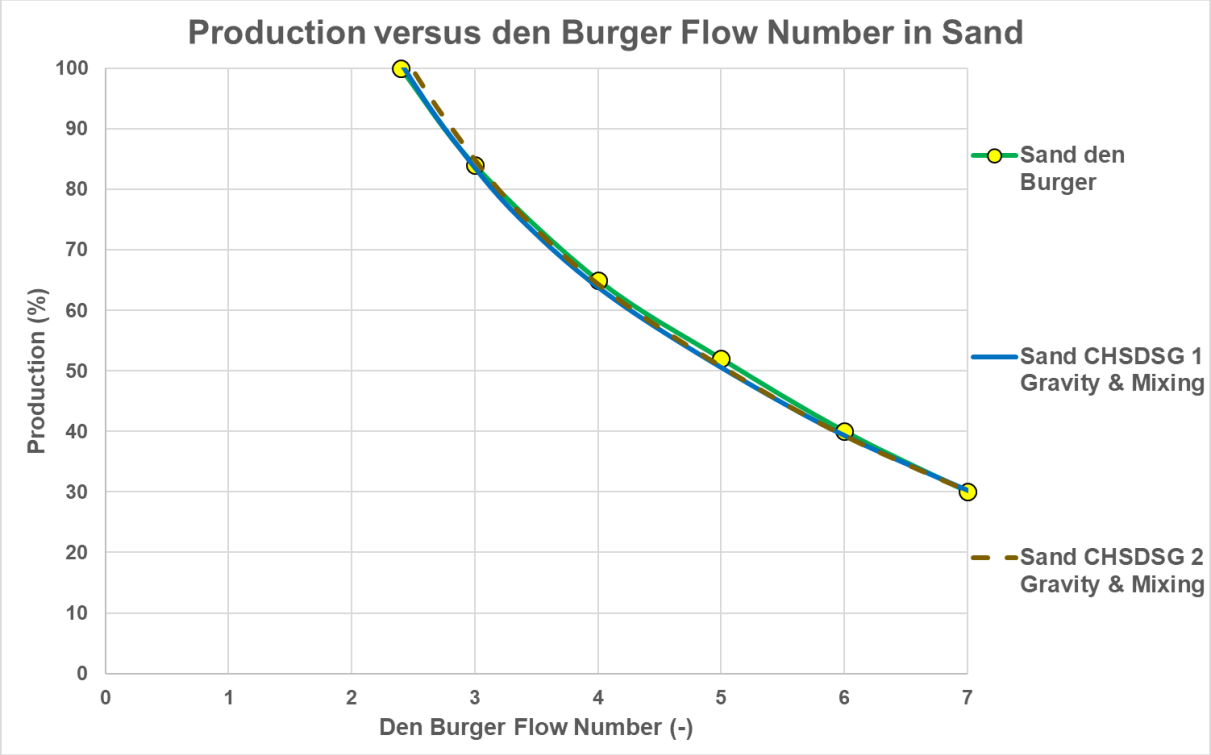

Figure 7-19: Production in sand, CHSDSG 1 & 2, prototype cutter head.

Figure 7-18 and Figure 7-19 show the spillage curves for the den Burger (2003) experiments for the preliminary and advanced models, the 0.4 m model cutter head and the 3.12 m prototype cutter head. The curves are almost the same, meaning the Bu dimensionless number is a good choice to describe spillage. The model of course is calibrated on these experiments, so a different shaped cutter head, different combinations of revolutions and mixture velocity and different solids may influence the location and shape of the spillage curve.

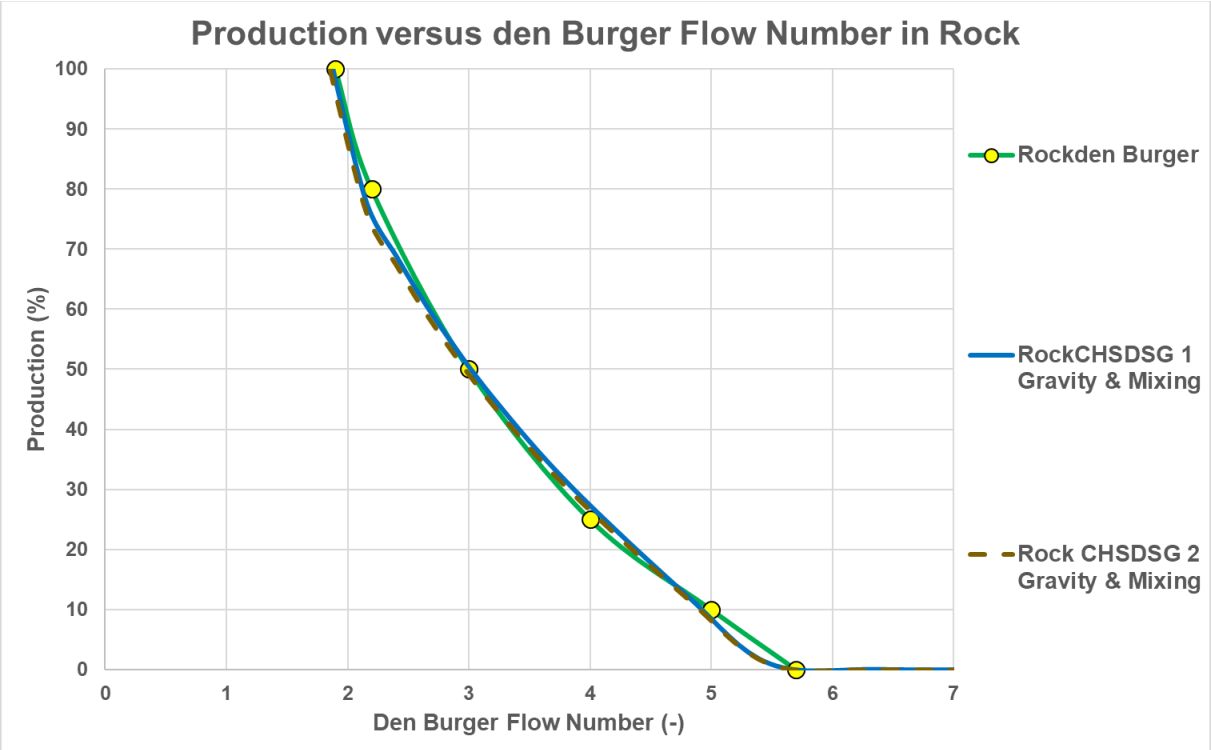

Figure 7-20: Production in rock, CHSDSG 1 & 2, model cutter head.

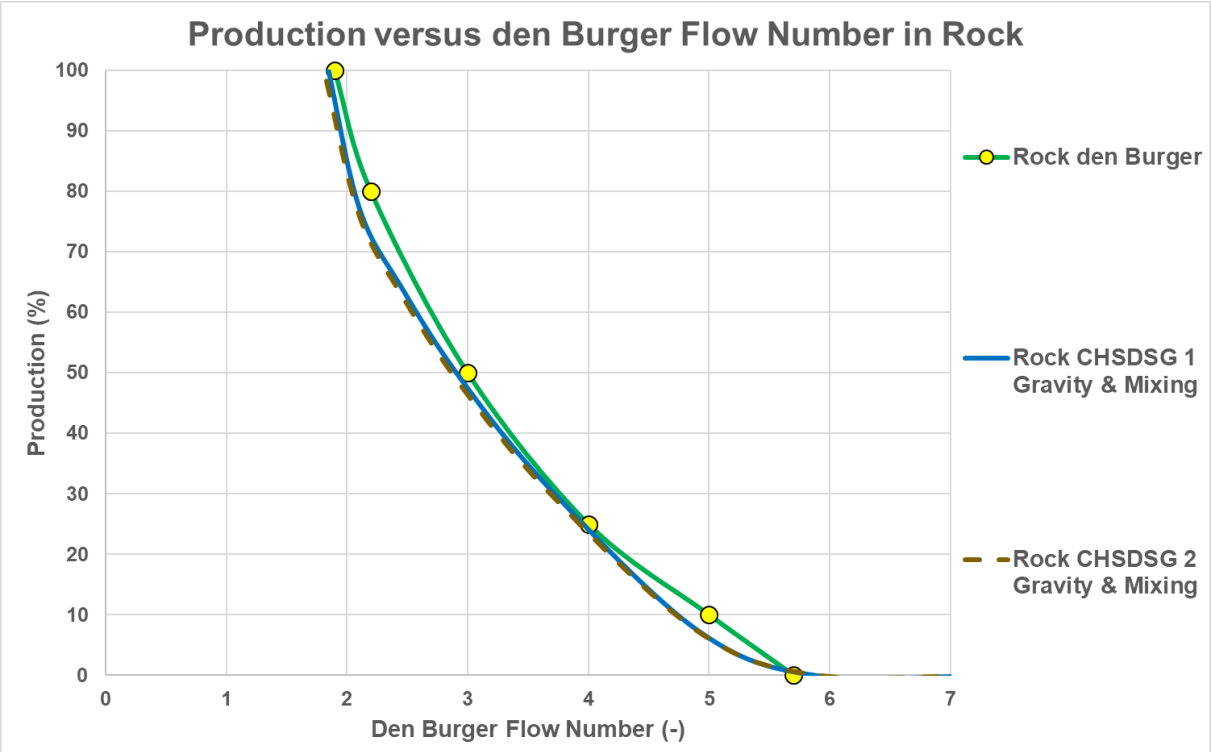

Figure 7-21: Production in rock, CHSDSG 1 & 2, prototype cutter head.

Figure 7-20 and Figure 7-21 show the spillage curves for the den Burger (2003) experiments for the preliminary and advanced models, the 0.4 m model cutter head and the 3.12 m prototype cutter head. For the model cutter head and the prototype cutter head the curves are very similar, which makes sense since the curves are calibrated on the model tests and the scale laws according to chapter 2 are applied.

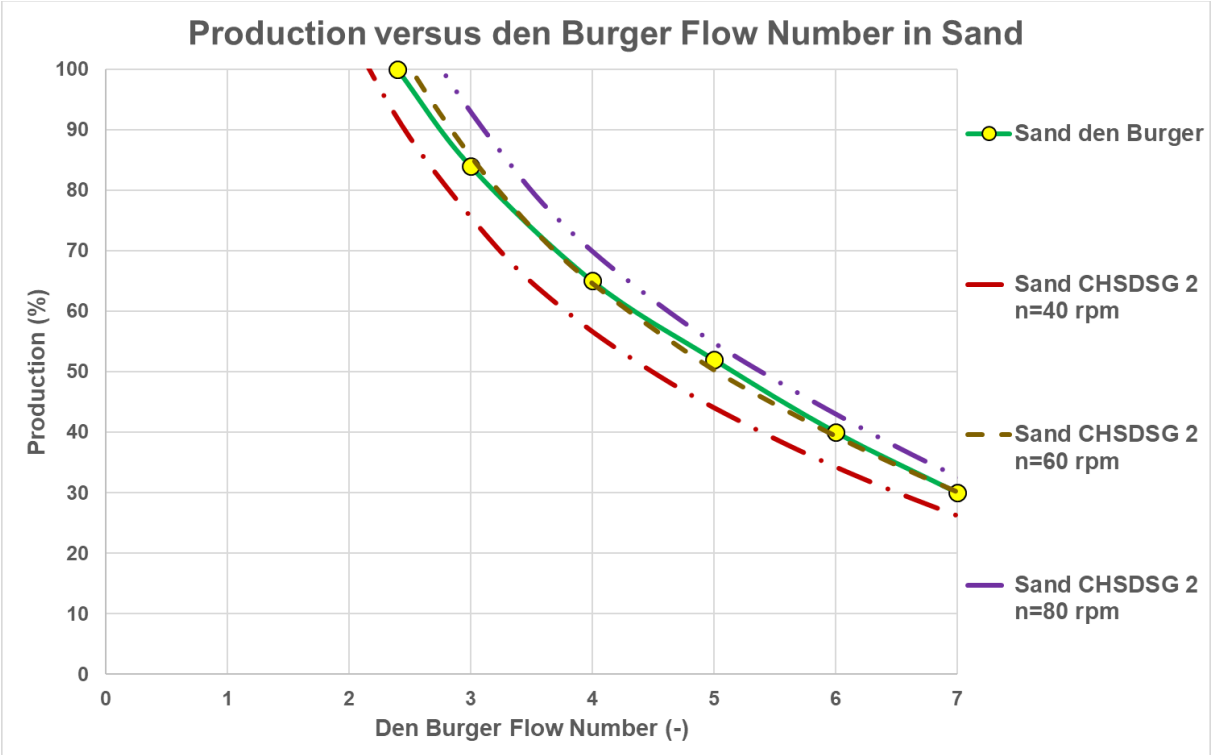

Figure 7-22: Production in sand, the advanced model, 3 different cutter head revolutions, model cutter head.

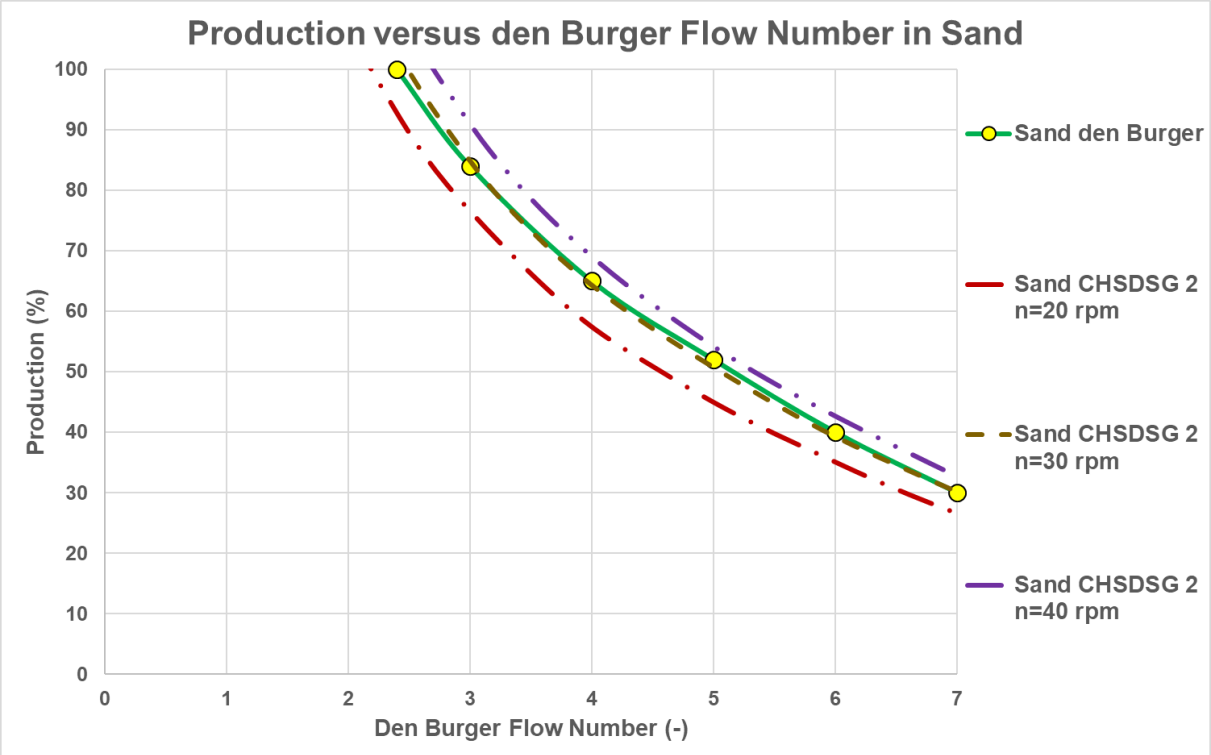

Figure 7-23: Production in sand, the advanced model, 3 different cutter head revolutions, prototype cutter head.

Figure 7-22 and Figure 7-23 show the effect of different cutter head revolutions when cutting sand. The cutter head revolutions influence the abscissa directly because the revolutions are present in the dimensionless flow number. So, it is expected that a decrease of the revolutions will move the curve to the left and an increase will move the curve to the right, which is clear from Figure 7-22 and Figure 7-23.

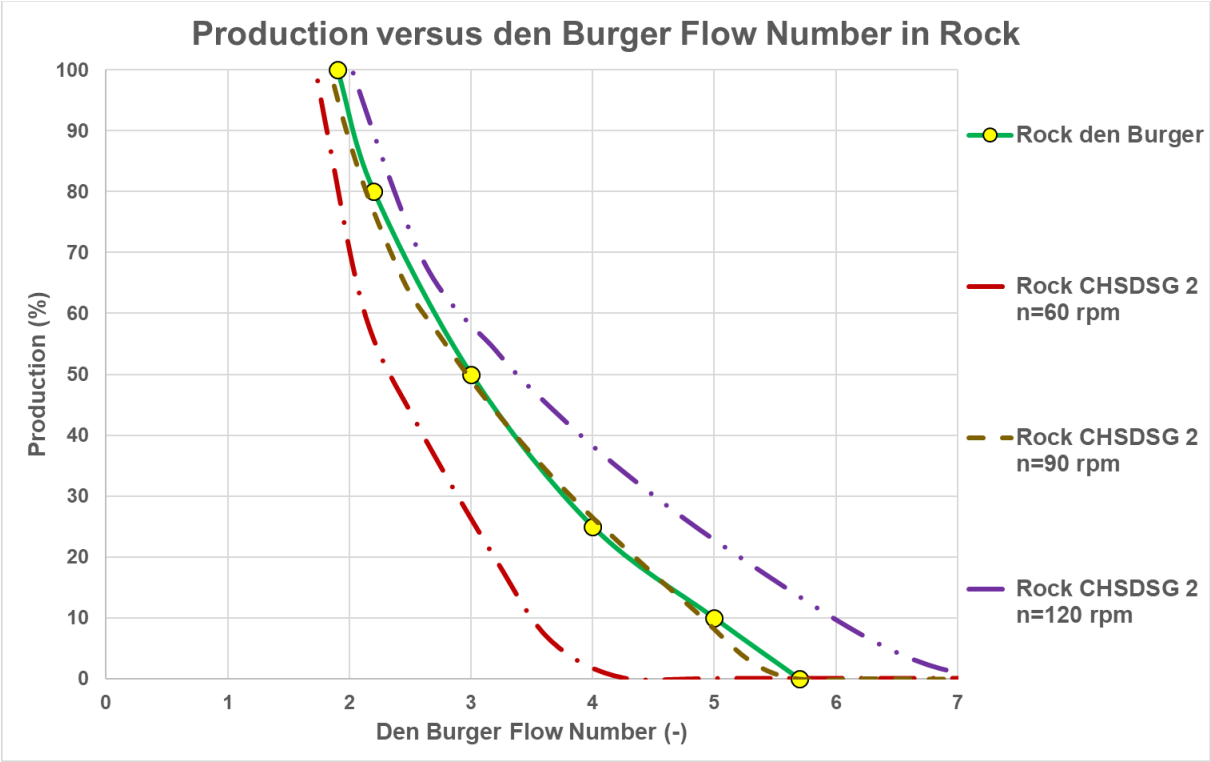

Figure 7-24: Production in rock, the advanced model, 3 different cutter head revolutions, model cutter head.

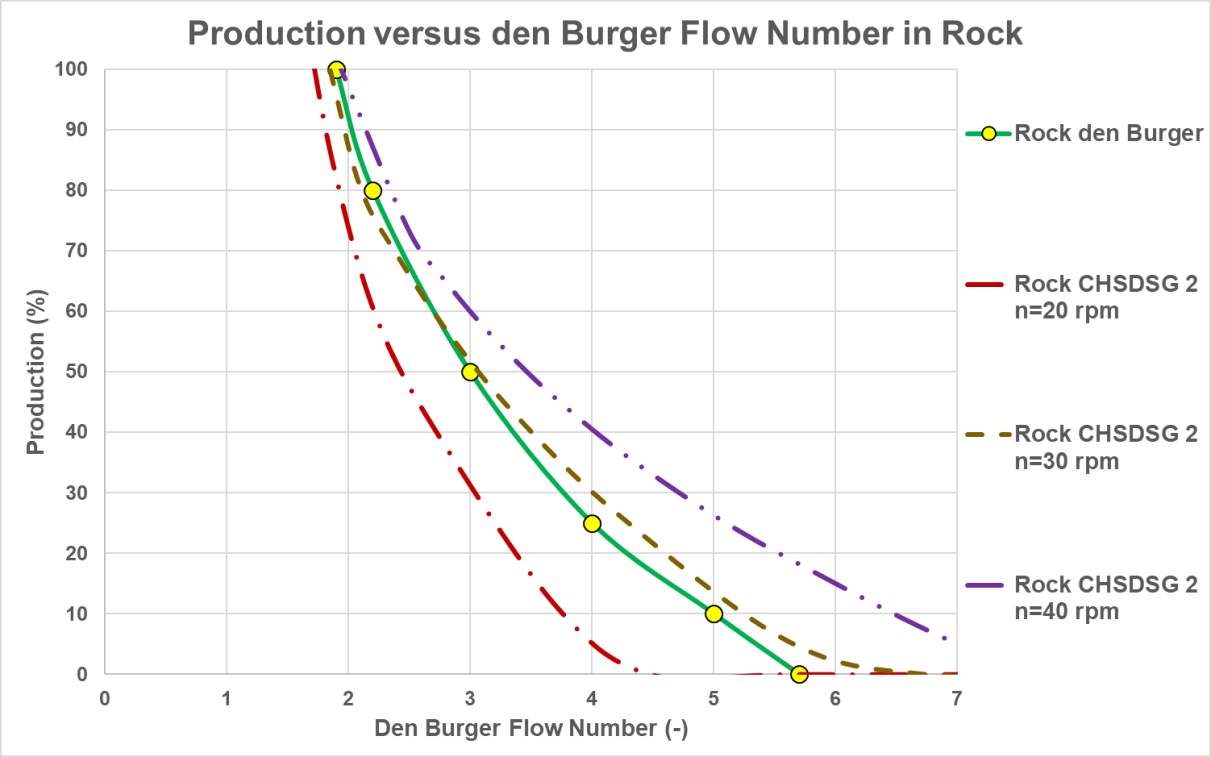

Figure 7-25: Production in rock, the advanced model, 3 different cutter head revolutions, prototype cutter head.

Figure 7-24 and Figure 7-25 show the effect of different cutter head revolutions when cutting rock. The cutter head revolutions influence the abscissa directly because the revolutions are present in the dimensionless flow number. So, it is expected that a decrease of the revolutions will move the curve to the left and an increase will move the curve to the right, which is clear from Figure 7-24 and Figure 7-25. The shape of the curves is different compared to the curves in sand.

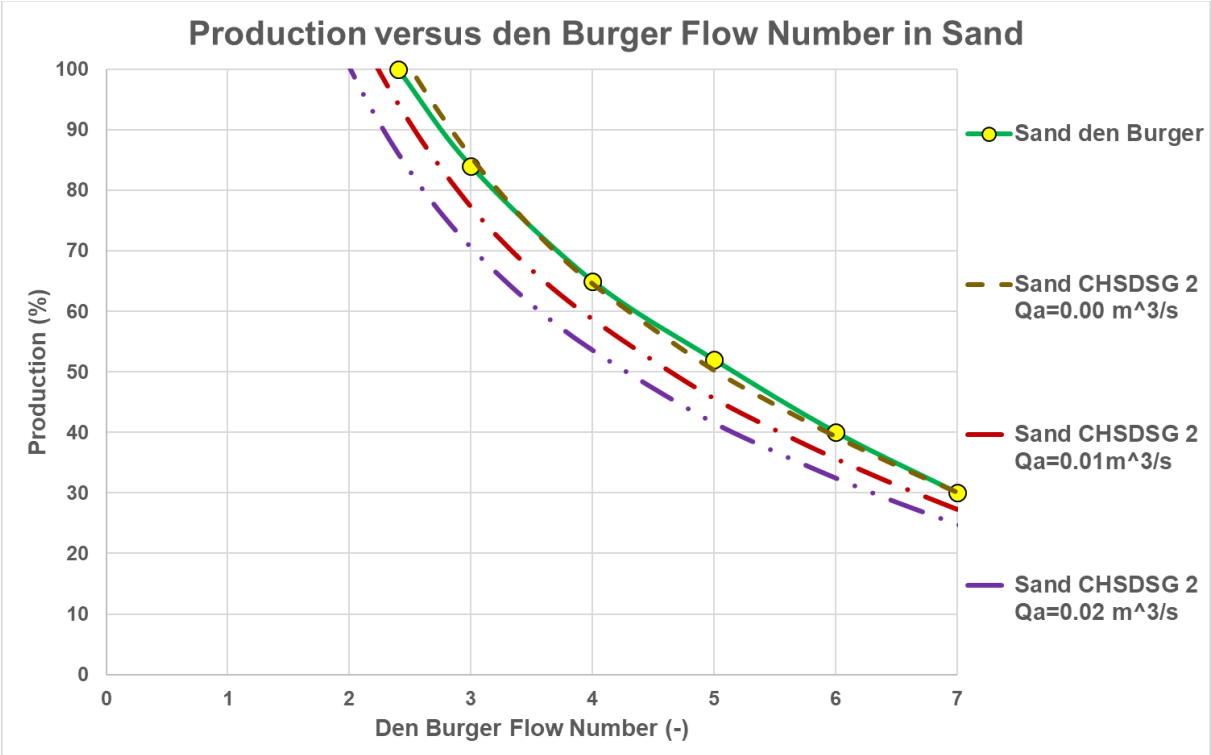

Figure 7-26: Production in sand, the advanced model, 3 different axial flows, model cutter head.

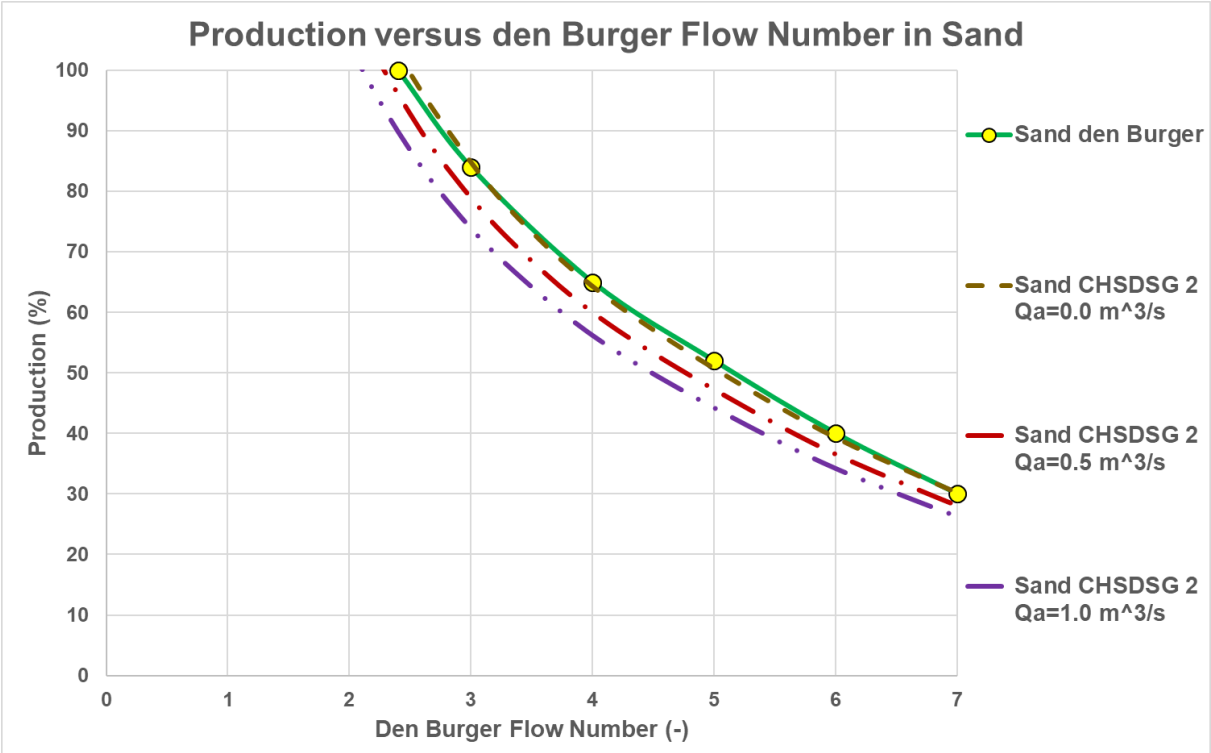

Figure 7-27: Production in sand, the advanced model, 3 different axial flows, prototype cutter head.

Figure 7-26 and Figure 7-27 show 3 curves for 3 different axial flows. The main reason for showing this is to investigate the influence of axial flow. Is the influence big or small? Axial flow increases the spillage and thus decreases the production. For the model cutter head, the mixture flow is about 0.07 m^3/s with a mixture velocity of 4 m/s. So, the axial flows used are about 15% and 30%. For the prototype cutter head, the mixture flow is about 5 m^3/s with a mixture velocity of 7 m/s. So, the axial flows used are about 10% and 20%. Each 1% axial flow results in about 0.5% increase in spillage or decrease of production. These numbers are determined at the point where the spillage is zero percent, close to operational conditions.

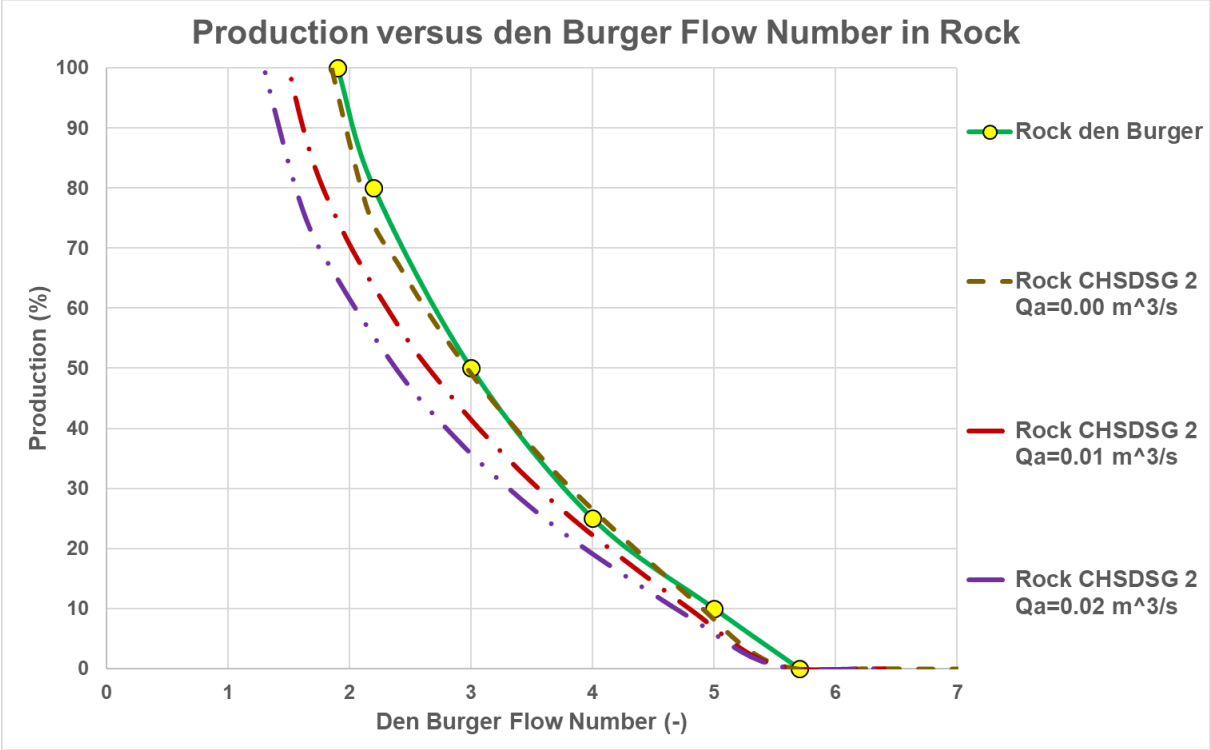

Figure 7-28: Production in rock, the advanced model, 3 different axial flows, model cutter head.

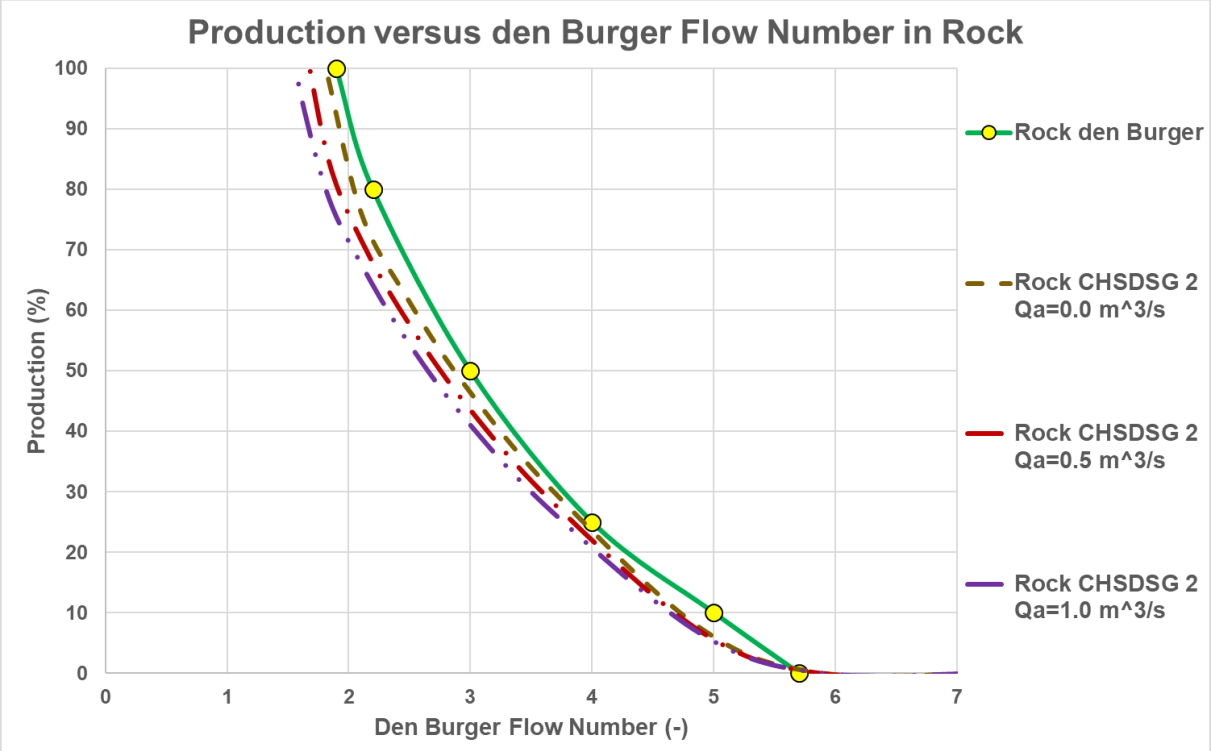

Figure 7-29: Production in rock, the advanced model, 3 different axial flows, prototype cutter head.

Figure 7-28 and Figure 7-29 show 3 curves for 3 different axial flows. The main reason for showing this is to investigate the influence of axial flow. Is the influence big or small? Axial flow increases the spillage and thus decreases the production. For the model cutter head, the mixture flow is about 0.043 m^3/s with a mixture velocity of 5.5 m/s. So, the axial flows used are about 22% and 44%. For the prototype cutter head, the mixture flow is about 5 m^3/s with a mixture velocity of 7 m/s. So, the axial flows used are about 10% and 20%. Each 1% axial flow results in about 0.5% increase in spillage or decrease of production for the prototype. For the model its about

1% per 1% axial flow. These numbers are determined at the point where the spillage is zero percent, close to operational conditions. The difference between sans and rock can be explained because of the difference in cut production. Here the scale laws according to chapter 2 are applied.

The prototype cutter head data are shown in Figure 7-4. In the graphs the flow number is varied by varying the mixture flow, while other parameters are kept constant on a curve.

Figure 7-18, Figure 7-19, Figure 7-20 and Figure 7-21 show the experimental data of den Burger (2003) versus the simulations with the preliminary and the advanced models. Both models are calibrated on these experimental data by adjusting **α** in the preliminary model and **ε** in the advanced model. For sand **α=0.162** and **ε=2.5.** For rock **α=0.21** and **ε=4.8.**

It should be noted that the by den Burger (2003) reported experimental data shows the envelope of maximum production. For each mixture velocity different curves are found with an increasing production with increasing revolutions up to a maximum production and a decreasing production with increasing revolutions passed the maximum, see Figure 7-30. The decreasing part of the curves is described well by the preliminary and the advanced model. The increasing part at low revolutions is not. It should be mentioned that den Burger (2003) carried out his experiments in rock with a 45° ladder angle, see Figure 7-31. This figure shows that the cutting process takes place at the lowest part of the cutter head, while the suction pipe is at a much higher location. Equation **(7-122)** takes the vertical distance (terminal settling velocity) and mixing effect into account.

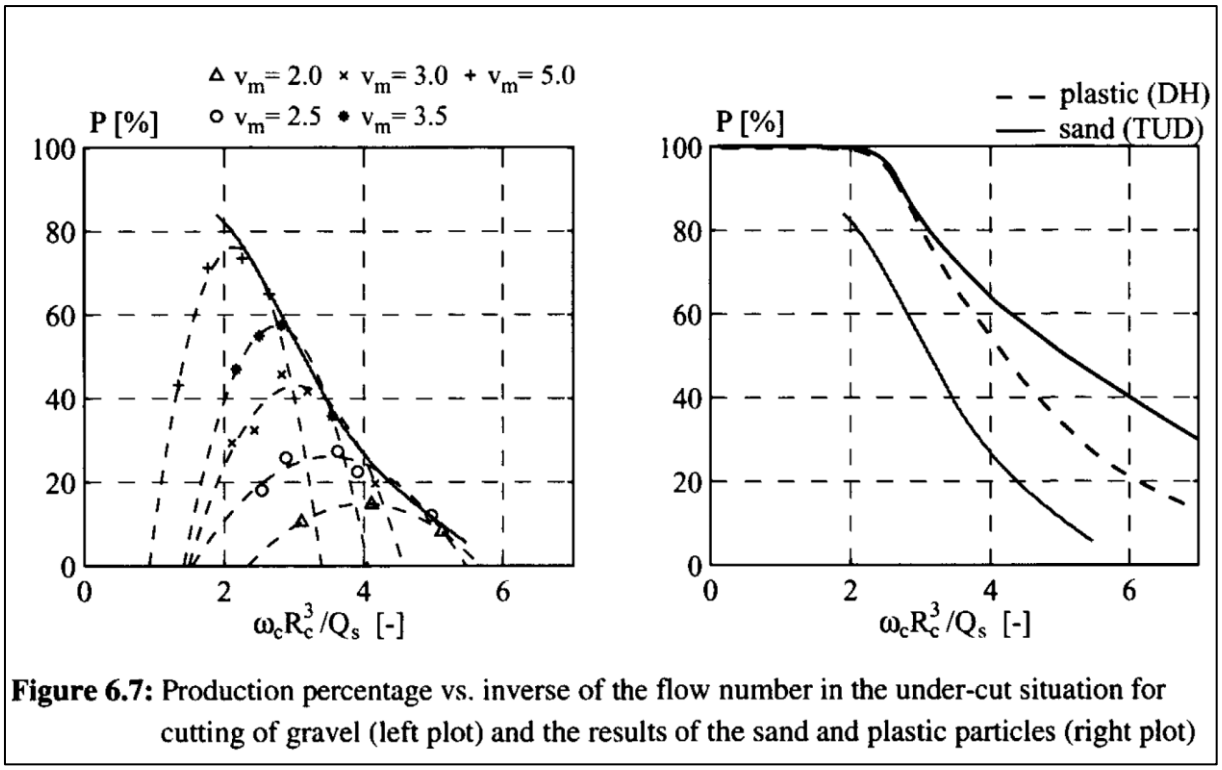

Figure 6.7: Production percentage vs. inverse of the flow number in the under-cut situation for cutting of gravel (left plot) and the results of the sand and plastic particles (right plot)

Figure 7-30: Production curves as a function of revolutions and mixture velocity den Burger (2003).

Another effect, which has not yet been considered is, is the rotating flow strong enough to bring the particles to the suction mouth? Figure 7-30 shows that at low revolutions the production increases with increasing revolutions. The figure suggests that below certain revolutions there is no production at all. Figure 7-31 shows that the cutting process takes place at the bottom of the cutter head. So, particles have to be lifted to flow to the suction mouth. This elevation depends on the ladder angle and dimensions of the cutter head. Particles will be lifted by drag forces generated by the rotating flow inside the cutter head. Now, drag forces are usually proportional to the velocity squared, in this case the circumferential velocity of the cutter head. The force that prevents the particles from being lifted is the gravitational force, resulting in a settling velocity. Based on this the ratio of the circumferential velocity of the cutter head to the terminal settling velocity, incorporating the ladder angle, squared, seems to be a good parameter to indicate the filling degree of the cutter head with particles.
This gives:

$$\mathbf{FillingDegree} = \xi \cdot \left(\frac{\frac{D_r \cdot 2 \cdot \pi \cdot n}{2 \cdot 60} \cdot \cos(\theta)}{v_t} \right)^2 \quad \textbf{and} \quad \mathbf{FillingDegree} \leq 1 \qquad \textbf{(7-123)}$$

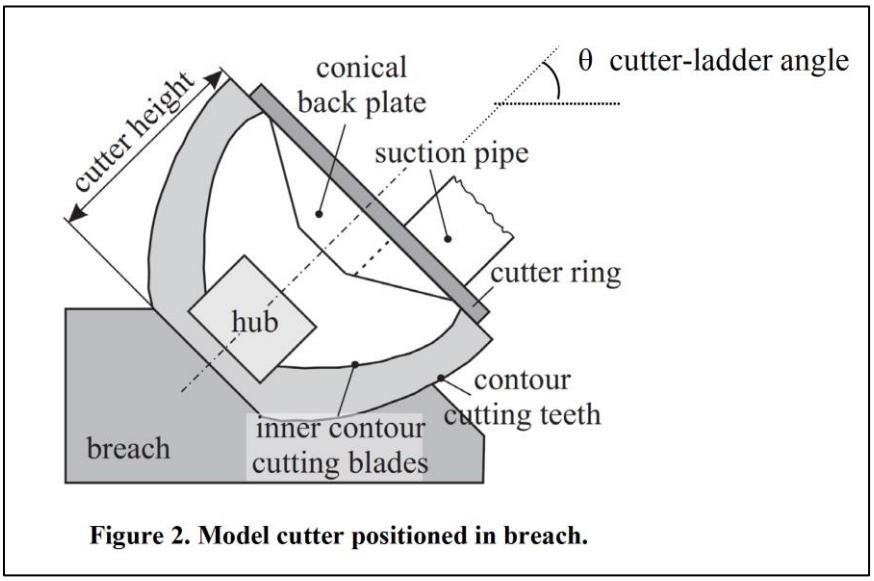

Figure 2. Model cutter positioned in breach.

Figure 7-31: The model cutter head in the bank.

With ξ=**0.15**. If the FD number is larger than 1, the filling degree equals 1, since a filling degree can never be higher that 100%. If the filling degree is, as an example, 80%, this means that 80% of the particles could reach the suction mouth. 20% of the particles never even move inside the cutter head, since they already left the cutter head immediately after cutting because of gravity. The spillage based on the flows in the cutter head of course only apply on the particles that entered the cutter head, the filling degree.

The final spillage can now be determined with (spillage from equation **(7-122)**):

$$\mathbf{FinalSpillage} = \mathbf{Spillage} \cdot \mathbf{FillingDegree} + (1 - \mathbf{FillingDegree}) \qquad \textbf{(7-124)}$$

Because of the limited amount of experimental data, here a simple linear approach is used. Since in reality the cutter head revolutions are fixed, the maximum production curve or minimum spillage curve should be used as determined before. The model including the filling degree effect is named the **CHSDSG 3** model.

The filling degree is based on turbulent settling and a turbulence-based drag force, giving the squared relation of equation **(7-123)**. For the Stokes region of the settling velocity, a linear relation for the filling degree is found. However, for this case the filling degree is already very high for very low revolutions, that this is not relevant. So the filling degree approach is only relevant for large particles of rock and gravel.

To match the experiments of den Burger, the factor ε is about 2.45 for sand and 4.4 for rock. This can be described by:

$$\varepsilon = 2.35 + (4.40 - 2.35) \cdot \frac{v_t}{0.45} \cdot \lambda^{-0.4} \qquad \textbf{(7-125)}$$

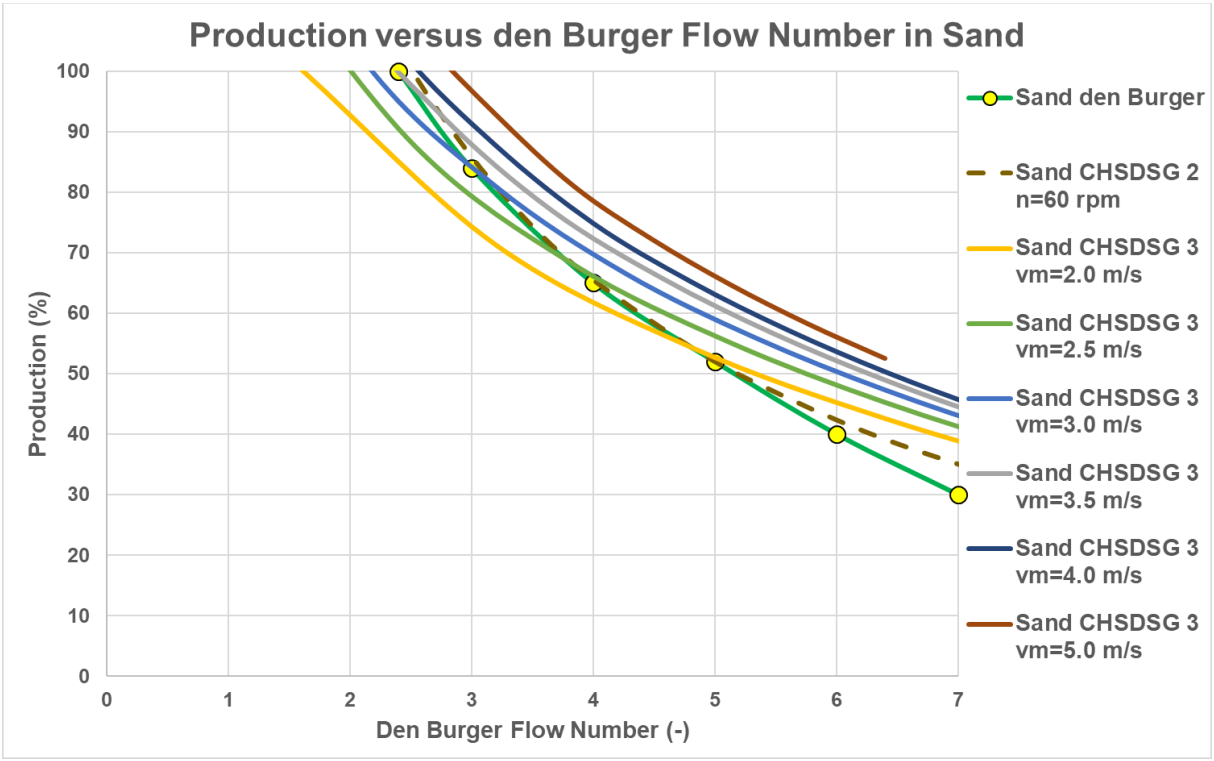

Figure 7-32: Production in sand, n from 20 to 200 rpm, including filling degree effect, model cutter head.

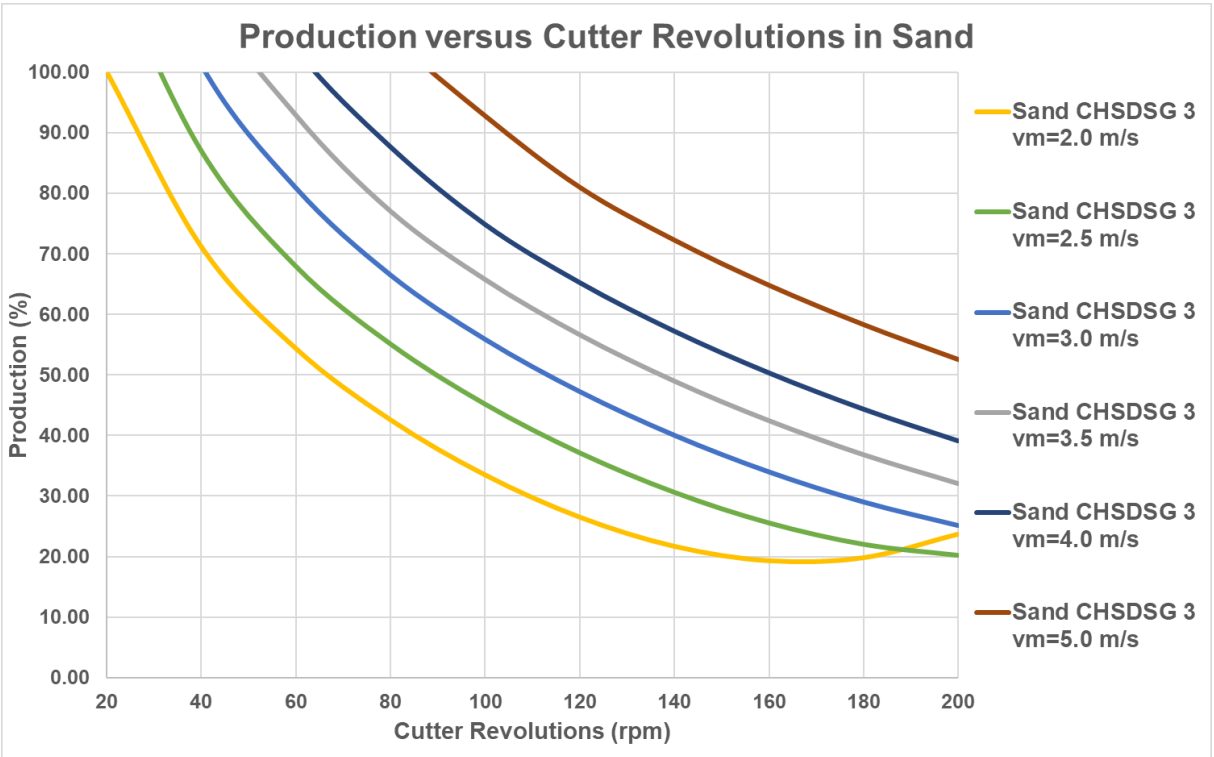

Figure 7-33: Production in sand, n from 20 to 200 rpm, including filling degree effect, model cutter head.

Figure 7-32 and Figure 7-33 show curves with this final spillage for values of **n** from 20 rpm to 200 rpm and mixture velocities of 2 m/s to 5 m/s for the model cutter head. The curves do not show a maximum, so they do not match with Figure 7-30, because the particles are so small that the filling degree is always 100%.

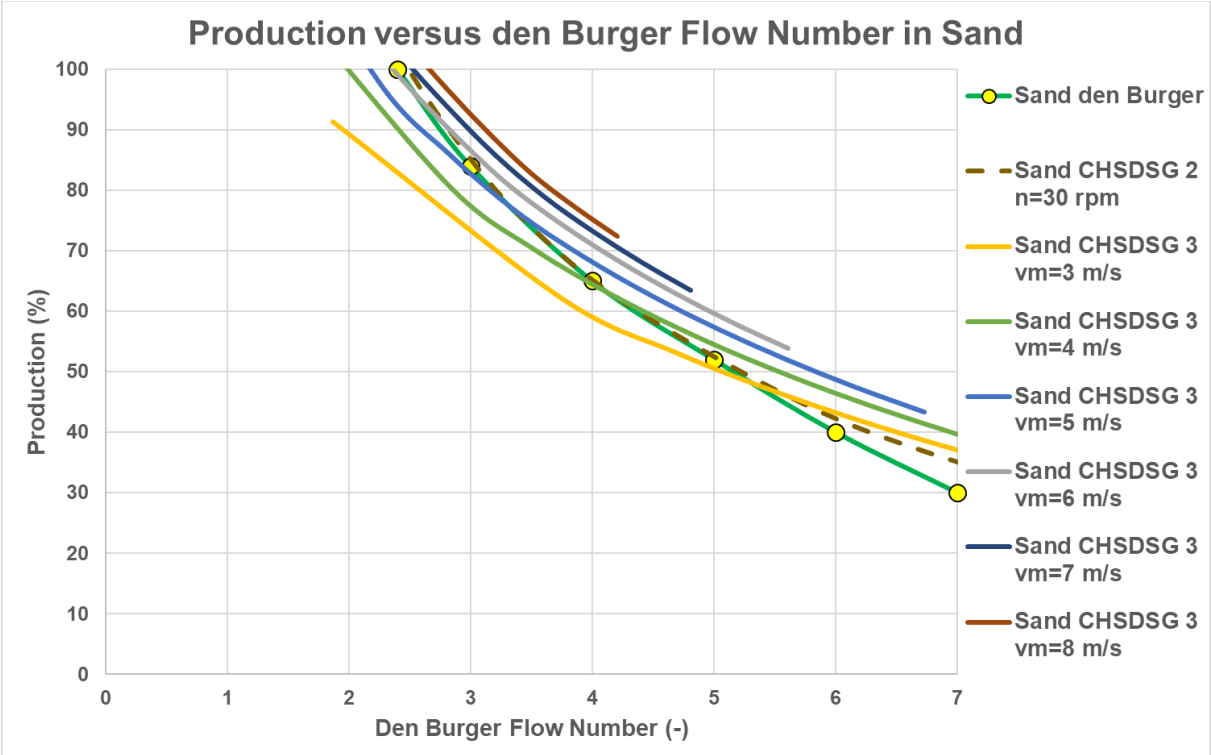

Figure 7-34: Production in sand n, from 10 rpm to 60 rpm, including filling degree effect, prototype cutter head.

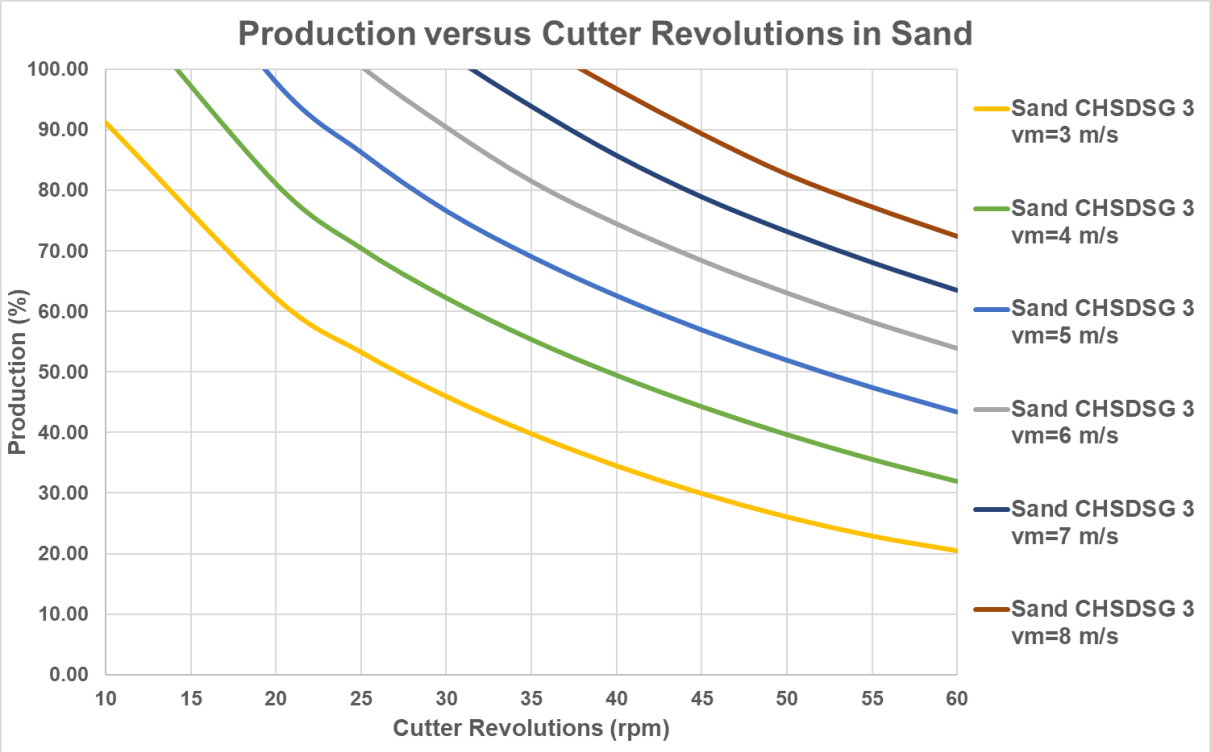

Figure 7-35: Production in sand, n from 10 rpm to 60 rpm, including filling degree effect, prototype cutter head.

Figure 7-34 and Figure 7-35 show curves with this final spillage for values of **n** from 10 rpm to 60 rpm and mixture velocities of 3 m/s to 8 m/s for the prototype cutter head. The curves do not show a maximum at about 35-40 rpm for the case considered. The curves do not match with Figure 7-30, because the particles are so small that the filling degree is always 100%.

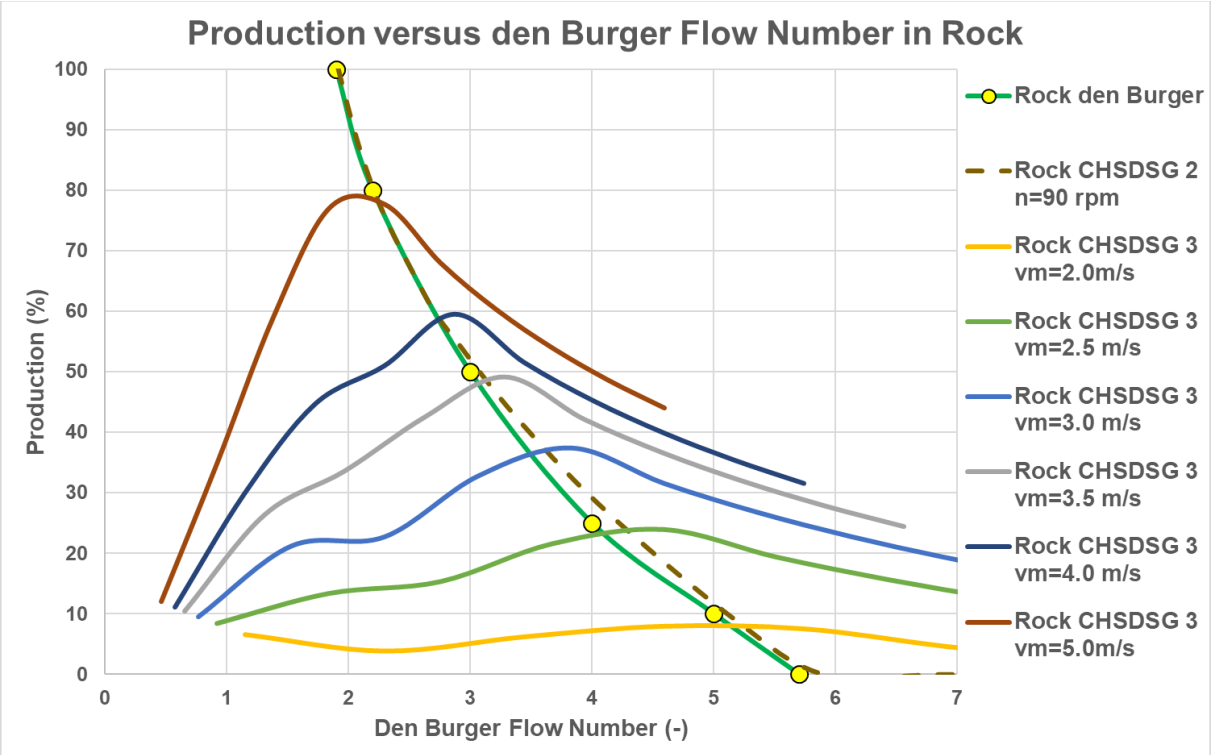

Figure 7-36: Production in rock n, from 20 to 200 rpm, including filling degree effect, model cutter head.

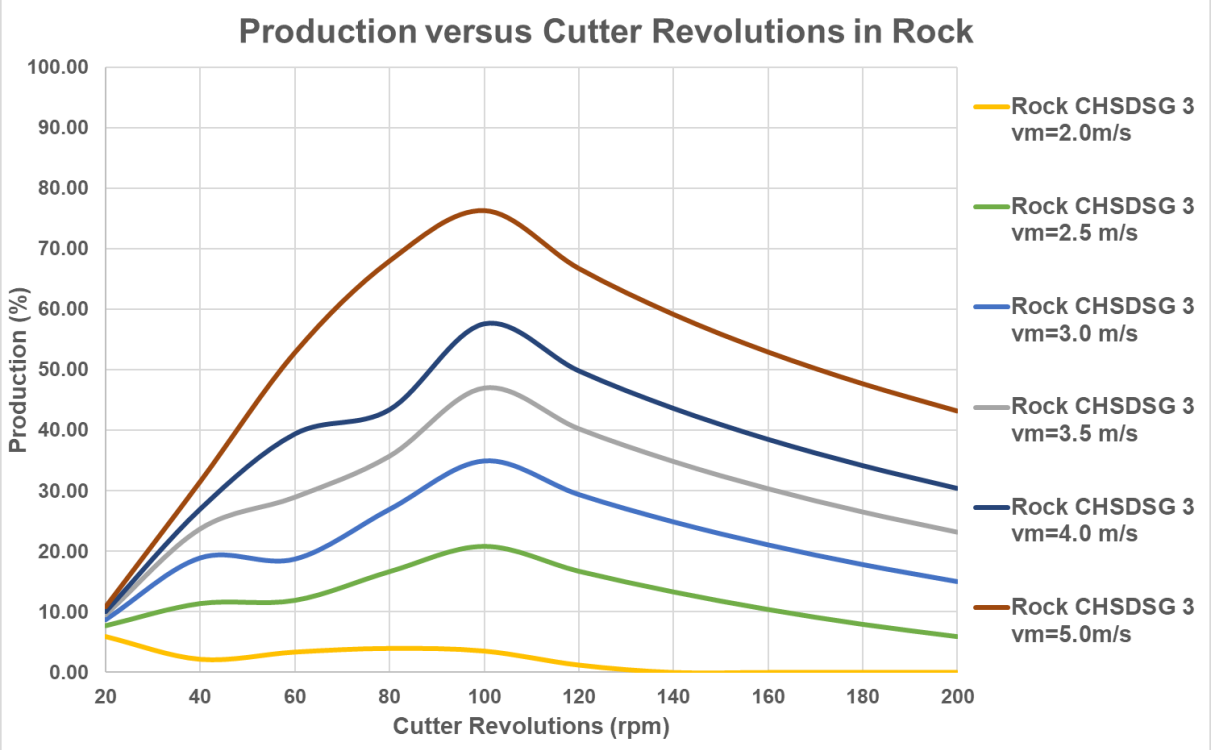

Figure 7-37: Production in rock, n from 20 to 200 rpm, including filling degree effect, model cutter head.

Figure 7-36 and Figure 7-37 show curves with this final spillage for values of **n** from 20 rpm to 200 rpm and mixture velocities of 2 m/s to 5 m/s for the model cutter head. The curves show a real maximum at 90-100 rpm, so they do match with Figure 7-30.

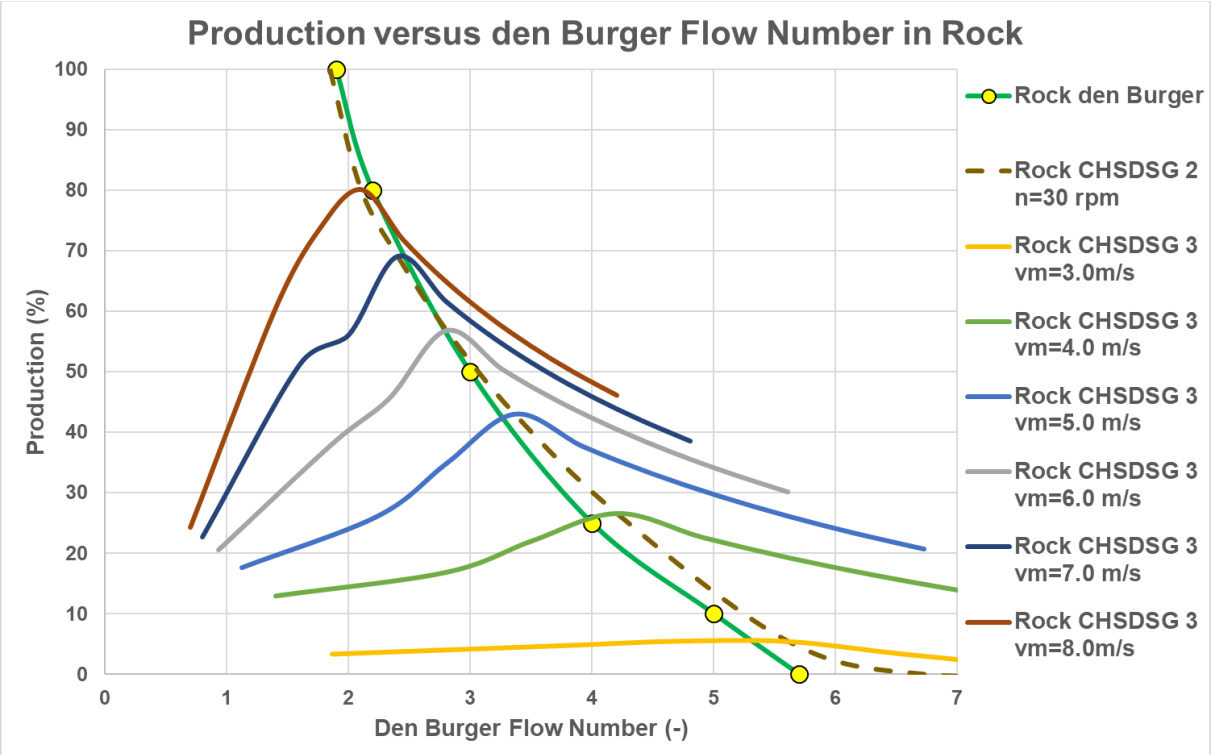

Figure 7-38: Production in rock, n from 10 rpm to 60 rpm, including filling degree effect, prototype cutter head.

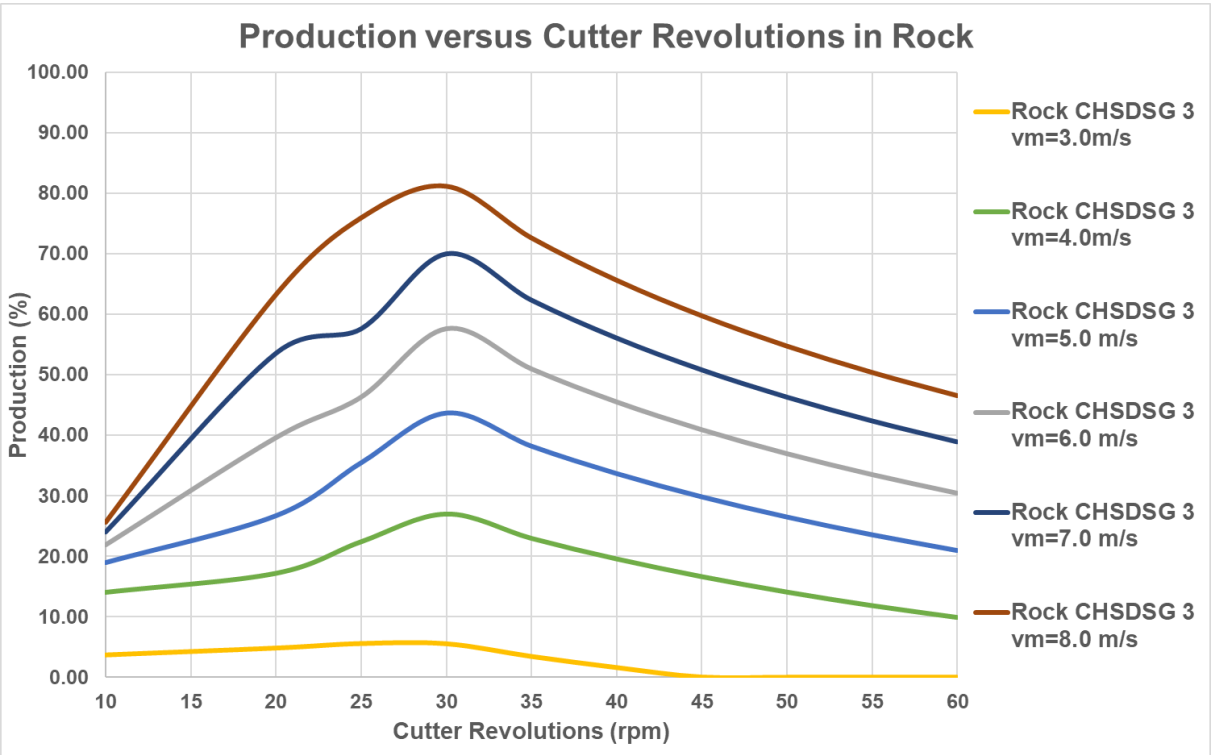

Figure 7-39: Production in rock, n from 10 rpm to 60 rpm, including filling degree effect, prototype cutter head.

Figure 7-38 and Figure 7-39 shows curve with this final spillage for values of **n** from 10 rpm to 60 rpm and mixture velocities of 3 m/s to 8 m/s for the prototype cutter head. The curves show a maximum at about 30 rpm for the case considered. The curves match with Figure 7-30. The scale laws according to chapter 2 are applied.

7.6. Conclusions and Discussion First Phase.

The preliminary model based on the affinity laws only contains the outer radii of the cutter head, the cutter head revolutions, the mixture flow, the axial flow and the cut production. This model matches well with the experimental data, also because it is calibrated on the experimental data. Still the shape of the maximum production curve for sand, gravel and plastic, match very well with the experimental data of den Burger (2003) for gravel and Delft Hydraulics for sand and plastic (see Mol (1977A)and (1977B), Moret (1977A) (1977B)). The detailed shape of the cutter head however is not yet included.

The advanced model based on the Euler equation for centrifugal pumps in its full form also contains the inner radii of the segments, the mixture densities, the inner and outer blade angles and the axial flow, where the preliminary model only uses the outer radii of the segments. Also, the part of the circumference cutting can be different for both segments, based on a cutter head with a certain ladder angle and the shape of the bank.

For the mixture density in segment 2 and also the axial flow, the carrier liquid density (water density) is assumed. Since equation **(7-61)** contains the mixture density in segment 1, the model is implicit because this density is only known after the widths of segments 1 and 2 are known. However, these widths depend on the mixture density. A good starting value can be found by assuming there is no spillage, so calculate the mixture density if all the solids leave the cutter head through the suction mouth. One can also apply a reasonable spillage percentage, like 25% and then calculate the mixture density.

The advanced model contains two iteration loops. The inner loop determines $\mathbf{w_1}$ based on a conical cutter head (here a cone angle of 79° is applied) and a certain mixture density. The outer loop iterates the mixture density to find the correct width of segment 1 $\mathbf{w_1}$. In reality the shape of the cutter head is more complicated. This can however be included in the iteration loop.

Both models behave the same, both qualitatively and quantitatively if the same factor $\boldsymbol{\alpha}$ is applied. The difference between the two models is the way $\boldsymbol{\alpha}$ is determined. In the preliminary model $\boldsymbol{\alpha}$ is just a constant. In the advanced model it depends on equation **(7-79)**, incorporating the inner radii, blade angles and mixture density. So, after calibration Figure 7-9, Figure 7-10, Figure 7-11 and Figure 7-12 are found.

Basically, the advanced model incorporates the geometry of the cutter head and mixture density differences in the factors $\boldsymbol{\varepsilon}$ and $\boldsymbol{\alpha}$**.** The dependency of the spillage on the cutter revolutions and the swing speed is the same in both models.

For the axial flow a formulation still has to be derived. One can first experiment with this flow to see how relevant this flow is. Increasing the axial flow will increase the width of segment 1 and thus the outflow of segment 1. In the advanced model, an increased outflow in segment 1 will also increase the spillage if the factor $\boldsymbol{\alpha}$ does not change. However, applying axial flow requires a new calibration with the experimental data, resulting in other proportionality factors. It is difficult to say whether and how this influences the spillage. In general, based on a sensitivity analysis, one can say that each 1% of mixture flow added as axial flow under operational conditions, will result in 0.5% to 1% of additional spillage.

The use of different cutting percentages for segments 1 and 2 does not affect the factor $\boldsymbol{\alpha}$, however it does affect the final spillage.

Figure 7-18, Figure 7-19, Figure 7-20 and Figure 7-21 show the productions for both the preliminary model (CHSDSG 1) and the advanced model (CHSDSG 2), both calibrated on the den Burger (2003) data for the model and the prototype cutter head. Of course, the results depend on the inputs used, so the two figures show trends and should not be used quantitatively. It is however proven here that it is possible to simulate the experimental data with a set of realistic inputs and also simulate correct trends.

Figure 7-32, Figure 7-33, Figure 7-34, Figure 7-35, Figure 7-36, Figure 7-37, Figure 7-38 and Figure 7-39 show the production graphs for sand and rock, model and prototype, including the filling degree effect (FD effect). These graphs show that there is a maximum production for the model cutter head cutting rock. Since the model is calibrated without this effect, the maximum production may occur at slightly different cutter head revolutions compared to the maximum occurring in the den Burger (2003) experiments. More experiments are required to carry out a thorough calibration. The FD effect seems to be valid for large particles with a high terminal settling velocity, so for rock and gravel. In sand the maximum production curves are not found.

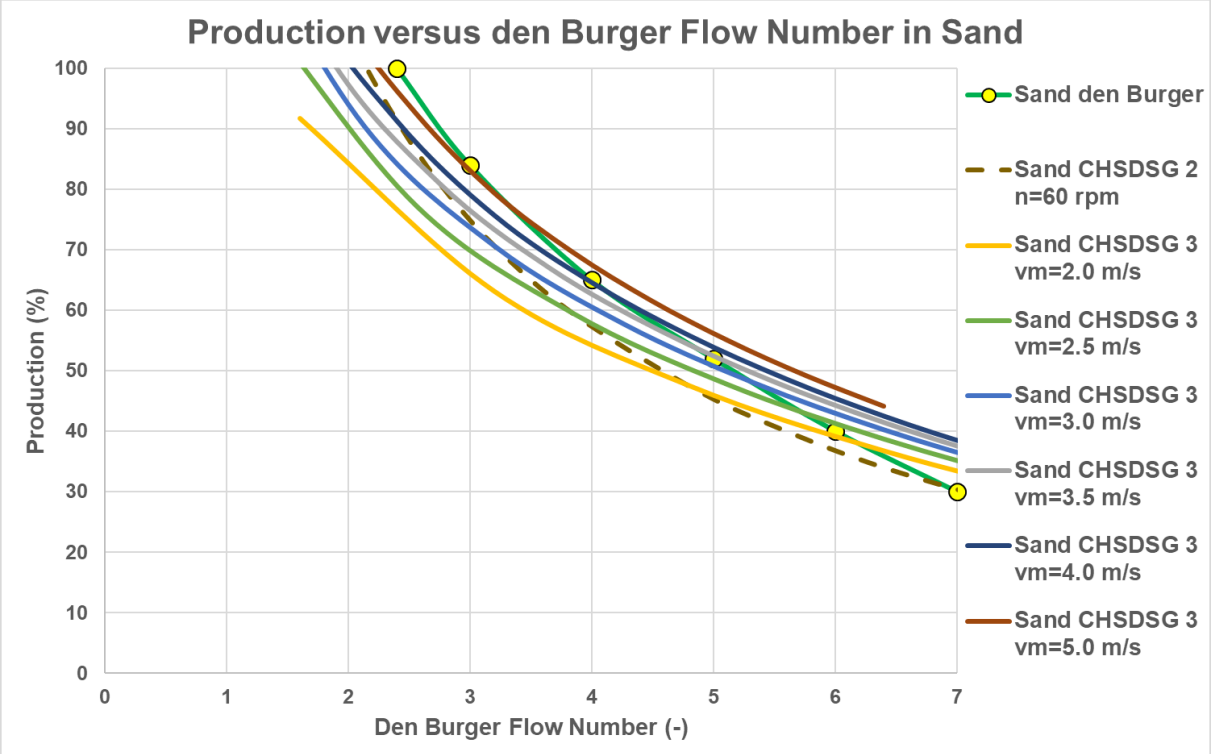

Figure 7-40: Production in sand, n from 20 to 200 rpm, including filling degree effect, model cutter head with ε=3.5.

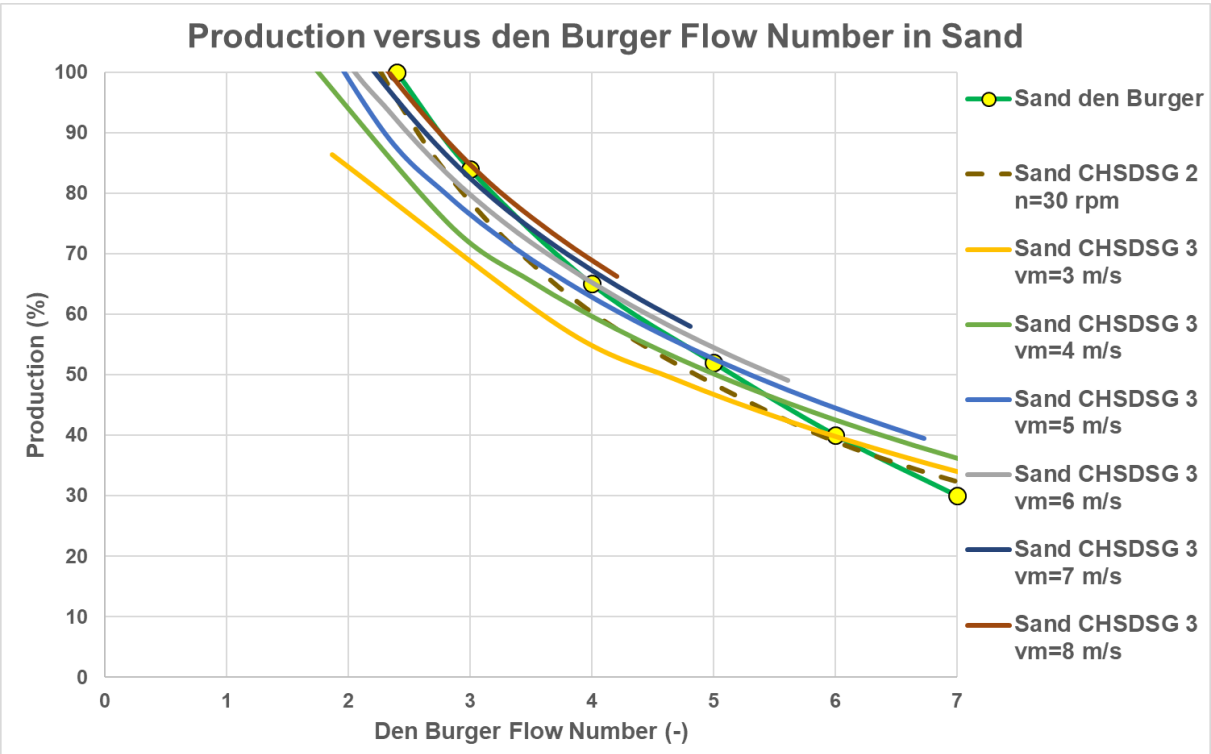

Figure 7-41: Production in sand, n from 10 to 60 rpm, including filling degree effect, prototype cutter head with ε=3.0.

Figure 7-32, Figure 7-33, Figure 7-34, Figure 7-35, Figure 7-36, Figure 7-37, Figure 7-38 and Figure 7-39 show an envelope that is shifted to the right compared to the experimental envelope. A shift of all the curves to the left can be achieved by increasing **ε** from 2.5 to 3.0 (prototype) - 3.5 (model) for sand in the model (see Figure 7-40 and Figure 7-41) and the prototype cutter head or adding a substantial axial flow of 0.03 m^3/s for the model or about 1 m^3/s for the prototype. So, it is very well possible to make the envelopes match as well, but most probably it should be done with a combination of adding some axial flow and increasing the constant **ε**. For rock, because of the gravity effect (terminal settling velocity), this is more complicated.

Figure 7-40 and Figure 7-41 show that the production curves for sand match the maximum production envelope well for increasing cutter head revolutions, very similar to the curves shown by den Burger (2003) in Figure 7-30 for rock/gravel. It should be mentioned however that den Burger (2003) used limited data, so the shapes of the curves in Figure 7-30 may differ from the shapes shown in this figure.

The scale laws from chapter 2 are applied to convert from model cutter head to prototype cutter head, since the mathematical model has been calibrated based on the model cutter head. Applying these scale laws gives very similar results for model and prototype cutter heads. The crucial factor here is that the terminal settling velocity also has to be scaled. If this is done properly, the production (spillage) curves are almost scale independent. This terminal settling velocity effect is not very important for fine and medium sands, but it is very important for gravels and rock.

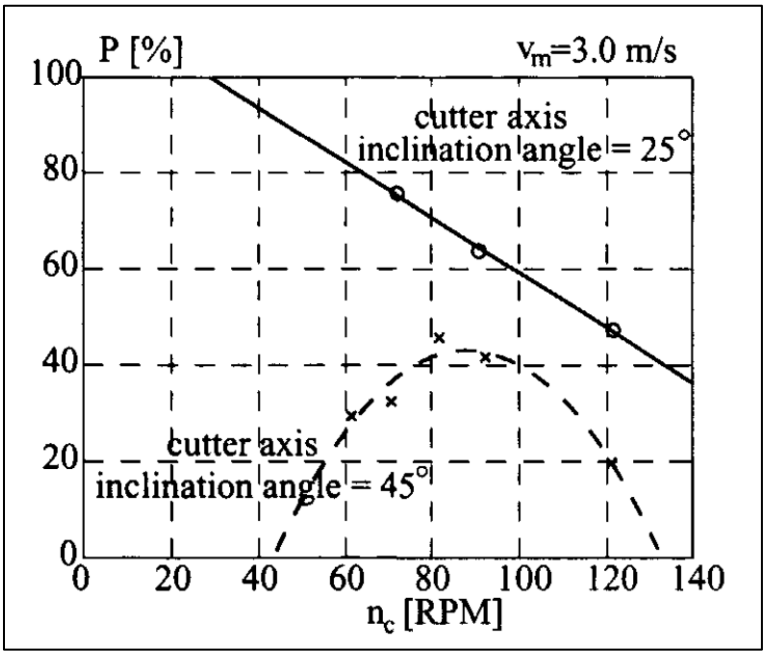

Figure 7-42: The influence of the ladder angle.

Figure 7-42 shows the influence of the ladder angle as measured by den Burger (2003). A smaller ladder angle gives less spillage and thus a higher production. The reason is probably the fact that the particles have to be elevated proportional to the ladder angle. The smaller the ladder angle the less elevation the less spillage. The particle settling velocity plays in important role in this. Figure 7-43 and Figure 7-44 show the production curves for the two ladder angles considered. The settling velocity of the particles used in the den Burger experiments was about 0.45 m/s, the grey curves. The grey curves match well with the experimental data points, for both the 25° ladder angle and the 45° ladder angle. The shapes of the curves are completely different compared to the shapes assumed by den Burger, but then there were not enough experimental data points to draw real conclusions about the shapes of the production curves. So also, for the 25° ladder angle there seems to be an optimum production, but its at about 60 rpm. So, it is now shown by the experimental data points.

Of course, every model can still be improved, however currently there is no additional experimental data to do so, so the full advanced model gives enough information for the time being. It is also possible to calibrate or improve the model with complimentary CFD calculations.

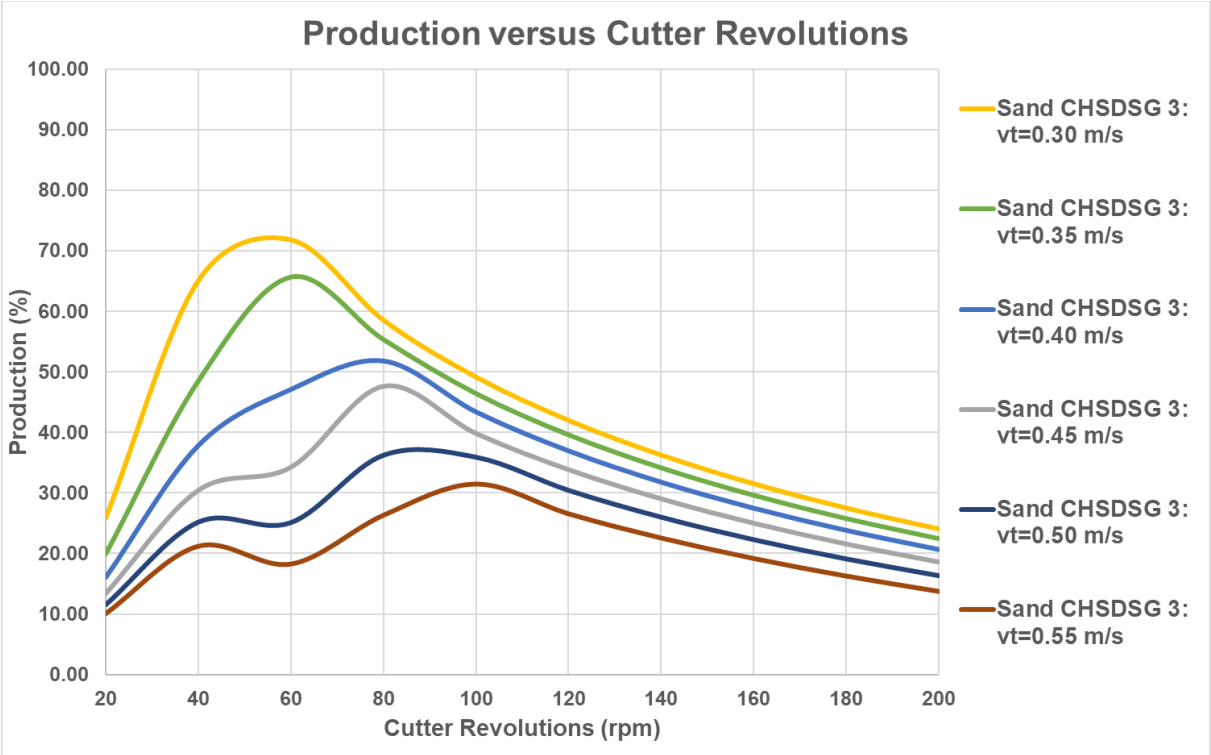

Figure 7-43: Production curves as a function of the settling velocity, ladder angle 45°.

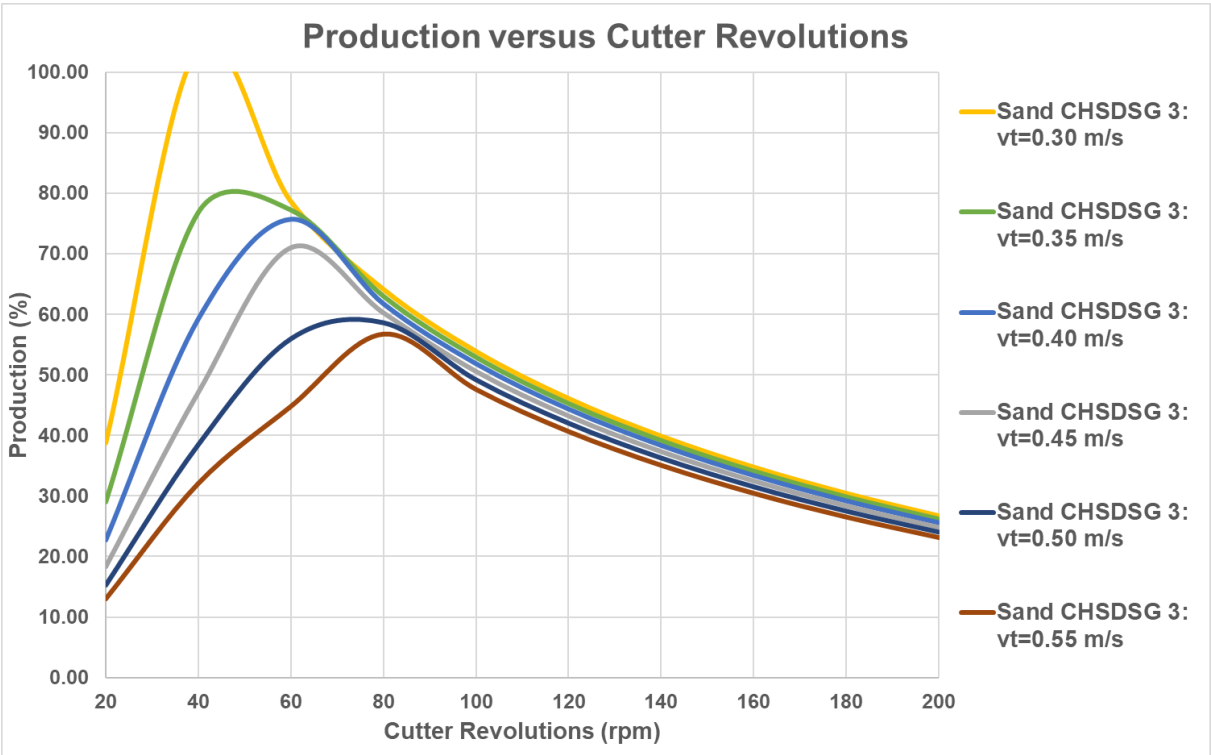

Figure 7-44: Production curves as a function of the settling velocity, ladder angle 25°.

The goal of developing an analytical model resulting in spillage of a cutter head has been reached. The advanced model (CHSDSG 3) gives the spillage as a function of the operational parameters, the swing speed, cutter revolutions, mixture flow, the cutter geometry and terminal settling velocity of the particles.

7.7. Miltenburg (1982) Experiments, a Cold Case.

Miltenburg (1982) carried out many experiments with 5 different cutter heads. This research was almost forgotten; however, the research was reported very detailed including the experimental data so it's like a cold case. Most of the experiments were carried out with a crown cutter head as shown in Figure 7-45. This cutter head has an outside diameter of 0.45 m (ring diameter 0.395 m) and a height of 0.29 m (excluding the ring). The experiments were carried out with revolutions of 100 rpm and 180 rpm and mixture velocities of 3 m/s, 4 m/s and 5 m/s. Because it was difficult to set these parameters exactly, there was some scatter in the values realized. About 50% of the cross section of the cutter head was actually cutting with swing speeds of on average 0.09 m/s, 0.18 m/s and 0.27 m/s. Also, here there was some scatter in the swing velocities. The combinations of revolutions and mixture velocities gave dimensionless Bu numbers of about 3 (n=100 rpm and v_m=5 m/s), 4 (n=100 rpm and v_m=4 m/s), 5.2 (n=100 rpm and v_m=3 m/s) and (n=180 rpm and v_m=5 m/s), 7 (n=180 rpm and v_m=4 m/s) and 9 (n=180 rpm and v_m=3 m/s). The grouping of the experimental data by Bu number is shown in Figure 7-48. The swing speed does not influence the Bu number. The figure shows a decreasing production with an increasing Bu number, as is expected based on the theoretical model. The scatter however is very large.

Figure 7-45: The crown cutter head used by Miltenburg (1982).

Miltenburg (1982) used 6 different configurations of the crown cutter head and of course carried out the experiments overcutting and undercutting. The 6 configurations are:

1. No skirts, short cone, suction mouth at 0°, see Figure 7-46 for the short cone, the base case.
2. No skirts, long cone, suction mouth at 0°, see Figure 7-46 for the long cone.
3. No skirts, long cone, suction mouth at +30°, see Figure 7-46 for the long cone.
4. No skirts, long cone, suction mouth at -30°, see Figure 7-46 for the long cone.
5. Skirts, long cone, suction mouth at 0°, see Figure 7-46 for the long cone and Figure 7-47 for skirts.
6. Skirts, long cone, suction mouth at +30°, see Figure 7-46 for the long cone and Figure 7-47 for skirts.

Besides the 6 configurations, each test has been carried out overcutting and undercutting. So, many subsets of experiments can be made. Although Figure 7-48 and Figure 7-49 seems to show a lot of scatter, the subsets will show that often there is a reason for the variation.

Figure 7-46: The crown cutter head (right), the short cone (left) and the long cone (right).

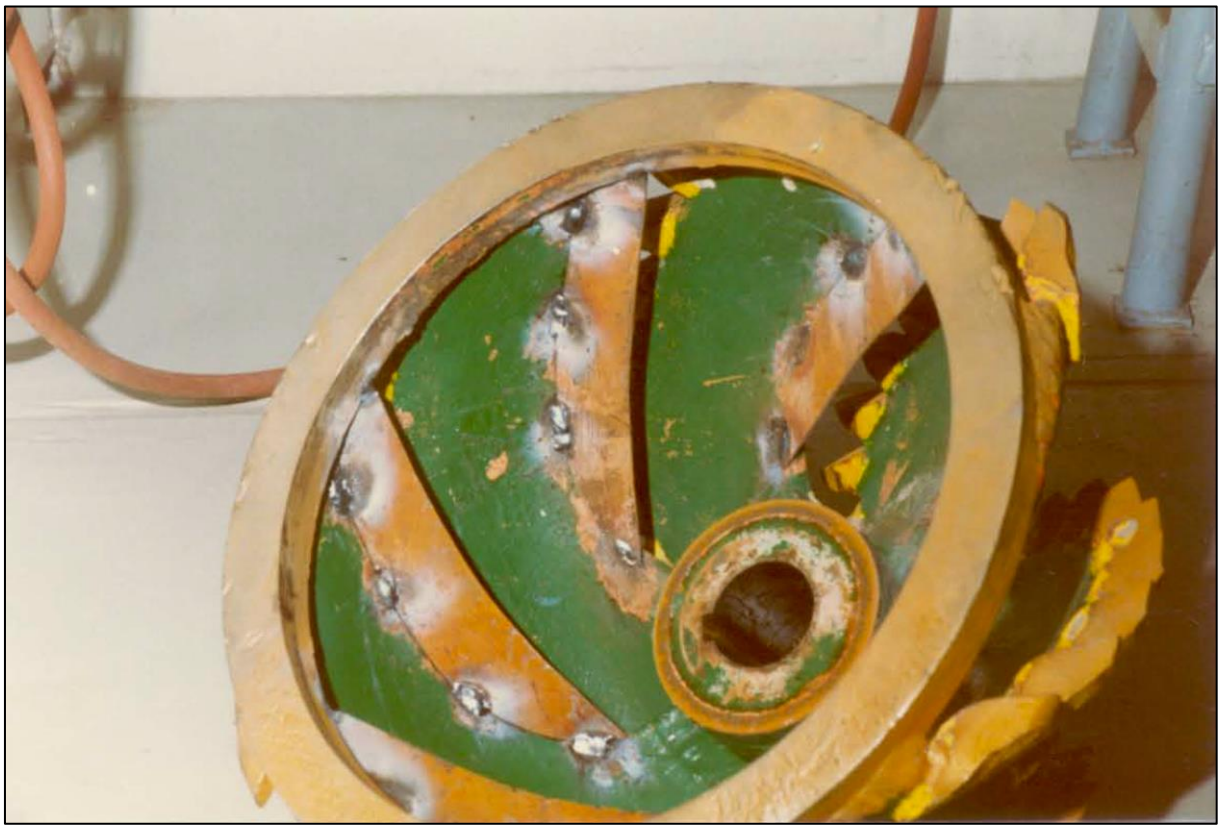

Figure 7-47: Skirts mounted inside the crown cutter head.

7.7.1. Miltenburg (1982) Experiments, All Data with Lower & Upper Limit.

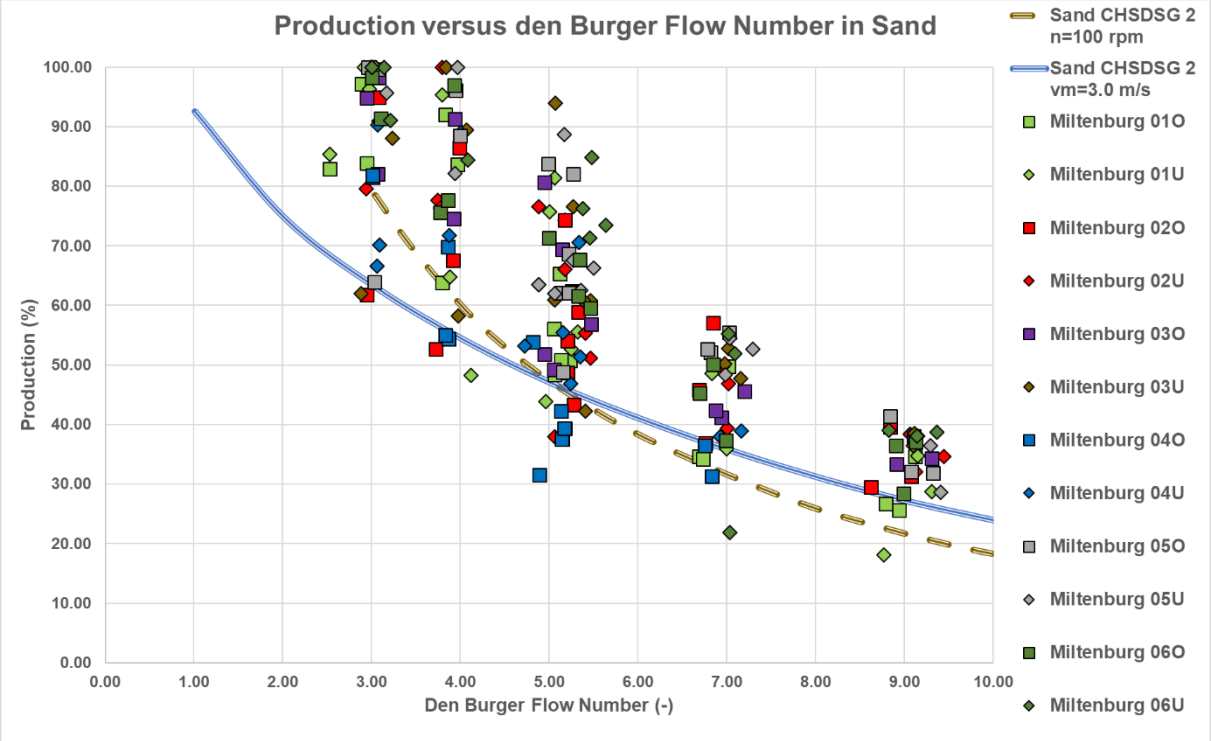

Figure 7-48: All experiments of Miltenburg (1982) with a rock cutter head in sand, with model lower limit.

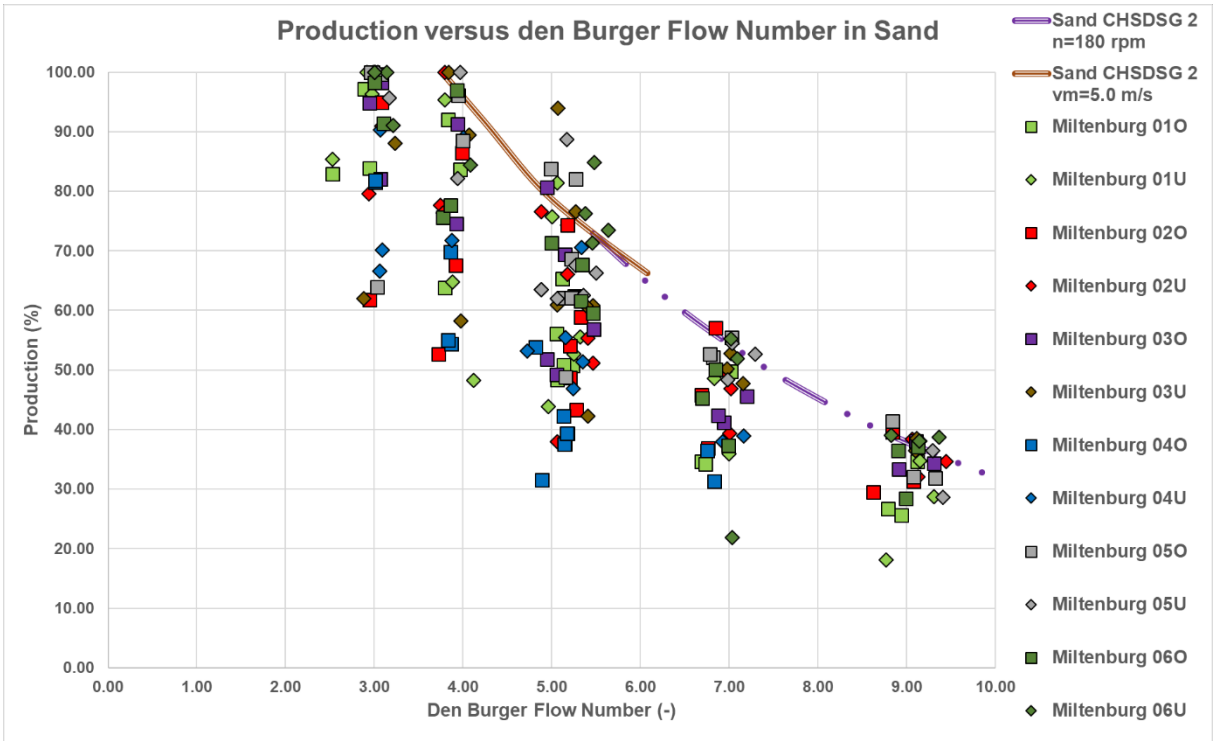

Figure 7-49: All experiments of Miltenburg (1982) with a rock cutter head in sand, with model upper limit.

Figure 7-48 and Figure 7-49 show all data for all 6 configurations and the lower and upper production limits of the CHSDSG 2 model (so without the filling ratio effect). The lower limit is determined from n=100 rpm and v_m=3 m/s. The upper limit is determined from n=180 rpm and v_m=5 m/s. From these figures it is clear that most (about 87.5%) of the data points are in between the upper and lower limit. If data points that are more or less on the limits are not counted to be outside, 92% is within the limits (16 points outside).

7.7.2. Miltenburg (1982) Experiments, Raw Data.

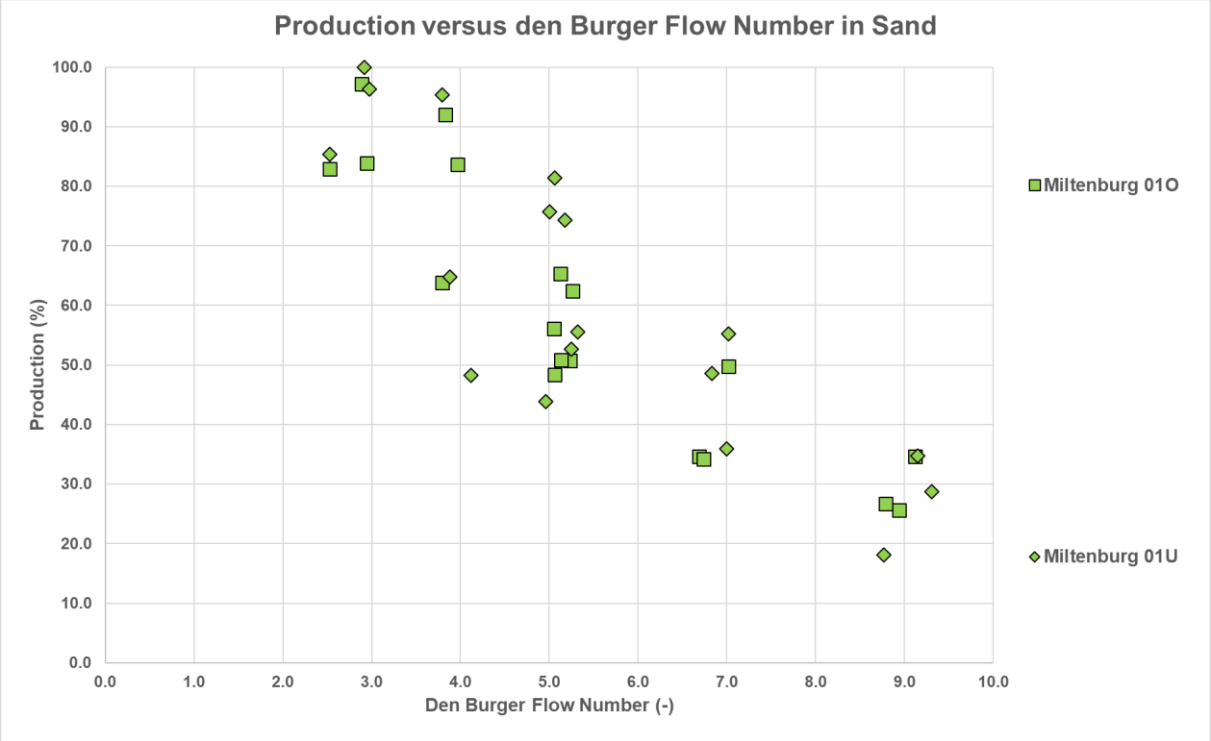

Figure 7-50: Miltenburg (1982) Experiments 01O and 01U, the base case (no skirts, short cone, sm at 0°).

Figure 7-50 shows that for this base case there is hardly any difference between the overcutting and the undercutting process.

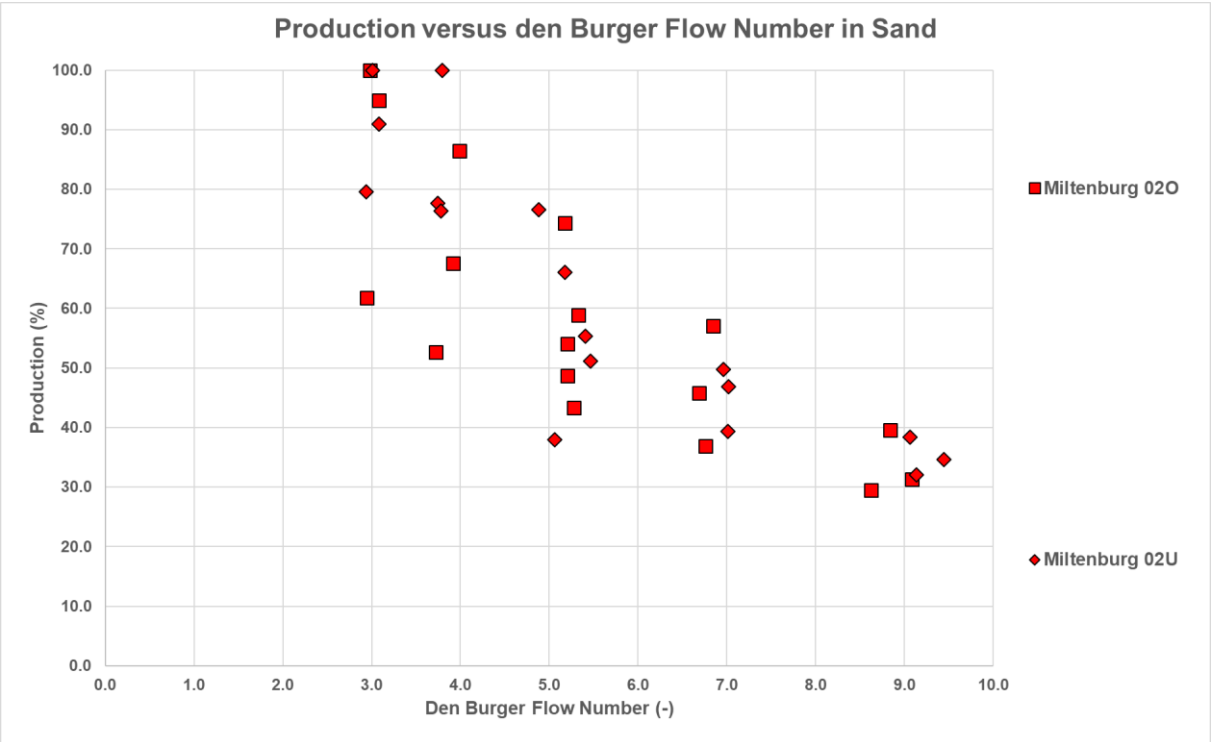

Figure 7-51: Miltenburg (1982) Experiments 02O and 02U (no skirts, long cone, sm at 0°).

Figure 7-51 shows a very light tendency of less spillage undercutting, but it's not significant enough to draw conclusions.

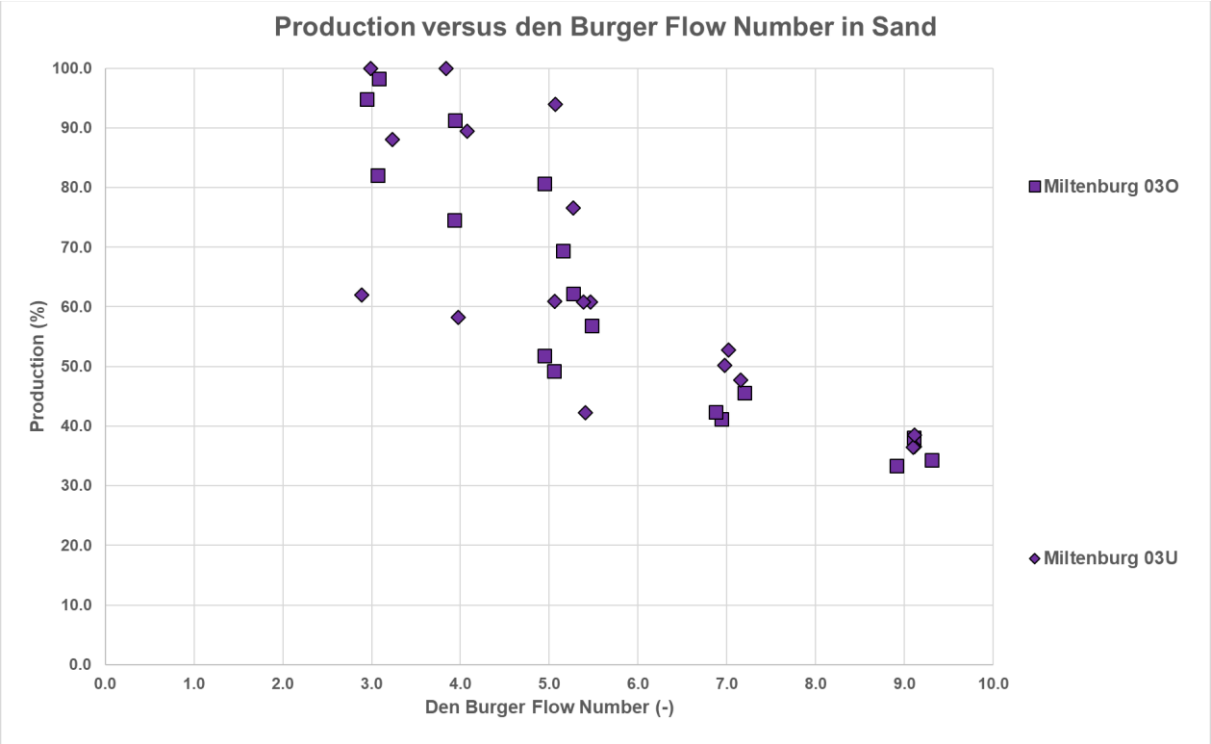

Figure 7-52: Miltenburg (1982) Experiments 03O and 03U (no skirts, long cone, sm at +30°).

Figure 7-52 does not show a difference in spillage between the overcutting and undercutting processes.

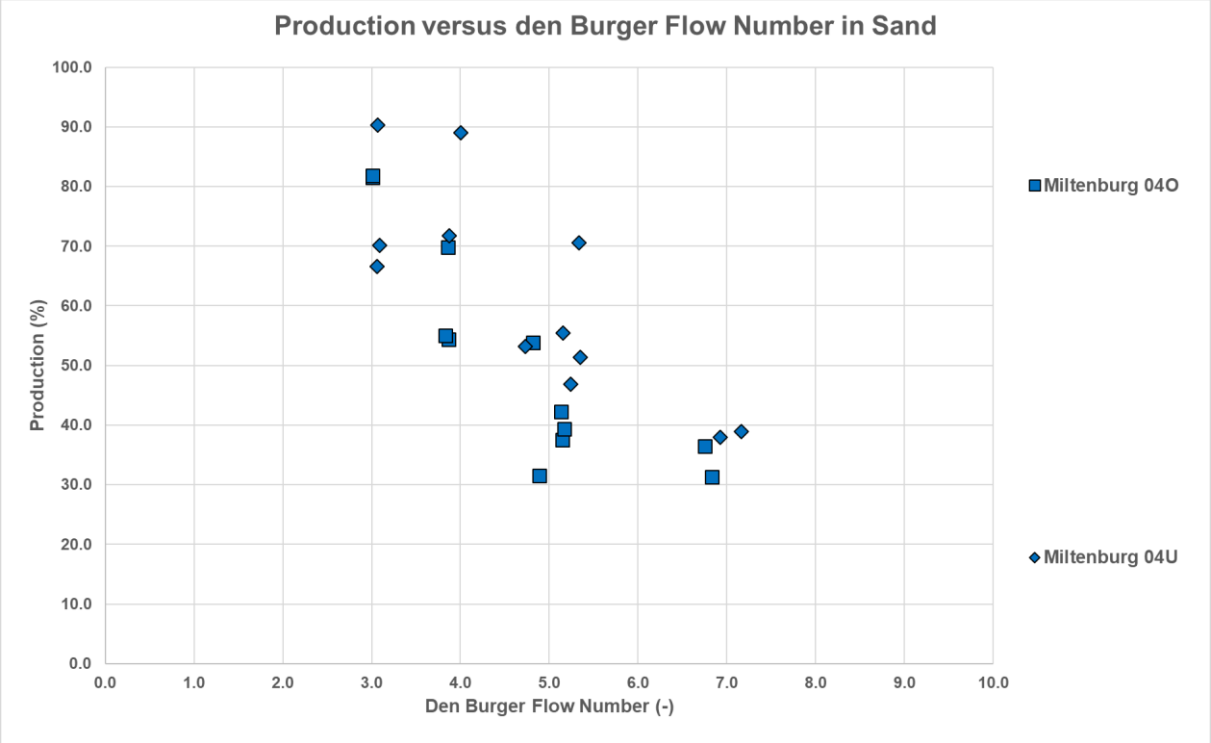

Figure 7-53: Miltenburg (1982) Experiments 04O and 04U (no skirts, long cone, sm at -30°).

Figure 7-53 shows less spillage for the undercutting experiments, compared to the overcutting experiments, especially at lower Bu numbers.

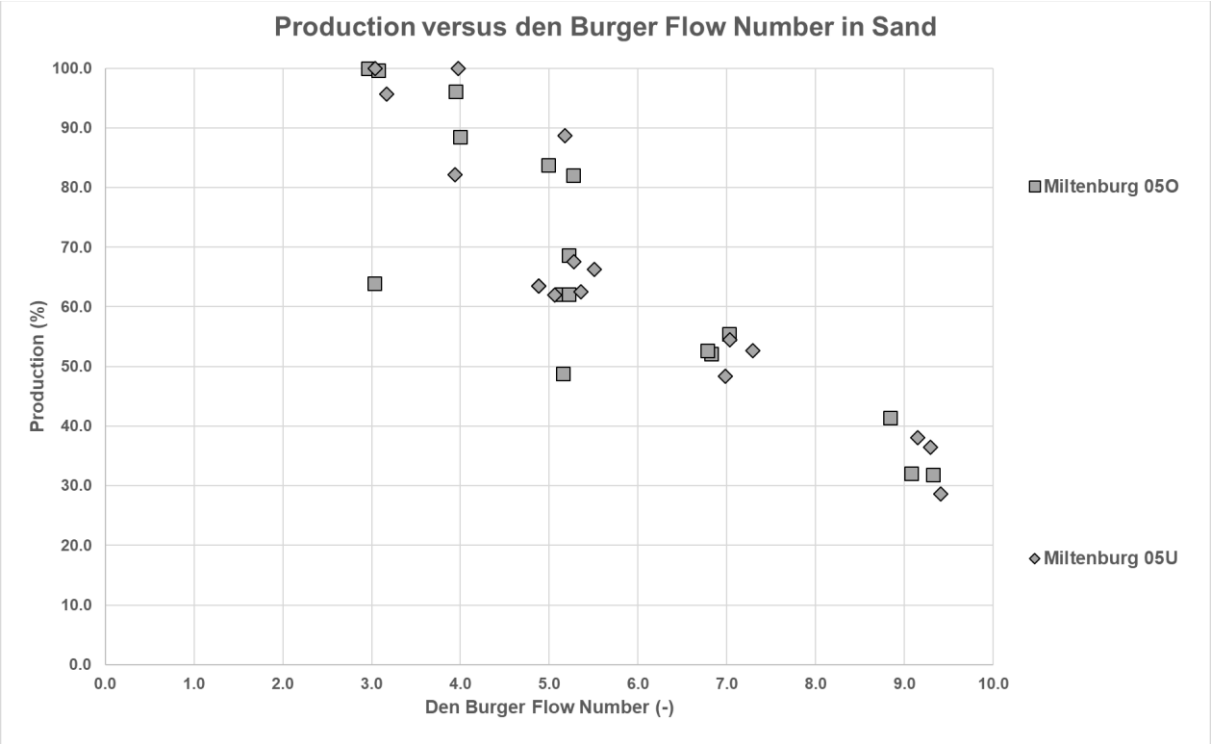

Figure 7-54: Miltenburg (1982) Experiments 05O and 05U (skirts, long cone, sm at 0°).

Figure 7-54 shows less spillage for the undercutting experiments, compared to the overcutting experiments, especially at lower Bu numbers. At high Bu numbers there is hardly a difference.

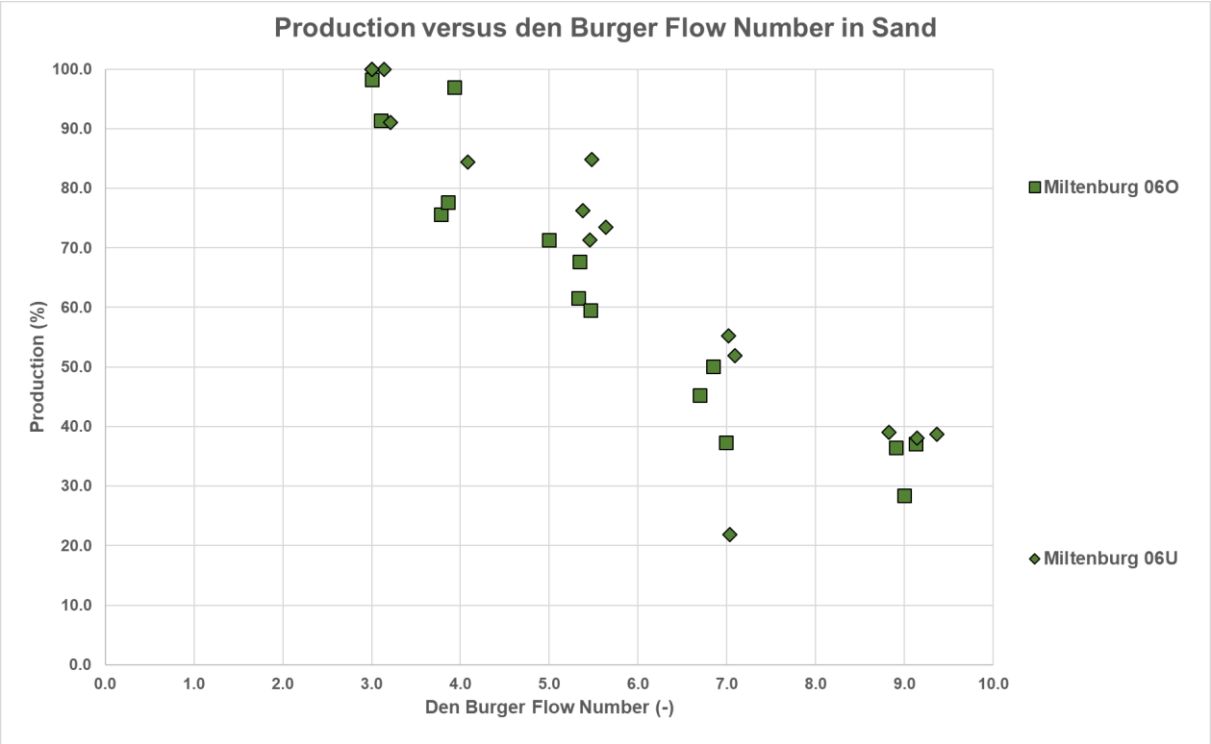

Figure 7-55: Miltenburg (1982) Experiments 06O and 06U (skirts, long cone, sm at +30°).

Figure 7-55 shows less spillage for the undercutting experiments, compared to the overcutting experiments, especially at lower Bu numbers. At high Bu numbers there is hardly a difference.

7.7.3. Miltenburg (1982) Experiments, Revolutions.

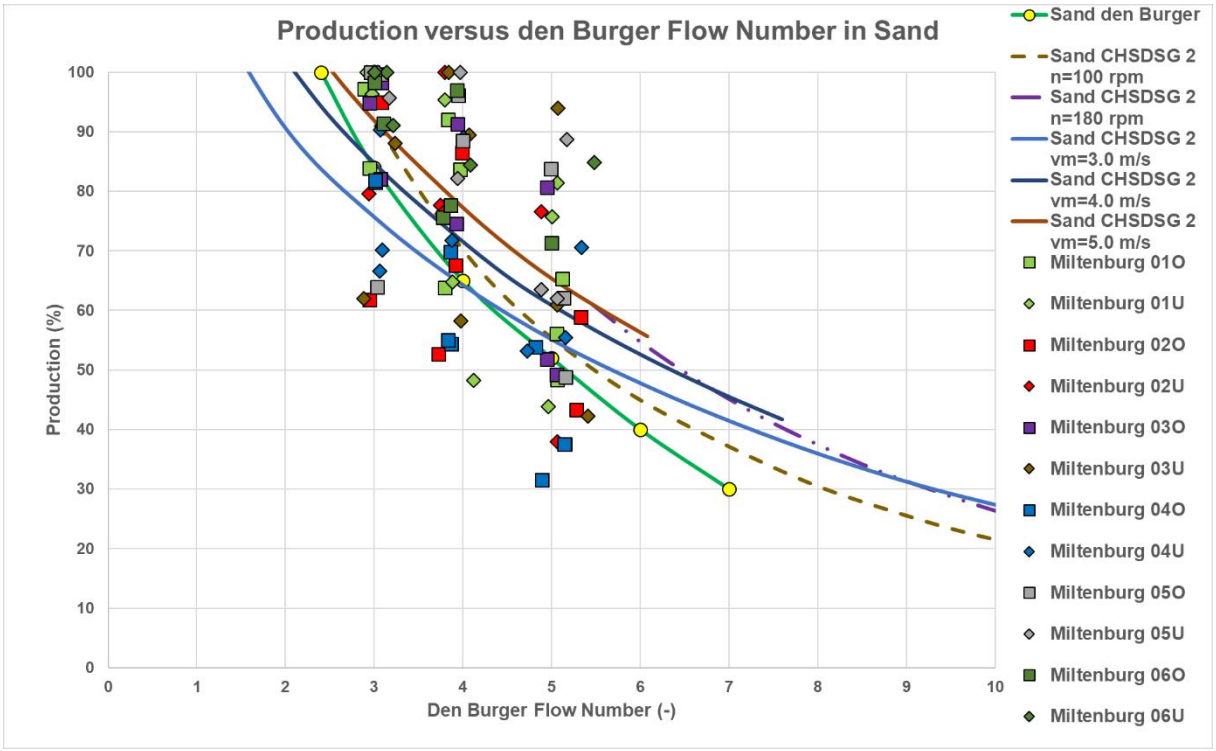

Figure 7-56: Experiments with revolutions of about 100 rpm.

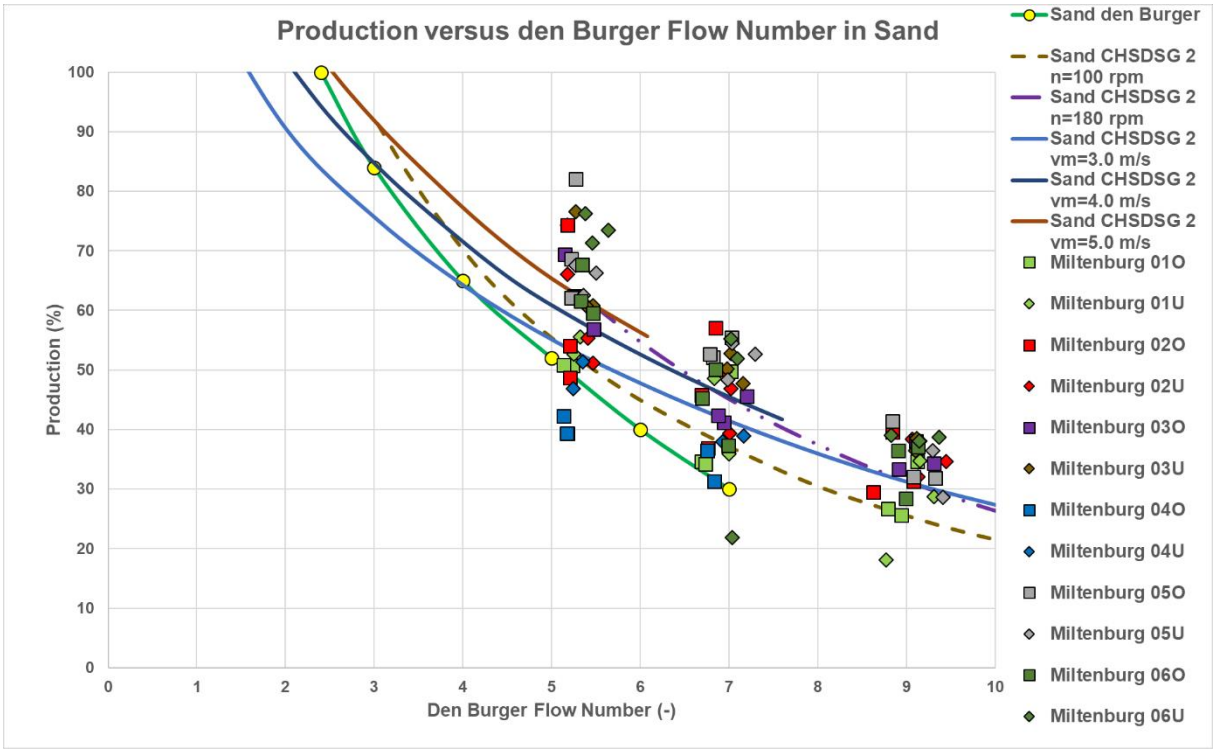

Figure 7-57: Experiments with revolutions of about 180 rpm.

Figure 7-56 and Figure 7-57 show clearly that higher revolutions give more spillage. However, at the highest Bu number of 9 the spillage is less than expected in chapters 2, 3 and 4 based on the den Burger (2003) observations. This implies that a correction of the model is required for large Bu numbers.

7.7.4. Miltenburg (1982) Experiments, Swing Speeds.

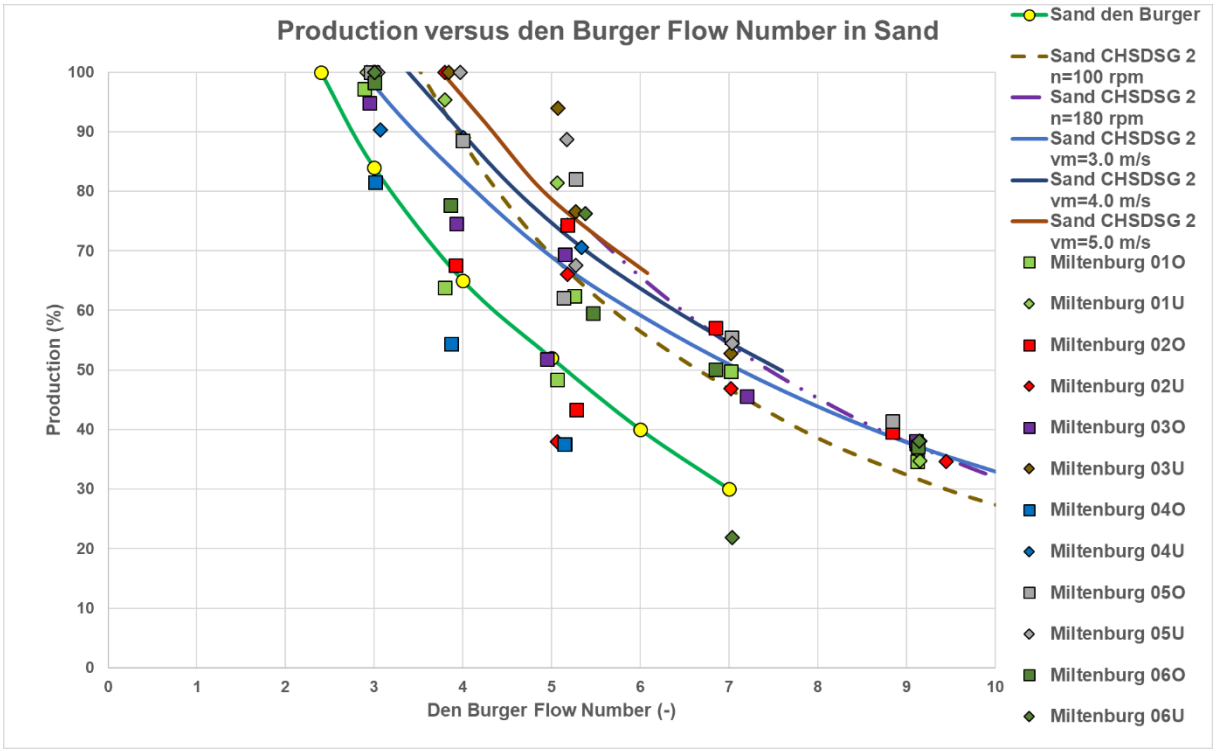

Figure 7-58: Experiments with a swing velocity of about 0.09 m/s.

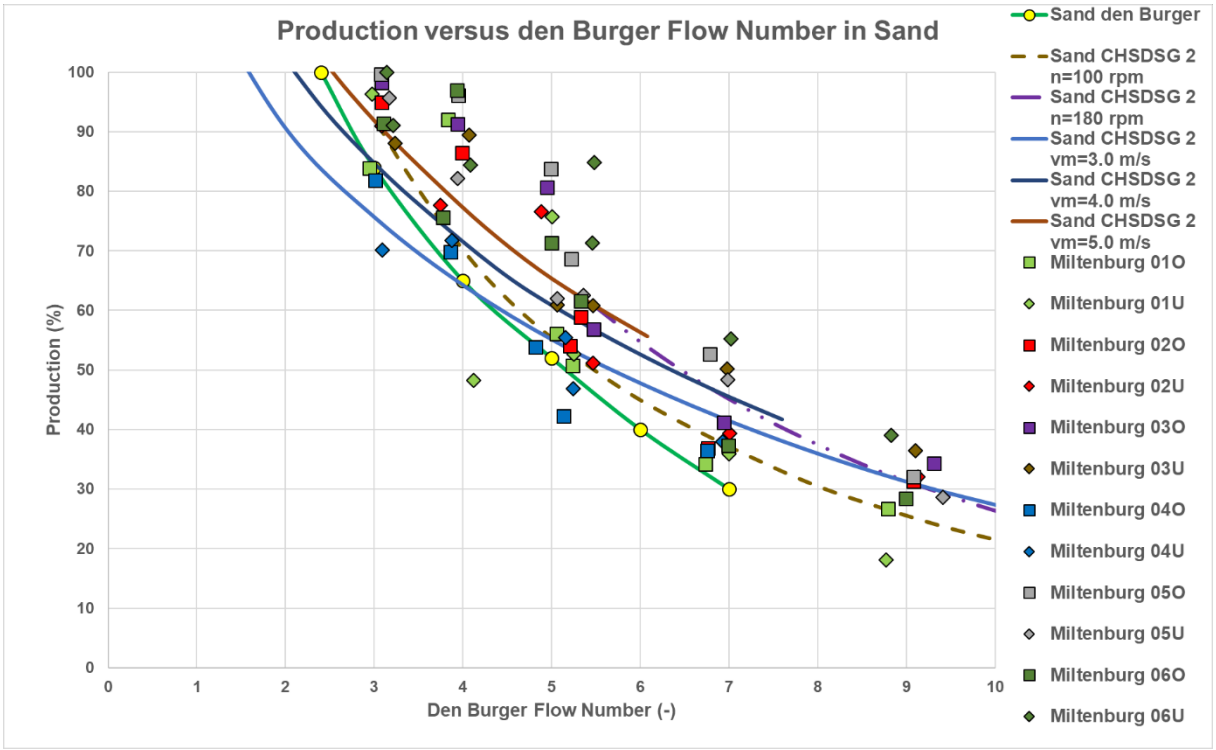

Figure 7-59: Experiments with a swing velocity of about 0.18 m/s.

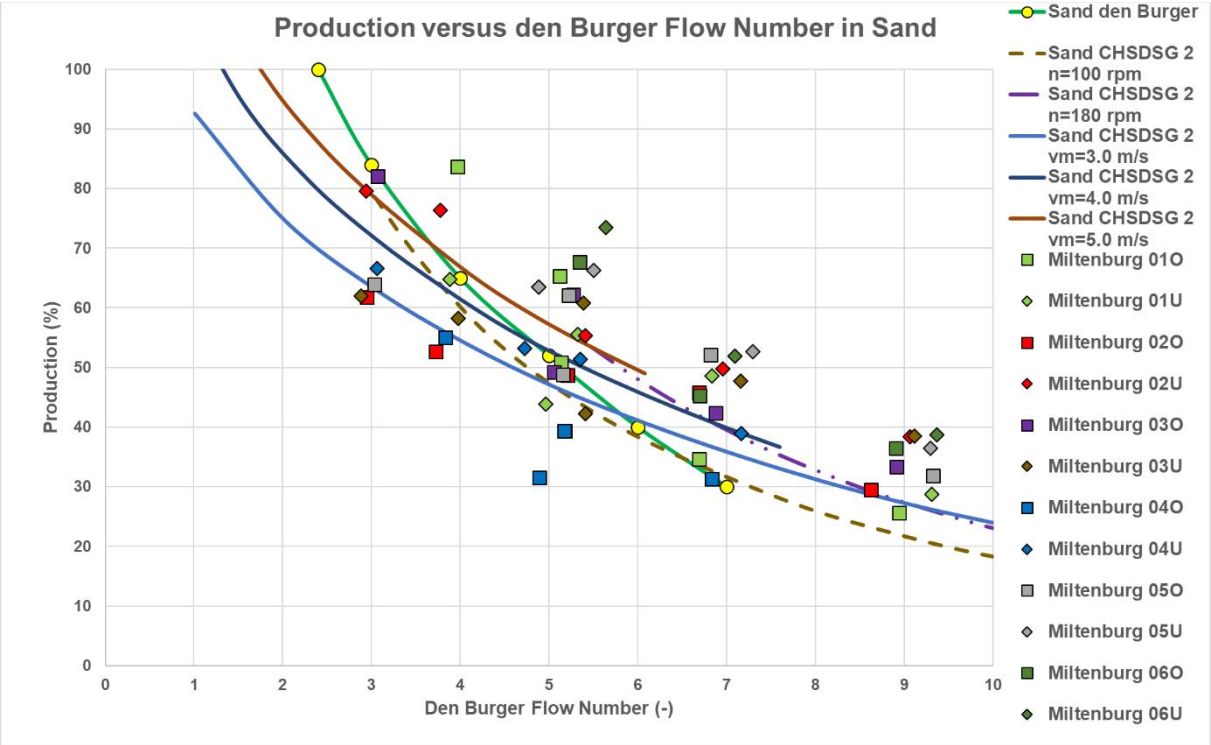

Figure 7-60: Experiments with a swing velocity of about 0.27 m/s.

Figure 7-58, Figure 7-59 and Figure 7-60 show the experimental data for 3 average swing speeds of 0.09 m/s (0.076-0.111 m/s), 0.18 m/s (0.162-0.207 m/s) and 0.27 m/s (0.240-0.333 m/s). Part of the scatter in these graphs is because of the range of swing speeds. Another part of the scatter is because of the 6 configurations and the overcutting and undercutting process, so this in fact is not really scatter.

The 3 figures show clearly that an increasing swing speed gives more spillage. The figures also show that the corrected CHSDSG 2 model overall gives a good prediction. The CHSDSG 2 model is corrected with an additional mixture forming term based on the Bu number.

$$\mathbf{Spillage} = \frac{Q_{1,out} \cdot \left(C_{vs} + \left(C_{vs,max} - C_{vs} \right) \cdot \left(0.1 \cdot \left(\frac{v_t \cdot \sin(\theta) \cdot \pi \cdot r_r^2}{Q_m} \right)^2 + \left(\frac{Bu}{10.8} \right)^3 - \left(\frac{Bu}{12} \right)^4 \right) \right)}{Q_s} \qquad \textbf{(7-126)}$$

$$\textbf{With :} \quad C_{vs,max} = \frac{Q_s}{Q_{1,out}}$$

The maximum concentration is limited to a value between 0.5 and 0.6, since this gives solid sand.

7.7.5. Miltenburg (1982) Experiments, Configuration Comparison.

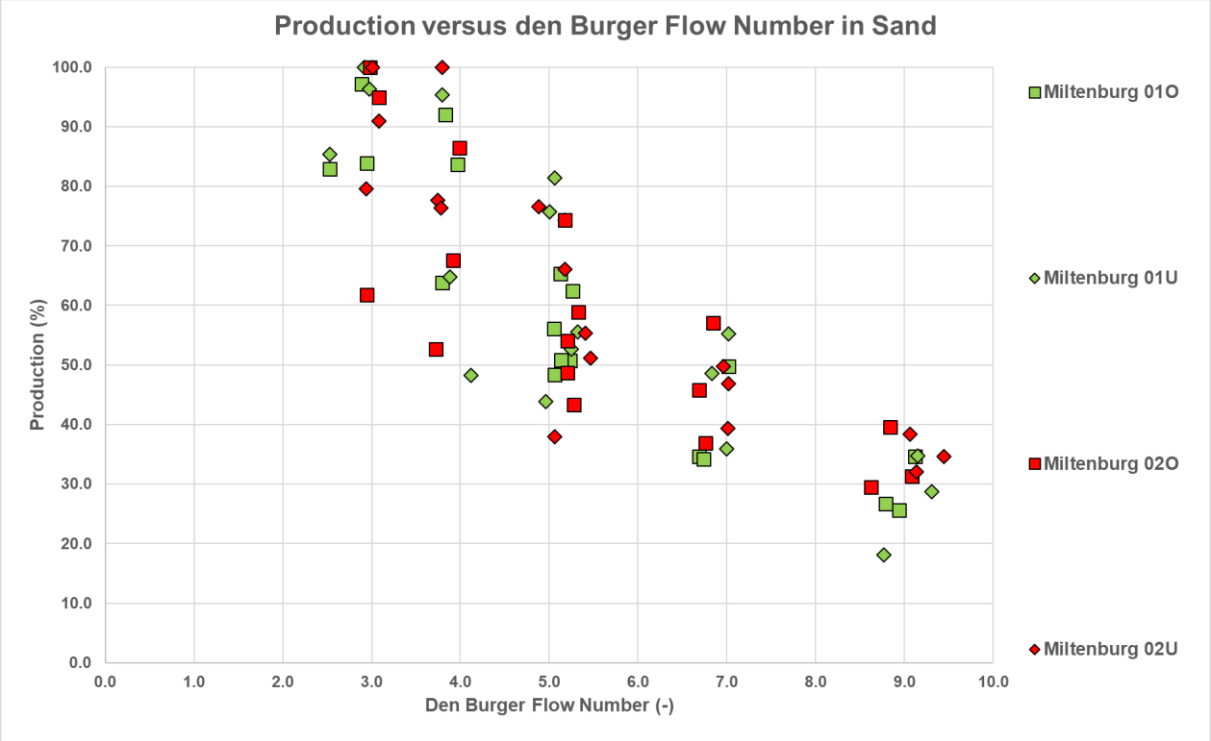

Figure 7-61: Configuration 01 (no skirts, short cone, sm at 0°) versus 02 (no skirts, long cone, sm at 0°).

Figure 7-61 compares configurations 01 and 02. Only at very high Bu numbers the long cone gives less spillage.

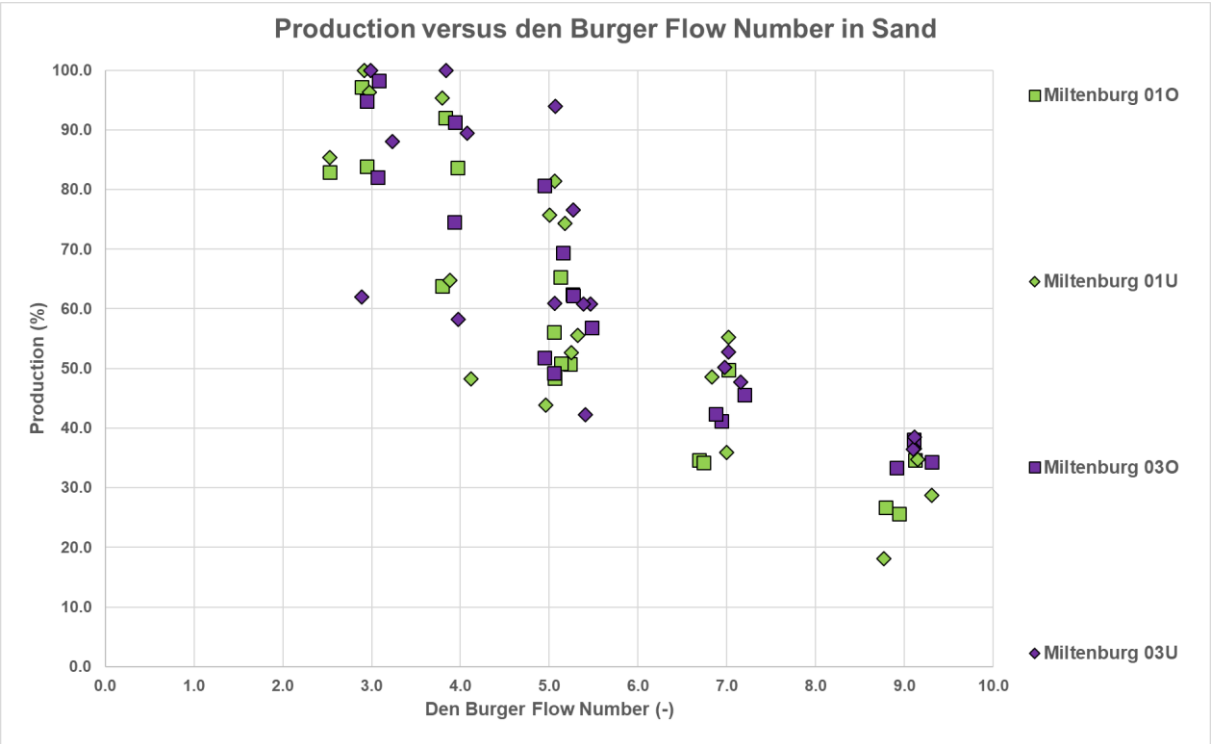

Figure 7-62: Configuration 01 (no skirts, short cone, sm at 0°) versus 03 (no skirts, long cone, sm at +30°).

Figure 7-62 compares configurations 01 and 03. Overall, the long cone with a rotated suction mouth gives less spillage, so a higher production.

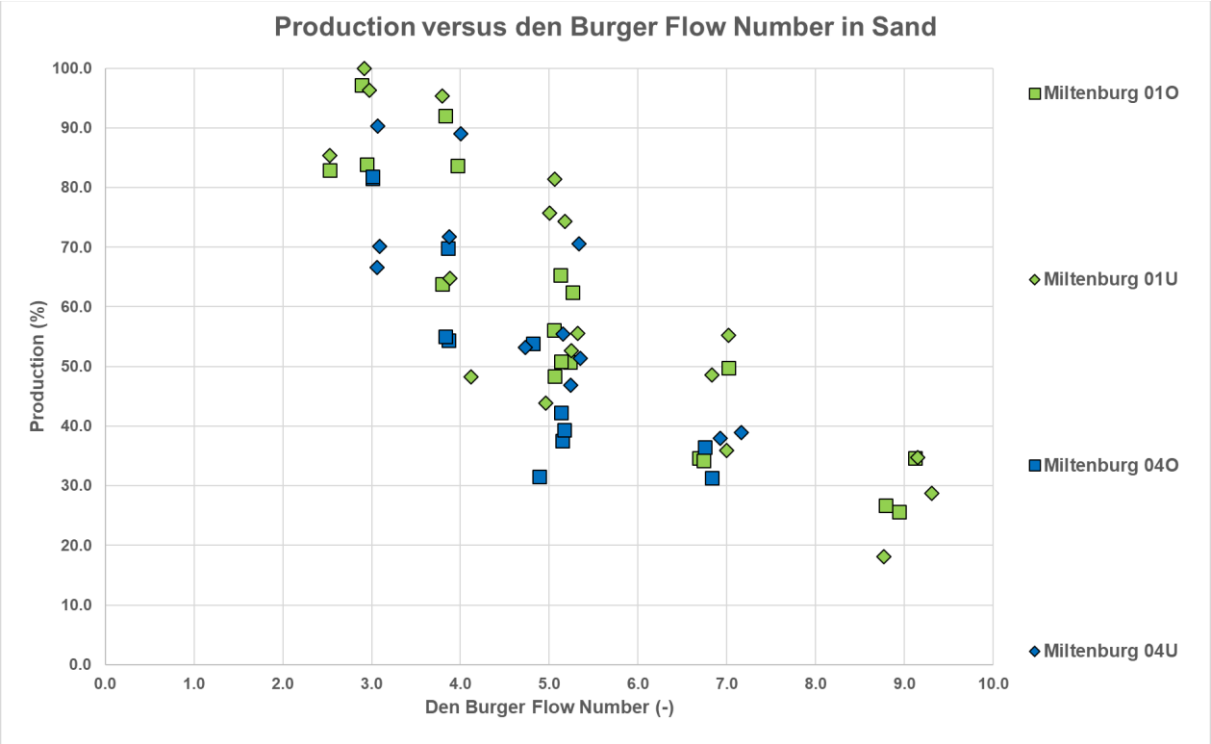

Figure 7-63: Configuration 01 (no skirts, short cone, sm at 0°) versus 04 (no skirts, long cone, sm at -30°).

Figure 7-63 compares configurations 01 and 04. Overall configuration 04 gives more spillage. Unfortunately, there were no data for the highest Bu number for configuration 04.

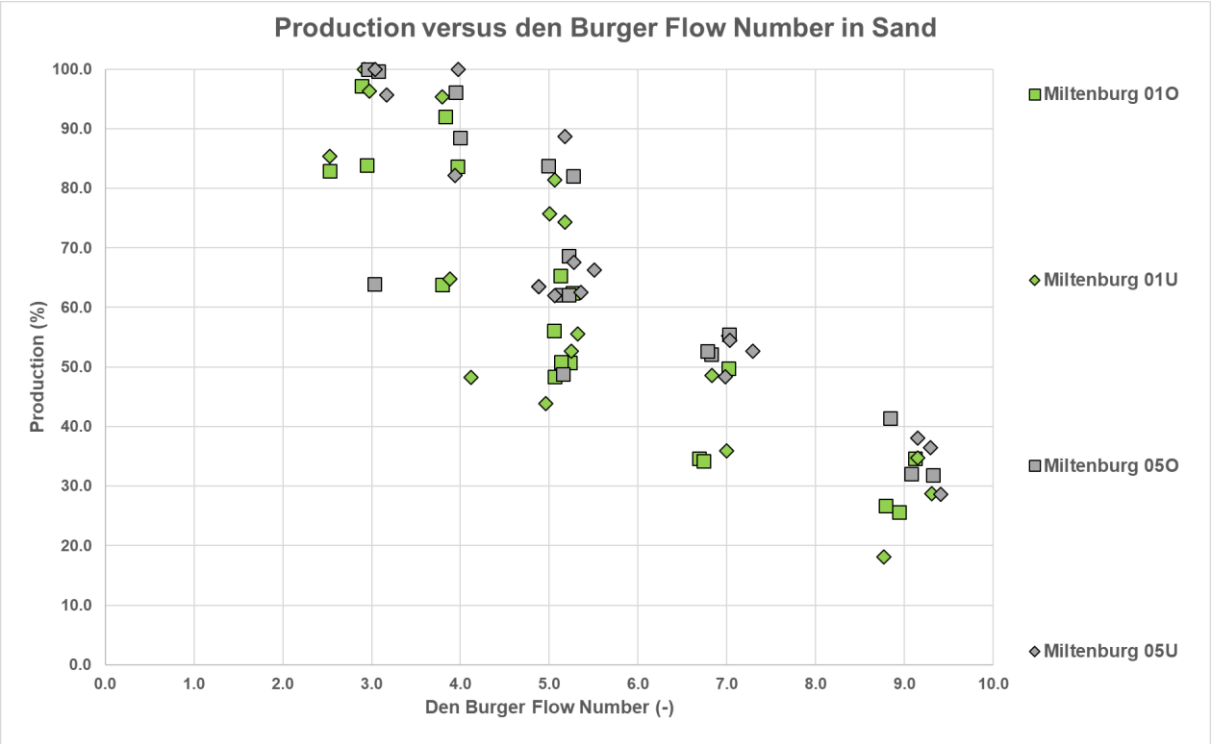

Figure 7-64: Configuration 01 (no skirts, short cone, sm at 0°) versus 05 (skirts, long cone, sm at 0°).

Figure 7-64 compares configurations 01 and 05. It is clear from this figure that configuration 05 gives less spillage over the full range of Bu numbers.

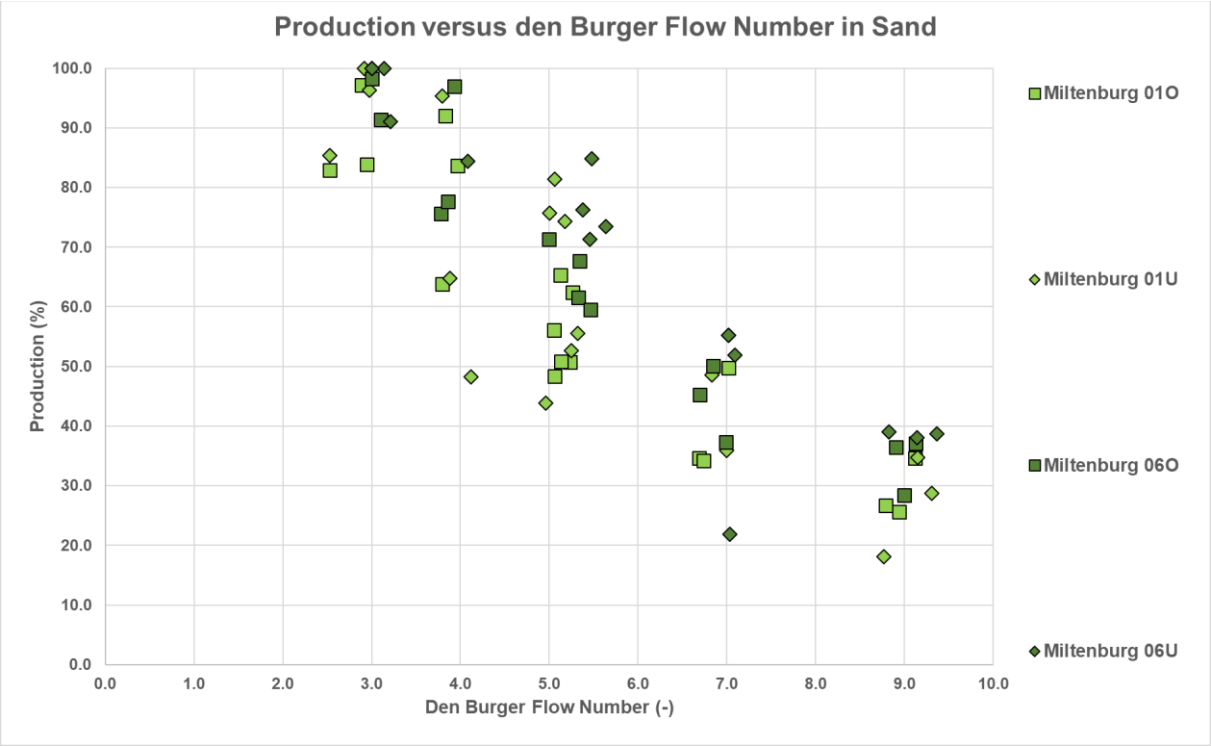

Figure 7-65: Configuration 01 (no skirts, short cone, sm at 0°) versus 06 (skirts, long cone, sm at +30°).

Figure 7-65 compares configurations 01 and 06. Also, here it is clear that configuration 06 gives les spillage over the full range of Bu numbers.

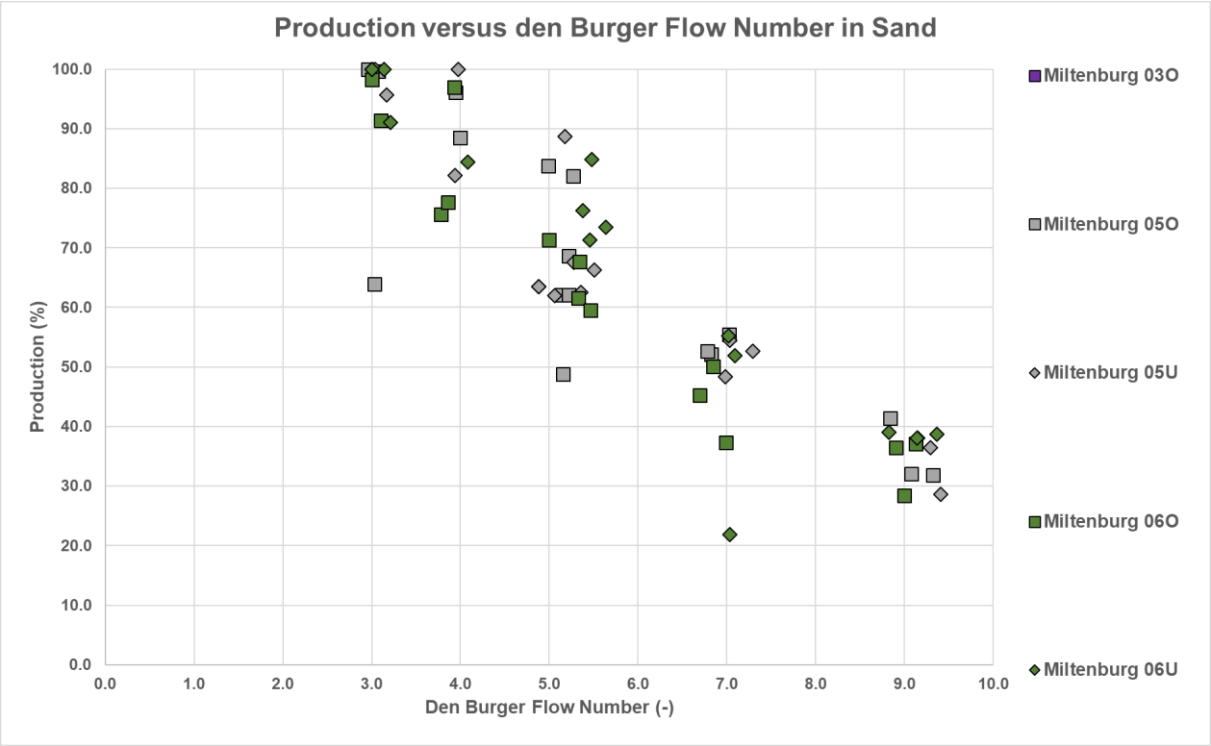

Figure 7-66: Configuration 05 (skirts, long cone, sm at 0°) versus 06 (skirts, long cone, sm at +30°).

Figure 7-66 compares configurations 05 and 06, the two configurations with the least spillage. One cannot really draw conclusions here, although configuration 06 may be a bit better. Both configurations seem to have about the same spillage over the full range of Bu numbers, maybe except some individual data points.

7.8. Final Conclusions.

The goal of this research, to develop an analytical model for the spillage of a cutter head, has been reached. The original idea to base this on the affinity laws of centrifugal pumps was successful but did not incorporate the detailed geometry of the cutter head. Using the Euler equation for centrifugal pumps gives a more detailed analytical model, not contradicting the affinity law model, since the affinity laws are a simplification of the Euler equation.

The basic concept of the model is, that above a certain rpm, there is an outflow of mixture near the ring of the cutter head and in inflow of water in the rest of the cutter head, so the top part. Further there is an outflow of mixture into the suction mouth and an inflow of sand because of the cutting process. In the model also, an axial inflow of water near the hub is incorporated, but this axial flow has not really been used in the validation of the model, since it's hard to quantify. Without this axial flow the model already gives good results.

The model is based on two continuity equations. The continuity of volume flow and the continuity of mass flow.

At first it is assumed that the mixture outflow near the ring and the mixture outflow through the suction mouth have the same solids concentration, based on the inflow of solids due to the cutting process. This assumption gives good predictions of the spillage and production at low Bu numbers, but not at high Bu numbers. At high Bu numbers (high revolutions, low mixture outflow), the spillage is underestimated in sand, but even more in rock. This is compared with the findings of Mol (1977A) and (1977B), Moret (1977A) and (1977B) and den Burger (2003). A term, increasing the concentration of the outflow near the ring is added, based on the Bu number is added. Of course, limiting this concentration to a reasonable maximum. This term gives a good correction for sand, but not yet for rock. So, a second term is added, based on the settling velocity of the particles in relation with the average mixture flow in the cutter head. This second term gives a good correction for gravel/rock.

The experimental data used so far is limited to Bu numbers of 6-7. When analyzing old data of Miltenburg (1982) Bu numbers up to 9 were found. Miltenburg carried out about 100 experiments, both overcutting and undercutting, with 6 different cutter head configurations and 5 different cutter heads. Most experiments were carried out with a crown rock cutter head, suitable for cutting rock and sand. So, these experimental data are used for the validation of the model. From these data it appeared that the model overestimated the spillage for very large Bu numbers. The model gave almost 100% spillage, while the data showed 60%-70% spillage. An additional term has been added to the concentration of the outflow near the ring to correct for this. This additional term is based on the Bu number. With this correction a good correlation is found between the model and the experimental data.

With the final model, 92% of the data points are within the upper and lower limit of the model, based on mixture flow and revolutions. The trends based on revolutions, mixture velocity and swing speed are well predicted, although individual experiments may deviate, because of the 6 configurations.

Configurations 01, 02 and 03 show hardly any difference in the spillage. These configurations have a short cone, a long cone and a suction mouth rotated 30° in the rotation direction of the cutter head. Configuration 04 with a long cone and a 30° rotation of the suction mouth, but now counter rotated with respect to the rotation direction of the cutter head, has a spillage of up to 20% more than the base case and also with respect to configurations 02 and 03. Configurations 05 and 06 with skirts and 06 with a suction mouth rotated 30° in the rotation direction of the cutter head, both have a spillage of about 10% less than the base case and also with respect to configurations 02 and 03. So, the main measure to reduce spillage is the use of skirts, resulting in about 10% less spillage. The difference between configuration 04 on one hand and configuration 05 and 06 on the other hand already give a scatter of 30% spillage. Figure 7-67 and Figure 7-68 show the data of configurations 01, 02 and 03 with the upper and lower limits according to the model. Now only 1 data point is above the upper limit and only 2 data points are below the lower limit, regarding the production. The whole area in-between the lower and upper limit is covered by the model developed. Configurations 04, 05 and 06 require a different value for the constant ε, which is set to 2.5 for the base case. Configuration 04 requires a larger value, while configurations 05 and 06 require a smaller value. The Miltenburg data do not show the filling ratio effect, most probably because only 2 cutter head revolutions were applied.

The den Burger number Bu should be determined using the cutter head diameter close to the ring. This diameter is often larger than the ring diameter. Since the centrifugal pump effect is determined by the actual diameter of the cutter head and not the ring diameter, the model input should also be the actual cutter diameter near the ring.

The scale laws from chapter 2 should be applied to convert from model to prototype. These scale laws give very good results regarding the similarity of production curves, comparing model and prototype.

All in all, the model presented here is very promising and has the advantage of easy implementation. However, to make a good prediction, the geometry of the cutter head and the operational parameters must be known. Using different cutter head geometries and particle diameters (sand, gravel or rock) may require different coefficients in the model.

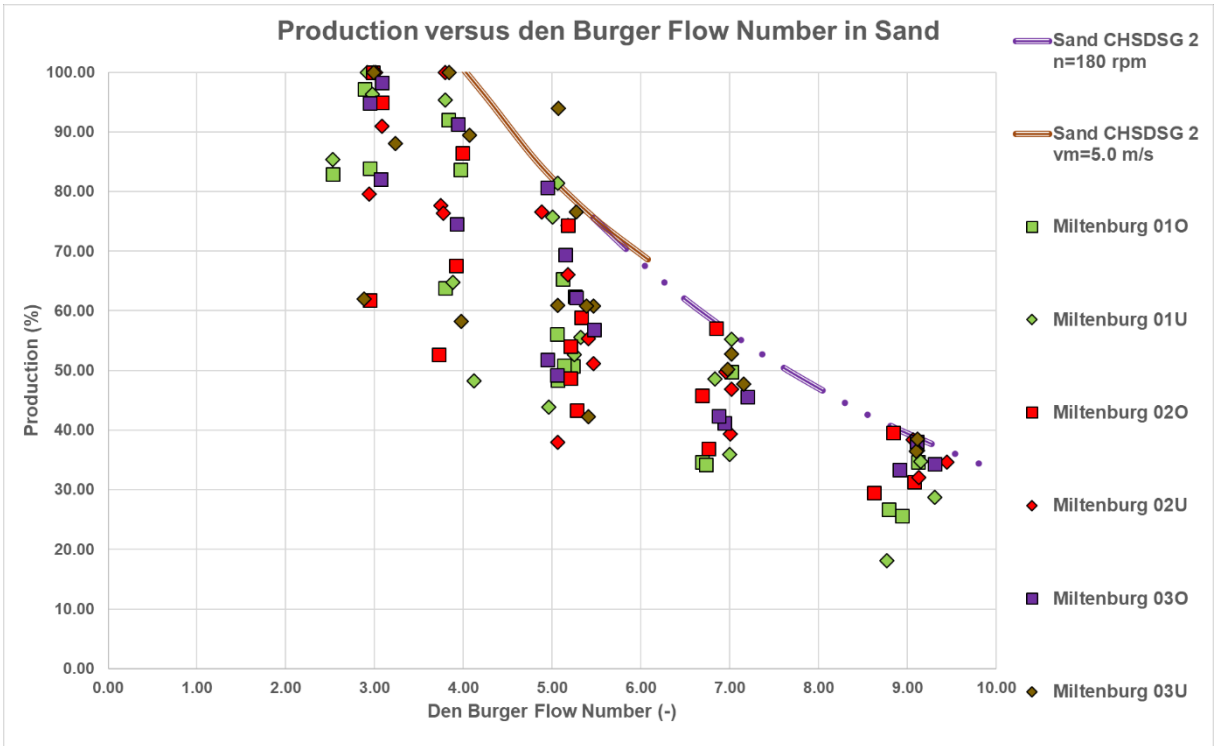

Figure 7-67: All experiments of Miltenburg (1982) with a rock cutter head in sand, with model upper limit.

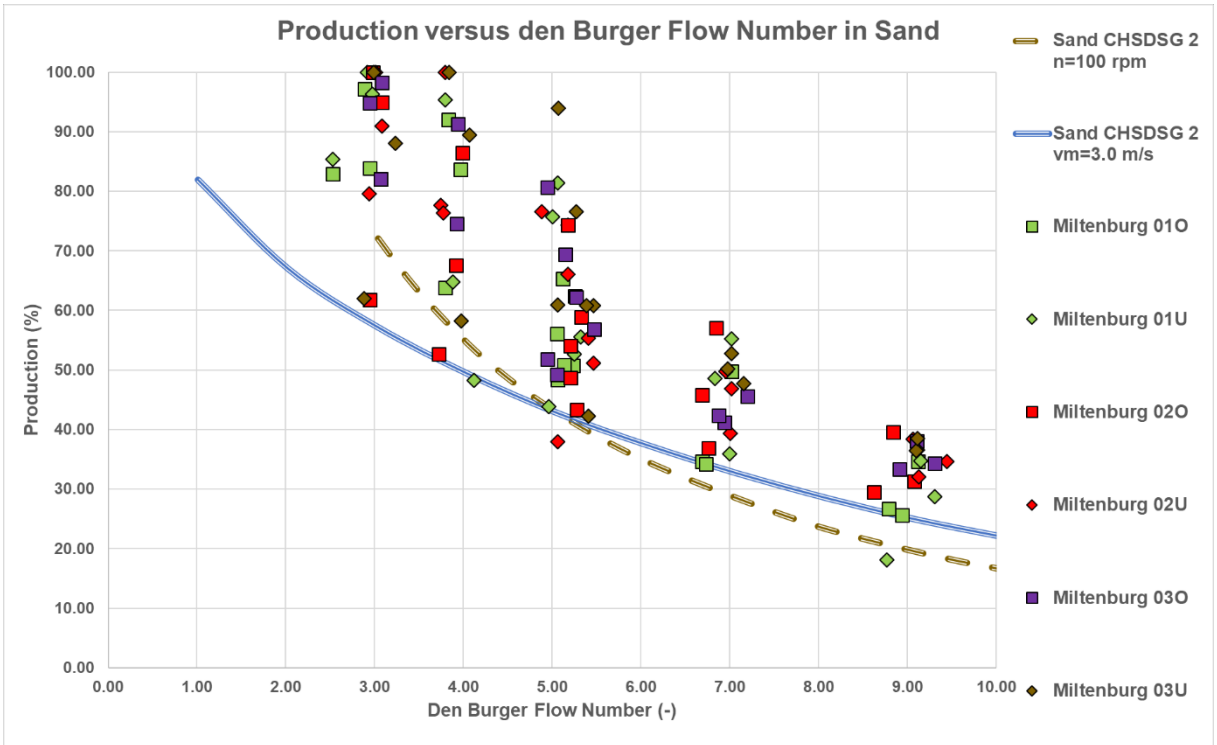

Figure 7-68: All experiments of Miltenburg (1982) with a rock cutter head in sand, with model lower limit.

7.9. Nomenclature

A_c	Cross section to be cut	m^2
$A_{c,p}$	Cross section to be cut prototype	m^2
$A_{c,m}$	Cross section to be cut model	m^2
A_p	Cross section suction pipe	m^2
$A_{p,p}$	Cross section suction pipe prototype	m^2
$A_{p,m}$	Cross section suction pipe model	m^2
Bu_p	Den Burger dimensionless number prototype	-
Bu_m	Den Burger dimensionless number model	-
Bu	Den Burger dimensionless number	-
C_{vs}	Spatial volumetric concentration	-
$D_{p,s}$	Pipe diameter suction pipe	m
D_r	Cutter ring diameter	m
f	Radii factor	-
FR	Filling ratio dimensionless number	-
n	Porosity	-
Δp	Pressure difference	kPa
Δp_E	Euler pressure difference	kPa
$\Delta p_{E,1}$	Euler pressure difference segment 1	kPa
$\Delta p_{E,2}$	Euler pressure difference segment 2	kPa
Δp_1	Pressure difference segment 1	kPa
Δp_2	Pressure difference segment 2	kPa
P_c	Percentage circumference involved in cutting (as a factor)	-
$P_{c,1}$	Percentage circumference involved in cutting (as a factor) segment 1	-
$P_{c,2}$	Percentage circumference involved in cutting (as a factor) segment 2	-
q	Specific flow (per meter width)	m^2/s
$q_{1,out}$	Specific outflow segment 1	m^2/s
$q_{2,out}$	Specific outflow segment 2	m^2/s
$q_{2,in}$	Specific inflow segment 2	m^2/s
Q	Flow	m^3/s
Q_a	Axial flow	m^3/s
Q_c	Cut production situ soil	m^3/s
$Q_{c,p}$	Cut production situ soil prototype	m^3/s
$Q_{c,m}$	Cut production situ soil model	m^3/s
Q_s	Cut production solids	m^3/s
Q_m	Mixture flow suction mouth	m^3/s
$Q_{m,p}$	Mixture flow suction mouth prototype	m^3/s
$Q_{m,m}$	Mixture flow suction mouth model	m^3/s
$Q_{1,out}$	Mixture outflow segment 1	m^3/s
$Q_{2,out}$	Mixture outflow segment 2	m^3/s
$Q_{2,in}$	Mixture inflow segment 2	m^3/s
r_o	Outer radius	m
r_i	Inner radius	m
$r_{o,1}$	Outer radius segment 1	m
$r_{i,1}$	Inner radius segment 1	m
$r_{o,2}$	Outer radius segment 2	m
$r_{i,2}$	Inner radius segment 2	m
$r_{c,a}$	Average outer cutter radius	m
r_r	Cutter ring radius	m
$r_{r,p}$	Cutter ring radius prototype	m
$r_{r,m}$	Cutter ring radius model	m
u_o	Circumferential velocity outer radius	m/s
u_i	Circumferential velocity inner radius	m/s
v_s	Swing speed	m/s
$v_{s,p}$	Swing speed prototype	m/s
$v_{s,m}$	Swing speed model	m/s
v_m	Mixture velocity suction pipe	m/s

$v_{m,p}$	Mixture velocity suction pipe prototype	**m/s**
$v_{m,m}$	Mixture velocity suction pipe model	**m/s**
v_t	Terminal settling velocity particles	**m/s**
$v_{t,p}$	Terminal settling velocity particles prototype	**m/s**
$v_{t,m}$	Terminal settling velocity particles model	**m/s**
w	Width (or height) of cutter head	**m**
w_1	Width segment 1	**m**
w_2	Width segment 2	**m**
α	Flow factor	**-**
α_1	Flow factor segment 1	**-**
α_2	Flow factor segment 2	**-**
β_o	Blade angle outer radius	**rad**
$\beta_{o,1}$	Blade angle outer radius segment 1	**rad**
$\beta_{o,2}$	Blade angle outer radius segment 2	**rad**
β_i	Blade angle inner radius	**rad**
$\beta_{i,1}$	Blade angle inner radius segment 1	**rad**
$\beta_{i,2}$	Blade angle inner radius segment 2	**rad**
ε	Factor pressure	**-**
ρ_l	Density carrier liquid (water)	**ton/m^3**
ρ_q	Density solids (quarts)	**ton/m^3**
ρ_m	Mixture density	**ton/m^3**
$\rho_{m,1}$	Mixture density segment 1	**ton/m^3**
$\rho_{m,2}$	Mixture density segment 2	**ton/m^3**
ω	Radial frequency cutter head	**rad/s**
ω_p	Radial frequency cutter head prototype	**rad/s**
ω_m	Radial frequency cutter head model	**rad/s**
ξ	Factor in FD (filling degree) dimensionless number	**-**
θ	Ladder angle	**rad**
λ_l	Length scale	**-**

Chapter 8: The Pump/Pipeline System.

8.1. Introduction.

A multi pump/pipeline system consists of components with different dynamic behaviour. To model such a system, one should start with simple mathematical descriptions of the sub-systems, to be able to determine the sensitivity of the behaviour of the system to changes in one of the sub-systems. The following sub-systems can be distinguished:
- The pump drive
- The centrifugal pump
- The sand/water slurry in the pipeline
- Flow control (if used)

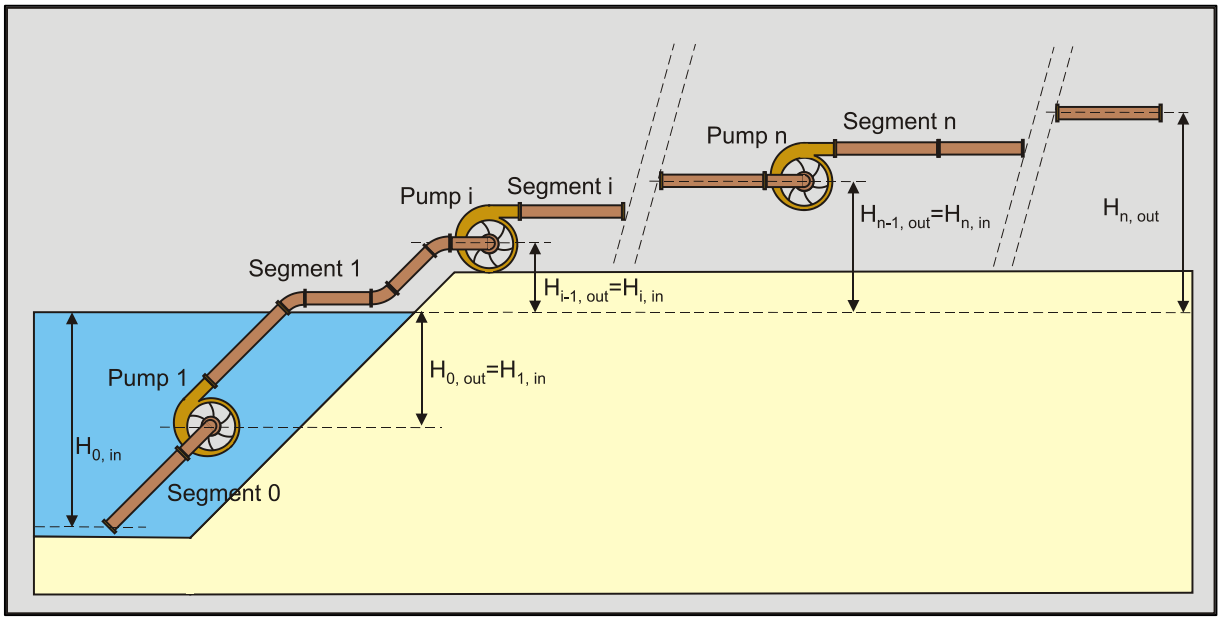

Figure 8-1: A pump –pipeline system.

The system is limited by cavitation at the entrance of each pump on one hand and by sedimentation of the solids resulting in plugging of the pipeline on the other hand. Cavitation will occur at high line velocities and/or at high solids concentrations in the suction pipe of the pump considered. Sedimentation will occur at line velocities below the so called critical velocity. The critical velocity depends on the grain distribution and on the solids concentration. In between these two limitations a stable transportation process is required. A steady state process is possible only if the solids properties and the solids concentration are constant in time. In practice however this will never be the case. Solids properties such as the grain size distribution will change as a function of time and place as will the solids concentration. The resistance of the slurry flow depends on the solids properties and concentration. If the total resistance of the slurry flow in a long pipeline is considered, changes of the solids properties and concentration at the suction mouth will result in slow changes of the total resistance, since only a small part of the pipeline is filled with the new slurry while most of the pipeline remains filled with the slurry that was already there, except from the slurry that has left the pipeline at the end. If the relatively short suction line is considered, this results in a much faster change of the vacuum at the inlet of the first pump.
The total head of a pump however, responds immediately to changes of the solids properties and concentration. If a sudden increase of the concentration is assumed, the total head of a pump will increase almost proportionally with the concentration. This will result in a higher flow velocity, but, because of the inertia of the slurry mass in the pipeline, the slurry mass will have to accelerate, so the flow velocity responds slowly on changes of the total head. The increase of the total head also causes an increase of the torque and power of the pump drive, resulting in a decrease of the pump drive revolutions and thus of the total head. Because of the inertia of pump and pump drive, there will not be an immediate response.
It is obvious that there is an interaction between all the different sub-systems. These interactions can be ranged from very slow to immediate. To be able to model the system, first the characteristic behaviour of the sub-systems should be known.

8.2. The Pump Drive.

Pump drives used in dredging are diesel direct drives, diesel/electric drives and diesel/hydraulic drives. In this paper the diesel direct drive, as the most common arrangement, is considered.
At nominal operating speed, the maximum load coincides with the nominal full torque point. If the torque is less then the nominal full torque, the engine speed usually rises slightly as the torque decreases. This is the result of the control of the speed by the governor. The extent of this depends upon the type of governor fitted.
If the engine load increases above the full torque point, the speed decreases and the engine operates in the full fuel range. With most diesel engines the torque will increase slightly as the speed decreases, because of a slightly increasing efficiency of the fuel pumps. When the load increases further, insufficient air is available to produce complete combustion and the engine stalls. The torque drops rapidly and heavily polluted gasses are emitted. The smoke limit has been reached. The speed range between the full torque point and the smoke limit is often referred to as the constant torque range.

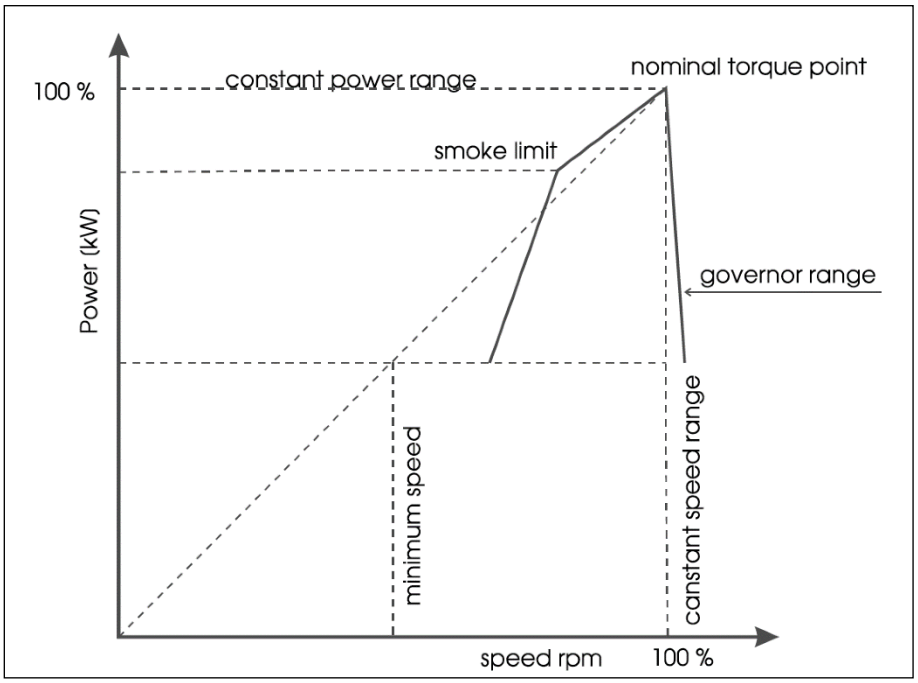

Figure 8-2: The speed-power curve of a diesel engine.

The torque/speed characteristic of the diesel engine can thus be approximated by a constant full torque upon the nominal operating speed, followed by a quick decrease of the torque in the governor range.
This characteristic however is valid for a steady state process of the diesel engine. When the speed of the diesel changes, the load will change, but also the inertia effects of the diesel have to be taken into account. The equation of motion of the diesel engine, gear box and centrifugal pump combination, reduced to the axis of the centrifugal pump, is:

$$\left(I_{d.e.} + I_{g.b.} + I_{c.p.}\right) \cdot \ddot{\varphi} = T_{d.e.} - T_{h.t.} \qquad \textbf{(8-1)}$$

In a steady state situation, the torque delivered by the diesel engine $T_{d.e.}$ equals the torque required by the hydraulic transport $T_{h.t.}$, so the angular acceleration of the diesel is zero. If $T_{d.e.}$ is greater then $T_{h.t.}$, the revolutions will increase, If $T_{d.e.}$ is smaller then $T_{h.t.}$, the revolutions will decrease. If the difference between these two torque's is approximated to be proportional with the difference between the actual angular velocity and the nominal operating angular velocity:

$$T_{d.e.} - T_{h.t.} = K_p \cdot \left(\dot{\varphi}_{s.p.} - \dot{\varphi}\right) \qquad \textbf{(8-2)}$$

The linear differential equation can be written as:

$$\left(I_{d.e.}+I_{g.b.}+I_{c.p.}\right)\cdot\ddot{\varphi}=K_p\cdot\left(\dot{\varphi}_{s.p.}-\dot{\varphi}\right) \tag{8-3}$$

With: $\left(I_{d.e.}+I_{g.b.}+I_{c.p.}\right)=I_t$ and $\tau_{d.e.}=\dfrac{K_p}{I_t}$ **(8-4)**

The solution of this first order system is:

$$\dot{\varphi}=\dot{\varphi}_0+\left(\dot{\varphi}_{s.p.}-\dot{\varphi}_0\right)\cdot\left(1-e^{-t/\tau_{d.e.}}\right) \tag{8-5}$$

In which $\dot{\varphi}_0$ is the angular velocity at an arbitrary time, defined as **t=0**. Using time domain calculations with a time step Δt, the angular velocity at time step **n** can now be written as a function of the angular velocity at time step **n-1** and the set point angular velocity $\dot{\varphi}_{s.p.}$ according to:

$$\dot{\varphi}_n=\dot{\varphi}_{n-1}+\left(\dot{\varphi}_{s.p.}-\dot{\varphi}_{n-1}\right)\cdot\left(1-e^{-\Delta t/\tau_{d.e.}}\right) \tag{8-6}$$

8.3. The Centrifugal Pump.

Figure 8-3: Centrifugal pumps.

The behaviour of centrifugal pumps can be described with the Euler impulse moment equation:

$$\Delta p_E = \rho_f \cdot u_o \cdot \left(u_o - \frac{Q \cdot \cot(\beta_o)}{2 \cdot \pi \cdot r_o} \right) - \rho_f \cdot u_i \cdot \left(u_i - \frac{Q \cdot \cot(\beta_i)}{2 \cdot \pi \cdot r_i} \right) \quad \textbf{(8-7)}$$

For a known pump this can be simplified to:

$$\Delta p_E = \rho_f \cdot (C_1 - C_2 \cdot Q) \quad \textbf{(8-8)}$$

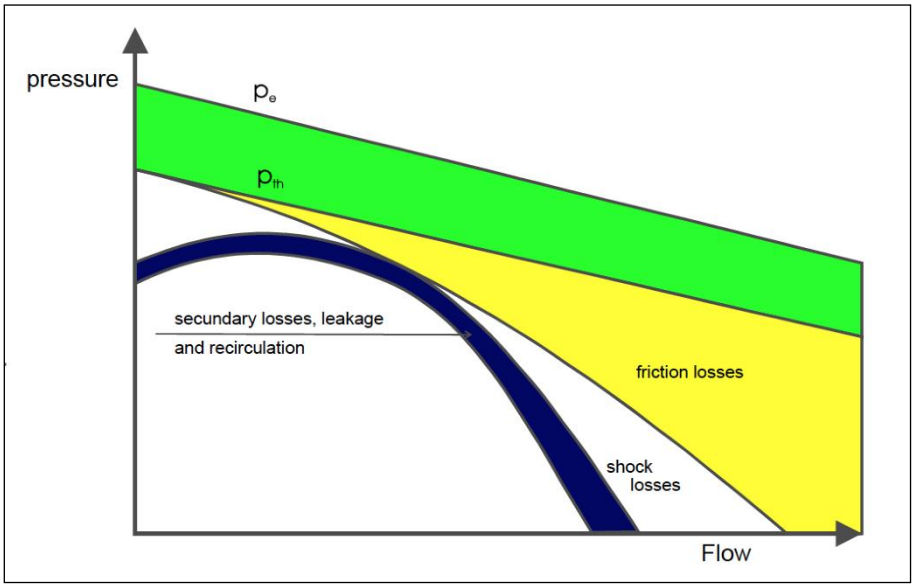

Figure 8-4: The pressure-flow curves.

Because of incongruity of impeller blades and flow, the finite number of blades, the blade thickness and the internal friction of the fluid, the Euler pressure Δp_E has to be corrected with a factor **k**, with a value of about 0.8. This factor however does not influence the efficiency. The resulting equation has to be corrected for losses from frictional contact with the walls and deflection and diversion in the pump and a correction for inlet and impact losses. The pressure reduction for the frictional losses is:

$$\Delta p_{h.f.} = C_3 \cdot \rho_f \cdot Q^2 \quad \textbf{(8-9)}$$

For a given design flow Q_d the impact losses can be described with:

$$\Delta p_{h.i.} = C_4 \cdot \rho_f \cdot (Q_d - Q)^2 \quad \textbf{(8-10)}$$

The total head of the pump as a function of the flow is now:

$$\Delta p_p = k \cdot \Delta p_E - \Delta p_{h.f.} - \Delta p_{h.i.} = \rho_f \cdot \left(k \cdot (C_1 - C_2 \cdot Q) - C_3 \cdot Q^2 - C_4 \cdot (Q_d - Q)^2 \right) \quad \textbf{(8-11)}$$

This is a second degree polynomial in **Q**. The fluid density ρ_f in the pump can be either the density of a homogeneous fluid (for water ρ_w) or the density of a mixture ρ_m passing the pump.
The total efficiency of the pump can be determined by dividing the power that is added to the flow $P_{fl} = \Delta p_p \cdot Q$ by the power that is output of the diesel engine $P_{d.e.} = k \cdot \Delta p_E \cdot Q + P_{d.f.}$ (in which $P_{d.f.}$ is the power required for the frictional losses in the gear box, the pump bearings, etc.), this gives:

$$\eta_p = \frac{(k \cdot \Delta p_E - \Delta p_{h.f.} - \Delta p_{h.i.}) \cdot Q}{k \cdot \Delta p_E \cdot Q + P_{d.f.}} \quad \textbf{(8-12)}$$

For the efficiency curve a third degree polynomial approximation satisfies, while the power and torque curves approximate straight lines. The pump characteristics usually will be measured for a specific impeller diameter and number of revolutions.

8.4. Affinity Laws.

In a dynamic system however, the pump revolutions will change. This is on one hand the result of the torque/speed curve of the pump drive, on the other hand of manual or automatic flow control. This means that the pump characteristics should also be known at different pump speeds.
The so-called affinity laws describe the influence of a different impeller diameter or revolutions on the pump head, flow and efficiency:

$$\frac{p_1}{p_2} = \frac{n_1^2}{n_2^2} \cdot \frac{D_1^2}{D_2^2}, \quad \frac{Q_1}{Q_2} = \frac{n_1}{n_2} \cdot \frac{D_1^2}{D_2^2}, \quad \eta_1 = \eta_2 \tag{8-13}$$

The efficiency does not change, but the value of the flow on the horizontal axis is shifted.
The affinity laws for the power and the torque can easily be derived from these equations.

$$\frac{P_1}{P_2} = \frac{p_1 \cdot Q_1 \cdot \eta_2}{p_2 \cdot Q_2 \cdot \eta_1} = \frac{n_1^3}{n_2^3} \cdot \frac{D_1^4}{D_2^4}, \quad \frac{T_1}{T_2} = \frac{P_1 \cdot n_2}{P_2 \cdot n_1} = \frac{p_1 \cdot Q_1 \cdot \eta_2 \cdot n_2}{p_2 \cdot Q_2 \cdot \eta_1 \cdot n_1} = \frac{n_1^2}{n_2^2} \cdot \frac{D_1^4}{D_2^4} \tag{8-14}$$

If a ratio for the revolutions $\varepsilon_n = \frac{n}{n_m}$ and a ratio for the diameter $\varepsilon_D = \frac{D}{D_m}$ are given, the head and efficiency curves at a speed **n** and an impeller diameter **D** can be determined by:

$$Q = Q_m \cdot \varepsilon_n^1 \cdot \varepsilon_D^2 \tag{8-15}$$

$$\Delta p_p = \alpha_0 \cdot Q^0 \cdot \varepsilon_n^2 \cdot \varepsilon_D^2 + \alpha_1 \cdot Q^1 \cdot \varepsilon_n^1 \cdot \varepsilon_D^0 + \alpha_2 \cdot Q^2 \cdot \varepsilon_n^0 \cdot \varepsilon_D^{-2} \tag{8-16}$$

$$\eta_p = \beta_0 \cdot Q^0 \cdot \varepsilon_n^0 \cdot \varepsilon_D^0 + \beta_1 \cdot Q^1 \cdot \varepsilon_n^{-1} \cdot \varepsilon_D^{-2} + \beta_2 \cdot Q^2 \cdot \varepsilon_n^{-2} \cdot \varepsilon_D^{-4} + \beta_3 \cdot Q^3 \cdot \varepsilon_n^{-3} \cdot \varepsilon_D^{-6} \tag{8-17}$$

In which n_m, D_m and Q_m are the revolutions, impeller diameter and flow used in the measurements of the head and efficiency curves.
Based on this theory, the characteristics of two pumps used in the case study in this chapter, are given in Figure 8-5 and Figure 8-6. Both pumps are limited by the constant torque behaviour of the corresponding diesel engine in the full fuel range.

Figure 8-5 and Figure 8-6 give the pump characteristics for clear water. If a mixture is pumped however, the pump head increases because of the mixture density as has been pointed out when discussing equation (8-11) and the pump efficiency decreases because a heterogeneous mixture is flowing through the pump. The decrease of the efficiency depends upon the average grain diameter, the impeller diameter and the solids concentration and can be determined with (according to Stepanoff):

$$\eta_m = \left(1 - C_t \cdot \left(0.466 + 0.4 \cdot \mathrm{Log10}\left(d_{50}\right)\right) / D\right) \tag{8-18}$$

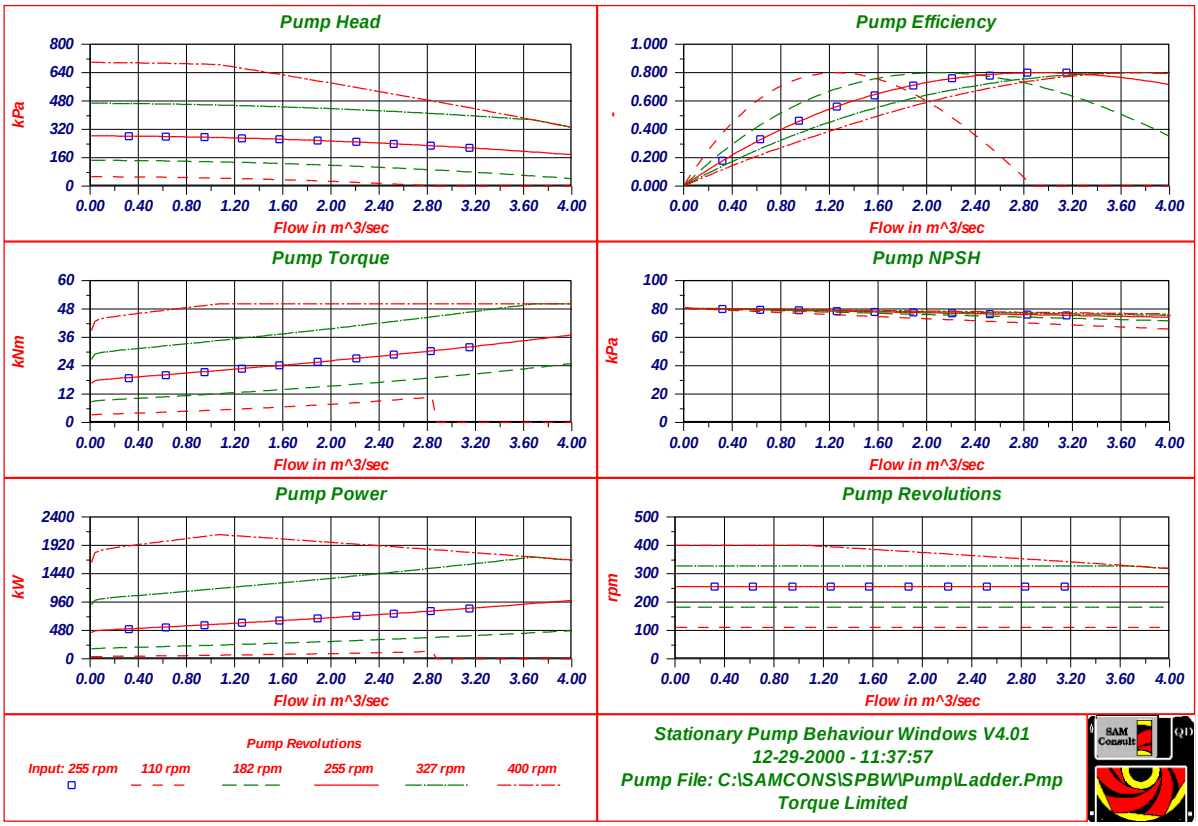

Figure 8-5: The characteristics of the ladder pump.

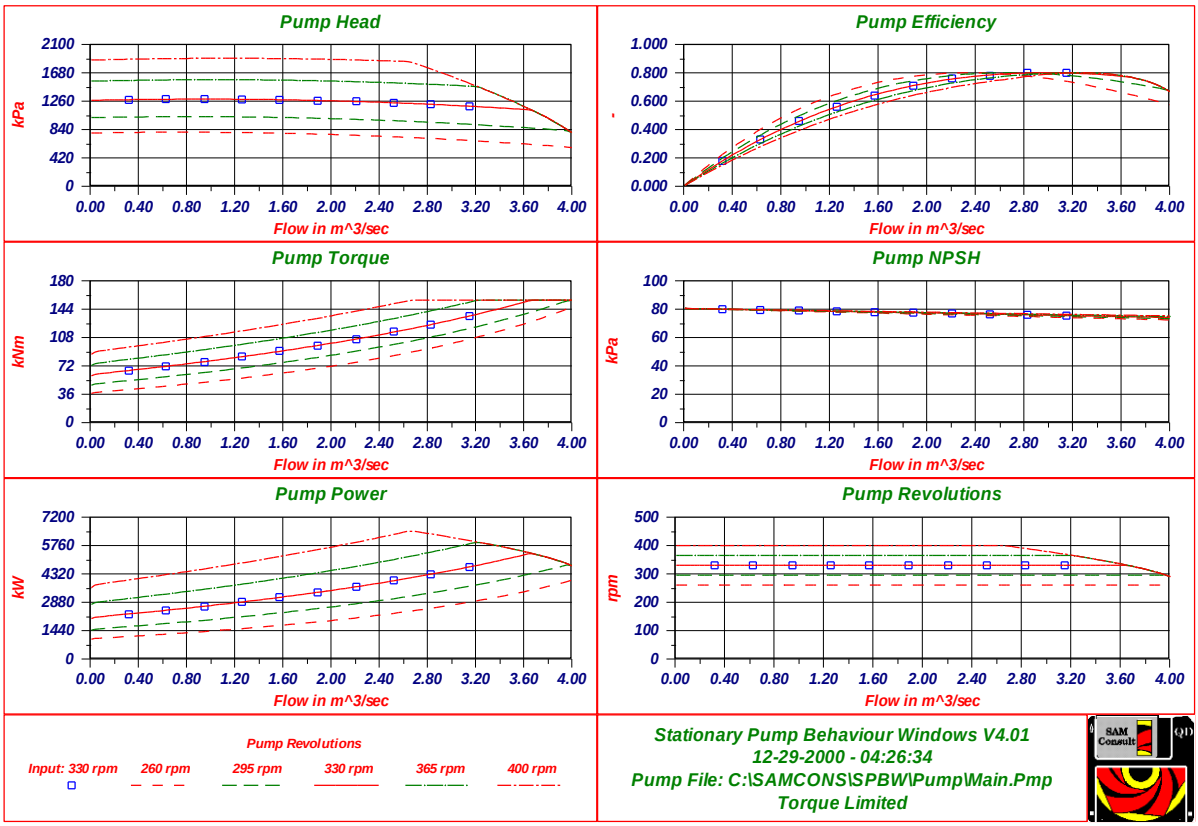

Figure 8-6: The characteristics of the main pump and the booster pump, torque limited.

8.5. Approximations.

The pump Q-H curve for water can be approximated by:

$$H = A + C \cdot Q^2 \quad \text{With: } A = f \cdot H_D \quad \text{and} \quad C = \frac{(1-f) \cdot H_D}{Q_D^2} \tag{8-19}$$

The pump efficiency curve can be approximated by:

$$\eta_m = \eta_{max} \cdot \left(1 - \left(\frac{Q_D - Q}{Q_D}\right)^2\right)^g \tag{8-20}$$

A factor **f** of about 1.25 and a power **g** of about 0.7 give good results. The design flow $\mathbf{Q_D}$ (m^3/s) and the design head $\mathbf{H_D}$ (kPa) follow from the requirements and can be used for one pump or for all pumps together.

8.6. The Total Head Losses.

The pressure at the inlet of the suction mouth of the cutter head or in the draghead is:

$$p_s = \rho_w \cdot g \cdot H_{sm} + 100 \tag{8-21}$$

The pressure losses from the suction mouth to the entrance of the first pump are:

$$p_{m,s} = \tfrac{1}{2} \cdot \rho_m \cdot v_{ls,s}^2 + \lambda_{w,s} \cdot \frac{L_s}{D_{p,s}} \cdot \tfrac{1}{2} \cdot \rho_w \cdot v_{ls,s}^2 + p_{s,s} + \sum_1^n \xi_{n,s} \cdot \tfrac{1}{2} \cdot \rho_m \cdot v_{ls,s}^2 + \rho_m \cdot g \cdot H_s + \rho_m \cdot L_s \cdot \dot{v}_{ls,s} \tag{8-22}$$

The pressure losses after the first pump (discharge losses) are:

$$p_{m,d} = \tfrac{1}{2} \cdot \rho_m \cdot \left(v_{ls,d}^2 - v_{ls,s}^2\right) + \lambda_{w,d} \cdot \frac{L_d}{D_{p,d}} \cdot \tfrac{1}{2} \cdot \rho_w \cdot v_{ls,d}^2 + p_{s,d} + \sum_1^n \xi_{n,d} \cdot \tfrac{1}{2} \cdot \rho_m \cdot v_{ls,d}^2 + \rho_m \cdot g \cdot H_d + \rho_m \cdot L_d \cdot \dot{v}_{ls,d} \tag{8-23}$$

The absolute pressure at the inlet of the first pump is p_s-$p_{m,s}$ and should be above a certain minimum.

$$p_s - p_{m,s} > p_{lim} \tag{8-24}$$

The last term in equations (8-22) and (8-23) is the contribution of acceleration or deceleration of the mixture.

In a stationary situation, the mixture density has to be smaller than a certain limit to avoid cavitation in the first pump.

$$\rho_m < \frac{\rho_w \cdot g \cdot H_{sm} + 100 - p_{lim}}{\tfrac{1}{2} \cdot v_{ls,s}^2 + \lambda_{w,s} \cdot \frac{L_s}{D_{p,s}} \cdot \tfrac{1}{2} \cdot v_{ls,s}^2 + \sum_1^n \xi_{n,s} \cdot \tfrac{1}{2} \cdot v_{ls,s}^2 + g \cdot H_s} \tag{8-25}$$

8.7. Numerical Simulation: Development Density Waves in Long Pipeline.

8.7.1. Abstract.

Slurry transport is used in dredging and mining to transport solid/liquid mixtures over a long distance. In slurry transport very often, multiple pumps are used. To describe the processes involved, very often a steady state approach is used. A steady state process however requires a constant density and solids properties in the system and thus at the suction mouth. In practice it is known, that the solids properties and the density change with respect to time. The density waves generated at the inlet of the system tend to transform their shape while moving along a pipeline. Under suitable conditions (a partially-stratified flow, low mean velocity of the mixture) high density waves tend to be amplified. This process is associated with the hydrodynamic interaction between the granular bed at the bottom of a pipeline and the suspension stream above the bed. The strongest amplification of high-density waves occurs at mixture velocities around or below the deposition limit value. The development of density waves and the mechanisms leading to the deformation of density waves were discussed recently (Matousek (2001)).

A numerical model that uses a simplified description of mechanisms governing the unsteady flow of partially-stratified slurry in order to simulate a development of a density wave along a long horizontal pipeline is presented. The model is two-dimensional, it handles the 2-D mass exchange within slurry flow. The vertical exchange of mass between the bed and the suspension layer above the bed is quantified using applied equations for the settling rate and the erosion rate. The adopted erosion-rate equation is preliminary and requires further investigation.

As a result of density fluctuations, the pump discharge pressure and vacuum will change with respect to time and the pipeline resistance will change with respect to time and place. A change of the discharge pressure will result in a change of the torque on the axis of the pump drive on one hand and in a change of the flow velocity on the other hand. The mixture in the pipeline must accelerate or decelerate. Since centrifugal pumps respond to a change in density and solids properties at the moment the mixture passes the pump, while the pipeline resistance is determined by the contents of the pipeline as a whole, this forms a complex dynamic system. The inertial pressure of the mixture must be added to the resistance of the mixture. In fact, the inertial pressure is always equal to the difference between the total pressure generated by the pumps and the total resistance of the mixture in the pipeline system. If this difference is positive (the pump pressure has increased due to an increase of the mixture density), the mixture will accelerate. If negative, the mixture will decelerate (Miedema (1996)).
As a result of the acceleration and deceleration, the mixture velocity (line velocity) will vary as a function of time. To realize a stable dredging process, it is required to have a line velocity that will not vary too much. The line velocity can be controlled by varying the revolutions of one of the dredge pumps, where the last pump is preferred.

Of course, the result of flow control depends on the pump/pipeline layout. If this layout has not been designed in a good way, flow control cannot correct a bad design. If this layout however has been designed properly, flow control can control the line speed and can prevent the occurrence of cavitation.

8.7.2. Introduction.

During dredging operations, the density of mixture transported along the pipeline of a conveying system varies in time and space. The density waves generated at the inlet of the system tend to transform their shape while moving along the pipeline. This process is associated with the hydrodynamic interaction between the granular bed at the bottom of a pipeline and the suspension stream above the bed. The strongest amplification of high-density waves occurs at mixture velocities around or below the deposition limit value. The development of density waves and the mechanisms leading to the deformation of density waves were discussed recently (Matousek (1997), (2001); Talmon (1999)).

Previously, the stratified flow in the long pipeline was analyzed by using the principles of a two-layer model with a fixed position of the interface between the layers. A two-layer model is a one-dimensional model that simplifies the internal structure of a settling-mixture flow into a flow pattern composed of a particle-rich lower layer and a particle-lean upper layer. The analysis of the wave-amplification process in a long pipeline requires further refinement to implement the effects of the mass exchange caused by the settling flux and the erosion flux through the interface between the layers. The modeling of the density-wave deformation requires that a one-dimensional two-layer model (longitudinal solids transport only) is replaced by a two-dimensional layered model that considers the vertical exchange of solids between the contact bed and the flow of suspension above the bed.

A model predicting the amplification of a density wave as a result of the exchange of solids mass in the direction perpendicular to the flow direction requires successful formula for both the settling flux and the erosion flux through the (virtual) interface between layers. The fluxes seem to be very sensitive to solids concentration at the interface, as must also be the formula determining the fluxes. Yet, the pick-up functions available for the prediction of the erosion flux are not reliable in the high concentrated flows typical for slurry pipelines.

8.7.3. Description of the 2-D Model for Unsteady Flow of Solids in a Pipeline.

8.7.3.1. Model Structure.

If the flow of solids is unsteady the flow structure (the velocity and concentration profiles) varies not only in time but also in space, i.e. along a pipeline length. To be able to simulate the unsteady flow on basis of its internal structure, we have to identify important parameters in both time domain and space domain. To handle the simulation in space domain properly, a pipeline must be divided into a number of elements. The flow in each element is split into two layers: the lower layer represents a granular bed (either stationary or sliding) and the upper layer represents the suspension flow. Since the solids flow is unsteady (the density of slurry varies along the pipelines and thus is different in different elements) the bed thickness is considered to be different in different elements. Figure 8-7 shows a slurry pipeline divided into elements for the model purposes.

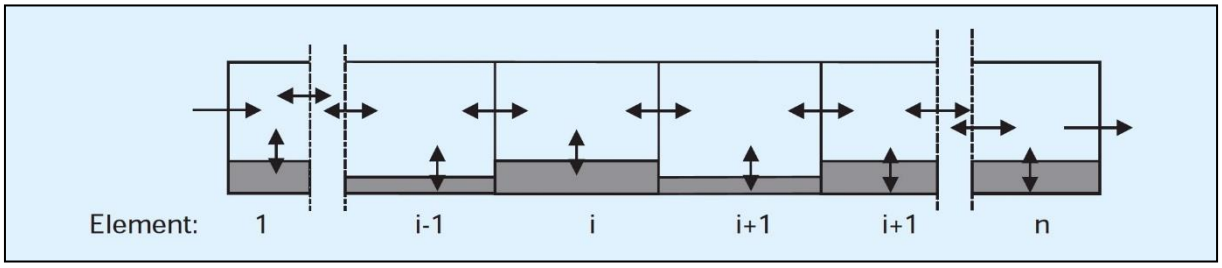

Figure 8-7: Elements of a pipeline filled with unsteady solids flow.

8.7.3.2. Modeled Transport Phenomena.

The conservation of mass must be satisfied in the model. The mass exchange takes place in two directions: horizontal and vertical. The horizontal transport of solids (the transport due to the pressure gradient in a pipeline) is given by the following equation:

$$\mathbf{dm = Q \cdot \Delta t \cdot C_{v,up} \cdot \rho_s} \qquad \textbf{(8-26)}$$

in which **dm** is mass differential in an element; **Q** is the flow rate of slurry; **Δt** is the time step; $\mathbf{C_{v,up}}$ is the volumetric concentration of solids in the upper layer and $\boldsymbol{\rho_s}$ is the density of the solid. During the simulation, at each moment given by **t**, the $\mathbf{C_{v,up}}$ is the only variable in different elements along the pipeline, the flow rate of slurry is considered constant. The horizontal transport of solid particles is influenced by horizontal turbulent diffusion, other possible effects as those of interparticle collisions are neglected. In the vertical direction, the mass exchange can be defined into two processes: settling and erosion. The Figure 8-8 summarizes the transport phenomena implemented in the 2-D model of unsteady flow of solids in a slurry pipeline.

8.7.3.3. Diffusion.

The turbulent-diffusion process is quite complex. In the simplified way, it can be modeled as similar to the molecular diffusion using:

$$\mathbf{f_{dif,x} = -k_x \cdot \frac{\partial \bar{c}}{\partial x}} \qquad \textbf{(8-27)}$$

in which $\mathbf{f_{dif,x}}$ is the diffusion flux due to turbulence in the x-direction and $\mathbf{k_x}$ is the factor of longitudinal dispersion. A suitable value for the factor $\mathbf{k_x}$ is subject to further investigation. The factor seems to be sensitive to the pipe diameter, particle size, slurry velocity and concentration. At this stage of investigation, the effect of turbulent diffusion is not taken into account in the 2-D model.

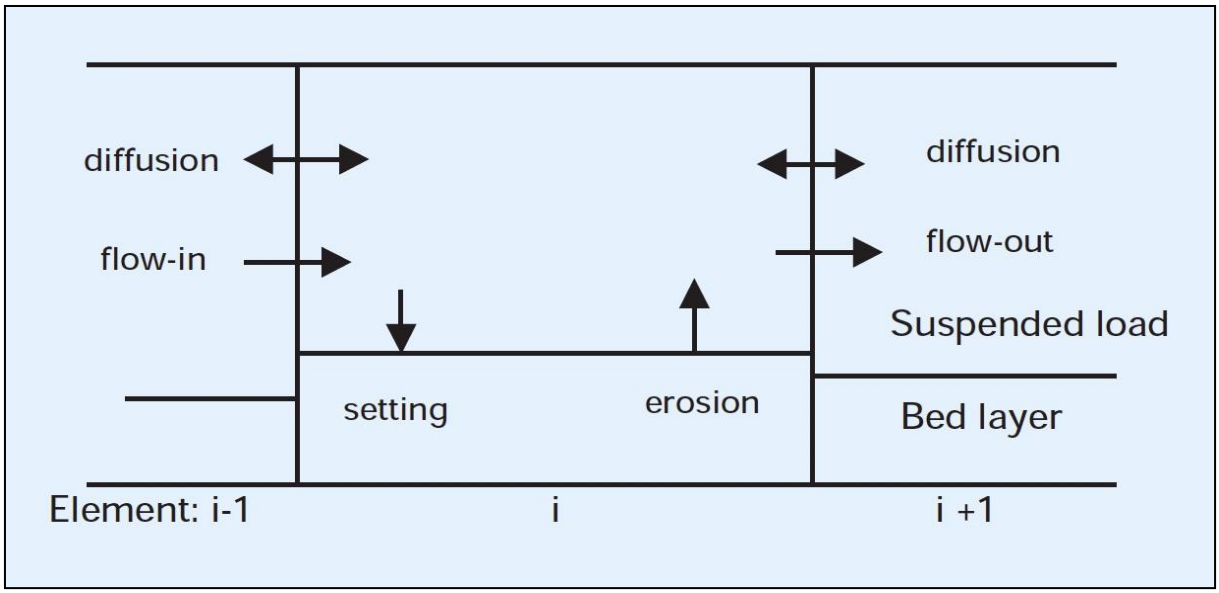

Figure 8-8: The transport phenomena simulated by the 2-D model.

8.7.3.4. Settling.

The dis-equilibrium between the solids settling rate and the erosion rate leads to the solids transport in the vertical direction (perpendicular to the main flow direction). This causes changes in the thickness of the bed and in the volumetric concentration of solid particles in the upper layer.

Settling processes present the ability of the particles to settle from upper layer to the bed layer. Normally the hindered settling velocity is applied to determine the settling process. It is derived as:

$$\mathbf{v_{th} = v_t \cdot (1 - C_{v,up})^m} \qquad \textbf{(8-28)}$$

in which $\mathbf{v_{th}}$ is the hindered settling velocity of solid particles; $\mathbf{v_t}$ is the terminal settling velocity of a solid particle and **m** is the empirical Richardson-Zaki coefficient.

8.7.3.5. Erosion.

The velocity of the suspension flow above the bed is higher than the bed velocity. If the velocity differential is high enough, the top of the bed is eroded. During the erosion process the particles from the top of the bed can be picked up by the suspension flow. The parameter called the erosion velocity evaluates the capability of the suspension flow to pick up particles from the granular bed. The erosion velocity has an opposite direction to the settling velocity. The equation for the erosion velocity is called the pick-up function.
Basically, the erosion velocity (the erosion rate) is dependent on the Shields number. The Shields number increases with the increasing relative velocity of the flow above the bed. The literature proposes a number of erosion-rate models. Unfortunately, the models are constructed for the conditions rather different from those in slurry pipelines, i.e. namely for flow of water or very low-concentrated mixture above a stationary bed (see e.g. Van Rijn (1984), Cao (1997), Fernandez-Luque (1974)). The equation for the erosion velocity:

$$\mathbf{v_e = 1.1 \cdot (\theta - \theta_{cr})} \qquad \textbf{(8-29)}$$

is used to plot the erosion flux in Figure 8-9. In Equation (8-29), θ is the Shields number and θ_{cr} is the critical Shields number (the threshold value for the initial erosion). The erosion flux is calculated as:

$$\mathbf{E = \rho_s \cdot v_e \cdot C_{vd}} \qquad \textbf{(8-30)}$$

Observations in a slurry pipeline indicate that the shear stress at the top of the bed and so the Shields number may vary significantly with the concentration of solids above the bed (e.g. Matousek (1997)). The classical erosion-velocity formulae do not include the effect of the solids concentration directly. For the purposes of slurry

pipelines this parameter should be implemented to the erosion-velocity equation. Furthermore, in the classical erosion-velocity formulae the exponent of Shields number is usually considered higher than 1. This means that the erosion flux simply keeps increasing with the increasing Shields number and so with the increasing solids concentration $\mathbf{C_{vd}}$. This provides unrealistically high values of erosion flux in highly concentrated flows as shown on Figure 8-9.
However, it can be expected that at extremely high concentrations of solids the hindering effects reduce the erosion process (Talmon (1999), Van Rhee & Talmon (2000)) so that the erosion rate diminishes. There are research results available on the effect of solids concentration on the erosion rate in a slurry pipeline. Therefore, as an initial approach, we consider the hindering effect as similar to that for the solids settling so that the hindering effect can be represented in the erosion-rate formula by the term $\mathbf{(0.55\text{-}C_v)^{\gamma}}$. The erosion velocity is then determined using the following equation:

$$\mathbf{v_e = \alpha \cdot (\theta - \theta_{cr})^{\beta} (0.55 - C_{v,up})^{\gamma}} \qquad \textbf{(8-31)}$$

in which $\boldsymbol{\alpha, \beta, \gamma}$ are the empirical coefficients. The constant 0.55 represents the concentration of solids in a loose-packed bed. The calibration of this simplified equation using a limited number of data (see below) led to the following preliminary form of the erosion-velocity equation:

$$\mathbf{v_e = 1.1 \cdot (\theta - \theta_{cr})^{1.9} \cdot (0.55 - C_{vd})^{0.9}} \qquad \textbf{(8-32)}$$

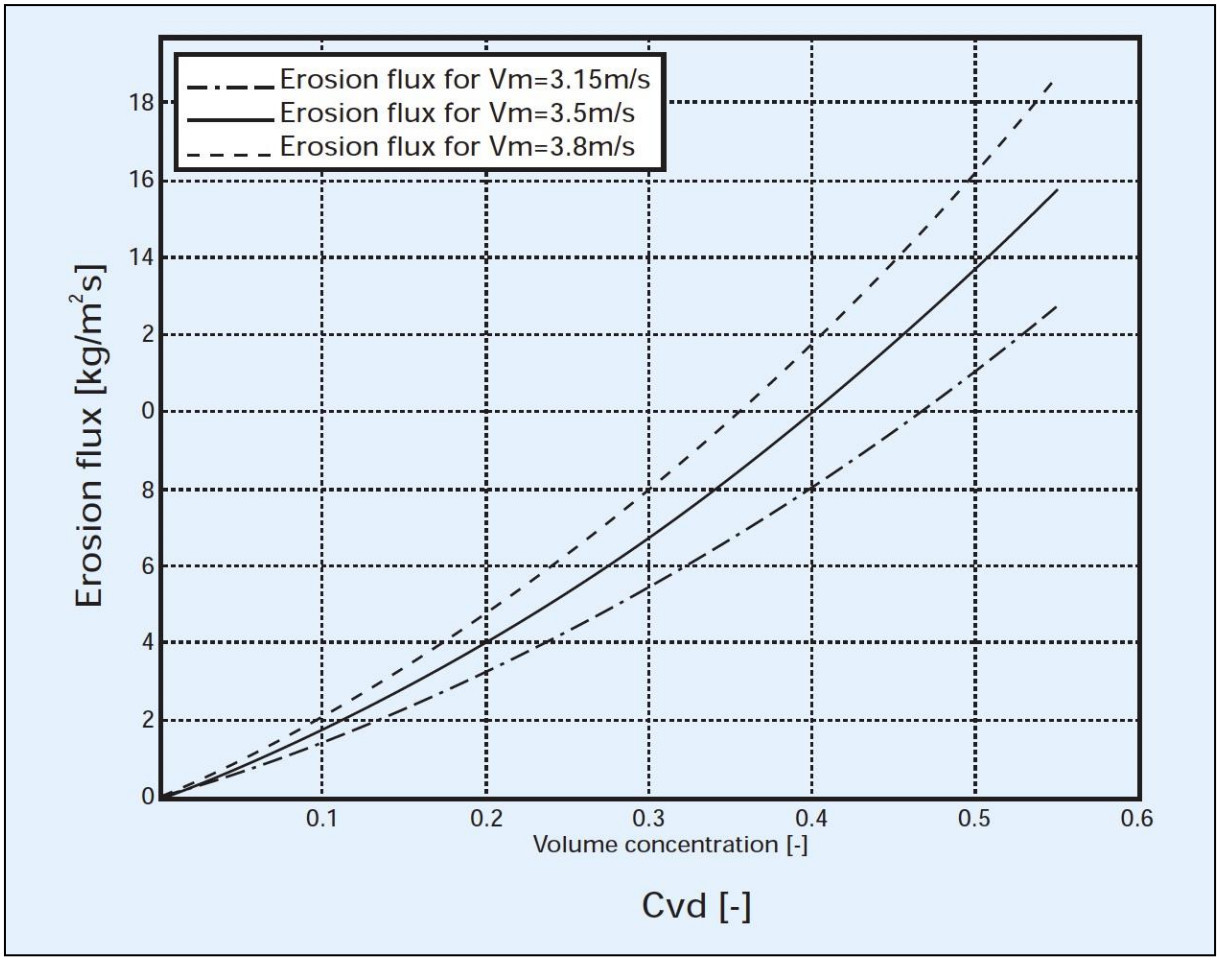

Figure 8-9: The erosion flux using the classical formula (equation (8-29)) for different solids concentrations and mean velocities of slurry in a pipeline.

This adapted erosion-rate equation provides a rather different shape of the curve than the classical model (compare Figure 8-9 and Figure 8-10). The adapted model seems to provide more realistic trends, but it must be stressed that the form of the model and the values of the coefficients have not been verified by experiments. A final form of the erosion-rate equation for slurry pipelines is a subject to further investigation.

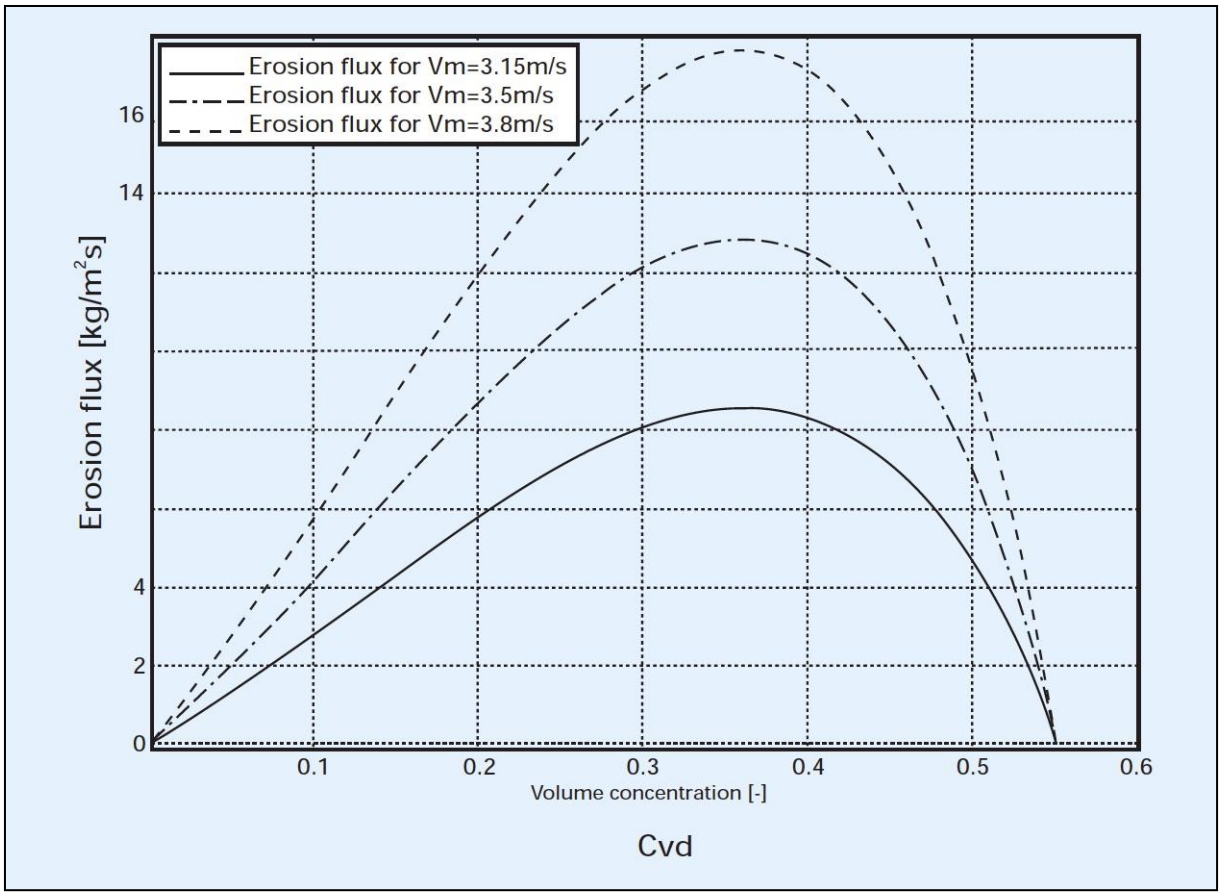

Figure 8-10: The erosion flux using the adapted formula (equation (8-32)) for different solids concentrations and mean velocities of slurry in a pipeline.

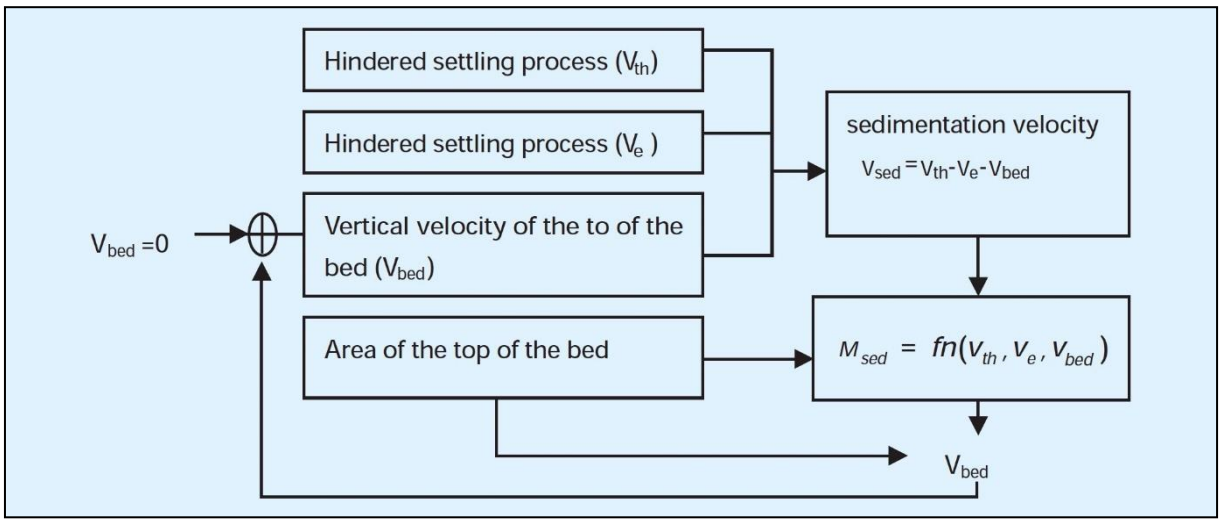

Figure 8-11: Computation of vertical mass exchange in the 2-D model.

8.7.3.6. Mass Exchange between Bed and Suspension Flow.

If there is dis-equilibrium between the settling flux and the erosion flux, the mass exchange takes place between the granular bed and the suspension flow and the thickness of the bed varies. The relative velocity that represents the mass exchange is called the sedimentation velocity, $\mathbf{v_{sed}}$, and can be defined as:

$$\mathbf{v_{sed} = v_{th} - v_e - v_{bed}} \qquad \textbf{(8-33)}$$

In equation (8-33), $\mathbf{v_{bed}}$ is the velocity of the top of the bed, i.e. the vertical velocity with which the top of the bed changes its position.

The sedimentation velocity represents the mass exchange between the contact bed and the suspension flow properly for channels in which the area through which the mass fluxes release does not change with the vertical position of the top of the bed, i.e. for rectangular channels. In circular pipelines, however, the area of the top of the bed varies significantly the vertical position of the top of the bed (with the bed thickness) and then an iteration is required to determine the sedimentation-velocity value. The iteration process is described in Figure 8-11.

8.7.4. Simulations.

The 2-D model is calibrated and tested using the data obtained from the measurements in a long 650-mm pipeline transporting the medium sand of d_{50} = 250 microns (for details over the measurements and data see Matousek (1997) and Matousek (2001)).

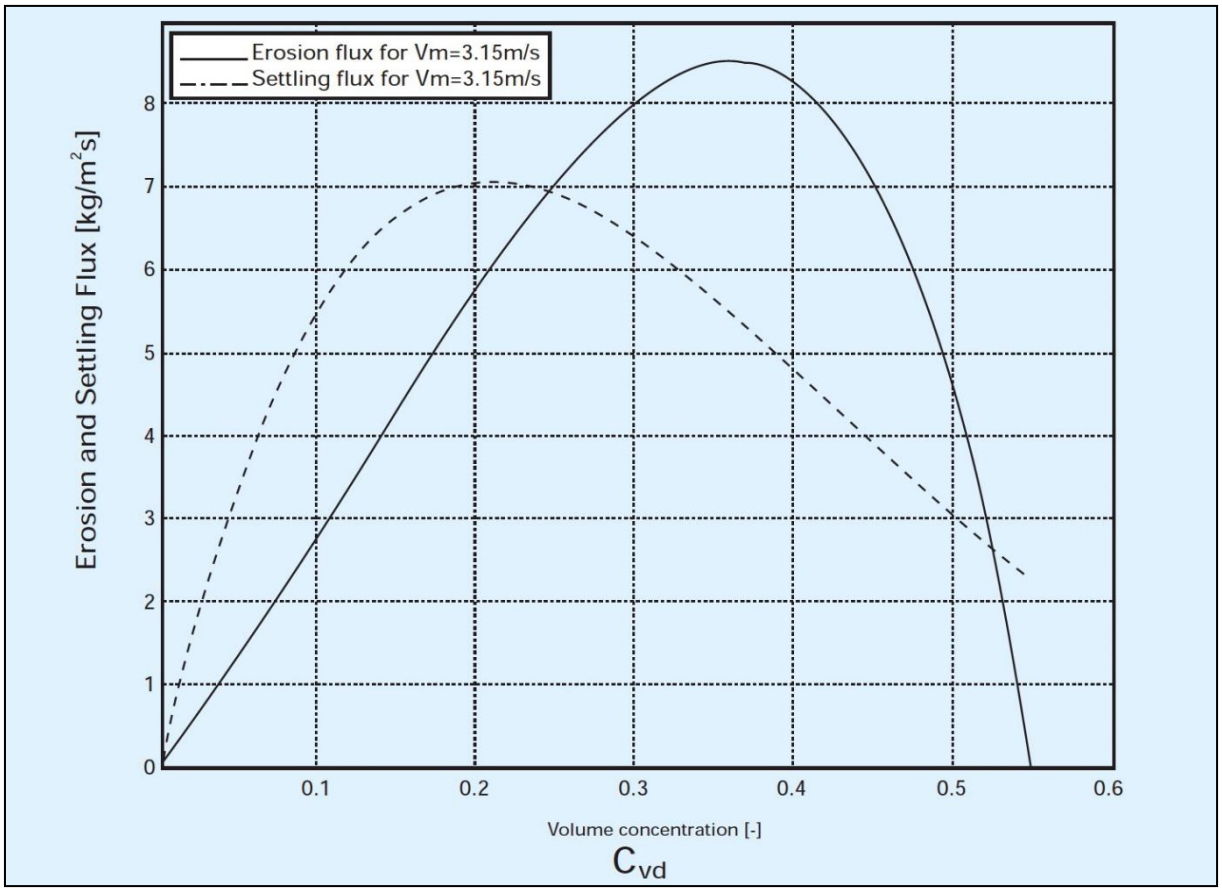

Figure 8-12: Comparison of settling and erosion fluxes according to the 2-D model in a 650-mm pipeline occupied by slurry of medium sand (d_{50}=0.25 mm) (v_m=3.15m/s).

8.7.4.1. Relation between settling and erosion fluxes

The measurements have shown that in flow near the deposition-limit velocity density peaks smaller than approximately 1250 kg/m^3 tended to flatten along the long horizontal pipeline while peaks larger than approximately 1400 kg/m^3 tended to amplify. Considering the vertical exchange of solids between the bed and the suspension as the mechanism responsible for the density-wave transformation, the observed phenomena can be interpreted as follows. In suspensions of density lower than approx. 1250 kg/m^3 the settling flux is bigger than the erosion flux, thus a portion of solid particles is transferred from the suspension to the bed, the thickness of the bed increases. In denser suspension (approx. denser than 1400 kg/m^3) the erosion flux from the top of the bed predominates and the particles are picked up from the bed, the density of suspension increases and the bed thickness decreases.

The adapted erosion-flux formula (Equation (8-29)) can be calibrated using the experimental data so that the calculated disequilibrium (see Figure 8-12) for the velocity near the deposition-limit value (3.15 m/s) shows the same trends as the measurements. The plot shows that for the above chosen conditions the model predicts the equilibrium between the settling flux and the erosion flux in slurry of the volumetric concentration of about 0.25 (slurry density of about 1415 kg/m^3). In the parts of the pipeline that are occupied by the slurry of density lower than this value the model predicts the predomination of the settling flux and thus gradual decrease of solids concentration in the suspension flow. In the parts occupied by the slurry of density higher than 1415 kg/m^3 (and lower than approximately 1930 kg/m^3) the model predicts the dominant effect of the erosion and thus a gradual increase of solids concentration in the suspension flow. The amplification of the high-density peaks does not occur at velocities significantly higher than the deposition-limit velocity. This is because the majority of particles is supported by turbulence (travels within suspension flow) and the bed is very thin. Under this condition the interaction is missing between two layers that is necessary for the development of the density waves.

The model with the implemented flux equations for vertical mass exchange can simulate a deformation of the density waves along a long horizontal pipeline. The plots in Figures 7 and 8 show the simulation results for the conditions described above (a pipeline of the diameter 650 mm and sand 250 microns). The pipeline is 1200 m long and the simulated time period is 360 seconds. One time-step in the simulation represents 0.3 second, i.e. 1200 steps are made during the entire simulation. The plots in the Figure 8-13 and Figure 8-14 indicate the volumetric concentration of solids in the suspension flow simulated in the element 1 (the position at the inlet to the pipeline), element 500 (the position 500 meter behind the inlet) and the element 800 (800 meter behind the inlet). The figures show how the set of density waves changes its shape while passing through the pipeline. In Figure 8-13, the slurry pipeline operates at the mean slurry velocity round the deposition-limit velocity (3.15 m/s). There is a granular bed of a considerable thickness at the bottom of the pipeline. The simulation indicates that due to the vertical exchange of mass between the bed and the suspension flow above the bed two large density peaks gradually increase and three small peaks gradually decrease while passing through the long pipeline from element No.1 to No.800. These trends are in accordance with those observed in the field pipeline during the tests (Matousek (2001)).

In Figure 8-14, the slurry pipeline operates at the mean slurry velocity far above the deposition-limit velocity (3.8 m/s). At this velocity the sliding bed at the bottom of the pipeline is very thin and tends to dissolve. This is primarily due to higher ability of carrier turbulence to keep particles suspended and also due to higher erosion than at velocity 3.15 m/s. Under these conditions the deformation of the density waves is different from that in the pipelines occupied by a thick bed. The waves change their shape much less than in the layered flow as can be seen in Figure 8-14. The front peaks of the set of the peaks tend to increase after entering the pipeline but their increase stops when the bed disappears in the pipeline and there is no material to feed the peaks. The rest of the peaks does not grow for the same reason. The increase of concentration of solids to the limit value 0.20 in the suspension flow in front of the set of the peaks in elements No. 500 and No. 800 indicates that the bed dissolved there already before the set of the peaks arrived. The concentration value 0.20 was reached when all particles traveled in suspension, thus there was no bed.

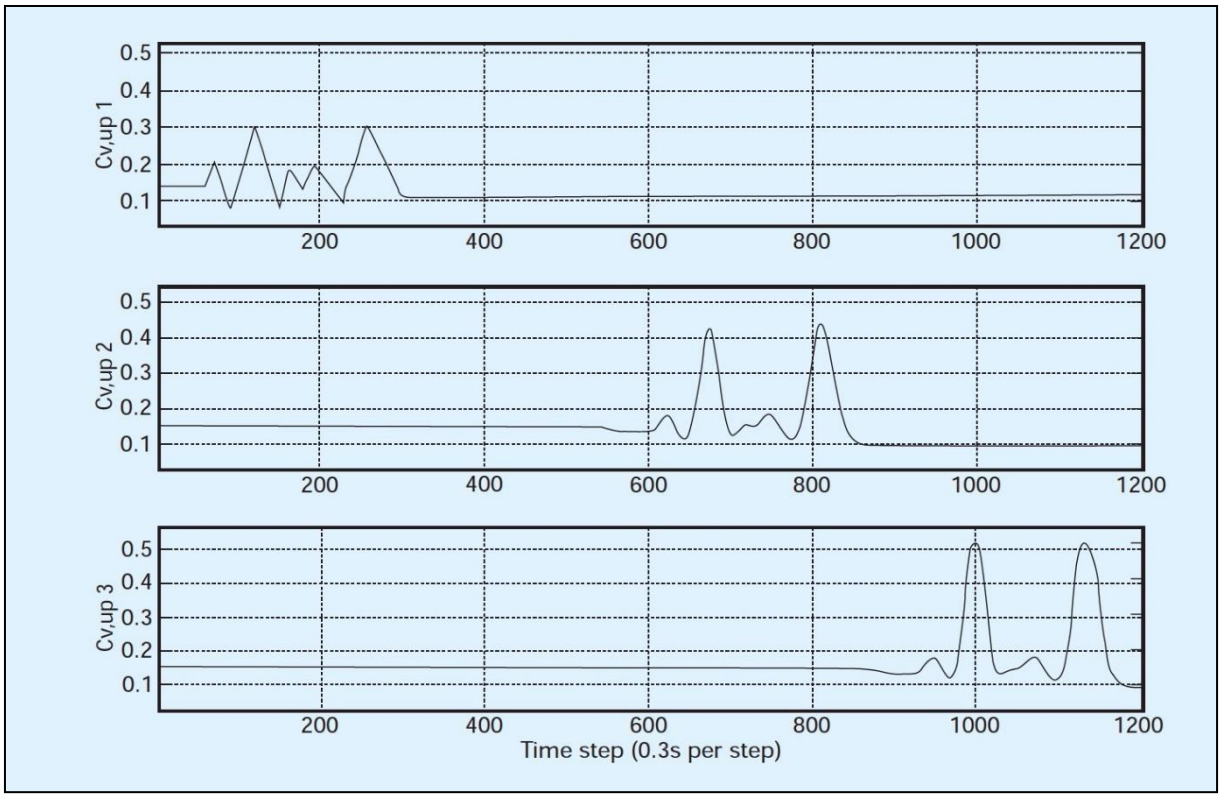

Figure 8-13: Deformation of density waves along the long pipeline (slurry velocity round the deposition limit velocity) observed at the inlet to the pipeline, 500 meter behind inlet and 800 meter behind inlet.

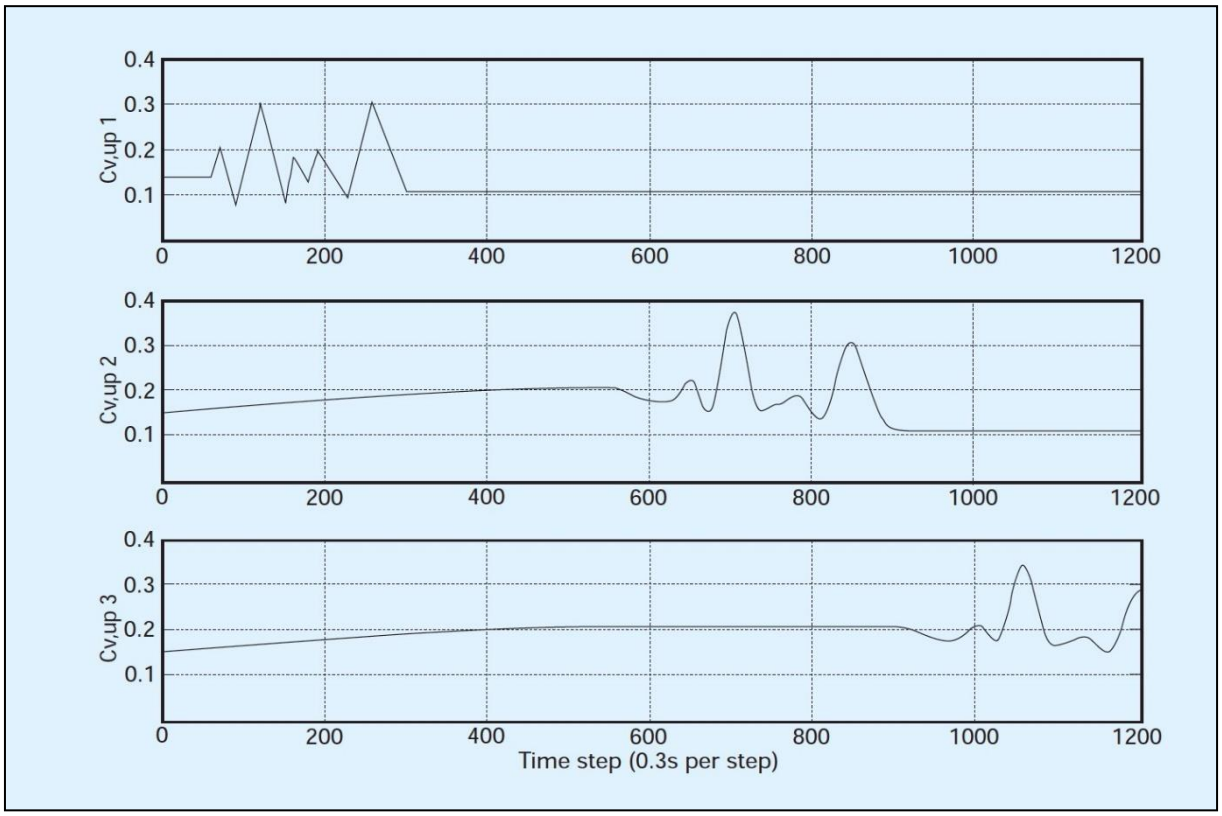

Figure 8-14: Deformation of density waves along the long pipeline (slurry velocity far above the deposition limit velocity) observed at the inlet to the pipeline, 500 meter behind inlet and 800 meter behind inlet.

8.8. The Pump/Pipeline System Description.

In a steady state situation, the revolutions of the pumps are fixed, the line speed is constant and the solids properties and concentration are constant in the pipeline. The working point of the system is the intersection point of the pump head curve and the pipeline resistance curve. The pump curve is a summation of the head curves of each pump according to equation (8-16). The resistance curve is a summation of the resistances of the pipe segments and the geodetic head according to equations (8-22) and (8-23). Figure 8-15 and Figure 8-16 show this steady state situation for the system used in the case study at 6 densities ranging from clear water upto a density of 1.6 ton/m^3. In reality, the solids properties and concentration are not constant in time at the suction mouth. As a result of this, the solids properties and concentration are not constant as a function of the position in the pipeline. To be able to know these properties as a function of the position in the pipeline, the pipeline must be divided into small segments. These segments move through the pipeline with the line speed. Each time step a new segment is added at the suction mouth, while part of the last segment leaves the pipeline. Because the line speed is not constant, the length of the segment added is not constant, but equals the line speed times the time step. For each segment the resistance is determined, so the resistance as a function of the position in the pipeline is known. This way also the vacuum and the discharge pressure can be determined for each pump. If vacuum results in cavitation of one of the pumps, the pump head is decreased by decreasing the pump density, depending on the time the pump is cavitating. The dynamic calculations are carried out in the time domain, because most of the equations used are non-linear. The time step used is about 1 second, depending on the speed of the PC and the other tasks Windows has to carry out.

8.9. The Segmented Pipeline.

In reality, the solids properties and concentration are not constant in time at the suction mouth. As a result of this, the solids properties and concentration are not constant as a function of the position in the pipeline. To be able to know these properties as a function of the position in the pipeline, the pipeline must be divided into small segments. These segments move through the pipeline with the line speed. Each time step a new segment is added at the suction mouth, while part of the last segment leaves the pipeline. Because the line speed is not constant, the length of the segment added is not constant, but equals the line speed times the time step. For each segment the resistance is determined, so the resistance as a function of the position in the pipeline is known. This way also the vacuum and the discharge pressure can be determined for each pump. If vacuum results in cavitation of one of the pumps, the pump head is decreased by decreasing the pump density, depending on the time the pump is cavitating.

As mentioned before, each segment contains the mixture properties. The two most important properties are the mixture density and the grain size distribution. If a homogeneous transport model is considered, the grain distribution can be replaced by the characteristic factor depending on the grain size distribution. For a heterogeneous or two-phase transport model, the problem becomes much more complicated.

The segments move through the pipeline with the line speed, assuming that all of the contents of a segment move at the same speed. However if part of the mixture has settled at the bottom of the pipeline, this part will move with a much smaller velocity then the average velocity, while the mixture above the sediment will move with a velocity higher then the average. In a stationary situation this does not matter, as long as the transport model used takes this into account (the Durand model takes this into account), but in a non-stationary situation there may be temporary accumulation of solids. Also dunes may occur, moving through the pipeline. To implement these phenomena a longitudinal diffusion model has to be developed. The current administrative system in the simulation software is suitable for storing the information required to describe these phenomena. However the information stored has to be extended, since two-phase flow requires storage of two components, the bed load and the suspended material.
With a time step in the simulation software of 0.1 to 0.2 seconds, the segment length varies (with a line speed of 5 m/s) from 0.5 to 1.0 m. The required length for a good description of dunes moving through the pipeline is unknown, but from experiments in our laboratory it seems a segment length of 0.5 m is still to high. An intuitive estimate of 0.1 to 0.2 m seems reasonable. The Durand model however has not been developed for a pipeline of only 0.1 m.

The mass conservation equation of a pipe segment can be described with equation (8-34). In this equation all terms give a mass flow. The sum of the mass flow of the suspended material and the bed load that enter a segment, should be equal to the sum of the suspended material and the bed load that leave the segment plus the material that settles in the segment. The last term on the right hand side is the settlement of suspended material into the bed. This term is positive when material settles (accumulates) in the segment.

$$Q_{in-s} + Q_{in-b} = Q_{out-s} + Q_{out-b} + Q_{s \rightarrow b} \qquad (8\text{-}34)$$

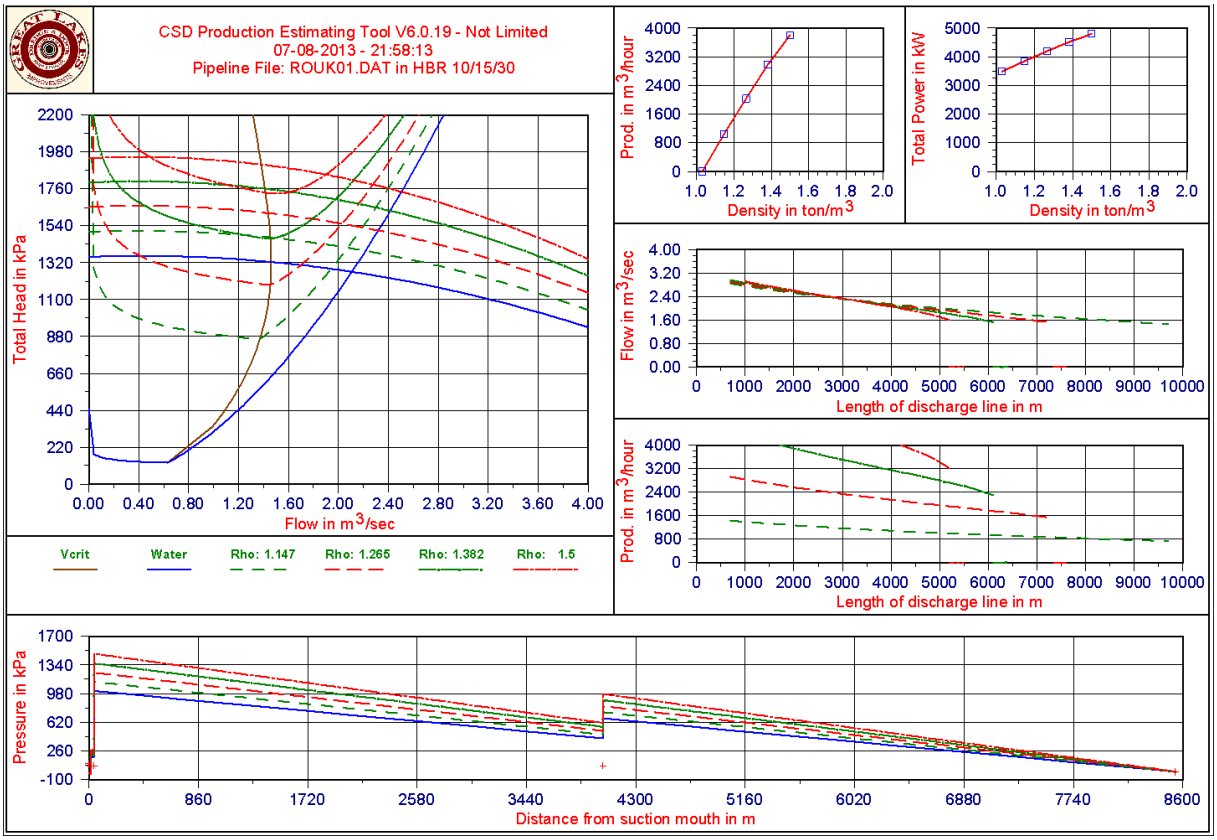

Figure 8-15: Characteristics of the pump/pipeline system, not limited.

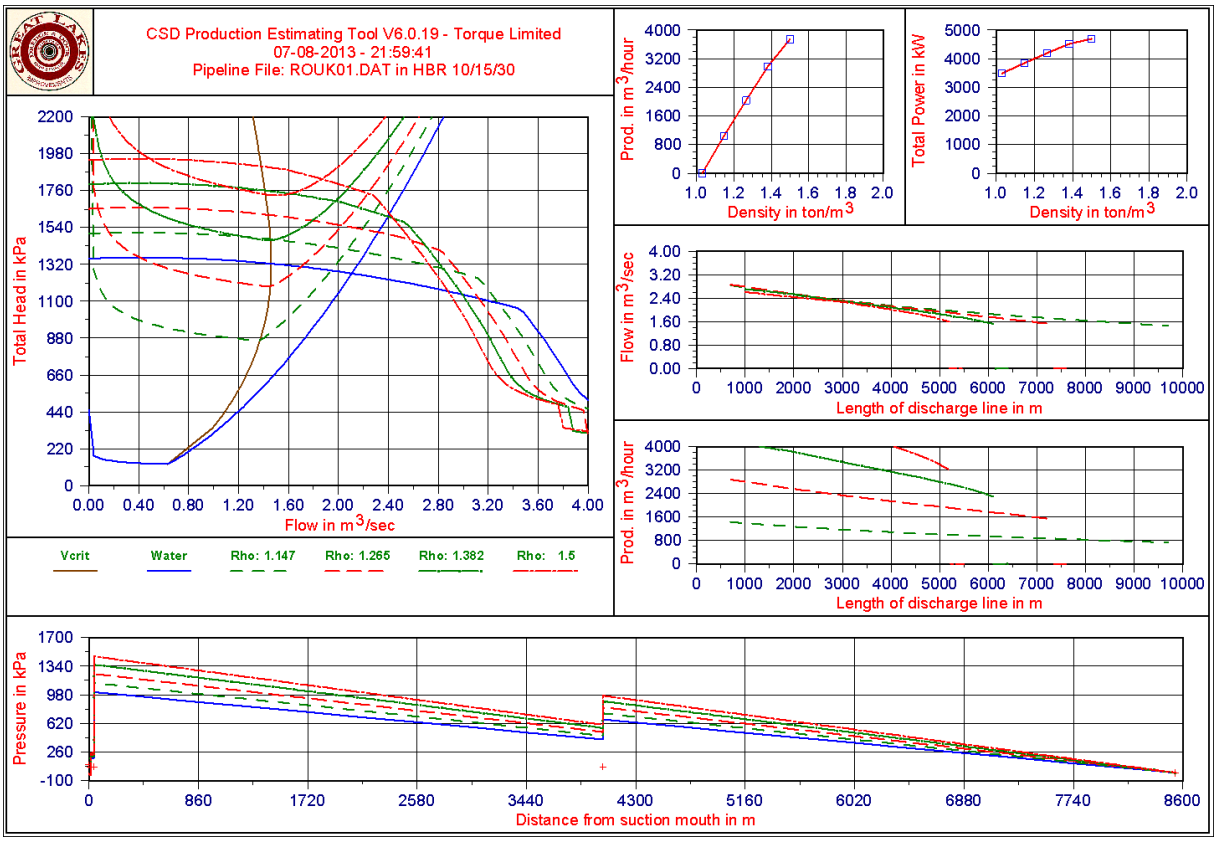

Figure 8-16: Characteristics of the pump/pipeline system, torque limited.

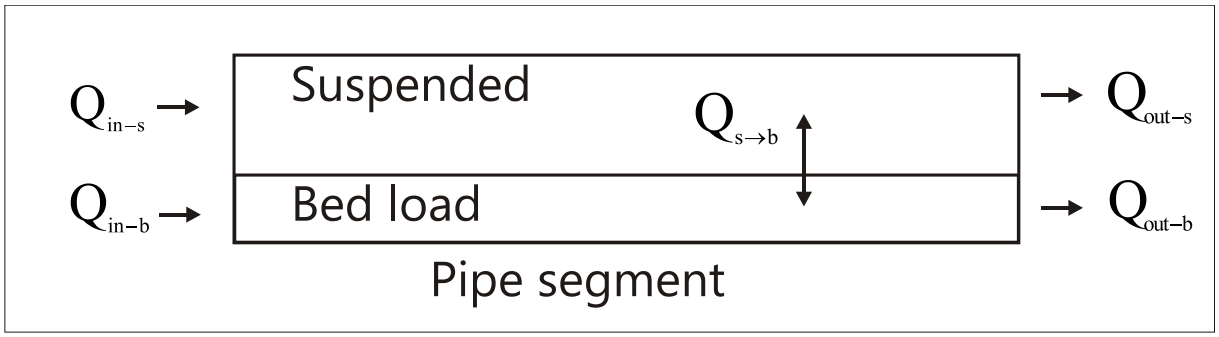

Figure 8-17: The mass equilibrium in a pipe segment.

The question is however; whether for a good description of the transport it suffices to administer the suspended load and the bed load in one segment moving through the pipeline. In fact the velocity of the suspended load will be higher then the average line speed and the velocity of the bed will be much smaller. The pipe segment should have to be split into two separate segments for the suspended load and for the bed load, moving at two different velocities through the system, in order to administer the two phase flow correctly. The current method of administering the contents of the segments is suitable for suspended load only at line speeds above the critical velocity.
A good description of the vertical diffusion between the suspended load and the bed load is not yet available and will be subject for further research. Erosion diffusion equations are used for hopper sedimentation as well, but these equation do not suffice Miedema and Vlasblom (1996).

8.10. The Inertial Effects in the Pipeline.

A steady state process requires a constant density and solids properties in the system and thus at the suction mouth. In practice it is known, that the solids properties and the density change with respect to time. As a result, the pump discharge pressure and vacuum will change with respect to time and the pipeline resistance will change with respect to time and place. A change of the discharge pressure will result in a change of the torque on the axis of the pump drive on one hand and in a change of the flow velocity on the other hand. The mixture in the pipeline has to accelerate or decelerate. Since centrifugal pumps respond to a change in density and solids properties at the moment the mixture passes the pump, while the pipeline resistance is determined by the contents of the pipeline as a whole, this forms a complex dynamic system.

The inertial pressure of the mixture has to be added to the resistance of the mixture. In fact, the inertial pressure is always equal to the difference between the total pressure generated by the pumps and the total resistance of the mixture in the pipeline system. If this difference is positive (the pump pressure has increased due to an increase of the mixture density), the mixture will accelerate. If negative, the mixture will decelerate.
As a result of the acceleration and deceleration, the mixture velocity (line velocity) will vary as a function of time. To realize a stable dredging process, it is required to have a line velocity that will not vary too much. The line velocity can be controlled by varying the revolutions of one of the dredge pumps, where the last pump is preferred. From the above one can distinguish the different effect by the time they require to change/occur:

1. Very fast (within a second), the change in discharge pressure of a centrifugal pump
2. Fast (seconds), the change in revolutions of the pump drive and the change in line speed (acceleration and deceleration)
3. Slow (minutes), filling up the pipeline with mixture or a change in mixture content

These effects can also be recognized in the equations describing the pump curve and the system curve. Equation (8-11) shows the effect of the fluid (mixture) density on the discharge pressure. Equation (8-6) shows the effect of a changing set point of the pump drive. Equations (8-22) and (8-23) contain the inertial effect in the most right term on the right hand side, while the effect of the changing mixture contents is described by the first term on the right hand side. Figure 8-15 and Figure 8-16 show the system curves and the pump curves for the system described in Figure 8-1, for 5 different densities, including clear water, for a stationary situation. The intersection points of each system and pump curve at one density are the working points for the system at that specific density.

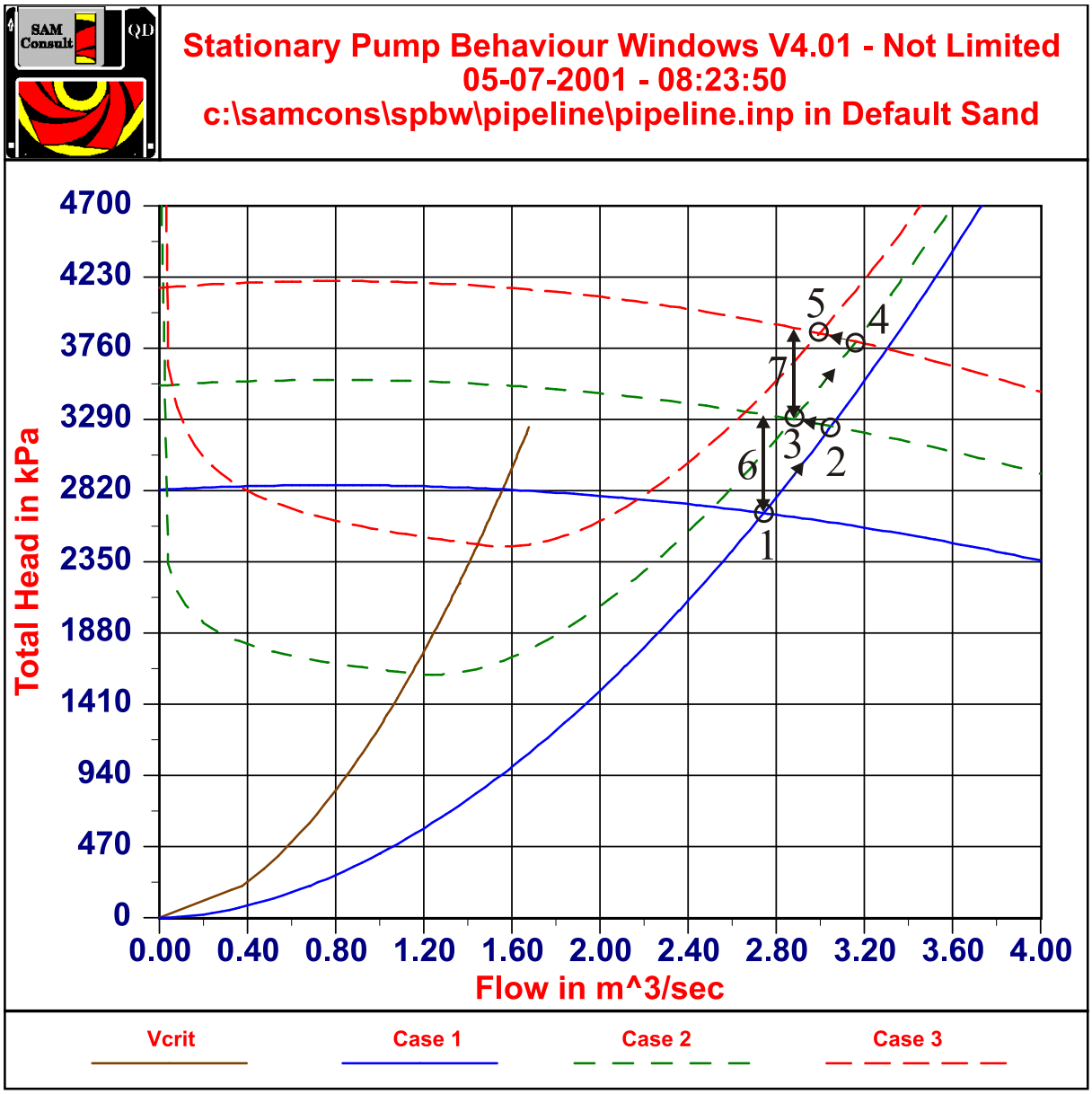

Figure 8-18: The system curves for 3 cases, accelerating.

Figure 8-18 is a representation of a number of phenomena that occur subsequently when the system (Figure 8-1) filled with water, is filled with mixture with a density of 1.6 ton/m^3. In this figure case 1 represents the system and the pump curve for the system filled with water. Case 2 represents the system with the pipeline filled with mixture up to a point just before the 3rd (booster) pump. Case 3 represents the system filled entirely with the mixture.

Now, what happens if a system filled with water is continuously filled with the mixture?

First the working point is point 1 in Figure 8-18. This is the intersection point of the pump and system curves for water. When mixture enters the system, within a few (about 8) seconds the mixture has reached the ladder and main pump, since the distance is only about 44 m and the line speed about 5 m/sec. At that moment, the discharge pressure of the ladder pump and main pump increase proportionally to the mixture density, resulting in a pump curve according to case 2 and a working point 2. The flow and thus the line speed will not change instantly because of the inertia of the fluid and solids mass in the pipeline. Number 6 shows the access pressure caused by the sudden increase of the discharge pressure. This access pressure has to take care of the acceleration of the pipeline contents. This acceleration will take in the order of 10-20 seconds.

The filling of the system continues and the resistance of the mixture slowly increases, so the working point moves from point 2 to point 3. With the line speed of 5 m/s, this will take about 400 seconds or almost 7 minutes. When the mixture reaches the booster pump, at once the discharge pressure increases, resulting in the pump curve

according to case 3, the top curve. The working point will move to point 4, while 7 represents the access pressure causing the acceleration of the pipeline contents. Moving from 3 to 4 will take 10-20 seconds. When the pipeline continues to be filled with mixture, the resistance increases, resulting in the working point moving from 4 to 5 in about 400 seconds.

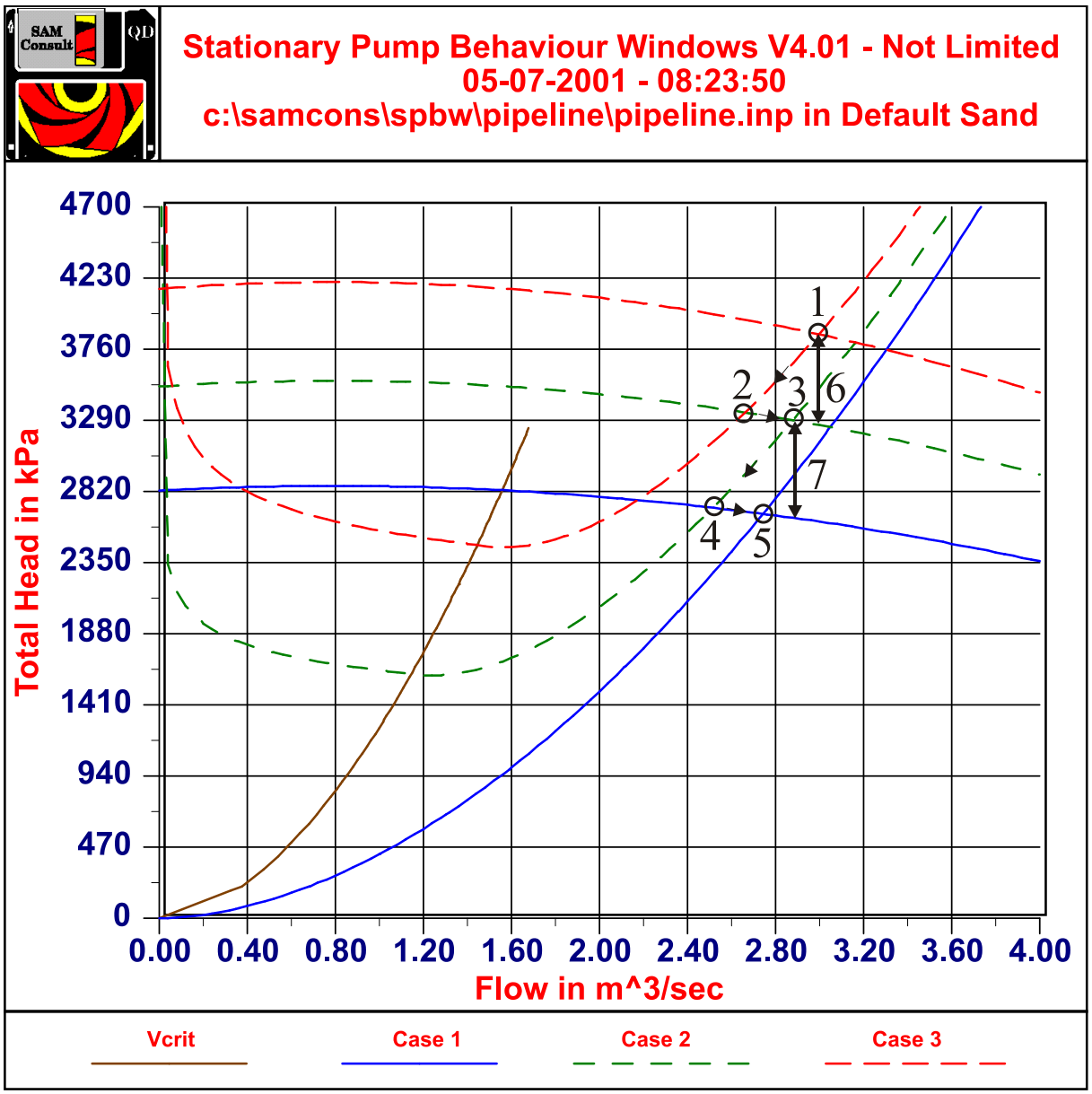

Figure 8-19: The system curves for 3 cases, decelerating.

Figure 8-19 shows the same procedure for a pipeline filled with a mixture of density 1.6 ton/m^3. In this case the pipeline, containing mixture of 1.6 ton/m^3, is filled with water, resulting in decreasing discharge pressures and pipeline resistance. The procedure is almost the inverse, but Figure 8-19 shows that the path followed is different. In working point 1, all the pumps and the pipeline are filled with the mixture. When the water reaches the ladder and main pump, the pump curve is decreased to case 2 and the new working point is point 2. 6 gives the deceleration pressure, so the contents of the pipeline will decelerate from 1 to 2 in about 10-20 seconds. From 2-3 the pipeline is filled with water up to the booster pump, resulting in a decrease of the resistance, taking about 400 seconds. When the water reaches the booster pump, the pump curve decreases again to case 1, resulting in working point 4. Again it takes 10-20 seconds to move from point 3 to point 4. At last the pipeline behind the booster pump is filled with water, resulting in a decrease of the resistance, taking about 400 seconds. The final working point is point 5. Both Figure 8-18 and Figure 8-19 give an example of the non-stationary effects in a multi-pump/pipeline system.

8.11. Case study.

The aim of this case study is twofold, first it shows events caused by the dynamic behaviour of the system that cannot be predicted by steady state calculations, second it shows the application of the above theory. A problem in defining a system and a scenario for the simulation is, that the system can consist of an infinite number of pump/pipeline combinations, while there also exists an infinite number of solids property/concentration distributions as a function of time. For this case study, a system is defined consisting of a suction line followed by three pump/pipeline units. The first pump is a ladder pump, with a speed of 200 rpm, an impeller diameter of 1.5 m and 1050 kW on the axis (see Figure 8-5). The second and the third pump run also at a speed of 200 rpm, have an impeller diameter of 2.4 m and 3250 kW on the axis (see Figure 8-6). The time constants of all three pumps are set to 4 seconds. The time constant of the density meter is set to 10 seconds. The suction line starts at 10 m below water level, has a length of 12 m and a diameter of 0.69 m. The ladder pump is placed 5 m below water level. The main pump and the booster pump are placed 10 m above water level. The pipeline length between ladder and main pump is 30 m, between main pump and booster pump 2000 m, as is the length of the discharge line. The pipe diameters after the ladder pump are 0.61 m. The total simulation lasts about 28 minutes and starts with the pipeline filled with water. After the pumps are activated, a mixture with a density of 1.6 ton/m^3 enters the suction mouth for a period of 2 minutes. A sand is used with a d_{15} of 0.25 mm, a d_{50} of 0.50 mm and a d_{85} of 0.75 mm. This density block wave moves through the system, subsequently passing the three pumps. For the simulation the following scenario is used:

00 minutes	start of simulation
01 minutes	start of ladder pump
04 minutes	start of main pump
07 minutes	start of booster pump
10 minutes	increase mixture density to about 1.6 ton/m^3
12 minutes	decrease mixture density to water density
12 minutes	take sample of density distribution in pipeline
17 minutes	take sample of density distribution in pipeline
22 minutes	take sample of density distribution in pipeline
28 minutes	stop simulation

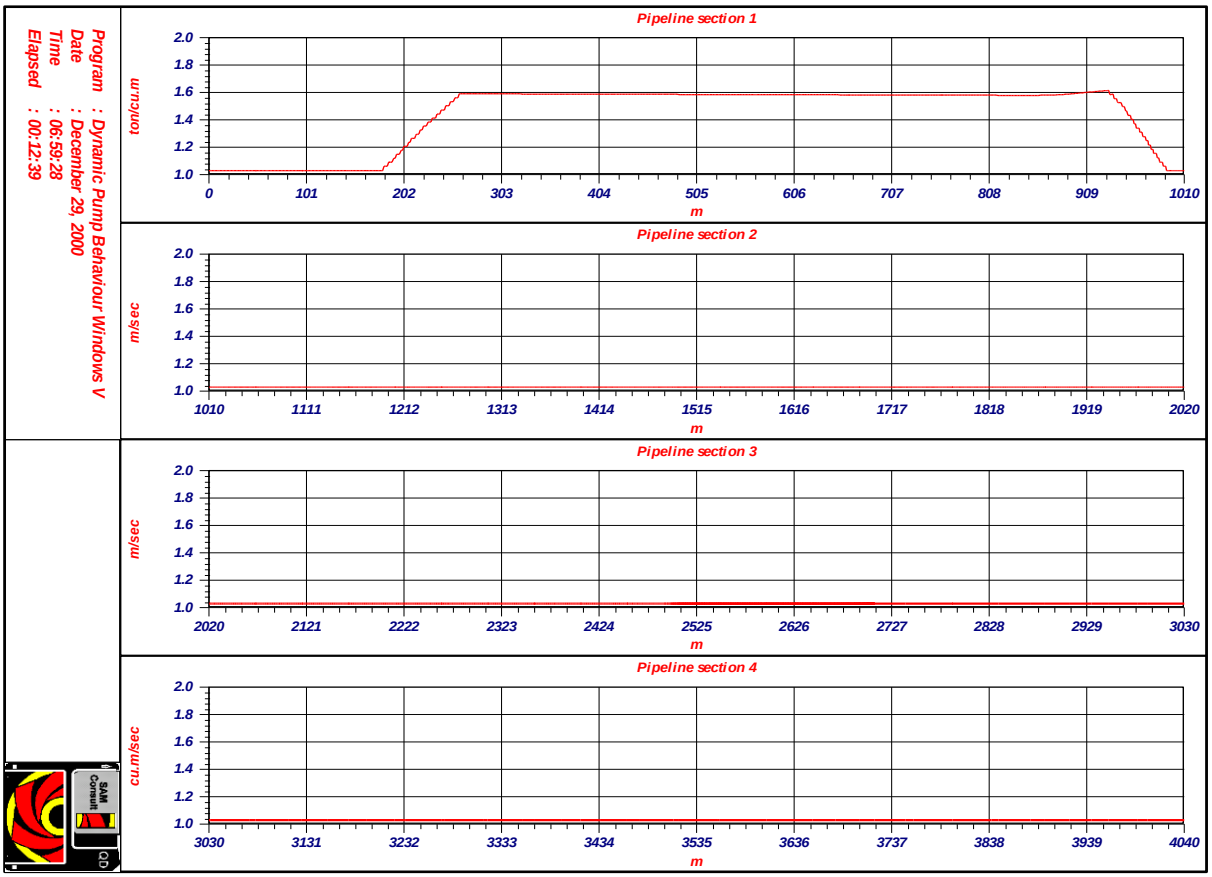

Figure 8-20: The density distribution in the pipeline after 12 minutes.

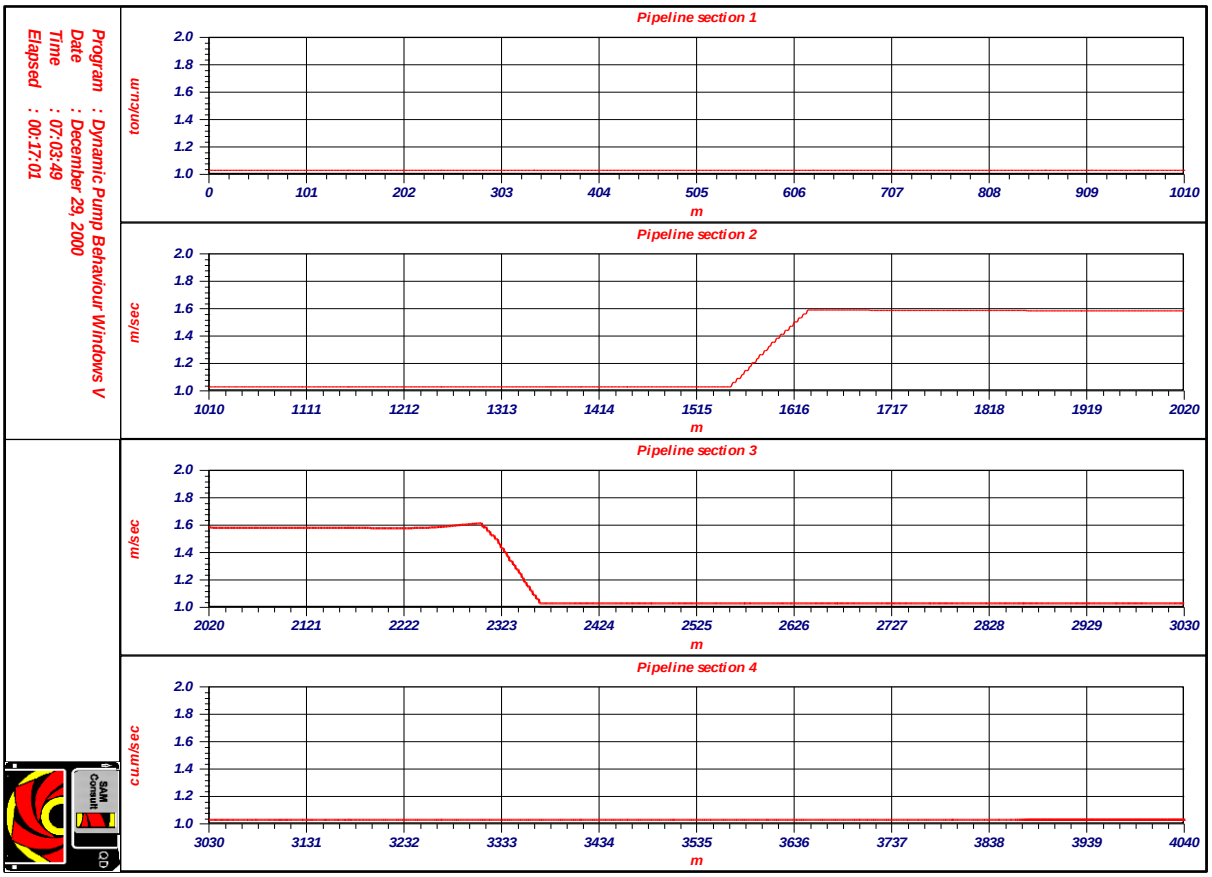

Figure 8-21: The density distribution in the pipeline after 17 minutes.

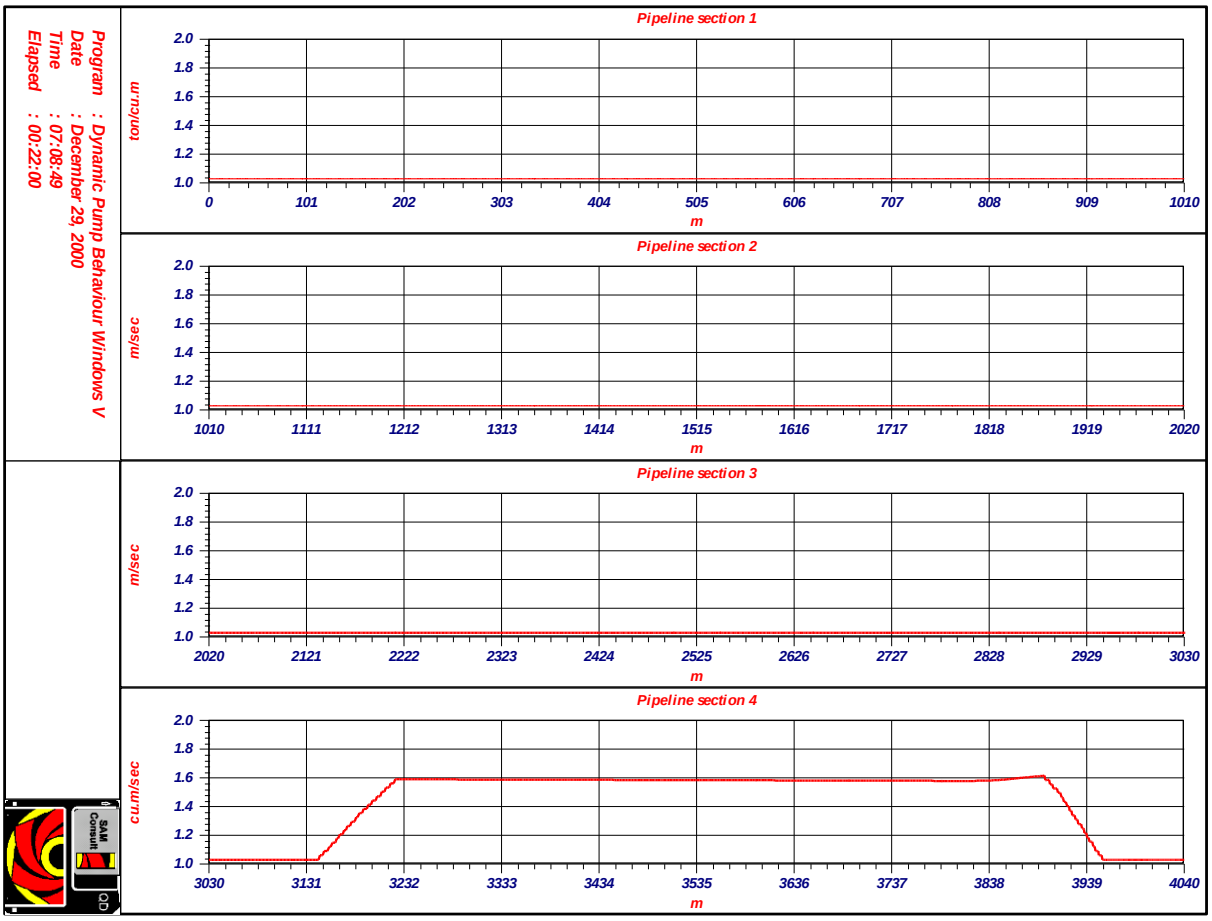

Figure 8-22: The density distribution in the pipeline after 22 minutes.

Figure 8-20, Figure 8-21 and Figure 8-22 show the density wave at 12, 17 and 22 minutes of simulation time. At 12 minutes the density wave occupies the suction line, the ladder pump and the main pump and part of the pipeline behind the main pump. At 17 minutes the density wave occupies the last part of the pipeline before the booster pump, the booster pump and the first part of the discharge line after the booster pump. At 22 minutes the density wave occupies the middle part of the discharge line. Figure 8-23 shows the line speed, the density, the total power consumed and the production as a function of time. The line speed, the density and the production are determined at the inlet of the ladder pump. The density is determined using the mathematical behaviour of a density transducer with a time constant of 10 seconds. Figure 8-24, Figure 8-25 and Figure 8-26 show the pump speed, power, vacuum and discharge pressure of the three pumps as a function of time.

As can be seen in Figure 8-23, the line speed increases slower then the pump speed, due to the inertial effect in the fourth term of equation (8-23). When the density wave passes the ladder and main pump (from 10 to 13 minutes), the discharge pressure of these pumps increases, resulting in a higher line speed. When the density wave passes the booster pump (from 16 to 19 minutes) the same occurs for the booster pump.
After about 10 minutes of simulation time, all three pumps are activated and a steady state situation occurs in the system. Then the mixture density at the suction mouth increases from water density to about 1.6 ton/m^3. First the resistance in the suction line increases, resulting in a sudden decrease of the ladder pump vacuum and discharge pressure. When the density wave reaches the ladder pump, the discharge pressure increases, due to the higher density. When after 2 minutes, the density decreases to the water density, first the resistance in the suction line decreases, resulting in an increase of the ladder pump vacuum and discharge pressure, followed by a decrease of the discharge pressure when the clear water reaches the ladder pump (see Figure 8-23). The distance between the ladder pump and the main pump is 30 m. With an average line speed of 5 m/s, the density wave passes the main pump 6 seconds after passing the ladder pump. The same phenomena as described for the ladder pump, occur 6 seconds later for the main pump (see Figure 8-25). Due to the increased discharge pressure of ladder and main pump during the density wave, the line speed will also increase (see Figure 8-23), but because of the inertial effects, this increase and 2 minutes later decrease is not as steep.

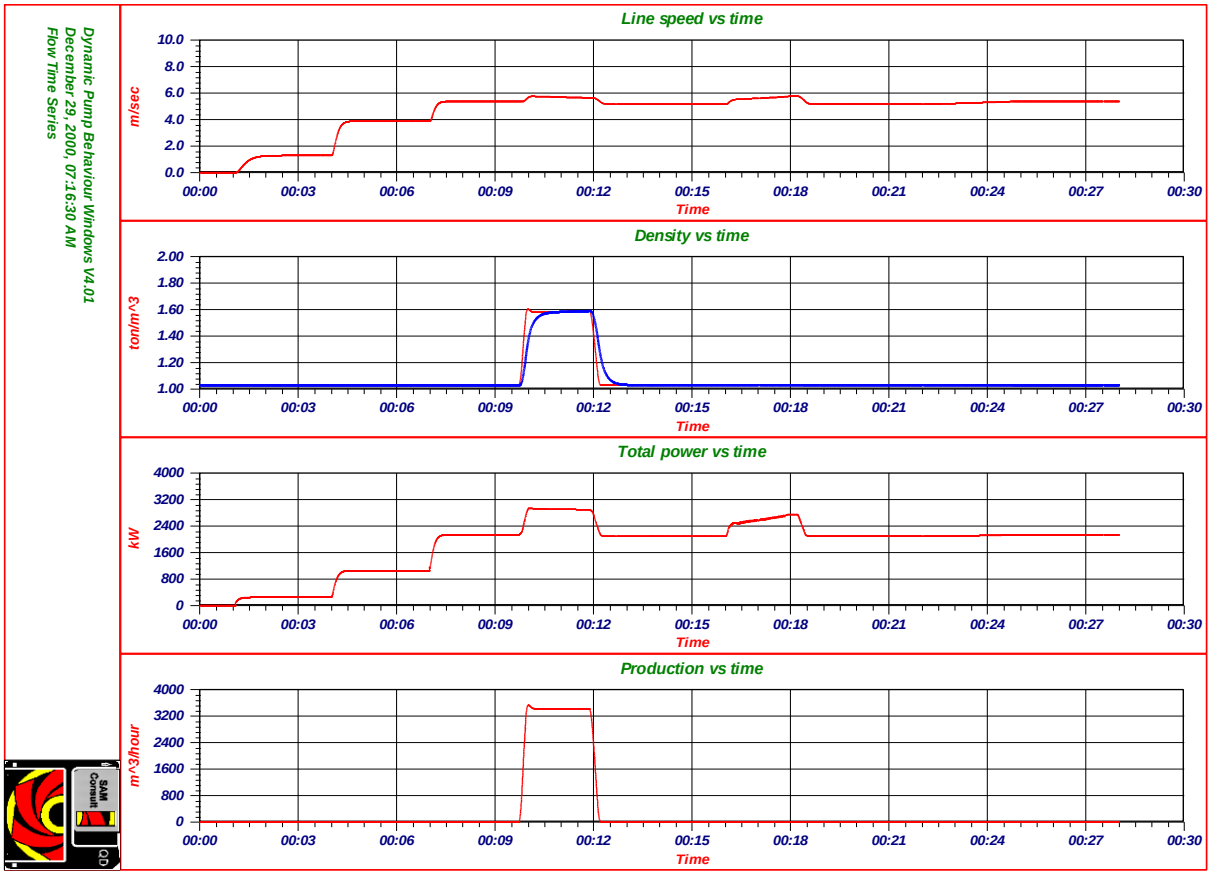

Figure 8-23: Line speed, density, total power and situ production as a function of time.

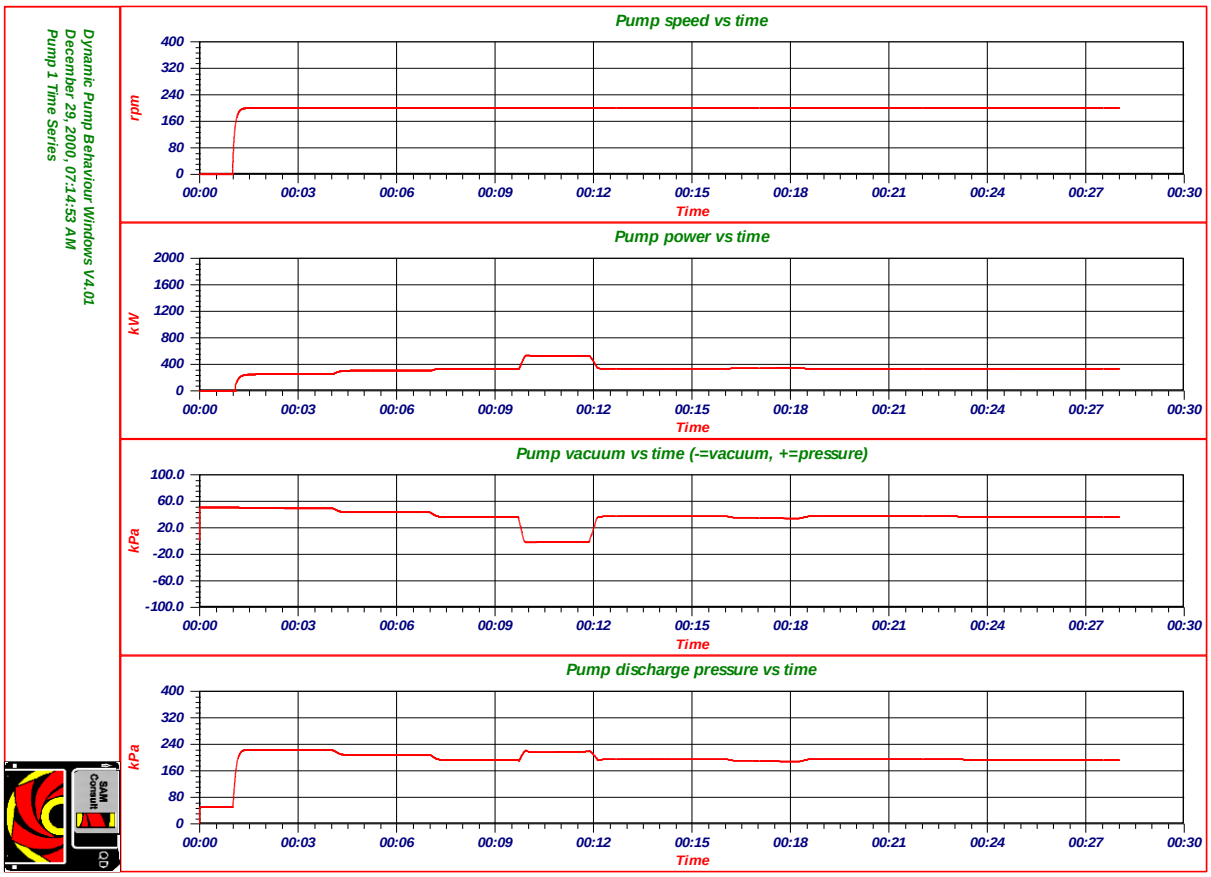

Figure 8-24: Speed, power, vacuum and discharge pressure of the ladder pump vs. time.

One could say that there is a time delay between the immidiate response of the discharge pressure of the pumps on changes in the density in the pumps and the response of the line speed on changes in the discharge pressure. At 12 minutes and about 15 seconds, the density wave has left the main pump, but has not yet reached the booster pump. The head of each pump is determined by the density of water, but the line speed is still determined by the head resulting from the mixture and thus to high. The resistance in the pipe between main and booster pump is high because of the mixture, resulting in a decrease of the booster pump vacuum and discharge pressure. As the line speed decreases, the booster pump vacuum and discharge pressure will stay in a semi-steady state situation. When the density wave reaches the booster pump, the total head of the booster pump increases, resulting in an increase of the line speed. This occurs after about 16.5 minutes of simulation time. Since the total head of ladder and main pump does not change, the booster pump vacuum will have to decrease to pull harder on the mixture in the pipeline before the booster pump. This results in the occurence of cavitation of the booster pump, limiting the total head of the booster pump and thus the line speed. The cavitation causes a very instable behaviour of the booster pump as is shown in Figure 8-26. Since the density wave moves from the suction line to the discharge line, the booster pump vacuum and discharge pressure both increase when the density wave moves through the booster pump. After 18.5 minutes the density wave leaves the booster pump. The total head of the booster pump decreases sharply, while the line speed decreases slowly. The fluid in the pipeline before the booster pump pushes and the fluid after the booster pump pulls, resulting in a quick increase of the booster pump vacuum and a decrease in the booster pump discharge pressure. As the line speed decreases, the discharge pressure will increase again. After 23 minutes of simulation time, the density wave starts leaving the pipeline. 2 minutes later the density wave has complete left the system. Because of the decreasing resistance during this time-span, the line speed will increase slightly, resulting in a small decrease of the vacuum and discharge pressure of each pump, while the total head remains constant. The total power will also increase slightly because of this.
To stabilise the line speed to a specific value, flow control can be used. Flow control adjusts the speed of the last pump, in this case the booster pump. If the line speed is higher then a set point, the booster pump speed is decreased, if the line speed is lower, the booster pump speed is increased. To determine the correct booster pump speed, the total head is considered to be a summation of the heads of all of the pumps in the system. The head of the booster pump is considered to be proportional to the square of the booster pump speed and the total resistance is considered to be proportional to the square of the line speed, this gives:

$$\Delta p_{l.p.} + \Delta p_{m.p.} + \Delta p_{b.p.} = \Delta p_{l.p.} + \Delta p_{m.p.} + \alpha \cdot n^2 = \beta \cdot c^2 \qquad \textbf{(8-35)}$$

When the flow control is active, the heads of the ladder pump and the main pump do not change, so for the set point of the line speed:

$$\Delta p_{l.p.} + \Delta p_{m.p.} + \Delta p_{b.p.} = \Delta p_{l.p.} + \Delta p_{m.p.} + \alpha \cdot n_{f.c.}^2 = \beta \cdot c_{f.c.}^2 \qquad \textbf{(8-36)}$$

Assuming that the sum of the heads of ladder and main pump equals the head of the booster pump times a factor γ and dividing equation (8-36) by equation (8-35), the following can be derived:

$$n_{f.c.} = n \cdot \sqrt{(\gamma + 1) \cdot \left(\frac{c_{f.c.}}{c}\right)^2 - \gamma} \qquad \textbf{(8-37)}$$

By substituting: $\varepsilon = \left(\frac{c_{f.c.} - c}{c}\right)$ and using Taylor series approximation, this gives:

$$n_{f.c.} = n + n \cdot \tfrac{1}{2} \cdot (\gamma + 1) \cdot \varepsilon \cdot (\varepsilon + 2) \qquad \textbf{(8-38)}$$

Equation (8-38) is used to simulate flow control. The same scenario as above is used, except for the flow control that is activated after 8 minutes of simulation time. The set point for the line speed is set to 5 m/sec. Figure 8-27 and Figure 8-28 show the results of this simulation. As can be seen, the line speed changes rapidly when the density wave reaches or leaves one of the pumps. In about 15 seconds the flow control has adjusted the line speed to the set point. Figure 8-28 shows that the occurrence of cavitation is almost surpressed using the flow control. The booster pump speed tends to slightly oscillate. This is caused by applying several first order systems in series, resulting in a second or third order system. If the factor γ is choosen to high, the system is fast but tends to oscillate. If this factor is to small, the system responds very slow. In the simulation a value of 2 is used.

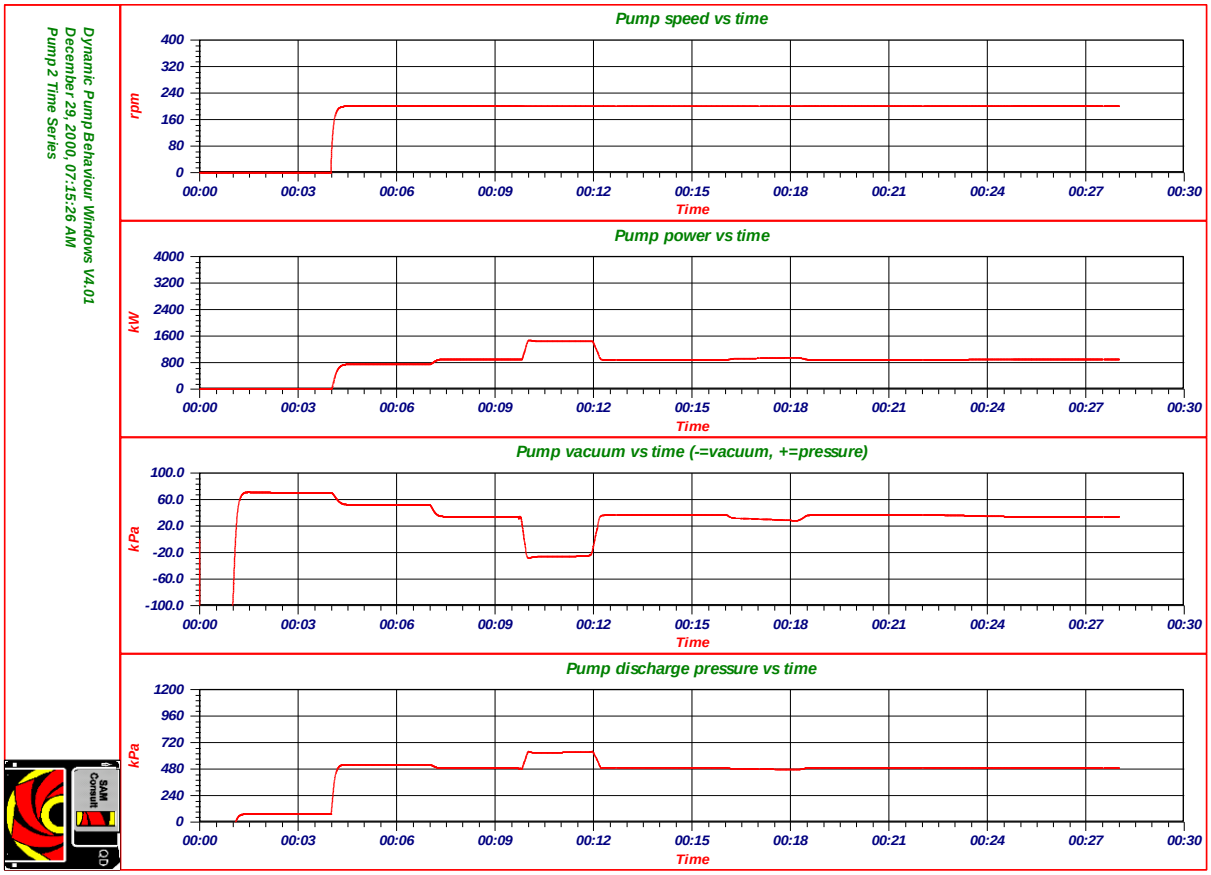

Figure 8-25: Speed, power, vacuum and discharge pressure of the main pump vs. time.

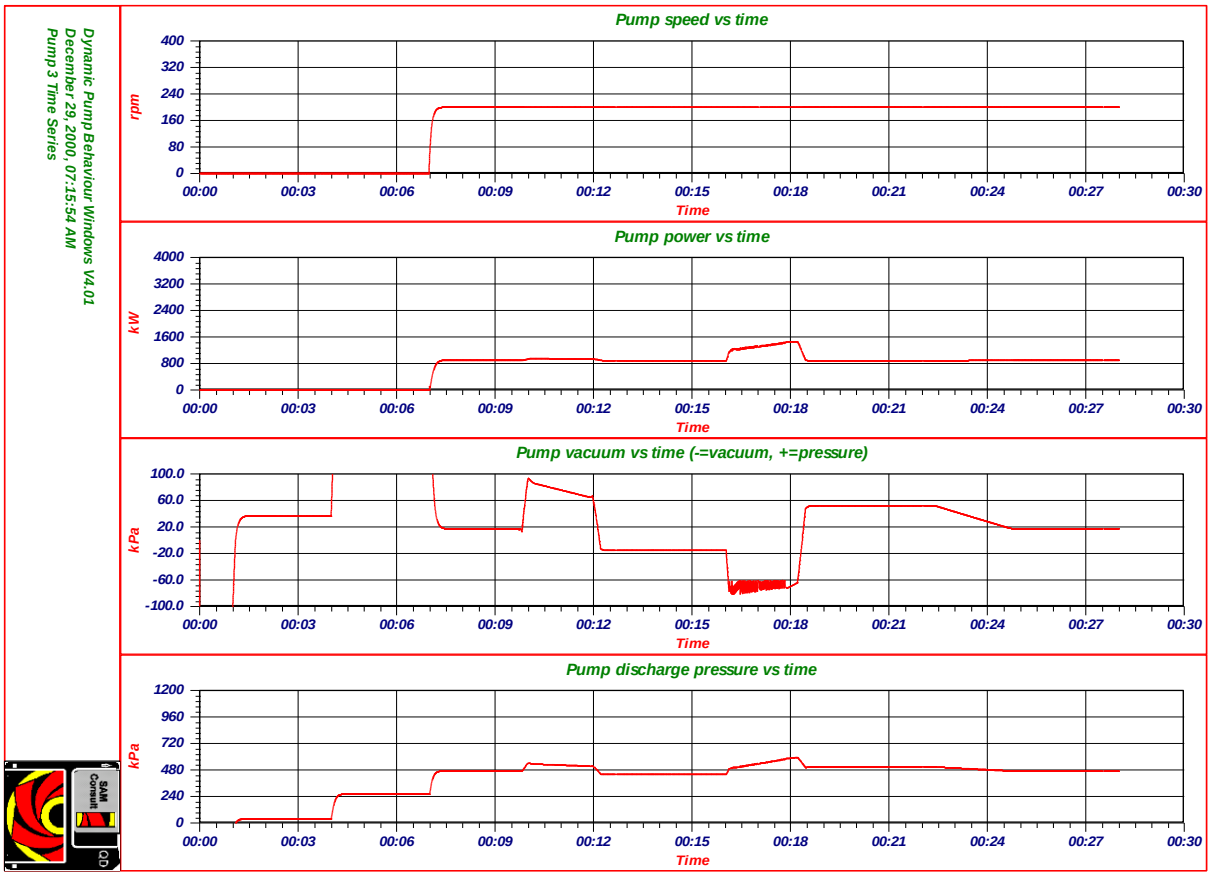

Figure 8-26: Speed, power, vacuum and discharge pressure of the booster pump vs. time.

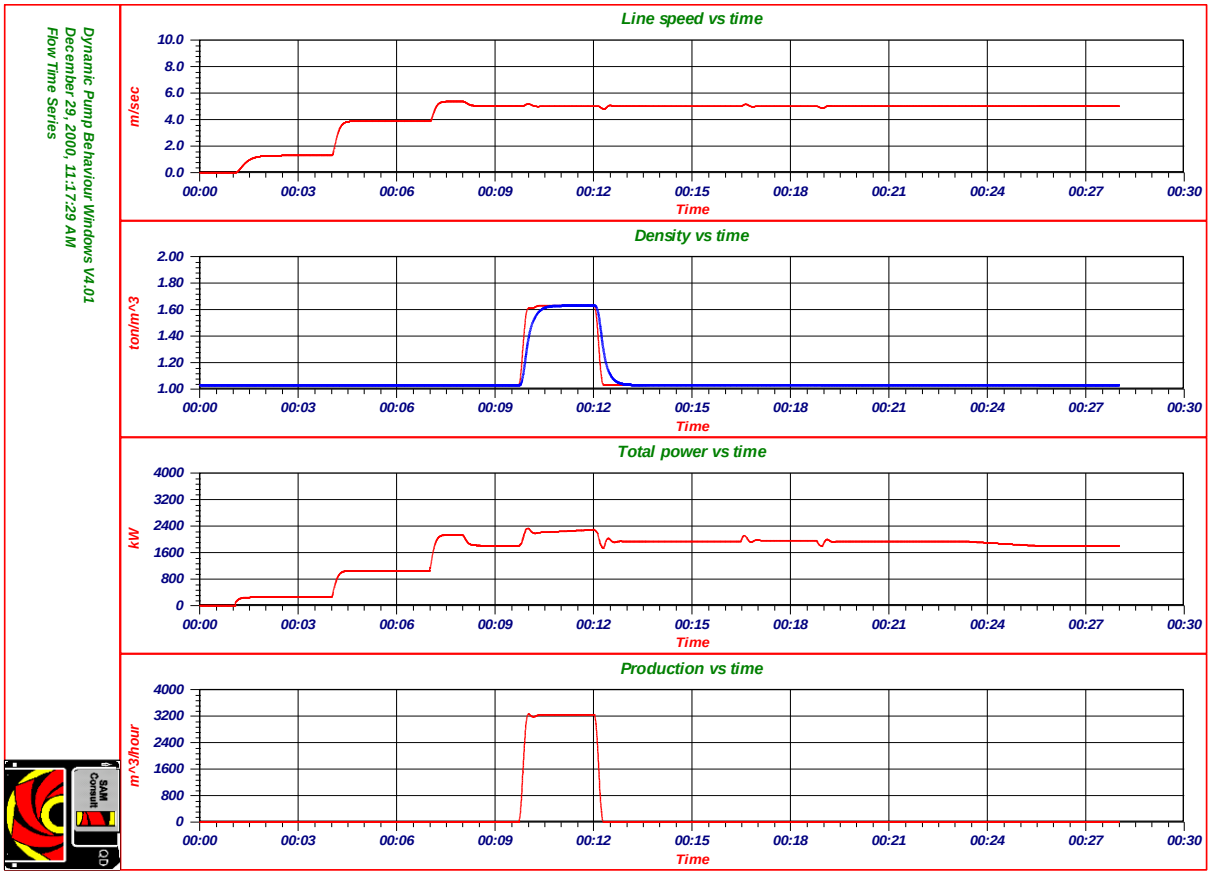

Figure 8-27: Line speed, density, total power and situ production as a function of time, with flow control.

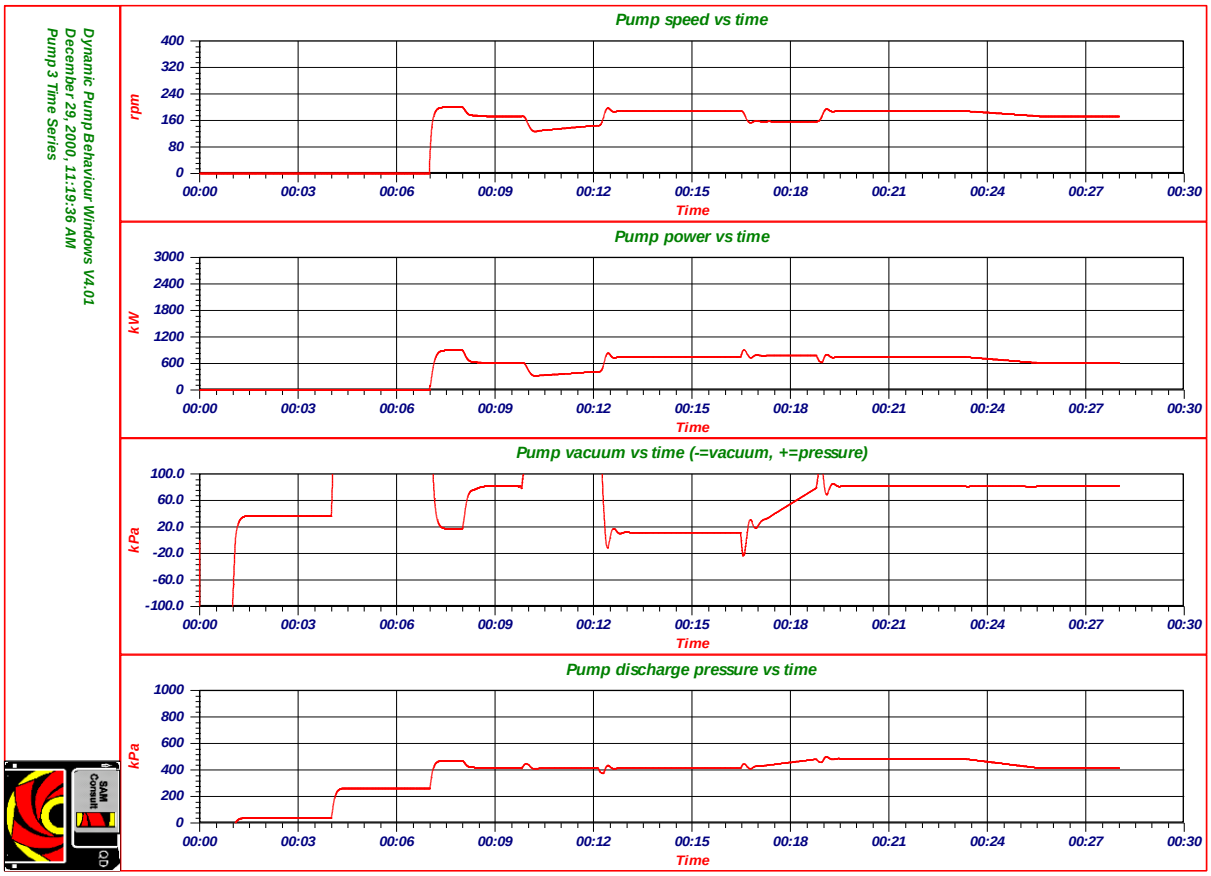

Figure 8-28: Speed, power, vacuum and discharge pressure of the booster pump vs. time, flow control.

8.12. Conclusions and Discussion.

The behaviour of a multi pump/pipeline system is hard to understand. As mentioned before, an infinite number of system configurations and soil conditions exist. Systems are usually configured, based on steady state calculations, while the dynamic behaviour is ignored. Combining the steady state approach for pipeline resistance with the dynamic behaviour of pumps, pump drives and the second law of Newton, the dynamic behaviour can be simulated. However, a number of assumptions had to be made.

These assumptions are:

1. There is no longitudinal diffusion in the pipeline.
2. The pump drive behaves like a constant torque system.
3. The pipeline resistance is determined using the Durand theory.
4. The centrifugal pump obeys the affinity laws.

Whether these assumptions are valid will be subject of further research. The simulations however show the occurrence of phenomena that are known in practice.

Multi pump/pipeline systems can be configured in an infinite number of configurations. Phenomena that occur in one configuration do not have to occur in other configurations. So the configuration to carry out simulations to examine certain phenomena has to be chosen carefully. The configuration used in this paper is suitable for simulation of most phenomena. The examples show, that moving from one working point to the next working point, does not occur instantaneously, but with a time delay, where the time delay depends on the phenomena.

The simulation model used is very well suitable for fully suspended load, but has a deficiency for two phase flow. The main shortcoming is the fact that suspended load and bed load move through the system at two different velocities, not being equal to the average line speed.

A second shortcoming is the lack of availability of a good model for the vertical diffusion between the suspended load and the bed load. This will be subject for further research.

One should consider that mathematical modelling is an attempt to describe reality without having any presumption of being reality.

8.13. Nomenclature.

$C_{1,2,3,4}$	Coefficients	-
C_D	Drag coefficient	-
C_{vt}	Transport concentration	-
C_v	Volumetric concentration	-
C_{vs}	Spatial concentration	-
C_x	Drag coefficient	-
d	Grain/particle diameter	**m**
D	Impeller diameter	**m**
D_p	Pipe diameter	**m**
Fr	Froude number	-
g	Gravitational constant	**m/sec^2**
H	Height/elevation	**m**
I	Mass moment of inertia	**ton·m^3**
k	Constant	-
Kp	Proportionality constant	**kNms/rad**
L	Length of pipeline	**m**
n	Revolutions	**rpm**
p	Pressure	**kPa**
P	Power	**kW**
Q	Flow	**m^3/sec**
r	Radius	**m**
Re	Reynolds number	-
T	Torque	**kNm**
u	Tangetial velocity	**m/sec**
v_t	Settling velocity grains	**m/sec**
v_{ls}	Line speed	**m/sec**
α,β	Coefficients	-
β	Blade angle	**rad**
ε	Wall roughness	**m**
ε	Ratio	-
η	Efficiency	-
φ	Rotation angle of centrifugal pump	**rad**
$\dot{\varphi}$	Angular velocity of centrifugal pump	**rad/sec**
$\ddot{\varphi}$	Angular acceleration of centrifugal pump	**rad/sec^2**
λ	Darcy Weisbach friction coefficient	-
ν	Kinematic viscosity	**m^2/sec**
ρ	Density	**ton/m^3**
τ	Time constant	**sec**
ξ	Friction coefficient	-
ψ	Shape factor	-
	Indices	
c	Concentration	
cr	Critical	
c.p.	Centrifugal pump	

D	Design	
d	Discharge	
d.e.	Diesel engine	
d.f.	Dry friction	
f	Fluid	
g	Geodetic	
gr	Grain	
g.b.	Gear box	
h.f.	Hydraulic friction	
h.i.	Hydraulic impact	
h.p.	Hydraulic power	
h.t.	Hydraulic transport	
i	In	
m	Mixture	
m	Measured	
n	Revolutions	
o	Out	
p	Proportional	
p	Pump	
p	Pipe	
q	Quarts	
s.p.	Set point	
t.	Total	
w	Water	
0	Initial value (boundary condition)	
n	Number of time step	
E	Euler	
15	% passing	
50	% passing	
85	% passing	

Chapter 9: Modeling of the Swing Winches of a Cutter Dredge.

9.1. Introduction.

The dredge motions consist of the six degrees of freedom of the pontoon complemented with the rotation of the ladder around the ladder bearings. This gives a total of 7 degrees of freedom (surge, sway, heave, roll, pitch, yaw and ladder rotation). For a dredge operating in still water, when wave forces are ignored, the motions in the horizontal plane are relevant (surge, sway and yaw) as well as the ladder rotation. The three pontoon motions can be reduced to the rotation around the spud if the spud is considered to be infinitely stiff. If the ladder rotation is considered not to be the result of a mass-spring system, but controlled by the ladder winch, only one equilibrium equation has to be solved, the rotation of the pontoon around the spud. The other 6 equilibrium equations are of interest when working offshore, when wave forces have to be taken into account, but using these equations increases the calculations to be carried out enormous.

9.2. The Motions of the Dredge.

The equilibrium equation of rotation around the spud is a second order non-linear differential equation, with the following external forces:

- The inertial forces of pontoon and ladder
- The water damping on pontoon and ladder
- The spring forces resulting from the swing wires
- The external forces resulting from the current
- The external forces resulting from the cutting process
- The external forces resulting from the swing winches
- The external forces resulting from the pipeline
- The reaction forces on the spud

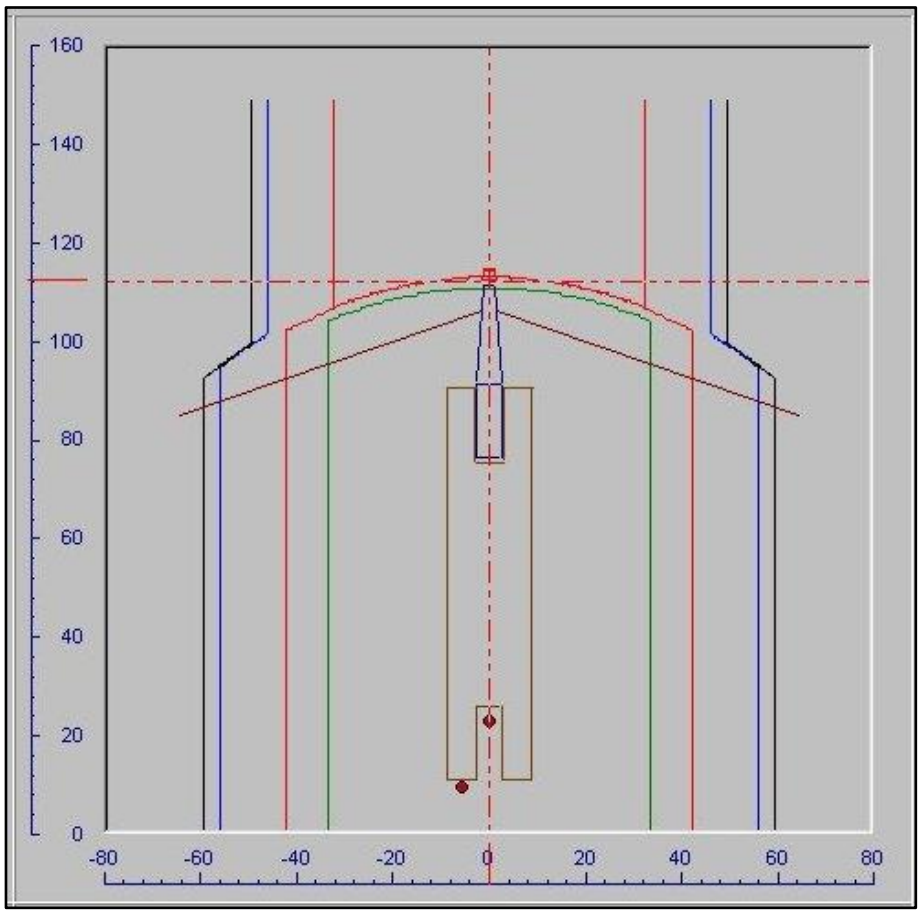

Figure 9-1: The display of the top view of the cutterdredge, also showing the channel.

1. The inertial forces (moments) determine whether there is an acceleration or deceleration of the rotation around the spud. These forces are the result of the equilibrium equation and thus of the external forces.
2. The water damping and the current forces depend on the value and the direction of the current and on the rotational speed of the pontoon around the spud.

3. The spring forces resulting from the swing wires and the forces resulting from the swing winches strongly depend on the characteristics of the winches and the wires and the winch control system. The position of the anchors in relation to the position of the spud and the position of the swing wire sheaves on the ladder determines the direction of the swing wire forces and thus of the resulting moments around the spud. Figure 4 shows the winch output of a research simulator.

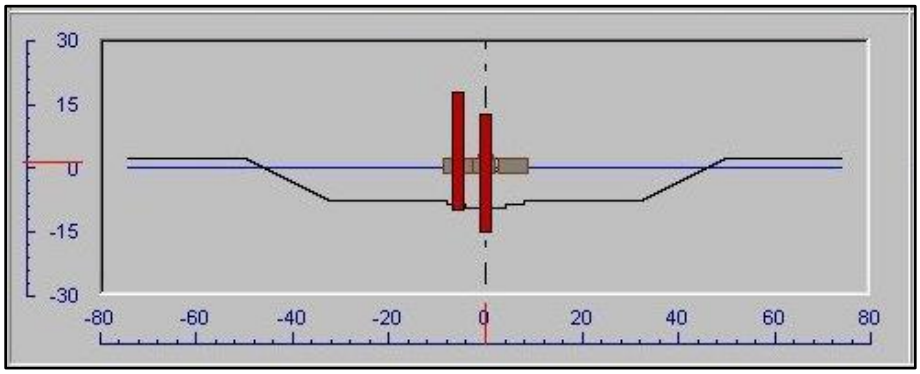

Figure 9-2: The display of the back view of the cutterdredge, also showing the cross-sectional channel profile.

4. The forces and moment excerted on the pontoon by the current influence the rotation around the spud depending on the current speed and the swing speed. For small values of the current speed this effect can however be neglected. For high values of the current speed the influence depends on the direction of the current and the swing angle. It may occur that the swing winches do not have enough power to pull back the pontoon out of a corner due to the angle of the swing wires and a high current speed.

5. The cutting forces and the cutting torque strongly influence the rotation around the spud, these will be discussed in the paragraph concerning the cutting forces.
6. The winch forces and the winch moment strongly influence the rotation around the spud, these will be discussed in the paragraph concerning the swing winch characteristics.

7. The forces resulting from the pipeline can be neglected if the position of the swivel elbow is close to the position of the work spud, because in this case this force hardly influences the rotation of the pontoon around the spud.

8. The reaction forces on the spud can be determined by the equilibrium equations of forces and complement this equilibrium. These forces however do not contribute to the moment around the spud.

The rotation of the pontoon around the spud is dominated by the cutting forces, the winch characteristics, the inertia of pontoon and ladder and placement of the anchors, while damping and current play a less important role. The equilibrium equation can be formulated as:

$$I_{yaw} \cdot \ddot{\varphi}_s + k_{yaw} \cdot \dot{\varphi}_s + c_{yaw} \cdot \varphi_s = M_{current} + M_{cutting} + M_{wires} + M_{pipe} + M_{spud} \qquad \textbf{(9-1)}$$

The water damping is combined with the current moment, the wire spring force, the pipeline moment and the spud moment are not taken into consideration. Equation 1 thus reduces to:

$$I_{yaw} \cdot \ddot{\varphi}_s = M_{current} + M_{cutting} + M_{wires} \qquad \textbf{(9-2)}$$

The equilibrium equation in question is non-linear, while some of the data is produced by interpolation from tables. This implies that the equation will have to be solved in the time domain, using a certain time step. This is also necessary because the simulation program has to interact with the console (the user input). To simulate the motions

of the dredge real time, a time step of at least two times per second is required. A time step of 5 to 10 times per second would be preferred.

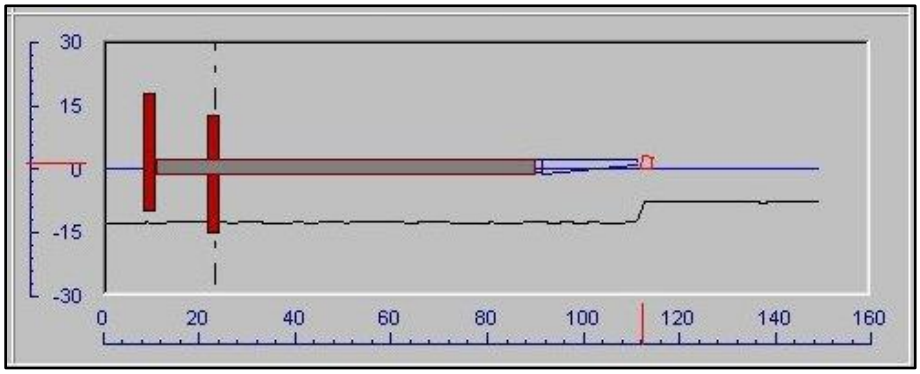

Figure 9-3: The display of the side view of the cutterdredge, also showing the longitudinal channel profile.

9.3. The Influence of the Swing Angle on the Wire Moment.

With fixed anchor positions, the angle of attack of the swing wires relative to the axis system of the pontoon, changes continuously with the value of the swing angle. With large swing angles this may result in a large decrease of the effective pulling or braking moment of the swing wires. This decrease of course depends on the anchor positions relative to the pontoon.

In this paper the following coordinate system definitions are applied:

1. The origin is placed in the centerline of the work spud.
2. The two wire sheaves are positioned on the centerline through the work spud and the cutterhead.
3. The positive swing direction is counter clock wise, with an angle of zero degrees when the centerline of the dredge matches the vertical axis (y-axis).
4. The distance from the center of the workspud to the center of the sheaves is L_{ss}.

With the coordinates if the swing sheaves on the ladder x_{ss} and y_{ss} according to:

$$x_{ss} = L_{ss} \cdot \sin(\varphi_s) \tag{9-3}$$

And

$$y_{ss} = L_{ss} \cdot \cos(\varphi_s) \tag{9-4}$$

The length of the port wire and the angle of the port wire with the centerline of the channel can be determined according to:

$$L_{pw} = \sqrt{(x_{ss} - x_{pw})^2 + (y_{ss} - y_{pw})^2} \tag{9-5}$$

and

$$\phi_{pw} = \arctan\left(\frac{x_{ss} - x_{pw}}{y_{ss} - y_{pw}}\right) \tag{9-6}$$

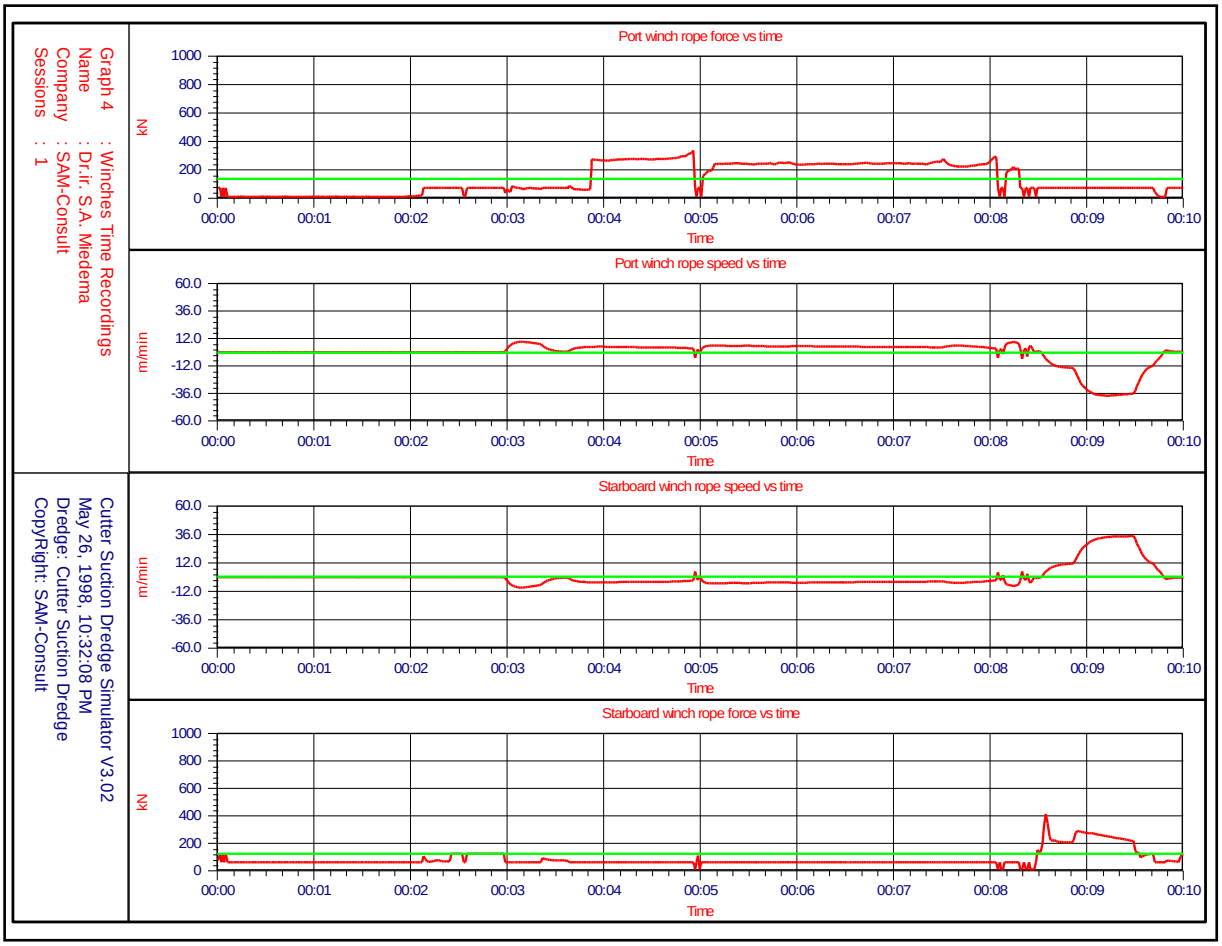

Figure 9-4: The output of the winch parameters.

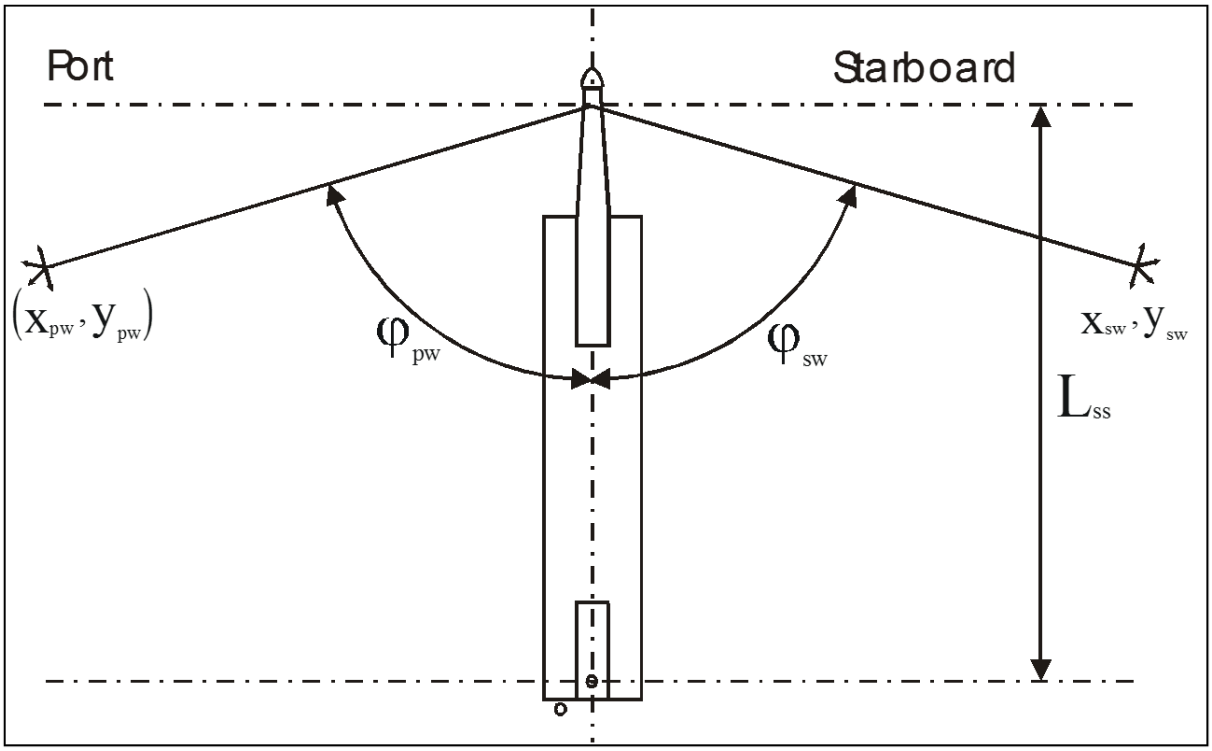

Figure 9-5: The coordinate system with the dredge in the neutral position.

The length of the starboard wire and the angle of the starboard wire with the centerline of the channel can be determined according to:

$$L_{sw} = \sqrt{(x_{ss} - x_{sw})^2 + (y_{ss} - y_{sw})^2} \tag{9-7}$$

and

$$\phi_{sw} = \arctan\left(\frac{x_{ss} - x_{sw}}{y_{ss} - y_{sw}}\right) \tag{9-8}$$

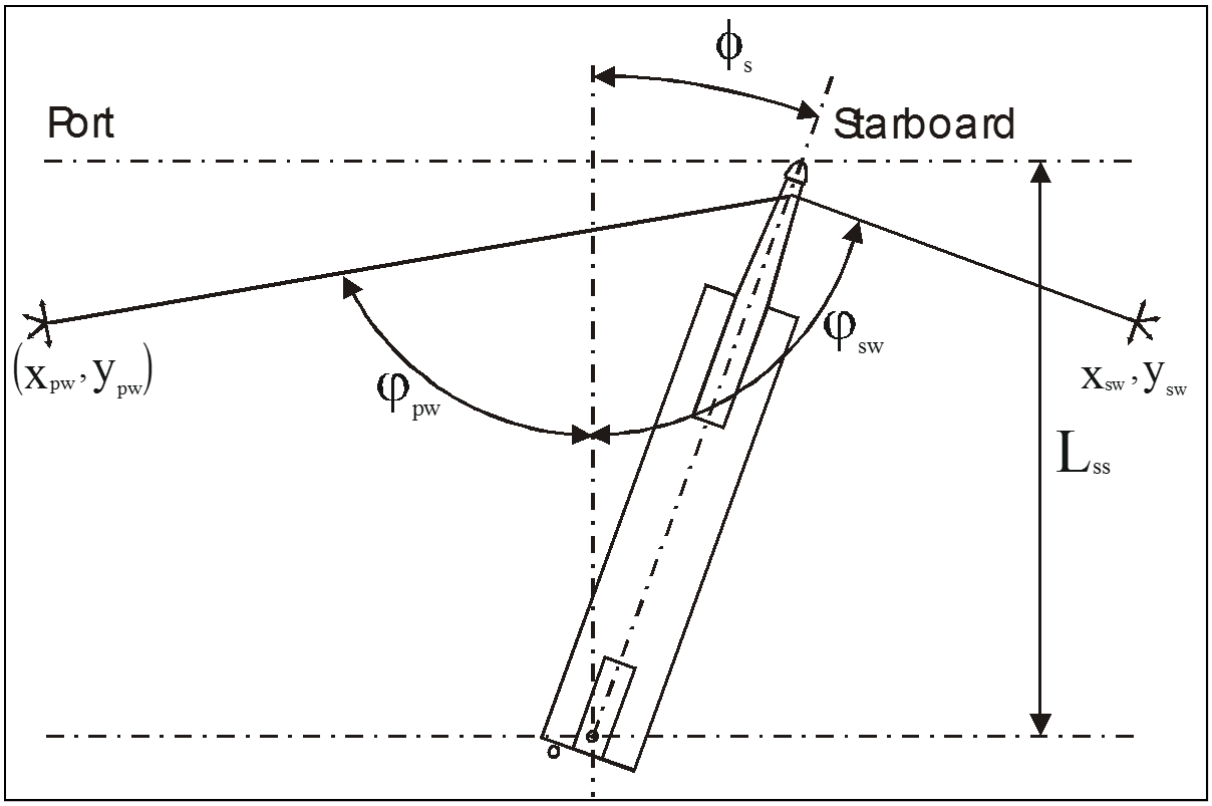

Figure 9-6: The coordinate system with the dredge at a swing angle ϕ_s.

The angle of the port wire with the centerline of the dredge is:

$$\phi_{pw} + \varphi_s \tag{9-9}$$

The angle of the starboard wire with the centerline of the dredge is:

$$\phi_{sw} - \varphi_s \tag{9-10}$$

The moment around the spud, resulting from the forces in the swing wires can now be determined by:

$$M_{wires} = F_{pw} \cdot L_{ss} \cdot \sin\left(\phi_{pw} + \varphi_s\right) - F_{sw} \cdot L_{ss} \cdot \sin\left(\phi_{sw} - \varphi_s\right) \tag{9-11}$$

The relation between the rope speed of the port wire and the angular speed of the dredge is now:

$$\dot{\varphi}_s \cdot L_{ss} = v_{pw} \cdot \sin\left(\phi_{pw} + \varphi_s\right) \tag{9-12}$$

The relation between the rope speed of the starboard wire and the angular speed of the dredge is now:

$$\dot{\varphi}_s \cdot L_{ss} = v_{sw} \cdot \sin\left(\phi_{sw} - \varphi_s\right) \tag{9-13}$$

This results in loss of effective power of both winches. The power mobilized by the winches to the angular speed of the dredge is:

$$P_{wm} = P_{pwm} - P_{swm} = F_{pw} \cdot v_{pw} \cdot \sin\left(\phi_{pw} + \varphi_s\right)^2 - F_{sw} \cdot v_{sw} \cdot \sin\left(\phi_{sw} - \varphi_s\right)^2 \tag{9-14}$$

The power consumed by the winches is:

$$P_w = P_{pw} + P_{sw} = F_{pw} \cdot v_{pw} + F_{sw} \cdot v_{sw} \tag{9-15}$$

9.4. The Winch Characteristics.

The torque speed characteristic of the winches consists of two parts if an electric drive is assumed. The first part runs from 0 revolution up to full revolutions and has a linear decrease of the torque, from a maximum at zero revolutions to the full torque at full revolutions. At this last point also the full power of the drive is reached. At higher revolutions the drive will use field weakening, while the power stays constant. In the simulator it is assumed that the characteristics for hauling and braking are equal. If one winch is in hauling mode, the other one will always be in braking mode.

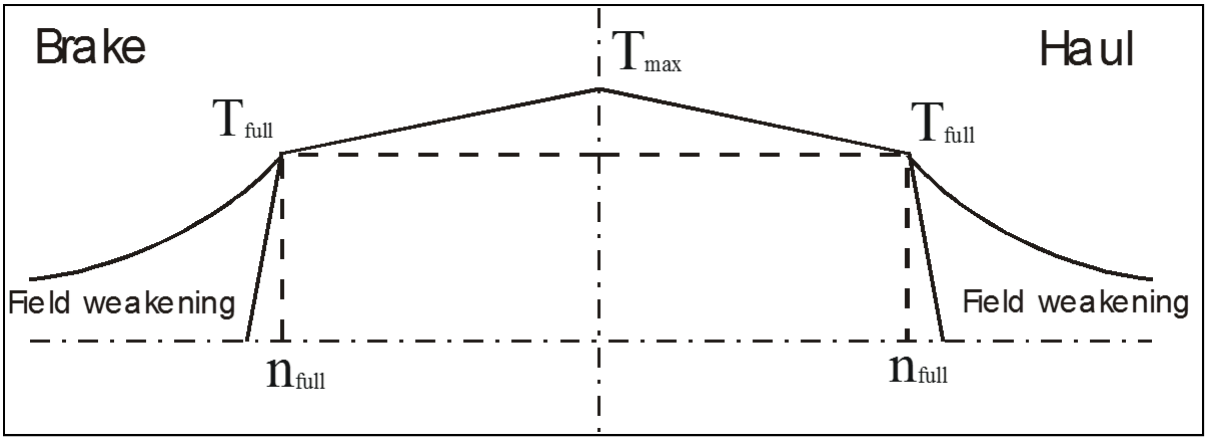

Figure 9-7: The torque-speed characteristic of the winches.

9.5. The Control System of the Winches.

The hauling winch is controlled by a setpoint for the winch revolutions. The braking winch is controlled by a setpoint for the braking torque. So for the hauling winch, the available torque results from the revolutions, while the pulling force also results from the drumdiameter and the number of layers on the drum. The mobilized torque also depends on the loads (cutter and current) and on the angular acceleration of the dredge around the spud pole.

Figure 9-8 shows the actual revolutions of the hauling winch, the setpoint of the hauling winch, the setpoint of the braking winch and the load curve for the hauling winch. The load curve includes the cutting process, the current and water damping and the braking winch. The difference between the available torque and the torque resulting for the loads is available for the acceleration of the pontoon. In the example given in Figure 9-8, it is assumed that the actual revolutions of the winch are smaller then the setpoint and that the available torque is larger then the required torque for compensating the loads.

The actual torque mobilized by the hauling winch, is always the resulting torque necessary to reach or stay on the setpoint. If in a certain situation, the torque available is less then the torque required, then the available maximum torque is assumed. In this case the working point is the intersection point of the load curve with the vertical dotted line through the setpoint of revolutions. The maximum available torque is not fully mobilized.

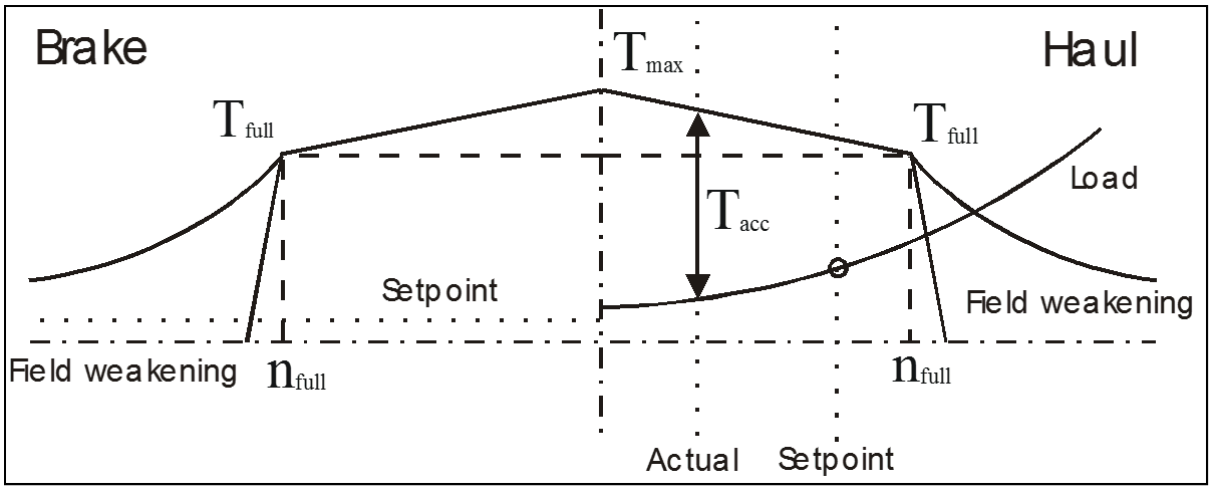

Figure 9-8: The torque-speed characteristic of the winches with the setpoints.
Case where the required torque is sufficient.

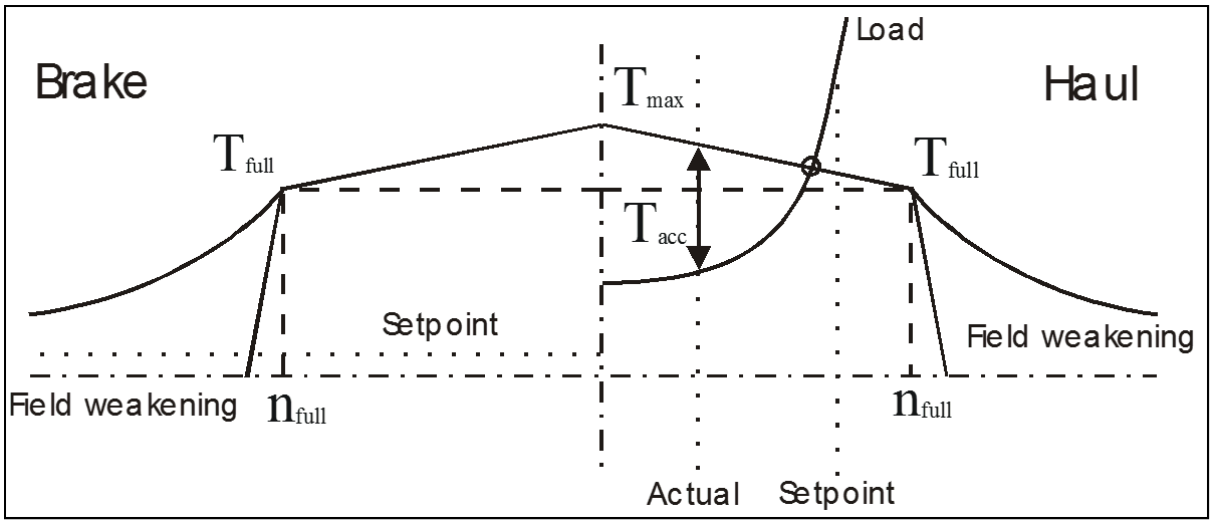

Figure 9-9: The torque-speed characteristic of the winches with the setpoints.
Case where the required torque in the setpoint is not sufficient.

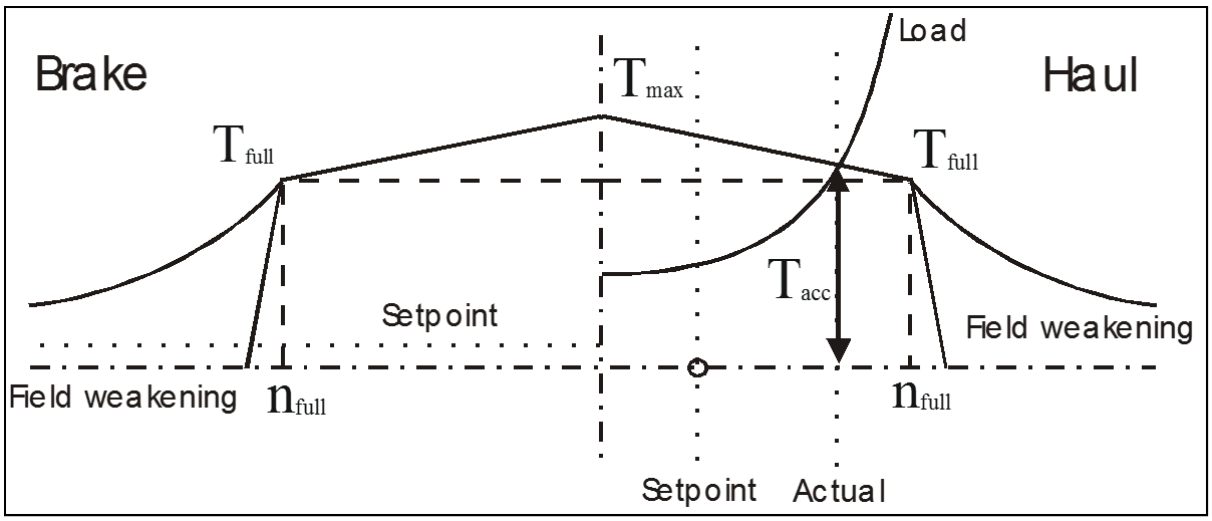

Figure 9-10: The torque-speed characteristic of the winches with the setpoints.
Case where the setpoint is smaller then the actual revolutions.

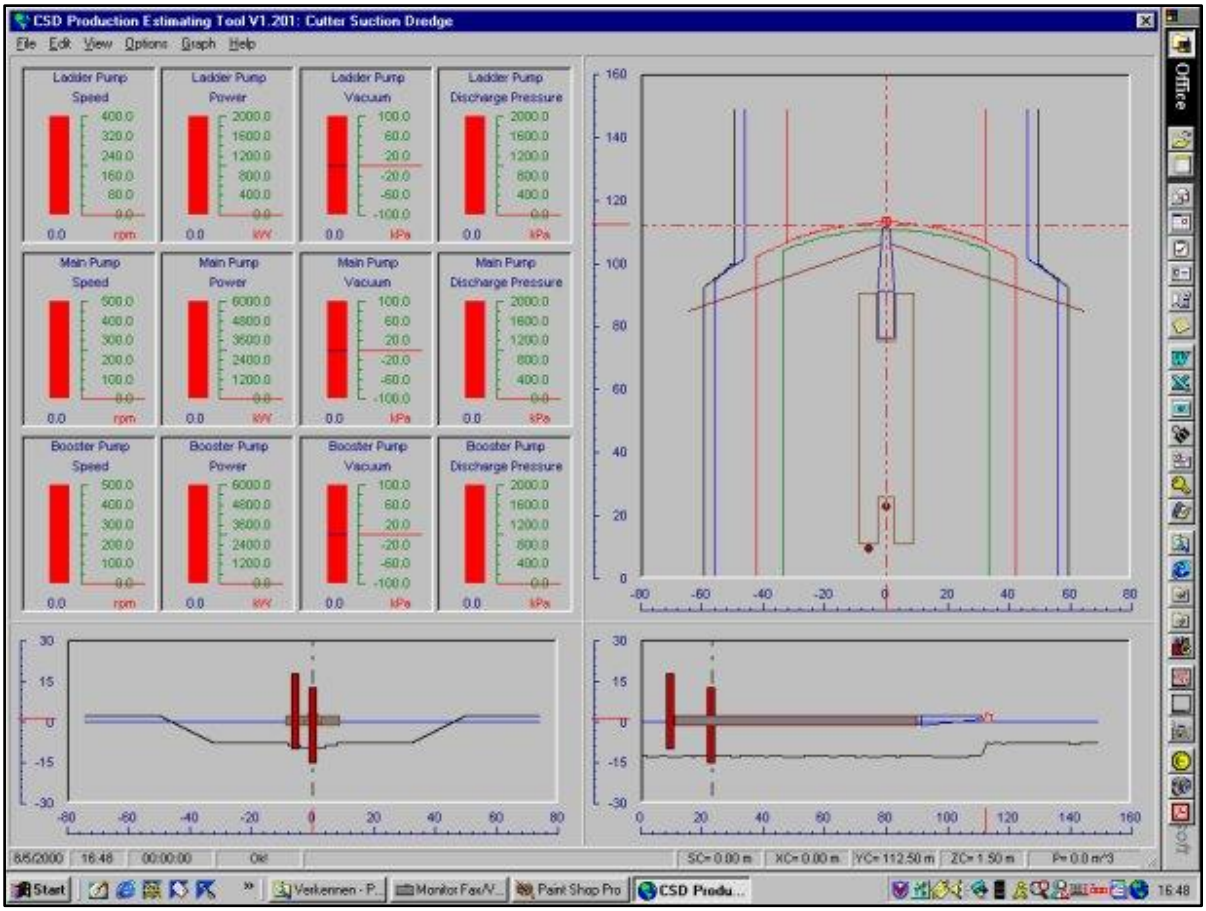

Figure 9-11: The dredge, winch and channel layout.

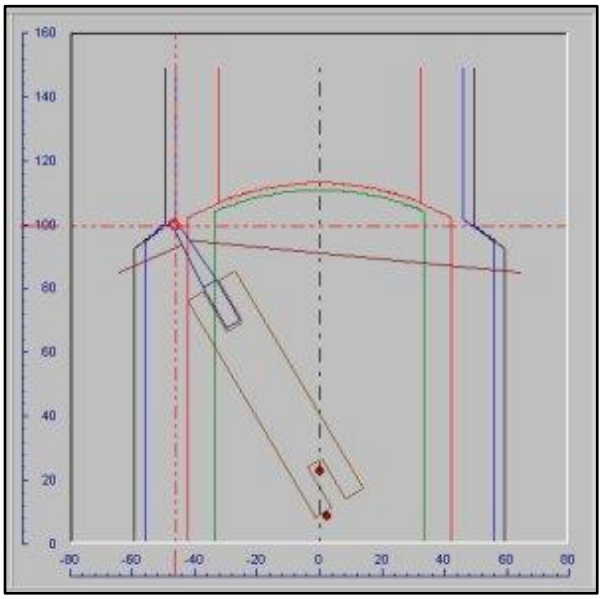

Figure 9-12: The dredge and anchor layout for case 1, port.

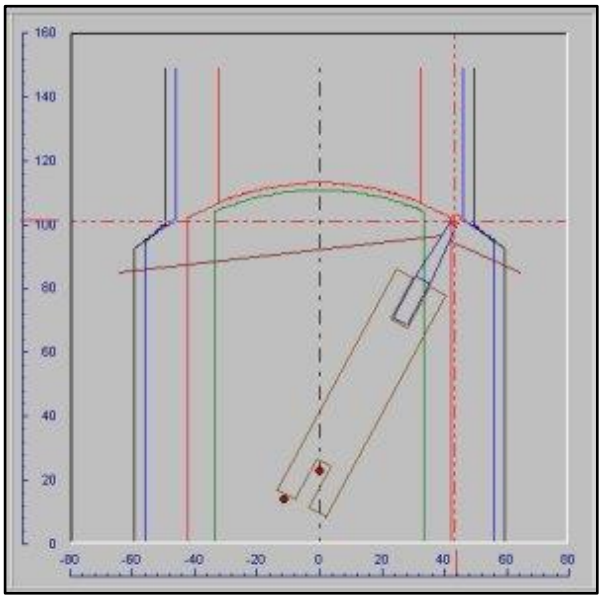

Figure 9-13: The dredge and anchor layout for case 1, starboard.

Figure 9-9 shows the case where the winch torque required in the setpoint is not sufficient. In this case, the working point is the intersection point of the load curve with the torque-speed curve. The maximum available torque is fully mobilized. The setpoint is not reached because there is not sufficient torque available.
Figure 9-10 shows the case where the setpoint is smaller then the actual revolutions. In this case, the pontoon will decelerate. The working point is the intersection point of the vertical through the setpoint and a minimum torque required keeping the wire from going slack.

9.6. Case Studies.

To show the behavior of the dredge-winch system two cases will be shown. In the first case the dredge starts on the centerline of the channel. The dredge and winch layouts are shown in Figure 9-11.

9.6.1. Case 1:

The winches have a drum diameter of 0.84 m, a full power of 158 kW at 8.87 rpm. The resulting full torque is 167 kNm. The anchor positions are symmetrical with respect to the centerline and are 65 m in horizontal direction and -21.5 m in vertical direction, away from the sheaves on the ladder. The ladder is not in contact with the bank and is moving free through the water. See Figure 9-12 and Figure 9-13.

The following actions are taken:

1. The setpoint for the swingspeed is set to 24 m/min to starboard.
2. The dredge swings from 0 to 30 degrees to starboard.
3. The setpoint for the swingspeed is set to 24 m/min to port.
4. The dredge swings from 30 degrees starboard to 30 degrees port.
5. The setpoint for the swingspeed is set to 24 m/min to starboard.
6. The dredge swings from 30 degrees port to the centerline.

Figure 9-14 shows the rope speeds and pulling forces for both the port and the starboard winch. It is clearly shown in the graphs in Figure 9-14 that, while the rope forces increase instantly, the rope speed increases or decreases according to a first or second order system. This is caused by the mass-spring-damper system according to equation 1, but also by the inertia of the winches themselves. In the simulator, the winches are modeled as a first order system. The winches and the dredge need some time to accelerate or decelerate.

The deceleration requires more time in case 1 then the acceleration, because the braking force is set to 30% of the maximum force, which is about 180 kN. The pulling force however, can be much higher, depending on the characteristic of the winches. Setting the braking force to a higher value, will increase the speed of the deceleration.

Typical for this case is, that the pulling wire is more and more perpendicular to the ladder when the swing angle approaches 30 degrees. This results in a decreasing pulling force, which can be seen in Figure 9-14. The braking force is set to a constant value and will only differ from this value if the braking force is larger then the torque-speed curve permits it to be. In that case the braking force will follow the torque speed curve.

9.6.2. Case 2:

The winches have a drum diameter of 0.84 m, a full power of 158 kW at 8.87 rpm. The resulting full torque is 167 kNm. The anchor positions are symmetrical with respect to the centerline and are 65 m in horizontal direction and +3.5 m in vertical direction, away from the sheaves on the ladder, as is shown in Figure 9-16 and Figure 9-17. The ladder is not in contact with the bank and is moving free through the water.

The following actions are taken:

1. The setpoint for the swingspeed is set to 24 m/min to starboard.
2. The dredge swings from 0 to 30 degrees to starboard.
3. The setpoint for the swingspeed is set to 24 m/min to port.
4. The dredge swings from 30 degrees starboard to 30 degrees port.
5. The setpoint for the swingspeed is set to 24 m/min to starboard.
6. The dredge swings from 30 degrees port to the centerline.

Figure 9-15 shows the rope speeds and pulling forces for both the port and the starboard winch. Because the anchors are moved 25 m forward in the channel, now the angle between the pulling wire and the ladder decreases when the dredge approaches the 30 degrees swing angle. This results in an increase of the pulling force as is visible in Figure 9-15. The start and stop behavior is almost equal to case 1.

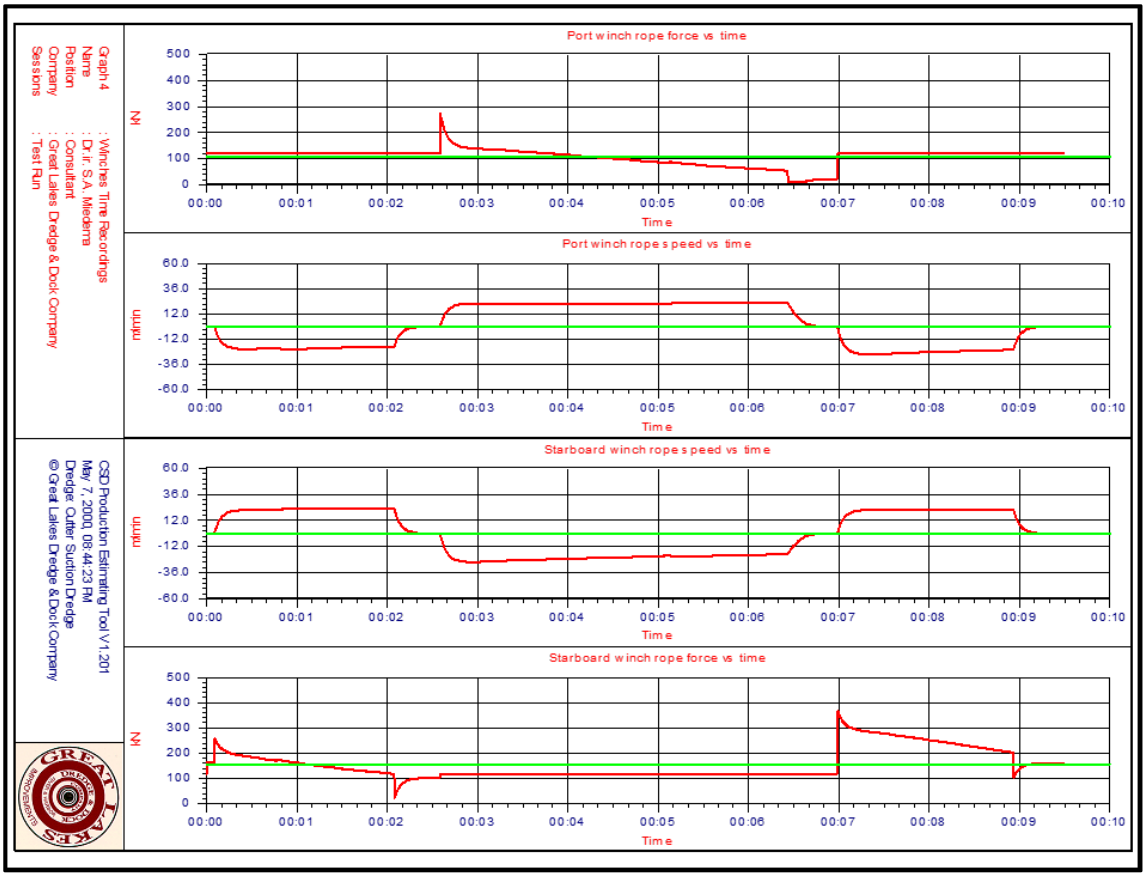

Figure 9-14: The rope speeds and forces for case 1.

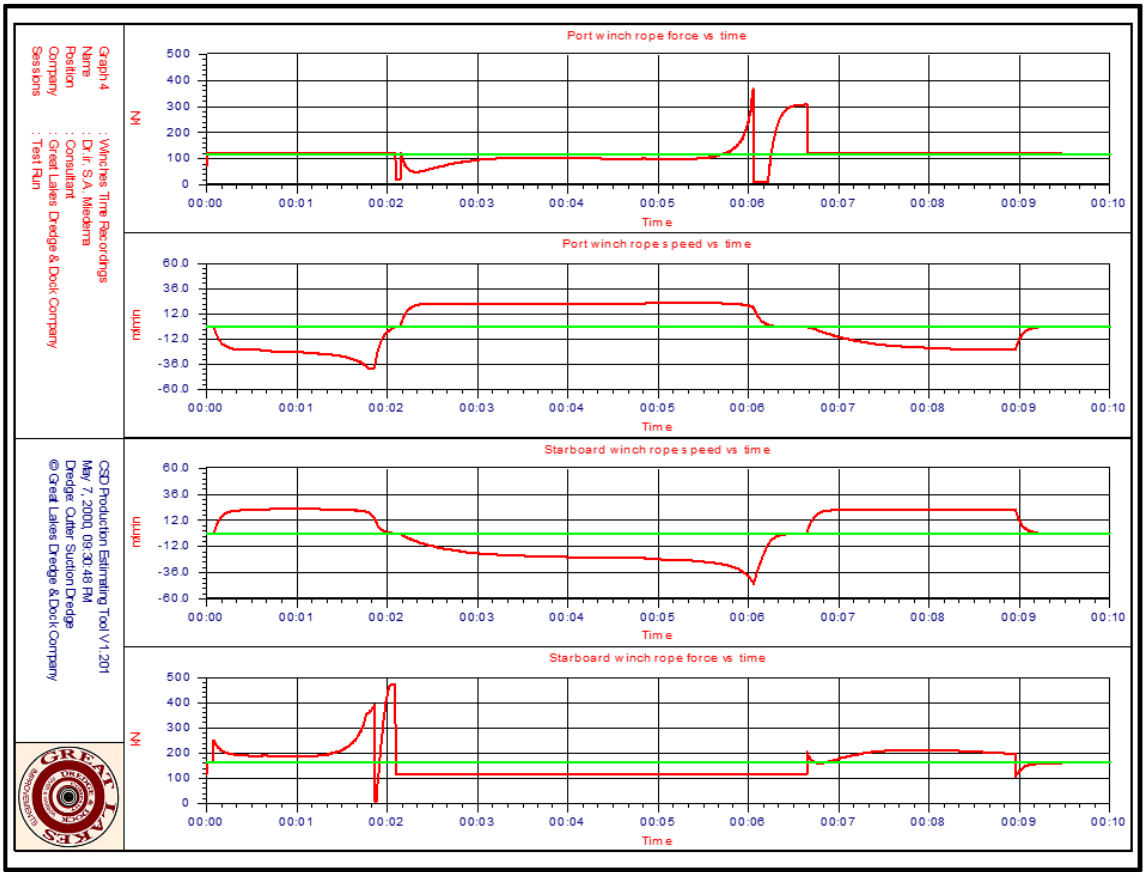

Figure 9-15: The rope speeds and forces for case 2.

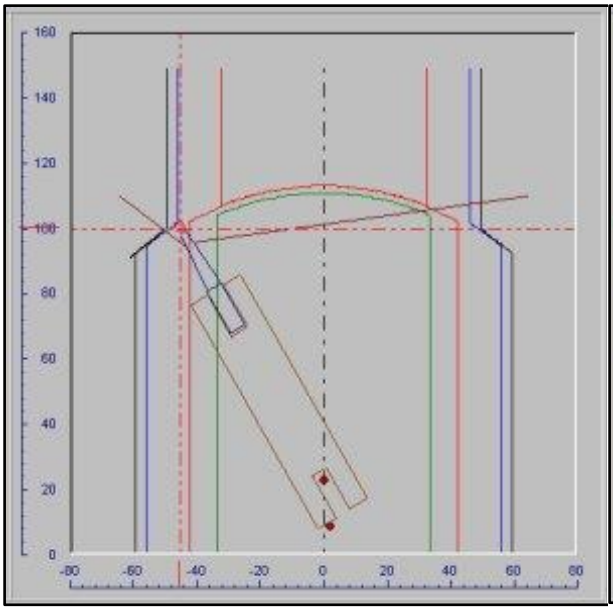

Figure 9-16: The dredge and anchor layout for case 2, port.

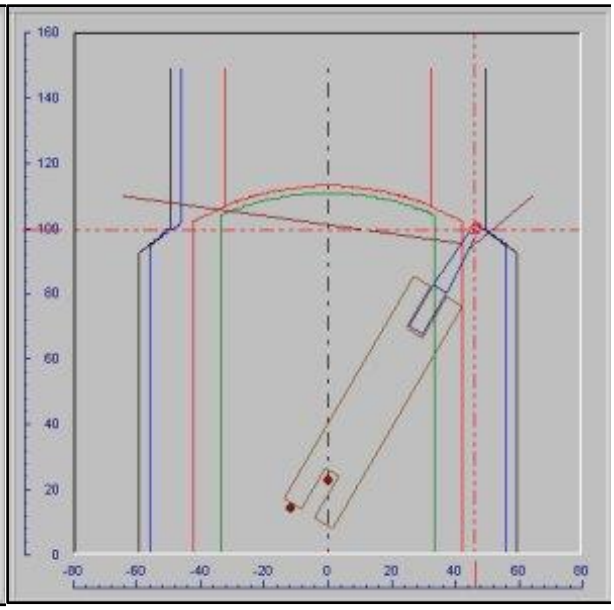

Figure 9-17: The dredge and anchor layout for case 2, starboard.

9.7. Conclusions.

The modeling of the winches and the wires consists of solving the equilibrium equation of motions of the dredge around the spudpole in combination with the characteristics of the winches. The two cases show that it takes about 10 seconds to accelerate to a swing speed of 24 m/min. The time required for the deceleration is of the same magnitude, but depends of course on the setpoint of the brake force.

The two cases also show, that the shape rope speed and force as a function of time, strongly depend on the position of the anchors relative to the sheave positions at the ladder. The two cases describe symmetrical configurations, which of course is not always the case. An infinite number of configurations can be chosen. Which configuration is the best depends on the work to be carried out and on the boundary conditions of the work to be carried out.

9.8. Nomenclature.

c_{yaw}	Spring constant of the yaw motion	**kNm/rad**
F_{pw}	Rope force of the port wire	**kN**
F_{sw}	Rope force of the starboard wire	**kN**
I_{yaw}	Mass moment of inertia of pontoon in yaw direction	**kNms^2/rad**
k_{yaw}	Damping coefficient of pontoon in yaw direction	**kNms/rad**
L_{pw}	Length of the port wire	**m**
L_{ss}	Distance from working spud to swing sheaves on ladder	**m**
L_{sw}	Length of starboard wire	**m**
$M_{current}$	Moment around the spud exerted by the current	**kNm**
$M_{cutting}$	Moment around the spud exerted by the cutting process	**kNm**
M_{pipe}	Moment around the spud exerted by the floating pipeline	**kNm**
M_{spud}	Moment around the spud exerted by the spud	**kNm**
M_{wires}	Moment around the spud exerted by the swing wires	**kNm**
n_{full}	Full revolutions of the swing winch	**rpm**
P_{pw}	Power of the port winch	**kW**
P_{pwm}	Power of the port winch mobilized on the dredge	**kW**
P_{sw}	Power of the starboard winch	**kW**
P_{swm}	Power of the starboard winch mobilized on the dredge	**kW**
P_{w}	Power of both winches	**kW**
P_{wm}	Power of both winches mobilized on the dredge	**kW**
T_{acc}	Winch torque available for acceleration or deceleration	**kNm**
T_{full}	Full torque of the winches	**kNm**
T_{max}	Maximum torque of the winches	**kNm**
v_{pw}	Rope speed of the port winch	**m/sec**
v_{sw}	Rope speed of the starboard winch	**m/sec**
x_{pw}	X coordinate of the port anchor	**m**
x_{ss}	X coordinate of the swing sheaves on the ladder	**m**
x_{sw}	X coordinate of the starboard anchor	**m**
y_{pw}	Y coordinate of the port anchor	**m**
y_{ss}	Y coordinate of the swing sheaves on the ladder	**m**
y_{sw}	Y coordinate of the starboard anchor	**m**
ϕ_s	Swing angle	**rad**
φ_{pw}	Port wire angle	**rad**
φ_{sw}	Starboard wire angle	rad

Chapter 10: The Trailing Suction Hopper Dredge.

10.1. Introduction

In the last decennia there has been a strong development in the enlargement of TSHD's (Trailing Suction Hopper Dredges) from roughly 10.000 m^3 in the early 90's up to 50.000 m^3 expected loading capacity nowadays. Because of the economy of the loading process, but also environmental regulations, it is important to predict the overflow losses that are occurring.
For the estimation of the sedimentation process in TSHD's a number of models have been developed. The oldest model used is the Camp (1936), (1946) and (1953) model which was developed for sewage and water treatment tanks. Camp and Dobbins (1944) added the influence of turbulence based on the two-dimensional advection-diffusion equation, resulting in rather complicated equations. Miedema (1981) used the Camp model to develop an analytical model. Groot (1981) added the effects of hindered settling. Vlasblom & Miedema (1995) and Miedema & Vlasblom (1996) simplified the Camp equations by means of regression and included a rising sediment zone, as well as hindered settling and erosion and an adjustable overflow. Van Rhee (2002C) modified the implementation of erosion in the Camp model, but concluded that the influence is small due to the characteristics of the model. Ooijens (1999) added the time effect, since the previous models assume an instantaneous response of the settling efficiency on the inflow of mixture. Yagi (1970) developed a new model based on the concentration distribution in open channel flow.
The models mentioned above are all black box approaches assuming simplified velocity distributions and an ideal basin. Van Rhee (2002C) developed a more sophisticated model, the 2DV model. This model is based on the 2D (horizontal and vertical) Reynolds Averaged Navier Stokes equations with a k-ε turbulence model and includes suspended sediment transport for multiple fractions.

10.2. The Loading Cycle of a Hopper Dredge

The loading cycle of a TSHD is considered to start when the hopper is filled with soil and starts to sail to the dump area. This point in the loading cycle was chosen as the starting point in order to be able to show the optimal load in a graph. The loading cycle then consists of the following phases:

- Phase 1: The water above the overflow level flows away through the overflow. The overflow is lowered to the sediment level, so the water above the sediment can also flow away. In this way minimum draught is achieved. Sailing to the dump area is started.

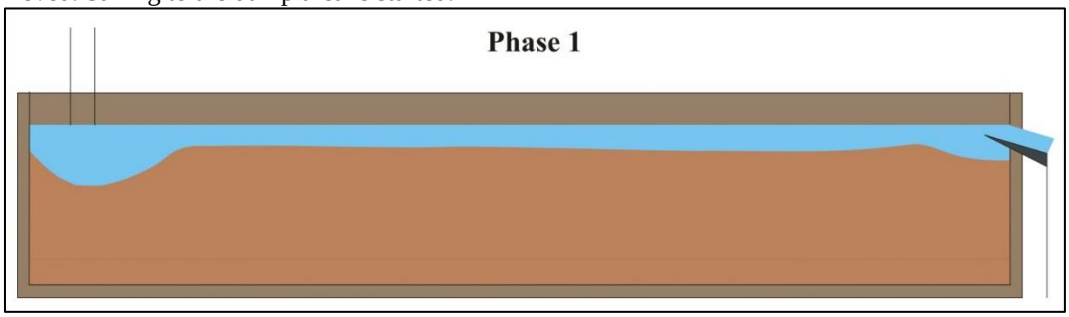

Figure 10-1: Phase 1 of the loading cycle.

- Phase 2: Continue sailing to the dump area.

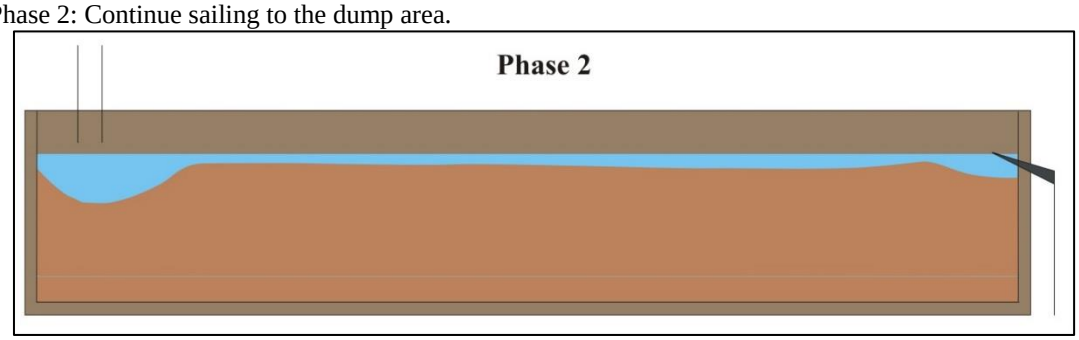

Figure 10-2: Phase 2 of the loading cycle.

- Phase 3: Dump the load in the dump area. Dumping can be carried out in 3 different ways, using the bottom dumping system, pumping ashore or rain bowing.

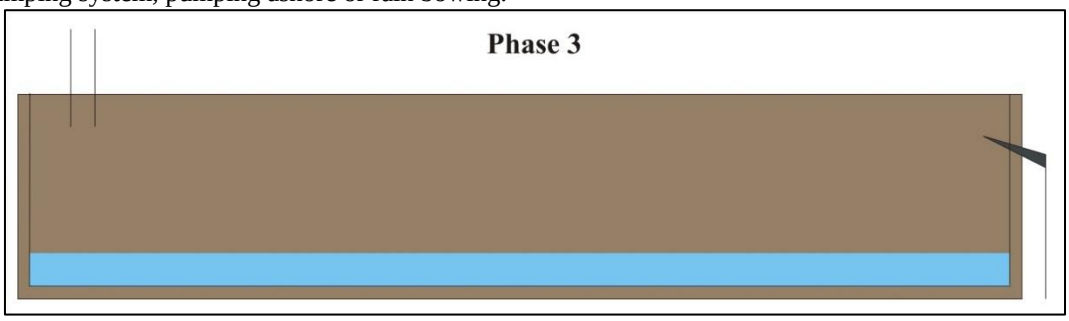

Figure 10-3: Phase 3 of the loading cycle.

- Phase 4: Pump the remaining water out of the hopper and sail to the dredging area. Often the water is not pumped out, but instead water is pumped in, to have the pumps as low as possible, in order to dredge a higher density, which should result in a shorter loading time.

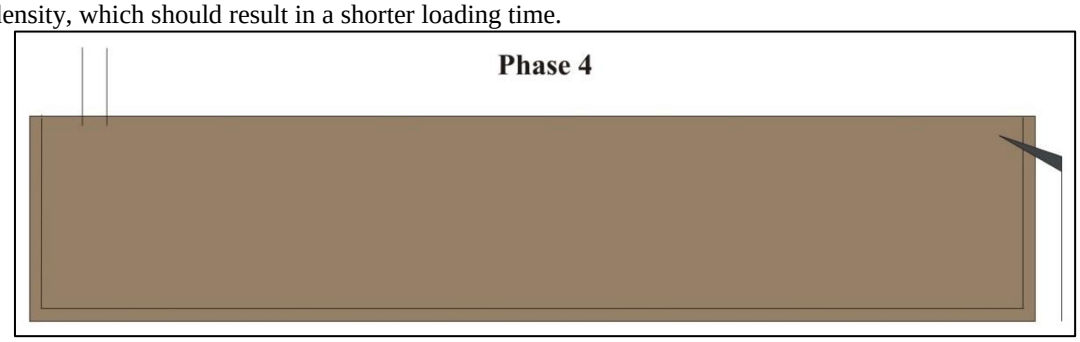

Figure 10-4: Phase 4 of the loading cycle.

- Phase 5: Start dredging and fill the hopper with mixture to the overflow level, during this phase 100% of the soil is assumed to settle in the hopper.

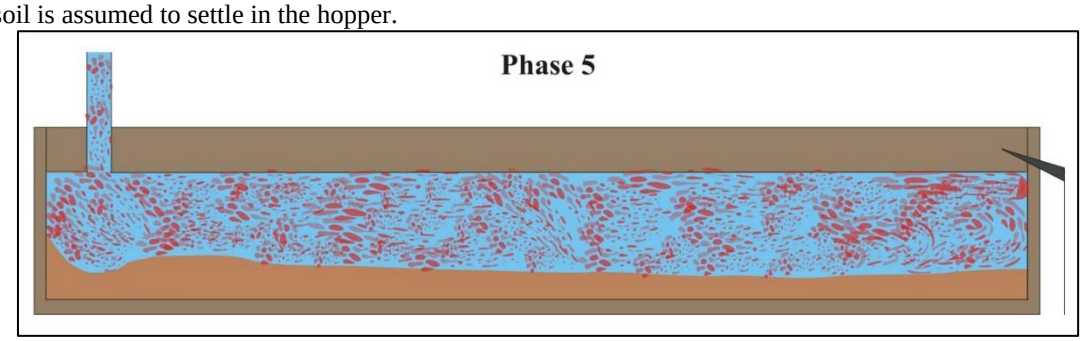

Figure 10-5: Phase 5 of the loading cycle.

- Phase 6: Continue loading with minimum overflow losses, during this phase a percentage of the grains will settle in the hopper. The percentage depends on the grain size distribution of the sand.

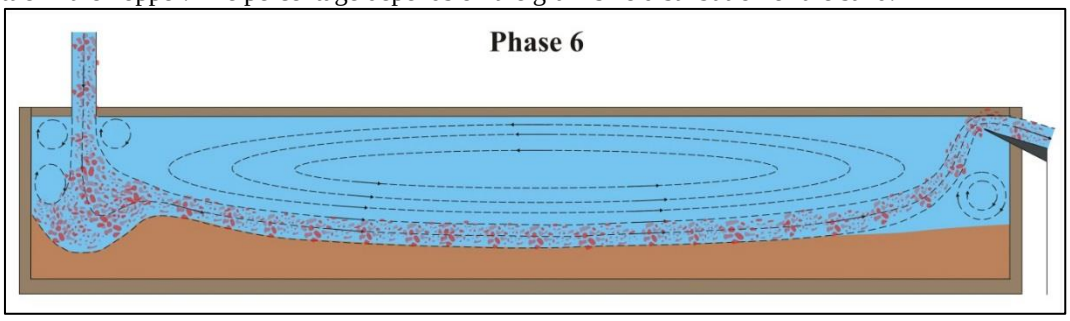

Figure 10-6: Phase 6 of the loading cycle.

- Phase 7: The maximum draught (CTS, Constant Tonnage System) is reached. From this point on the overflow is lowered.

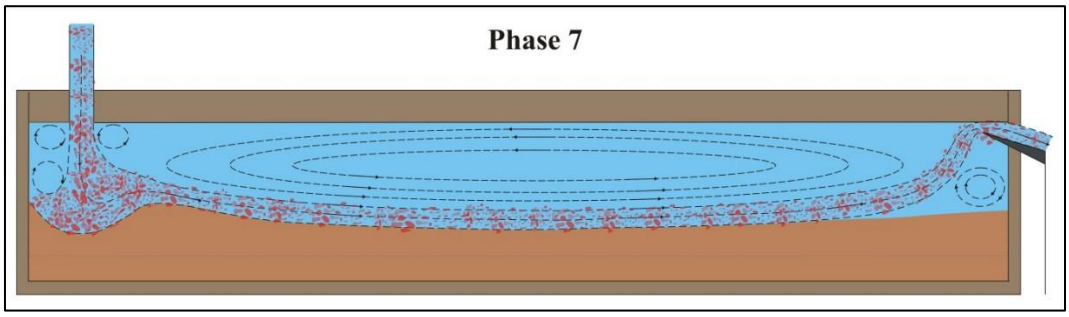

Figure 10-7: Phase 7 of the loading cycle.

- Phase 8: The sediment in the hopper is rising due to sedimentation, the flow velocity above the sediment increases, resulting in scour. This is the cause of rapidly increasing overflow losses.

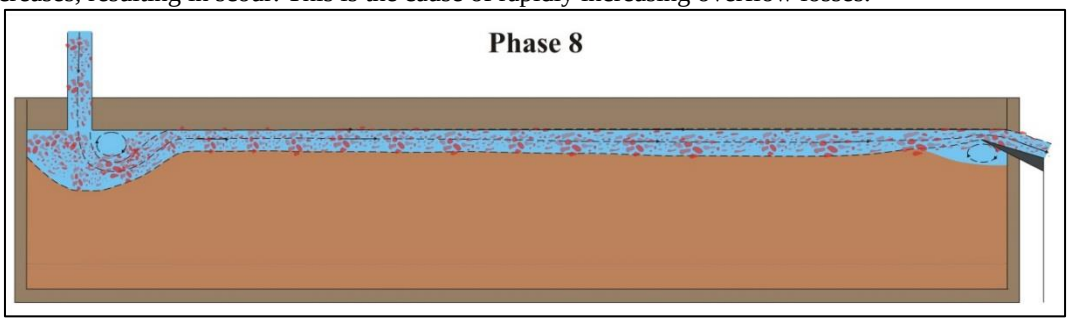

Figure 10-8: Phase 8 of the loading cycle.

Figure 10-9 and Figure 10-10 show the total load, the effective load, the TDS and the overflow losses during these phases. The way each phase occurs in the cycle, depends on the type of hopper dredge, the working method and of course, the type of soil to be dredged.

Basically there are two main methods for loading the hopper. The 'Constant Volume System' (CVS). This system has a fixed overflow level so the effective volume of the hopper is constant. The TSHD is designed for filling the hopper with sediment with a density of 1.9-2.0 ton/m^3. The 'Constant Tonnage System' (CTS). The system has an adjustable overflow level. The hopper is designed for a density of 1.3-1.7 ton/m^3 in combination with a maximum tonnage. When the content of the hopper reaches the maximum tonnage, the overflow is lowered in order to keep the tonnage of the hopper content constant. This system has certain advantages, like reaching the maximum tonnage sooner than with CVS, resulting in the pumps to be as low as possible, giving a higher mixture density. De Koning (1977) has compared both systems.
The sedimentation in the hopper occurs during the phases 5, 6, 7 and 8. During phase 5 the hopper is filled with mixture until the overflow level is reached. During this phase 100% of the soil is assumed to stay in the hopper and settle. When the overflow level is reached, phase 6, depending on the grain distribution, a specified percentage of the soil will not settle and will leave the hopper via the overflow. During this phase scouring does not have much influence on the sedimentation process. When the maximum weight of the hopper contents is reached, the overflow will be lowered continuously in order to keep the weight of the hopper contents constant at its maximum (only CTS system). When the sediment level rises, phase 8, the flow velocity above the sediment increases and scouring will re suspend settled particles. The overflow losses increase with time. The transition between phase 5 and 6 is very sharp, as is the transition between the phases 6 and 7 for the graph of the total load, but this does not exist in the graph of the effective load (Figure 10-10). However, the transition between the phases 7 and 8 is not necessarily very sharp. When this transition occurs depends on the grain distribution of the soil dredged. With very fine sands this transition will be near the transition between phases 6 and 7, so phase 7 is very short or may not occur at all. With very coarse sands and gravel scouring is minimal, so phase 8 is hardly present. In this case the sediment level may be higher than the overflow level. With silt the phases 7 and 8 will not occur, since after reaching the overflow level the overflow losses will be 100%.

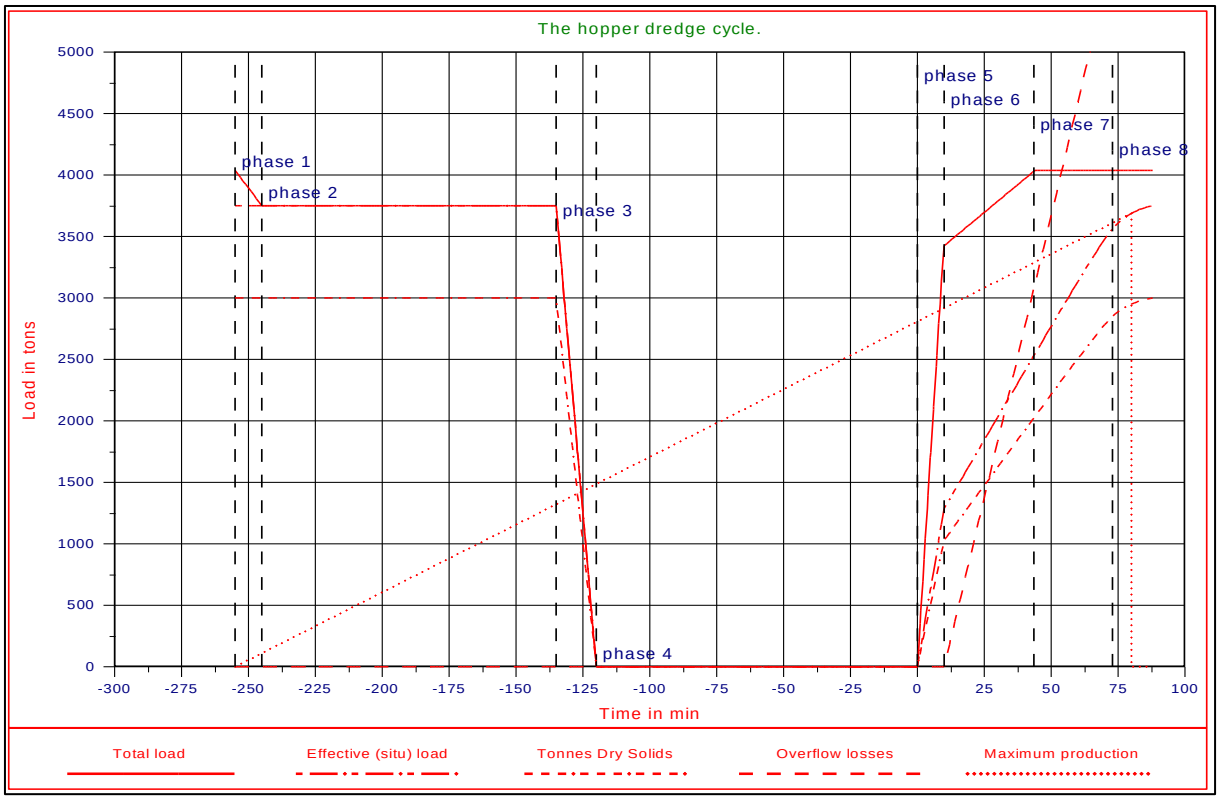

Figure 10-9: The loading cycle of a TSHD.

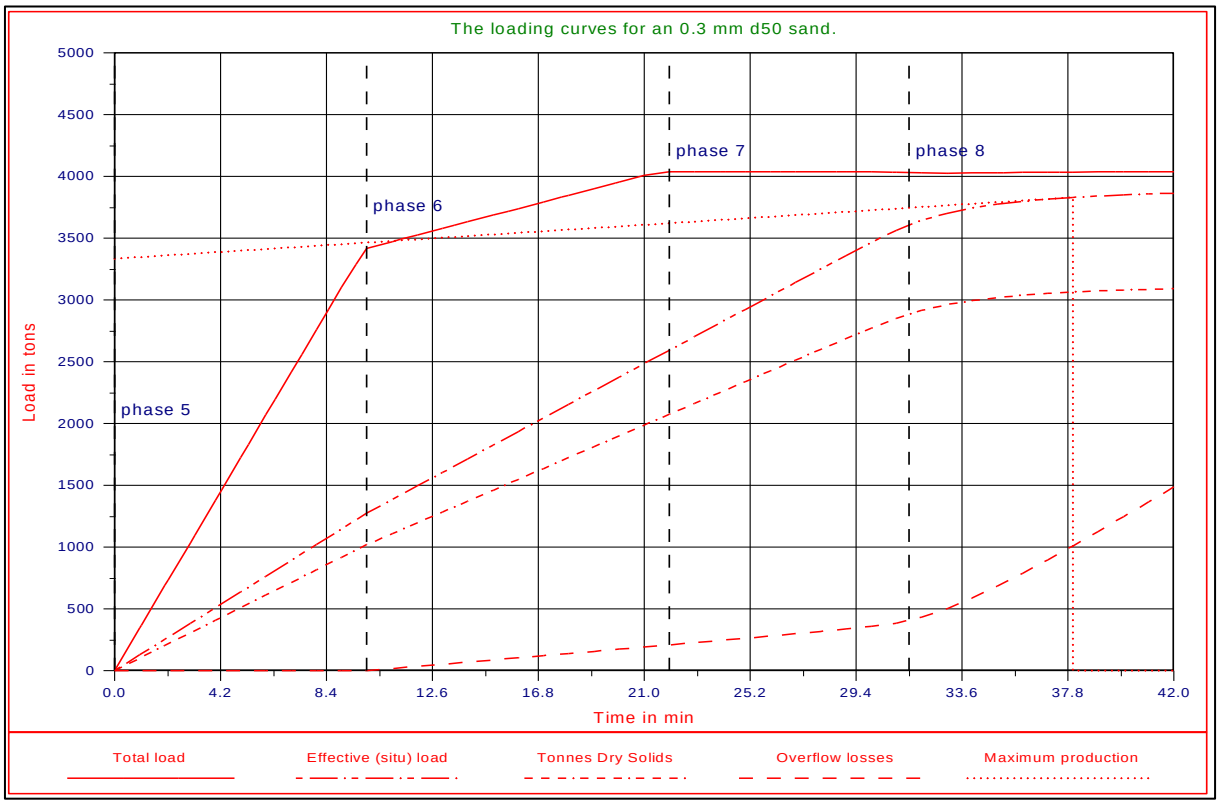

Figure 10-10: The loading part of the cycle of a TSHD.

So far the total load in the hopper has been described. A contractor is, of course, interested in the "Tonnes Dry Solids" (TDS) or situ cubic meters. The total load or gross load consists of the sediment with water in the pores and a layer of water or mixture above the sediment. The TDS consists of the weight of the soil grains only. The net weight in the hopper consists of the weight of the sediment, including the weight of the pore water. If the porosity of the sediment is considered to be equal to the in-situ porosity, then the volume of the sediment in the hopper equals the removed situ-volume. Although, in practice, there will be a difference between the in-situ porosity and the sediment porosity, here they will be considered equal. The net weight (weight of the sediment $\mathbf{W_s}$) is equal to the weight in the hopper $\mathbf{W_h}$ minus the weight of the water above the sediment $\mathbf{W_w}$:

$$W_s = W_h - W_w \tag{10-1}$$

The net volume (volume of the sediment $\mathbf{V_s}$) is equal to the volume of the hopper $\mathbf{V_h}$ minus the volume of the water above the sediment $\mathbf{V_w}$.

$$V_s = V_h - V_w \tag{10-2}$$

Multiplying the volumes with the densities gives:

$$V_s \cdot \rho_s = W_h - V_w \cdot \rho_w \quad \text{and} \quad V_w = V_h - V_s \tag{10-3}$$

$$V_s \cdot \rho_s = W_h - (V_h - V_s) \cdot \rho_w \tag{10-4}$$

$$V_s \cdot (\rho_s - \rho_w) = W_h - V_h \cdot \rho_w \tag{10-5}$$

Rearranging the terms of equation **(10-5)** gives an expression for the volume of situ cubic meters.

$$V_s = \frac{(W_h - V_h \cdot \rho_w)}{(\rho_s - \rho_w)} \tag{10-6}$$

Multiplying the situ volume $\mathbf{V_s}$ with the situ density $\boldsymbol{\rho_s}$ gives for the situ weight $\mathbf{W_s}$:

$$W_s = V_s \cdot \rho_s = \frac{(W_h - V_h \cdot \rho_w) \cdot \rho_s}{(\rho_s - \rho_w)} \tag{10-7}$$

To find the weight of the sand grains only (without the pore water), the situ density $\boldsymbol{\rho_s}$ has to be replaced by the quarts density (or particle density) $\boldsymbol{\rho_q}$:

$$TDS = W_s \cdot \frac{\rho_s - \rho_w}{\rho_q - \rho_w} \cdot \frac{\rho_q}{\rho_s} = \frac{(W_h - V_h \cdot \rho_w) \cdot \rho_q}{(\rho_q - \rho_w)} \tag{10-8}$$

The net weight (situ weight) according to equation **(10-7)** can be approximated by the total weight of the load in the hopper minus the weight of the same volume of water and the result multiplied by 2. For the TDS this factor is about 1.2, according to equation **(10-8)**. This is of course only valid for a specific density of the sediment of 2 tons per cubic meter.

With these equations the hopper cycle for the net weight and the TDS can be derived, this is shown in Figure 10-9 and Figure 10-10. The hopper dredge is optimally loaded, when the effective load (weight) or the TDS divided by the total cycle time $\mathbf{dW_s/dt}$ reaches its maximum. This is shown in Figure 10-9 and Figure 10-10 and is the reason for the starting point of the loading cycle in Figure 10-9.

10.3. The Calculation Model.

Consider a rectangular hopper of width **W**, height **H** and length **L**. A mixture with a mixture density ρ_m and with a specified grain distribution is being dredged. Depending on the operational conditions such as dredging depth, the pump system installed, the grain distribution (PSD, Particle Size Distribution) and mixture density ρ_m, a mixture flow **Q** will enter the hopper. If the porosity **n** of the sediment is known, the flow of sediment can be determined according to:

The mass flow of the mixture into the hopper is:

$$Q_{in} \cdot \rho_m = Q_{in} \cdot (\rho_w \cdot (1-C_v) + \rho_q \cdot C_v) \quad \textbf{(10-9)}$$

The mass flow of the solids into the hopper is now:

$$\frac{dTDS}{dt} = Q_{in} \cdot \rho_q \cdot \frac{(\rho_m - \rho_w)}{(\rho_q - \rho_w)} = Q_{in} \cdot C_v \cdot \rho_q \quad \textbf{(10-10)}$$

From this, the mass flow of situ sediment into the hopper is:

$$\frac{dW_s}{dt} = Q_{in} \cdot C_v \cdot (\rho_q + e \cdot \rho_w) \quad \textbf{(10-11)}$$

With:

$$e = \frac{n}{(1-n)} \quad \textbf{(10-12)}$$

Part of this mass flow will settle in the hopper and another part will leave the hopper through the overflow. The ratio between these parts depends on the phase of the loading process. During phase 5 the hopper is loaded to the overflow level, so the mass flow into the hopper will stay in the hopper. This means that the total settling efficiency η_b during this phase equals 1. During phase 6 the loading continues until the maximum load in the hopper is reached (CTS). If scouring does not occur, the mass flow that will settle into the sediment can be calculated with equation (10-13) and (10-14), where the settling efficiency η_b should be determined with equation (10-56) and (10-57), 0.

The mass flow of the solids staying in the hopper is now:

$$\frac{dTDS}{dt} = Q_{in} \cdot C_v \cdot \rho_q \cdot \eta_b \quad \textbf{(10-13)}$$

From this, the mass flow of situ sediment into the hopper is:

$$\frac{dW_s}{dt} = Q_{in} \cdot C_v \cdot (\rho_q + e \cdot \rho_w) \cdot \eta_b \quad \textbf{(10-14)}$$

During phase 7 the loading continues, but with a CTS, the overflow is lowered to ensure that the total weight in the hopper remains constant. As scour does not yet occur, the above equation is still valid. During phase 8 scouring occurs. If scouring does occur, the mass flow that will settle into the sediment can also be calculated with equation (10-13) and (10-14), but the settling efficiency should be determined with equation (10-56) and (10-57) taking into account the effect of scouring. Scouring is the cause of increasing overflow losses. Scour depends upon the velocity of the flow above the sediment. Since in a hopper the sediment is not removed, the sediment level rises during the loading of the hopper. This means that the height of the mixture flow above the sediment decreases during the loading process, resulting in an increasing flow velocity. The scour velocity can now be determined by:

$$s_s = \frac{Q_{in}}{B \cdot H_w} \quad \textbf{(10-15)}$$

The height of the water/mixture layer $\mathbf{H_w}$ above the sediment, is equal to the overflow height **H** minus the sediment height $\mathbf{H_s}$:

$$\mathbf{H_w = H - H_s = H - \frac{W_s}{\rho_s \cdot W \cdot L}} \qquad \textbf{(10-16)}$$

The overflow height **H** is a constant for a Constant Volume System (CVS), but this height changes for a CTS, because the overflow is lowered from the moment, the maximum weight in the hopper is reached. If a maximum weight $\mathbf{W_m}$ is considered, the height of the layer of water above the sediment $\mathbf{H_w}$ for a CTS can be determined by:

$$\mathbf{H_w = \frac{W_m - \rho_S \cdot H_s \cdot B \cdot L}{\rho_W \cdot B \cdot L}} \qquad \textbf{(10-17)}$$

The hopper loading curve can now be determined by first calculating the time required to fill the hopper (phase 6), given a specified mixture flow $\mathbf{Q_{in}}$. From the mixture density $\boldsymbol{\rho_m}$ the mass and given a specified porosity, the volume of the sediment can be calculated. From this point the calculations are carried out in small time steps (phases 7 and 8). In one time step, first the height of the sediment and the height of the water layer above the sediment are determined. The height of the water layer can be determined with equation (10-16) for a CVS hopper and equation (10-17) for a CTS hopper. With equation (10-15) the scour velocity can now be determined. Using equations (10-55) the fraction of the grains that will be subject to scour can be determined. If this fraction $\mathbf{p_s}$ is zero equation (10-50) has to be used to determine the mass flow that will stay in the hopper. If this fraction is not equal to zero equation (10-56) has to be used. Equations (10-13) and (10-14) can now be used to determine the mass flow. This mass flow multiplied by the time step results in an increment of the sediment mass that is added to the already existing mass of the sediment. The total sediment mass is the starting point for the next time step. This is repeated until the overflow losses are 100%. When the entire loading curve is known, the optimum loading time can be determined. This is shown in Figure 10-9, where the dotted line just touches the loading curve of the effective (situ) load or the TDS. The point determined in this way gives the maximum ratio of effective load or TDS in the hopper and total cycle time. In chapter 2 and chapter 3 the determination of the settling efficiency $\boldsymbol{\eta_b}$ will be discussed in detail.

10.4. The Layer Thickness of the Layer of Water above Overflow Level

Where an obstacle is constructed on the bottom of an open channel, the water surface is raised and passes over it. Structures of this type are called weirs. Aside from special cases, flow over weirs may be regarded as steady, i.e. unchanging with respect to time, and suddenly varied, as in most hydraulic structures. The most important problem arising in connection with weirs is the relationship between the discharge over the weir and the characteristics of the weir. Many authors have suggested various relationships (e.g. Poleni, Weissbach, Boussinesq, Lauck, Pikalow) generally along the same theoretical lines and with similar results. So it seems satisfactory to introduce only the relationship of Weissbach.

$$\mathbf{Q_{out} = \frac{2}{3} \cdot C_e \cdot b \cdot \sqrt{2 \cdot g} \left(\left(h + \frac{v^2}{2 \cdot g} \right)^{3/2} - \left(\frac{v^2}{2 \cdot g} \right)^{3/2} \right)} \qquad \textbf{(10-18)}$$

If $\mathbf{h/(M+h)}$ tends towards zero (because **h** is small compared to **M**) then $\mathbf{v^2/2gh}$ also tends towards zero; so a simplified relationship can be reached as introduced first by Poleni about 250 years ago:

$$\mathbf{Q_{out} = \frac{2}{3} \cdot C_e \cdot b \cdot h \cdot \sqrt{2 \cdot g \cdot h}} \qquad \textbf{(10-19)}$$

The above equation (10-19) gives the relation between the layer thickness h and the flow $\mathbf{Q_{out}}$ for the stationary process. During the dredging process of a TSHD however, the process is not always stationary. At the start of the loading process when the overflow level is reached the layer of water will build up, while at the end when the pumps stop the layer thickness will decrease to zero. If the TSHD makes turns and the poor mixture is pumped overboard directly,

also the layer thickness will decrease and as soon as the mixture is pumped back in the hopper the layer will build up again.

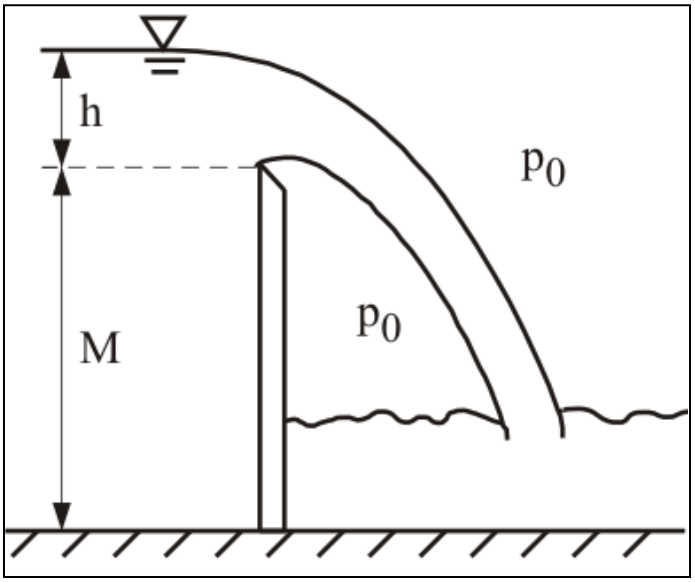

Figure 10-11: A sharp crested weir.

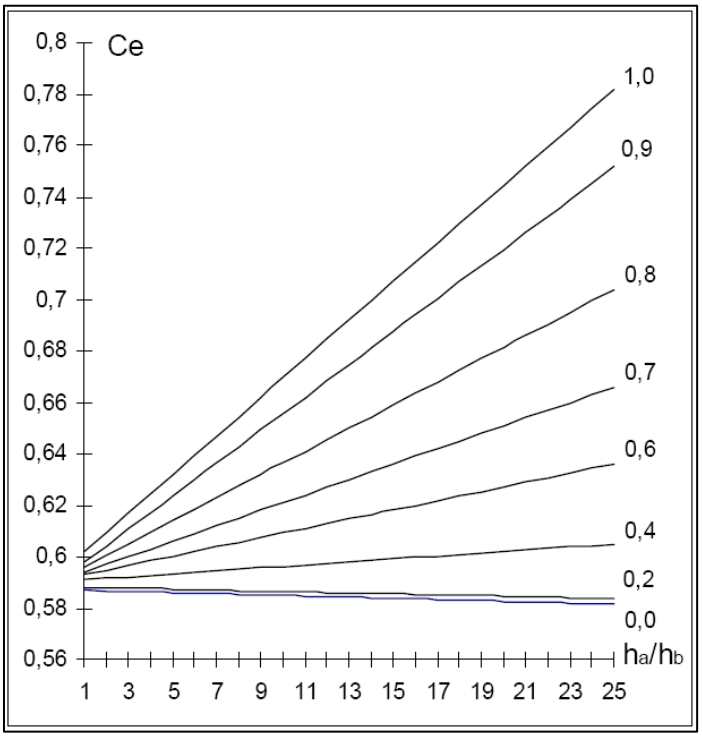

Figure 10-12: Values for the coefficient C_e as a function of $h_a/h_b=h/M$.

First the increase of the layer thickness will be considered. This increase per unit of time multiplied by the width and the length of the hopper equals the difference between the flow into the hopper and the flow leaving the hopper through the overflow according to:

$$b \cdot L \cdot \frac{dh}{dt} = Q_{in} - Q_{out} \qquad \textbf{(10-20)}$$

Substituting equation (10-19) in this equation gives a non-linear differential equation of the first order for the layer thickness **h**.

$$b \cdot L \cdot \frac{dh}{dt} = Q_{in} - C_e \cdot \frac{2}{3} \cdot \sqrt{2 \cdot g} \cdot b \cdot h^{3/2} \qquad \textbf{(10-21)}$$

This equation can be solved numerically, for example in Excel, using the starting condition **t=0**, **h=0** and the following two equations:

$$\Delta h = \frac{Q_{in} - C_e \cdot \frac{2}{3} \cdot \sqrt{2 \cdot g} \cdot b \cdot h^{3/2}}{b \cdot L} \cdot \Delta t \qquad \textbf{(10-22)}$$

$$h_{i+1} = h_i + \Delta h \qquad \textbf{(10-23)}$$

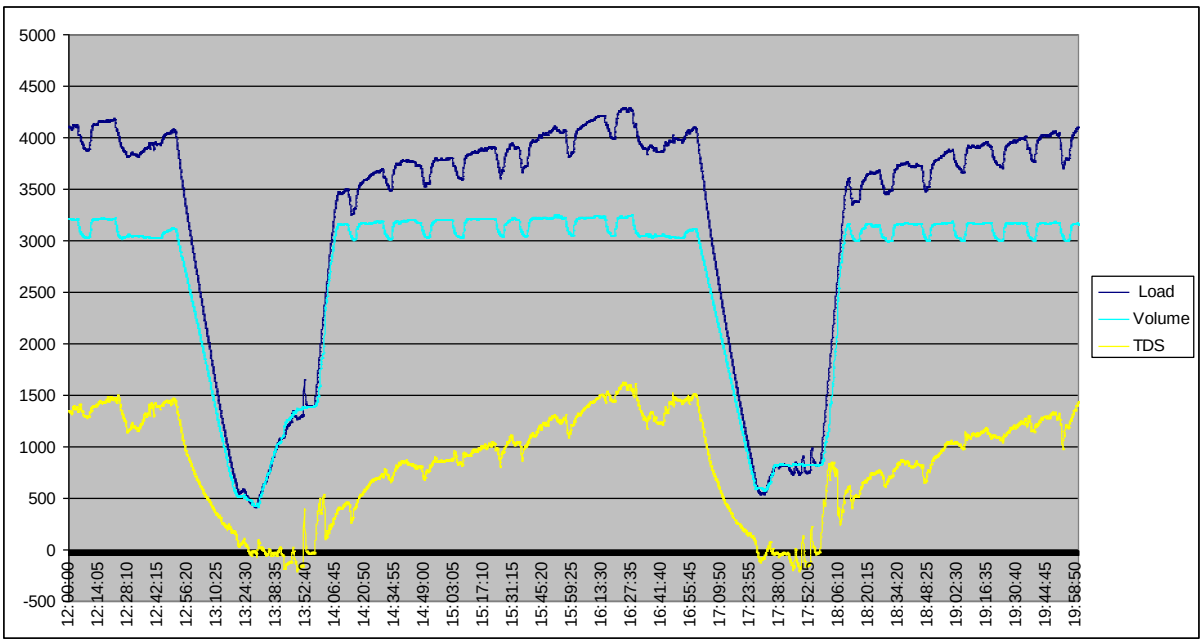

Figure 10-13: An example of a loading cycle of a TSHD with many turns.

In the equilibrium situation where $Q_{in}=Q_{out}$, the maximum layer thickness h_{max} is found according to:

$$h_{max} = \left(\frac{Q_{in}}{C_e \cdot \frac{2}{3} \sqrt{2 \cdot g} \cdot b} \right)^{2/3} = \left(\frac{Q_{in}}{2.95 \cdot C_e \cdot b} \right)^{2/3} \qquad \textbf{(10-24)}$$

From the start, **t=0**, until the maximum layer thickness is reached, h_{max}, the layer thickness **h** is a function of time that can be approximated according to:

$$h(t) = \left(\frac{Q_{in}}{2.95 \cdot C_e \cdot b} \right)^{2/3} \cdot \left(1 - e^{\frac{-t}{0.452 \cdot L \cdot \left(\frac{2.95 \cdot C_e \cdot b}{Q_{in}} \right)^{1/3}}} \right) = h_{max} \cdot \left(1 - e^{-\frac{t}{\tau}} \right) \qquad \textbf{(10-25)}$$

$$\tau = 0.452 \cdot L \cdot \left(\frac{2.95 \cdot C_e \cdot b}{Q_{in}} \right)^{1/3} = 0.452 \cdot L \cdot h_{max}^{-1/2} \qquad \textbf{(10-26)}$$

The decrease of the layer thickness h when the pumps are stopped or the poor mixture is pumped overboard follows from equation (10-20) when Q_{in} is set to zero, this can be approximated by:

$$\Delta h = \frac{-C_e \cdot \frac{2}{3} \cdot \sqrt{2 \cdot g} \cdot b \cdot h^{3/2}}{b \cdot L} \cdot \Delta t \qquad (10\text{-}27)$$

$$h_{i+1} = h_i + \Delta h \qquad (10\text{-}28)$$

Solving this gives:

$$h(t) = h_{max} - \frac{h_{max}}{\left(1 + C_d \cdot h_{max}^{2/3} \cdot t^{4/3}\right)} \quad \text{with:} \quad C_d = \frac{(3.27 + 0.0486 \cdot b)}{b^{0.22}} \cdot L^{-1.284} \qquad (10\text{-}29)$$

Figure 10-15 shows the discharge and the loading of the layer of water above the overflow level for a hopper with a length of 40 m, a width of 9 m and a height of 9 m and a flow of 5.8 m^3/sec. Both the exact solution and the approximation are shown versus an in situ measurement. The effective width of the overflow is assumed to be equal to the width of the hopper.

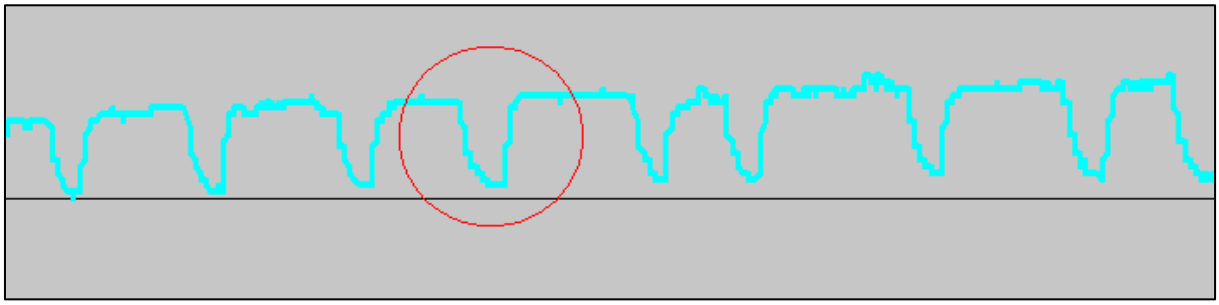

Figure 10-14: A close up of the hopper volume registration.

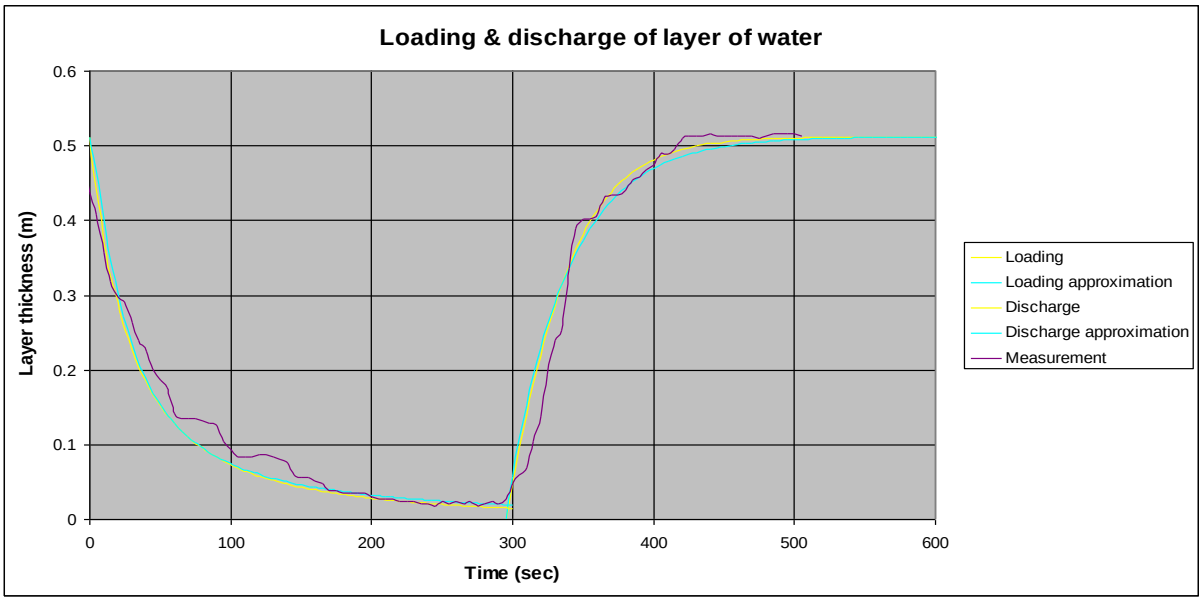

Figure 10-15: The layer thickness during a turn, registration and approximation.

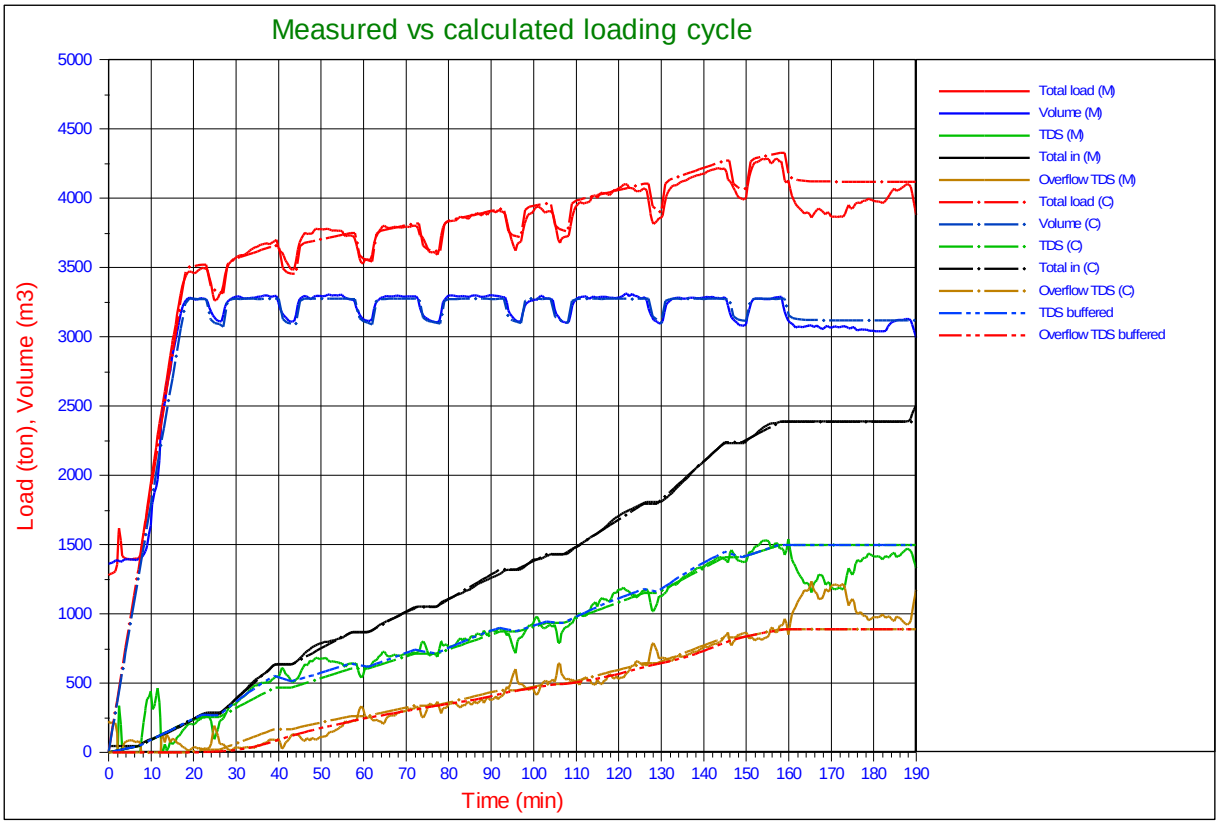

Figure 10-16: The cycle as registered is simulated with the theoretical model.

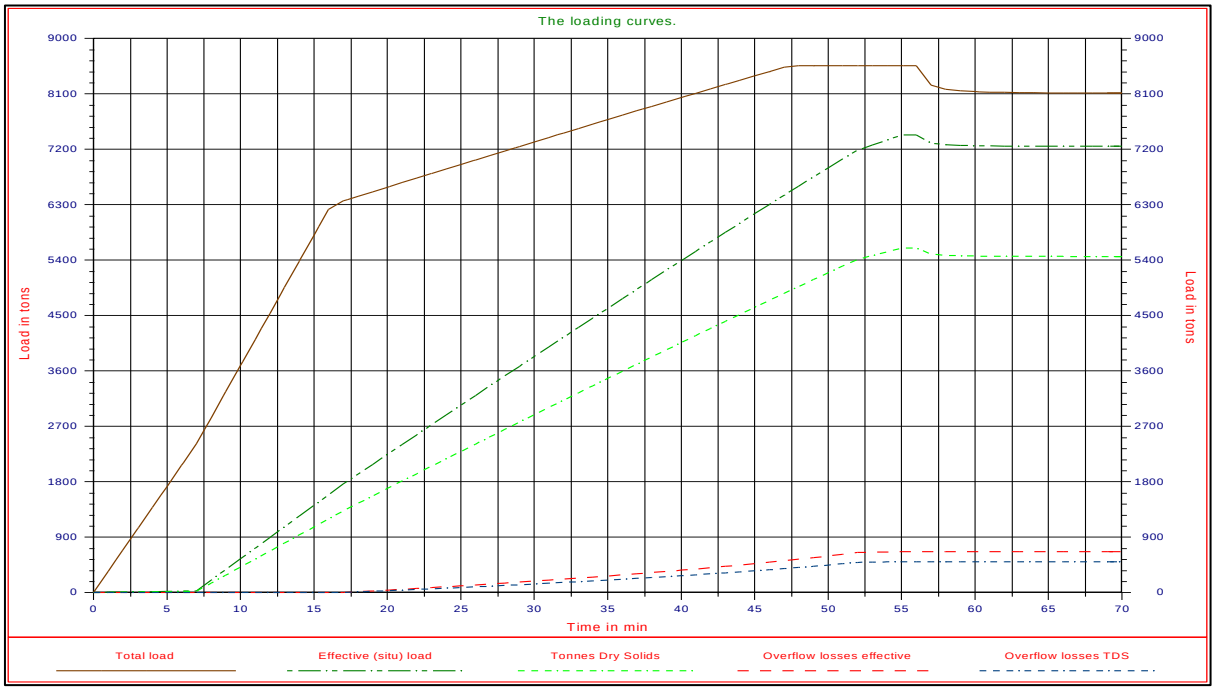

Figure 10-17: The decreasing of the height of the layer of water above the overflow at the end of the cycle.

10.5. The Storage Effect.

In the Miedema & Vlasblom model (1996) upon entrance of a particle in the hopper it is decided whether the particle will settle or not. In reality the particles that will not settle first have to move through the hopper before they reach the overflow. This means that these particles are part of the TDS in the hopper during the time they stay in the hopper. Ooijens (1999) discovered that using the time delay to determine the overflow losses improved the outcome of the Miedema & Vlasblom model (1996) considerably. Overflow losses with time delay can be derived from the overflow losses without a time delay according to the following equation:

$$ov_b(t) = \frac{1}{\tau} \cdot \int_{t-\tau}^{t} ov_c(t) \cdot dt + \frac{s}{\tau} \cdot \int_{0}^{t-\tau} (ov_c(t) - ov_b(t)) \cdot dt \qquad (10\text{-}30)$$

The first term in equation (10-30) gives the time delay for the situation with a constant bed height. Since the height of the bed increases during the loading process, the rising bed pushes part of the mixture out of the hopper. This is represented by the second term on the right hand.

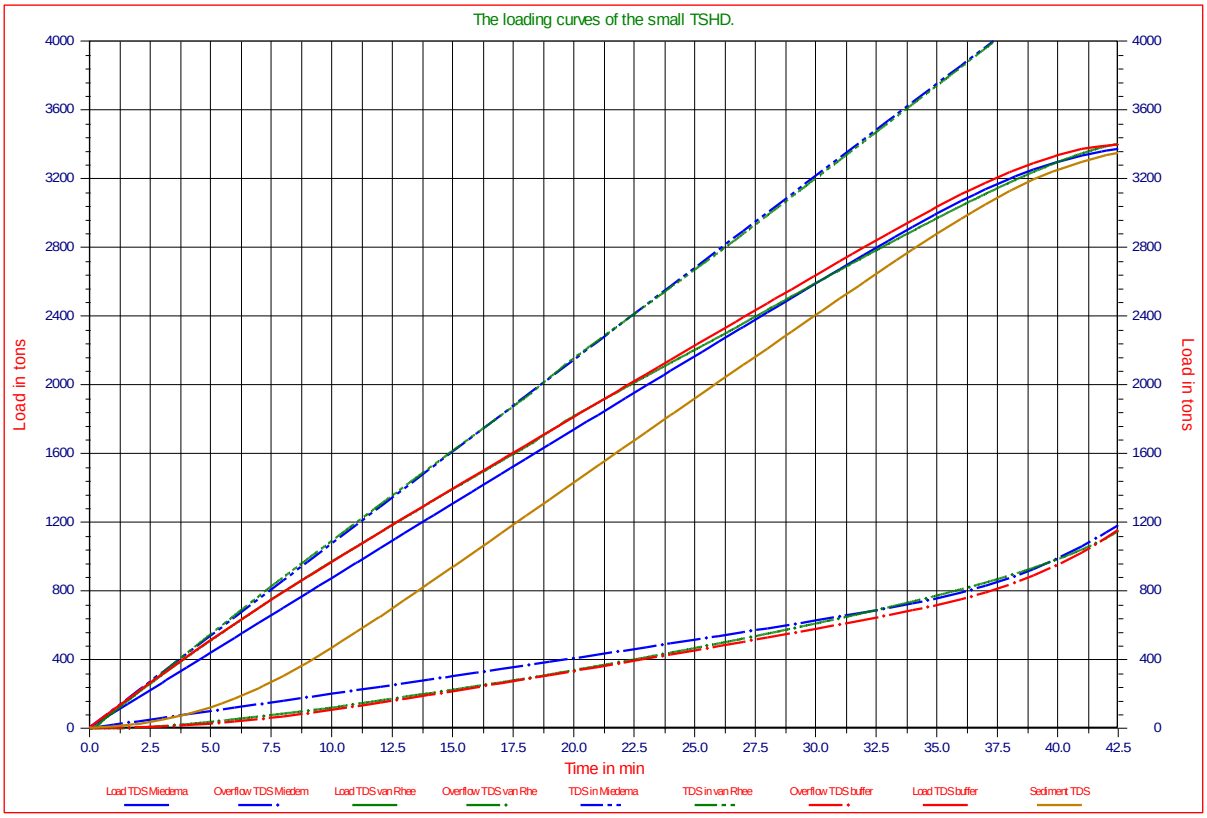

Figure 10-18: Loading curves according to Miedema & van Rhee (2007) with and without time delay.

Figure 10-18 shows the loading and overflow curves with and without the time delay or storage effect for a case considered by Miedema & van Rhee (2007). Table 10-1 gives the main data of the TSHD used in this case.

Table 10-1: The data of the TSHD used.

Hopper	Load	Volume	Length	Width	Empty height	Flow	Hopper load v_0	Mixture density
	ton	m^3	m	m	m	m^3/sec	m/sec	ton/m^3
Small	4400	2316	44.0	11.5	4.577	4	0.0079	1.3

From top to bottom Figure 10-18 contains 9 curves. The first two curves (blue and green) are almost identical and represent the TDS that enters the hopper. Since the flow and the density are constant, these curves are straight. The 3rd curve (red) represents the total TDS in the hopper according to the Miedema & Vlasblom (1996) model, so including the TDS that is still in suspension above the sediment of which part will leave the hopper through the overflow. The 4th curve (green) represents this according to van Miedema & van Rhee (2007). The 5th curve (blue)

represents the TDS that will stay in the hopper excluding the time delay effect, according to Miedema & Vlasblom (1996). The 6th (brown) curve represents the TDS in the sediment in the hopper. The 7th curve (blue) is the overflow losses according to Miedema & Vlasblom (1996), so excluding the time delay or buffering effect. The 8th curve (green) represents the overflow losses according to the 2DV model of van Rhee (2002C), which automatically includes the time delay effect. The 9th curve (red) represents the overflow losses according to the Miedema & Vlasblom (1996) model including the time delay effects according to equation (10-30).

10.6. The Hopper of a TSHD as an Ideal Settlement Basin.

As stated before, the ideal settlement basin is a rectangular basin with an entrance zone, a settlement and sedimentation zone and an overflow zone. The hopper geometry and configuration aboard of the TSHD can be quite different from the ideal situation, so a method to schematize the hopper dimensions is required.

1. The height **H** of the hopper can be defined best as the hopper volume divided by the hopper area **L·W**. This means that the base of the ideal hopper, related to the maximum overflow height is at a higher level than the ship's base. This assumption results in a good approximation at the final phases (7 and 8) of the loading process, while in phase 6 of the loading process the hopper is filled with mixture and so the material stays in the hopper anyway.

2. Near the loading chute of the hopper or in cases where a deep loading system is used, the turbulence of the flow results in a good and sufficient distribution of the concentration and particle size distribution over the cross-section of the hopper, so the entrance zone can be kept small. For example between the hopper bulkhead and the end of the loading chute.

3. In the ideal settlement basin there are no vertical flow velocities except those resulting from turbulence. However in reality vertical velocities do occur near the overflow, therefore it is assumed that the overflow zone starts where the vertical velocities exceed the horizontal velocities. An estimate of where this will occur can easily be made with a flow net.

4. Although the presence of beams and cylinder rods for the hopper doors does increase the turbulence, it is the author's opinion, that an additional allowance is not required, neither for the hopper load parameter, nor for the turbulence parameter.

5. As is shown in Figure 10-6 and Figure 10-7, a density current may occur during the loading phases 6 and 7, resulting in a non-uniform velocity and density distribution. This does not affect the so called hopper load parameter as is proven in 0, so for the schematization of the hopper a uniform velocity and density distribution are assumed.

6. The validity of the schematizations and simplifications will be proven by some examples with model and prototype tests.

10.7. The Modified Camp Model.

Sedimentation is a treatment process where suspended particles, like sand and clay are re-moved from the water. Sedimentation can take place naturally in reservoirs or in compact settling installations. Sedimentation is applied in groundwater treatment installations for backwash water treatment and in TSHD's. In horizontal flow settling tanks water is uniformly distributed over the cross-sectional area of the tank in the inlet zone. A stable, non-turbulent, flow in the settling zone takes care for the settling of suspended matter in the settling zone. The sludge accumulates on the bottom, or is continuously removed. In the outlet zone the settled sludge must be prevented from being re-suspended and washed out with the effluent. Sedimentation occurs because of the difference in density between suspended particles and water. The following factors influence the sedimentation process: density and size of suspended particles, water temperature, turbulence, stability of flow, bottom scour and flocculation:

- Density, the higher the density of the particles, the faster the particles settle
- Size, the larger the particles are, the faster they settle
- Temperature, the lower the temperature of the water is, the higher the viscosity is, so the slower the particles settle
- Turbulence, the more turbulent the flow is, the slower the particles settle
- Stability, instability can result in short circuit flow, influencing the settling of particles
- Bottom scour, by bottom scour settled particles are re-suspended and washed out with the effluent

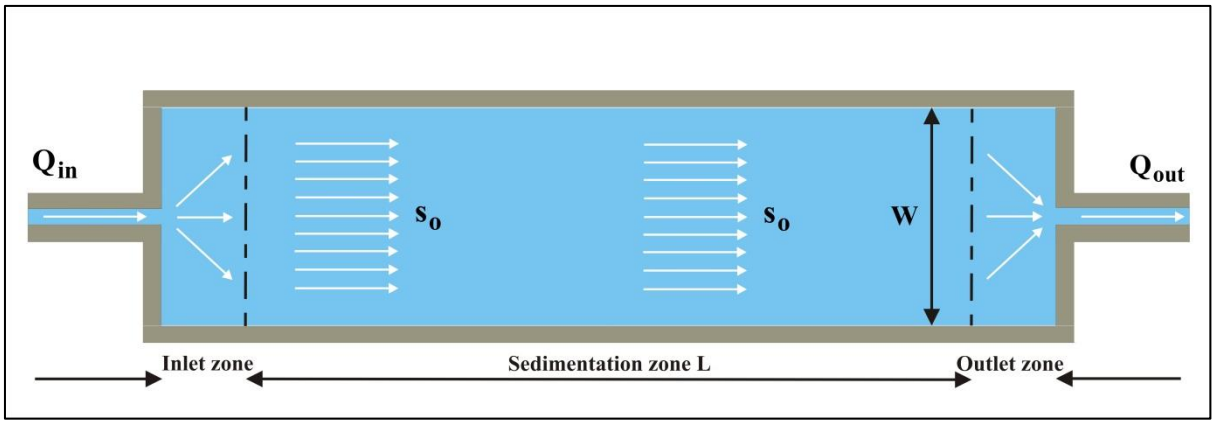

Figure 10-19: The top view of the ideal basin.

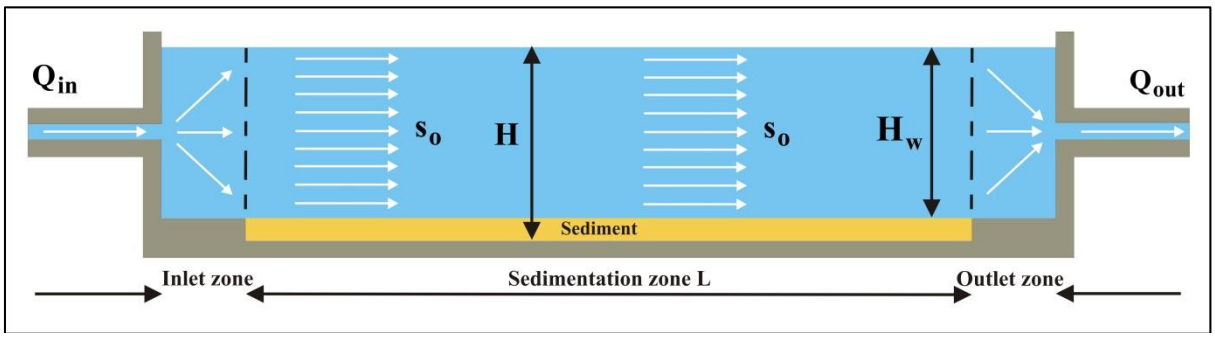

Figure 10-20: The side view of the ideal basin.

The ideal settlement basin consists of an entrance zone where the solid/fluid mixture enters the basin and where the grain distribution is uniform over the cross-section of the basin, a settlement zone where the grains settle into a sediment zone and a zone where the cleared water leaves the basin, the overflow zone. It is assumed that the grains are distributed uniformly and are extracted from the flow when the sediment zone is reached. Each particle stays in the basin for a fixed time and moves from the position at the entrance zone, where it enters the basin towards the sediment zone, following a straight line. The slope of this line depends on the settling velocity v and the flow velocity above the sediment $\mathbf{s_o}$. Figure 10-19 shows a top view of the ideal settlement basin. Figure 10-20 shows the side view and Figure 10-21, Figure 10-22 and Figure 10-23 the path of individual grains. All particles with a diameter $\mathbf{d_o}$ and a settling velocity $\mathbf{v_o}$ will settle, a particle with this diameter, entering the basin at the top, reaches the end of the sediment zone. Particles with a larger diameter will all settle, particles with a smaller diameter will partially settle. Miedema & Vlasblom (1996) adapted the Camp model to be used for hopper sedimentation. The biggest difference between the original Camp (1936), (1946) and (1953) model and the

Miedema & Vlasblom model is the height H_w above the sediment zone. In the Camp model this is a fixed height, in the Miedema & Vlasblom model this height decreases during the loading process.

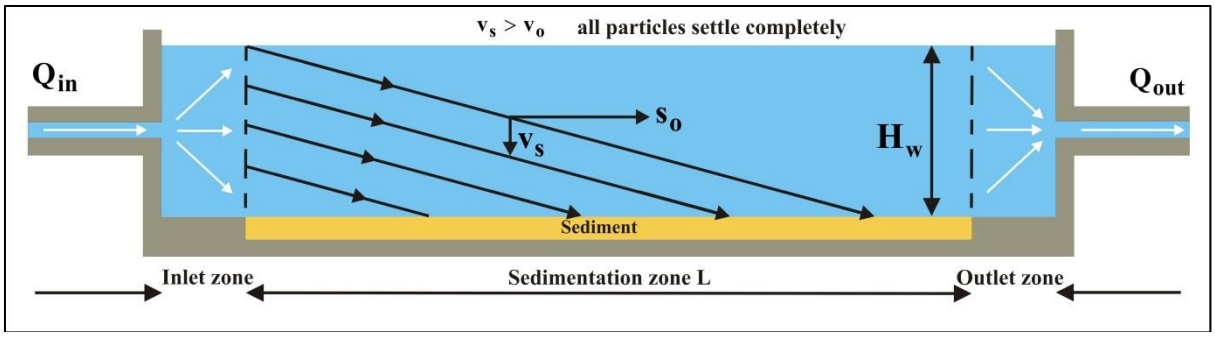

Figure 10-21: The path of a particle with a settling velocity greater than the hopper load parameter.

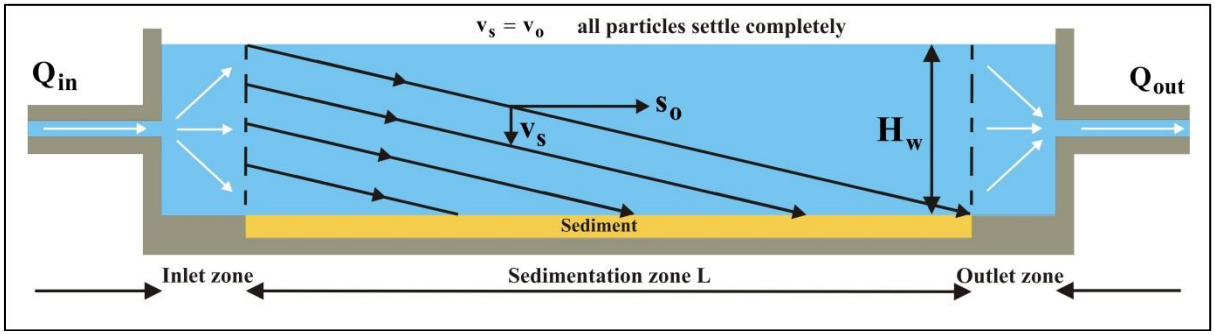

Figure 10-22: The path of a particle with a settling velocity equal to the hopper load parameter.

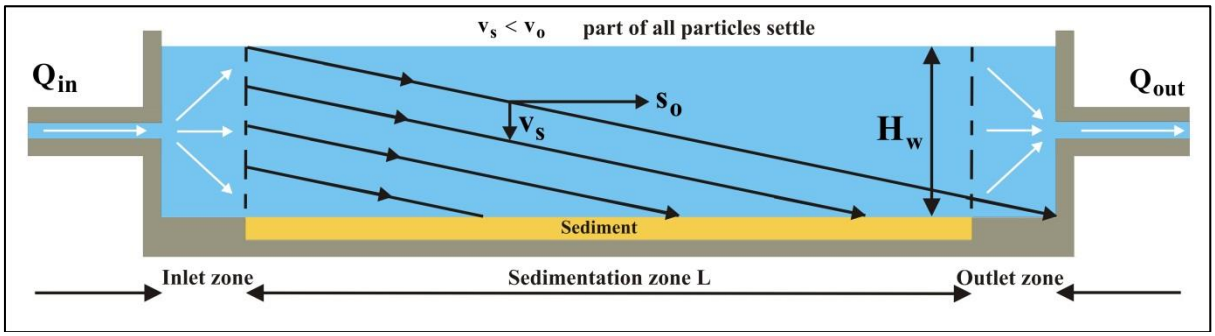

Figure 10-23: The path of a particle with a settling velocity smaller than the hopper load parameter.

The average horizontal velocity s_o in the basin, when the height H_w above the sediment is known (see equations (10-16) and (10-17)), equals to:

$$s_o = \frac{Q_{in}}{W \cdot H_w} \tag{10-31}$$

The hopper load parameter v_o is defined as the settling velocity of a particle that enters the basin (hopper) at the top and reaches the sediment at the end of the basin, after traveling a distance **L,** see Figure 10-22. This can be determined according to (with a uniform velocity distribution):

$$\frac{v_o}{s_o} = \frac{H_w}{L} \text{ thus: } v_o = s_o \cdot \frac{H_w}{L} = \frac{Q_{in}}{W \cdot L} \tag{10-32}$$

If the velocity distribution is non-uniform, like in Figure 10-24, the hopper load parameter can be derived by integrating the horizontal velocity **s(z)** over the time the particle, entering at the top of the basin, needs to reach the sediment at the end, so traveling a horizontal distance **L**.

$$\int_0^T s(z)\cdot dt = L \qquad (10\text{-}33)$$

With:

$$T = \frac{H_w}{v'_o} \quad , \quad z = v'_o \cdot t \quad , \quad dz = v'_o \cdot dt \quad , \quad Q_{in} = W \cdot \int_0^{H_w} s(z)\cdot dz \qquad (10\text{-}34)$$

Equation (10-33) can be written as:

$$\frac{1}{v'_o}\cdot\int_0^{H_w} s(z)\cdot dz = \frac{1}{v'_o}\cdot\frac{Q_{in}}{W} = L \qquad (10\text{-}35)$$

Thus the hopper load parameter does not change because of a non-uniform velocity distribution.

$$v'_o = \frac{Q_{in}}{W\cdot L} = v_o \qquad (10\text{-}36)$$

During the transport of a particle from the top of the inlet to the overflow however, the sediment level rises by $\Delta H = v_{sed}\cdot\Delta t$, where Δt equals the traveling time of the particle and v_{sed} equals the sediment (bed) rise velocity. The thickness of the layer of fluid above the sediment thus decreases from H_w when the particle enters the hopper to $H_w - \Delta H$ when the particle reaches the sediment at the end of the hopper due to the settling velocity of the particle. The average thickness H_a of the layer of water above the sediment during the transport of the particle is now:

$$H_a = H_w - 0.5\cdot\Delta H \qquad (10\text{-}37)$$

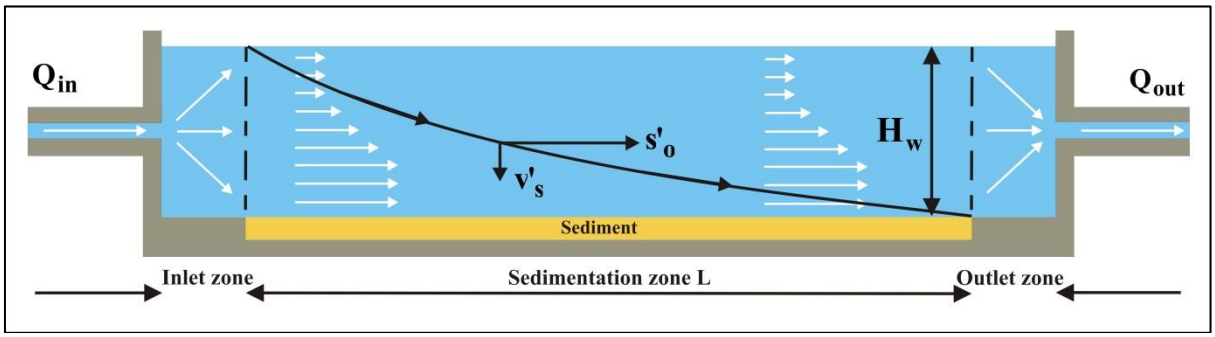

Figure 10-24: The path of a particle with a non-uniform velocity distribution.

The average horizontal velocity s_o in the hopper during the stay of the particle in the hopper is thus:

$$s_o = \frac{Q_{in}}{W\cdot(H_w - 0.5\cdot\Delta H)} = \frac{Q_{in}}{W\cdot H_a} \qquad (10\text{-}38)$$

The time it takes for the particle to be transported over the length of the hopper is thus:

$$\Delta t = \frac{L}{s_o} = \frac{W\cdot L\cdot H_a}{Q_{in}} \qquad (10\text{-}39)$$

The vertical distance traveled by a particle that enters the hopper at the top and just reaches the sediment at the end of the hopper is (see Figure 10-25):

$$v_{oo}\cdot\Delta t = v_{oo}\cdot\frac{W\cdot L\cdot H_a}{Q_{in}} = H_w - \Delta H = H_a - 0.5\cdot\Delta H \qquad (10\text{-}40)$$

This gives for the settling velocity of such a particle:

$$v_{oo} = \frac{Q_{in}}{W \cdot L \cdot H_a} \cdot (H_a - 0.5 \cdot \Delta H) = \frac{Q_{in}}{W \cdot L} \cdot \left(1 - \frac{0.5 \cdot \Delta H}{H_a}\right) \quad \textbf{(10-41)}$$

With:

$$\Delta H = v_{sed} \cdot \Delta t = v_{sed} \cdot \frac{W \cdot L \cdot H_a}{Q_{in}} \quad \textbf{(10-42)}$$

This gives for the modified hopper load parameter:

$$v_{oo} = \frac{Q_{in}}{W \cdot L} - \frac{v_{sed}}{2} \quad \textbf{(10-43)}$$

A smaller hopper load parameter means that smaller grains will settle easier. From Figure 10-21 the conclusion can be drawn that grains with a settling velocity greater than v_o will all reach the sediment layer and thus have a settling efficiency η_g of 1. Grains with a settling velocity smaller then v_o, Figure 10-23, will only settle in the sedimentation zone, if they enter the basin below a specified level. This gives for the modified settling efficiency of the individual grain:

$$\eta_{gg} = \left(\frac{v_s}{v_{oo}}\right) \quad \textbf{(10-44)}$$

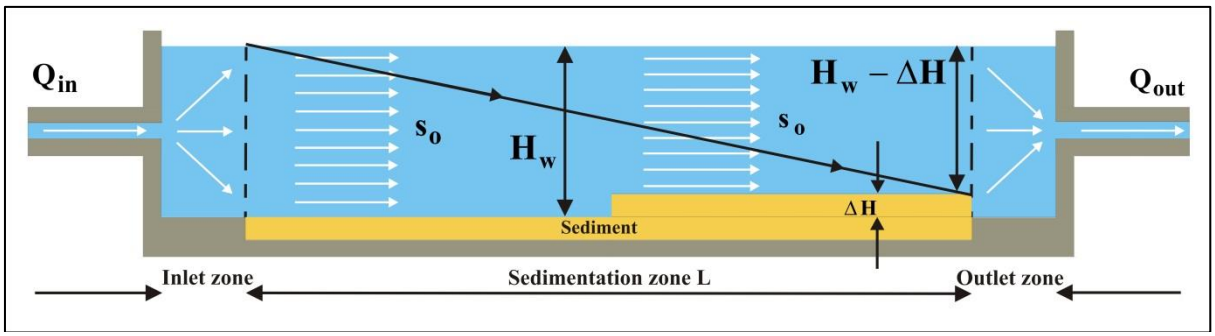

Figure 10-25: The effect of a rising sediment level.

In the case of a non-uniform velocity distribution, Figure 10-24, the settling efficiency can also be defined as the ratio of the horizontal distances traveled in the time a particle needs to reach the sediment, although this is not 100% true because the ratio of the vertical distance traveled gives the exact settling efficiency, it's a good approximation:

$$\eta_g = \left(\frac{L_{v_o}}{L_v}\right) \quad \textbf{(10-45)}$$

The horizontal distance traveled by a particle in the time to reach the sediment level is:

$$L_v = \int_0^T s(z) \cdot dt \quad \textbf{(10-46)}$$

With:

$$T = \frac{H_w}{v_s} \quad , \quad z = v_s \cdot t \quad , \quad dz = v_s \cdot dt \quad , \quad Q_{in} = W \cdot \int_0^{H_w} s(z) \cdot dz \qquad \textbf{(10-47)}$$

Equation (10-47) can be written as:

$$\frac{1}{v_s} \cdot \int_0^{H_w} s(z) \cdot dz = \frac{1}{v_s} \cdot \frac{Q_{in}}{W} = L_v \qquad \textbf{(10-48)}$$

This also gives a settling efficiency according to:

$$\eta_g = \left(\frac{v_s}{v_o} \right) \qquad \textbf{(10-49)}$$

The settling efficiency of a particle with a settling velocity smaller than the hopper load parameter v_o, does not change due to a non-uniform velocity distribution. If the fraction of grains with a settling velocity greater than v_o equals p_o, then the settling efficiency for a grain distribution η_b can be determined by integrating the grain settling efficiency for the whole grain distribution curve, according to Figure 10-26. The blue surface equals the basin settling efficiency according to equation (10-50).

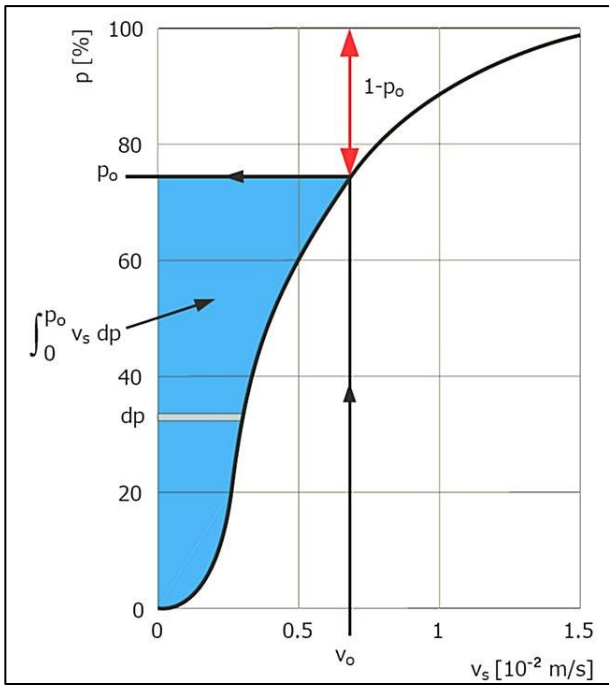

Figure 10-26: Determination of the basin settling efficiency.

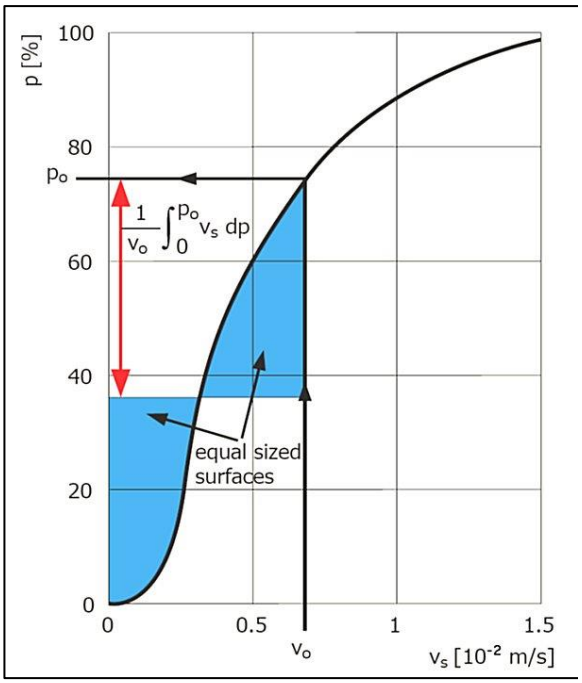

Figure 10-27: A graphical method to determine the settling efficiency.

$$\eta_b = \left(1 - p_o\right) + \int_0^{p_o} \eta_g \cdot dp \qquad \textbf{(10-50)}$$

In theory a particle is removed from the water when it reaches the bottom of the settling tank. In practice, however, it is possible that re-suspension of already settled particles occurs.
When the sediment level in the hopper is rising, the horizontal velocity increases and there will be a point where grains of a certain diameter will not settle anymore due to scour. First the small grains will not settle or erode and when the level increases more, also the bigger grains will stop settling, resulting in a smaller settling efficiency. The effect of scour is taken into account by integrating with the lower boundary p_s. The fraction p_s is the fraction of the grains smaller then d_s, matching a horizontal velocity in the hopper of s_s.
The shear force of water on a spherical particle is:

$$\tau = \frac{1}{4} \cdot \lambda \cdot \frac{1}{2} \cdot \rho_w \cdot s_s^2 \qquad \textbf{(10-51)}$$

The shear force of particles at the bottom (mechanical friction) is proportional to the submerged weight of the sludge layer, per unit of bed surface (see Figure 10-28):

$$f = \mu \cdot N = \mu \cdot (1-n) \cdot (\rho_q - \rho_w) \cdot g \cdot d \qquad \textbf{(10-52)}$$

In equilibrium the hydraulic shear equals the mechanical shear and the critical scour velocity can be calculated. The scour velocity for a specific grain with diameter $\mathbf{d_s}$, according to Huisman (1973-1995) and (1980) is:

$$s_s = \sqrt{\frac{8 \cdot \mu \cdot (1-n) \cdot (\rho_q - \rho_w) \cdot g \cdot d_s}{\lambda \cdot \rho_w}} \qquad \textbf{(10-53)}$$

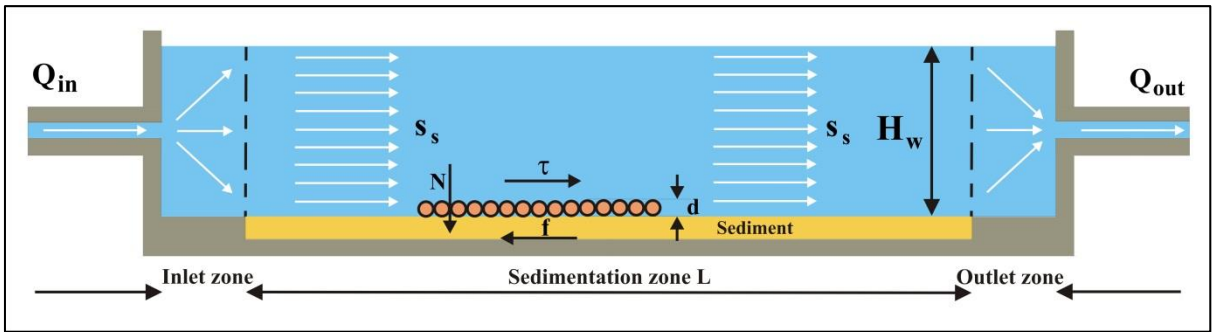

Figure 10-28: The equilibrium of forces on a particle.

With $\mu \cdot (1-n) = 0.05$ and $\lambda = 0.03$ this gives:

$$s_s = \sqrt{\frac{40 \cdot (\rho_q - \rho_w) \cdot g \cdot d_s}{3 \cdot \rho_w}} \qquad \textbf{(10-54)}$$

The particle diameter of particles that will not settle due to scour (and all particles with a smaller diameter) is:

$$d_s = \frac{3 \cdot \rho_w}{40 \cdot (\rho_q - \rho_w) \cdot g} \cdot s_s^2 \qquad \textbf{(10-55)}$$

Knowing the diameter $\mathbf{d_s}$, the fraction $\mathbf{p_s}$ that will not settle due to scour can be found if the PSD of the sand is known. Equation (10-54) is often used for designing settling basins for drinking water. In such basins scour should be avoided, resulting in an equation with a safety margin. For the prediction of the erosion during the final phase of the settling process in TSHD's a more accurate prediction of the scour velocity is required, which will be discussed in another chapter. The settling efficiency η_g, but this only occurs at the end of the loading cycle, can now be corrected for scour according to:

$$\eta_b = (1 - p_o) + \int_{p_s}^{p_o} \eta_g \cdot dp \qquad \textbf{(10-56)}$$

When $p_s > p_o$ this results in:

$$\eta_b = (1 - p_s) \qquad \textbf{(10-57)}$$

10.8. The Influence of Turbulence.

For the ideal settlement basin laminar flow is assumed. Turbulent flow will reduce the settling velocity of the grains and thus the total settling efficiency. Whether turbulent flow occurs, depends on the Reynolds number of the flow in the basin. Using the hydraulic radius concept this number is:

$$\mathbf{Re} = \frac{\mathbf{Q_{in}}}{\nu \cdot (\mathbf{W} + 2 \cdot \mathbf{H_w})} \tag{10-58}$$

For a given flow $\mathbf{Qi_n}$ and viscosity ν the Reynolds number depends on the width **W** and the height $\mathbf{H_w}$ of the layer of fluid in the basin. A large width and height give a low Reynolds number. However this does not give an attractive shape for the basin from an economical point of view, which explains why the flow will be turbulent in existing basins.

Dobbins (1944) and Camp (1946) and (1953) use the two-dimensional turbulent diffusion equation to determine the resulting decrease of the settling efficiency.

$$\mathbf{s(z)} \cdot \frac{\partial \mathbf{c}}{\partial \mathbf{x}} = \varepsilon_z \cdot \frac{\partial^2 \mathbf{c}}{\partial \mathbf{z}^2} + \left(\mathbf{v(c)} + \frac{\partial \varepsilon_z}{\partial \mathbf{z}} \right) \cdot \frac{\partial \mathbf{c}}{\partial \mathbf{z}} + \varepsilon_x \cdot \frac{\partial^2 \mathbf{c}}{\partial \mathbf{x}^2} \tag{10-59}$$

Assuming a parabolic velocity distribution instead of the logarithmic distribution, neglecting diffusion in the x-direction and considering the settling velocity independent of the concentration reduces the equation to:

$$\left(\mathbf{s_t} - \mathbf{k} \cdot (\mathbf{h} - \mathbf{z})^2 \right) \cdot \frac{\partial \mathbf{c}}{\partial \mathbf{x}} = \varepsilon_z \cdot \frac{\partial^2 \mathbf{c}}{\partial \mathbf{z}^2} + \mathbf{v} \cdot \frac{\partial \mathbf{c}}{\partial \mathbf{z}} \tag{10-60}$$

Because of the parabolic velocity distribution, the turbulent diffusion coefficient ε_z is a constant. A further simplification is obtained if the velocity **s** is assumed constant throughout the depth, meaning that the constant of the parabola **k** approaches zero. In this case the turbulent diffusion equation becomes:

$$\frac{\partial \mathbf{c}}{\partial \mathbf{t}} = \mathbf{s} \cdot \frac{\partial \mathbf{c}}{\partial \mathbf{x}} = \varepsilon_z \cdot \frac{\partial^2 \mathbf{c}}{\partial \mathbf{z}^2} + \mathbf{v} \cdot \frac{\partial \mathbf{c}}{\partial \mathbf{z}} \tag{10-61}$$

Huisman (1973-1995) in his lecture notes derives the diffusion-dispersion equation in a more general form, including longitudinal dispersion.

$$\frac{\partial \mathbf{c}}{\partial \mathbf{t}} + \frac{\partial (\mathbf{s} \cdot \mathbf{c})}{\partial \mathbf{x}} = \frac{\partial}{\partial \mathbf{x}} \cdot \left(\varepsilon_x \cdot \frac{\partial \mathbf{c}}{\partial \mathbf{x}} \right) + \frac{\partial}{\partial \mathbf{z}} \cdot \left(\mathbf{v} \cdot \mathbf{c} + \varepsilon_z \cdot \frac{\partial \mathbf{c}}{\partial \mathbf{z}} \right) \tag{10-62}$$

Assuming a steady and uniform flow, the longitudinal dispersion coefficient is independent of **x** and the settling velocity **v** independent of **z**. This reduces the equation 18 to:

$$\mathbf{s} \cdot \frac{\partial \mathbf{c}}{\partial \mathbf{x}} = \varepsilon_z \cdot \frac{\partial^2 \mathbf{c}}{\partial \mathbf{z}^2} + \mathbf{v} \cdot \frac{\partial \mathbf{c}}{\partial \mathbf{z}} + \varepsilon_x \cdot \frac{\partial^2 \mathbf{c}}{\partial \mathbf{x}^2} \tag{10-63}$$

By means of computations Huisman (1973-1995) shows that the retarding effect of dispersion may be ignored for the commonly applied width to depth ratio 3 to 5. This reduces equation (10-62) to equation (10-59) of Dobbins and Camp.

Groot (1981) investigated the influence of hindered settling and the influence of different velocity distributions using the following equation:

$$\mathbf{s} \cdot \frac{\partial \mathbf{c}}{\partial \mathbf{x}} = \mathbf{v(c)} \cdot \frac{\partial \mathbf{c}}{\partial \mathbf{z}} + \mathbf{c} \cdot \frac{\partial \mathbf{v(c)}}{\partial \mathbf{c}} \cdot \frac{\partial \mathbf{c}}{\partial \mathbf{z}} + \frac{\partial}{\partial \mathbf{z}} \cdot \left(\varepsilon(\mathbf{x}, \mathbf{z}) \cdot \frac{\partial \mathbf{c}}{\partial \mathbf{z}} \right) \tag{10-64}$$

The velocity distribution, the diffusion coefficient distribution and the distribution of the initial concentration did not have a significant influence on the computed results, but the results were very sensitive on the formulation of hindered settling. This formulation of course influences the settling velocity in general. Equation (10-63) can be solved analytically using separation of variables. The boundary conditions used by Camp and Dobbins describe the rate of vertical transport across the water surface and the sediment for **x=∞** and the concentration distribution at the inlet, these are:

$$\varepsilon \cdot \frac{\partial c}{\partial z} + v \cdot c = 0$$ at the water surface **(10-65)**

$$\varepsilon \cdot \frac{\partial c}{\partial z} + v \cdot c = 0$$ at the sediment for **x=∞**, for the no-scour situation **(10-66)**

$$c = f(z)$$ at the entrance for **x=0** **(10-67)**

This method, resulting in Figure 10-29, Figure 10-30 and Figure 10-31, gives the removal ration due to turbulence for a single grain. The removal ratio can be determined by summation of a series.
Solving equation (10-64) gives ($\mathbf{v \cdot H / 2 \cdot \varepsilon_z}$) as the independent parameter on the horizontal axis and the removal ratio ($\mathbf{v/v_o}$=settling efficiency) on the vertical axis. Using a parabolic velocity distribution this can be substituted by:

$$\frac{v \cdot H}{2 \cdot \varepsilon_z} = \frac{v}{s_o} \cdot \frac{3}{\kappa} \cdot \sqrt{\frac{8}{\lambda}} = 122 \cdot \frac{v}{s_o}$$ with: κ**=0.4** and λ**=0.03** **(10-68)**

Figure 10-29, Figure 10-30 and Figure 10-31 give the removal ratio or settling efficiency for individual particles for values of λ of 0.01, 0.02 and 0.03.

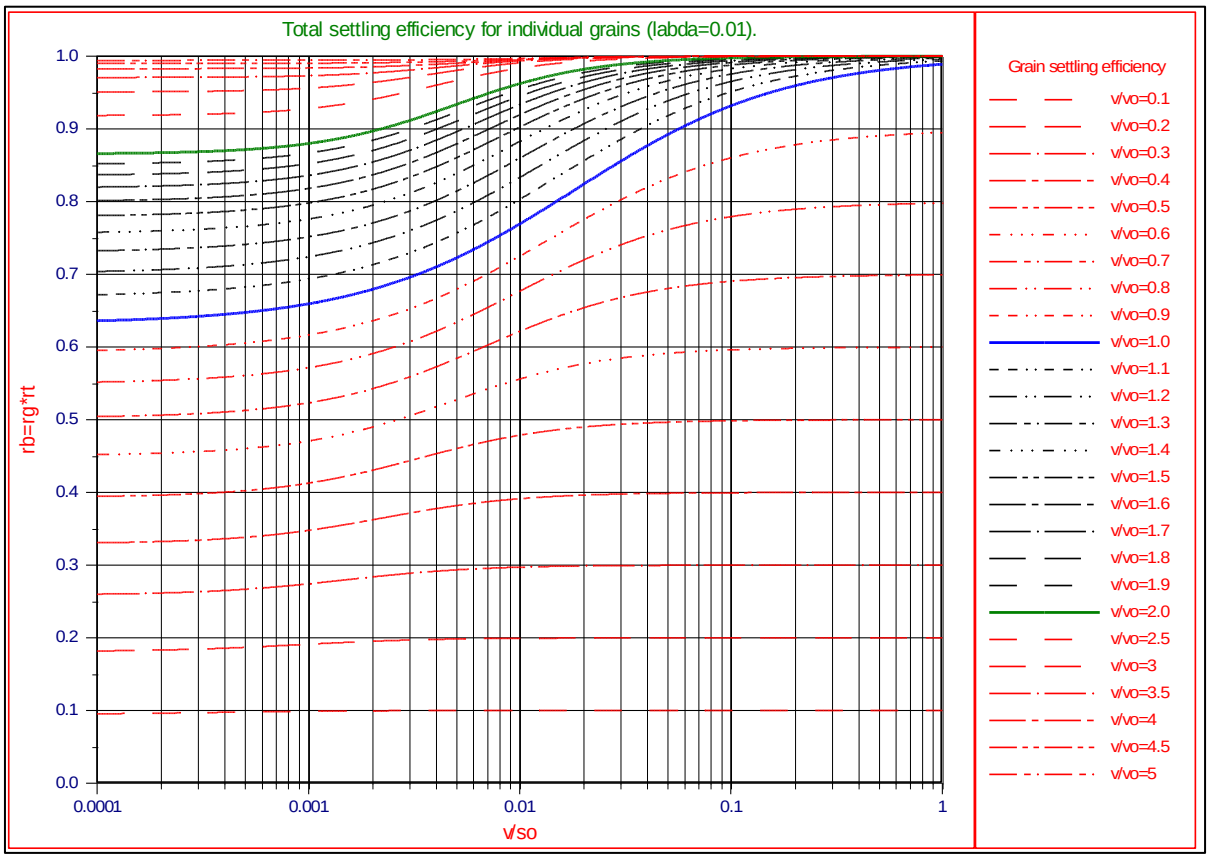

Figure 10-29: The total settling efficiency for λ=0.01.

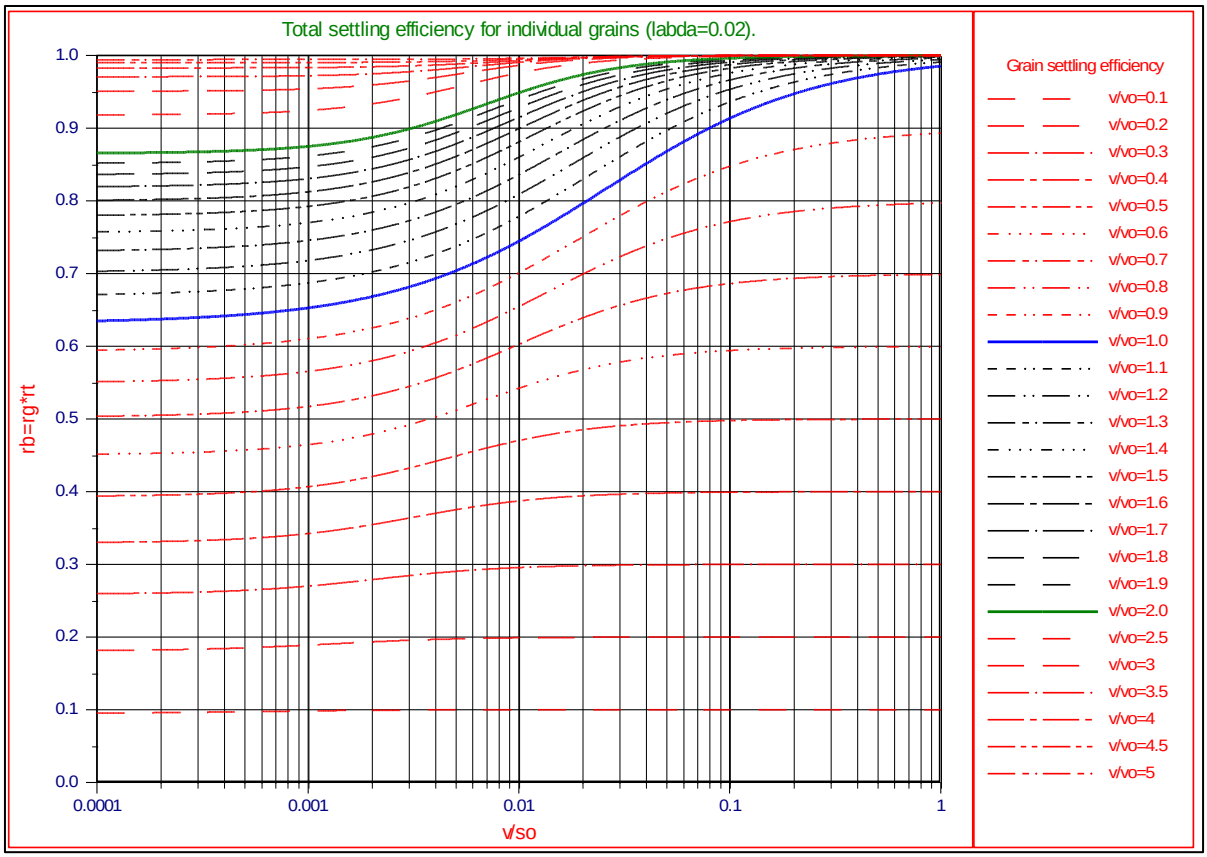

Figure 10-30: The total settling efficiency for λ=0.02.

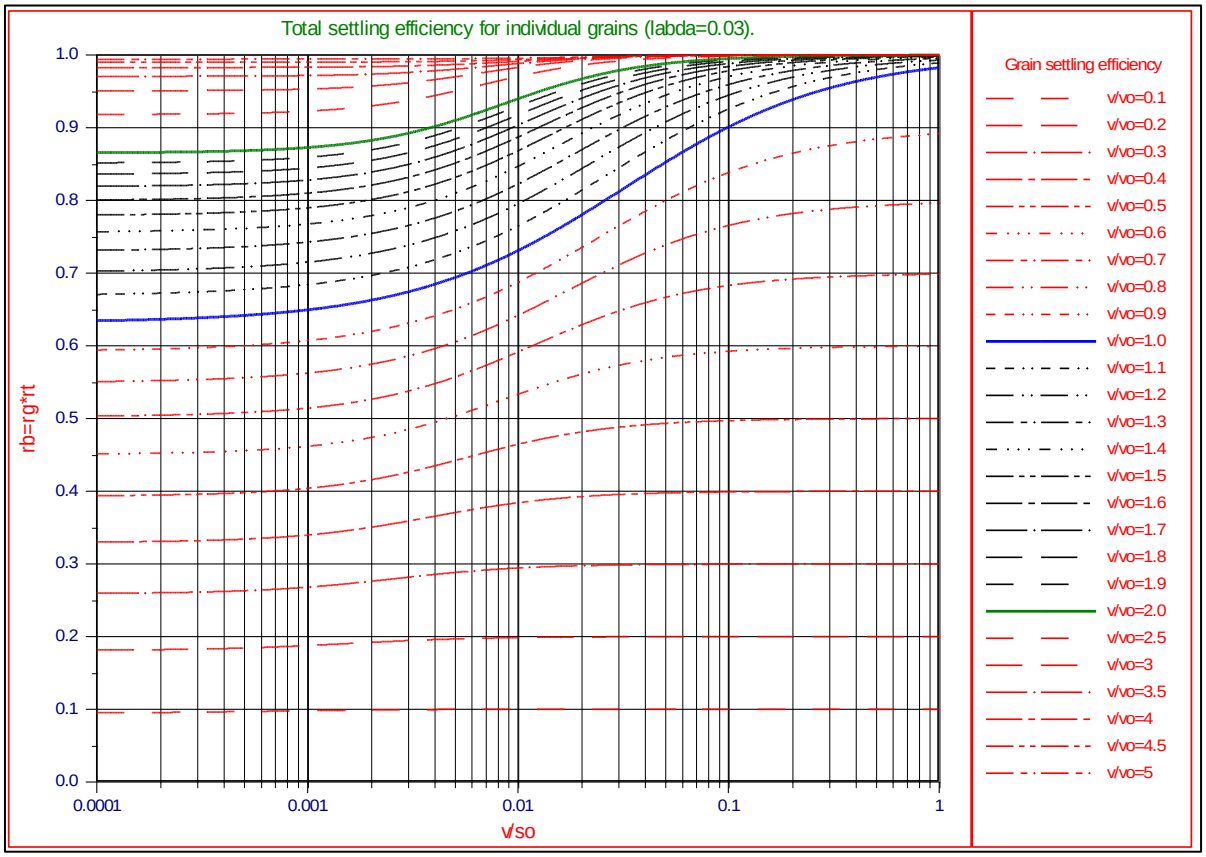

Figure 10-31: The total settling efficiency for λ=0.03.

The settling efficiency for $v/v_o<1$ can be approximated by equation (10-69), while equation (10-70) gives a good approximation for the case $v/v_o>1$:

$$\eta_t = \eta_g^0 \cdot \left(1 - .184 \cdot \eta_g^{+.885-.20\cdot\eta_g} \cdot \left(1 - \mathrm{TanH}\left(\eta_g^{-.13-.80\cdot\eta_g} \cdot \left(\mathrm{Log}\left(\frac{v}{s_o}\right) - .2614 - .5\cdot\mathrm{Log}(\lambda) + \eta_g^{-.33-.94\cdot\eta_g}\right)\right)\right)\right) \quad \textbf{(10-69)}$$

$$\eta_t = \eta_g^{-1} \cdot \left(1 - .184 \cdot \eta_g^{-.69-.38\cdot\eta_g} \cdot \left(1 - \mathrm{TanH}\left(\eta_g^{+.77-.08\cdot\eta_g} \cdot \left(\mathrm{Log}\left(\frac{v}{s_o}\right) - .2614 - .5\cdot\mathrm{Log}(\lambda) + \eta_g^{+1.01-.18\cdot\eta_g}\right)\right)\right)\right) \quad \textbf{(10-70)}$$

The effect of turbulence is taken into account by multiplying the settling efficiency with the turbulence efficiency η_t according to Miedema & Vlasblom (1996). Since the turbulence efficiency is smaller than 1 for all grains according to the equations (10-69) and (10-70), the basin settling efficiency can be determined with equation (10-71), where p_s equals 0 as long as scour does not occur. So the total settling efficiency is now:

$$\eta_b = \int_{p_s}^{1} \eta_g \cdot \eta_t \cdot dp \quad \textbf{(10-71)}$$

10.9. The Modified Hopper Load Parameter.

The basic Camp theory assumes that the settled grains are removed constantly, resulting in a constant height H_w of the settlement zone. In the hopper of the TSHD this is not the case, resulting in a rising sediment zone and a decreasing height H_w during the sedimentation process. The rising sediment zone influences the effective or modified hopper load parameter v_{oo}. This influence can be determined as follows (see also Figure 10-25 and equation (10-43)):

$$\frac{dH_w}{dt}\cdot L\cdot W\cdot c_{bed} = Q\cdot\left(c_{in}-c_{out}\right) \qquad \textbf{(10-72)}$$

With the effective or modified settling efficiency η_{gg} of a grain, including the effect of the rising sediment zone:

$$\eta_{gg}=\frac{c_{in}-c_{out}}{c_{in}} \text{ thus: } c_{in}-c_{out}=\eta_{gg}\cdot c_{in} \text{ with: } \eta_{gg}=\left(\frac{v_s}{v_{oo}}\right) \qquad \textbf{(10-73)}$$

The velocity at which the sediment zone is rising is:

$$\frac{dH_w}{dt}\cdot L\cdot W\cdot c_{bed} = Q\cdot\eta_{gg}\cdot c_{in}$$

thus: **(10-74)**

$$\frac{dH_w}{dt}=\frac{Q}{L\cdot W}\cdot\frac{c_{in}}{c_{bed}}\cdot\eta_{gg}=v_o\cdot\frac{c_{in}}{c_{bed}}\cdot\eta_{gg}=v_o\cdot\kappa\cdot\eta_{gg}$$

The time an element of mixture stays in the hopper is:

$$\Delta t=\frac{L}{s_o}=\frac{V}{Q}=\frac{L\cdot(H_w-0.5\cdot\Delta H)\cdot W}{Q}=\frac{L\cdot H_a\cdot W}{Q} \qquad \textbf{(10-75)}$$

During the time an element of mixture stays in the hopper, the sediment level is raised by:

$$\Delta H=\frac{dH}{dt}\cdot\Delta t=v_o\cdot\kappa\cdot\eta_{gg}\cdot\frac{L\cdot H_a\cdot W}{Q}=H_a\cdot\kappa\cdot\eta_{gg} \qquad \textbf{(10-76)}$$

The effective or modified hopper load parameter v_{oo}, being the setting velocity of a grain that just reaches the (raised) sediment zone at the end of the hopper is now:

$$\frac{v_{oo}}{s_o}=\frac{H_w-\Delta H}{L}=\frac{H_a-0.5\cdot\Delta H}{L}=\frac{H_a}{L}\cdot\left(1-0.5\cdot\kappa\cdot\eta_{gg}\right) \qquad \textbf{(10-77)}$$

Substituting s_o in this equation gives:

$$v_{oo}=v_o\cdot\left(1-0.5\cdot\kappa\cdot\eta_{gg}\right) \qquad \textbf{(10-78)}$$

Now there are two cases, first the case where the settling velocity of a grain v_s is greater than or equal to the effective hopper load parameter v_{oo}. In this case the effective settling efficiency is 1. This results in an effective hopper load parameter of:

$$v_{oo}=v_o\cdot\left(1-0.5\cdot\kappa\right) \qquad \textbf{(10-79)}$$

The second case is the case where the settling velocity of a grain v_s is smaller than the effective hopper load parameter v_{oo}. In this case the effective settling efficiency will be smaller then 1, according to equation (10-73). This gives the following effective hopper load parameter:

$$v_{oo} = v_o \cdot \left(1 - 0.5 \cdot \kappa \cdot \frac{v_s}{v_{oo}}\right) \qquad \textbf{(10-80)}$$

Since in this equation, the effective hopper load parameter v_{oo} depends on itself, this has to be solved as a quadratic equation, resulting in:

$$v_{oo} = \frac{1}{2} \cdot v_o + \sqrt{\frac{1}{4} \cdot v_o \left(v_o - 2 \cdot \kappa \cdot v_s\right)} \qquad \textbf{(10-81)}$$

With: $v_s = \alpha \cdot v_o$ this gives: $v_{oo} = \frac{1}{2} \cdot v_o + \frac{1}{2} \cdot v_o \cdot \sqrt{1 - 2 \cdot \kappa \cdot \alpha}$

Now the question is, for which value of α is the effective hopper load parameter v_{oo} equal to the settling velocity of the grain v_s. At this value the effective settling efficiency η_{gg} equals 1. The following value for the effective hopper load parameter is valid.

$$v_{oo} = \alpha \cdot v_o \quad \text{this gives: } \alpha = 1 - 0.5 \cdot \kappa = 1 - 0.5 \cdot \frac{c_{in}}{c_{bed}} \text{ or } c_{in} = 2 \cdot c_{bed} \cdot (1 - \alpha) \qquad \textbf{(10-82)}$$

This gives the following conditions for the settling efficiency to be smaller than 1:

$$\alpha < 1 - 0.5 \cdot \frac{c_{in}}{c_{bed}} \text{ or } c_{in} < 2 \cdot c_{bed} \cdot (1 - \alpha) \qquad \textbf{(10-83)}$$

In all other cases the effective settling efficiency equals 1, resulting in the following velocity of the rising sediment level:

$$\frac{dH_w}{dt} = \frac{Q}{L \cdot W} \cdot \kappa = v_o \cdot \kappa \qquad \textbf{(10-84)}$$

Figure 10-32, Figure 10-33, Figure 10-34, Figure 10-35, Figure 10-36 and Figure 10-37 show the resulting modified hopper load parameters and the settling velocities as a function of the relative concentration in a model hopper with **L=11.34 m**, **W=2.04 m**, **H=2 m** and **Q=0.1 m^3/sec** for grain diameters of 0.08, 0.10, 0.12, 0.14, 0.16 and 0.18 mm. It is clear from these figures that the modified hopper load parameter decreases linearly according to equation (10-80), with a settling efficiency of 1 as long as the modified hopper load parameter is smaller than the settling velocity. From the intersection point of the two curves to higher relative concentrations, the modified hopper load parameter increases again. The settling velocity v_s include the effects of hindered settling according to Richardson and Zaki (1954) with an exponent of 4.65 in the examples. The unmodified hopper load parameter is 4.3 mm/sec in these examples.

Figure 10-38 shows the sedimentation velocity dH_w/dt for grain diameters of 0.1, 0.15 and 0.2 mm. As can be seen the grain with a diameter of 0.2 mm gives a straight line, because the effective settling efficiency is equal to 1 for all concentrations. The grain with a diameter of 0.15 mm has a settling efficiency equal to 1 up to a relative concentration of about 0.65. Above this relative concentration the effect of hindered settling causes the sedimentation velocity to decrease. The grain with a diameter of 0.1 mm has a settling efficiency smaller than 1 from the beginning and the sedimentation velocity is determined by the hindered settling effect all the way.

Of course in the interpretation of the examples in this chapter one has to consider that real sand often consists of a graded PSD and not just one diameter. Still the examples show the influence of hindered settling on the modified hopper load parameter and they show that this effect should not be neglected. If a graded PSD is considered, the total settling efficiency should be used to determine the modified hopper load parameter. In 0 an analytical model will be derived to determine the settling efficiency for graded sand.

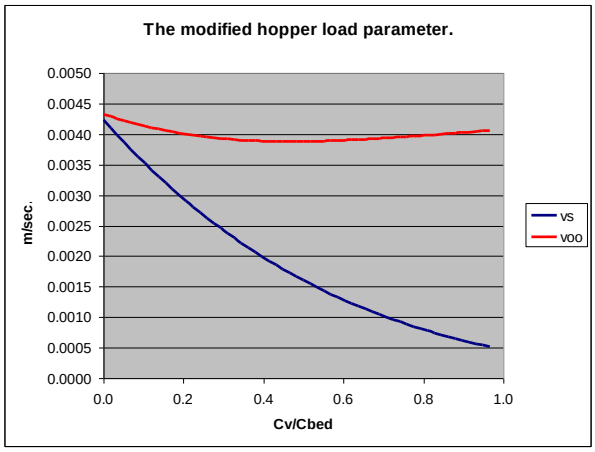

Figure 10-32: d=0.08 mm.

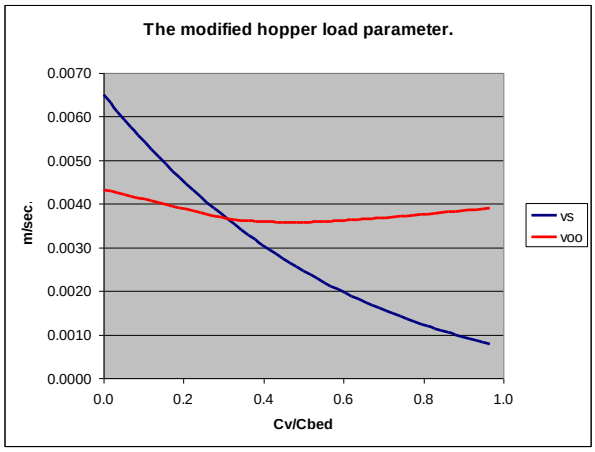

Figure 10-33: d=0.10 mm.

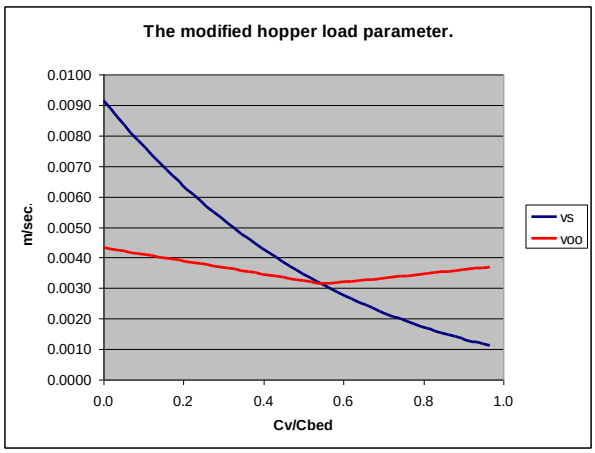

Figure 10-34: d=0.12 mm.

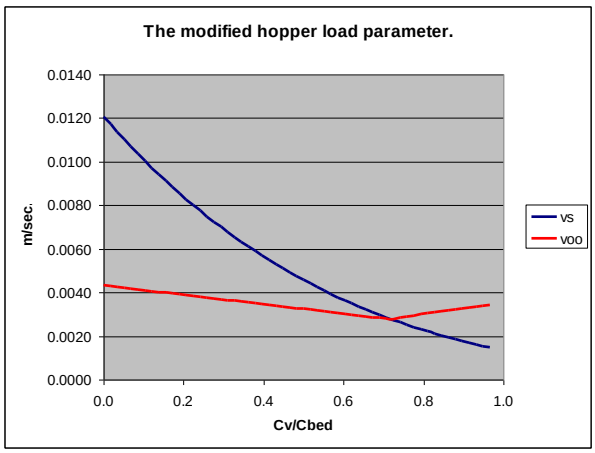

Figure 10-35: d=0.14mm.

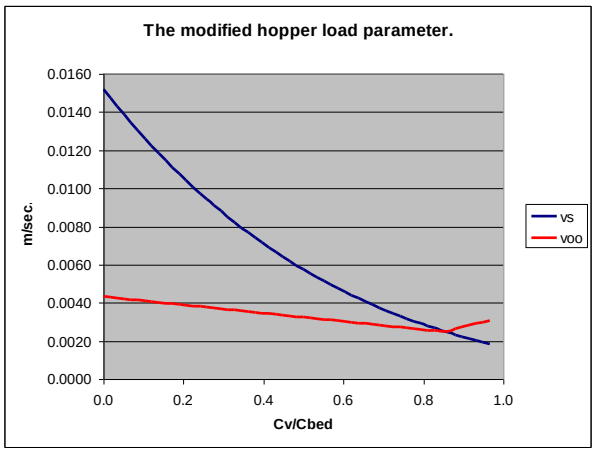

Figure 10-36: d=0.16 mm.

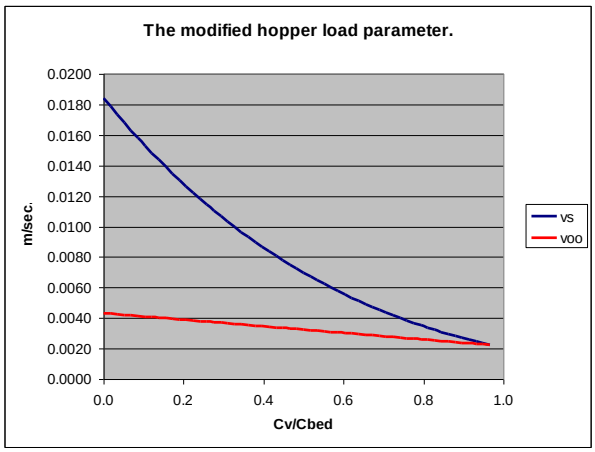

Figure 10-37: d=0.18 mm.

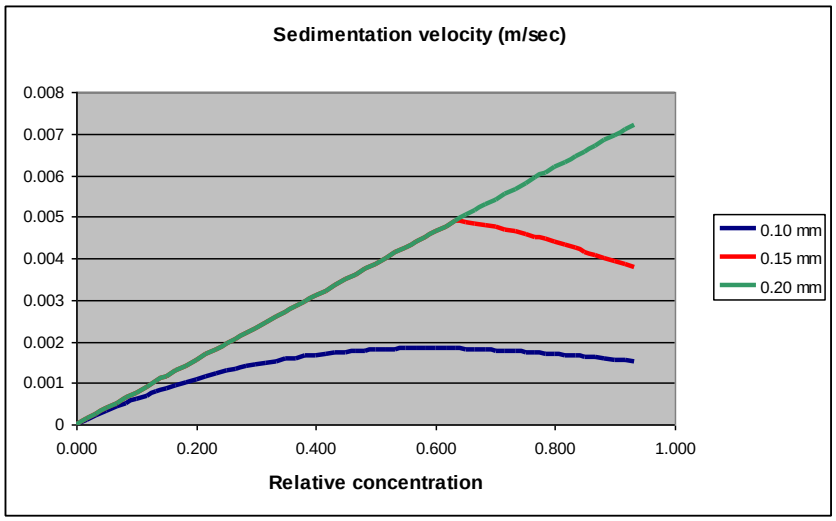

Figure 10-38: The sedimentation velocity dH_w/dt as a function of the relative concentration for 3 grain diameters.

10.10. The Influence of Hindered Settling on the Production.

10.10.1. Theory.

Hindered settling is the main cause for the settling efficiency and the sedimentation velocity to decrease with an increasing relative concentration for small grains as is shown in Figure 10-38. An interesting question is how does this influence de production of a TSHD, based on a full dredging cycle. First we define the production to be the total load in tons, divided by the total cycle time according to:

$$P = \frac{W_{max}}{T_{cycle}} = \frac{W_f + W_l}{T_s + T_f + T_l} \qquad \textbf{(10-85)}$$

To simplify the cycle we divide it in 3 phases:

1. The sum of sailing time, dumping time, etc. T_s.
2. The time to fill the hopper to the overflow level T_f, loading W_f tons.
3. The time to fill the hopper completely after the overflow level has been reached T_l, loading W_l tons.

For this derivation it is assumed that we consider a CVS TSHD and it is assumed that the hopper can be filled completely with sand with a settling efficiency as derived before. The volume of sand loaded during phase 2 and the load and the time required are now:

$$V_f = \frac{c_{in}}{c_{bed}} \cdot V_{max} \text{ thus: } W_f = V_f \cdot \rho_{bed} \text{ and } T_f = \frac{V_{max}}{Q} \qquad \textbf{(10-86)}$$

For the load and the volume during phase 3, now the following equations can be derived, assuming the hopper will be filled with a factor λ:

$$W_l = W_{max} - W_f \text{ and } V_l = \lambda \cdot V_{max} - V_f \text{ and } W_l = V_l \cdot \rho_{bed} \qquad \textbf{(10-87)}$$

The time to load this value can be simplified by assuming a certain average settling efficiency during this phase, being equal to the effective settling efficiency η_{gg} as described earlier:

$$V_l = Q \cdot \frac{c_{in}}{c_{bed}} \cdot \eta_{gg} \cdot T_l \text{ thus: } T_l = \frac{V_l}{Q \cdot \frac{c_{in}}{c_{bed}} \cdot \eta_{gg}} = \frac{V_l}{Q \cdot \kappa \cdot \eta_{gg}} \qquad \textbf{(10-88)}$$

Substituting the equations (10-86), (10-87) and (10-88) in equation (10-85) gives the following production:

$$P = \frac{\lambda \cdot V_{max} \cdot \rho_{bed}}{T_s + \frac{V_{max}}{Q} \cdot \left\{ \frac{\lambda - \kappa \cdot (1 - \eta_{gg})}{\kappa \cdot \eta_{gg}} \right\}} \qquad \textbf{(10-89)}$$

The calculations have been carried out for a 2500 m^3 hopper with a mixture flow Q of 3.33 m^3/sec and a total time T_s of 100 minutes. The settling efficiencies as derived with equation (10-78), including hindered settling, and as used in Figure 10-38, are also used to create Figure 10-39, Figure 10-40 and Figure 10-41.The A-curves are calculated with equation (10-89), while the B-curves are calculated with software, using a graded sand.
The figures clearly show a continuous increase of the production for the 0.1, 0.15 and 0.2 mm sand. The shape of the curve is determined by the mixture flow and the total delay time T_s in the denominator of equation (10-89). Of course the shape of the curves depends strongly on the TSHD chosen, the total delay time and the mixture flow and should be determined with the right values for the different parameters involved.
Figure 10-39, Figure 10-40 and Figure 10-41 however prove that a decreasing sedimentation velocity as is shown in Figure 10-38, does not imply a decreasing final production when the effects of hindered settling are taken into account with an increasing relative concentration. The main reason for this is the fact that during the filling phase of the hopper up to overflow level, there are no losses. The figures show a clear increase in production at the smaller relative concentrations, while the productions are almost equal for the high productions. For example, at a relative concentration of 0.3, the 0.1 mm sand has a production of about 0.5 ton/sec, the 0.15 mm sand a production of about 0.55 ton/sec and the 0.2 mm sand a production of 0.56 ton/sec. Coarser sands will not have a much higher

production since the main part of the PSD is above the hopper load parameter. Sands finer than the 0.1 mm sand will have a smaller production due to the increased overflow losses.

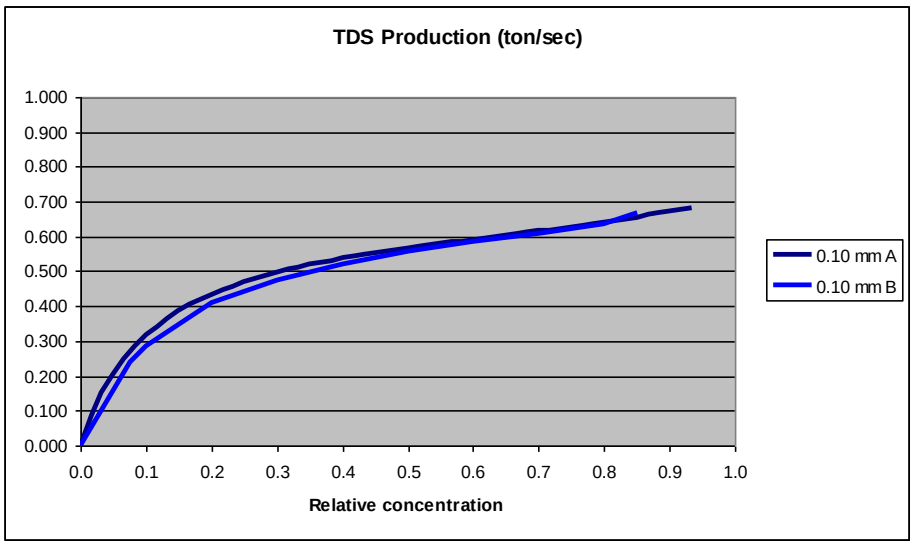

Figure 10-39: The production as a function of the relative concentration for an 0.10 mm grain diameter.

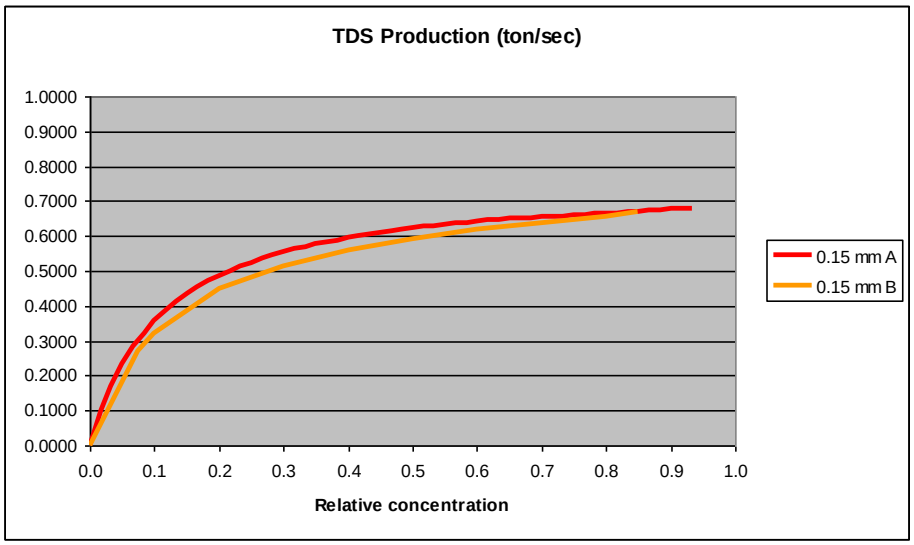

Figure 10-40: The production as a function of the relative concentration for an 0.15 mm grain diameter.

10.10.2. Implementation.

The current simulation model is based on the theory as published in 3 publications and applied in some other publications. The basic theory was published in Terra et Aqua (Miedema (2008A)). Some special considerations and the one equation analytical model were published in the Journal of Dredging Engineering (Miedema (2009A)). Now how does this theory relate to reality? Figure 10-42 shows a measurement of the dredging cycle of a small TSHD using the Constant Volume System. In this figure the total load in the hopper, the total volume of the load in the hopper and the TDS in the hopper are shown, but many other signals like the density and the flow velocity were also available.

The measurements contain many turns and some other effects. After dumping, water is flowing back into the hopper, resulting in a partially filled hopper at the moment the real dredging starts. Due to a time delay between the registration of the density signal and the flow signal, the TDS (which is a derived signal) may become negative momentary. Due to some trim of the TSHD during the loading, it looks like the hopper volume is slightly increasing.
After the loading is stopped, the layer of water above the overflow has to flow away, resulting in a decrease of the total load and a decrease of the total volume. The measured decrease is bigger than would be expected. This is

most probably caused by the Bernouilli effect when the TSHD starts sailing to the dump site. A higher sailing speed results in a smaller pressure measured by the transducers, resulting in an apparent decrease of the total load. When the TSHD approaches the dump site and reduces the sailing speed, the apparent load increases again.

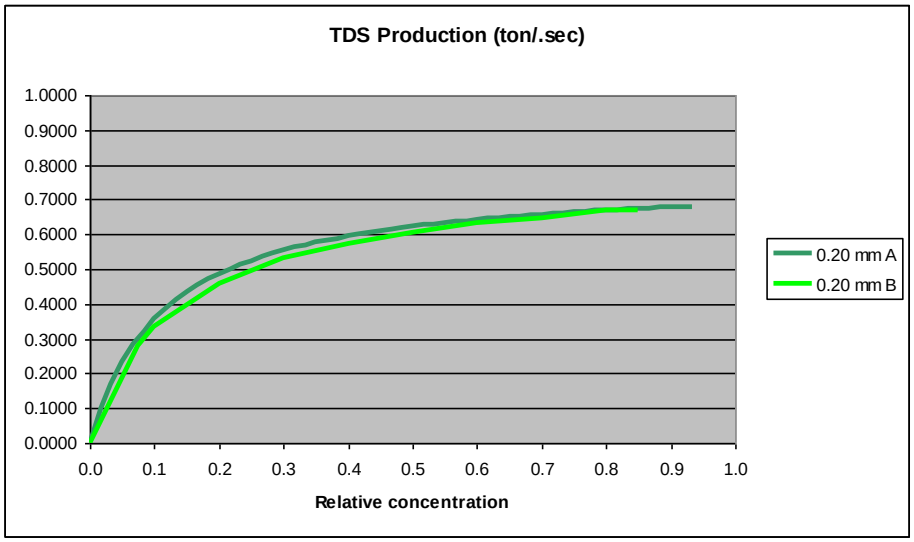

Figure 10-41: The production as a function of the relative concentration for an 0.20 mm grain diameter.

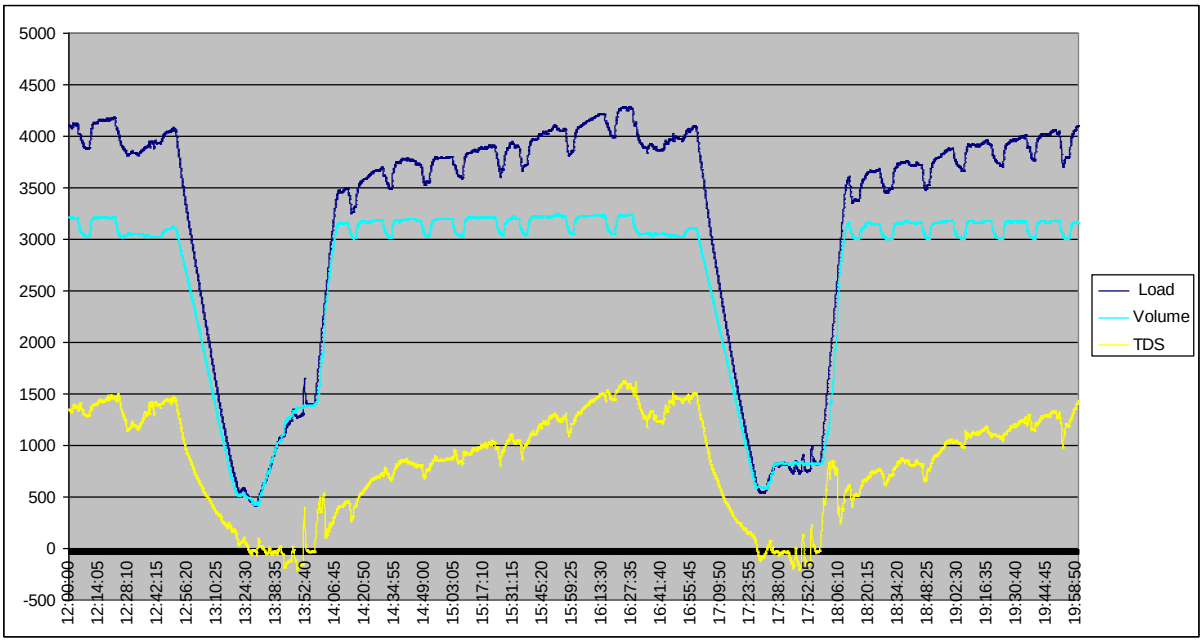

Figure 10-42: An example of a loading cycle of a TSHD with many turns.

The measurements were corrected for the effects of trim and time delays and compared with a simulation. To carry out the simulation it was important to reconstruct the input of the TSHD as accurately as possible. The input consisted of the density and flow signals. Figure 10-43 shows the corrected measurements (M) from Figure 10-42 and the results of the simulation (C). The first two lines to look at are the Total in (M) and (C), which show the total TDS going into the TSHD. All other signals are the result of what enters the hopper. It is clear that the measured Total in (M) is almost equal to the simulated Total in (C), although there are some small momentary deviations.

The other signals in Figure 10-43 are, the Total load (M) & (C), the Volume (M) & (C), the TDS (M) & (C) & buffered and finally the Overflow TDS (M) & (C) & buffered. From the figure it is clear that the simulations match the measurements very well and also that the buffered TDS and the buffered Overflow TDS match the measurements better than the un-buffered signals. It should be mentioned that the loading is stopped before erosion becomes important, so erosion behavior is not verified in these measurements. The behavior of flow over a weir, which occurs each turn is simulated very well, while the cumulative overflow losses and thus also the TDS are simulated well by applying the time effect or buffer effect.

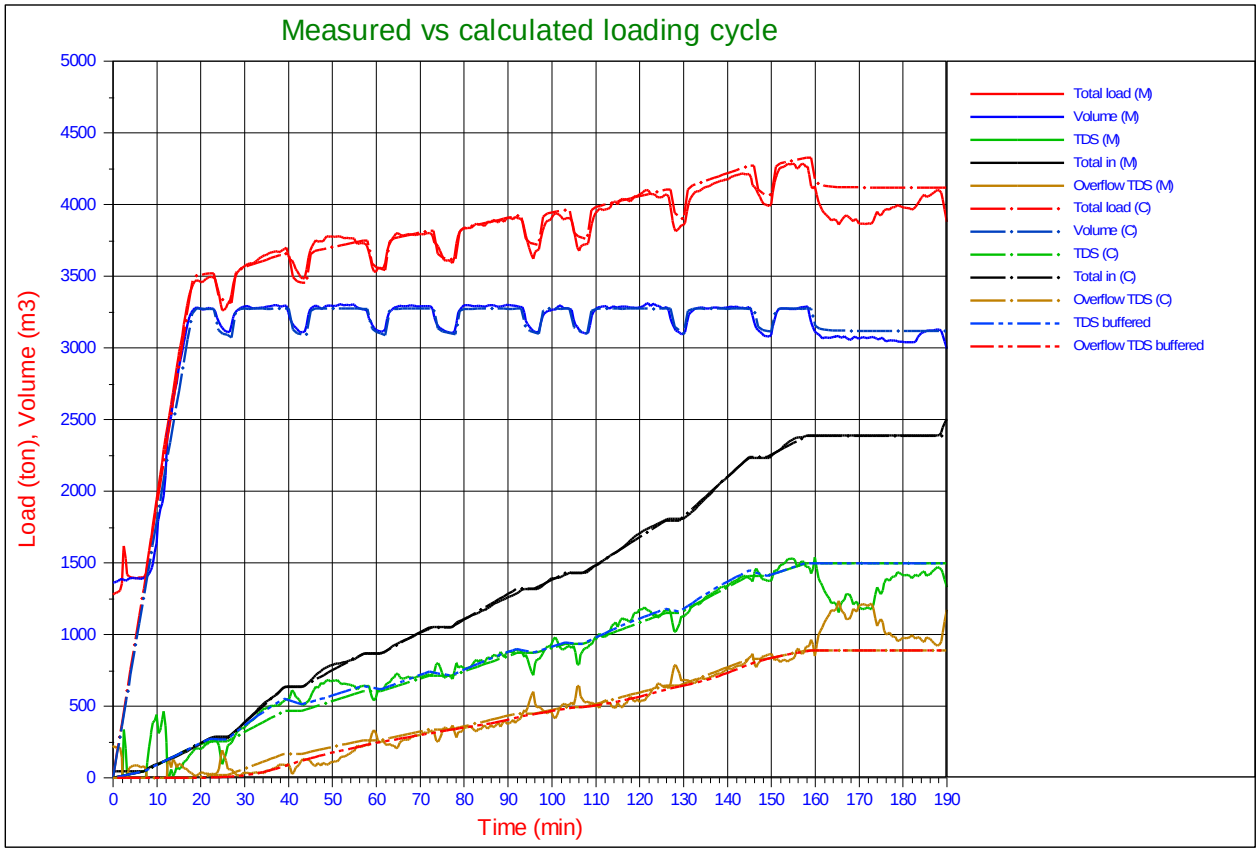

Figure 10-43: Simulation & Measurement.

Figure 10-44 shows the cumulative overflow losses and efficiency as a function of the mixture concentration calculated with the one equation analytical model for 3 cases. The hopper was filled with water for 100% when the loading started, the hopper was filled for 50% and the hopper was empty, so 0% water. The cumulative efficiency, being the efficiency of one full cycle, continues to decrease with increasing concentration, due to the effect of hindered settling for the first case where we start with a 100% filled hopper. The sand used was an 0.1 mm sand, meaning that the sedimentation velocity is also decreasing with increasing concentration. When the hopper is filled for 50% or 0%, the efficiency decreases first, but increases later at the higher mixture concentrations. The reason is that it is assumed that the efficiency is 100% until the overflow level is reached and the influence of this becomes bigger at the higher concentrations.

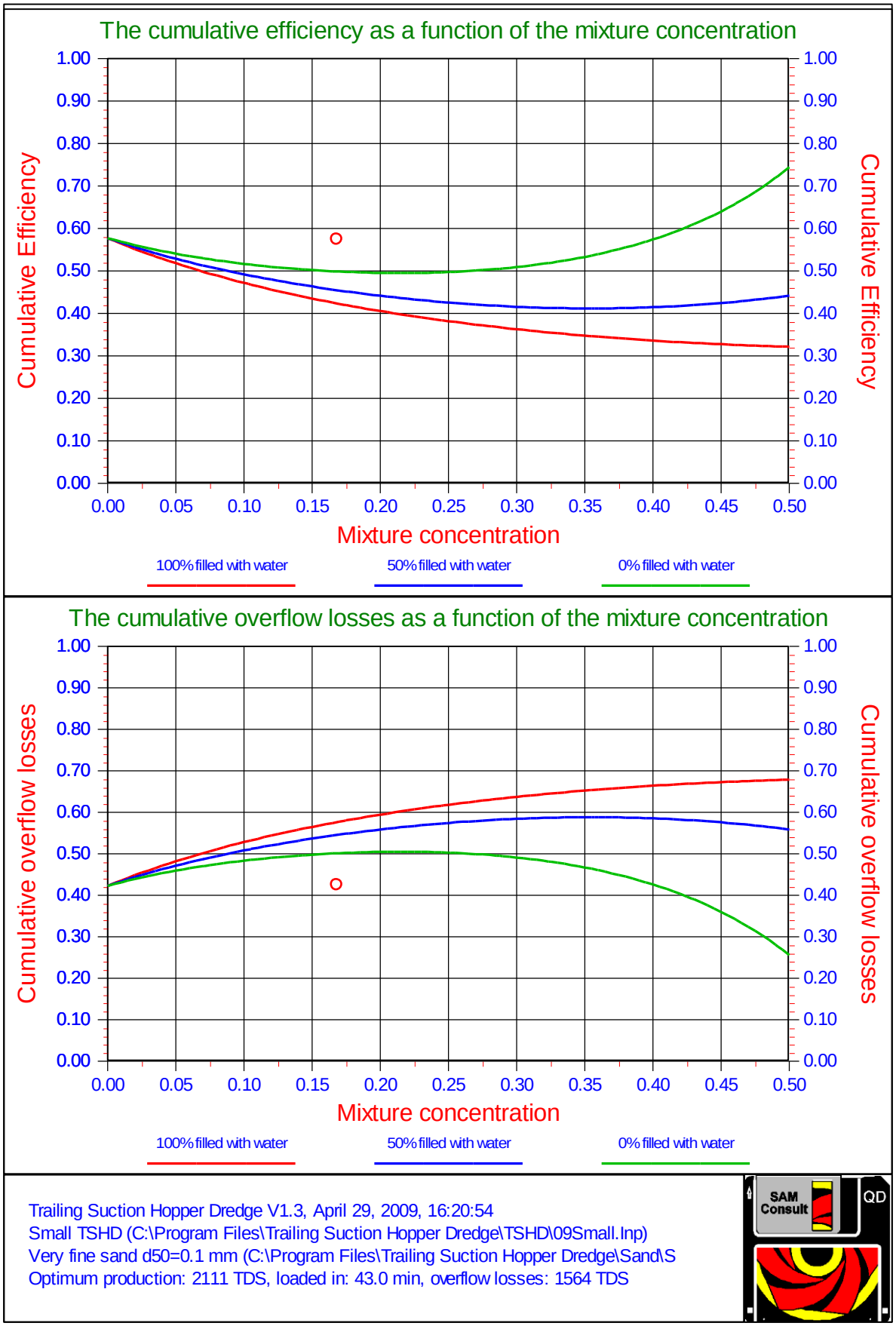

Figure 10-44: The overflow losses compared with an analytical model for the Small TSHD.

10.11. Analytical Considerations.

10.11.1. The Bed Rise or Sedimentation Velocity.

Suppose a vertical element of the hopper with length and width equal to 1m consists of 3 layers. At the top a layer of water with a concentration of particles equal to zero, in the middle a layer of mixture with an average concentration c_b and at the bottom a layer of sediment with a concentration c_{bed}. All the particles in the mixture layer have a vertical settling velocity v_c (including the hindered settling effect), while the sediment is moving up with a velocity v_{sed}, the so-called sedimentation or bed rise velocity because of the sedimentation of the particles. Now the question is, what is the value of this sedimentation velocity if c_b, c_{bed} and v_c are known and constant during a certain time interval.

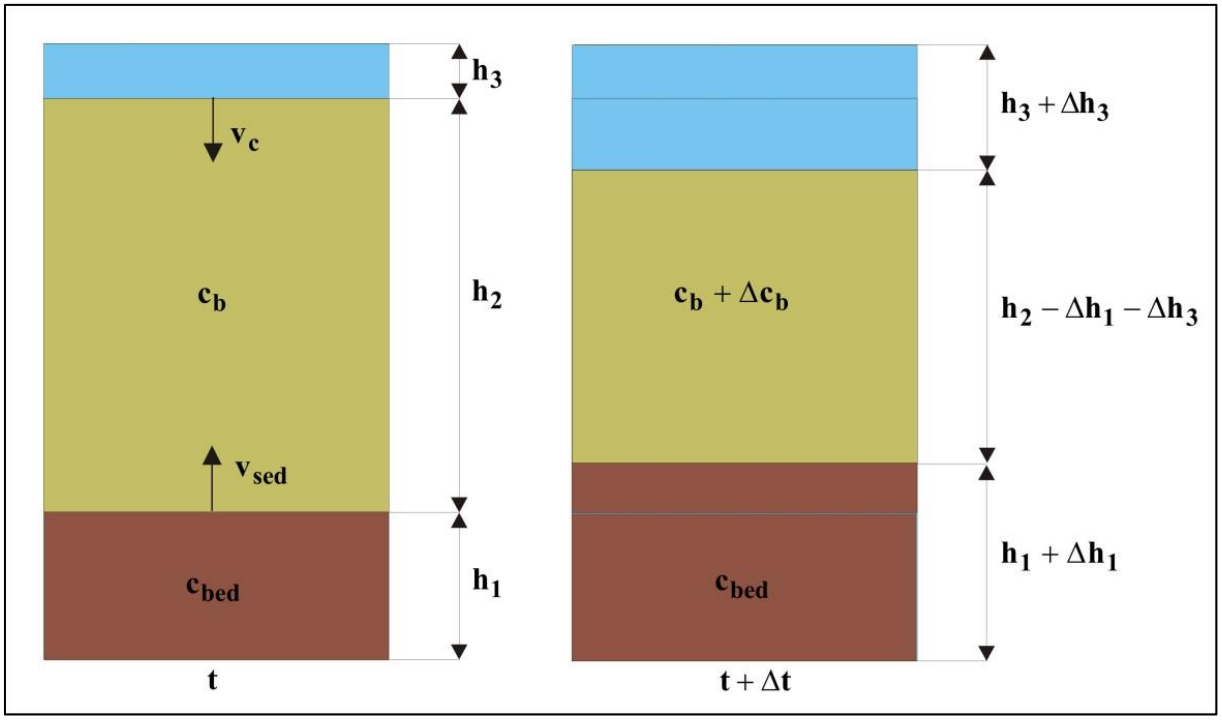

Figure 10-45: A segment of a hopper at 2 subsequent time steps.

Figure 10-45 shows the hopper at 2 subsequent time steps. During one time step, the mixture moves down with the settling velocity v_c, causing the sediment to rise with the bed rise velocity v_{sed}. There is no mass added during the time step, so the sum of the mixture mass and the sediment mass remains constant. At time **t** (left figure) the total mass in TDS in the hopper is:

$$TDS = h_1 \cdot c_{bed} + h_2 \cdot c_b \qquad (10\text{-}90)$$

A time step Δt later (right figure), if the total mass in TDS in the hopper is assumed to be constant:

$$TDS = (h_1 + \Delta h_1) \cdot c_{bed} + (h_2 - \Delta h_1 - \Delta h_3) \cdot (c_b + \Delta c_b) \qquad (10\text{-}91)$$

This gives:

$$\Delta h_1 \cdot c_{bed} + (-\Delta h_1 - \Delta h_3) \cdot c_b + (h_2 - \Delta h_1 - \Delta h_3) \cdot \Delta c_b = 0 \qquad (10\text{-}92)$$

Neglecting the double derivatives this gives:

$$\Delta h_1 \cdot (c_{bed} - c_b) = \Delta h_3 \cdot c_b - h_2 \cdot \Delta c_b \qquad (10\text{-}93)$$

If the particles in the mixture layer all move downwards with the same settling velocity v_c, then the increment of the concentration Δc_b in the second term on the right hand side equals zero, resulting in the following relation for the sedimentation or bed rise velocity:

$$v_{sed} = v_c \cdot \frac{c_b}{c_{bed} - c_b} \qquad \text{with :} \quad v_c = v_s \cdot (1 - C_v)^{\beta} \tag{10-94}$$

$$\text{With :} \quad \Delta h_1 = v_{sed} \cdot \Delta t \qquad \Delta h_3 = v_c \cdot \Delta t \tag{10-95}$$

Van Rhee (2002C) already derived this equation based on a finite element near the bed surface. If this equation is derived for a small element near the surface of the sediment, the concentration near the bed (the near bed concentration) does not have to be equal to the average concentration as used in the derivation above. Other researchers, Ooijens et al. (2001) and Braaksma et al. (2007), used this equation for determining the global overflow losses and just like van Rhee use the concentration of the dredged mixture c_{in} as a first approximation for the near bed concentration c_b. This may lead however to results that are physically impossible.

10.11.2. The Dimensionless Overflow Rate.

Based on the conservation of mass it can be proven that in general the near bed concentration c_b and the mixture concentration c_{in} are not equal.

If the increase of the sand mass in the sediment (bed) is considered as:

$$Q_{m_{bed}} = v_{sed} \cdot c_{bed} \cdot W \cdot L \tag{10-96}$$

Then the total sand mass in the hopper at the end of the loading process, assuming a constant sedimentation velocity, after a time T equals to:

$$TDS_{bed} = Q_{m_{bed}} \cdot T = v_{sed} \cdot c_{bed} \cdot W \cdot L \cdot T \tag{10-97}$$

The total mass of TDS that has entered the hopper during this time equals to:

$$TDS_{in} = Q_{m_{in}} \cdot T = Q_{in} \cdot c_{in} \cdot T \tag{10-98}$$

The cumulative overflow losses are equal to the amount of mass that entered the hopper, minus the amount that has settled, divided by the amount that has entered the hopper, according to:

$$ov_{cum} = 1 - \eta_{cum} = \frac{TDS_{in} - TDS_{bed}}{TDS_{in}} = \frac{Q_{in} \cdot c_{in} \cdot T - v_{sed} \cdot c_{bed} \cdot W \cdot L \cdot T}{Q_{in} \cdot c_{in} \cdot T} = 1 - \frac{W \cdot L}{Q_{in}} \cdot v_{sed} \cdot \frac{c_{bed}}{c_{in}} \tag{10-99}$$

Using the unmodified hopper load parameter $v_o = Q_{in}/W \cdot L$ and equation (10-94) for the sedimentation velocity, this gives:

$$ov_{cum} = 1 - \eta_{cum} = 1 - \frac{W \cdot L}{Q_{in}} \cdot v_c \frac{c_b}{c_{bed} - c_b} \cdot \frac{c_{bed}}{c_{in}} = 1 - \frac{v_c}{v_o} \cdot \frac{c_b}{c_{in}} \cdot \frac{c_{bed}}{c_{bed} - c_b} \tag{10-100}$$

Ooijens et al. (2001) uses this equation for determining the cumulative overflow losses. Van Rhee (2002C) defined a dimensionless overflow rate S^*, based on the sedimentation velocity according to equation (10-94):

$$S^* = \frac{v_o}{v_c} \cdot \frac{c_{in}}{c_b} \cdot \frac{c_{bed} - c_b}{c_{bed}} = H^* \cdot \frac{c_{in}}{c_b} \cdot \frac{c_{bed} - c_b}{c_{bed}} \quad \text{and} \quad S'^* = H^* \cdot \frac{c_{bed} - c_{in}}{c_{bed}} \tag{10-101}$$

The second equation for **S'*** is valid if $c_b=c_{in}$. This however has no physical meaning. Substituting equation (10-101) in equation (10-100) gives a relation between the cumulative overflow losses ov_{cum} and the dimensionless overflow rate **S***:

$$ov_{cum} = 1 - \frac{1}{S^*} \qquad \text{or} \qquad \eta_{cum} = \frac{1}{S^*} \tag{10-102}$$

Since the overall settling efficiency can never be greater than 1, this means that **S*** should always be greater or equal to 1. Besides, the name dimensionless overflow rate does not seem to be appropriate, because **S*** equals to the reciprocal of the cumulative settling efficiency and not to the cumulative overflow losses.

10.11.3. The Near Bed Concentration.

Both van Rhee (2002C) and Ooijens et al. (2001) state that making the near bed concentration c_b equal to the mixture concentration c_{in}, is a good first approximation. For course particles with a settling velocity v_c higher than the unmodified hopper load parameter v_o, equation (10-100) leads to negative overflow losses and equation (10-101) will gives an **S*** smaller than 1. This leads to the conclusion that for an overall approach, the near bed concentration should not be chosen equal to the mixture concentration. From equation (10-100), the following equation can be derived for the overall settling efficiency:

$$\eta_{cum} = \frac{v_c}{v_o} \cdot \frac{c_b}{c_{in}} \cdot \frac{c_{bed}}{c_{bed} - c_b} \tag{10-103}$$

From this equation, an equation for the near bed concentration c_b can be derived:

$$c_b = \frac{\eta_{cum} \cdot c_{bed}}{\left(\eta_{cum} + \frac{v_c}{v_o} \cdot \frac{c_{bed}}{c_{in}}\right)} = \frac{\eta_{cum} \cdot c_{bed} \cdot c_{in}}{\left(\eta_{cum} \cdot c_{in} + \frac{v_c}{v_o} \cdot c_{bed}\right)} = c_{bed} \cdot \frac{\eta_{cum} \cdot \frac{c_{in}}{c_{bed}}}{\left(\eta_{cum} \cdot \frac{c_{in}}{c_{bed}} + \frac{v_c}{v_o}\right)} \tag{10-104}$$

Thus:

$$\frac{c_b}{c_{bed}} = \frac{\eta_{cum} \cdot \frac{c_{in}}{c_{bed}}}{\left(\eta_{cum} \cdot \frac{c_{in}}{c_{bed}} + \frac{v_c}{v_o}\right)} = \frac{\eta_{cum} \cdot \kappa}{\left(\eta_{cum} \cdot \kappa + \frac{v_c}{v_o}\right)} \tag{10-105}$$

$$\textbf{With :} \qquad \kappa = \frac{c_{in}}{c_{bed}}$$

Now two cases can be considered:

1. There are hardly any overflow losses, which means that the particle settling velocity is much higher then the hopper load parameter.
2. The particle settling velocity is smaller than the hopper load parameter.

In both cases it is assumed that the loading process starts with a hopper full of water, otherwise the filling of the hopper up to overflow level is part of the cumulative settling efficiency, while there are no overflow losses during this phase, so a to high settling efficiency is found. If the loading process starts with an empty hopper or a partially filled hopper, this part of the filling process should not be considered when determining the cumulative settling efficiency, for the purpose of determining the correct near bed concentration.

Case 1: $\eta=1$

$$\frac{c_b}{c_{bed}} = \frac{\kappa}{\left(\kappa + \frac{v_c}{v_o}\right)} \tag{10-106}$$

Since in this case the velocity ratio v_c/v_o is always greater than 1, the near bed concentration c_b will always be smaller than the mixture concentration c_{in}. The greater the settling velocity of the particle, the smaller the near bed concentration. In other words, the ratio c_b/c_{bed} will always be smaller than κ the ratio c_{in}/c_{bed}. Physically this means that the particles settle faster than they are supplied by the inflow of mixture.

Case 2: $\eta_p = \frac{v_c}{v_o} < 1$

$$\frac{c_b}{c_{bed}} = \frac{\eta_{cum} \cdot \kappa}{\left(\eta_{cum} \cdot \kappa + \eta_p\right)} \qquad \textbf{(10-107)}$$

If the PSD is very narrow graded, the cumulative settling efficiency η_{cum} is equal to the settling efficiency of the particle considered η_p leading to the following equation:

$$\frac{c_b}{c_{bed}} = \frac{\kappa}{(\kappa + 1)} \qquad \textbf{(10-108)}$$

The near bed concentration c_b in this case is always smaller than the mixture concentration c_{in}. Physically this is caused by the overflow losses.

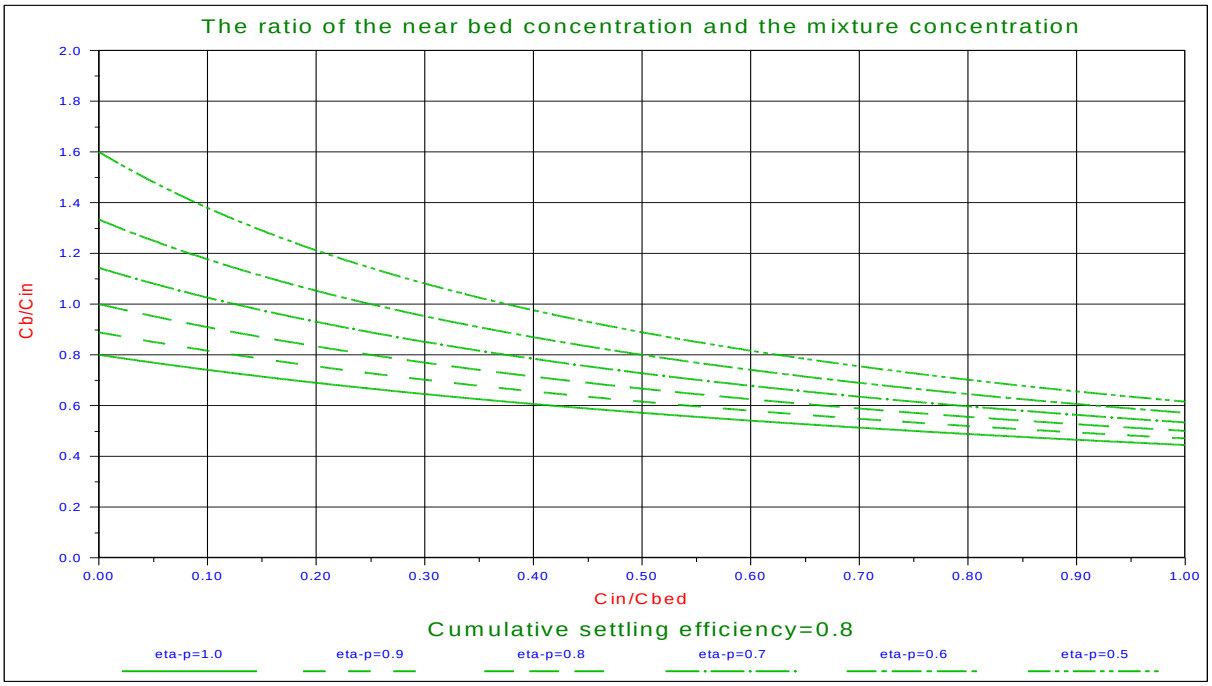

Figure 10-46: The ratio between c_b and c_{in}.

If the PSD is not narrow graded, the cumulative settling efficiency η_{cum} can be smaller of greater than the particle settling efficiency η_p, where it is assumed that the particle efficiency for the d_{50} is chosen.
If the PSD is steep for the grains smaller than the d_{50} and well graded for the grains larger than the d_{50}, the cumulative settling efficiency η_{cum} will be greater than the particle settling efficiency η_p. Figure 10-46 shows that in this case the near bed concentration c_b is greater than the mixture concentration c_{in} for small mixture concentrations and smaller than the mixture concentration for high mixture concentrations. Physically this is caused by the fact that the larger particles dominate the settling efficiency. For example, the cumulative settling efficiency in Figure 10-46 is chosen 0.8. For a particle settling efficiency η_p of 0.6, the ratio λ is greater than 1 for a value of κ smaller than 0.25. The ratio λ between the near bed concentration c_b and the mixture concentration c_{in} is:

$$\lambda = \frac{c_b}{c_{bed} \cdot \kappa} = \frac{c_b}{c_{in}} = \frac{\eta_{cum}}{\left(\eta_{cum} \cdot \kappa + \eta_p\right)} \qquad \textbf{(10-109)}$$

If the PSD is steep for the grains larger than the d_{50} and well graded for the grains smaller than the d_{50}, the cumulative settling efficiency η_{cum} will be smaller than the particle settling efficiency η_p for the d_{50} resulting in a ratio λ that is always smaller then 1, so the near bed concentration c_b is always smaller than the mixture concentration c_{in}. Physically this is caused by the fact that the smaller particles dominate the cumulative settling efficiency.

10.11.4. The Overall Bed Rise or Sedimentation Velocity.

Based on the conservation of mass it has been proven that the near bed concentration c_b should not be chosen equal to the mixture concentration. In fact the near bed concentration c_b can be smaller or greater than the mixture concentration c_{in}, depending on the PSD of the sand. The loading process considered, should start at the moment the overflow level is reached, otherwise a to high cumulative settling efficiency is chosen. If equation (10-105) is substituted in equation (10-94), the following equation for the sedimentation or bed rise velocity is found:

$$v_{sed} = v_c \cdot \frac{c_b}{c_{bed} - c_b} = v_c \cdot \frac{c_{in} \cdot \dfrac{\eta_{cum}}{\eta_{cum} \cdot \kappa + \dfrac{v_c}{v_o}}}{c_{bed} - c_{in} \cdot \dfrac{\eta_{cum}}{\eta_{cum} \cdot \kappa + \dfrac{v_c}{v_o}}} = v_o \cdot \eta_{cum} \cdot \kappa \qquad \textbf{(10-110)}$$

In other words:

$$L \cdot W \cdot v_{sed} \cdot c_{bed} = Q \cdot c_{in} \cdot \eta_{cum}$$

$$\text{With:} \quad v_o = \frac{Q}{L \cdot W} \qquad \textbf{(10-111)}$$

$$\kappa = \frac{c_{in}}{c_{bed}}$$

From the point of view of conservation of mass this is logic, so the circle is round again. The derivation is for the whole loading cycle, from the moment the overflow level is reached to the moment the hopper is economically full. Some aspects of the loading process however are not taken into account:

1. The filling of the hopper up to the overflow level. Since it is assumed that there are no overflow losses during this phase, this will increase the cumulative settling efficiency and thus the bed rise velocity. This also gives a higher near bed concentration, which is valid for the whole loading cycle, but not realistic for the loading after the overflow level has been reached.
2. The occurrence of scour at the end of the loading cycle. This will decrease the average sedimentation velocity resulting in a lower cumulative settling efficiency. The calculated near bed concentration will also decrease, which is not representative for the main part of the loading cycle. Fortunately the scour does not occur very long if the loading stops at the most economical point, so this influence is not very important.

Equation (10-102) implies that the factor **S*** should always be greater than 1. Van Rhee ((2002C), page 72 and page 205) however found values for **S*** between 0.5 and 1 with the approximation that the near bed concentration c_b equals the mixture concentration c_{in}. For this case he found the following empirical relation between the cumulative overflow losses and the dimensionless overflow rate:

$$ov_{cum} = 0.39 \cdot (S'^{*} - 0.43) \qquad \textbf{(10-112)}$$

To explain this, the example from chapter 8 of van Rhee (2002C) will be reproduced. Van Rhee used the TSHD Cornelia, a hopper with **L=52m**, **W=11.5m**, **H=8.36m**, **Q=5.75m^3/sec**, c_{bed}**=0.54**, c_{in}**=0.15**, η_{cum}**=0.92** and d_{50}**=0.235mm**. This gives v_c**=14.8mm/sec** including the hindered settling effect, v_o**=9.6mm/sec**, κ**=0.278**, **H*=0.648**, **S*=0.47** and ov_{cum}**=0.015** if c_b**=**c_{in}.

From equation (10-105) it can be seen however that $c_b=0.513 \cdot c_{in}$. This gives **S*=1.09** according to equation (10-101) and (10-102), which in fact is a self-fulfilling prophecy and $ov_{cum}=0.259$ according to equation (10-140) using **S*=1.09**. The real cumulative overflow losses were 0.08, so the empirical equation (10-140) for the overflow losses is not very accurate. In fact using the approximation of $c_b=c_{in}$ does not match the conservation of mass principle and should only be applied as a first approximation.

Equation (10-140) has been derived by van Rhee ((2002C) , page 72) based on a set of model tests, see Table 10-2. Recalculating the values for c_b with equation (10-105) and **S*** with equation (10-101) gives a new relation between the cumulative overflow losses ov_{cum} and **S***. This gives a 100% correlation matching equation (10-101), but this is a self-fulfilling prophecy, since the near bed concentration has been derived from the cumulative overflow losses. Table 10-2, Figure 10-47 and Figure 10-48 show the original data from van Rhee (2002C), while Figure 10-49 shows the results of the recalculation.

The original equation (10-94) for the bed rise velocity however is still valid for a small element of sediment and mixture at a certain moment of the loading process if the correct near bed concentration c_b is used. For the overall approach equation (10-110) should be used to calculate the average bed rise velocity.

Table 10-2: The model tests as carried out by van Rhee (2002C).

Test	ρ_{in}	c_{in}	Q	v_o	d_{50}	ov_{cum}	H*	S'* ($c_b=c_{in}$)	c_b	S* ($c_b<>c_{in}$)
1	1310	0.18	0.099	2.75	0.140	0.01	0.75	0.50	0.105	1.01
2	1210	0.11	0.139	3.86	0.146	0.02	0.70	0.55	0.068	1.02
4	1460	0.27	0.100	2.78	0.147	0.04	1.25	0.62	0.201	1.04
5	1350	0.20	0.100	2.78	0.102	0.25	1.60	1.00	0.165	1.33
6	1420	0.24	0.137	3.81	0.107	0.42	2.60	1.43	0.218	1.72
7	1100	0.05	0.140	3.89	0.089	0.23	1.10	1.00	0.037	1.30
8	1500	0.29	0.075	2.08	0.103	0.25	2.20	1.02	0.255	1.33
9	1260	0.14	0.138	3.83	0.096	0.27	1.62	1.18	0.130	1.37
10	1310	0.18	0.101	2.81	0.105	0.18	1.30	0.88	0.139	1.22
11	1290	0.16	0.137	3.81	0.106	0.21	1.60	1.12	0.149	1.27
12	1480	0.28	0.101	2.81	0.105	0.32	2.55	1.22	0.255	1.47
13	1480	0.28	0.102	2.83	0.104	0.29	2.60	1.24	0.264	1.41
15	1370	0.21	0.138	3.83	0.101	0.35	2.35	1.43	0.203	1.54
16	1130	0.06	0.141	3.92	0.103	0.23	1.00	0.88	0.046	1.30
17	1290	0.16	0.142	3.94	0.104	0.29	1.75	1.22	0.148	1.40
18	1280	0.16	0.140	3.89	0.111	0.28	1.48	1.05	0.128	1.38
19	1180	0.10	0.100	2.78	0.100	0.11	0.85	0.70	0.063	1.12

Ooijens et al. (2001) also published data of research carried out to validate the model of the sedimentation velocity. He used equation (10-94) with $c_b=c_{in}$. Figure 10-50 shows the measurements and prediction of Ooijens et al. (2001) and the prediction using the near bed concentration according to equation (10-105). The cumulative efficiency η_{cum}, required in equation (10-105) has been calculated using the modified Camp model of Miedema and Vlasblom (1996). It is obvious that using the near bed concentration according to equation (10-105) results in a better match with the measured data. Ooijens et al. (2001) used a hopper with **L=11.34m**, **W=2.0m**, **H=1.4-2.4m**, **Q=0.1m^3/sec**, d_{50}**=0.1mm** and densities up to 1.6 ton/m^3. For the calculations a bed concentration c_{bed} of 0.55 has been used.

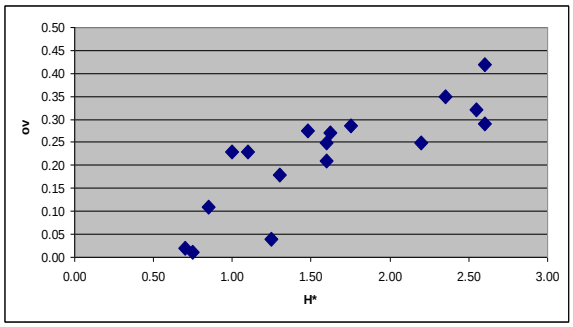

Figure 10-47: Overflow losses vs H*.

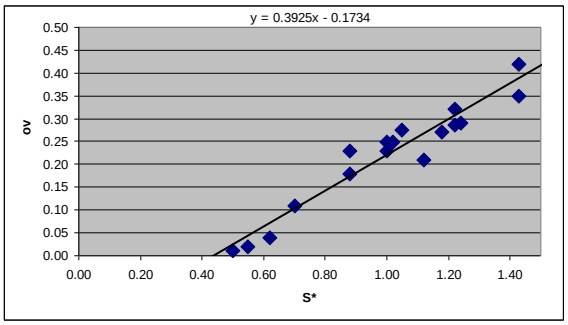

Figure 10-48: Overflow losses vs S'*.

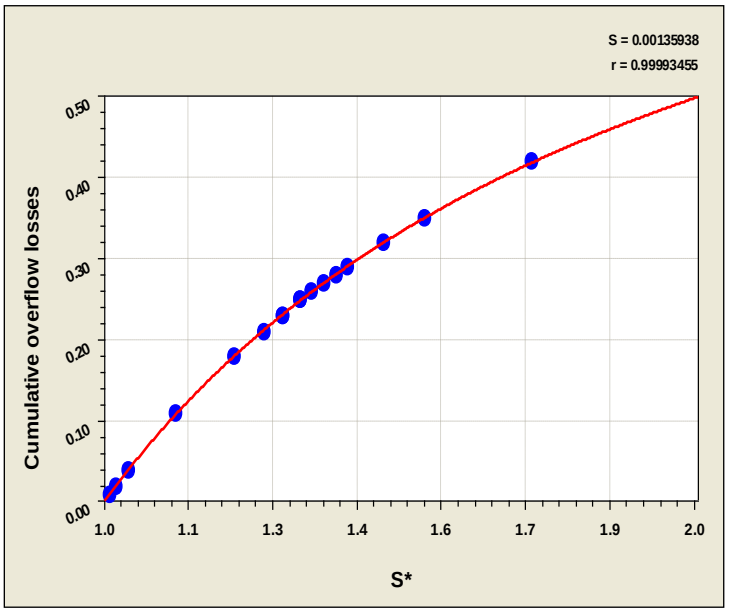

Figure 10-49: The cumulative overflow losses vs S*, c_b re-calculated.

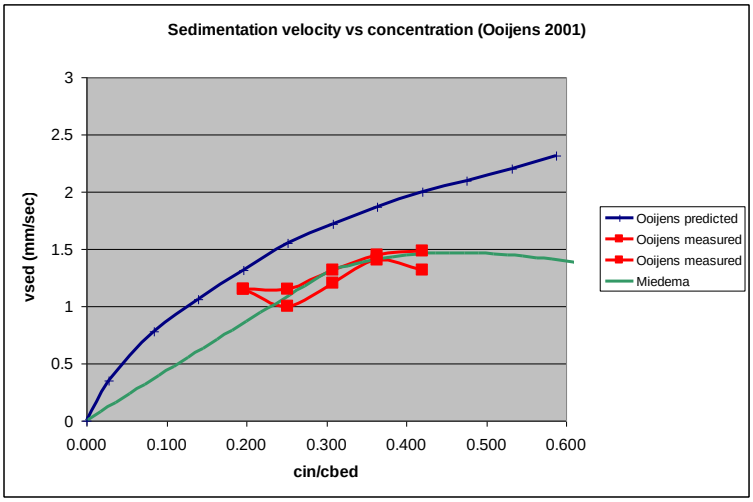

Figure 10-50: The sedimentation velocity measured by Ooijens et al. (2001).

10.11.5. The Concentrations during the Loading Cycle.

Equation (10-105) gives the average near bed concentration, averaged during the total loading process. In fact the concentration calculated with equation (10-105) equals the average mixture concentration above the bed. The momentary near bed concentration however may differ from the average. If a hopper with a height **H** and a sediment level **h** is considered, the following equation can be derived based on the conservation of mass principle, starting with a hopper full of water at t=0, and assuming a uniform concentration distribution with concentration $c_b(t)$ above the sediment level and a concentration c_{bed} in the sediment.

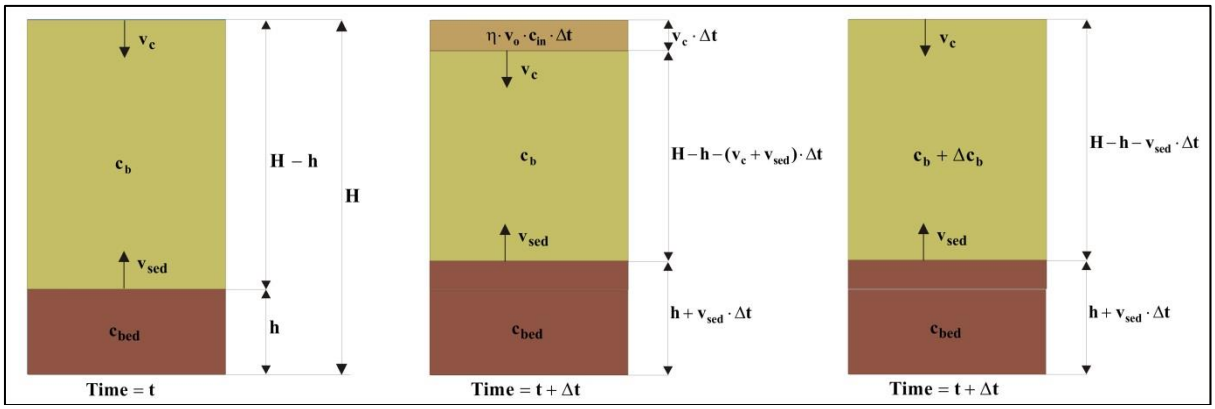

Figure 10-51: The concentrations during the loading cycle.

Further assuming a hopper with a width and a length of 1 m, the total mass TDS in the hopper at any moment of time equals the amount of TDS that has entered the hopper and stayed in the hopper during this time, assuming a constant settling efficiency **η**:

$$h \cdot c_{bed} + (H-h) \cdot c_b = \eta \cdot v_o \cdot c_{in} \cdot t \qquad \textbf{(10-113)}$$

The left hand side shows the amount of mass in the sediment ($h \cdot c_{bed}$) and above the sediment ($(H-h) \cdot c_b$), while the right hand side shows the amount of mass that has entered the hopper ($\eta \cdot v_o \cdot c_{in} \cdot t$) at a time **t** after the loading has started. This can be rewritten as:

$$h \cdot (c_{bed} - c_b) + H \cdot c_b = \eta \cdot v_o \cdot c_{in} \cdot t \qquad \textbf{(10-114)}$$

Taking the derivative with respect to time gives:

$$(c_{bed} - c_b) \cdot \frac{dh}{dt} + (H-h) \cdot \frac{dc_b}{dt} = \eta \cdot v_o \cdot c_{in} \qquad \textbf{(10-115)}$$

With the sedimentation velocity according to equation 5:

$$\frac{dh}{dt} = v_{sed} = v_c \cdot \frac{c_b}{c_{bed} - c_b} \qquad \textbf{(10-116)}$$

This gives for the derivative of the near bed concentration:

$$\frac{dc_b}{dt} = \frac{\eta \cdot v_o \cdot c_{in} - v_c \cdot c_b}{H-h} \qquad \textbf{(10-117)}$$

Or:

$$(H-h) \cdot \frac{dc_b}{dt} + v_c \cdot c_b - \eta \cdot v_o \cdot c_{in} = 0 \qquad \textbf{(10-118)}$$

Solving equation (10-118) for a constant sediment level **h** gives:

$$\frac{c_b}{c_{in}} = \eta \cdot \frac{v_o}{v_c} \cdot \left(1 - e^{-\frac{v_c}{H-h} \cdot t} \right) \qquad \textbf{(10-119)}$$

Now an expression has been found for the average near bed concentration (equation (10-105)) and an expression for the momentary near bed concentration (equation (10-119)).
For the case of the Cornelia, as discussed before, equations (10-116) and (10-117) have been solved numerically. The results are shown in Figure 10-52 and Figure 10-53 it is obvious that the near bed concentration has to build up, causing a time delay in the momentary sediment level, with respect to the sediment entered in the hopper. The vertical distance between the momentary sediment level and the level of the sediment in, is the amount of sediment still in suspension.
It should be noted here that the near bed concentration is assumed to be the concentration of all the mixture above the sediment. Although this is not in accordance with the definition of van Rhee (2002C), it gives more insight in the loading process.

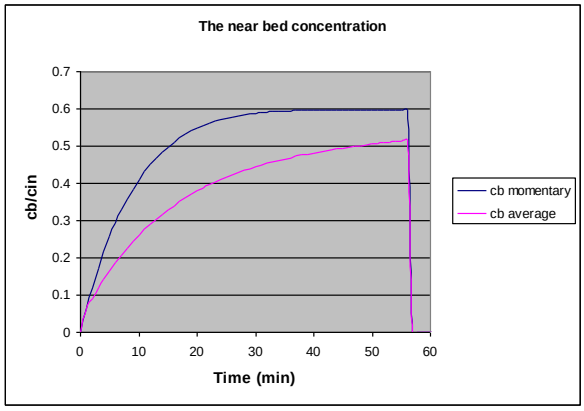

Figure 10-52: The near bed concentration, v_c=14.8 mm/sec.

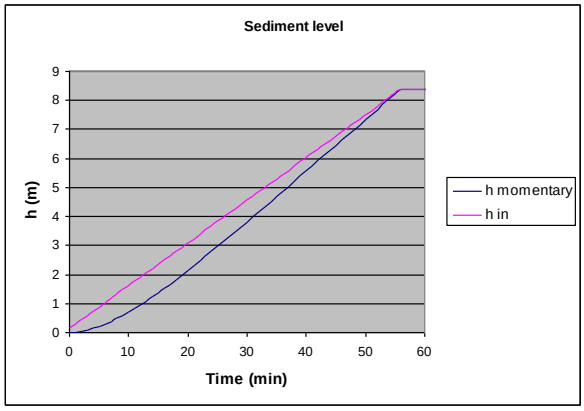

Figure 10-53: The sediment level, v_c=14.8 mm/sec.

The case considered in Figure 10-52 and Figure 10-53, has a sand with a settling velocity of 14.8 mm/sec, so a rather course sand. It is interesting to see what these figures would look like for finer sands. If two other cases are considered, sand with a settling velocity of 9.6 mm/sec (equal to the hopper load parameter) and sand with 50% of this settling velocity, 4.8 mm/sec, including the hindered settling effect. This gives values for the **S*** of 0.72 and 1.44 (assuming $c_b=c_{in}$). The estimated overflow losses according to equation (10-140) are now 11.31% and 39.39%, but since the estimation was 6.5% too low for the sand with a settling velocity of 14.8 mm/sec, as discussed before, this 6.5% is added to the estimation, giving 17.8% and 45.9%. So the settling efficiencies are estimated to 0.822 and 0.541.

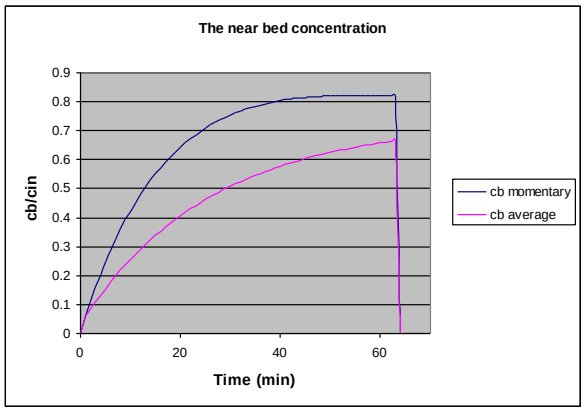

Figure 10-54: The near bed concentration, vc=9.6 mm/sec.

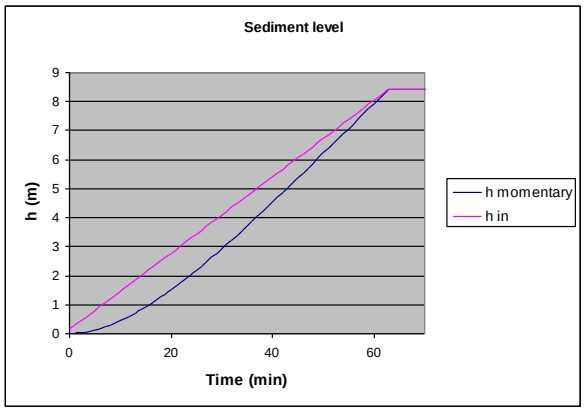

Figure 10-55: The sediment level, vc=9.6 mm/sec.

From these figures it can be seen that a smaller grain with a smaller settling velocity will result in a higher near bed concentration as also was concluded from Figure 10-46 and equation (10-139). The smallest grain gives a momentary near bed concentration which is higher than the incoming mixture concentration at the end of the

loading process, while the average near bed concentration is still below the incoming mixture concentration. Another conclusion that can be drawn and also makes sense, is that the time required for the mixture to settle increases when the settling velocity decreases. This is in accordance with equation (10-119).

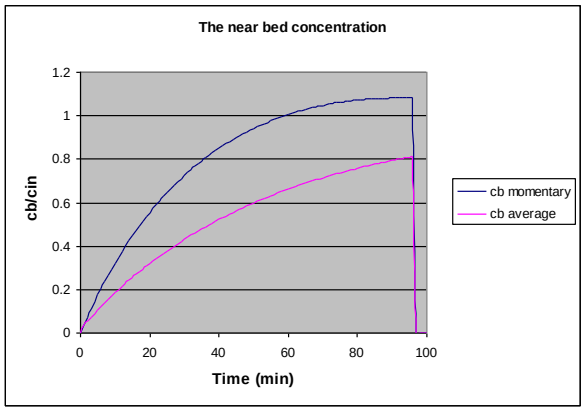

Figure 10-56: The near bed concentration, vc=4.8 mm/sec.

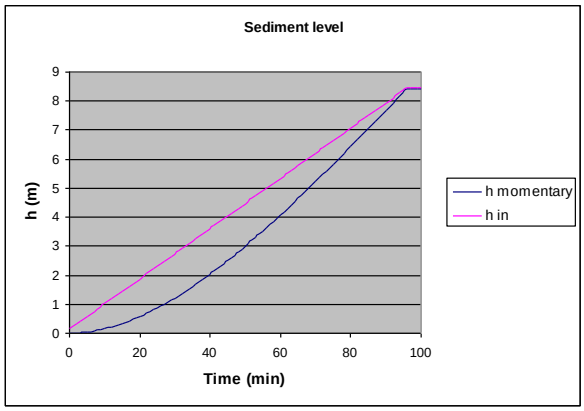

Figure 10-57: The sediment level, vc=4.8 mm/sec.

The fact that the near bed concentration (here it is the average concentration in the hopper above the bed) is different from the incoming mixture concentration also implies that this near bed concentration should be used for determining the hindered settling effect. In most cases this will result in a near bed concentration smaller than the incoming mixture concentration, but in specific cases the near bed concentration is higher.

10.12. Analytical Model to Predict the Overflow Losses

10.12.1. The Analytical Model

After discussing the empirical equation (10-140) of van Rhee (2002C), it is interesting to see if there is a more theoretical background behind this equation. Of course equation (10-102) has been found, but using it in combination with the near bed concentration according to equation (10-105), is a self-fulfilling prophecy. Equation (10-140) at least gives a first estimate of the overflow losses, although some questions can be asked about the validity as already mentioned by van Rhee (2002C).
One of the omissions of equation (10-140) is, that it is based on tests with a certain grading of the sand, so the question would be, how accurate is this equation if sand with another grading is used. To investigate this, an old analytical model of Miedema (Miedema S. , The flow of dredged slurry in and out hoppers and the settlement process in hoppers, 1981) is used. The model is based on the Camp (1946) approach and published by Miedema and Vlasblom (Miedema & Vlasblom, Theory of Hopper Sedimentation, 1996). The settling efficiency η_b at a certain moment of the hopper loading process is defined as:

$$\eta_b = (1 - p_o) + \int_{p_{fs}}^{p_o} \frac{v_c}{v_o} \cdot dp \qquad \textbf{(10-120)}$$

One should read Miedema & Vlasblom (1996) for the derivation of this equation. Basically, there are 3 areas in this equation. The area from 0 to p_{fs} are the particles that will not settle due to scour, or because they are to small (fines), the area from p_{fs} to p_o, which are the particles that settle partially, some reach the sediment but some don't and leave the hopper through the overflow, and last but not least the area above p_o which are the particles that settle 100%. To find an analytical solution for this equation, the PSD should be approximated by a straight line according to:

$$\log(d) = a \cdot p - b \qquad \textbf{(10-121)}$$

A number of examples of PSD's according to equation (10-141) are shown in Figure 10-58. Equation (10-141) can also be written as:

$$p = \frac{\log(d) + b}{a} \qquad \textbf{(10-122)}$$

Now the grains that cause overflow losses are usually grains that settle in the Stokes region, according to:

$$v_s = 424 \cdot R_d \cdot \mu \cdot d^2 \qquad \textbf{(10-123)}$$

Hindered settling can be taken into account with the well-known Richardson and Zaki equation:

$$v_c = 424 \cdot R_d \cdot \mu \cdot d^2 \cdot (1 - C_v)^{\beta} \qquad \textbf{(10-124)}$$

This can be rewritten as equation (10-125) to show the grain diameter as a function of the settling velocity.

$$d = \left(\frac{v_c}{424 \cdot R_d \cdot \mu \cdot (1 - C_v)^{\beta}} \right)^{1/2} \qquad \textbf{(10-125)}$$

The number 424 is based on the original Stokes equation but can be changed using the variable μ. The particle diameter that matches the hopper load parameter v_o, the particle that will just settle 100% is now:

$$d_o = \left(\frac{v_o}{424 \cdot R_d \cdot \mu \cdot (1 - C_v)^{\beta}} \right)^{1/2} \qquad \textbf{(10-126)}$$

This gives for the fraction of the particles that will settle 100%, p_o:

$$p_o = \frac{\log(d_o) + b}{a} \tag{10-127}$$

For the particles that settle partially the second term on the right hand side of equation (10-120) has to be solved according to:

$$p_1 = \int_{p_{fs}}^{p_o} \frac{v_c}{v_o} \cdot dp = \int_{p_{fs}}^{p_o} \frac{424 \cdot R_d \cdot \mu \cdot d^2 \cdot (1 - C_v)^{\beta}}{v_o} \cdot dp = \int_{p_{fs}}^{p_o} \frac{424 \cdot R_d \cdot \mu \cdot (1 - C_v)^{\beta} \cdot e^{2 \cdot (a \cdot p - b) \cdot \ln(10)}}{v_o} dp \tag{10-128}$$

$$p_1 = \frac{1}{2 \cdot a \cdot \ln(10)} \cdot \frac{424 \cdot R_d \cdot \mu \cdot (1 - C_v)^{\beta}}{v_o} \cdot e^{-2 \cdot b \cdot \ln(10)} \cdot \left(e^{2 \cdot a \cdot p_o \cdot \ln(10)} - e^{2 \cdot a \cdot p_{fs} \cdot \ln(10)} \right) \tag{10-129}$$

This gives for the settling efficiency of the whole PSD:

$$\eta = (1 - p_o) + p_1 \tag{10-130}$$

Equation (10-130) does not include the turbulence effect as described by Miedema & Vlasblom (Miedema & Vlasblom, Theory of Hopper Sedimentation, 1996), because here it is the aim to find a simple equation to predict overflow losses. Of course this will give an error, but the magnitude of the settling efficiency found will be correct. The derivation until now assumes that the loading process starts with a hopper full of water, so from the beginning of the loading process the settling efficiency is active. In reality though, it is possible that the loading process starts with an empty hopper or a partially filled hopper. When the hopper at the start of the loading process has to be partially filled with mixture for a fraction α, and it is assumed that all the particles that enter the hopper before the overflow level has been reached will settle, then the sediment level will already reach a fraction ε of the height of the hopper when the overflow level has been reached. This fraction ε can be calculated with:

$$\varepsilon = \alpha \cdot \left(\frac{\rho_{in} - \rho_w}{\rho_{bed} - \rho_w} \right) \tag{10-131}$$

Since this has an effect on the cumulative settling efficiency η_{cum}, the settling efficiency has to be corrected by:

$$ov_{cum} = \frac{ov \cdot (1 - \varepsilon)}{1 - \varepsilon \cdot ov} \tag{10-132}$$

The cumulative overflow losses are now:

$$\eta_{cum} = 1 - ov_{cum} \tag{10-133}$$

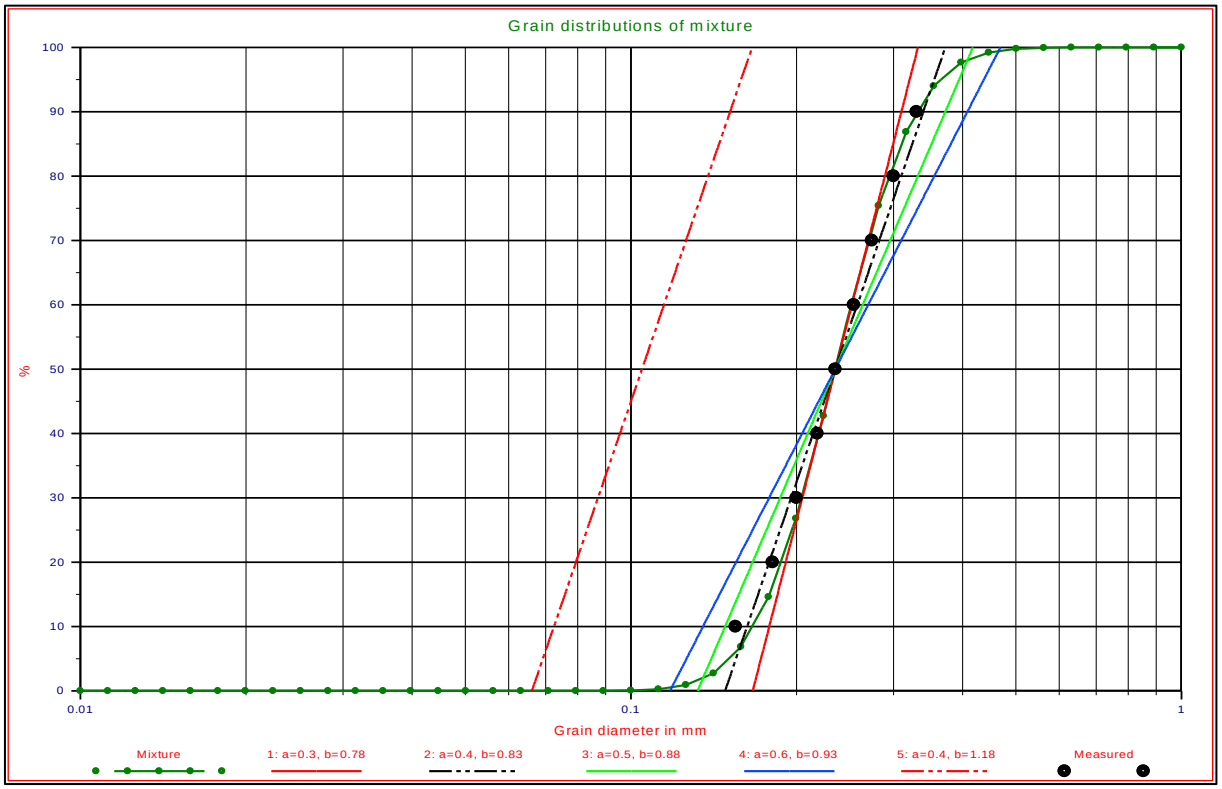

Figure 10-58: The PSD's as used in the examples.

10.12.2. Verification of the Analytical Model

The analytical model found has been verified using the data from van Rhee (2002C), as given in Table 10-2. Figure 10-59 shows the cumulative overflow losses of the analytical model, the empirical equation (10-140) and the measured data of Table 10-2, as a function of the dimensionless overflow rate **S*** assuming $c_b=c_{in}$, as a function of the concentration and as a function of the dimensionless overflow rate **S*** with c_b calculated according to equation (10-105).

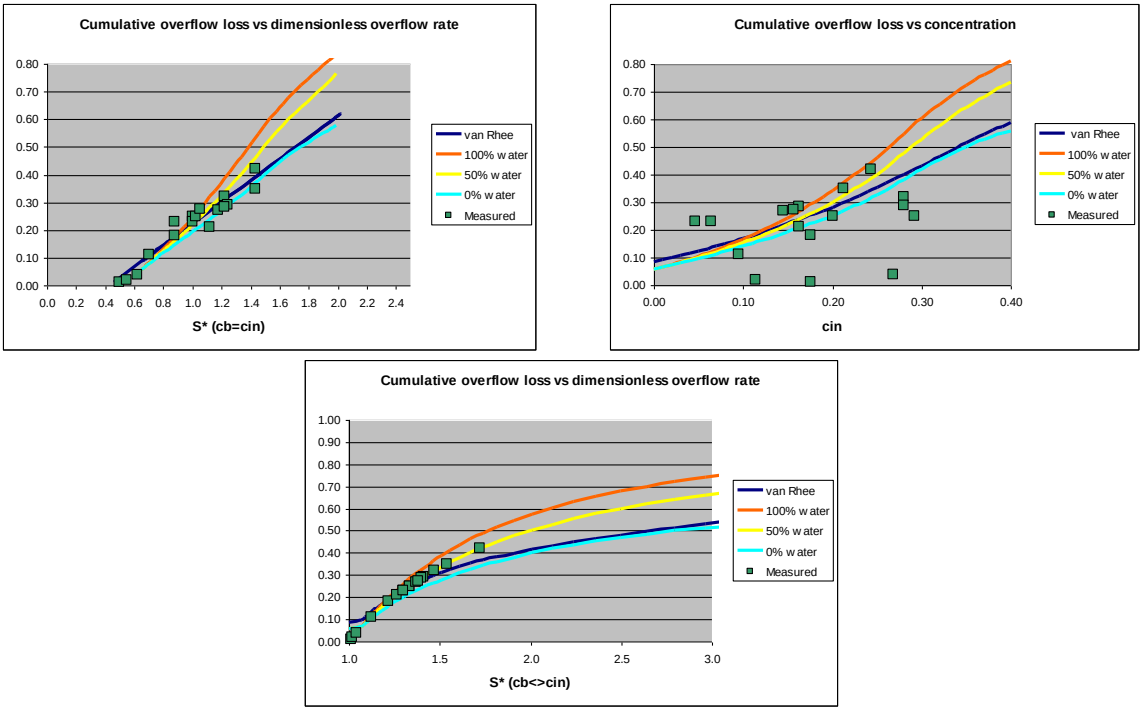

Figure 10-59: Comparing van Rhee (chapter 4) with the analytical model. (Q=0.125, L=12, W=3, H=2, d_{50}=0.105, a=0.4, b=1.18, β=4.47, n=0.4, μ=1)

The analytical model has been computed for a hopper filled with 0%, 50% and 100% water at the start of the loading process. It should be noted that the measurements of van Rhee (2002C) from Table 10-2 are carried out with a hopper with about 50% of water at the start of the loading process. So the analytical model for 50% initial hopper filling should be compared with the empirical equation (10-140). It is obvious that the analytical model matches the empirical equation (10-140) up to a value of **S*** of 1.2 in the top left graph, up to a concentration c_{in} of 0.2 in the top right graph and up to a value of **S*** of 1.5 in the bottom graph. For these computations, the settling velocity has been calculated using the iterative method based on the drag coefficient and using the Richardson and Zaki equation for hindered settling. Van Rhee (2002C) however states that the hindered settling process is more complicated for well graded sand. In the experiments sand according to Figure 10-58 sand number 5 has been used. In such sand there is interaction between smaller and larger particles regarding the hindered settling effect. If this is taken into account by the principle of hindered density, which means, that the larger particles settle in a heavier mixture of the smaller particles according to:

$$\rho_f = \frac{C_v}{2}\cdot\rho_q + \left(1-\frac{C_v}{2}\right)\cdot\rho_w \qquad \textbf{(10-134)}$$

Giving a relative density R_d of:

$$R_d = \frac{\rho_q - \rho_f}{\rho_f} \qquad \textbf{(10-135)}$$

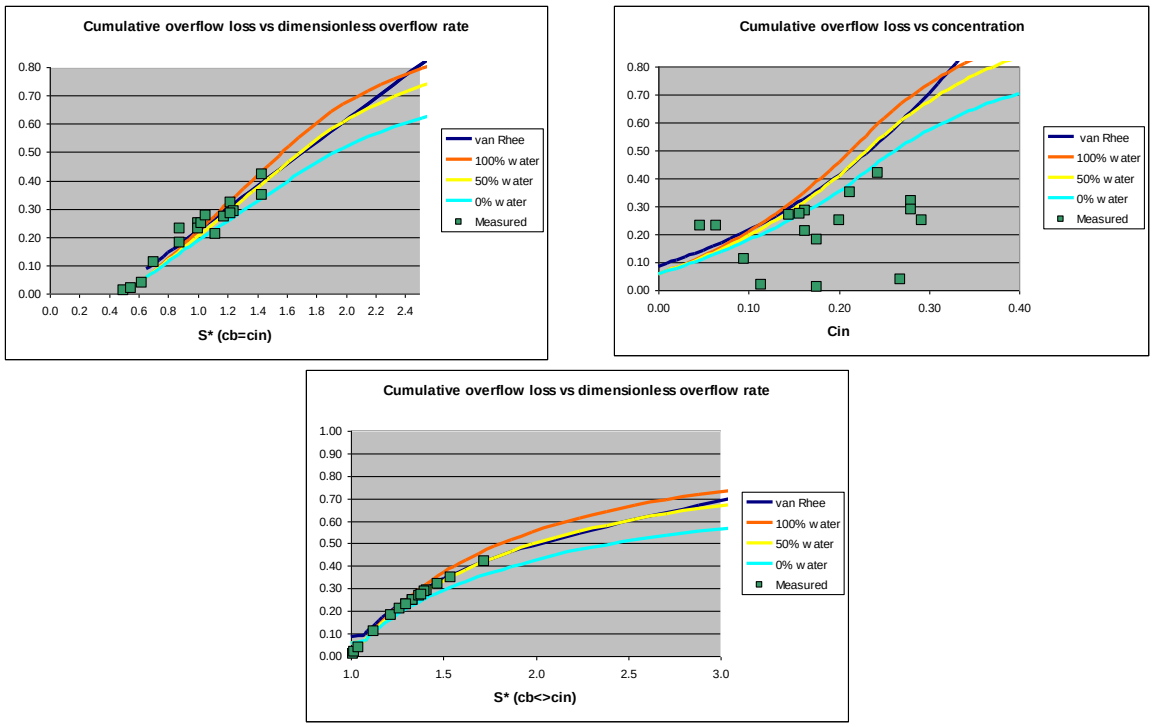

Figure 10-60: Comparing van Rhee (chapter 4) with the analytical model, including the hindered density effect.
(Q=0.125, L=12, W=3, H=2, d_{50}=0.105, a=0.4, b=1.18, β=4.47, n=0.4, μ=1)

Using equation (10-134) in the equations (10-126) and (10-129), gives an improved result according to Figure 10-60. It is obvious from this figure that the analytical model with 50% filling at the start of the loading process matches the empirical equation perfectly. Which proves the validity of the analytical model derived and gives a more physical background to the empirical equation of van Rhee (2002C). Now the question is, does the analytical model give good predictions in other cases. Van Rhee (2002C) tested equation (10-140) on the measurements of the Cornelia as mentioned before and found cumulative overflow losses of 1.5%, while the measurements gave cumulative overflow losses of 8%. One of the reasons for this might be that the model tests on which equation (10-140) is based are carried out with sand with a certain grading, see Figure 10-58 sand number 5. The tests with the Cornelia used sand with another grading. First the overflow losses are computed with the same grading as in the model tests which is sand number 2 in Figure 10-58.

The results of this computation are shown in Figure 10-62. The top left figure shows the results according to equation (10-140) with $\mathbf{c_b=c_{in}}$. Now cumulative overflow losses are found of about 2% at **S*=0.47**, similar to the 1.5% of van Rhee (2002C). In these calculations, the hindered density effect has not been used because of the narrow grading of the PSD.

From Figure 10-58 it can be seen however that the fines are not taken into account properly and it is the fines that cause the higher cumulative overflow losses. If sand number 4 is used however, taking into account the fines, Figure 10-64 is the result giving cumulative overflow losses of about 8% for **S*=0.47** in the top left graph. It is clear that finding the right model PSD is difficult and sand number 4 is a little bit jumping to conclusions, but it is also clear that using a PSD that matches the real sand closer will result in a better prediction of the overflow losses.

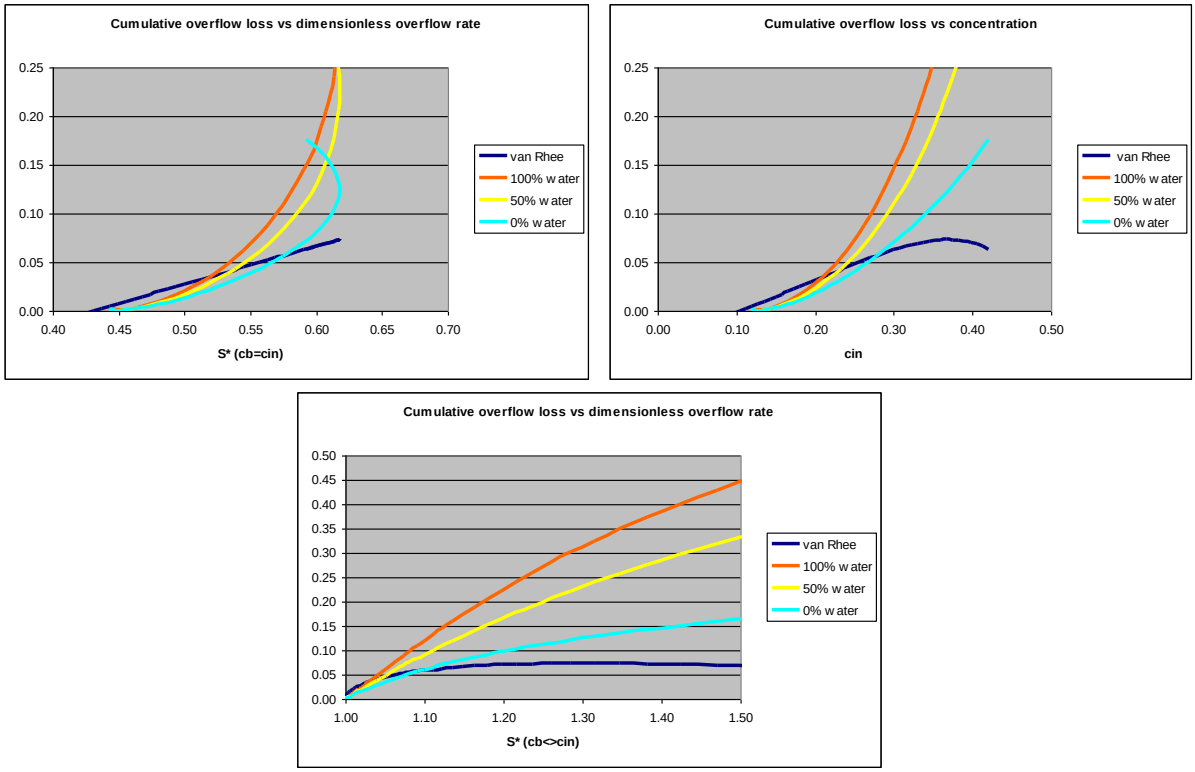

Figure 10-61: Comparing van Rhee (chapter 8) with the analytical model (a=0.3, b=0.78). (Q=6, L=52, W=11.5, H=8.36, d_{50}=0.235, a=0.3, b=0.779, β=3.7, n=0.46, μ=0.725)

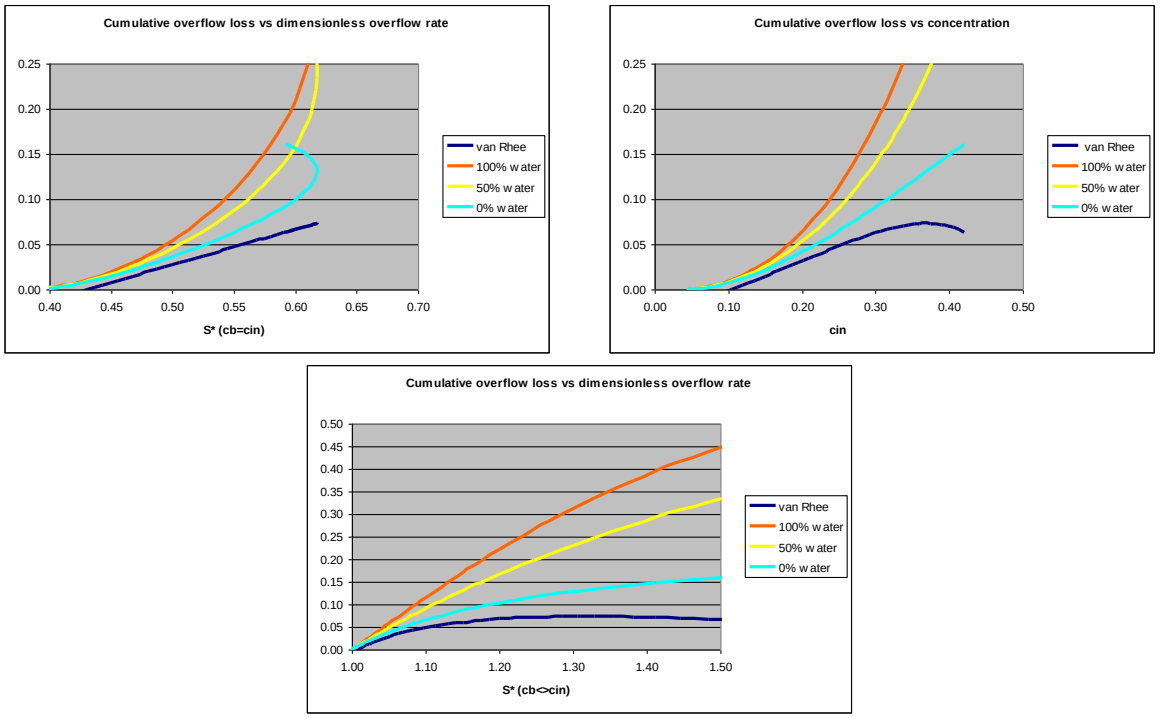

Figure 10-62: Comparing van Rhee (chapter 8) with the analytical model (a=0.4, b=0.83). (Q=6, L=52, W=11.5, H=8.36, d_{50}=0.235, a=0.4, b=0.829, β=3.7, n=0.46, μ=0.725)

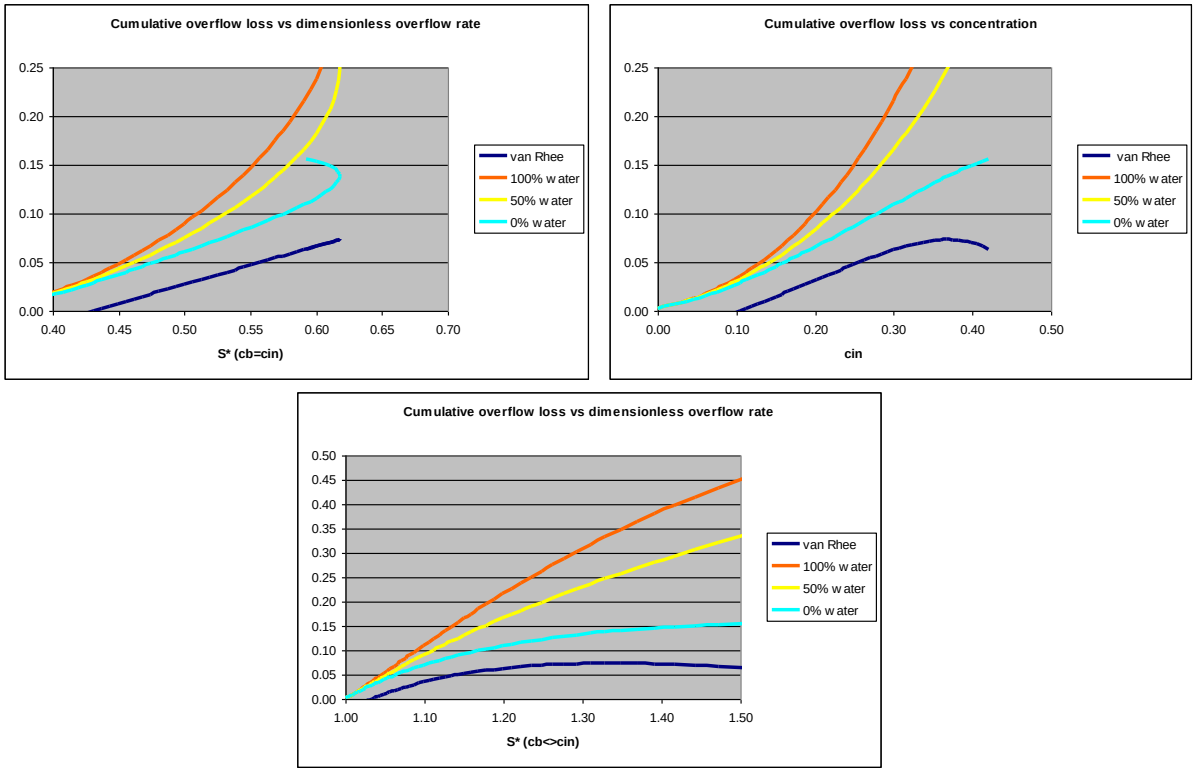

Figure 10-63: Comparing van Rhee (chapter 8) with the analytical model (a=0.5, b=0.88). (Q=6, L=52, W=11.5, H=8.36, d_{50}=0.235, a=0.5, b=0.879, β=3.7, n=0.46, μ=0.725)

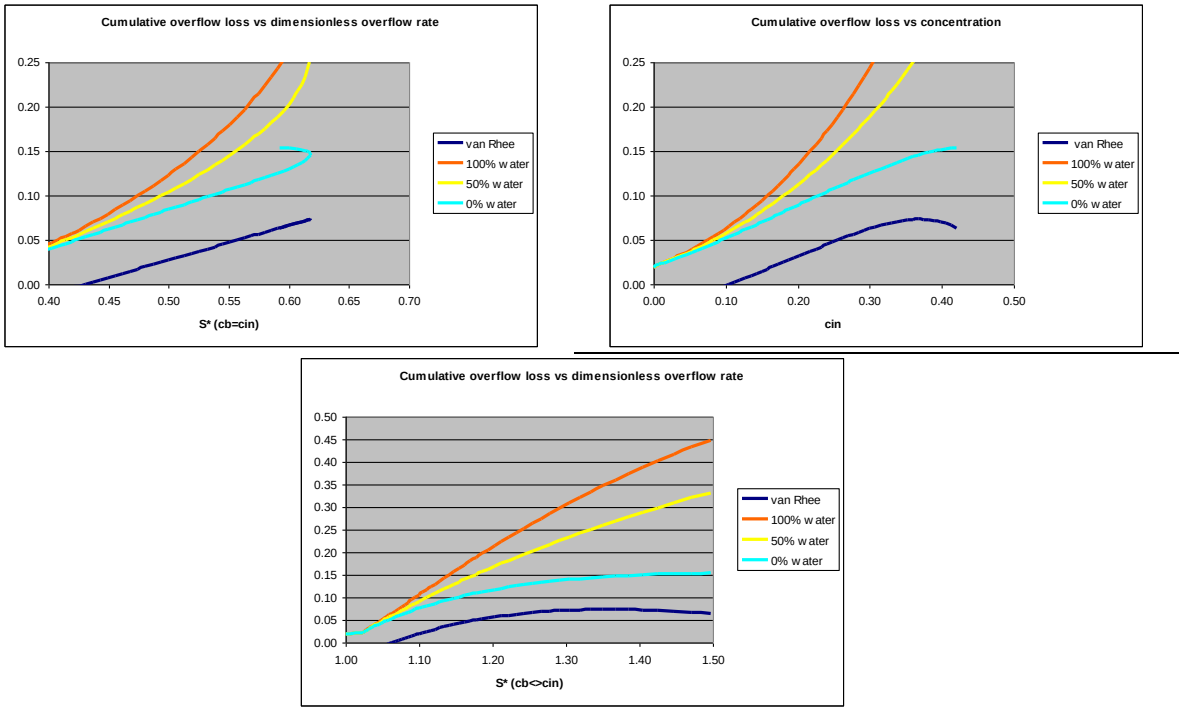

Figure 10-64: Comparing van Rhee (chapter 8) with the analytical model (a=0.6, b=0.93). (Q=6, L=52, W=11.5, H=8.36, d_{50}=0.235, a=0.6, b=0.929, β=3.7, n=0.46, μ=0.725)

10.13. Comparing the Miedema and the van Rhee Models.

10.13.1. Introduction.

This chapter is based on Miedema & van Rhee (2007).
In the past two decades the size of TSHD's has tripled and there are plans for TSHD's in the range of 50.000 m^3. When enlarging hoppers there are some limitations like the draught of the vessel and the line velocity in the suction lines. It's interesting to compare the influences of length, width, height ratio's, flow capacity and some other parameters on the production and the overflow losses of TSHD's. To do so, mathematical models have been developed to simulate the sedimentation process in the hopper. Two models will be used and compared, first the model of Vlasblom/Miedema (1995), Miedema/Vlasblom (1996) and Miedema (2008A) and second the more sophisticated 2DV model of van Rhee (2002C), which is verified and validated with model and prototype tests. Both models are explained briefly. With the two models 3 cases are analyzed, a 2316 m^3, a 21579 m^3 and a 36842 m^3 hopper. The results of the case studies give the following conclusions and recommendations:

- The two models give the same magnitude for the overflow losses, but the shape of the curves is different due to the differences in the physical modeling of the processes.
- Due to the lower losses the computed optimal loading time will be shorter for the Vlasblom /Miedema approach.
- The strong point of the van Rhee model is the accurate physical modeling, giving the possibility to model the geometry of the hopper in great detail, but also describing the physical processes in more detail.
- The van Rhee model is verified and validated with model and prototype tests and can be considered a reference model for other models.
- The strong point of the Miedema/Vlasblom model is the simplicity, giving a transparent model where result and cause are easily related.

From a scientific point of view it is interesting to compare the sophisticated van Rhee model with the simplified models and to do so, the van Rhee (2002C) model is compared with the Miedema (2008A) model. The comparison consists of a number of cases regarding real TSHD's. The following TSHD's will be compared:

Table 10-3: The data of the TSHD's used.

Hopper	Load	Volume	Length	Width	Empty height	Flow	Hopper load v_0	Mixture density
	ton	m^3	m	m	m	m^3/sec	m/sec	ton/m^3
Small	4400	2316	44.0	11.5	4.577	4	0.0079	1.3
Jumbo	41000	21579	79.2	22.4	12.163	14	0.0079	1.3
Mega	70000	36842	125.0	30.0	9.825	19	0.0051	1.3

Further it is assumed that all 3 TSHD's have a design density of 1.9 ton/m^3 and they operate according to the CVS system (no adjustable overflow). This gives a sand fraction of 0.54 and a porosity of 0.46. For the calculations a sand with a $\mathbf{d_{50}}$ of 0.4 mm is chosen, according to figure 1. The particle size distribution is chosen in such a way that there is a reasonable percentage of fines in order to have moderate overflow losses.

10.13.2. Case Studies with the Camp/Miedema Model.

The calculations according to the modified Camp/Miedema model as developed by Miedema (1981) and published by Vlasblom & Miedema (1995), Miedema & Vlasblom (1996) and Miedema (2008A) are carried out with the program TSHD (developed by Miedema). The effects of hindered settling, turbulence and scour and an adjustable overflow are implemented in this program as described previously.
The program assumes that first the hopper is filled with mixture up to the overflow level and all the grains entering the hopper during this phase will stay in the hopper, so the overflow losses are 0 during this phase. The table below shows the filling time, the total load and the TDS at the end of this phase.

Table 10-4: The hopper content after the filling phase.

Hopper	Load	Volume	Flow	Filling time	Total load	TDS	Overflow losses	Mixture density
	ton	m^3	m^3/sec	min	ton	ton	%	ton/m^3
Small	4400	2316	4	9.65	3011	1039	20.0	1.3
Jumbo	41000	21579	14	25.69	28053	9678	20.0	1.3
Mega	70000	36842	19	32.32	47895	16523	16.6	1.3

After this phase the program will determine the total settling efficiency and based on this the increase of the sediment and the overflow losses in time steps of 1 minute. Each time step the program checks whether or not scour occurs and if so which fraction of the PSD will not settle due to scour. Usually first there is a phase where scour does not occur. The overflow losses are determined by the settling efficiency according to the equations (10-69) and (10-70). If the hopper has a CTS system, each time the necessary overflow level is calculated and the overflow level is adjusted. In the cases considered a CVS system is assumed, so the overflow level is fixed. When the sediment level is so high that the velocity above the bed is very high, scour starts. This will happen at the end of the loading process. In the calculations the loading process is continued for a while, so the effect of scour is clearly visible. The results of the calculations are show in Figure 10-66, Figure 10-67 and Figure 10-68 for the Small, Jumbo and Mega hopper. The initial overflow losses of 20, 20 and 16.6% match the values of the hopper load parameter as mentioned in Table 10-3. The Mega hopper has a smaller hopper load parameter and thus also smaller initial overflow losses (without scour).

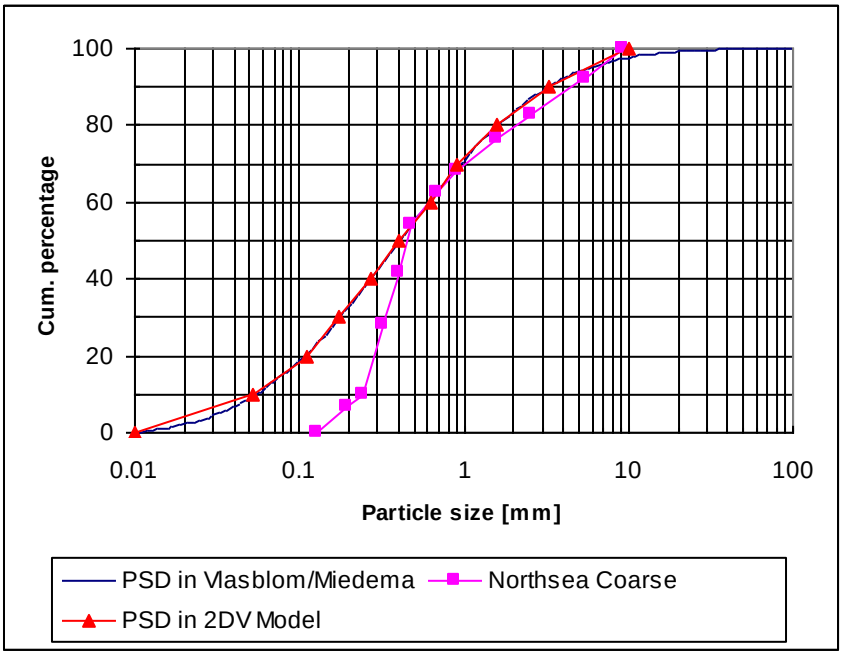

Figure 10-65: The 0.4 mm grain distribution.

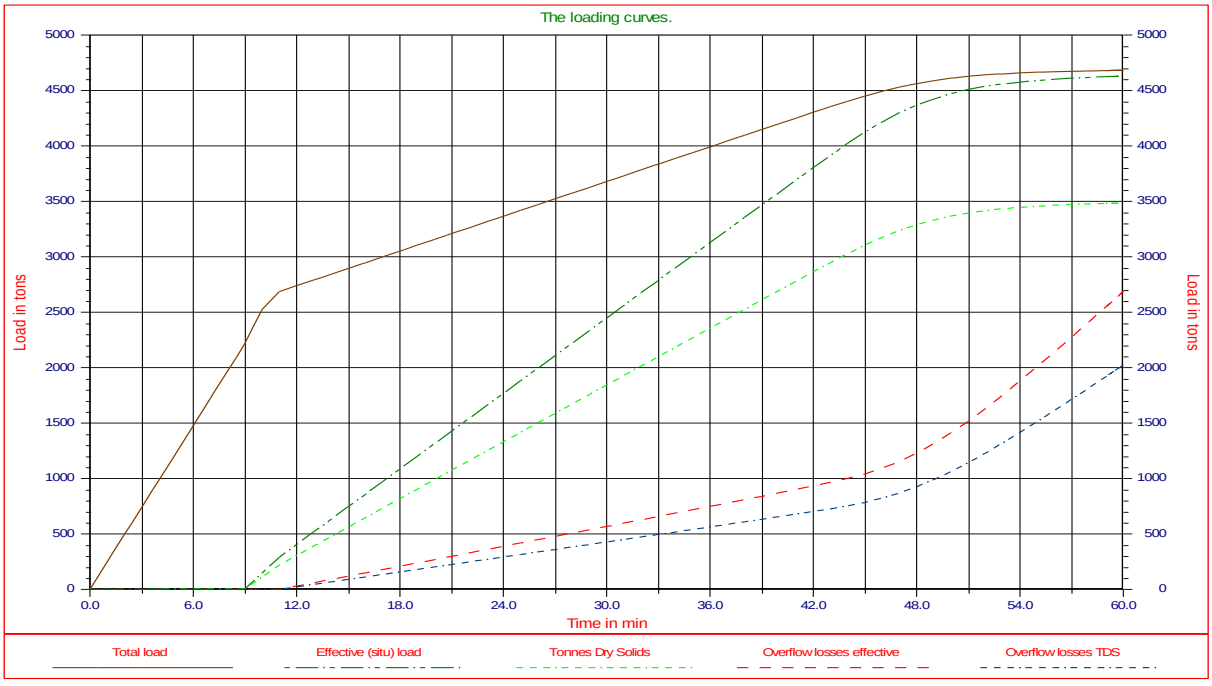

Figure 10-66: The loading curves of the Small TSHD.

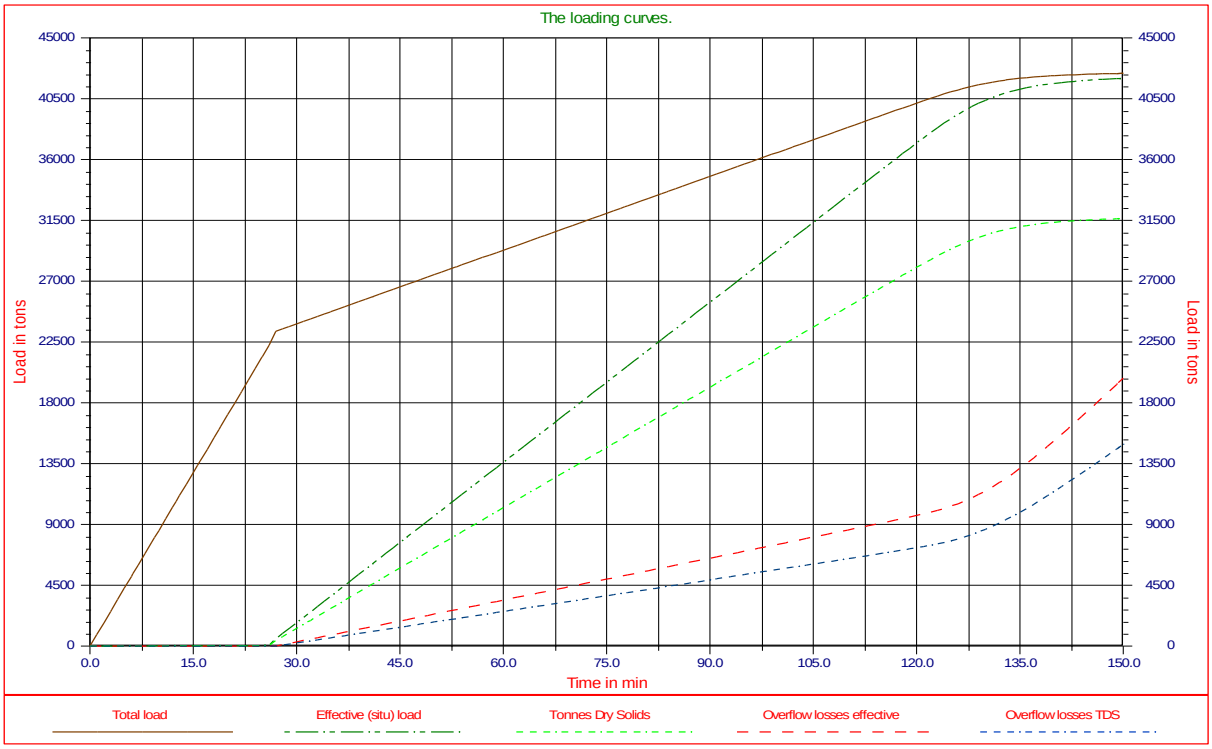

Figure 10-67: The loading curves of the Jumbo TSHD.

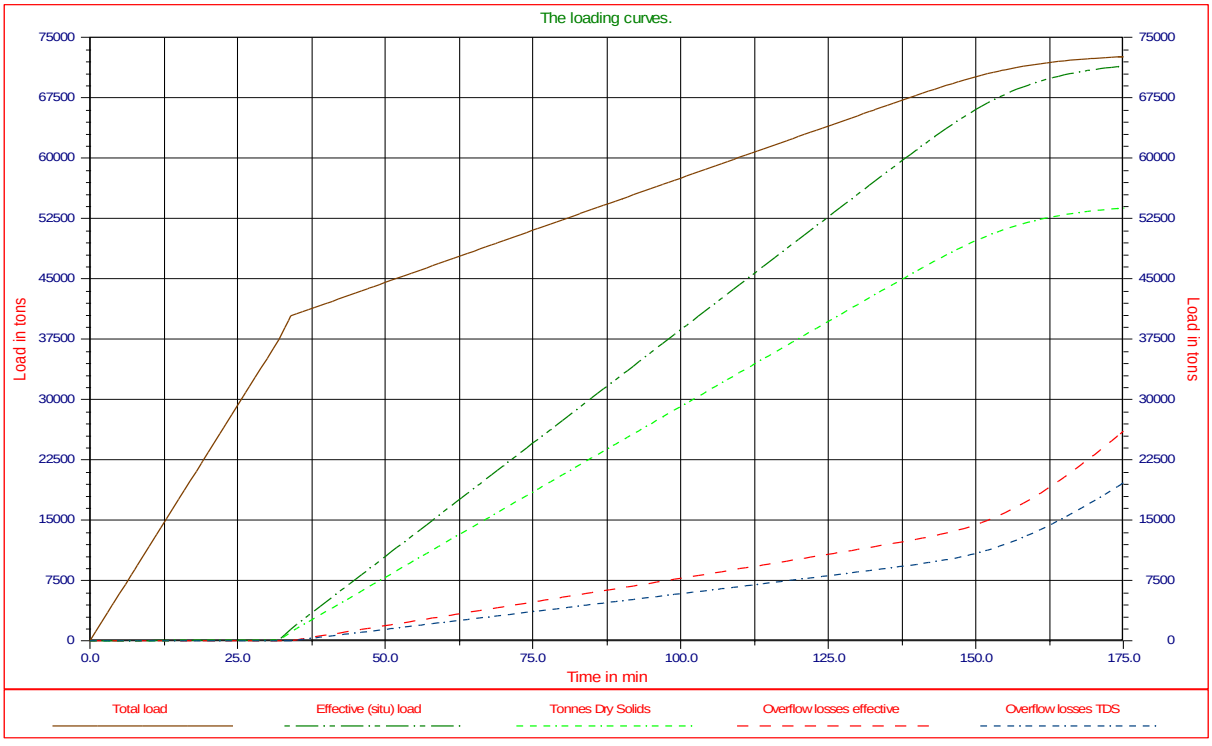

Figure 10-68: The loading curves of the Mega TSHD.

It should be noted that the optimum loading time, the loading time with the maximum production, depends on the total cycle, including sailing times, dumping time, etc. Since the calculations with the 2DV model start with a hopper full of water, also here first the hopper is filled with water, so the two models can be compared.

10.13.3. The 2DV Model

The settlement model described above provides a good approximation of the overflow losses. The influence of grain size, discharge, concentration and hopper geometry can be taken into account. Some influences however are not included in the model. For instance the influence of the inflow location, variation of water level at the start of dredging is not included. To overcome these limitations the 2DV hopper sedimentation model was developed (Van Rhee (2002A)). The model is based on the Reynolds Averaged Navier Stokes equations with a k-epsilon turbulence model. The model includes the influence of the overflow level of the hopper (moving water surface) and a moving sand bed due to the filling of the hopper. The influence of the particle size distribution (PSD) is included in the sediment transport equations. A summary of the model is described in Van Rhee (2002C). The total model is based on three modules (see Figure 10-69).

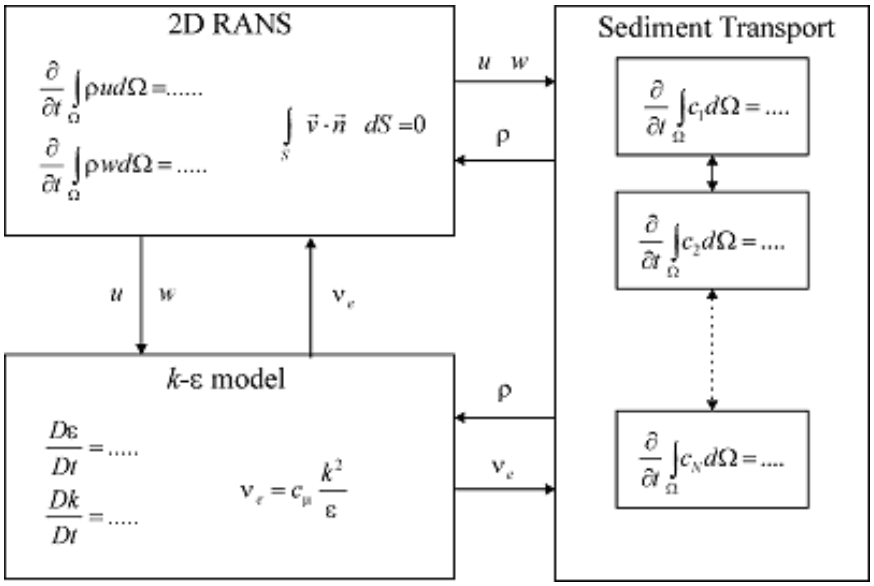

Figure 10-69: Overview of the 2DV model.

In the 2D RANS module the Reynolds Averaged Navier Stokes equations are solved (the momentum equations). The sediment transport module computes the distribution of suspended sediment in the hopper while the k-epsilon module is necessary for the turbulent closure. The modules have to be solved simultaneously because the equations are strongly coupled. In the momentum equations the density is present which follows from the sediment transport equations. The diffusive transport of sediment is governed by turbulence predicted by the k-epsilon model. The turbulence on the other hand is influenced by the density gradients computed in the sediment transport module.

Boundary conditions

The partial differential equations can be solved in case boundary conditions are prescribed. Different boundaries can be distinguished: Walls (sediment bed and side walls), water surface, inflow section and outflow section. At the walls the normal flow velocity is zero. The boundary condition for the flow velocity at the wall is computed using a so-called wall function (Rodi (1993), Stansby (1997)). The boundary conditions for the turbulent energy **k** en dissipation rate **ε** are consistent with this wall function approach. For the sediment transport equations the fluxes through vertical walls and water surface is equal to zero since no sediment enters or leaves the domain at these boundaries. At the sand bed for every fraction the sedimentation flux $\mathbf{S_i}$ is prescribed (the product of the near bed concentration and vertical particle velocity of a certain fraction). The influence of the bottom shear stress on the sedimentation is modeled using a reduction factor **R**.

$$\mathbf{S_i = R \cdot c_i \cdot w_{zj}}$$

$$\mathbf{R} = \begin{cases} \mathbf{1 - \frac{\theta}{\theta_0}} & \boldsymbol{\theta < \theta_0} \\ \mathbf{0} & \boldsymbol{\theta \geq \theta_0} \end{cases} \qquad \textbf{(10-136)}$$

This simple relation between the reduction factor and Shields parameter **θ** is based on flume tests (Van Rhee (2002B)). The critical value for the Shields parameter proved to be independent of the grain size for the sands

tested (d50 < 300 μm). It will be clear that this approach can only be used when overall sedimentation (like in a hopper of a TSHD) will take place. When the Shields value exceeds the critical value no sedimentation will take place, but sediment already settled will not be picked up with this approach. Hence net erosion is not (yet) possible in the model.

At the inflow section the velocity and concentration is prescribed. The outflow boundary is only active when overflow is present, so when the mixture level in the hopper exceeds the overflow level. In that case the outflow velocity is prescribed, and follows simply from the ratio of the overflow discharge and the difference between the hopper and overflow level. For the other quantities the normal gradients are equal to zero (Neumann condition).
At the water surface a rigid-lid assumption is used since surface wave phenomena are not important for the subject situation. A rigid-lid can be regarded as a smooth horizontal plate covering the water surface in the hopper. Depending on the total volume balance inside the hopper this "plate" will be moved up and down.

Numerical approach
The momentum and sediment transport equations are solved using the Finite Volume Method to ensure conservation. The transport equations for the turbulent quantities k and are solved using the Finite Difference method. A Finite Difference Method is allays implemented on a rectangular (Cartesian) grid. Although a Finite Volume Method can be applied on any grid it is advantageous to use a Cartesian approach for this method as well especially when a staggered arrangement of variables is used. In general the flow domain is however not rectangular. The water surface can be considered horizontal on the length scale considered, but a sloping bottom will not coincide with the gridlines. Different approaches are possible. The first method is to use a Cartesian grid and to adjust the bottom cells (cut-cell method). Another method is to fit the grid at the bottom. In that case a boundary fitted non-orthogonal grid can be used. A third method is using grid transformation. By choosing an appropriate transformation the equations are solved on a Cartesian domain in transformed co-ordinates. Although this transformation allows for a good representation of a curved topography the method has the disadvantage that due to truncation errors in the horizontal momentum equation artificial flows will develop when a steep bottom encounters density gradients. These unrealistic flows can be partly suppressed when the diffusion terms are locally discretized in a Cartesian grid (Stelling (1994)). Since however in a hopper both large density gradients as steep bottom geometry can be present it was decided to develop the model in Cartesian co-ordinates with a cut-cell approach at the bed.
The computational procedure can only be outlined here very roughly. The flow is not stationary hence the system is evaluated in time. The following steps are repeated during time:

- Update the velocity field to time $\mathbf{t_{n+1}}$ by solving the NS-equations together with the continuity equation using a pressure correction method (SIMPLE-method (Patankar (1980)) using the density and eddy viscosity of the old time step $\mathbf{t_n}$.
- Update the turbulent quantities and to time $\mathbf{t_{n+1}}$ using the velocity field of $\mathbf{t_{n+1}}$. Compute the eddy-viscosity for the new time.
- Use the flow field of $\mathbf{t_{n+1}}$ to compute the grain velocities for the next time and update the concentrations for all fractions and hence the mixture density to time $\mathbf{t_{n+1}}$.
- Compute the new location for the bed level and mixture surface in the hopper

Results
The 2DV model is used to simulate the loading process for the three different cases. At the start of the simulation the hopper is filled with water. The results are shown in Figure 10-70, Figure 10-71 and Figure 10-72. In these figures the TDS in the hopper (settled in the bed and in suspension) and the cumulative overflow losses are plotted versus loading time.

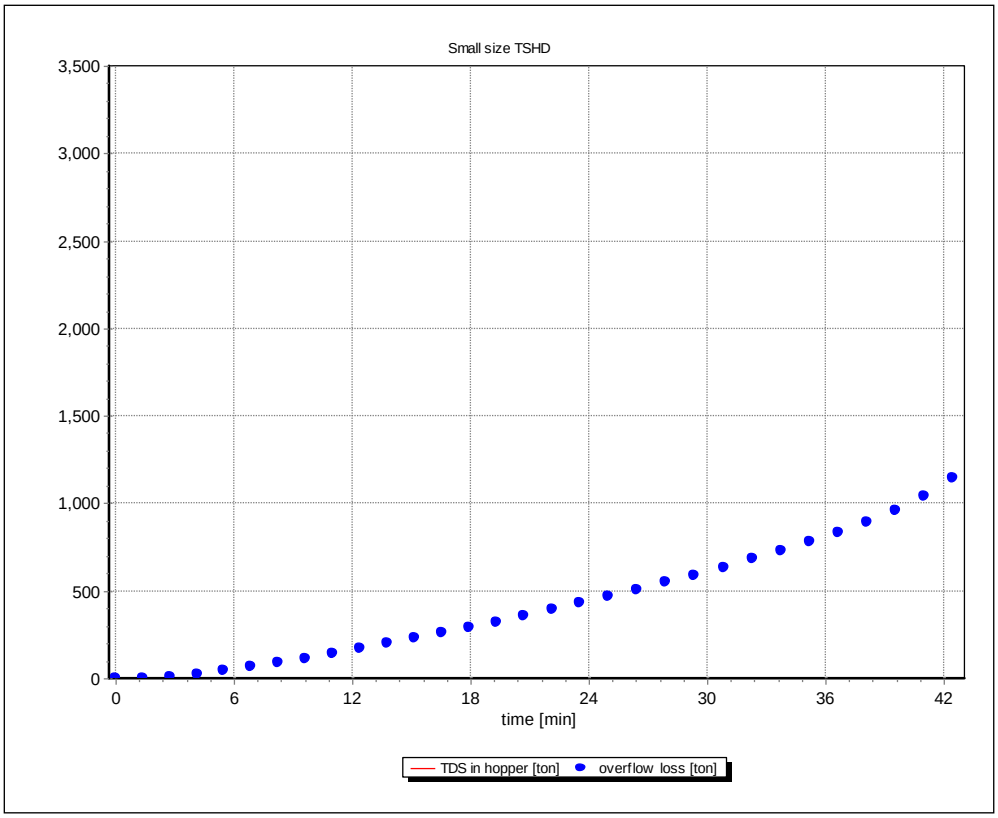

Figure 10-70: Loaded TDS and overflow losses as a function of time for a Small size TSHD.

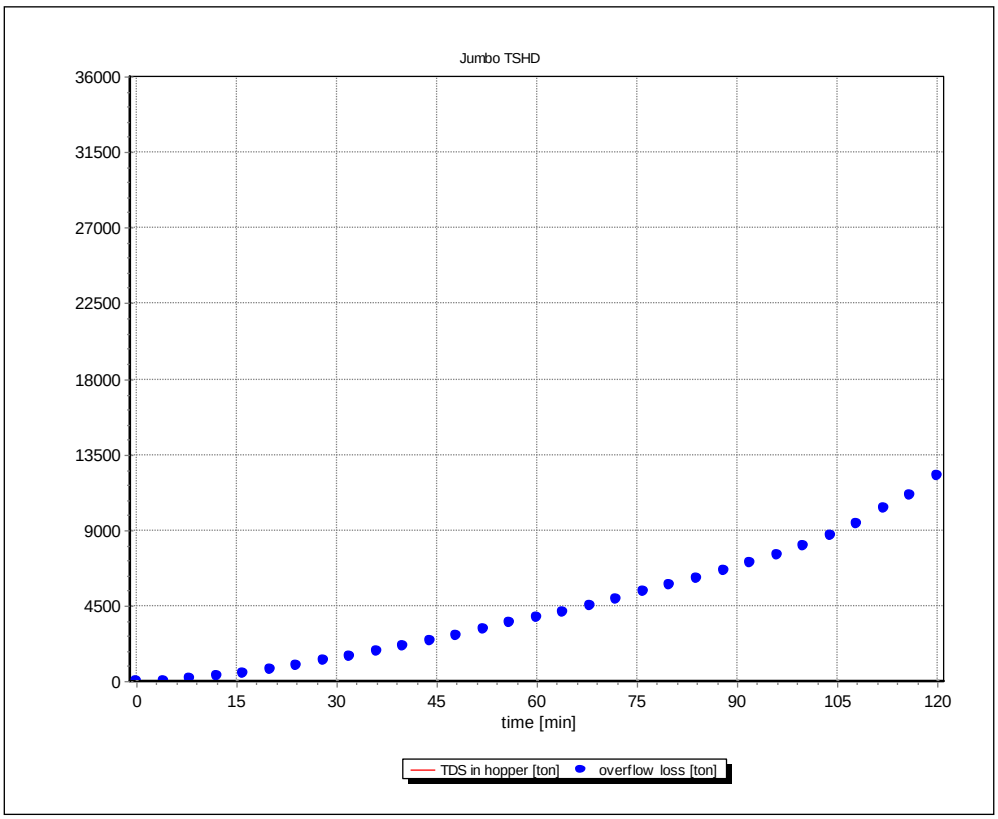

Figure 10-71: Loaded TDS and overflow losses as a function of time for Jumbo TSHD.

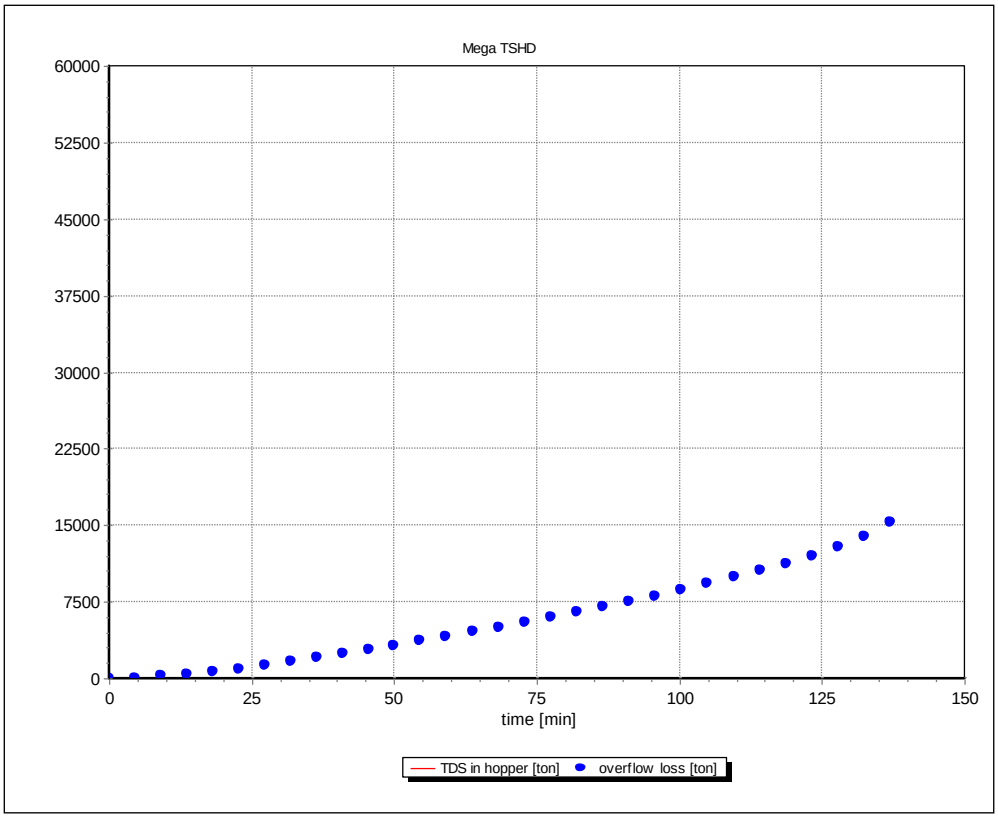

Figure 10-72: Loaded TDS and overflow losses as a function of time for a mega TSHD.

10.13.4. Comparison of the Two Models.

To compare the results of the two methods, first the differences in the models are summarized:

1. The physical modeling of the two methods is different; Miedema/Vlasblom/Camp is based on the Camp approach, while the 2DV model is based on the Reynolds Averaged Navier Stokes equations.
2. The van Rhee model starts with a hopper full of water, while the Miedema/Vlasblom/Camp model starts with an empty hopper.
3. The Miedema/Vlasblom/Camp model assumes 100% settling of the grains during the filling phase of the hopper.
4. The van Rhee model includes a layer of water above the overflow level, while the Miedema/Vlasblom/Camp model doesn't by default. But to compare the two models the height of the overflow level has been increased by the thickness of this layer of water and the results are shown in the Figure 10-73, Figure 10-74 and Figure 10-75. With the layer thickness according to: $\mathbf{H_l = \left(\frac{Q}{1.72 \cdot b} \right)^{2/3}}$, where the constant 1.72 may vary. The width **W** is chosen for the width of the overflow **b** in the calculations. This gives a layer thickness of 34 cm for the small hopper and 51 cm for the Jumbo and the Mega hopper.

The results of the Small hopper and the Jumbo hopper are similar due to the same hopper load parameter of 0.0079 m/sec. The Mega hopper has a smaller hopper load parameter of 0.0051 m/sec, resulting in relatively smaller overflow losses. To compare the two models the graphs of the two models are combined and similarities and differences are discussed:

Similarities:

1. The overflow rate seems to be quite similar for all 3 hoppers, until the Miedema/Vlasblom/Camp approach reaches the scour phase. From this moment on the overflow rate increases rapidly.
2. It is obvious that at the end of the loading both models find the same amount of sand in all cases, since this matches the maximum loading capacity of the hopper in question. This observation explains the fact that the overflow losses of both models are almost the same at the time where the van Rhee simulation

stops (42 minutes for the Small hopper, 112 minutes for the Jumbo hopper and 137 minutes for the Mega hopper).

Differences:

1. The overflow losses in the van Rhee model are lower in the first phase, because in the Miedema/Vlasblom/Camp approach this occurs instantly, while the van Rhee approach considers the time the mixture needs to flow through the hopper and the effect of scour is very limited because a uniform flow velocity distribution over depth is assumed (leading to very low horizontal flow velocities) in this model. Only at the end of the loading stage the effect of the horizontal flow velocity on sedimentation becomes noticeable. For instance for the Small hopper the TDS loading curve is a straight line from the start of overflow up to 33 min after start dredging. After that time the loading rate decreases as a result of the increasing horizontal velocity. At t = 45 min the hopper is completely filled. Hence the influence of the velocity during the final loading stage is present for about 12 minutes.
2. In the 2DV model velocity distribution is not prescribed, but is determined by physics and depends on the inflow conditions. In general, due to the large density difference between the inflowing mixture and fluid already present in the hopper, density currents will develop. This will lead to a larger velocity close to the sand bed surface. Hence the effect of the flow velocity on sedimentation will be present from the start of dredging. This influence does not increase much during loading. The effect is more spread out over the loading cycle. The loading rate decreases gradually, but remains on a reasonable level unto the moment that the hopper is fully loaded. In the Miedema/Vlasblom/Camp loading rate reduces to zero at full load..
3. If optimum loading time is considered, the two models differ in that the van Rhee model gives 43, 112 and 137 minutes, while this will be around 38, 99 and 120 minutes in the Miedema/Vlasblom/Camp approach. Both models start with a hopper full of water, so this should be considered. The overflow losses in the final phase of the loading process are similar for both models.

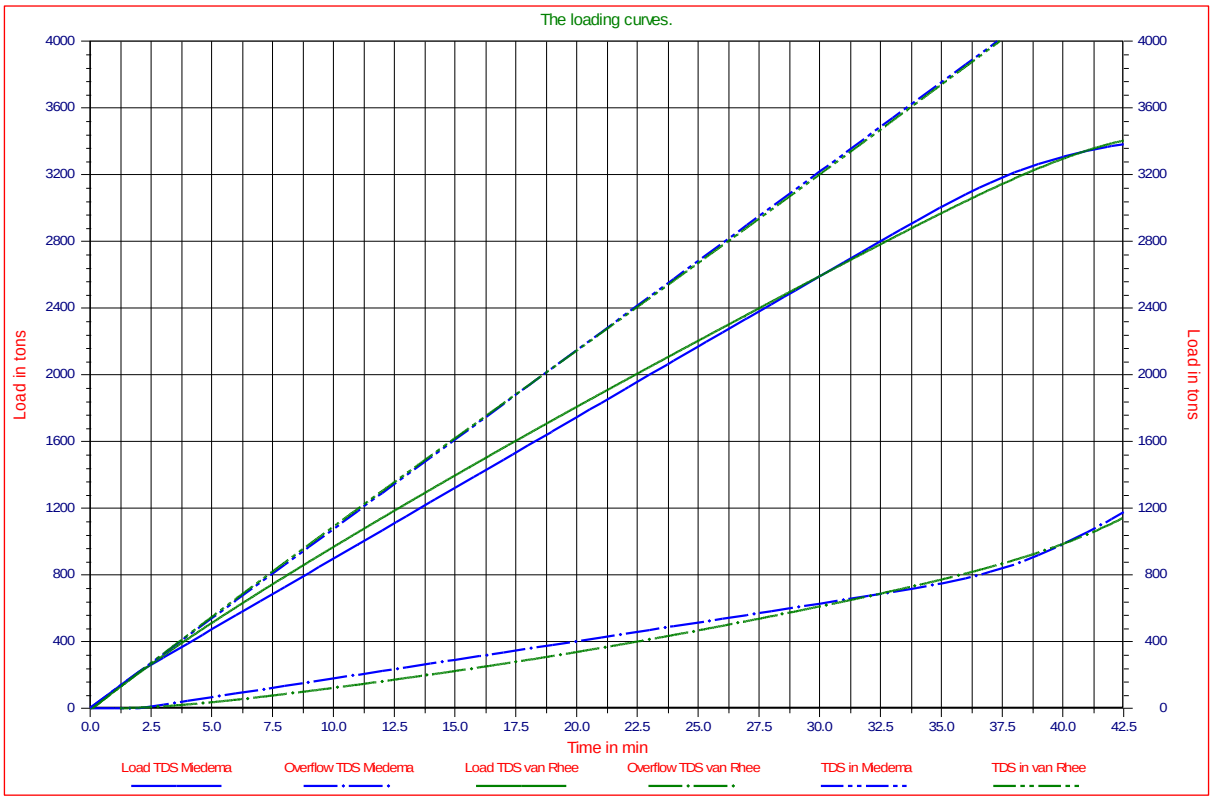

Figure 10-73: Comparison of the two models for the Small hopper.

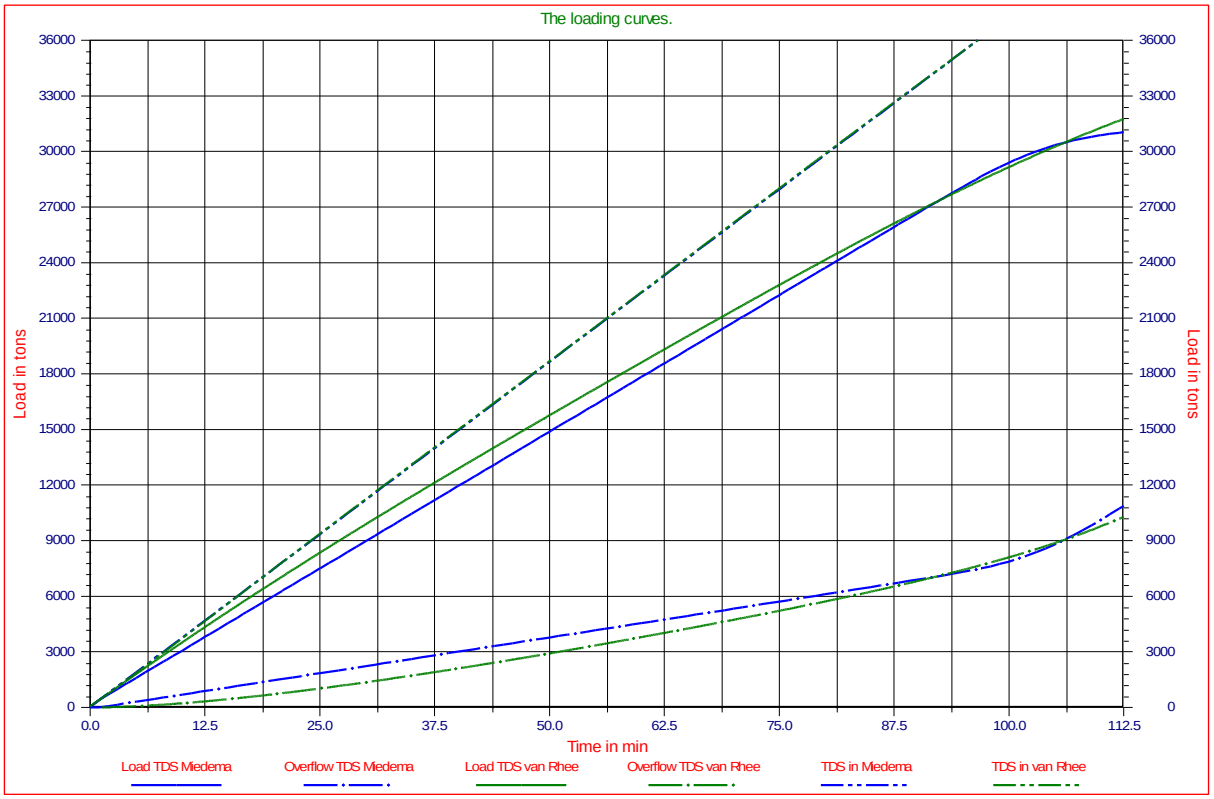

Figure 10-74: Comparison of the two models for the Jumbo hopper.

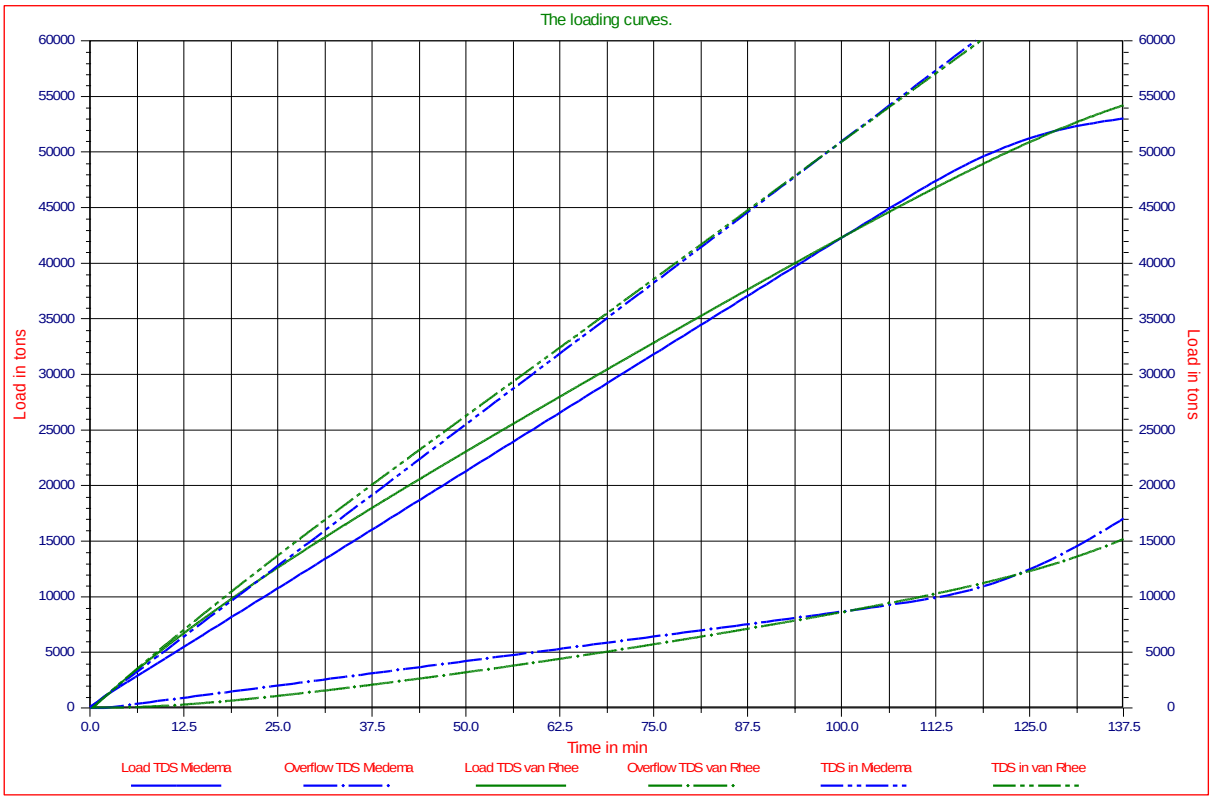

Figure 10-75: Comparison of the two models for the Mega hopper.

10.13.5. Conclusions

- The two models give the same magnitude for the overflow losses, but the shapes of the curves are different due to the differences in the physical modeling of the processes.
- Due to the lower losses the computed optimal loading time will be shorter for the Miedema/Vlasblom /Camp approach.
- The strong point of the van Rhee model is the accurate physical modeling, giving the possibility to model the geometry of the hopper in great detail, but also describing the physical processes in more detail.
- The van Rhee model is verified and validated with model and prototype tests and can be considered a reference model for other models.
- The strong point of the Miedema/Vlasblom/Camp model is the simplicity, giving a transparent model where result and cause are easily related.

10.14. A Sensitivity Analysis of the Scaling of TSHS's.

The loading process of TSHD's contains a number of non-linearity's:

1. The real hopper load parameter will vary during the loading process.
2. The turbulence settling efficiency.
3. The behavior of the layer of water above the overflow.
4. The behavior of hindered settling.
5. The effective concentration in the hopper.
6. The so called storage effect.

Based on all these non-linearity's it is not expected that TSHD's can be scaled easily, however the research in this paper shows that with the right choice of scale laws the TSHD's can be scaled rather well.
4 TSHD's are chosen, derived from Miedema & van Rhee (2007), but adapted to the scale laws. With each of these TSHD's simulations are carried out in 4 types of sand, 400 µm, 250 µm, 150 µm and 100 µm sand.

10.14.1. Scale Laws.

To compare TSHD's of different dimensions scale laws have to be applied in order to create identical loading processes. Scale laws should be based on the physical and the operational processes that occur. Further the shape of the hopper should be identical and the relation with the flow should match. It is however also important to decide which parameter or parameters to choose for the comparison of the TSHD's. When can the conclusion be drawn that two hoppers with different dimensions behave identical. The main parameter that is chosen for this comparison are the cumulative overflow losses. The cumulative overflow losses are the overflow losses expressed as TDS (Tonnes Dry Solids) divided by the total amount of TDS that has entered the hopper, from the start of the loading process until the moment of optimum loading.
The first important parameter to consider is the hopper load parameter (HLP) as described in equation (10-137). Here the hopper load parameter without the effect of the bed rise velocity is considered, because the bed rise velocity changes during the loading process and would result in changing scale laws. As stated before, the hopper load parameter is the settling velocity of a grain that will settle for 100%. Larger grains will also settle for 100%, but smaller grains will settle with a smaller percentage.

$$v_o = s_o \cdot \frac{H_w}{L} = \frac{Q_{in}}{W \cdot L} \qquad \textbf{(10-137)}$$

If two TSHD's with different dimensions have the same hopper load parameter, it can be expected that under similar conditions, the momentary overflow losses are equal and thus also the cumulative overflow losses. However the hopper load parameter does not take into consideration the effects of turbulence efficiency, hindered settling, and the storage effect and so on.

A second scale law could be that the ratios between Length, Width and Height are identical. If a length scale λ is considered this gives:

$$\lambda = \frac{L_1}{L_2} = \frac{W_1}{W_2} = \frac{H_1}{H_2} \quad \textbf{and} \quad \frac{HLP_1}{HLP_2} = 1 \quad \textbf{and} \quad \frac{Q_1}{Q_2} = \lambda^2 \quad \textbf{and} \quad \frac{T_{f1}}{T_{f2}} = \frac{V_1 / Q_1}{V_2 / Q_2} = \lambda \qquad \textbf{(10-138)}$$

Because the hopper load parameter is considered to be a constant, the flow **Q** will scale with the square of the length scale λ. The filling time T_f, which is the time to fill the hopper up to the overflow level also scales with the length scale λ. To have similar processes for determining the optimum loading time, the travelling time, which is the sum of the sailing time to and from the dump area and the dumping time, should also be scaled with the length scale, assuming that the loading time is proportional to the filling time. Since the horizontal flow velocity in the hopper equals the flow **Q** divided by the width **W** and the height **H** of the hopper, the horizontal flow velocity is a constant and does not depend on the length scale. This also follows from the fact that the hopper load parameter is a constant. If it is assumed that the maximum line velocity in the suction pipes is a constant, for example 7 m/s and because the line velocity equals the flow velocity divided by 2 and divided by the cross section of one pipe, this implies that the pipe diameter should be proportional to the square root of the flow and thus be proportional to the length scale λ.
Because sand is difficult to scale and in reality the sand will be the same independent of the TSHD used, it is assumed that the sand is the same for all hopper sizes. This implies that the settling velocities are the same and looking at the equations (10-69) and (10-70) this means that the grain settling efficiency η_g does not depend on the

hopper size and the ratio v_s/s_o does not depend on the hopper size, since the horizontal flow velocity s_o does not depend on the hopper size. The resulting turbulence efficiency as calculated with equations (10-69) and (10-70) is thus not dependent on the hopper size, although it will change during the loading process.

10.14.2. The TSHD'S used.

Based on the scale laws and based on Miedema & van Rhee (2007), 4 TSHD's are chosen in a range from small to Mega. The main dimensions and additional parameters of these hoppers can be found in table 1 and 2.

Table 10-5: The main dimensions of the 4 TSHD's.

Hopper	Length (m)	Width (m)	Empty height (m)	Volume (m^3)	Design density (ton/m^3)	Maximum load (ton)	HLP (m/sec)
Small	40	10	5.0	2000	1.5	3000	0.008
Large	60	15	7.5	6750	1.5	10125	0.008
Jumbo	80	20	10.0	16000	1.5	24000	0.008
Mega	100	25	12.5	31250	1.5	46875	0.008

Table 10-6: Additional and derived quantities.

Hopper	Flow (m^3/sec)	Pipe diameter (m)	Filling time (min)	Sailing time (min)	Hydraulic diameter (m)	Reynolds number	Mixture density (ton/m^3)
Small	3.2	0.54	10.4	104	10	$0.64*10^6$	1.3
Large	7.2	0.81	15.6	156	15	$0.96*10^6$	1.3
Jumbo	12.8	1.08	20.8	208	20	$1.28*10^6$	1.3
Mega	20.0	1.35	26.0	260	25	$1.60*10^6$	1.3

Table 10-5 and Table 10-6 show a wide range of TSHD's from Small (2000 m^3) to Mega (31250 m^3) . As can be noted in the tables, the hopper load parameters are constant at 0.008 m/sec, which is the settling velocity of a grain a bit bigger than 100 µm. The design density of the TSHD's is chosen at 1.5 ton/m^3, which implies that the loading process will follow the Constant Tonnage Loading process. The total sailing and dumping time is chosen 10 times the filling time, which of course is arbitrary, but the resulting sailing times seem to be representative for the reality. The mixture density is chosen at 1.3 ton/m^3, which is high enough to take the influence of hindered settling into account. It should be noted that the Reynolds numbers of the horizontal flow in the hopper are not constant; the Reynolds numbers are proportional to the length scale λ. The question is whether or not this will influence the loading process. As stated before, it does not influence the turbulent settling efficiency, but it could influence the scour in the final phase of the loading process. Scour is influenced by the viscous friction of the fluid flowing over the bed. This friction depends on the relative roughness and the Reynolds number. The roughness of the sediment has the magnitude of the grain diameter which is in the range of 0.1-0.5 mm, while the hydraulic diameters of the 4 TSHD's are in the magnitude of 10-25 m. The largest relative roughness would occur for a 0.5 mm grain and a hydraulic diameter of 10 m, giving 0.0005/10=0.00005. The friction coefficient will be between 0.0175 and 0.0171, which hardly has an effect on the scour. Although there will always be some effect, it is not expected that this effect will have a big influence on the similarity of the loading processes of the 4 TSHD's. The sediment density is chosen at 1.9 ton/m^3, which means that the TDS is about 76% of the weight of the wet sediment.

For carrying out the simulations 4 grain distributions are chosen. All 4 grain distributions have a $\mathbf{d_{15}}$ for grains with a settling velocity smaller than the hopper load parameter in order to be sure there will be significant overflow losses. If grain distributions were chosen with almost 100% of the grains having a settling velocity above the hopper load parameter, this would result in very small cumulative overflow losses and a good comparison would be difficult. Table 10-7 gives the $\mathbf{d_{15}}$, $\mathbf{d_{50}}$ and $\mathbf{d_{85}}$ of the 4 grain distributions, while figure 12 shows the full PSD's.

Table 10-7: The characteristics of the 4 grain distributions.

	400 µm	250 µm	150 µm	100 µm
d_{15}	70 µm	80 µm	80 µm	50 µm
d_{50}	400 µm	250 µm	150 µm	100 µm
d_{85}	2000 µm	750 µm	300 µm	200 µm

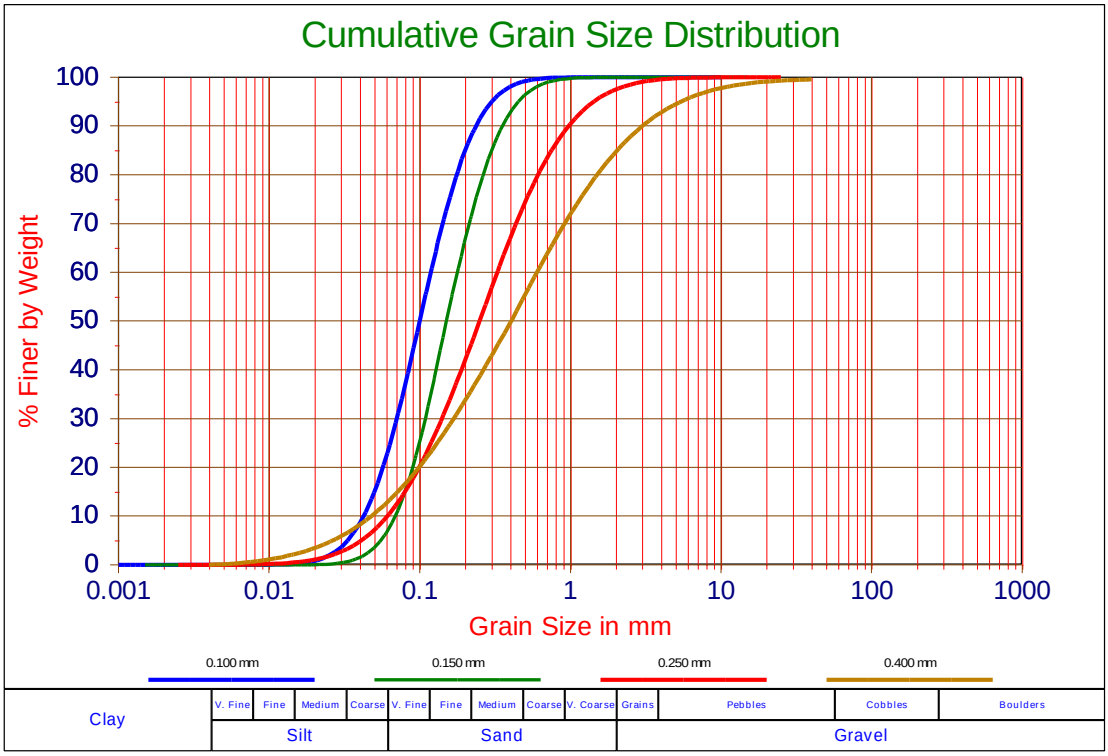

Figure 10-76: The 4 grain distributions.

10.14.3. Simulation Results.

The simulations of the loading process of the 4 TSHD's are carried out with software based on the model published by Miedema (2008A), including turbulence efficiency, hindered settling, the storage effect, the layer of water above the overflow and more. The results of these simulations are summarized in Table 10-8, Table 10-9, Table 10-10 and Table 10-11.

Table 10-8: The simulation results with the 0.400 mm sand.

400 µm sand	Loading time (min)	TDS (ton)	Overflow losses TDS (ton)	Cumulative overflow losses (%)	Production (ton/min)
Small	31.0	2174	476	18.0%	16.1
Large	46.5	7349	1594	17.8%	36.2
Jumbo	62.0	17440	3758	17.7%	64.5
Mega	77.5	34089	7313	17.7%	100.9

Table 10-9: The simulation results with the 0.250 mm sand.

250 µm sand	Loading time (min)	TDS (ton)	Overflow losses TDS (ton)	Cumulative overflow losses (%)	Production (ton/min)
Small	31.0	2146	503	19.0%	15.9
Large	46.5	7258	1685	18.8%	35.8
Jumbo	61.8	17218	3923	18.6%	63.7
Mega	77.3	33662	7651	18.5%	99.7

Table 10-10: The simulation results with the 0.150 mm sand.

150 µm sand	Loading time (min)	TDS (ton)	Overflow losses TDS (ton)	Cumulative overflow losses (%)	Production (ton/min)
Small	32.2	2104	645	23.5%	15.4
Large	48.2	7114	2149	23.2%	34.8
Jumbo	64.2	16887	3923	23.0%	62.0
Mega	80.3	33030	7651	23.0%	96.9

Table 10-11: The simulation results with the 0.100 mm sand.

100 µm sand	Loading time (min)	TDS (ton)	Overflow losses TDS (ton)	Cumulative overflow losses (%)	Production (ton/min)
Small	43.0	2111	1564	42.6%	14.3
Large	64.7	7145	5292	42.6%	32.3
Jumbo	86.0	16952	12452	42.3%	57.6
Mega	107.7	33149	24368	42.4%	90.1

To visualize the simulations, the graphs of the simulations of the Small TSHD and the Mega TSHD can be found in the Figure 10-77, Figure 10-78, Figure 10-79, Figure 10-80, Figure 10-81, Figure 10-82, Figure 10-83 and Figure 10-84. From these graphs and the above tables it will be clear that the cumulative overflow losses do not depend on the size of the TSHD in quantity and in shape op de loading and overflow curves. To understand the above tables and the following figures, they will be explained and discussed each.

Table 10-8, Table 10-9, Table 10-10 and Table 10-11 show the loading times in the second column, it is clear that the loading times are almost proportional to the length scale λ and they increase with increasing overflow losses. The finer the sand, the longer the loading time. The third column gives the TDS at the point of optimum loading. The TDS of a hopper filled with sediment is about 76% of the weight of the sediment, but since there is still some water on top of the sediment at the moment of optimum loading the TDS is a bit less. This means that the maximum TDS of the Small TSHD is 2280 tons, for the Large TSHD 7695 tons, for the Jumbo TSHD 18240 tons and for the Mega TSHD 35625 tons, so the assumption is correct. The TDS does not depend on the type of sand. The fourth column gives the overflow losses in tons TDS. Again TDS means, only the weight of the solids, excluding the pore water and the water on top of the sediment. The fifth column gives the cumulative overflow losses, which are almost constant for each type of sand. For the 400 µm sand about 17.8%, for the 250 µm about 18.7%, for the 150 µm sand about 23.2% and for the 100 µm sand about 42.4%. These cumulative overflow losses are the overflow losses in TDS, divided by the total amount of TDS that has entered the hopper. It is clear that the cumulative overflow losses do not seem to depend on the size of the TSHD, given the scale laws applied in the simulations. Apparently the scale laws applied are the correct scale laws for scaling TSHD's in order to get similar loading and sedimentation processes. It is interesting however to compare the cumulative overflow losses with the grain size distribution curves of the sands used. The hopper load parameter of 0.008 m/s matches a grain with a diameter of 0.112 mm. If the percentage of grains smaller than this diameter is considered and compared we the overflow losses, the following numbers are found. For the 400 µm sand, about 20% smaller than 0.112 mm and cumulative overflow losses of 17.8%, for the 250 µm sand, about 20% smaller than 0.112 mm and 18.7% cumulative overflow losses, for the 150 µm sand, about 26% smaller than 0.112 mm and 23.2% cumulative overflow losses and for the 100 µm sand, about 52% smaller than 0.112 mm and 42.4% cumulative overflow losses. Apparently, but not unexpected, the cumulative overflow losses have a strong relation with the percentage of the grains smaller than the grain diameter matching the hopper load parameter. There is however not a fixed relation, because the grains smaller than the diameter matching the hopper load parameter will still settle partially and this depends strongly on the steepness of the cumulative grain size distribution. In the examples given it is clear that the 400 µm sand and the 250 µm sand, both have about 20% smaller and both have a cumulative overflow loss of about 20%. The simulations however also take hindered settling, the effect of the concentration on the settling velocity, into account and in reality the TSHD might make turns, resulting in a more complicated loading process. The overflow losses will also depend on the concentration as will be discussed later. The last column shows the production and of course the production is decreasing if the cumulative overflow losses are increasing.

Figure 10-77 and Figure 10-78 give the loading curves of the Small and the Mega TSHD in order to see if not only the cumulative overflow losses are independent of the size of the TSHD, but also the shape of the loading curves. To understand these graphs the different curves are explained. The loading process starts with an empty hopper, so there is no water in the hopper. First for 10.4 minutes for the Small hopper and 26.0 minutes for the Mega hopper, the hopper is filled with mixture of 1.3 ton/m3. After that the loading continues until after about 22.4 minutes for the Small hopper and 57 minutes for the Mega hopper, the maximum load is reached as can be found in table 1, seventh column. After reaching the maximum load, the loading continues while the overflow is lowered in such a way that the total load in the hopper remains constant, replacing water above the sediment with sediment. After about 40 minutes for the Small hopper and about 100 minutes for the Mega hopper, the sediment level is so high and the layer of water above the sediment is so thin, that very high flow velocities occur above the sediment, preventing the grains the settle and resulting in scour. After a short while hardly any grains will settle and the optimum loading point is reached. Continuing after this point will result in a decrease of production and is thus useless.

The black solid line at the top is the total load in the hopper and it is obvious that this line stays at the maximum load once this is reached. The blue solid line is the total volume in the hopper, it can be seen that after reaching the maximum load, the total volume is decreasing because the overflow is lowered. The dashed red line shows the tangent method to determine the optimum loading point. The dashed brown line shows the weight of the sediment in the hopper, including the weight of the pore water. At the end of the loading this line is just below the maximum load line, because there is still a layer of water above the sediment, which does not count in the sediment weight. The black solid straight line gives the amount of TDS that enters the hopper, so the sum of sediment TDS and overflow TDS should be equal to this line. The highest solid brown line is the amount of TDS in the hopper, while the lowest solid brown line is the sediment volume. Finally the solid red line gives the overflow losses in TDS. It can be seen that until the mixture in the hopper reaches the overflow level, there are no overflow losses. After the hopper is filled the overflow losses follow an almost straight line, which curves to a steeper line when scour starts to occur.
Although the scales of Figure 10-77 and Figure 10-78 are different, it is clear that the different loading curves have similar shapes, so not only the cumulative overflow losses are independent of the size of the hopper, also the momentary overflow losses are.

Figure 10-79 and Figure 10-80 show the loading curves including the storage effect. So what exactly is this storage effect? When grains enter the hopper, it can already be calculated which fraction of the grains will settle and which fraction of the grains will leave the hopper through the overflow. Figure 10-77 and Figure 10-78 are based on such a calculation. Grains that will leave through the overflow however, first have to travel through the hopper before they actually leave the hopper through the overflow. One can say that these grains are temporary stored in the hopper, the so called storage effect. This means that if suddenly the loading process would stop before the optimum is reached, there are more grains and thus TDS in the hopper then would follow from the Figure 10-77 and Figure 10-78. It also means that the overflow losses at such a moment would be less. The amount of grains that will leave the hopper, but are still inside, depends on the time it takes for a particle to move from the entrance to the overflow and this depends on the flow velocity. The flow velocity will increase when the sediment level increases and at the end of the loading cycle this velocity is so high that the storage effect can be neglected. In the Figure 10-79 and Figure 10-80 the top thick solid black lines show the amount of TDS in the hopper (compare with Figure 10-77 and Figure 10-78, these contain the same lines but solid brown). Just above the thick solid black lines are the thin solid green lines. The difference between the thick solid black line and the thin solid green line is the amount of TDS that will leave through the overflow, but has not yet left. The thin solid brown line below the thick solid black line show how many grains have already settled, the difference between the two lines is the amount of grains that will settle, but has not yet settled. Finally the thick solid black line at the bottom gives the overflow losses as have already been shown in Figure 10-77 and Figure 10-78. The thin red line, below this line give the amount of TDS that have already left the hopper.

Figure 10-81 and Figure 10-82 show the grain distribution curves of the 100 µm for the Small and the Mega TSHD. The original distribution is the lines with the dots. Left from these are the red lines which give the distribution of the grains leaving the overflow, on average from the start of the loading until the optimum loading point. Right from the original distribution is the solid green line, showing the average distribution in the hopper. It can be concluded that the grain distributions are similar for the Small and the Mega TSHD.

Figure 10-83 and Figure 10-84 show the influence of the concentration and the amount of water in the hopper at the moment the loading starts, on the cumulative overflow losses and the cumulative efficiency. The dot in both graphs shows the result of the simulation carried out. It is obvious that Figure 10-83 and Figure 10-84 show similar graphs. The lines in the graphs are determined by an equation, derived as an attempt to predict the overflow losses with just one equation. The green solid line shows the cumulative overflow losses when the hopper is completely empty at the start of the loading process. The blue line when the hopper is filled with 50% water and the red line when its filled with 100% water. The graph shows the overflow losses as a function of the mixture concentration. These graphs are still experimental, but give good tendencies of the overflow losses.

10.14.4. Conclusions & Discussion.

The question before this research started, was how do the cumulative overflow losses behave when TSHD's are scaled from small to very big. The second question was, are that scale laws that should be applied when scaling TSHD's in order to create similar or maybe even identical processes.

First the answer on the second question, there are scale laws that should be applied and the main law is, to keep the hopper load parameter constant and from there derive the scale laws for the flow and other dimensions, but don't scale the sand.
If the scale laws are applied correctly, the simulations show that scaling the TSHD has hardly any influence on the cumulative overflow losses and the loading processes are similar.
The overflow losses however depend strongly on the position of the grain diameter match the hopper load parameter in the particle size distribution diagram. The fraction of the sand with diameters smaller than this diameter has a very strong relation with the cumulative overflow losses.

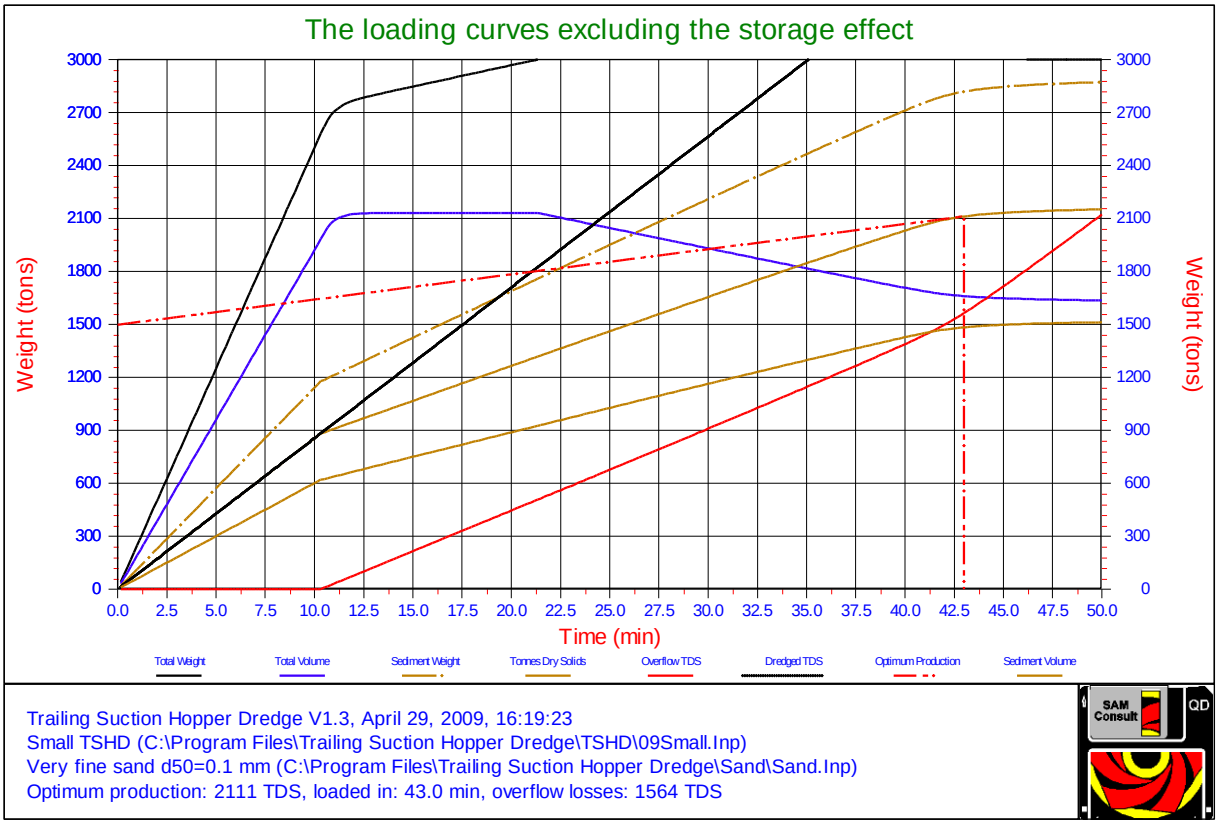

Figure 10-77: The loading curves for the Small TSHD.

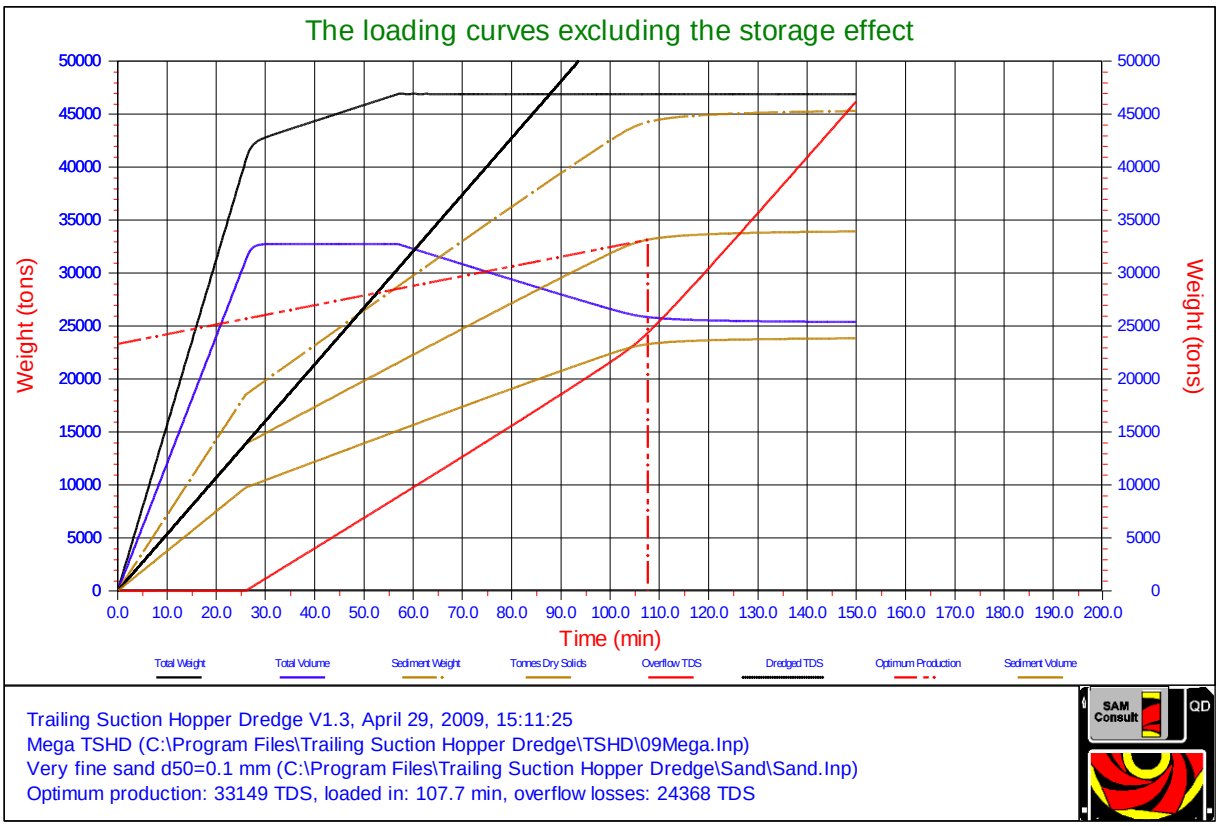

Figure 10-78: The loading curves for the Mega TSHD.

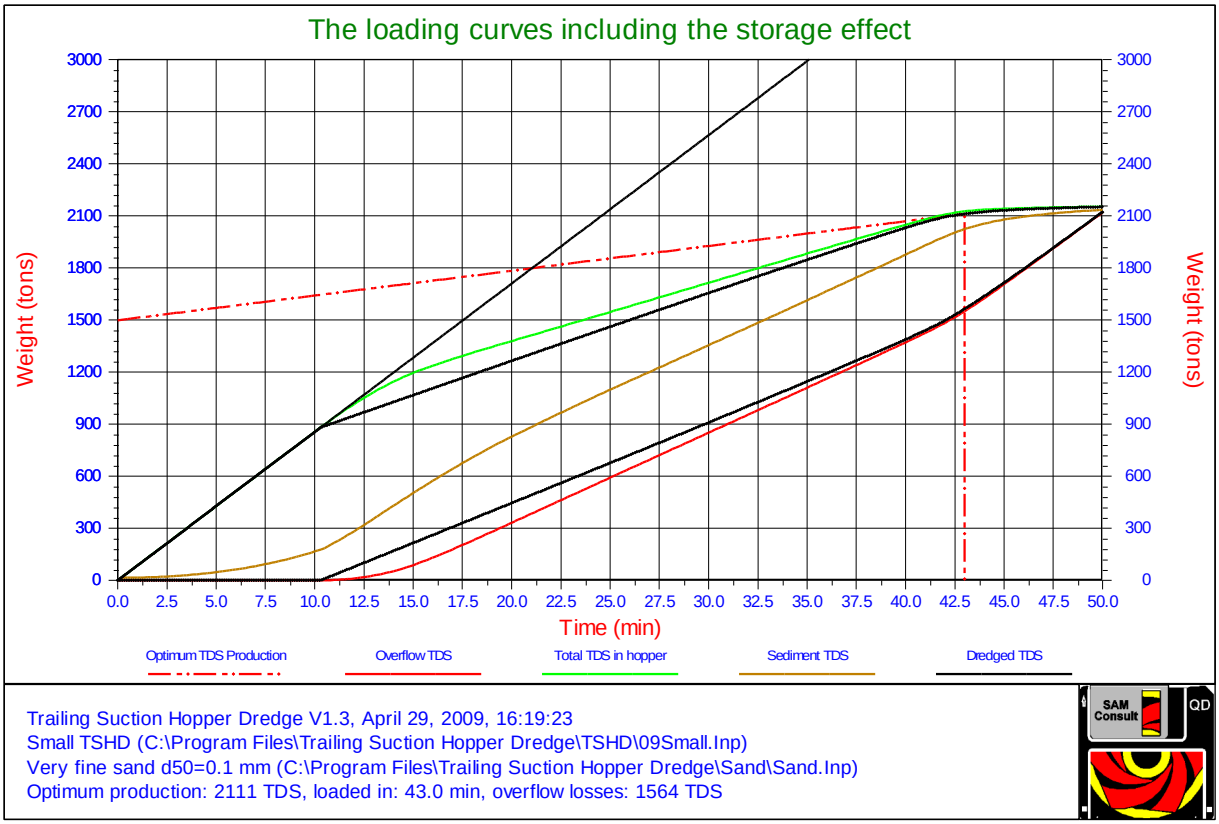

Figure 10-79: The loading curves including the storage effect for the Small TSHD.

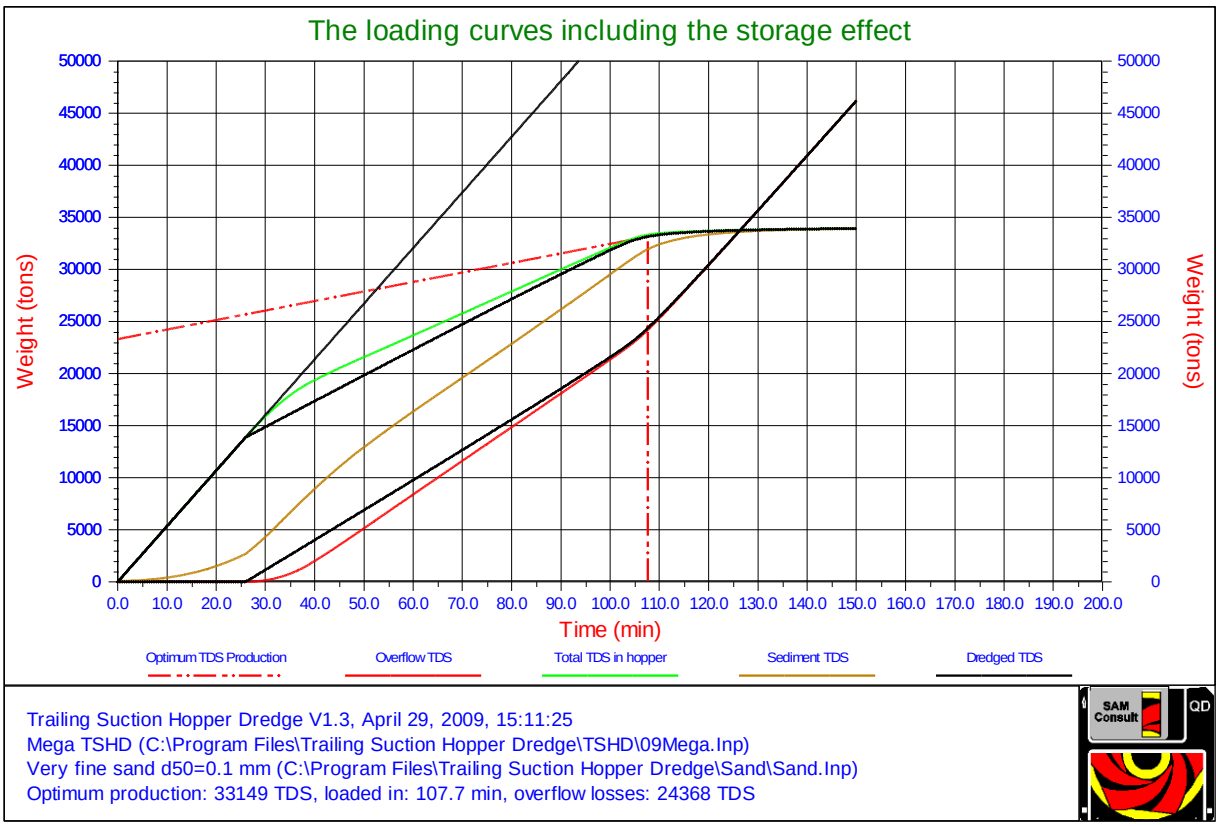

Figure 10-80: The loading curves including the storage effect for the Mega TSHD.

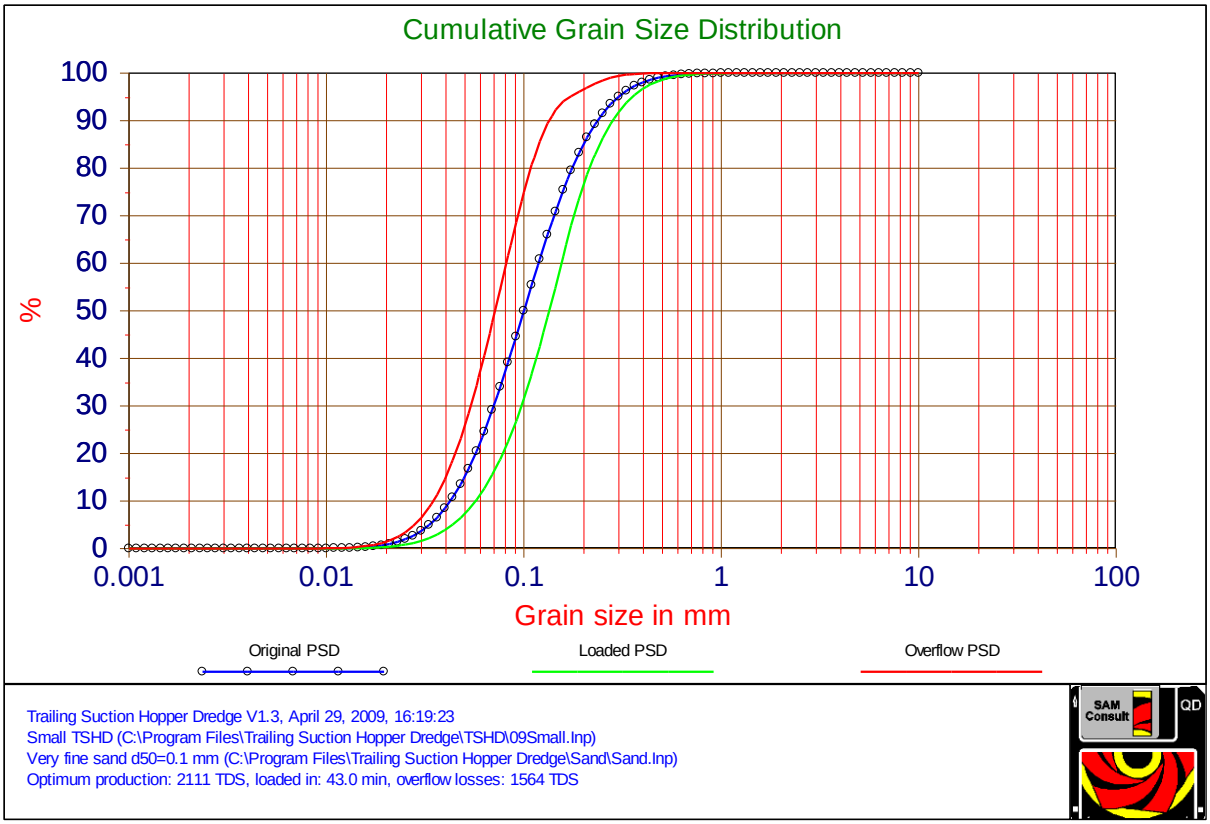

Figure 10-81: The grain distribution curves, original, overflow losses and sediment for the Small TSHD.

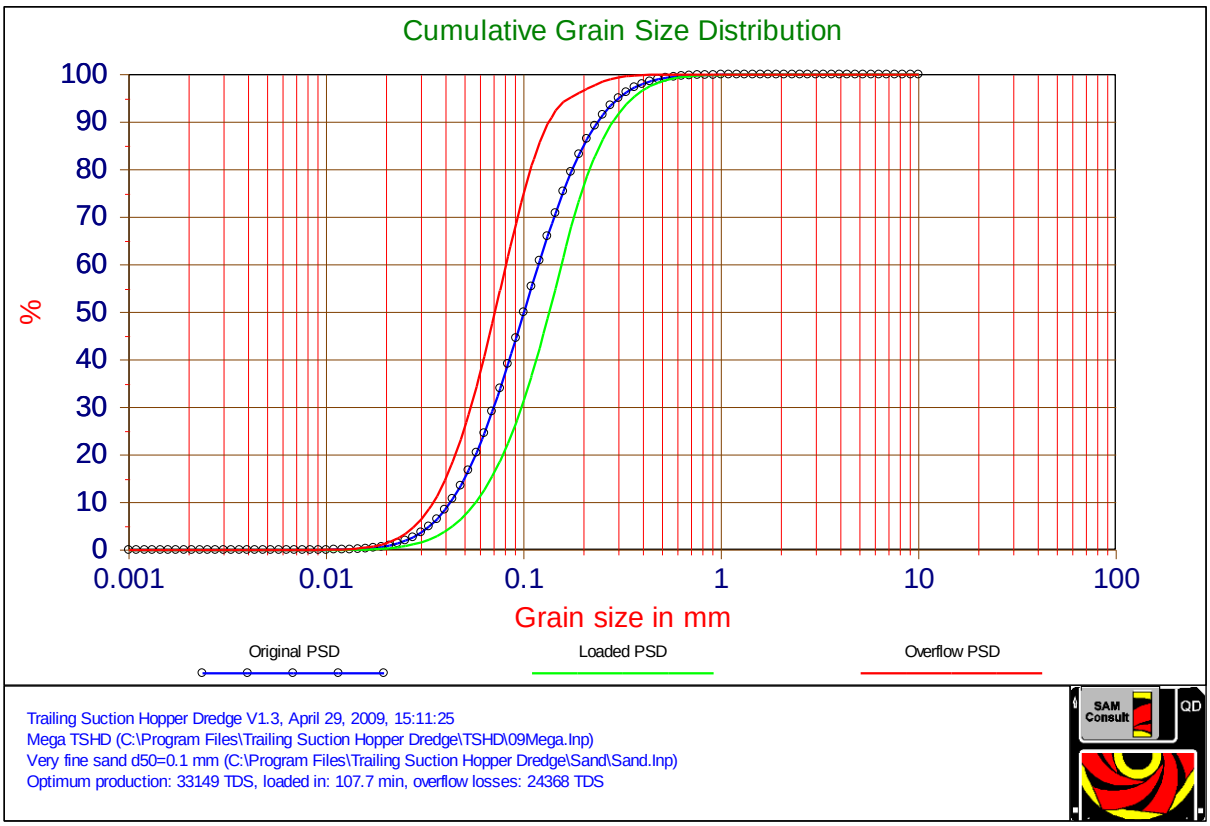

Figure 10-82: The grain distribution curves, original, overflow losses and sediment for the Mega TSHD.

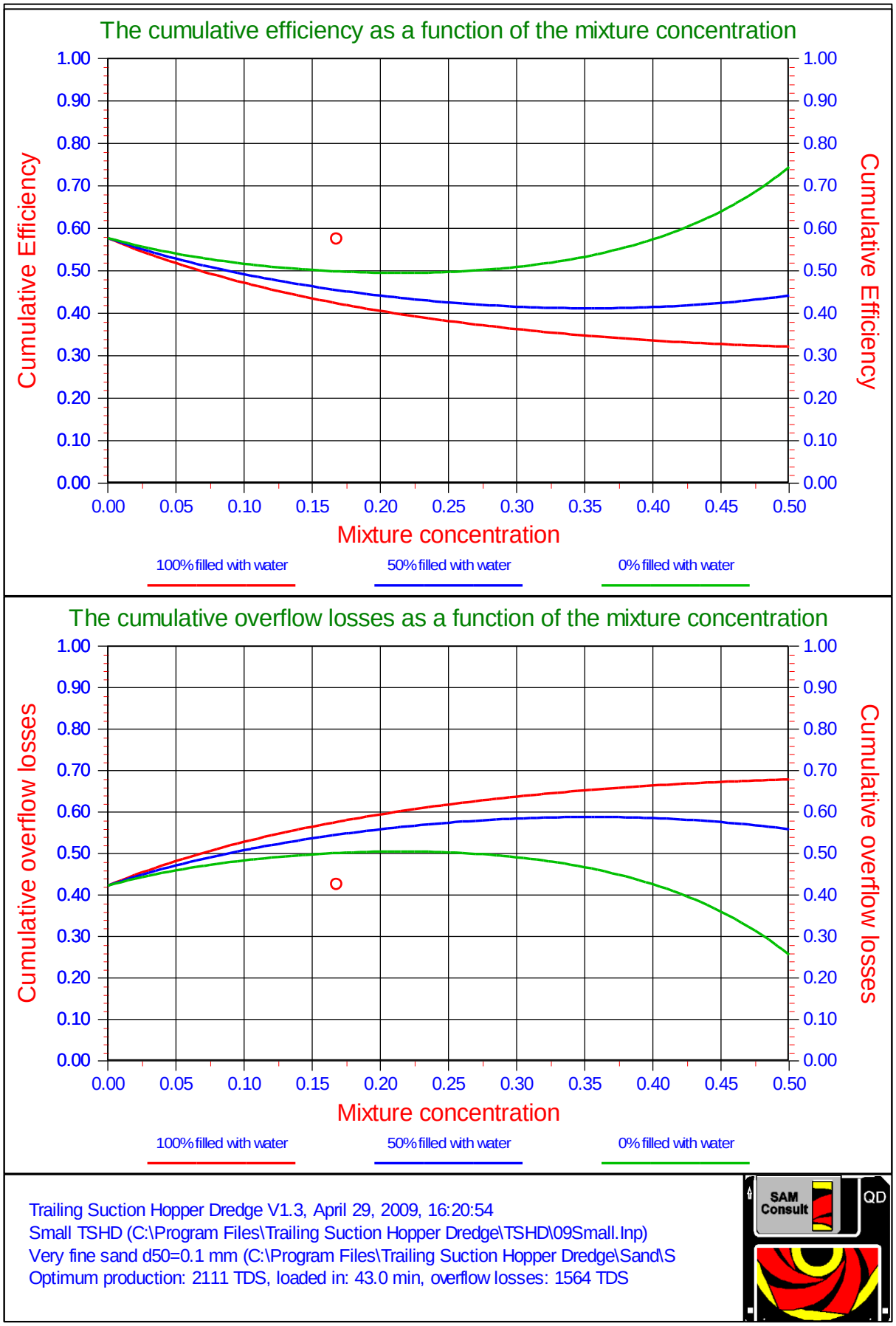

Figure 10-83: The overflow losses compared with an analytical model for the Small TSHD.

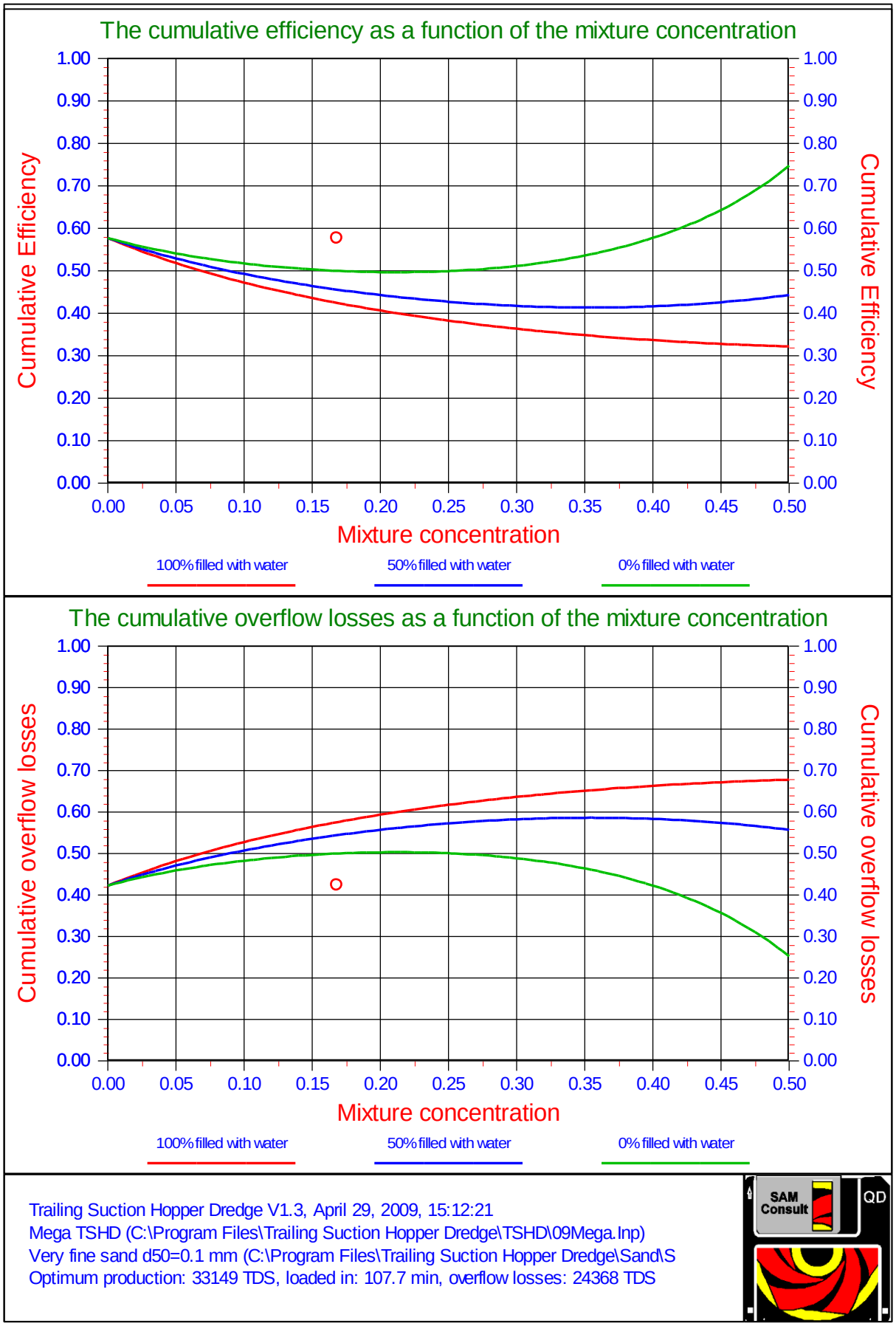

Figure 10-84: The overflow losses compared with an analytical model for the Mega TSHD.

10.16. Conclusions & Discussion.

The Camp and Dobbins model can be used to estimate loading time and overflow losses; however, the model should be tuned with measurements of the overflow rate in tons/sec as well as the particle size distribution in the overflow, as a function of time. The model can then also be used for the calculation of the decaying of the overflow plume in the dredging area.
If the model is used for the calculation of the production rate of the dredge a distinction has to be made whether the production is expressed in T.D.S./sec or in m^3/sec. In the first case the theory can be applied directly, while in the second case it has to be realized, that the overflow losses in T.D.S./sec do not always result in the same overflow loss in m^3/sec, since fine particles may situate in the voids of the bigger ones. The loss of fines does not reduce the total volume, but increases the void ratio. Although the fines leave the hopper in this case, they do not result in a reduction of the volume of the settled grains.
Those fractions which can be considered to apply to the overflow losses and those which do not, can be estimated from the difference between the real particle size distribution and the optimal particle size distribution, giving a maximum dry density, the so called Fuller distribution. If the gradient of the distribution curve for the fines is less steep then the corresponding gradient of the Fuller distribution, than that fraction of fines will not effectively contribute to the overflow losses if they are expressed in m^3/sec. In such a case, in-situ, the fines were situated in the voids of the courser grains. If the gradient is however steeper, the fines also form the grain matrix and the volume of settled grains will decrease if the fines leave the hopper through the overflow.
In the model a number of assumptions are made. Except from numerical values for the parameters involved, the Camp and Dobbins approach is used for the influence of turbulence, while separately the influence of scour is used instead of using it as a boundary condition.

The models of Miedema & Vlasblom (1996) and van Rhee (2002C) give the same magnitude for the overflow losses, but the shapes of the curves are different due to the differences in the physical modeling of the processes. Due to the lower losses the computed optimal loading time will be shorter for the Vlasblom /Miedema approach. The strong point of the van Rhee model is the accurate physical modeling, giving the possibility to model the geometry of the hopper in great detail, but also describing the physical processes in more detail. The van Rhee model is verified and validated with model and prototype tests and can be considered a reference model for other models. The strong point of the Miedema/Vlasblom model is the simplicity, giving a transparent model where result and cause are easily related.

One question before this research started, was how do the cumulative overflow losses behave when TSHD's are scaled from small to very big. The second question was, are that scale laws that should be applied when scaling TSHD's in order to create similar or maybe even identical processes.

First the answer on the second question, there are scale laws that should be applied and the main law is, to keep the hopper load parameter constant and from there derive the scale laws for the flow and other dimensions, but don't scale the sand. If the scale laws are applied correctly, the simulations show that scaling the TSHD has hardly any influence on the cumulative overflow losses and the loading processes are similar.
The overflow losses however depend strongly on the position of the grain diameter with respect to the hopper load parameter in the particle size distribution diagram. The fraction of the sand with diameters smaller than this diameter has a very strong relation with the cumulative overflow losses. A large silt fraction will increase these overflow losses.

Finally we have noted that the modified Hopper Load Parameter will reduce in magnitude compared with the unmodified Hopper Load Parameter. For particles with a settling efficiency greater than 1, this will not influence the settling efficiency, but for particles with a settling efficiency near 1 or smaller than 1, this may increase the settling efficiency slightly. So the sedimentation velocity in this respect has a positive effect on the cumulative settling efficiency. The current model seems to give rather accurate predictions. This conclusion is based on the comparison with the van Rhee model on one hand and the comparison with real data on the other hand.

Four effects are considered that were not part of the original Miedema & Vlasblom (1996) model, based on the Camp model. Those effects have been added later to the model by Miedema (2008A), (2008B), (2009A), (2009B), (2010) and Miedema & van Rhee (2007).

- Equations (10-25) and (10-29) give a good estimate of the thickness of the layer of water above the overflow level and Figure 10-15 proves that this estimate is accurate.
- The Shields approach is based on a fundamental force and moment equilibrium on grains and has been proven by many scientists in literature. Now the question is, which Shields curve to use. **Figure 10-85** shows 7 levels of erosion as defined by Delft Hydraulics (1972). To decide which of these 7 levels is appropriate for the

physics of the final stage of hopper loading, these physics should be examined. During this final stage, a high density mixture is flowing over the sediment. Part of the particles in this mixture flow will settle, part will not settle because the settling velocity is to low and part will not settle because of erosion and suspension. This process differs from the erosion process in the fact that there is not water flowing over the sediment, but a high density mixture. In fact the mixture is already saturated with particles and it is much more difficult for a particle to get eroded that in a clean water flow. One could call this hindered erosion. From the experience until now with the erosion model described (Miedema & van Rhee (2007)) and comparing it with other models, level 7 from Figure 10-85 should be chosen, this level is achieved by using **β=0.475**.

- The concentration of the mixture above the bed, often called the near bed concentration $\mathbf{c_b}$, can be estimated with equation **(10-139)**, and based on a black box approach. This concentration is used to determine the hindered settling effect on the settling velocity. Although equation **(10-139)** will not give the near bed concentration at a certain place at a certain time, it is derived for the entire hopper and loading cycle, it's a good estimate for determining the cumulative overflow losses.
- The storage, time delay or buffer effect can be implemented by using equation (10-30). Miedema & van Rhee (2007) compared both the Miedema & Vlasblom (1996) model, including the features as discussed here, and the sophisticated 2DV model, van Rhee (2002C). The result is shown in Figure 10-18. It is clear from this figure that there is a difference between the two methods if the storage effect is omitted in the Miedema & Vlasblom model, but including this storage effect gives almost the same results.
- It looks like the modified model gives results that match the van Rhee (2002C) model closely; of course the models are compared for just a few cases, specifically regarding the grain distributions used. This is remarkable because the physics of the two models are different. The van Rhee (2002C) model is based on the density flow as shown in Figure 10-6 and Figure 10-7, where there is an upward flow in the hopper. The modified model as presented here is based on the old Camp theory and assumes a uniform inflow of particles over the height of the hopper, as shown in Figure 10-20, a horizontal flow of the mixture and vertical downward transport of particles. So it seems that the dominating parameter in both models is the so called hopper load parameter, since this is the upward flow velocity in the van Rhee model and it is the settling velocity of a particle entering the hopper at the top and just reaching the sediment at the other end of the hopper in the Miedema & Vlasblom model.

Using the equations to determine the near bed concentration as derived here are based on known cumulative overflow losses and should thus not be used to predict overflow losses because that is a self-fulfilling prophecy. The modeling should be used to verify experiments where the near bed concentration is measured.
The use of the sedimentation or bed rise velocity to determine the sedimentation process when loading a TSHD with sand can only give good predictions if the correct near bed concentration is used and measured. Using the assumption that the near bed concentration equals the inflowing mixture concentration may lead to results that do not obey the conservation of mass principle.
Using the empirical equation (10-140) of van Rhee (2002C) to predict the overflow losses with the assumption that $\mathbf{c_b=c_{in}}$ is a good first approximation, but with some restrictions. It should be noted that van Rhee used the assumption of $\mathbf{c_b=c_{in}}$ to find this equation by curve fitting. The dimensionless overflow rate **S*** in this equation has to be considered to be the reciprocal of the settling efficiency, that is the correct physical meaning.
The analytical model derived in this paper matches this empirical equation, but has the advantage that sands with different grading can be taken into account.
The model derived for the sedimentation velocity, the near bed concentration and the overflow losses matches both the experiments as carried out by van Rhee (2002C) and Ooijens et al. (2001).
The model however is very sensitive for the values of the parameters **a** and **b** describing the PSD in equation (10-141), but with correct values, the model gives a very good prediction of the cumulative overflow losses.

$$\lambda = \frac{c_b}{c_{bed}\cdot\kappa} = \frac{c_b}{c_{in}} = \frac{\eta_{cum}}{\left(\eta_{cum}\cdot\kappa+\eta_p\right)} \qquad \textbf{(10-139)}$$

$$ov_{cum} = 0.39\cdot(S'^{*}-0.43) \qquad \textbf{(10-140)}$$

$$\log(d) = a\cdot p - b \qquad \textbf{(10-141)}$$

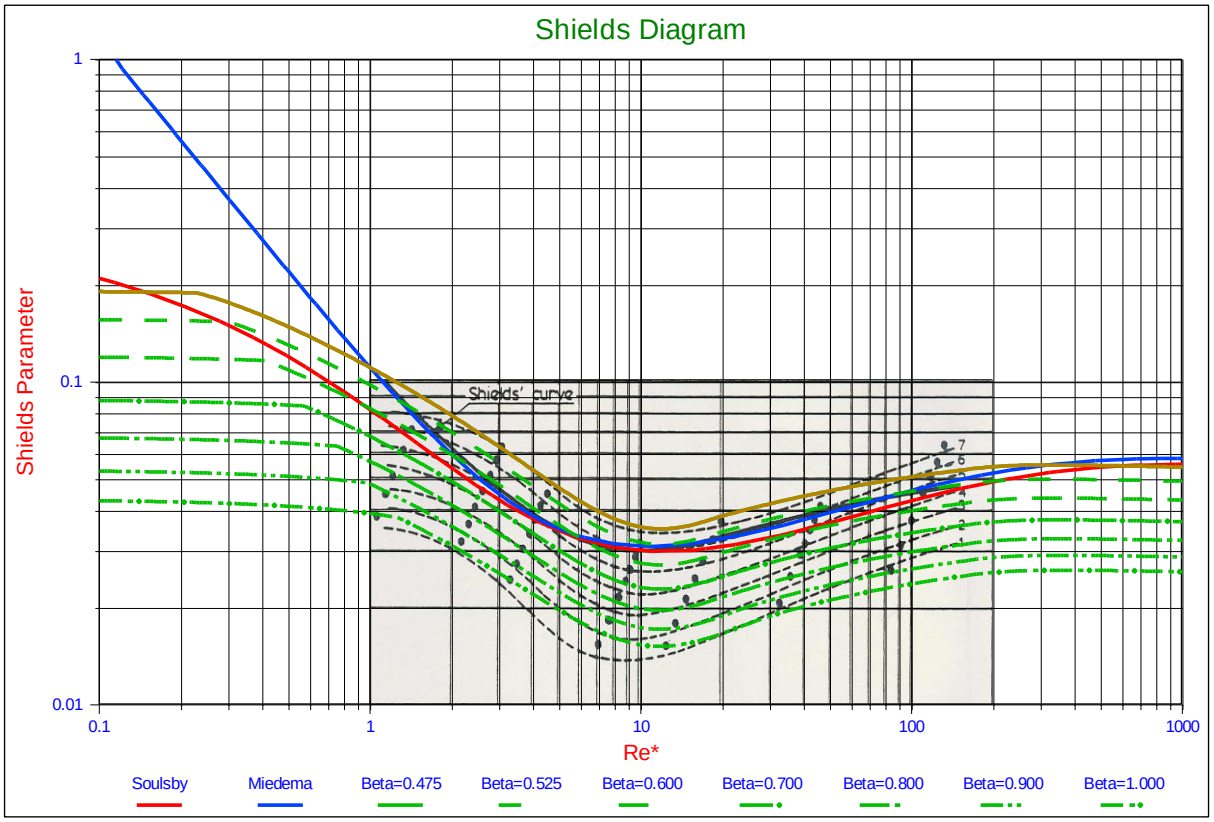

Figure 10-85: The 7 levels of erosion according to Delft Hydraulics (1972).

10.17. Nomenclature

a	Steepness of the PSD	**mm**
b	Offset of the PSD	**mm**
b	Width of the weir	**m**
c_b	Near bed concentration	**-**
c_{bed}	Bed/sediment concentration	**-**
c_{in}	Volume concentration	**-**
c_v , c_i	Volumetric concentration	**-**
C_e	Dimensionless discharge (contraction) coefficient with a value near 0.6.	**-**
C_d	Coefficient	**-**
C_D	Drag coefficient	**-**
C_L	Lift coefficient	**-**
d	Grain diameter	**mm**
d_o	Grain diameter matching the hopper load parameter	**mm**
d_{50}	Grain diameter at 50% of PSD	**mm**
d_s	Grain diameter (scour)	**m**
F_D	Drag force	**kN**
F_L	Lift force	**kN**
F_w	Submerged weight	**kN**
g	Gravitational constant (9.81)	**m/sec^2**
h	Height	**m**
h	is the overfall height (measured about a distance of 5·h upstream from the crest)	**m**
h_{max}	Maximum water layer thickness	**m**
H	Height of hopper	**m**
H_w	Height of the water above the sediment	**m**
H*	Dimensionless hopper load parameter	**-**
L	Length of basin	**m**
M	Height of the weir crest above the headwater bottom	**m**
n	Porosity	**-**

ov	Overflow losses	**-**
ov_{cum}	Cumulative overflow losses	**-**
p	Fraction of grains	**-**
p_o	Fraction of grains that settle partially (excluding turbulence)	**-**
p_{fs} , p_s	Fraction of grains that do no settle due to scour or fines	**-**
p_0	Atmospheric pressure	**kPa**
Q	Mixture flow	**m^3/sec**
$Q_{in, out}$	Mixture flow (in or out)	**m^3/sec**
Q_m	Mixture flow (mass)	**ton/sec**
R_d	Relative density	**-**
R	Reduction factor	**-**
s_o	Flow velocity in basin	**m/sec**
s_s	Scour velocity	**m/sec**
S*	Dimensionless overflow rate	**-**
S	Sedimentation flux	
t, T	Time	**sec**
TDS	Tonnes dry solid	**ton**
u_*	Shear velocity	**m/sec**
U_{cr}	Critical velocity above bed	**m/sec**
v	Mean velocity in the headwater this is equal to **Q/b (M + h)**	**m/sec**
v_c	Settling velocity including hindered settling	**m/sec**
v_o	Hopper load parameter	**m/sec**
v_s	Settling velocity of individual particle	**m/sec**
v_{sed}	Sedimentation/bed rise velocity	**m**
W	Width of basin	**m**
α	Fraction of hopper to be filled with mixture at start of loading process	**-**
α	Velocity factor	**-**
β	Power for hindered settling	**-**
β	Height factor	**-**
ε	Fraction of hopper filled with sediment when reaching the overflow	**-**
ρ_f	Density of fluid	**ton/m^3**
ρ_q	Density of particles (quarts=2.65)	**ton/m^3**
ρ_w	Density of water (1.025)	**ton/m^3**
ρ_m	Density of a sand/water mixture	**ton/m^3**
ρ_q	Density of quarts	**ton/m^3**
ρ_s	Density of sediment	**ton/m^3**
η	Settling efficiency	**-**
η_{cum}	Cumulative settling efficiency	**-**
η_g	Settling efficiency individual grain	**-**
η_b	Settling efficiency for basin	**-**
η_t	Turbulence settling efficiency for individual grain	**-**
η_p	Settling efficiency individual particle	**-**
λ	Concentration ratio c_b/c_{in}	**-**
λ	Viscous friction coefficient	**-**
κ	Concentration ratio c_{in}/c_{bed}	**-**
κ	Ratio mixture concentration versus bed concentration	**-**
μ	Settling velocity factor	**-**
μ	Friction coefficient	**-**
τ	Time constant	**sec**
ν	Kinematic viscosity	**St**
θ	Shields parameter	**-**

Chapter 11: Production Estimation of Water Jets and Cutting Blades in Drag Heads

11.1. Abstract.

Many models have been derived for the forces, power and specific energy of soil cutting, sand, clay and rock. Very often modern drag heads also use waterjets to excavate the soil, in this case sand. A good model to determine the production, power and specific energy of waterjets in a drag head has never been published.
In order to develop a model for the production and thus mixture density in a drag head, such a model is required. The mixture density and mixture velocity in its turn are required for existing hopper sedimentation models. Now these inputs are a best guess.
This paper shows the derivation and validation of a model to determine production, power and specific energy of the waterjets in a drag head. The model assumes that the jet production does not depend on the water depth and the assumption that for cutting sand at zero water depth, the specific energy is equal for a certain blade angle. The law of conservation of misery, in this case conservation of a minimum amount of energy required. By making the jet power and the non-cavitating cutting power equal, a useful equation is derived, including the sand soil mechanical parameters. A simplification of the dilatancy to permeability ratio makes the equation practical. With some data available, the model (equation) is validated/calibrated.
Based on the non-cavitational cutting process and an assumption regarding the equilibrium of moments on the visor, the cut production is added to the jet production, so the total production can be determined. Depending on the modeling, a maximum can be found or a slightly increasing production with increasing trailing speed is found.

11.2. Introduction.

For production estimation and overflow losses in dredging with a Trailing Suction Hopper Dredge (TSHD), one of the main inputs is the mixture density cq. concentration combined with the mixture velocity. Based on the mixture density and velocity, knowing the Particle Size Distribution (PSD), overflow losses and thus loading times can be determined (Miedema (1996), (2016)). So, the mixture density and velocity are essential for a good estimate. The mixture velocity can be estimated accurately enough, based on the pump pipeline layout and experience with the dredge. However, the mixture concentration cannot. The mixture concentration depends on the type of soil, but also on the excavation method. Old drag heads only used erosion to fluidize the sand. After that cutting blades were mounted inside the visor of the drag head. The visors are fixed or flexible. Later water jets were added in the heel of the drag head and more recently also jets were added into the cutting teeth. The latter is based on Miedema (1987) and de Jong (1988B), to neutralize the pore vacuum pressures. To estimate the mixture concentration (solids production), the exact drag head layout has to be known and models should be available for all the physical processes involved. The physics of the cutting process has been described in books and publications (Miedema (1987), (2014), however the physics of water jetting in sand not enough. Not enough means, that there does not exist a public model to determine the production in drag heads using water jets, including the soil mechanical parameters like the permeability or the porosity.
So, assuming the production is fully determined by water jets, a model is derived here based on the assumption that the energy required to excavate the soil, does not depend on the excavation method (the law of conservation of misery). Now let's compare sand cutting with blades and fluidizing sand with water jets. The energy required to cut 1 m^3 of sand depends on the blade geometry (blade height, blade width, blade angle and layer thickness), the soil mechanical parameters (permeability, porosity, dilatation and friction angles), operational parameters (water depth and cutting velocity) and whether the cutting is cavitational or non-cavitational. Since water jetting is never cavitational and since water jetting depends on the pressure difference over the nozzle and thus does not depend on the water depth, water jetting should be compared with non-cavitational sand cutting at zero meters water depth. Using a water depth for the cutting process would only introduce a correction factor of **10/(z+10)**. Some parameters are similar in both the cutting and the jetting process, while others are not applicable. Blade width and layer thickness can be replaced by drag head width and water jet penetration depth. Cutting velocity equals the trailing speed. Permeability and porosity (dilatation) are important in both processes. Blade height, blade angle and friction angles are not present in water jets and will become part of calibration constants. On the other hand, jet pressure (difference) and volume flow are not part of the cutting process but will be part of the jetting model.
Resuming, a water jetting model for a drag head is developed, based on jet pressure and flow, drag head width and trailing speed and sand permeability, resulting in the penetration depth. The specific energy resulting from the model is calibrated on a cutting configuration and model tests.

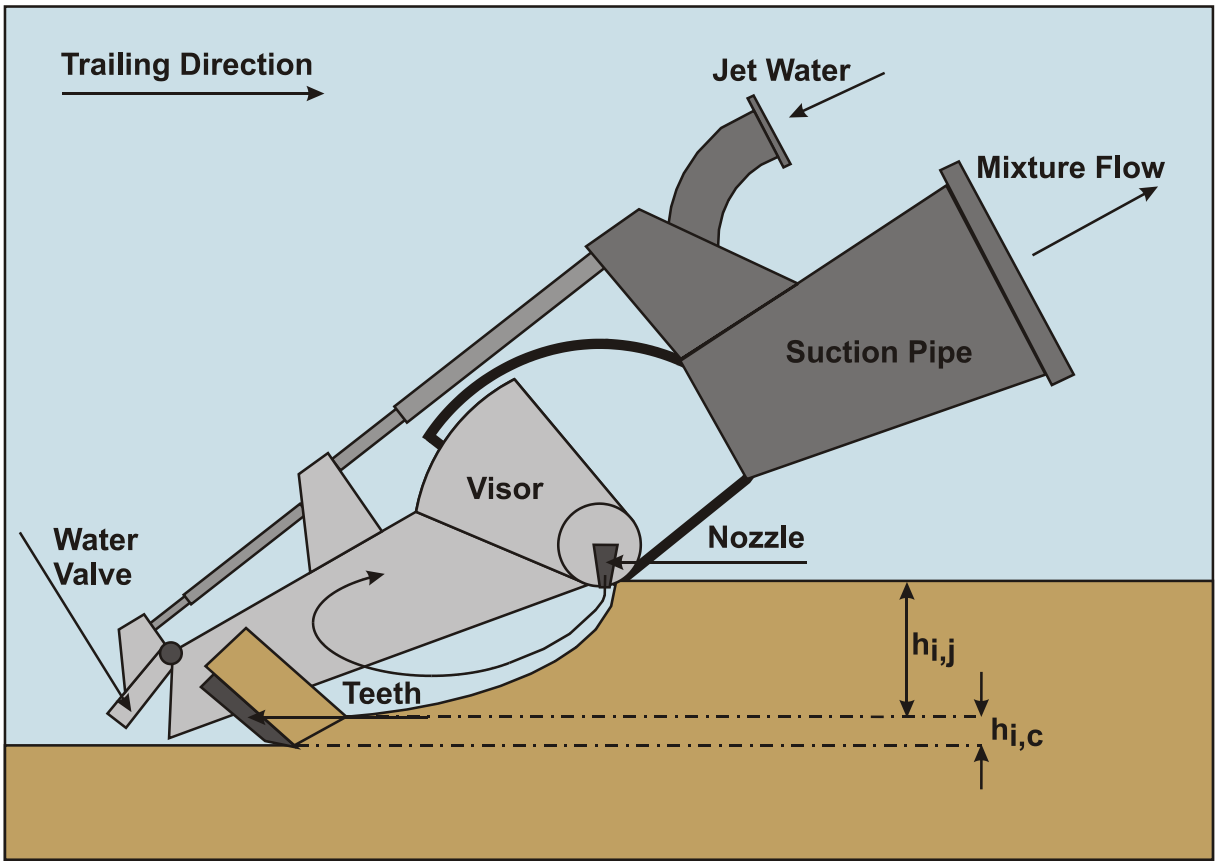

Figure 11-1: A draghead with visor, teeth and nozzles.

11.3. Waterjets in the Draghead.

Instead of cutting sand with a drag head, it is also possible to fluidize the sand with waterjets (see Figure 11-1 the nozzle). The fluidization process depends on the differential jet pressure and the jet flow. Where the jet flow can be determined by using the Bernouilli equation applied to the differential jet pressure and the internal cross section of the nozzle. The momentum of the flow determines the penetration depth of the water jet. If the jets are close enough and the penetration depth matches the cutting depth, the cutting process is replaced by a jetting process. Since the total efficiency (from diesel to jet) of the jetting process is much higher than the total efficiency (from diesel through propeller to drag head) of the cutting process and the required net jet power is also much less than the net cutting power, the installed power for water jet pumps is much less than the power used by the propulsion system to generate the cutting forces, resulting in a much smaller fuel consumption.
Waterjets however have the disadvantage that the penetration depth depends on the type of sand, especially on the permeability of the sand. A smaller value of the permeability will reduce the penetration depth. If the penetration depth is smaller than the layer thickness that would be cut by the blades in the drag head, the blades will still have to cut the difference. If the permeability is larger it's possible that more sand is fluidized than the amount entering the drag head based on the depth of the tip of the blades, so part of the jetting energy is wasted.
A model is presented here based on the assumption that the energy required to fluidize the sand is equal to the energy required to cut the sand at zero water depth with a small blade angle. Since the working principle of waterjets is based on the differential pressure over the nozzle of a waterjet, this does not depend on the water depth. The model assumes all the sand up to the penetration depth is fluidized, where in reality this may not be the case.

11.4. The Basic Model.

The situ production $\mathbf{Q_{s,dh}}$ of 1 drag head equals the layer thickness (in this case the penetration depth of the jets) $\mathbf{h_{i,j}}$ times the width of the blades $\mathbf{w_{dh}}$ times the trailing speed $\mathbf{v_c}$, similar to the production when cutting with blades.

$$\mathbf{Q_{s,dh} = h_{i,j} \cdot w_{dh} \cdot v_c} \qquad \textbf{(11-1)}$$

So, the penetration depth equals:

$$h_{i,j} = \frac{Q_{s,dh}}{w_{dh} \cdot v_c} \tag{11-2}$$

The situ production of 1 drag head also equals the installed jet pump power P_j divided by the specific energy E_{sp}:

$$Q_{s,dh} = \frac{P_{j,dh}}{E_{sp}} \tag{11-3}$$

This gives for the penetration depth:

$$h_{i,j} = \frac{P_{j,dh}}{E_{sp}} \cdot \frac{1}{w_{dh} \cdot v_c} \tag{11-4}$$

The flow Q_j leaving one waterjet, equals the jet water velocity v_j times the cross section of the jet opening, including the effect of the contraction coefficient α:

$$Q_j = v_j \cdot \frac{\pi}{4} \cdot \left(\alpha \cdot D_j\right)^2 \tag{11-5}$$

According to the Bernouilli law, the jet water velocity v_j can be expressed in terms of the pressure difference over the nozzle Δp_j, so:

$$v_j = \left(\frac{2 \cdot \Delta p_j}{\rho_l}\right)^{1/2} \tag{11-6}$$

The jet water flow of one nozzle is dependent on the differential pressure and the nozzle diameter, according to:

$$Q_j = \left(\frac{2 \cdot \Delta p_j}{\rho_l}\right)^{1/2} \cdot \frac{\pi}{4} \cdot \left(\alpha \cdot D_j\right)^2 \tag{11-7}$$

The jet water power for one nozzle equals the differential pressure Δp_j times the flow Q_j giving:

$$P_j = \Delta p_j \cdot Q_j = \Delta p_j \cdot \left(\frac{2 \cdot \Delta p_j}{\rho_l}\right)^{1/2} \cdot \frac{\pi}{4} \cdot \left(\alpha \cdot D_j\right)^2 \tag{11-8}$$

The jet power required for one nozzle is now:

$$P_j = \left(\frac{2}{\rho_l}\right)^{1/2} \cdot \frac{\pi}{4} \cdot \alpha^2 \cdot \Delta p_j^{3/2} \cdot D_j^2 \tag{11-9}$$

Giving for one nozzle, using the different values for the water density (1.025 ton/m^3) and the contraction coefficient (0.91):

$$P_j = 0.9 \cdot \Delta p_j^{3/2} \cdot D_j^2 \tag{11-10}$$

Since the jet pump process also has an efficiency (about 0.9) the installed jet pump power for 1 drag head containing n_j nozzles is:

$$P_{j,dh} = \frac{0.9 \cdot \Delta p_j^{3/2} \cdot D_j^2 \cdot n_j}{\eta_j} \approx \Delta p_j^{3/2} \cdot D_j^2 \cdot n_j \tag{11-11}$$

Now the situ production of 1 nozzle $\mathbf{Q_s}$ is:

$$\mathbf{Q_s = \frac{\Delta p_j \cdot \left(\frac{2 \cdot \Delta p_j}{\rho_l}\right)^{1/2} \cdot \frac{\pi}{4} \cdot \left(\alpha \cdot D_j\right)^2}{E_{sp}}} \qquad \textbf{(11-12)}$$

The penetration depth $\mathbf{h_i}$ is, using equation (11-1):

$$\mathbf{h_{i,j} = \frac{\Delta p_j \cdot \left(\frac{2 \cdot \Delta p_j}{\rho_l}\right)^{1/2} \cdot \frac{\pi}{4} \cdot \left(\alpha \cdot D_j\right)^2}{E_{sp} \cdot w_j \cdot v_c}} \qquad \textbf{(11-13)}$$

The question is now, which specific energy $\mathbf{E_{sp}}$ to use in this equation. Assuming the specific energy for jetting equals the specific energy for non-cavitating cutting, this gives (Miedema (2014)):

$$\mathbf{E_{sp} = c_1 \cdot \frac{\rho_l \cdot g \cdot h_{i,j} \cdot v_c \cdot \varepsilon}{k_m}} \qquad \textbf{(11-14)}$$

This gives for the penetration depth $\mathbf{h_i}$**:**

$$\mathbf{h_{i,j} = \frac{\Delta p_j \cdot \left(\frac{2 \cdot \Delta p_j}{\rho_l}\right)^{1/2} \cdot \frac{\pi}{4} \cdot \left(\alpha \cdot D_j\right)^2}{c_1 \cdot \rho_l \cdot g \cdot h_{i,j} \cdot v_c^2 \cdot w_j} \cdot \frac{k_m}{\varepsilon}} \quad \textbf{or} \quad \mathbf{h_{i,j}^2 = \frac{\Delta p_j \cdot \left(\frac{2 \cdot \Delta p_j}{\rho_l}\right)^{1/2} \cdot \frac{\pi}{4} \cdot \left(\alpha \cdot D_j\right)^2}{c_1 \cdot \rho_l \cdot g \cdot v_c^2 \cdot w_j} \cdot \frac{k_m}{\varepsilon}} \qquad \textbf{(11-15)}$$

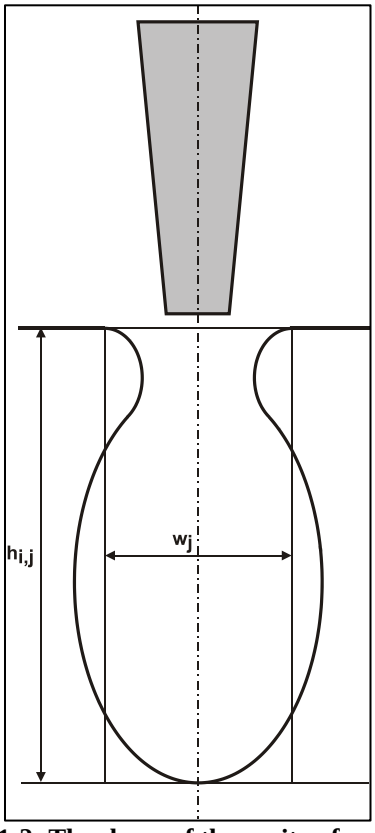

Figure 11-2: The shape of the cavity of a single jet.

11.5. Permeability and Dilatation.

The ratio of the mean permeability $\mathbf{k_m}$ to the dilatation $\boldsymbol{\varepsilon}$ in sand cutting, requires some investigation. The mean permeability is the average of the initial (situ) permeability $\mathbf{k_i}$ and the maximum permeability $\mathbf{k_{max}}$ after the sand has passed the shear plane in sand cutting. The dilatation is the volume increase due to the shearing of the sand. The mean permeability and the dilatation are related. An increase in dilatation also results in an increase of the maximum permeability and thus an increase of the mean permeability.

So, the mean permeability and the dilatation are:

$$\mathbf{k_m = \frac{k_i + k_{max}}{2} \quad and \quad \varepsilon = \frac{n_{max} - n_i}{1 - n_{max}}} \tag{11-16}$$

How to simplify this into known parameters (see also van Rhee (2015))?

The Kozeny-Carman equation is one of the most widely accepted and used equations of permeability as a function of the characteristics of the soil. The Kozeny-Carman equation (or Carman-Kozeny equation) is a relation used in the field of fluid dynamics to calculate the pressure drop of a fluid flowing through a packed bed of solids. It is named after Josef Kozeny and Philip C. Carman. This equation was originally proposed by Kozeny (1927) and was then modified by Carman (1937) and (1956) to become the Kozeny-Carman equation. It is not appropriate for either soil with effective size above 3 mm or for clayey soils. This equation is only valid for laminar flow. The equation is given as:

$$\mathbf{k = d_e^2 \cdot \frac{\gamma_l}{\mu_l} \cdot \frac{e^3}{1+e} \cdot C \quad or \quad k = 8.3 \cdot 10^{-3} \cdot \frac{g}{\nu_l} \cdot \frac{n^3}{(1-n)^2} \cdot d_{10}^2 \quad with: \quad \nu_l = \frac{\mu_l}{\rho_l} \; and \; \gamma_l = \rho_l \cdot g} \tag{11-17}$$

This equation holds for flow through packed beds with particle Reynolds numbers up to approximately 1.0, after which point frequent shifting of flow channels in the bed causes considerable kinetic energy losses. This equation can be expressed as "*flow is proportional to the pressure drop and inversely proportional to the fluid viscosity*", which is known as Darcy's law.
Now it is assumed that the relation between the permeability and the porosity follows Kozeny-Carman, although the absolute value of the permeability may be incorrect, due to the use of the $\mathbf{d_{10}}$, which is not necessarily true. This gives for the ratio of the final maximum permeability and the initial permeability (with $\mathbf{n_{max}}$ about 0.5):

$$\mathbf{\frac{k_{max}}{k_i} = \frac{\frac{n_{max}^3}{(1-n_{max})^2}}{\frac{n_i^3}{(1-n_i)^2}} = 0.5 \cdot \frac{(1-n_i)^2}{n_i^3}} \tag{11-18}$$

For the ratio of the mean permeability to the initial permeability it can be stated that:

$$\mathbf{\frac{k_{max} + k_i}{2 \cdot k_i} = \frac{\frac{n_{max}^3}{(1-n_{max})^2} + \frac{n_i^3}{(1-n_i)^2}}{2 \cdot \frac{n_i^3}{(1-n_i)^2}} = \frac{0.5 + \frac{n_i^3}{(1-n_i)^2}}{2 \cdot \frac{n_i^3}{(1-n_i)^2}} = \frac{1}{4} \cdot \frac{(1-n_i)^2}{n_i^3} + \frac{1}{2}} \tag{11-19}$$

Dividing this ratio by the dilatation gives the dilatation ratio (with $\mathbf{n_{max}}$ about 0.5):

$$\mathbf{\frac{k_{max} + k_i}{2 \cdot k_i \cdot \varepsilon} = \frac{\frac{1}{4} \cdot \frac{(1-n_i)^2}{n_i^3} + \frac{1}{2}}{\varepsilon} = \frac{\frac{1}{4} \cdot \frac{(1-n_i)^2}{n_i^3} + \frac{1}{2}}{\frac{n_{max} - n_i}{1 - n_{max}}} = \frac{\frac{1}{4} \cdot \frac{(1-n_i)^2}{n_i^3} + \frac{1}{2}}{1 - 2 \cdot n_i}} \tag{11-20}$$

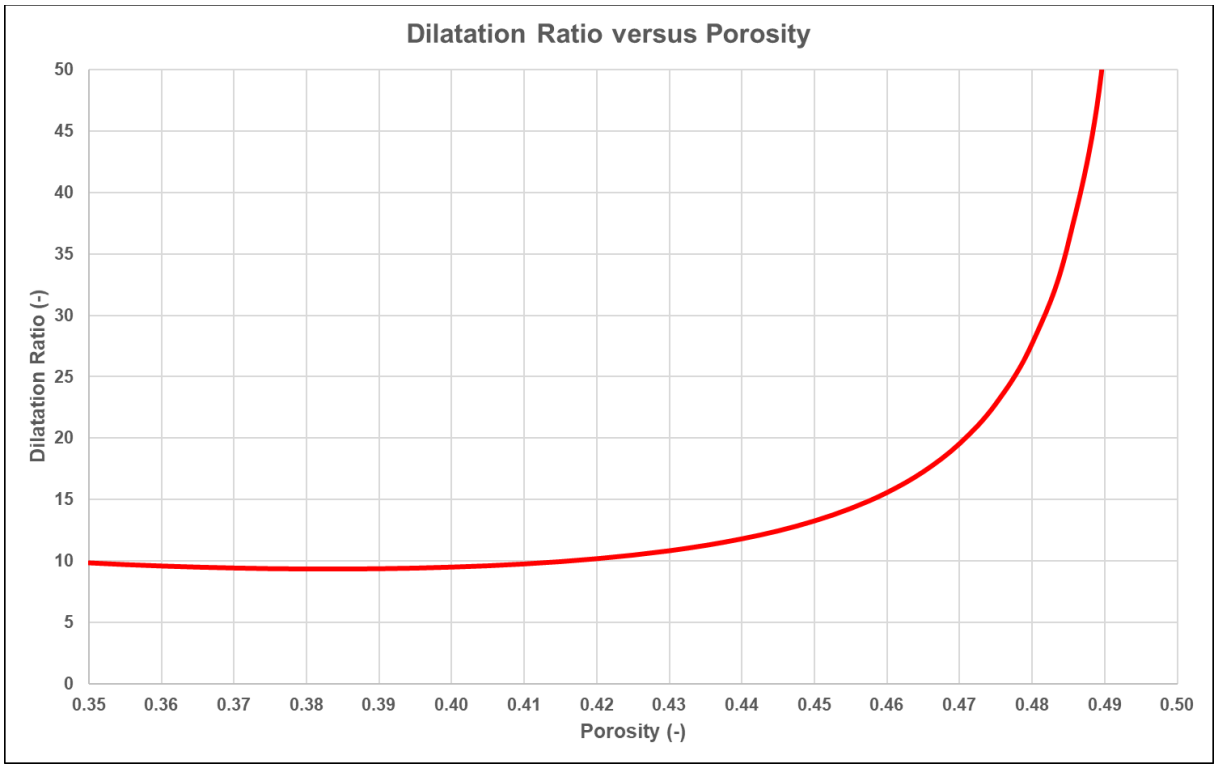

Figure 11-3. The dilatation ratio versus the porosity.

Figure 11-3 shows the behavior of equation (11-20), assuming a maximum porosity of 50%. From experience (Miedema (2014)) the maximum porosity will be close to this 50%. A slightly higher or lower maximum porosity will not significantly change the result of equation (11-20) if the initial porosity is small enough. If the initial porosity is closer to the maximum porosity of about 50%, the dilatation ratio increases, which will result in a larger penetration depth. Using a constant dilatation ratio of about 10 is accurate for small initial porosities and conservative with regard to production estimation for large initial porosities. In this case however, the penetration depth will exceed the cutting depth of the blades anyway. This cutting depth limits the production.
So, using the Kozeny Carman equation to determine the permeability, the following is found:

$$\frac{k_m}{\varepsilon} \approx 10 \cdot k_i \tag{11-21}$$

11.6. The Model Simplified.

There are still several unknowns in equation (11-15). The differential pressure Δp_j, nozzle diameter D_j, initial permeability k_i and trailing speed v_c are the inputs of the model. The contraction coefficient α has a value close to 0.91 The density of the water ρ_l has a value of about 1.025 ton/m^3. Since the jetting process does not know about blade angles, a c_1 value has to be chosen calibrated on experiments. A c_1 value of 0.12 is found, matching a 15° blade. Giving for the penetration depth, using the dilatation ratio:

$$h_{i,j}^2 = \frac{\Delta p_j \cdot \left(\frac{2 \cdot \Delta p_j}{\rho_l}\right)^{1/2} \cdot \frac{\pi}{4} \cdot \left(\alpha \cdot D_j\right)^2}{c_1 \cdot \rho_l \cdot g \cdot v_c^2 \cdot w_j} \cdot 10 \cdot k_i \tag{11-22}$$

The effective width of the fluidized area will be related to the penetration depth and the trailing speed according to (with v_1 the velocity where the width equals the penetration depth), see Figure 11-4:

$$w_j = \left(\frac{v_c}{v_1}\right)^{\beta} \cdot h_{i,j} \tag{11-23}$$

Substituting this in equation (11-23) gives:

$$h_{i,j}^2 = \frac{\Delta p_j \cdot \left(\frac{2 \cdot \Delta p_j}{\rho_l}\right)^{1/2} \cdot \frac{\pi}{4} \cdot \left(\alpha \cdot D_j\right)^2}{c_1 \cdot \rho_l \cdot g \cdot v_c^2 \cdot \left(\frac{v_c}{v_1}\right)^{\beta} \cdot h_{i,j}} \cdot 10 \cdot k_i \qquad \textbf{(11-24)}$$

This can be simplified to:

$$h_{i,j}^3 = 10 \cdot \frac{\left(\frac{2}{\rho_l}\right)^{1/2} \cdot \frac{\pi}{4} \cdot \alpha^2}{c_1 \cdot \rho_l \cdot g} \cdot \frac{\Delta p_j^{3/2} \cdot D_j^2 \cdot k_i}{v_c^{2+\beta} \cdot v_1^{-\beta}} = 8 \cdot \frac{\Delta p_j^{3/2} \cdot D_j^2 \cdot k_i}{v_c^{2+\beta} \cdot v_1^{-\beta}} \qquad \textbf{(11-25)}$$

Based on the experiments of van Rhee (1986), (1987A) and (1987B), β and v_1 are both about unity, giving:

$$h_{i,j} = 2 \cdot \frac{\Delta p_j^{1/2} \cdot D_j^{2/3} \cdot k_i^{1/3}}{v_c} \quad \text{and} \quad w_j = 2 \cdot \Delta p_j^{1/2} \cdot D_j^{2/3} \cdot k_i^{1/3} \qquad \textbf{(11-26)}$$

Giving a constant width. The situ production (fluidized area times trailing speed) of one nozzle can be determined by:

$$Q_s = h_{i,j} \cdot w_j \cdot v_c = 2 \cdot \frac{\Delta p_j^{1/2} \cdot D_j^{2/3} \cdot k_i^{1/3}}{v_c} \cdot v_c \cdot 2 \cdot \frac{\Delta p_j^{1/2} \cdot D_j^{2/3} \cdot k_i^{1/3}}{v_c} \cdot v_c = 4 \cdot \Delta p_j \cdot D_j^{4/3} \cdot k_i^{2/3} \qquad \textbf{(11-27)}$$

Apparently, the production of one nozzle is a constant and not depending on the trailing speed, given the assumption and simplification that β and v_1 are both about unity. This can be related to the jet power, including the jet process efficiency, with:

$$P_j = \Delta p_j^{3/2} \cdot D_j^2 \quad \Rightarrow \quad Q_s = 4 \cdot k_i^{2/3} \cdot P_j^{2/3} \qquad \textbf{(11-28)}$$

The equations use the differential pressure in kPa, the nozzle diameter in m and the permeability in m/s as well as the trailing speed. Equations found in literature often use other units like MPa, cm or mm and cm/s.
In this model some values are used for the contraction coefficient, the jet pump process efficiency, the water density and so on. Using different values may alter the equations slightly. The purpose here is to create rules of the thumb that are accurate enough.

11.7. Validation.

For the validation, experiments mentioned by de Jong (1988A), (1988B) and (1987) are used. These experiments were originally carried out by van Rhee (1986), (1987A) and (1987B), however these reports are confidential.
Experiments were carried out in a sand with a d_{50} of 190 µm, a nozzle diameter D_j of 30 mm, a pressure Δp_j of 6 bar and a permeability k_i of 0.00006 m/s. The resulting penetration depth and effective width are shown in:

Table 11-1. Experiments in a 190 µm sand.

v_c (m/s)	$h_{i,j}$ (m)	A (m^2)	w_j (m)		$h_{i,j}$ (m) eq (11-26)	w_j (m) eq (11-26)
0.49	0.35	0.0630	0.179		.378	.185
0.90	0.20	0.0375	0.188		.206	.185
1.67	0.13	0.0286	0.221		.111	.185

Experiments were also carried out in a sand with a d_{50} of 105 µm, a nozzle diameter D_j of 14 mm, a pressure Δp_j of 7.5 bar and a permeability k_i of 0.00008 m/s. The resulting penetration depth and effective width are shown in:

Table 11-2. Experiments in a 105 µm sand.

v_c (m/s)	$h_{i,j}$ (m)	A (m^2)	w_j (m)		$h_{i,j}$ (m) eq (11-26)	w_j (m) eq (11-26)
1.00	0.137	0.0160	0.116		.137	.137
1.55	0.100	0.0136	0.140		.088	.137
2.00	0.058	0.0074	0.128		.069	.137

Although the results from equation (11-26) (last two columns) do not match perfectly, the correlation is good enough for a rough production estimate, considering that the correlation is good around a trailing speed of 1 m/s as is often used in practice.

Figure 11-4. The effective width to penetration depth ratio, van Rhee (1986), (1987A) and (1987B) .

11.8. Drag Head Production.

Vlasblom (2003-2007) , in his lecture notes, mentioned an equation to determine the production of one jet (nozzle) based on the momentum of the jet nozzle flow, giving (the contraction coefficient is part of the proportionality constant):

$$Q_{m,q} = 0.1 \cdot \rho_l \cdot Q_j \cdot \sqrt{\frac{2 \cdot \Delta p_j}{\rho_l}} = 0.1 \cdot \rho_l \cdot \frac{\pi}{4} \cdot D_j^2 \cdot \sqrt{\frac{2 \cdot \Delta p_j}{\rho_l}} \cdot \sqrt{\frac{2 \cdot \Delta p_j}{\rho_l}} = 2 \cdot 0.1 \cdot \frac{\pi}{4} \cdot \Delta p_j \cdot D_j^2 \qquad (11\text{-}29)$$

This equation gives the quarts production by weight and not the volumetric production. In order to compare this production with equation (11-27), it has to be transformed to volumetric production. Assuming a porosity of 60% this gives:

$$Q_s = \frac{Q_{m,q}}{\rho_q \cdot (1 - n_i)} = \frac{2 \cdot 0.1 \cdot \frac{\pi}{4}}{\rho_q \cdot (1 - n_i)} \cdot \Delta p_j \cdot D_j^2 \approx 0.1 \cdot \Delta p_j \cdot D_j^2 \qquad (11\text{-}30)$$

It is interesting to check whether the equations derived here match or conflict with the Vlasblom equation and to analyze what is the difference.

Equation (11-27) as derived here, can be written as:

$$Q_s = 4 \cdot \left(\frac{k_i}{D_j} \right)^{2/3} \Delta p_j \cdot D_j^2 \qquad (11\text{-}31)$$

So:

$$Q_s = 0.1 \cdot \Delta p_j \cdot D_j^2 = 4 \cdot \left(\frac{k_i}{D_j} \right)^{2/3} \Delta p_j \cdot D_j^2 \quad \Rightarrow \quad 4 \cdot \left(\frac{k_i}{D_j} \right)^{2/3} = 0.1 \qquad (11\text{-}32)$$

For a 1-inch nozzle (0.0254 m) and a permeability of 0.0001 m/s, this matches. So apparently the Vlasblom equation is a good first estimate for an average sand with permeability of 0.0001 m/s and a 1 inch nozzle. If the ratio of the permeability to the nozzle diameter is a constant (0.004), the match is exact. For other combinations of nozzle diameter and permeability the factor 0.1 is not accurate enough.

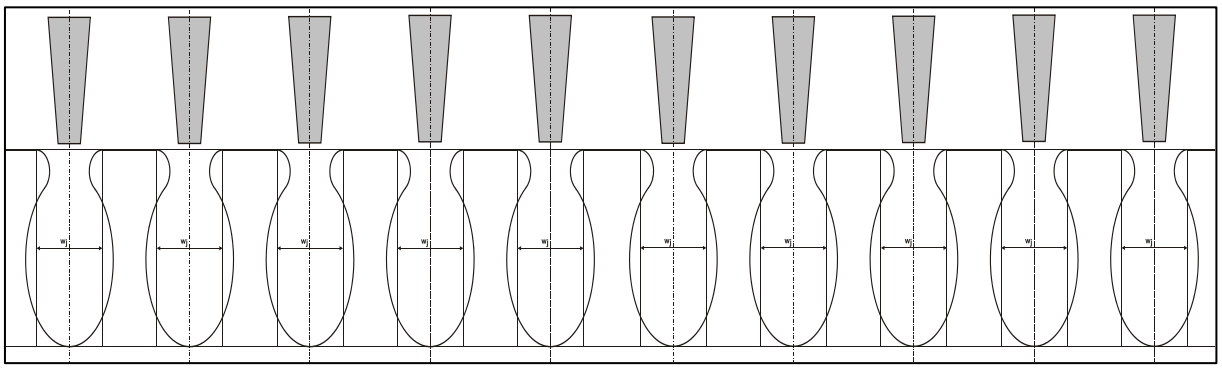

Figure 11-5: The cavity width is smaller than the distance between the nozzles.

In order to determine the production of a drag head as a function of the trailing speed, a number of cases have to be distinguished however. The effective width of the fluidized area of one nozzle is a constant given by:

$$w_j = 2 \cdot \Delta p_j^{1/2} \cdot D_j^{2/3} \cdot k_i^{1/3} \qquad (11\text{-}33)$$

If this width is smaller than the distance between the nozzles (see Figure 11-5), this width should be chosen, otherwise the distance between the nozzles according to (see Figure 11-6):

$$\begin{aligned} 2 \cdot \Delta p_j^{1/2} \cdot D_j^{2/3} \cdot k_i^{1/3} > \frac{w_{dh}}{n_j} \quad &\Rightarrow \quad w_j = \frac{w_{dh}}{n_j} \\ 2 \cdot \Delta p_j^{1/2} \cdot D_j^{2/3} \cdot k_i^{1/3} < \frac{w_{dh}}{n_j} \quad &\Rightarrow \quad w_j = 2 \cdot \Delta p_j^{1/2} \cdot D_j^{2/3} \cdot k_i^{1/3} \end{aligned} \qquad (11\text{-}34)$$

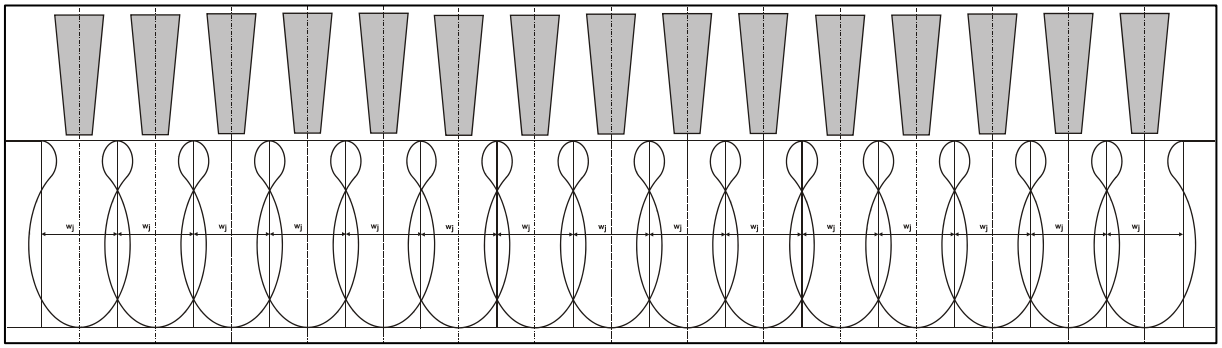

Figure 11-6: The cavity width equals to the distance between the nozzles.

In both cases the supposed width of the fluidized area is a constant, see also Figure 11-12. Now assuming that the tip of the blades have a penetration depth of h_c, with a certain maximum value $h_{c,max}$ and assuming that only the

sand above the tip of the blades will enter the suction system, that means that the production is linear with the trailing speed as long as the penetration depth h_i exceeds the maximum cutting depth $\mathbf{h_{c,max}}$, giving:

$$\mathbf{Q_s = h_{c,max} \cdot w_j \cdot v_c} \quad \text{and} \quad \mathbf{Q_{s,dh} = h_{c,max} \cdot w_j \cdot v_c \cdot n_j} \tag{11-35}$$

If the jet penetration depth h_i is smaller than the maximum cutting depth, here it is assumed that the cutting depth $\mathbf{h_c}$ equals the jet penetration depth $\mathbf{h_i}$, giving for the production:

$$\mathbf{Q_s = h_{i,j} \cdot w_j \cdot v_c} \quad \text{and} \quad \mathbf{Q_{s,dh} = h_{i,j} \cdot w_j \cdot v_c \cdot n_j}$$

or **(11-36)**

$$\mathbf{Q_s = 2 \cdot \Delta p_j^{1/2} \cdot D_j^{2/3} \cdot k_i^{1/3} \cdot w_j} \quad \text{and} \quad \mathbf{Q_{s,dh} = 2 \cdot \Delta p_j^{1/2} \cdot D_j^{2/3} \cdot k_i^{1/3} \cdot w_j \cdot n_j}$$

In this case it is obvious that the production is a constant, not depending on the trailing speed. It should be mentioned that in reality the tip of the blades will be below the penetration depth of the nozzles, resulting in a higher production. Equation (11-36) is thus conservative for the case where the jet penetration depth $\mathbf{h_i}$ is smaller than the maximum cutting depth $\mathbf{h_{c,max}}$.
The model is calibrated (based on the experiments of van Rhee (1986), (1987A) and (1987B)) for a differential pressure of 10 bar, a nozzle diameter of 2.54 cm (1 inch), a permeability of 0.0001 m/s, a maximum cutting depth of 0.3 m, a drag head width of 4 m, 16 nozzles, a suction pipe diameter of 0.762 m (30 inch) and a line speed of 6 m/s. The jet power required is about 1.03 MW. The resulting mixture density in the suction pipe is shown in Figure 11-7. For this particular case, the maximum production is reached at a trailing speed of 0.85 m/s.

Figure 11-7. Mixture density jet production versus the trailing speed.

The mixture concentration can be determined with:

$$\mathbf{C_{vs} = \frac{Q_{s,dh} \cdot (1 - n_i)}{Q_m} = \frac{h_{i,j} \cdot w_j \cdot v_c \cdot n_j \cdot (1 - n_i)}{\frac{\pi}{4} \cdot D_p^2 \cdot v_{ls}} = \frac{2 \cdot \Delta p_j^{1/2} \cdot D_j^{2/3} \cdot k_i^{1/3} \cdot w_j \cdot n_j \cdot (1 - n_i)}{\frac{\pi}{4} \cdot D_p^2 \cdot v_{ls}}} \tag{11-37}$$

The mixture density is now:

$$\rho_m = C_{vs} \cdot \rho_q + (1 - C_{vs}) \cdot \rho_l \qquad \textbf{(11-38)}$$

This mixture density is based only on the jet production. It is however the question how much this density will increase because of the cut production. To consider this a very simplified model is created. Suppose the drag head has a visor with a submerged weight of 5.5 ton and the visor can rotate freely, so no cylinder. The visor point of gravity has a horizontal distance of 1 m with respect to the visor bearing. The visor angle is considered almost constant, giving an angle between the horizontal and the line from the visor bearing to the tip of the blade of 30° and a line length of 2 m. Further, assuming a blade angle of 30°. The sand has an internal friction angle of 35° and an initial permeability of 0.0001 m/s. The ratio blade height to layer thickness cut is assumed to be 1.
Assuming the non-cavitational cutting forces can be determined with (Miedema (2014)):

$$F_h = \frac{c_1 \cdot \rho_l \cdot g \cdot v_c \cdot h_{i,c}^2 \cdot w_{dh} \cdot \varepsilon}{k_m} \quad \textbf{with:} \quad c_1 = 0.0427 \cdot e^{0.0509 \cdot \varphi}$$

$$F_v = \frac{c_2 \cdot \rho_l \cdot g \cdot v_c \cdot h_{i,c}^2 \cdot w_{dh} \cdot \varepsilon}{k_m} \quad \textbf{with:} \quad c_2 = 0.0343 \cdot e^{0.0341 \cdot \varphi} \qquad \textbf{(11-39)}$$

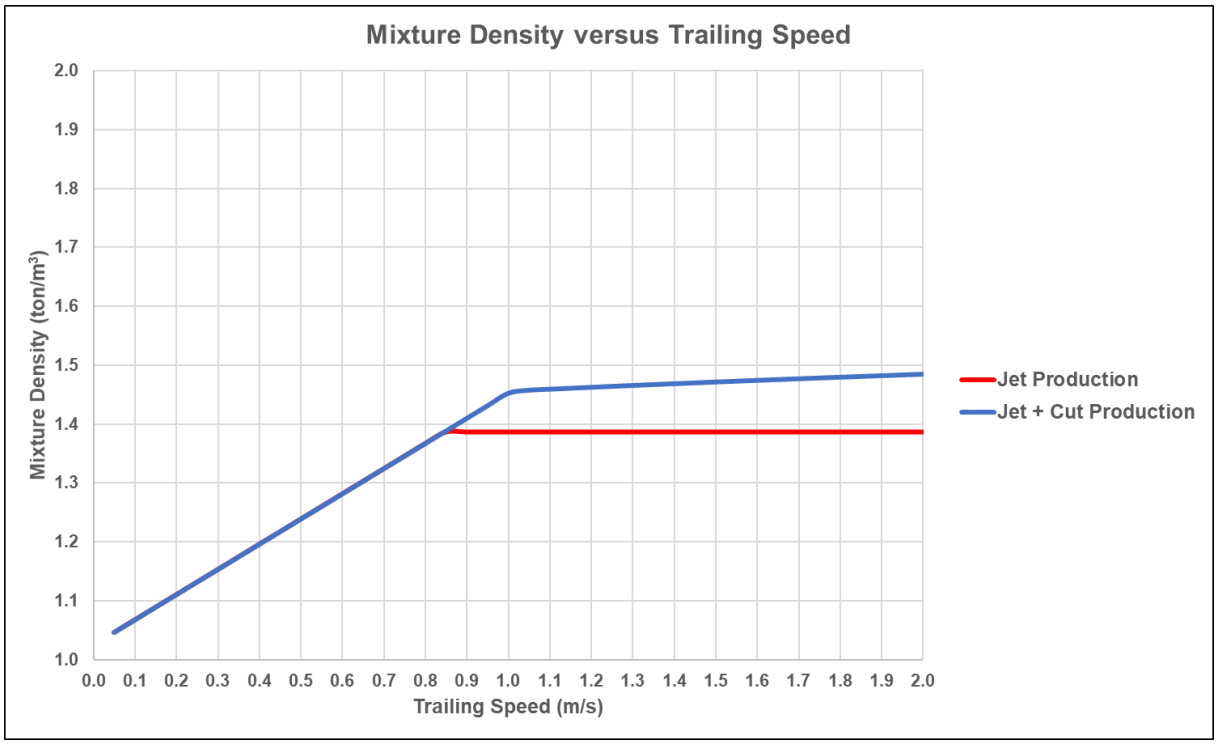

Figure 11-8. Mixture density jet + cut production versus the trailing speed, β=1.0, see equation (11-23).

Substituting equation (11-21) gives:

$$F_h = \frac{c_1 \cdot \rho_l \cdot g \cdot v_c \cdot h_{i,c}^2 \cdot w_{dh}}{10 \cdot k_i} \quad \textbf{and} \quad F_v = \frac{c_2 \cdot \rho_l \cdot g \cdot v_c \cdot h_{i,c}^2 \cdot w_{dh}}{10 \cdot k_i} \qquad \textbf{(11-40)}$$

Since the water density times the gravitational constant almost equals 10, this gives:

$$F_h = \frac{c_1 \cdot v_c \cdot h_{i,c}^2 \cdot w_{dh}}{k_i} \quad \textbf{and} \quad F_v = \frac{c_2 \cdot v_c \cdot h_{i,c}^2 \cdot w_{dh}}{k_i} \qquad \textbf{(11-41)}$$

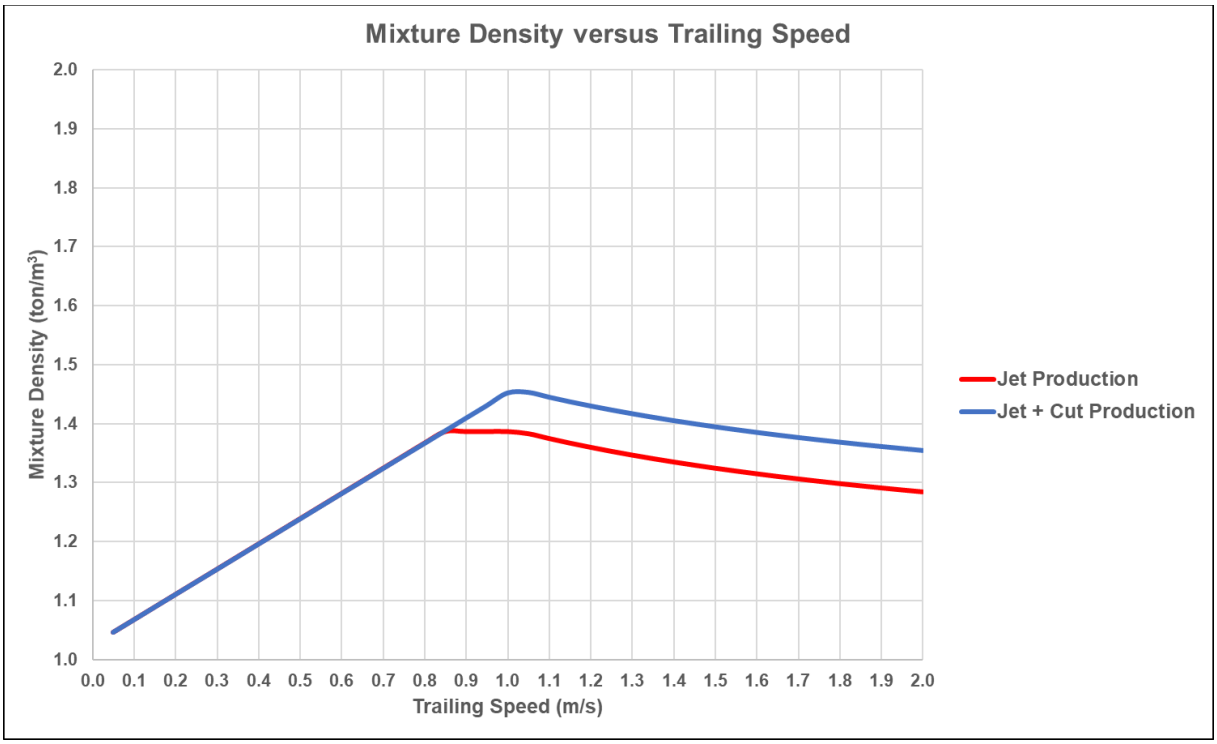

Figure 11-9. Mixture density jet + cut production versus the trailing speed, β=0.5, see equation (11-23).

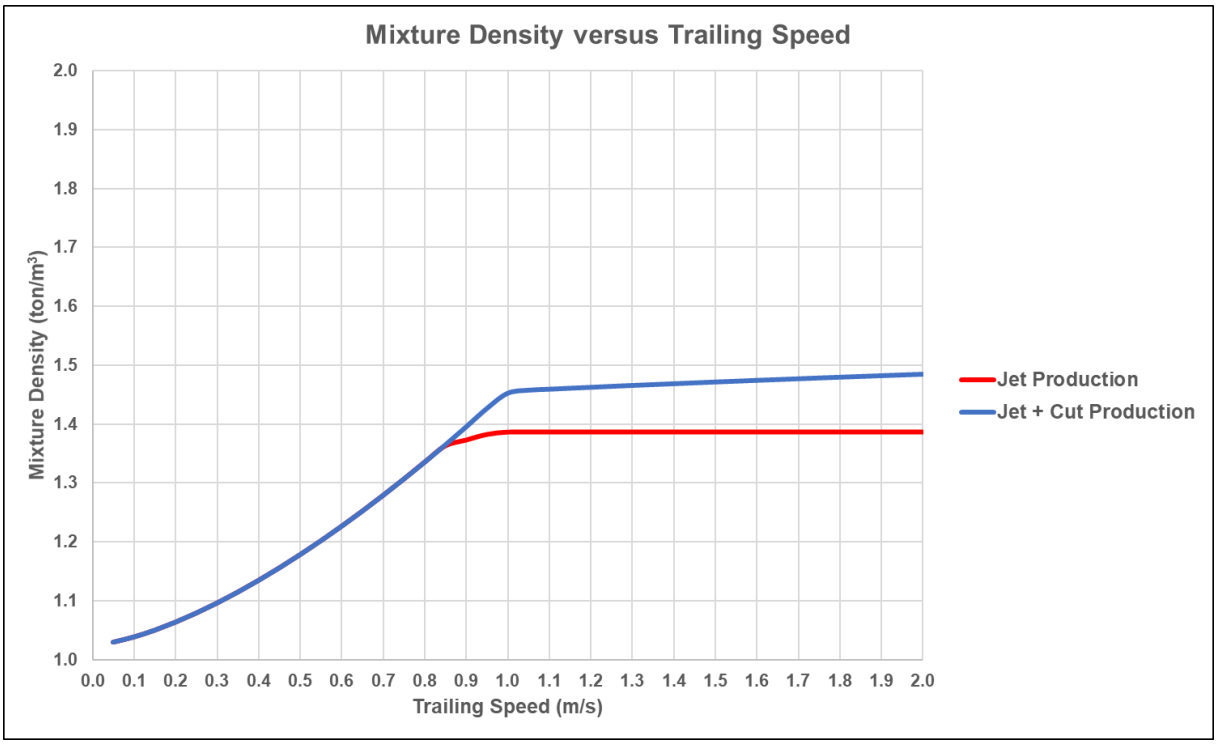

Figure 11-10. Mixture density jet + cut production versus the trailing speed, β=1.5, see equation (11-23).

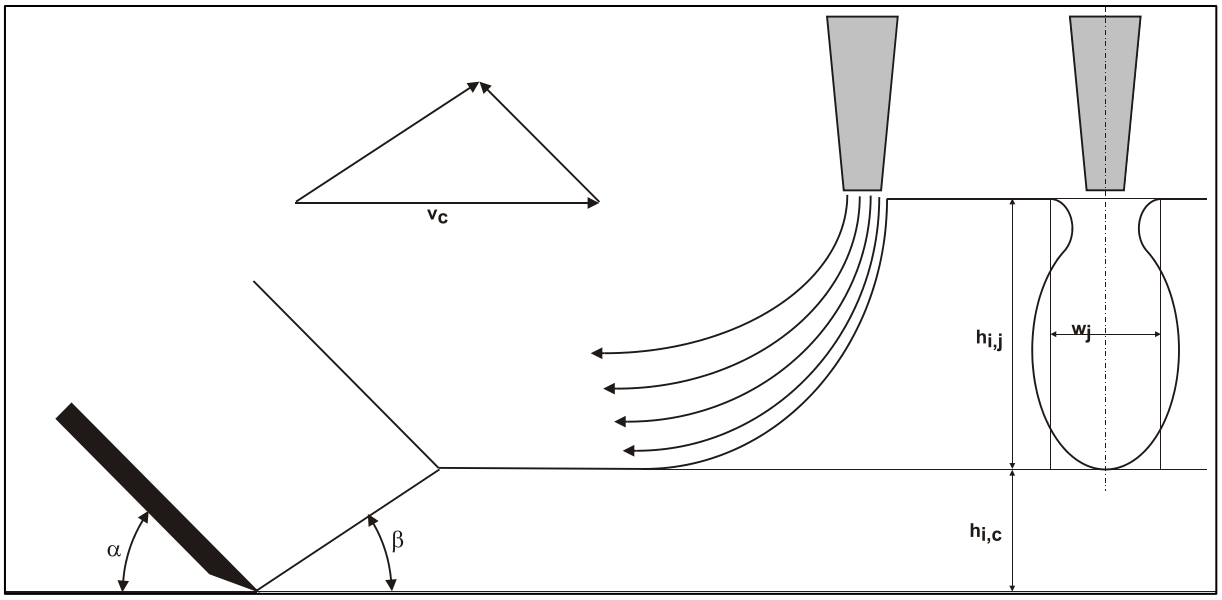

Figure 11-11: The layer jetted and the layer cut.

The equilibrium of moments around the visor bearing is:

$$F_G \cdot L_G = F_h \cdot L_h - F_v \cdot L_v \qquad \textbf{(11-42)}$$

Substituting equation (11-41) gives:

$$F_G \cdot L_G = \frac{v_c \cdot h_{i,c}^2 \cdot w_{dh}}{k_i} \cdot \left(c_1 \cdot L_h - c_2 \cdot L_v\right) \qquad \textbf{(11-43)}$$

So, the layer thickness cut by the blades is, see Figure 11-11:

$$h_{i,c}^2 = \frac{F_G \cdot L_G \cdot k_i}{v_c \cdot w_{dh} \cdot \left(c_1 \cdot L_h - c_2 \cdot L_v\right)} \qquad \textbf{(11-44)}$$

The total layer thickness is the sum of the layer thickness jet and the layer thickness cut. If the total layer thickness found this way is larger than the maximum layer thickness, the maximum layer thickness $h_{c,max}$ should be chosen for the production calculation. The mixture concentration can now be determined with:

$$\textbf{if} \quad h_{i,j} + h_{i,c} > h_{c,max} \quad \textbf{then} \quad C_{vs} = \frac{h_{c,max} \cdot w_{dh} \cdot v_c \cdot \left(1 - n_i\right)}{\frac{\pi}{4} \cdot D_p^2 \cdot v_{ls}}$$

else

$$C_{vs} = \frac{\left(Q_{s,dh} + Q_c\right) \cdot \left(1 - n_i\right)}{Q_m} = \frac{\left(h_{i,j} \cdot w_j \cdot n_j + h_{i,c} \cdot w_{dh}\right) \cdot v_c \cdot \left(1 - n_i\right)}{\frac{\pi}{4} \cdot D_p^2 \cdot v_{ls}} \qquad \textbf{(11-45)}$$

$$= \frac{\left(2 \cdot \Delta p_j^{1/2} \cdot D_j^{2/3} \cdot k_i^{1/3} \cdot w_j \cdot n_j + h_{i,c} \cdot w_{dh} \cdot v_c\right) \cdot \left(1 - n_i\right)}{\frac{\pi}{4} \cdot D_p^2 \cdot v_{ls}}$$

The mixture density is now:

$$\rho_m = C_{vs} \cdot \rho_q + \left(1 - C_{vs}\right) \cdot \rho_l \qquad \textbf{(11-46)}$$

Figure 11-8, Figure 11-9 and Figure 11-10 show the resulting mixture density for the case considered. Above a certain trailing speed, the jet+cut production results in a slightly increasing mixture density with increasing trailing speed. If c_2 is positive (vertical force downwards directed), this increases the layer cut thickness. It is however the question whether this is realistic, since there will also be an upwards force on the bottom of the blade, compensating for the downwards force. For positive values of $\mathbf{c_2}$ it may be safer to choose $\mathbf{c_2}$ equal to zero. This may underestimate the production slightly.

11.9. Conclusions.

Based on the law of conservation of misery, the specific energy for fluidizing sand with water jets is assumed to be equal to the specific energy of sand cutting under atmospheric conditions with a blade angle of about 15°. This assumption results in a set of equations for jet penetration depth, jet production and jet power. Validation of these (calibrated) equations with experimental data, gives a good match, so apparently the above assumption is valid enough within certain boundaries. The proportionalities in the equations may differ slightly if other values for water density, contraction coefficient and so on are taken, however no significant changes are expected.
The final production equations assume the cutting blades have additional production. It may be expected that when using a flexible visor, there is an equilibrium of cutting moment, visor weight moment and cylinder moment around the visor bearing, resulting in a certain layer thickness to be cut, increasing the production and thus mixture density. This is shown clearly in Figure 11-8, Figure 11-9 and Figure 11-10. In case the effective width of the fluidized area is smaller than the distance between the nozzles, the blades will cut the remaining sand. This will result in cutting forces and moments and may thus affect the visor angle and maximum cutting depth. This effect is taken into account in equation (11-44), but neglected in the examples in Figure 11-8, Figure 11-9 and Figure 11-10.
A power not equal to unity for the width to penetration depth ratio will give a dependency of the production to the trailing speed. This effect however is expected to be small. A power smaller than 1 gives a decreasing production at trailing speeds higher than the trailing speed where the penetration depth reaches the maximum visor depth. A power larger than 1 gives a curvature to the production at trailing speeds below the trailing speed where the penetration depth reaches the maximum visor depth. In the examples given this is at a trailing speed of about 0.85 m/s. 3D effects and overlapping of fluidized areas are not taken into account in the equations derived. The latter effects require more experimental research and a more detailed model. The model can also be used to determine the distance between the nozzles in a certain type of sand.

It is expected that above a certain trailing speed, the jet production is more or less a constant. If the layer to be cut is taken into account, then the cutting forces of the non-cavitational cutting process depend linear on the cutting velocity. Since these cutting forces have to give a constant moment around the visor bearing (based on visor weight and cylinder pressure), the layer thickness cut will be reversely proportional to the square root of the trailing speed, because the cutting forces are proportional to the layer thickness cut squared. So, the cut production will still be proportional to the square root of the trailing speed. This means that the total production, jet production plus cut production, will increase slightly with the trailing speed. How much depends on the ratio jet production to cut production, and thus specifically to the permeability of the sand and other soil mechanical parameters, the weight of the visor and if present the cylinder pressure.
The contribution of the cut production is subject to further research, since here a simplified method is used. A constant submerged weight moment around the visor bearing is assumed. This moment will probably be visor angle dependent. A cylinder moment is omitted, this could be added to the submerged weight moment, since it's also a driving moment to open the visor. The cutting forces should be visor angle dependent and also the arms resulting in the cutting moment, the resisting moment that wants to close the visor. In the current model a moment resulting from a pressure difference over the visor is omitted. The MSc study of de Jonge (2017) shows that this contribution is just about 5% of the submerged weight moment and may be neglected.
Resuming it can be stated that the model derived here gives a good first estimate for the **water jet production** in a drag head. One should however realize that the validity is based on experiments with a certain range of parameters, meaning the model is valid for this range of parameters. The goal of developing a drag head production model is reached.

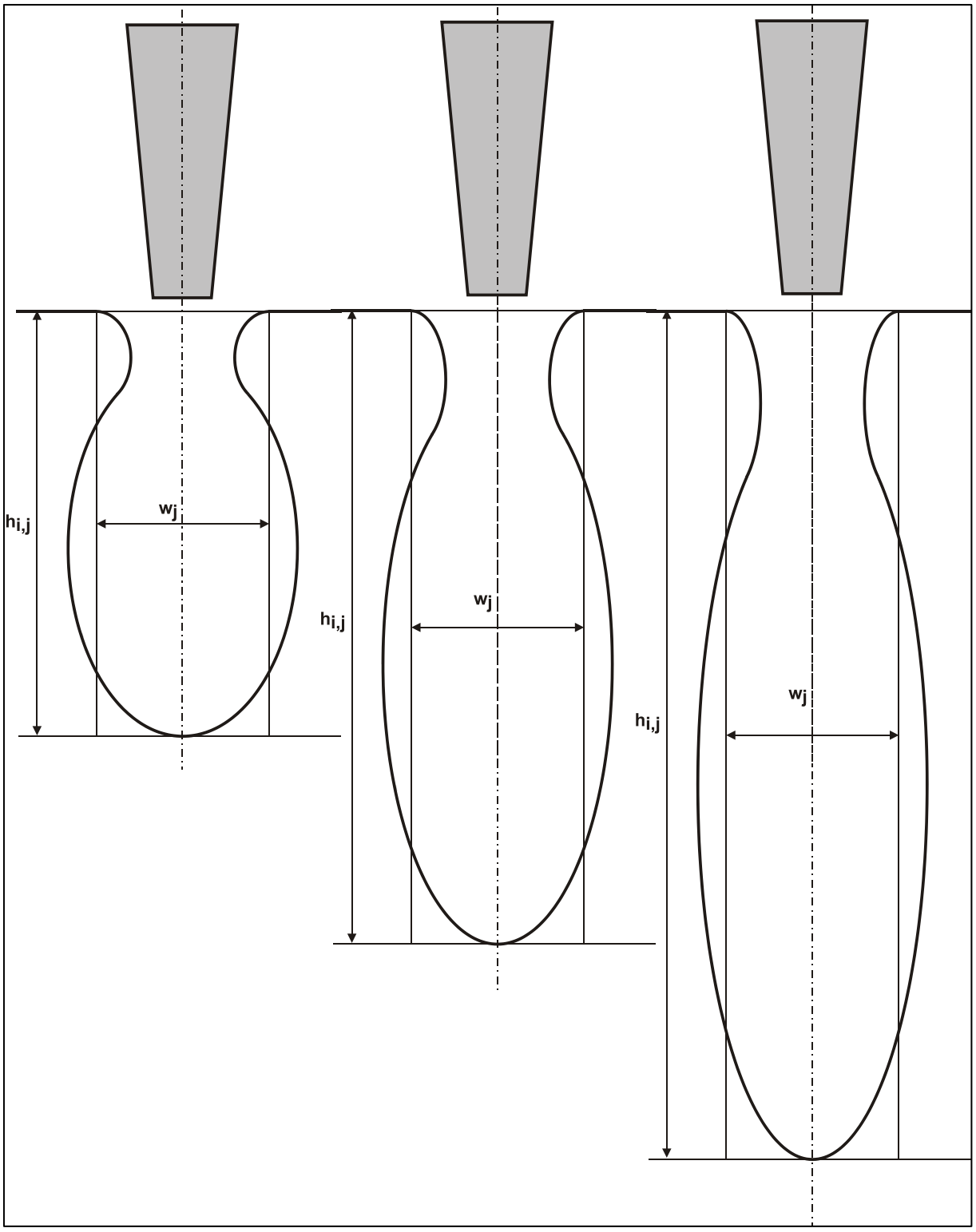

Figure 11-12: The cavity for high speed, medium speed and low trailing speed (the cavity width is constant here).

11.10. Nomenclature

c_1	Proportionality constant cutting process horizontal force	-
c_2	Proportionality constant cutting process vertical force	-
C_{vs}	Spatial volumetric concentration	-
d_e	Particle diameter	m
d_{10}	Particle diameter 10% passing	m
D_j	Nozzle diameter	m
D_p	Suction pipe diameter	m
e	Void ratio	-
F_G	Submerged weight of visor	kN
F_h	Horizontal cutting force	kN
F_v	Vertical cutting force	kN
E_{sp}	Specific energy	kPa
g	Gravitational constant (9.81 m/s^2)	m/s^2
h_c	Depth tip of blade in visor	m
$h_{c,max}$	Maximum depth tip of blade in visor	m
$h_{i,j}$	Jet penetration depth or layer thickness jet	m
$h_{i,c}$	Cut layer thickness	m
k	Permeability in general	m/s
k_i	Initial permeability situ sand	m/s
k_{max}	Permeability after shearing (cutting)	m/s
k_m	Mean permeability	m/s
L_G	Horizontal distance point of gravity visor to visor bearing	m
L_h	Vertical distance visor bearing to tip of cutting blade (related to horizontal force moment)	m
L_v	Horizontal distance visor bearing to tip of cutting blade (related to vertical force moment)	m
n	Porosity in general	-
n_i	Initial porosity	-
n_{max}	Porosity after shearing (cutting)	-
n_j	Number of nozzles in one drag head	-
Δp_j	Differential pressure over nozzle	kPa
P_j	Jet power used in one nozzle	kW
$P_{j,dh}$	Jet power used in one drag head	kW
Q_j	Jet flow	m^3/s
Q_s	Fluidized volume flow situ sand water jet	m^3/s
$Q_{s,dh}$	Fluidized volume flow situ sand in one drag head	m^3/s
$Q_{m,q}$	Quartz mass flow of one nozzle	ton/s
v_1	Trailing speed where the penetration depth equals the effective width of the fluidized area	m/s
v_c	Trailing velocity or cutting velocity	m/s
v_j	Jet flow velocity	m/s
v_{ls}	Line speed (cross sectional average mixture velocity)	m/s
w_j	Effective width fluidized area or blade width, cavity width	m
w_{dh}	Width of a drag head	m
α	Contraction coefficient	-
β	Power of effective width trailing speed dependency	-
ε	Dilatation	-
ρ_l	Liquid density (in this case sweet water or salt water)	ton/m^3
ρ_q	Density of quartz	ton/m^3
ρ_m	Mixture density	ton/m^3
γ_l	Liquid density times g	kN/m^3
η_j	Jet pump process efficiency	-
ν_l	Kinematic viscosity	m^2/s
μ_l	Dynamic viscosity	Pas

Chapter 12: The Closing Process of Clamshell Dredges in Water-Saturated Sand.

12.1. Abstract.

The literature reveals little about the prediction of the closing process of clamshell dredging buckets when cutting sand or clay under water. The results of research carried out, mostly relates to the use of clamshells in dry bulk materials. While good prediction of the forces (in dry materials) involved are possible by measuring the closing curve, the very prediction of the closing curve of clamshells in general, seems to be problematic. Because the dredging business is concerned with water-saturated sand or clay has to be dredged, the research into the closing process of clamshell grabs had to start from scratch (except for the kinematics of clamshells). In 1989 the research carried out by Great Lakes Dredge & Dock Company resulted in a numerical method of calculating the closing process of clamshell grabs in water saturated sand and clay, which simulates the closing of a clamshell so that production and forces can be predicted. The calculation method is based on the non-linear equations of motion of the buckets and the sand cutting theory Miedema. A clay cutting theory is implemented in the numerical model but will not be taken into consideration in this paper. In 1991, Great Lakes and the Delft University of Technology carried out laboratory research in which a scale model clamshell was used. This research, carried out in dry and in water saturated sand, resulted in a verification and validation of the calculation method with respect to the closing curve, the angular velocity and the pulling force in the closing wire. This paper contains results of the lecture notes of Vlasblom (2003-2007), a literature survey, the equations of motion of a clamshell grab, background to the sand cutting theory, results of the computer program CLAMSHELL (1989), and it will give some of the results of the research carried out with respect to verification and validation of the computer program, whilst a short preview into future research is given.

12.2. Introduction to Clamshell Dredging.

The grab dredger is the most common used dredger in the world, especially in North America and the Far East. It is a rather simple and easy to understand stationary dredger with and without propulsion (Figure 12-1). In the latter the ship has a hold that it stores the dredge material, otherwise barges transport the material. The dredgers can be moored by anchors or by poles (spuds).

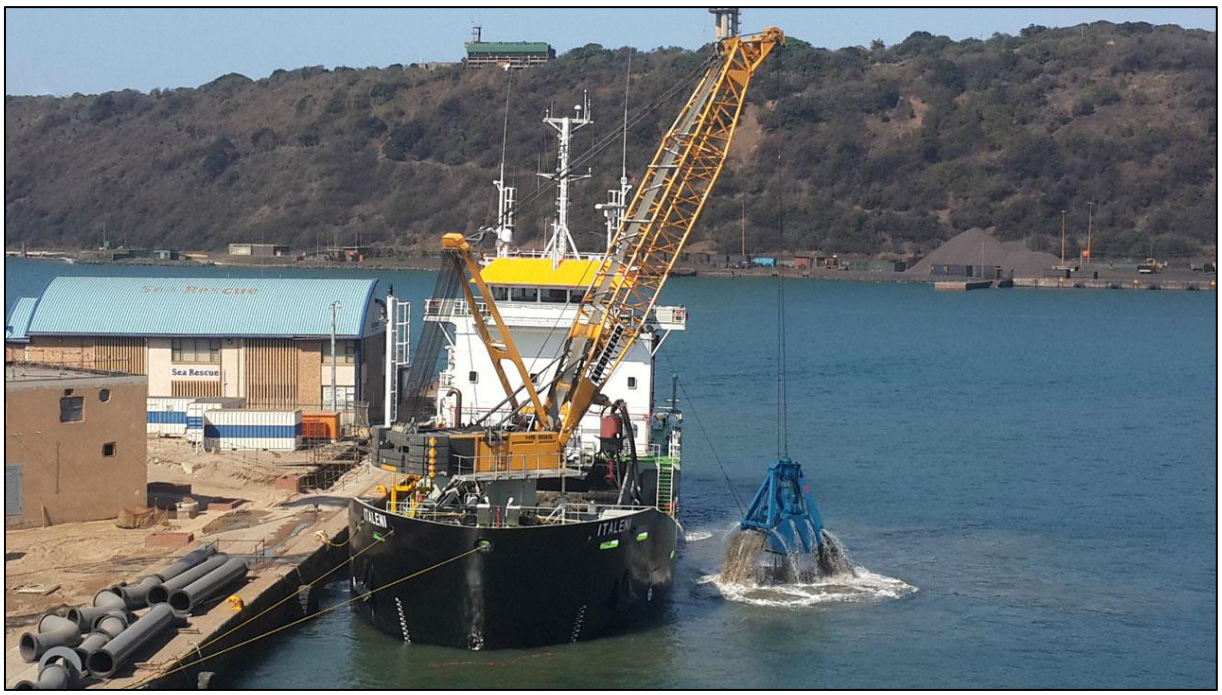

Figure 12-1: Self-propelled grab hopper dredge.

Figure 12-2: Grab bucket reclaimer.

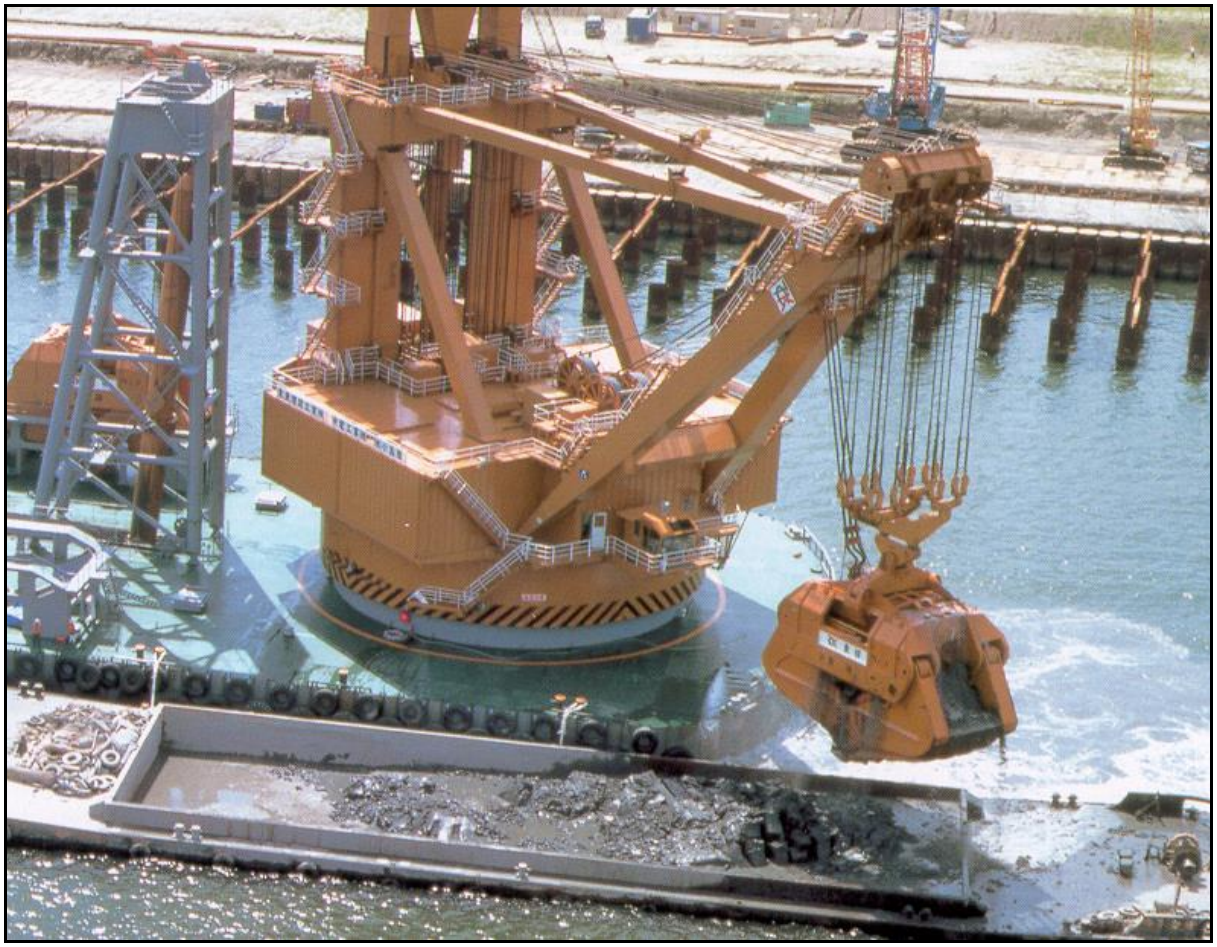

Figure 12-3: The largest grab in the world (200 m^3)

The most common types are boom type clamshell dredgers with a boom that can swing around a vertical axis. Beside these, but considerably less in number, are the overhead cranes (Figure 12-2), with the trolleys, like the ones used for the transshipment of bulk goods in ports. The capacity of a grab dredger is expressed in the volume of the grab. Grab sizes varies between less than 1 m^3 up to 200 m^3 (Figure 12-3). Figure 12-4 shows a distribution of grab sizes.

The opening of the grab is controlled by the closing and hoisting wires or by hydraulic cylinders. To ensure that the grab does not spin during hoisting and lowering many cranes are equipped with a tag line, running from half way the boom straight to the grab. For clamshell dredgers the method of anchoring and the positioning system plays an important role for the effectiveness of the dredger. The volume to be dredged at a position decreases with the angle from the centerline. So dredging areas from -90° to +90 ° from the centerline is not always effective. In Figure 12-5 a top view and a projection of the dredging area is shown. The width of the dredging area is $\mathbf{R \cdot \sin(\zeta)}$ and the width of the cut is L, so the surface of the effective dredging area is: $\mathbf{A_{eff} = L \cdot R \cdot \sin(\zeta)}$ which equals: $\mathbf{A_{eff} = \zeta \cdot \frac{2 \cdot \pi}{360^{\circ}} \cdot R \cdot L'}$.

The mean dredging (swing) efficiency as a function of the swing angle of the crane being $\frac{L'}{L}$ follows from equalization of both equations: $\frac{L'}{L} = \frac{\sin(\zeta)}{\zeta} \cdot \frac{360^{\circ}}{2 \cdot \pi}$ (Figure 12-6).

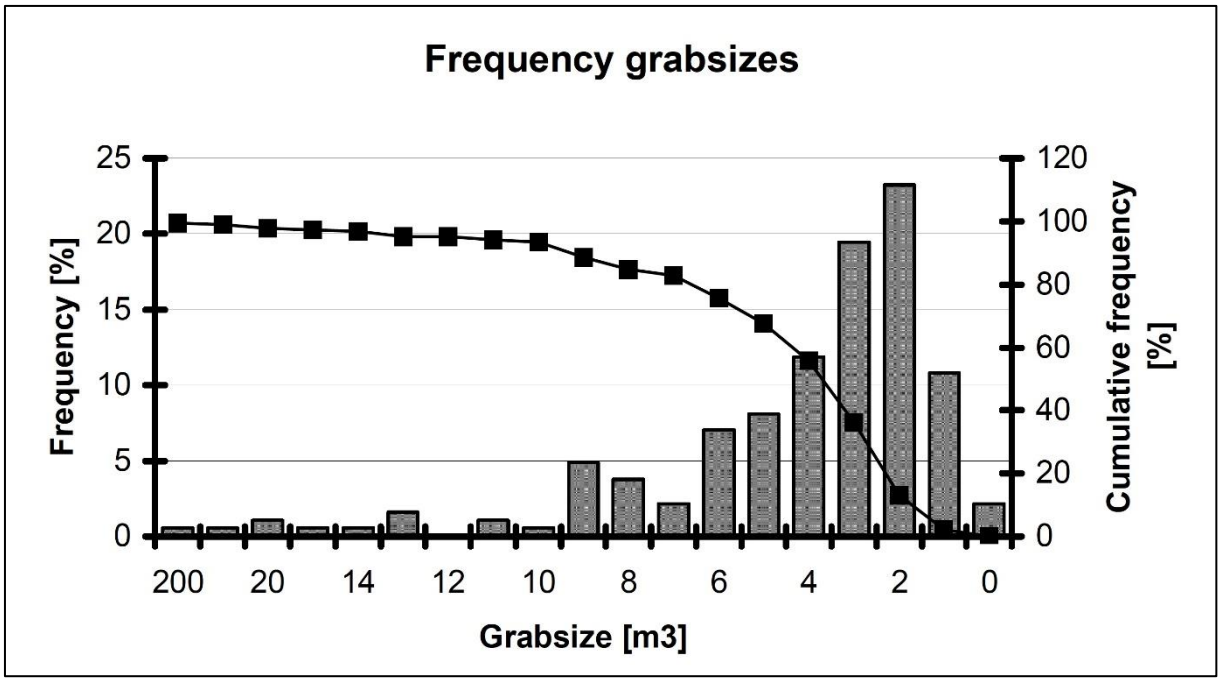

Figure 12-4: A rough overview of the most common grab sizes.

It is important to localize every bite of the grab by means of a positioning system. This helps the dredge master to place the next bit after the foregoing. The dredging process is discontinuously and cyclic:

- Lowering of the grab to the bottom
- Closing of the grab by pulling the hoisting wire
- Hoisting starts when the bucket is complete closed
- Swinging to the barge or hopper
- Lowering the filled bucket into the barge or hopper
- Opening the bucket by releasing the closing wire.

Releasing the aft wires and pulling the fore wires does the movement of the pontoon. When the dredgers have spud poles, this movement is done by a spud operation, which is more accurate than executed by wires. The principle of this hoisting operation is given in Figure 12-7 below. For a good crane-working behavior the cable cranes have two motors:

- The hoisting motor, which drives the hoisting winch and

- The closing motor, which controls the closing and the opening the grab.

In order to avoid spinning of the clamshell a so-called tag wire is connected to the clamshell.

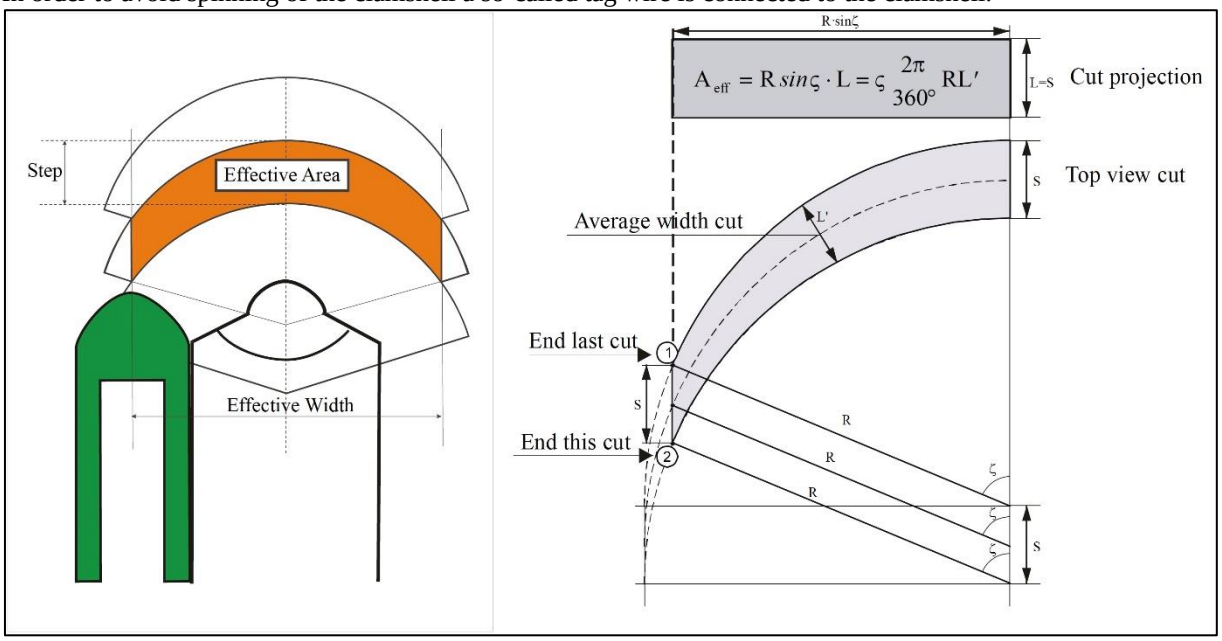

Figure 12-5: The effective dredging area.

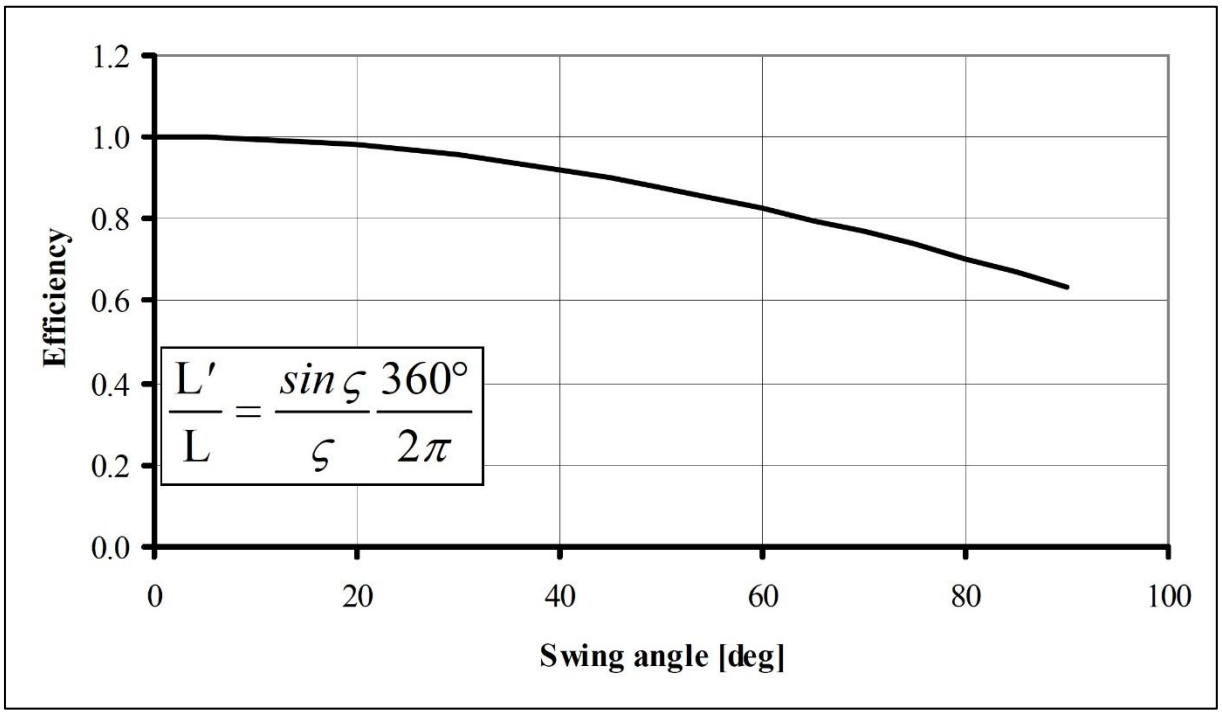

Figure 12-6: The swing efficiency.

The crane-working behavior is now as follows:

no.	Cycle Part	Position Yaws	Hoisting Winch	Closing Winch
1	ease	open	eases	eases
2	dig	closing	hoists	hoists
3	hoist	closed	hoists	hoists
4	swing	closed	rest	rest
5	ease	closed	eases	eases
6	dump	opening	eases	rest
7	hoist	open	hoists	hoists

8	swing	open	rest	rest

The large grab dredgers are used for bulk dredging. While the smaller ones are mostly used for special jobs, such as:

- Difficult accessible places in harbors
- Small quantities with strongly varying depth.
- Along quay walls where the soil is spoiled by wires and debris
- Borrowing sand and gravel in deep pits
- Sand and gravel mining
- Dredging in moraine areas where big stones can be expected.

.

The production of a grab depends strongly on the soil. Suitable materials are soft clay, sand and gravel. Though, boulder clay is dredged as well by this type of dredger. In soft soils light big grabs are used while in more cohesive soils heavy small grabs are favorable. The dredging depth depends only on the length of the wire on the winches. However, the accuracy decreases with depth. For mining of minerals dredging depths can reach more than 100 m.

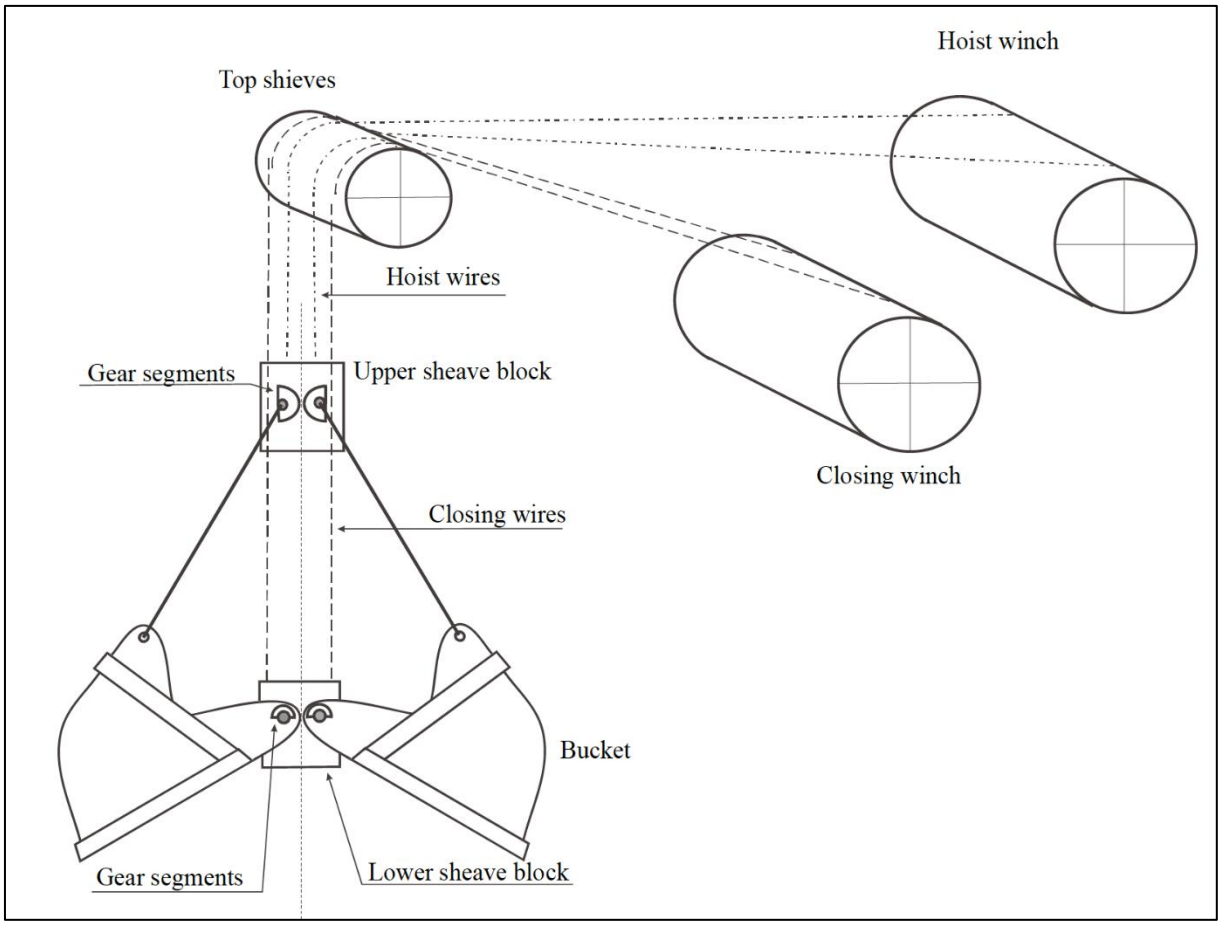

Figure 12-7: Hoisting system of cable clamshells.

12.3. Important Design Aspects.

The clamshell (Figure 12-8) most common and is used in silty, clayey and sandy materials. In mud the yaws in general have flat plates without teeth. In sand, clay and gravel, the yaws are fitted with, in each other grabbing teeth. The two halves, shells, rotate around a hinge in the **lower sheave block** and are connected with the **upper sheave block** by rods. The closure/hoist cable is reefed several times between the head and the disc block to generate enough closing force. In mud the yaws in general have flat plates without teeth. In sand, clay and gravel, the yaws are fitted with, in each other grabbing teeth. For the removal of contaminated soil closed clamshells are used to avoid spillage.

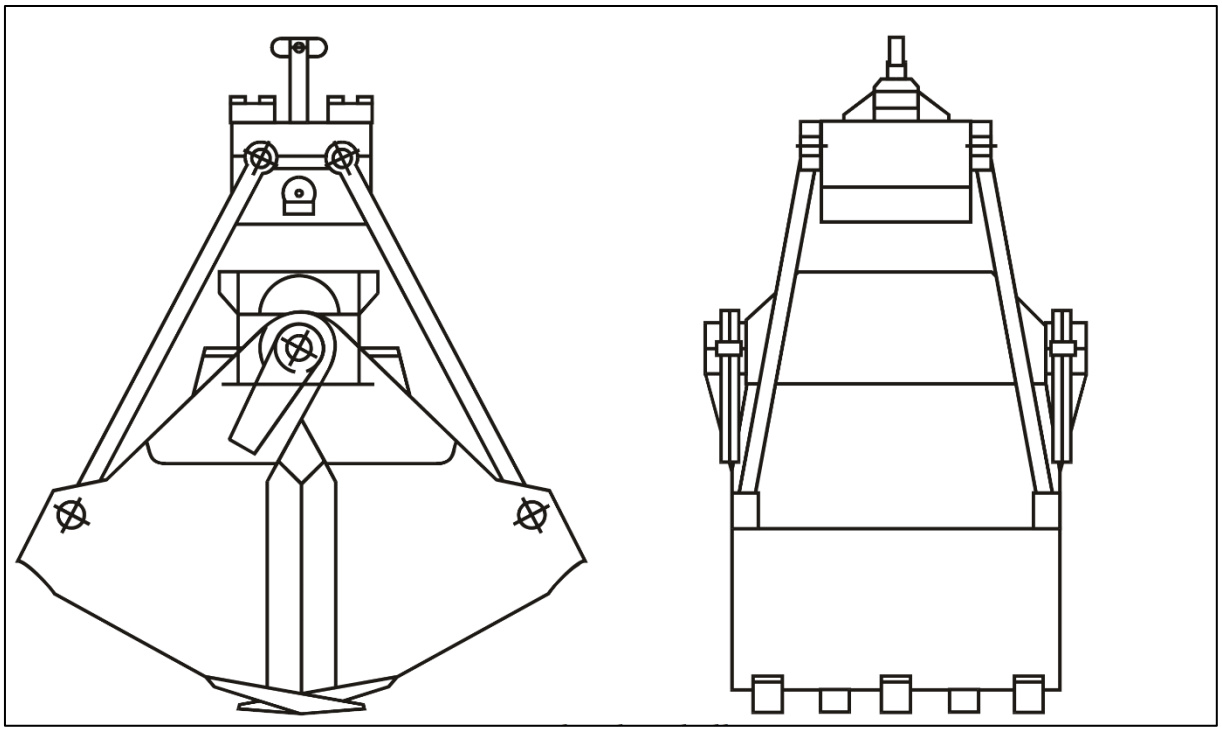

Figure 12-8: The clamshell.

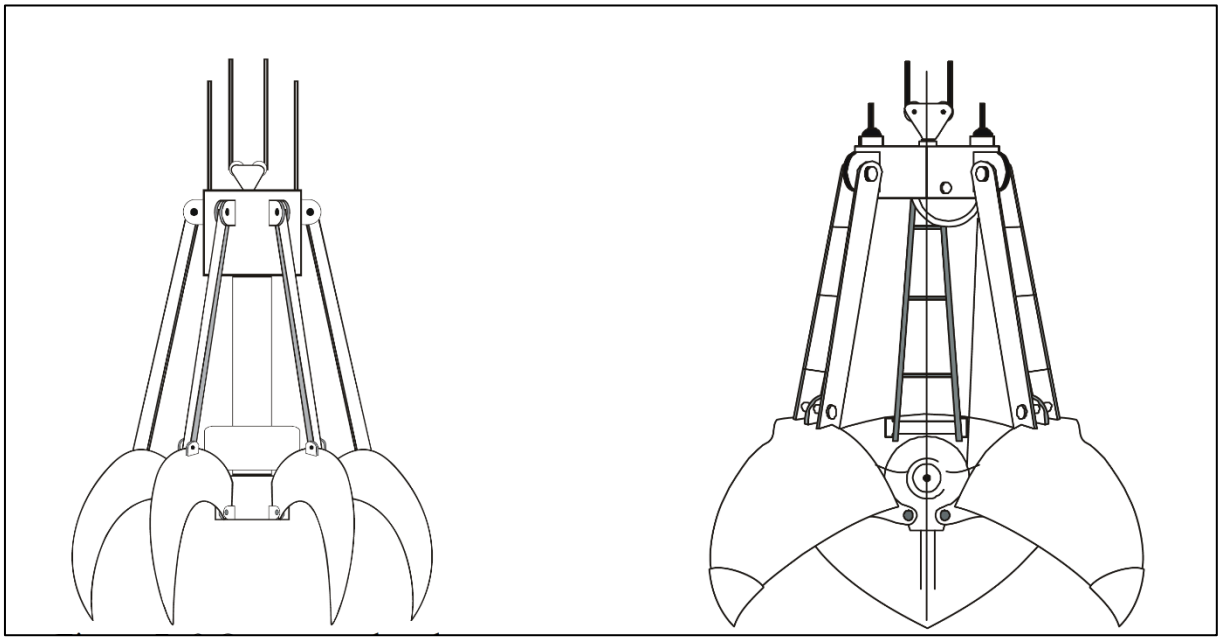

Figure 12-9: The orange peel grab and the cactus grab.

The orange peel grab (Figure 12-9) is often used for the removal of large irregular pieces of rock and other irregular pieces. This type of grab has 8 yaws that in general do not close very well. The **cactus bucket** (Figure 12-9) is used in the occurrence of both coarse and fine material at the same time. This grab has 3 or 4 yaws that close well in the closed position and form a proper bucket. The size of the bucket depends on the required production capacity of the crane.

The size of the grab depends on the capacity of the crane. The construction weight is determined, besides by the size also by the required strength and therefore by the type of soil to be dredged. So, a grab suitable for the dredging of silt will be relatively large in volume and light in weight, while for the dredging of heavy clay or rocks a relatively small but heavy bucket will be used. However, because the hoist force remains constant, with increasing weight of the grab the load weight must decrease. For this reason, the efficiency of the grab is expressed as

$\eta = \frac{\text{paying load in tons}}{\text{paying load} + \text{grab weight}}$. Research carried out in Japan has found the following relation between the ratio of the mass of the material in and the mass of the bucket: $K_s = L \cdot \sqrt{\frac{B}{2 \cdot M_{bucket}}}$ (Figure 12-10).

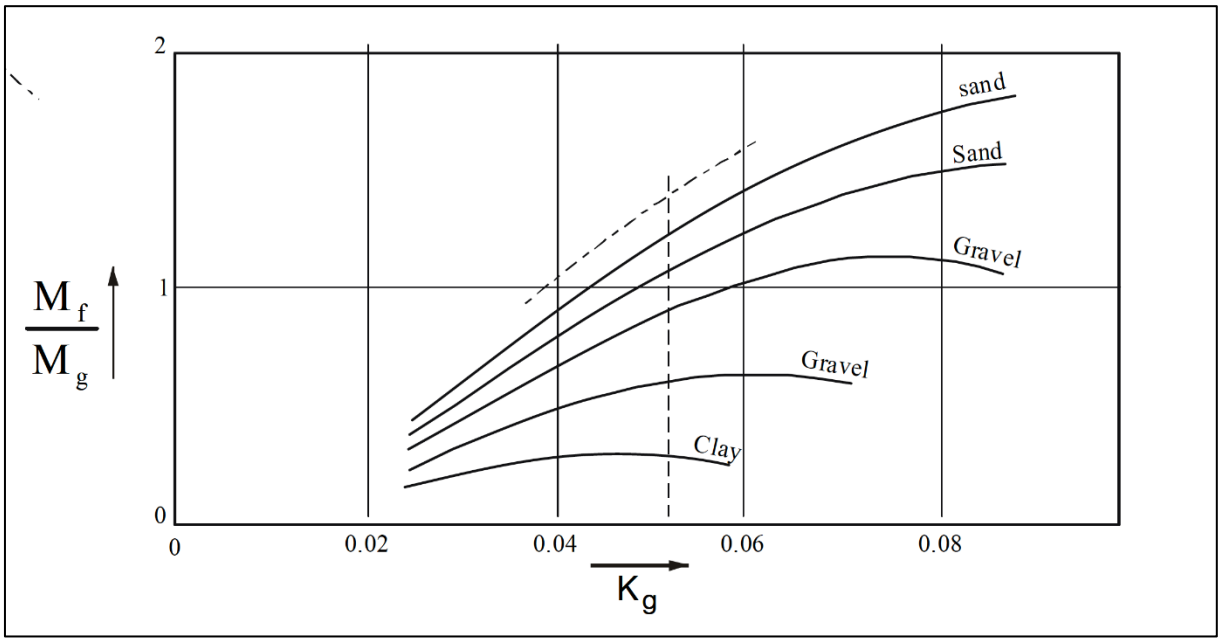

Figure 12-10: Fill mass and bucket mass ratio.

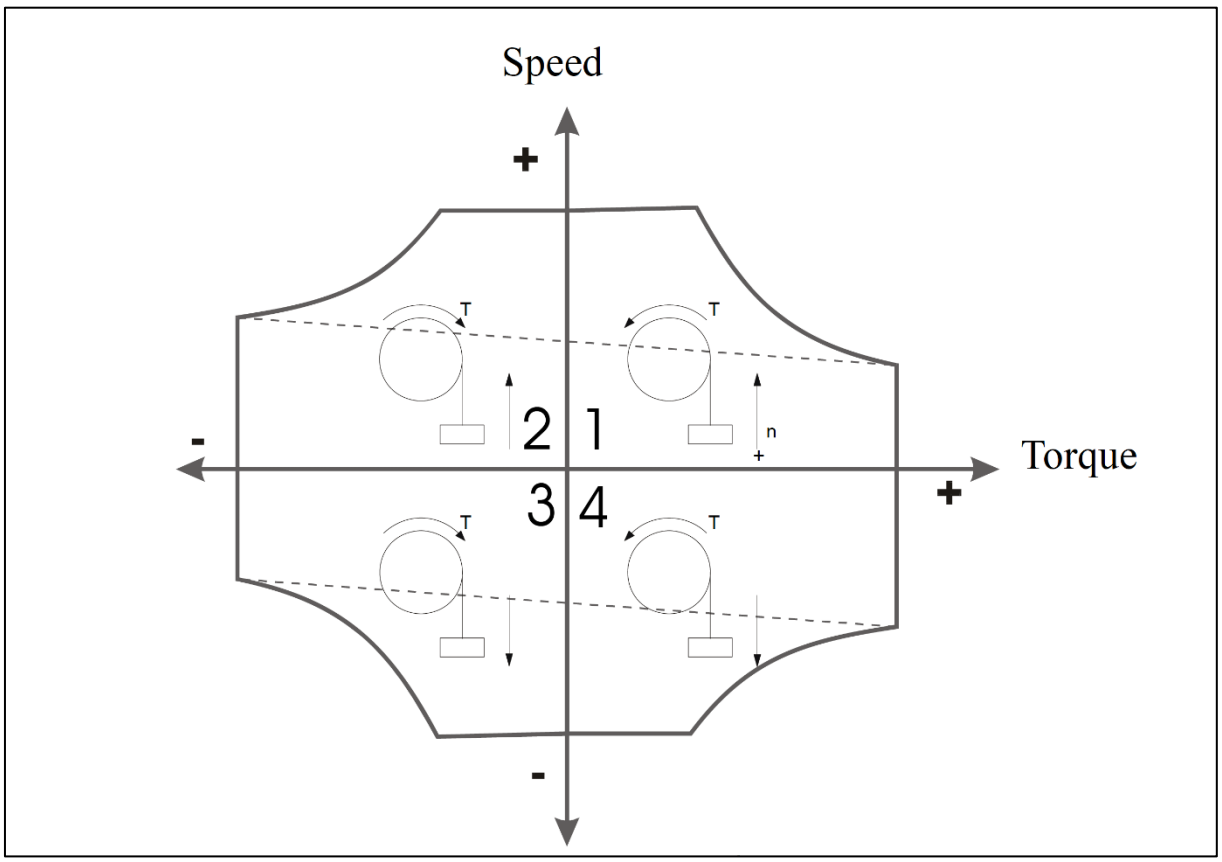

Figure 12-11: Four quadrants system. winch drive.

The winch drive systems are mainly electric (direct current or thyristor-controlled d-c motor connect to the 3-phase board net system) and has the 4 quadrants system (Figure 12-11).

Non-self-propelled grab dredgers consist of simple pontoons on which the crane is positioned. The deck is heavy reinforced not only for foundation of the crane but also where heavy loads can be expected, in particular where the grabs are stored. Winces for the movement of the pontoon are placed on deck as well as the accommodation for the crew when necessary. In many cases a standard crane is placed on the pontoon. The boom of the crane is movable with a simple wire system. During dredging the boom is kept in a fixed position as much as possible. This avoids the need for a horizontal load path. The length of the pontoon is in many cases longer than necessary in order to keep barges alongside. The positioning of the pontoon is either by anchors (4 to 6) or by 2 or 3 spud poles. In the last case 2 fixed spuds are situated at on the sides of the pontoon and one walking spud aft. An idea about the lightweight in relation to grab size is given in (Figure 12-13) and is in the order of 100 times the grab size.

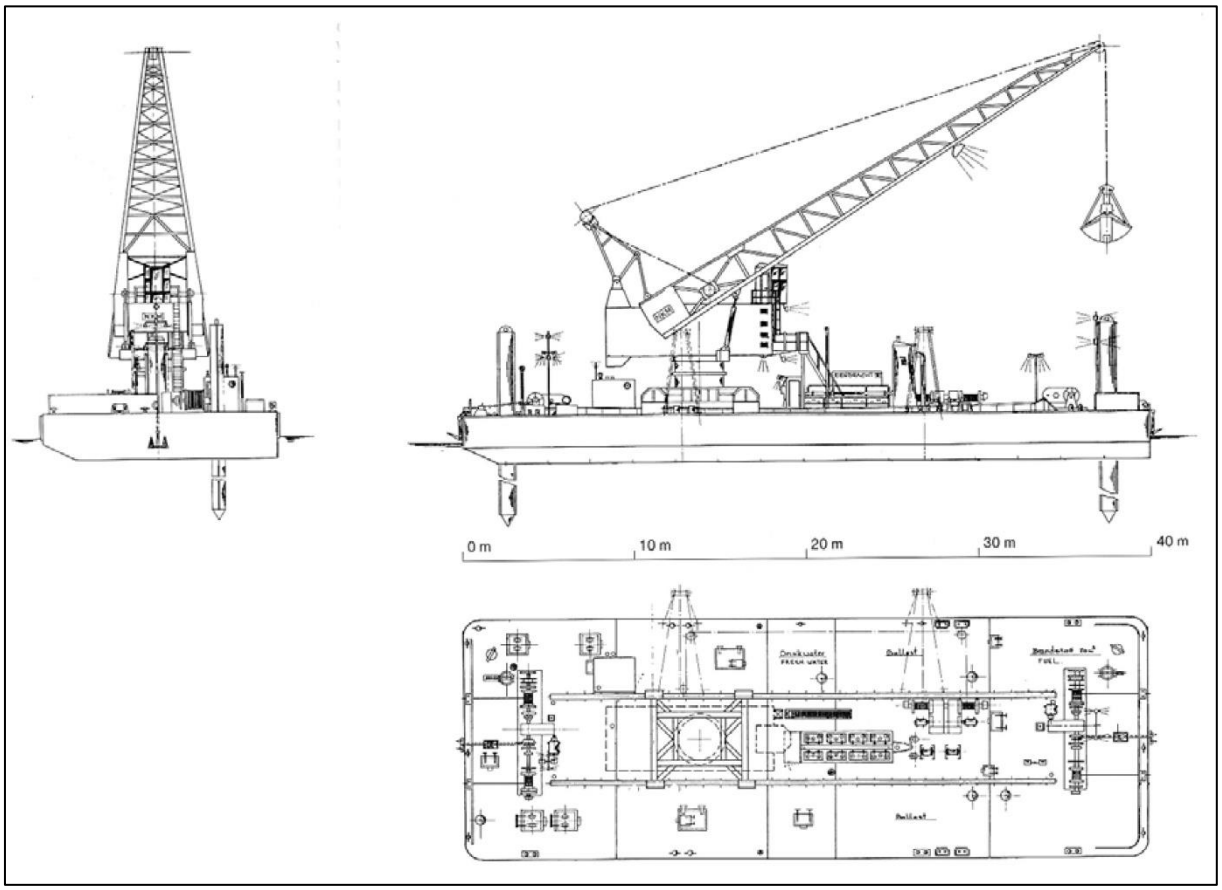

Figure 12-12: Plan view of Grab crane Eendracht, BOSKALIS.

The lightweight of the pontoon is low compared to that of the other dredgers. The relation between light weight and pontoon volume is shown in Figure 12-14. The L/B and B/T ratios f the pontoons are respectively between 2 and 3 and 4 to 6 (Figure 12-15). Special attention needs the stability of the dredge because of the varying and eccentrics loads. Free fluid levels should be avoided.

The most interesting part of the dredging process takes place during the digging in the soil when the grab is closing. When the grab is dropped on the soil the yaws (cutting edges) penetrate vertically into the soil. This is called the initial penetration. This initial penetration is very important for the total production. If the closing cable is pulled up, the lower sheave block and the upper sheave block are pulled together and as a result the grab closes. During this process the hoisting cable is kept slack to allow the grab to penetrate deeper into the soil. The closing wire however is still pulling and this way carrying part of the weight of the clamshell (grab). In very soft soil like silt or soft clay, the hoisting cable may be kept tight to prevent a too large penetration. The calculation of the path of the grab and the forces occurring is carried out by solving the equations of motion of the clamshell in the time domain, applying the cutting theory for sand or clay. The friction forces on the sides of the yaws (buckets) are also taken into account. During the excavation the cutting edge will follow a certain path through the soil. During this movement the lower sheave block moves upwards while the upper sheave block moves downwards.

The closing curve is very important when dredging contaminated soils. Storage of these soils is very expensive, so digging underlaying uncontaminated soils has to be avoided as much as possible. Therefore, grab dredgers dredging contaminated soil types tend to have horizontal closing curves. For production purposes the determination of the closing curve is insufficient. For this the excavating or digging curve is necessary. The closing curve is determined by keeping the upper block fixed, the digging curve is determined when the upper block is not fixed. The latter is determined by calculating the forces on the grab yaws and the disc blocks at every timestep during the closing process.

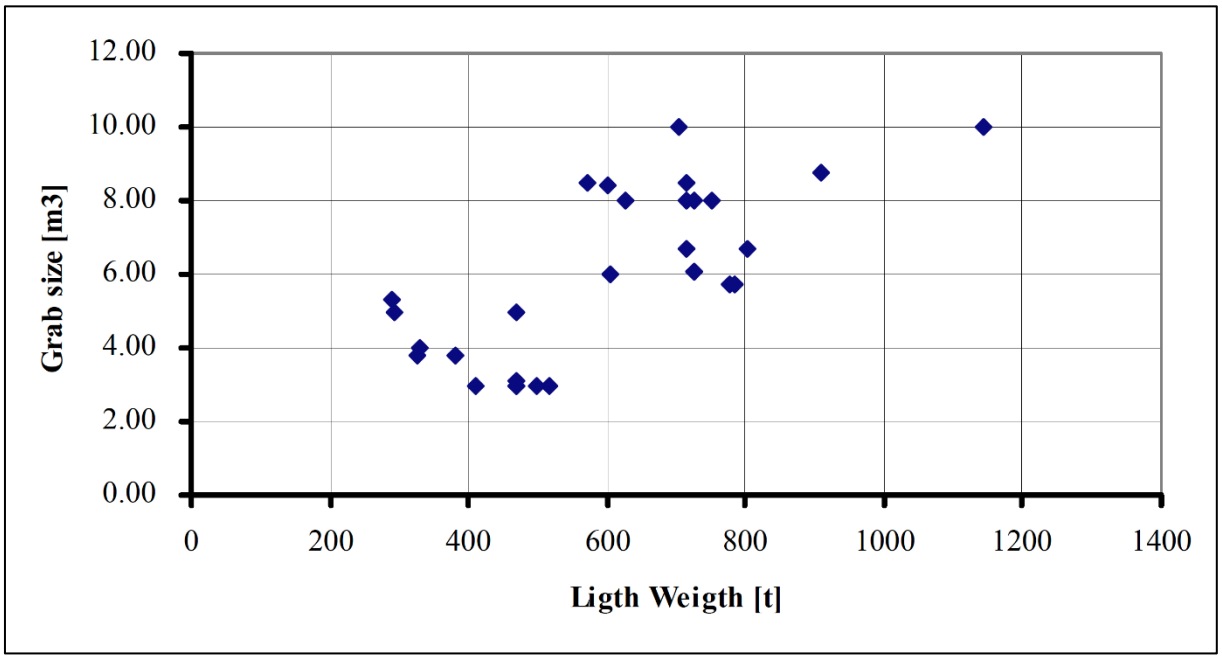

Figure 12-13: Light weight of grab dredge pontoons.

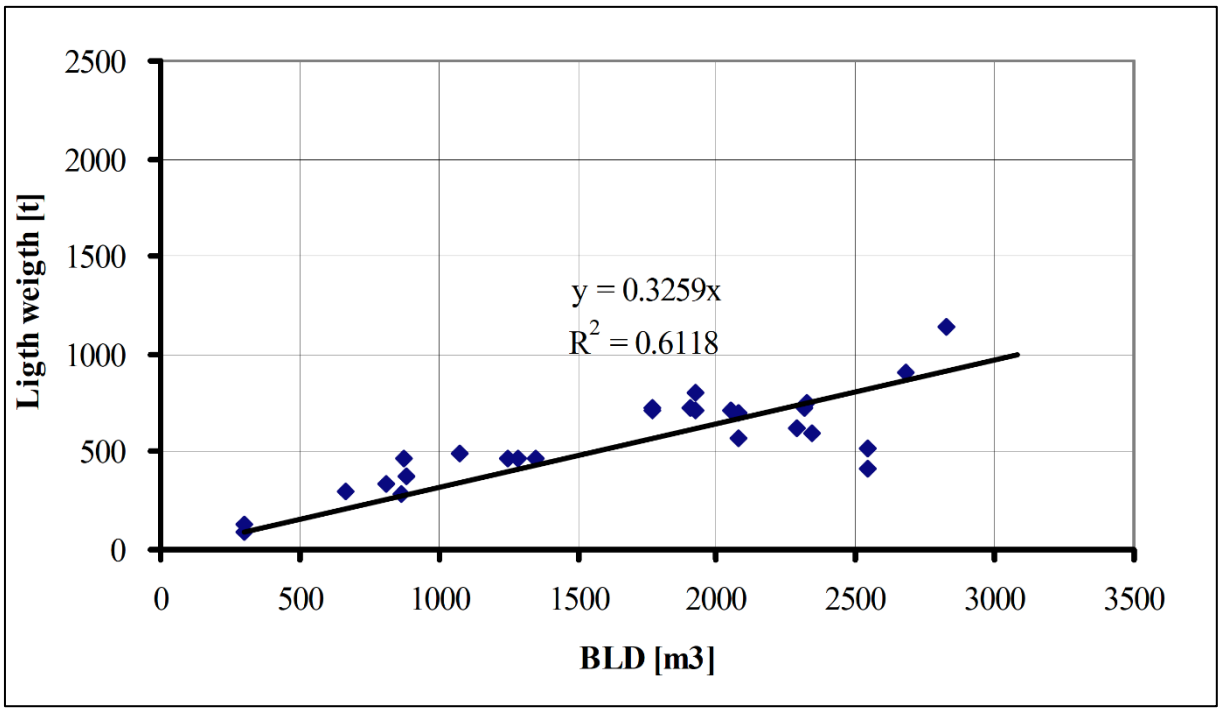

Figure 12-14: Pontoon volume.

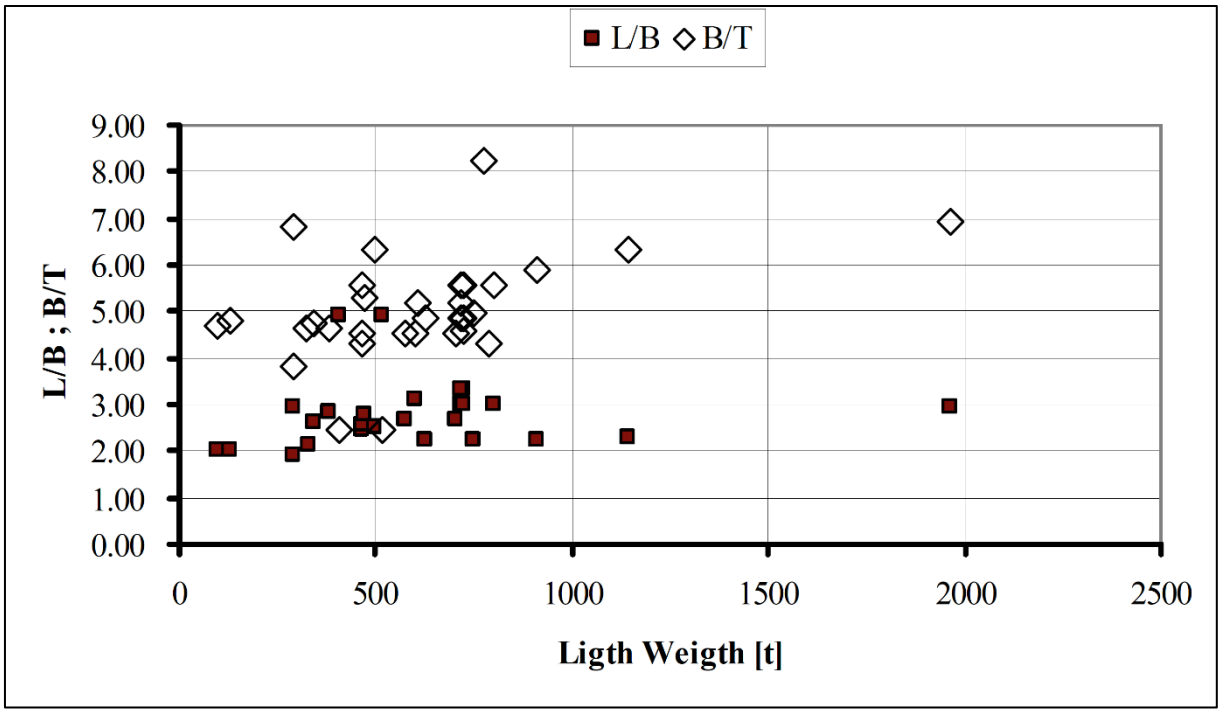

Figure 12-15: L/B and B/T ratios.

12.4. Introduction to Clamshell Research & Production.

It is important for dredging contractors to be able to predict the production of their dredges. Many studies have been carried out with respect to cutter suction dredges and hopper dredges. From the literature it became clear that, although many researchers have investigated the closing process of clamshell grabs, no one had succeeded in predicting their closing process. Since many clamshell grabs are being used in dredging industry in the U.S.A. and the Far East, it is important to have a good prediction of the production of clamshells in different types of soil. This was the reason for Great Lakes Dredge & Dock to start fundamental research into the processes involved in the digging of clamshell grabs in cooperation with Delft University of Technology. In 1989 this resulted in the computer program CLAMSHELL (1989), which simulates the digging process of clamshell grabs in water saturated sand and clay. Although the results of the program were promising, there was a need for verification and validation of the program by means of measurements. Model research was carried out at the Dredging Engineering Research Laboratory of the Delft University of Technology, Wittekoek (1991A), (1991B) and (1991C). The results of the measurements correlate very well with the computer program. The program is used by Great Lakes for production estimates and as well for the design of new clamshell grabs. Figure 12-16 shows the largest clamshell grab used in dredging, the Chicago (not operational anymore), owned by Great Lakes Dredge & Dock Company. Figure 12-17 shows the 50 cubic yard clamshell of the Chicago. Figure 12-18 shows the clamshell against human size.

12.5. The History of Clamshell Research.

The first grab reported was designed by Leonardo da Vinci (1452-1519) in the 15th century. Although the basic working principles remained the same, grab designs have improved dramatically as a result of trial and error, though research has had some influence. The following reviews some of the results found of research carried out in this century. Pfahl (1912) investigated the influence of the deadweight of a grab with respect to the payload for grabs of 1 m^3 to 2.25 m^3. He concluded that the payload has a linear relation with the deadweight. Ninnelt (1924) carried out research similar to Pfahl (1912) and confirmed Pfahl' s conclusions. Niemann (1935) experimented with model clamshells. He investigated the deadweight, the bucket's shape, the soil mechanical properties, the payload and the rope force. Special attention was paid to the width of the grab, leading to the conclusion that the payload is proportional to the width of a grab. The research also led to a confirmation of the work of Pfahl (1912) and Ninnelt (1924). Tauber (1958) conducted research on prototype and model grabs. Contrary to Nieman (1935) he found that enlarging the grab does not always lead to an increasing payload. The optimum ratio between the grab width and the grab span was found to be in between 0.6 and 0.75.

Figure 12-16: The largest clamshell grab used in dredging, the Chicago, in full operation.

Torke (1962) studied the closing cycle of a clamshell in sand for three different 39.5 kg model grabs. He first determined the closing path of the buckets experimentally, after which he reconstructed the filling process and the rope forces. His results were promising, even though he did not succeed in predicting the closing curve. An important conclusion reached by Torke (1962) is, that the payload is inversely proportional to the cutting angle of the bucket edges. In a closed situation, the cutting angle should be as near to horizontal as possible. Wilkinson (1963) performed research on different types of grabs and concluded that wide span grabs are more efficient then clamshell grabs. He also concluded that no model laws for grabs exist and that existing grabs are proportioned in about the best way possible. The best grab is a grab that exerts a torque on the soil that is as high as possible especially towards the end of the closing cycle. Hupe and Schuszter (1965) investigated the influence of the mechanical properties of the soil such as the angle of internal friction. They concluded that grabs intended to handle rough materials like coal should be larger and heavier. Dietrich (1968) tested a 0.6 m^3 grab and measured the payload for different values of the deadweight, the grab area, the cutting angle and the grain size. He concluded that in hard material 80% of the closing force is used for penetrating the soil, while in soft material this takes only 30% of the force. The width/span ratio should be between 0.6 and 0.7 matching Tauber's (1958) conclusions, while the cutting angle should be about 11 to 12 degrees with the horizontal in a closed situation matching Torke' s (1962) conclusions. Gebhardt (1972) derived an empirical formulation for the penetration forces in materials with grain sizes from 30 to 50 mm. Grain size and distribution are parameters in the equation, but the mechanical properties of the soil such as the angle of internal friction are absent. He also concludes that a uniform grain distribution results in relatively low penetration forces. Teeth are only useful in rough materials, but they have a negative effect in fine materials with respect to the penetration forces. Scheffler (1972) made an inventory of grab dimensions and design tendencies in several Eastern European countries. He concludes that most of the grabs are not used to their full potential and also that 80% of the closing force is used for penetration in rough materials confirming the work of Dietrich (1968). Scheffler, Pajer and Kurth (1976) give an overview of the mechanical aspects of several types of grabs. The soil/grab interaction moreover is too simplified or absent. They concluded that after fifty years of research the understanding of grabs is still limited. They refer to Wilkinson (1963) as having derived the best conclusions about grab model testing but regret that prototype results are not available.

Bauerslag (1979) investigated the process of grabbing ores of 55 mm with a motor grab. As with Torke (1962) he first measured the closing curve (digging path) and then reconstructed the closing process.

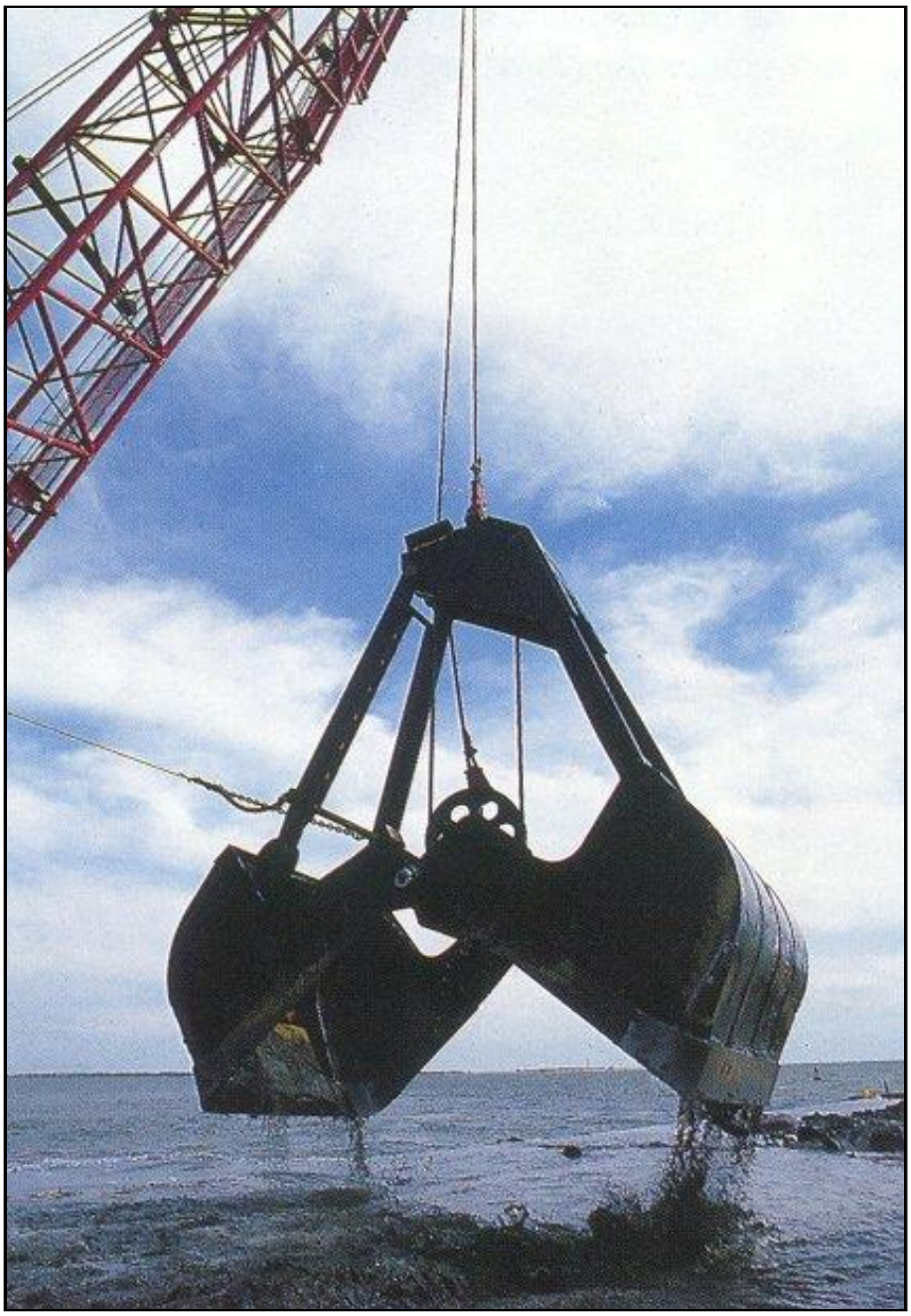

Figure 12-17: The 50 cubic yard clamshell buckets.

From the literature survey it can be concluded, that much research has been carried out in order to find the optimum geometry of clamshells with respect to the payload. The influence of the nature of the bulk material, however, has been underestimated, while no research has been carried out with respect to the use of clamshells under water. Several researchers manage to reconstruct the filling process of a clamshell, once the closing curve is known, but not one of them is able to predict the closing curve. One of the main problems is that grabs are designed by mechanical engineers, while the bulk material taken by the grab often behaves according to the rules of soil mechanics, the field of the civil engineer. This results in a communications problem. To be able to simulate and thus predict the closing process of clamshells, one needs to study the clamshell operation, kinematics, dynamics (equations of motion) and the soil mechanical behavior of the material taken. This will lead to a better understanding of the processes involved.

Figure 12-18: The clamshell buckets versus human size.

12.6. The Operation and Kinematics of a Clamshell.

Clamshell grabs as used in dredging industry, consist of six main bodies that can be distinguished as is shown in Figure 12-19. These six bodies are the upper sheave block, the lower sheave block, the two arms and the two buckets. In between the two sheave blocks the closing wire (rope) is reefed with a certain number of parts of line. The hoisting (and lowering) wire is mounted on top of the upper sheave block. A cycle of the grabbing process in a soil which is hard to dig consists of first lowering the clamshell fully opened and placing it on the soil to be excavated. When the clamshell is resting on the soil the hoisting wire is kept slack, so the clamshell will penetrate vertically into the soil by its own weight. This is called the initial penetration. The distance between the two sheave blocks is at a maximum during the initial penetration. Secondly the closing wire is hauled in, resulting in the two sheave blocks being pulled towards each other and thus causing the closing of the buckets. During this second stage, the hoisting wire is kept slack, so the buckets are allowed to penetrate into the soil. In soft soils it may be necessary to keep the hoisting wire tight, because otherwise the clamshell might penetrate too deeply into the soil, resulting in a lot of spillage. In this paper, only hard to dig sands will be considered. At the end of the second stage the clamshell is closed and will be raised with the hoisting (and the closing) wire. Figure 12-20 shows the stages of the closing cycle of the clamshell. The amount of soil taken by the clamshell depends on the kinematics and the weight distribution of the clamshell and on the mechanical properties of the soil to be dredged.

12.7. The Equations of Motion of a Clamshell.

In order to calculate the closing curve of a clamshell, the equations of motion of the moving parts of the clamshell have to be solved. The type of clamshell considered has six main bodies that are subject to motions. These bodies are the upper sheave block, the lower sheave block, the two arms and the two buckets. Because the arms have a small rotational amplitude and translate vertically with the upper sheave block, they are considered as part of the upper sheave block. The error made by this simplification is negligible. If a clamshell is considered to be symmetrical with respect to its vertical axis, only the equations of motion of one halve of the clamshell have to be solved. The other half is subject to exactly the same motions but mirrored with respect to the vertical axis. Since there are three main bodies left, three equations of motion have to be derived. In these equations' weights are considered to be submerged weights and masses are considered to be the sum of the steel masses and the hydro-mechanical added masses. The weights and the masses as used in the equations of motion are also valid for one half of the clamshell. The positive directions of motions, forces and moments are as depicted in Figure 12-21.

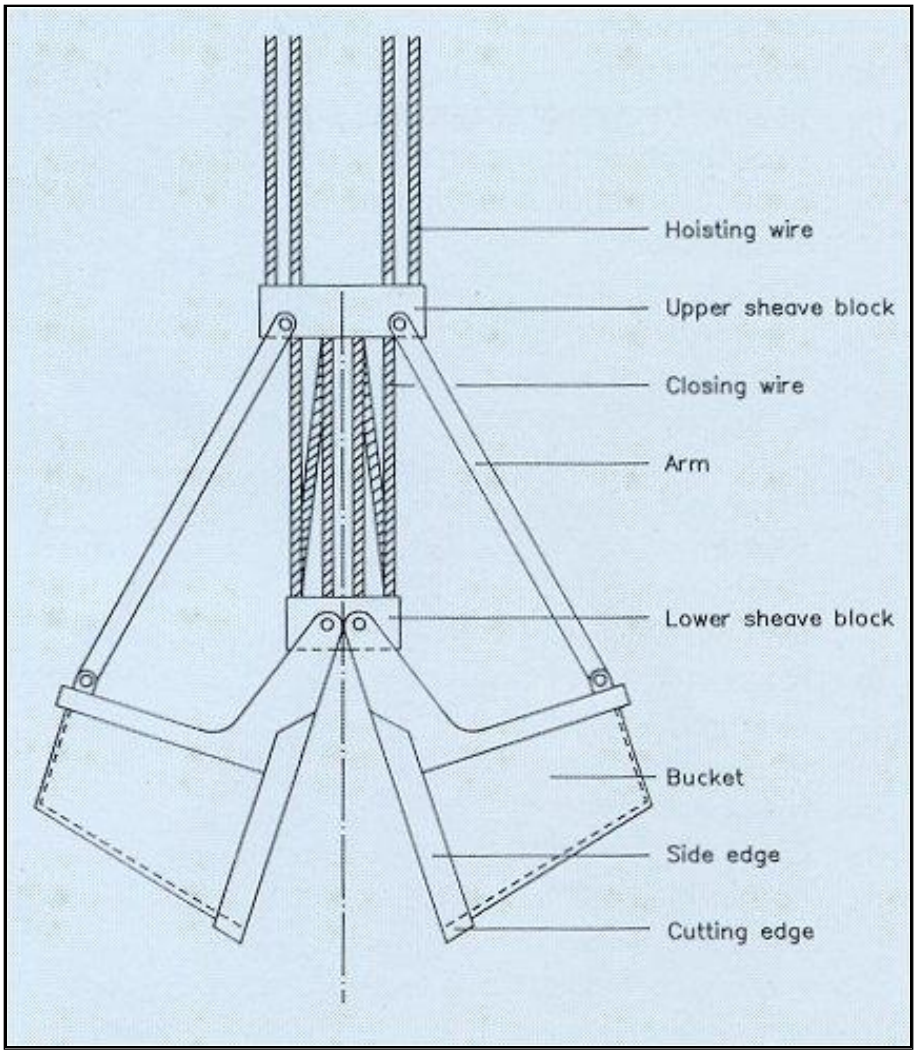

Figure 12-19: The nomenclature of the clamshell buckets.

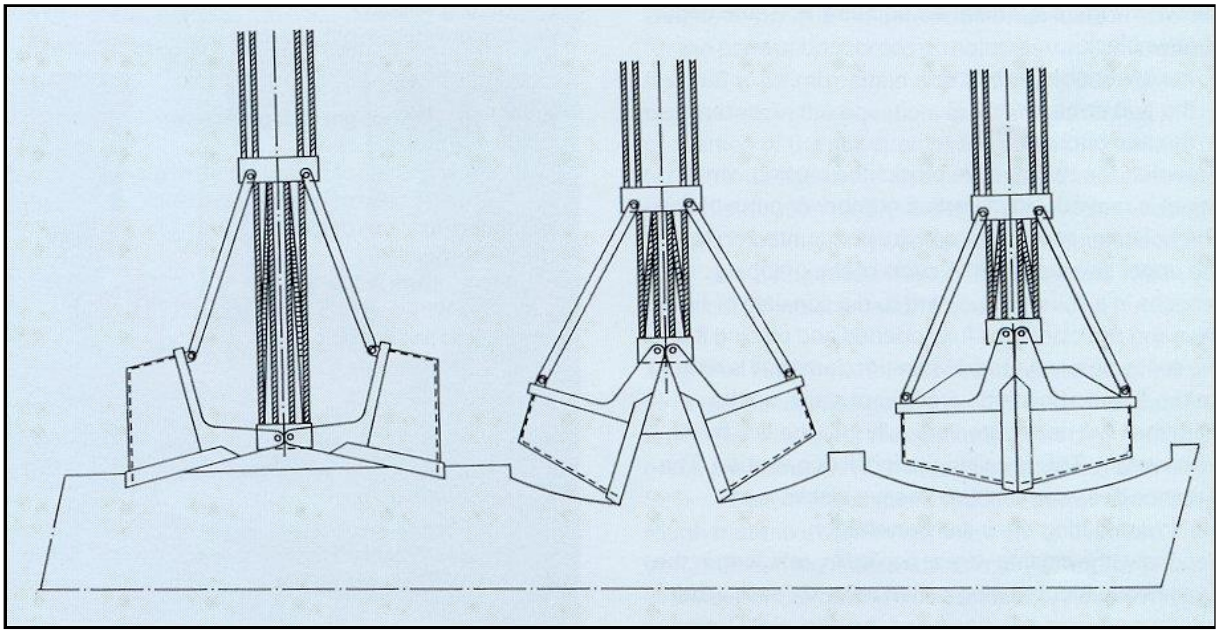

Figure 12-20: Three stages of the closing process.

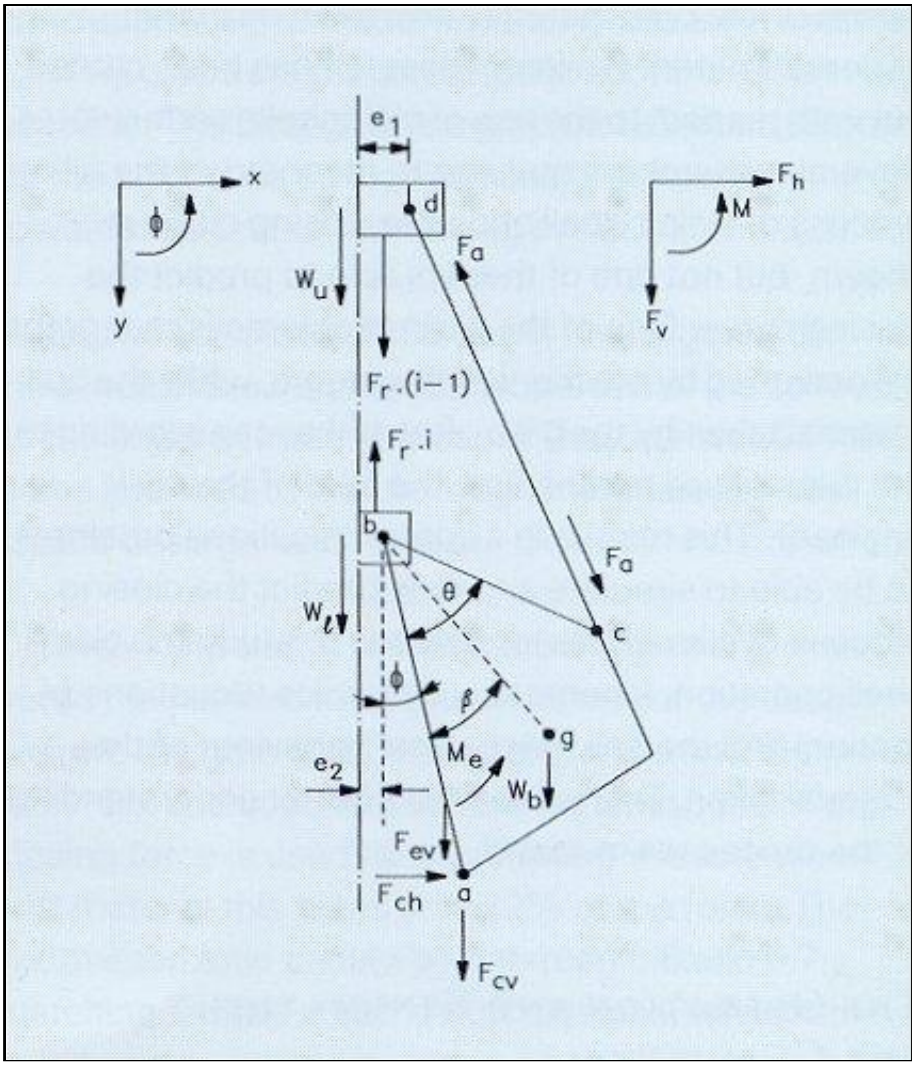

Figure 12-21: The parameters involved (forces and moments distinguished in the clamshell model).

For the upper sheave block the following equation can be derived from the equilibrium of forces:

$$\mathbf{m_u \cdot \ddot{y}_u = F_r \cdot (i-1) + W_u - F_a \cdot \cos(\alpha)} \qquad \textbf{(12-1)}$$

The motions of the lower sheave block should satisfy the equilibrium equation of forces according to:

$$\mathbf{m_i \cdot \ddot{y}_i = -F_r \cdot i + W_1 + W_b - m_b \cdot \ddot{y}_b + m_b \cdot bg \cdot \cos(\phi+\beta) \cdot \dot{\phi}^2 + F_a \cdot \cos(\alpha) + F_{cv} + F_{ev}} \qquad \textbf{(12-2)}$$

For the rotation of the bucket the following equilibrium equation of moments around the bucket bearing is valid:

$$\mathbf{I_b \cdot \ddot{\phi} = -W_b \cdot bg \cdot \sin(\phi+\beta) + m_b \cdot y_b \cdot bg \cdot \sin(\phi+\beta) - F_a \cdot \cos(\alpha) \cdot bc \cdot \sin(\phi+\theta)}$$

$$\mathbf{+F_a \cdot \sin(\alpha) \cdot bc \cdot \cos(\phi+\theta) + F_{ch} \cdot ab \cdot \cos(\phi) - F_{cv} \cdot ab \cdot \sin(\phi) - M_e} \qquad \textbf{(12-3)}$$

As can be seen, equations **(12-1)**, **(12-2)** and **(12-3)** form a system of three coupled non-linear equations of motion. Since in practice the motions of a clamshell depend only on the rope speed and the type of soil dredged, the three equations of motion must form a dependent system, with only one degree of freedom. This means that relations must be found between the motions of the upper sheave block, the lower sheave block and the bucket. A first relation can be found by expressing the rope force as the summation of all the vertical forces acting on the clamshell, this gives:

$$F_r = W_b - m_b \cdot \ddot{y}_b + W_u - m_u \cdot \ddot{y}_u + W_l - m_l \cdot \ddot{y}_l + F_{cv} + F_{ev} + m_b \cdot bg \cdot \cos(\phi + \beta) \cdot \dot{\phi}^2 \quad \textbf{(12-4)}$$

Since there are four degrees of freedom in the equations thus derived:

$$\ddot{y}_b, \ddot{y}_1, \ddot{y}_u, \ddot{\phi} \quad \textbf{(12-5)}$$

One of them has to be chosen as the independent degree of freedom, whilst the other three have to be expressed as a function of the independent degree of freedom. For the independent degree of freedom, φ is chosen as the closing angle of the bucket.

To express the motions of the upper and the lower sheave blocks as a function of the bucket rotation, the following method is applied.

The angle of an arm with the vertical **α**, can be expressed in the closing angle of the bucket by:

$$\alpha = \arcsin\left[\frac{e_2 - e_1 + bc \cdot \sin(\phi + \theta)}{dc}\right] \quad \textbf{(12-6)}$$

The distance between the upper and the lower sheave blocks can now be determined by:

$$|y_u - y_1| = dc \cdot \cos(\alpha) - bc \cdot \cos(\phi + \theta) \quad \textbf{(12-7)}$$

As can be seen, the only unknown variable in equations **(12-6)** and **(12-7)** is the closing angle **φ**. All other variables are constants, depending only on the geometry of the clamshell. A function **η(φ)** can know be defined, which is the derivative of the distance between the sheave blocks with respect to the closing angle of the buckets.

$$\eta(\phi) = \frac{d|y_u - y_1|}{d\phi} \quad \textbf{(12-8)}$$

If during a small time interval **Δt** the length of the closing rope l and the closing angle **φ**, are subject to small changes **Δl** and **Δφ**, the change of the vertical position of the upper sheave block Δy_u can be calculated with:

$$\Delta y_u = \Delta l_r - i \cdot \Delta\phi \cdot \eta(\phi) \quad \textbf{(12-9)}$$

The change of the vertical position of the lower sheave block Δy_l can be expressed by:

$$\Delta y_1 = \Delta l_r - (i-1) \cdot \Delta\phi \cdot \eta(\phi) \quad \textbf{(12-10)}$$

In equations **(12-9)** and **(12-10)** **i** is the number of parts of line. Dividing the equations **(12-9)** and **(12-10)** by the time increment **Δt** gives the equations for the velocities of the upper and the lower sheave block. For the upper sheave block equation **(12-11)** is valid.

$$\dot{y}_u = \dot{l}_r - i \cdot \dot{\phi} \cdot \eta(\phi) \quad \textbf{(12-11)}$$

The velocity of the lower sheave block can be calculated with:

$$\dot{y}_l = \dot{l}_r - (i-1) \cdot \dot{\phi} \cdot \eta(\phi) \quad \textbf{(12-12)}$$

The vertical accelerations of the upper and lower sheave block can be calculated by taking the derivative of equations **(12-11)** and **(12-12)** with respect to the time, this gives for the upper sheave block:

$$\ddot{y}_u = \ddot{l}_r - i \cdot \ddot{\phi} \cdot \eta(\phi) - i \cdot \dot{\phi}^2 \cdot \frac{d\eta(\phi)}{d\phi} \quad \textbf{(12-13)}$$

and for the lower sheave block:

$$\ddot{y}_l = \ddot{l}_r - (i-1)\cdot\ddot{\phi}\cdot\eta(\phi) - (i-1)\cdot\dot{\phi}^2\cdot\frac{d\eta(\phi)}{d\phi} \qquad \textbf{(12-14)}$$

The vertical acceleration at the center of gravity of the bucket can be expressed as a function of the vertical acceleration of the lower sheave block and the angular acceleration of the bucket according to:

$$\ddot{y}_b = \ddot{y}_l - \ddot{\phi}\cdot bg\cdot\sin(\phi+\theta) \qquad \textbf{(12-15)}$$

The three vertical accelerations can now be expressed as a function of the rotational bucket acceleration. Velocities and motions can be derived by means of integrating the accelerations if boundary conditions are given. The force in the clamshell arm can be calculated from equation **(12-1)** if the rope force $\mathbf{F_r}$ and the vertical acceleration of the upper sheave block are known.

The vertical cutting force $\mathbf{F_{cv}}$, the vertical force on the side edges $\mathbf{F_{ev}}$ and the torque on the side edges $\mathbf{M_e}$ will be discussed in the next paragraph.

Since the equations of motion are non-linear, the equations have to be solved numerically. The solution of this problem is a time domain solution, in this case using the Newton Rapson iteration method and the teta integration method to prevent numerical oscillations.

12.8. The Forces Exerted on the Buckets by Sand.

The buckets of the clamshell are subject to forces and resulting moments exerted out by the sand on the buckets. The forces and moments can be divided into forces and moments as a result of the cutting forces on the cutting edges of the buckets and forces and moments as a result of the soil pressure and friction on the side edges of the buckets.

Figure 12-21 shows the forces and moments that will be distinguished in the clamshell model. The cutting forces on the cutting edges of the buckets can be calculated with the cutting theory of Miedema (1987) and (1989) presented at WODCON XII in 1989. This theory is based on the equilibrium of forces on the layer of sand cut and on the occurrence of pore under pressures. Since the theory has been published extensively, the theory will be summarized with the following equations: If cavitation does not occur the horizontal force on the cutting edge If cavitation does not occur the horizontal force on the cutting edge can be calculated with:

$$F_{ch} = c_1\cdot\rho_w\cdot g\cdot v_c\cdot h_i^2\cdot b\cdot\frac{e}{k_m} \qquad \textbf{(12-16)}$$

$$F_{cv} = c_2\cdot\rho_w\cdot g\cdot v_c\cdot h_i^2\cdot b\cdot\frac{e}{k_m} \qquad \textbf{(12-17)}$$

If cavitation does occur the horizontal force on the cutting edge can be calculated with:

$$F_{ch} = d_1\cdot\rho_w\cdot g\cdot(z+10)\cdot h_i\cdot b \qquad \textbf{(12-18)}$$

For the vertical cutting force:

$$F_{cv} = d_2\cdot\rho_w\cdot g\cdot(z+10)\cdot h_i\cdot b \qquad \textbf{(12-19)}$$

The proportionality coefficients $\mathbf{c_1}$, $\mathbf{c_2}$, $\mathbf{d_1}$ and $\mathbf{d_2}$ can be found in Miedema (1987) or (1989).

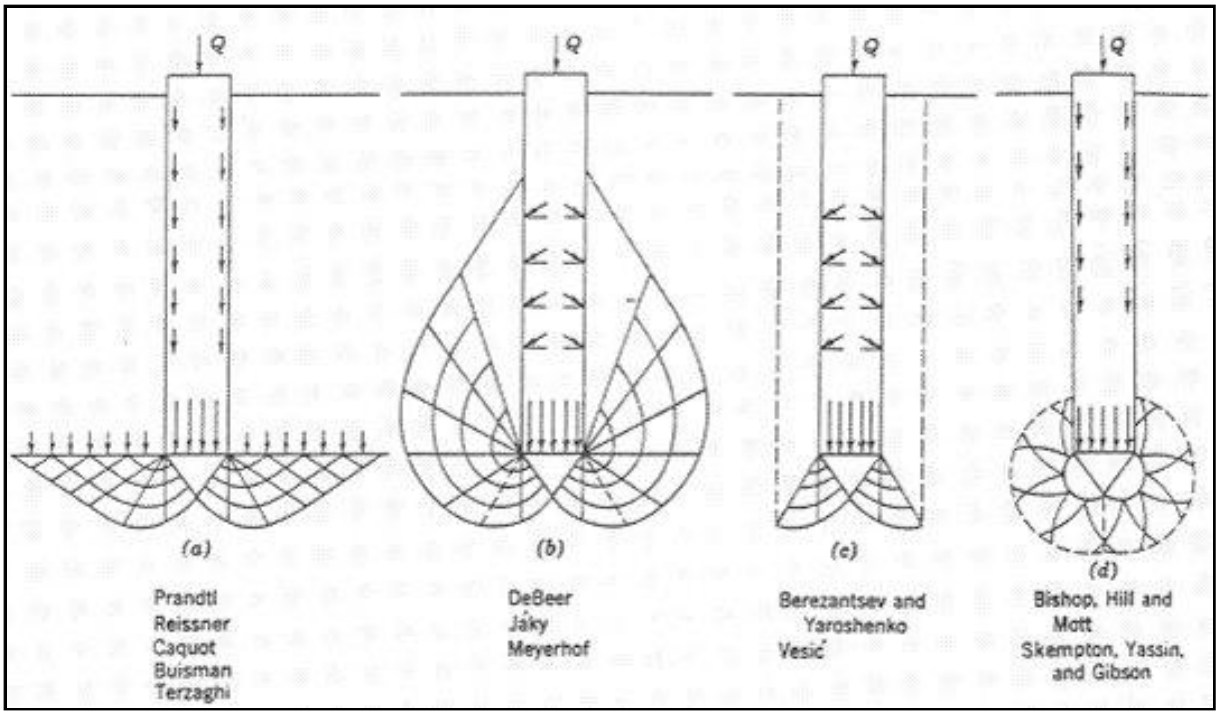

Figure 12-22: Typical failure patterns that might occur under deep foundations (Lambe & Whitman (1979))

The forces and moments on the side edges were unknown when the research started. At first it was assumed that the forces were negligible when cutting sand. From the model experiments Wittekoek (1991A), (1991B) and (1991C) carried out, it appeared that the computer program CLAMSHELL (1989) resulted productions that were too high. Changing the mechanical properties of the soil within the accuracy range could not solve this problem. Implementing pressure and friction forces on the side edges improved the calculated results drastically. The forces on the side edges are modeled as the forces on strip footings, Lambe & Whitman (1979). Figure 12-22 shows some typical failure patterns that might occur under foundations. The general equation for the pressure force on a strip footing is:

$$F_e = A_e \cdot (c \cdot N_c + \gamma_s \cdot \delta \cdot N_\gamma / 2 + \gamma_s \cdot h_i \cdot N_q) \qquad \textbf{(12-20)}$$

The friction force on the side surfaces of the buckets can be derived by integrating the shear stress over the side surfaces. It appeared from the research that this part of the forces is negligible in sand. The coefficients N_c, N_γ and N_q can be calculated according to different theories. The best-known theory is the theory of Terzaghi for shallow foundations. Theories for shallow and deep foundations have been developed by De Beer, Meyerhof, Brinch Hansen, Caquot-Kerisel, Skempton-Yassin-Gibson, Berantzef, Vesic and Terzaghi. Lambe & Whitman (1979) give an overview of these theories.
The different theories mentioned are based on different failure patterns of the soil. All theories are based on drained conditions, meaning that excess pore pressures can dissipate readily. This assumption is reasonable for static foundations, but not for the digging process of clamshells. During the digging process pore under pressures will occur, increasing the soil pressure on the side edges.

Two problems now occur in modeling the forces on the side edges. The first problem is, which theory to choose for the side edge forces under drained conditions such as those occurring during the initial penetration and the digging process in dry sand. The second problem involves the modeling of the influence of pore pressures on the side edge forces as it occurs when cutting saturated sand.

The first problem was solved by examining the initial penetration and the digging curves that occurred with 8 tests in dry sand. It required some trial and error to find satisfactory coefficients for equation **(12-20)**. The second problem was solved by examining the initial penetration and the measured digging curves in saturated sand. Although the resulting equation for the force on the side edges is empirical, it is based on a combination of Terzaghi's foundation theory and Miedema's cutting theory.

$$F_e = A_e \cdot (\gamma_s \cdot h_i / 2 + \gamma_w \cdot \Delta_p) \cdot N_q \qquad \textbf{(12-21)}$$

The pore under pressure **Δp** in equation **(12-21)** follows from the sand cutting theory of Miedema (1987). The parts of equation **(12-20)** containing N_c and N_γ appeared to be negligible and thus cannot be found in equation **(12-21)**. To calculate this penetration the empirical formula of Gebhart (1972) can also be used, but does not consider the pore pressures:

$$F_e = 0.14 \cdot e^{0.0019 d_m} \cdot K_f \cdot 1.26^{(\rho_s - 1)} + 0.21 \cdot 10^{-3} e^{(0.0175 d_m)} \cdot (B - 900) + 1.21 \cdot 10^{-3} \cdot e^{(0.0145 d_m)} \cdot (h - 300) \qquad \textbf{(12-22)}$$

12.9. The Research Carried Out.

For the verification and validation of the calculation method as described in the previous paragraphs, a test rig was built in the Dredging Engineering Research Laboratory of the Delft University of Technology. The test rig consisted of a model clamshell grab, a container filled with 100 μm sand, a vibration device, a cone penetrometer and a data-acquisition system. Figure 12-23 gives an impression of the test stand. Figure 12-25 shows the model clamshell used. On the model clamshell two displacement transducers were mounted, to measure the vertical position and the closing angle. In the closing wire a force transducer was mounted to measure the closing force. The vibration device was used to compact the sand and thus make it possible to get sand with different soil mechanical properties. The cone penetrometer was used to determine the cone resistance of the sand.

By means of calibration diagrams (Miedema (1987)), when the cone resistance is known, the density, the angle of internal friction, the soil interface friction angle and the permeability of the sand could be determined. All transducers were connected with the data-acquisition system, so the data could be processed by a computer. The aim of the research was to do tests in dry and saturated sand, compare the results with simulations of the CLAMSHELL program, and adjust the calculation method if necessary. Since the calculation method is fundamental, it should not matter on which scale the tests are carried out. As explained in the previous paragraph, the forces exerted on the buckets by the sand include a part determined by the mechanical properties of the dry sand and a part determined by the mechanical properties of the saturated sand. Also, the forces consist of part acting on the cutting edges of the buckets and a part acting on the side edges of the buckets.

From Miedema (1987) and (1989) the cutting forces on the cutting edges can be calculated in dry and in saturated sand. What would occur on the side edges was not known when this research started. To quantify the side edge forces, first 8 tests were carried out in dry sand. Since the force of the closing wire was measured and the real cutting forces could be calculated, the forces on the side edges remained. Repeating this with 14 tests in saturated sand gave a good impression of the influence of saturation on the side edge forces. As a result of these tests, an equation was derived for the side edge forces in dry and in saturated sand as described in the previous paragraph.

Figure 12-26, Figure 12-27, Figure 12-28 and Figure 12-29 give an example of the test results and the simulations. Figure 12-26 is the result of a test in dry sand with 10 minutes vibration time. Figure 12-27 is the result of a simulation with the same mechanical properties of the soil. As can be seen, the digging curves correlate well. The closing force calculated is very smooth, while the closing force measured shows irregularities as a result of the occurrence of discrete shear surfaces in the sand (chipping). The correlation is reasonable, however. Figure 12-28 is the result of a test in saturated sand with 15 minutes vibration time. Figure 12-29 is the result of a simulation with the same mechanical properties of the soil. Again, the digging curves correlate well. The shape of the simulated closing force as a function of the span differs slightly from the measured shape, but the magnitude of the measured and the calculated closing force correlate well. The angular velocity was derived from the signals of the displacement transducers. The shape of this signal from test and simulation correlates well, although irregularities occur in the measured angular velocity.

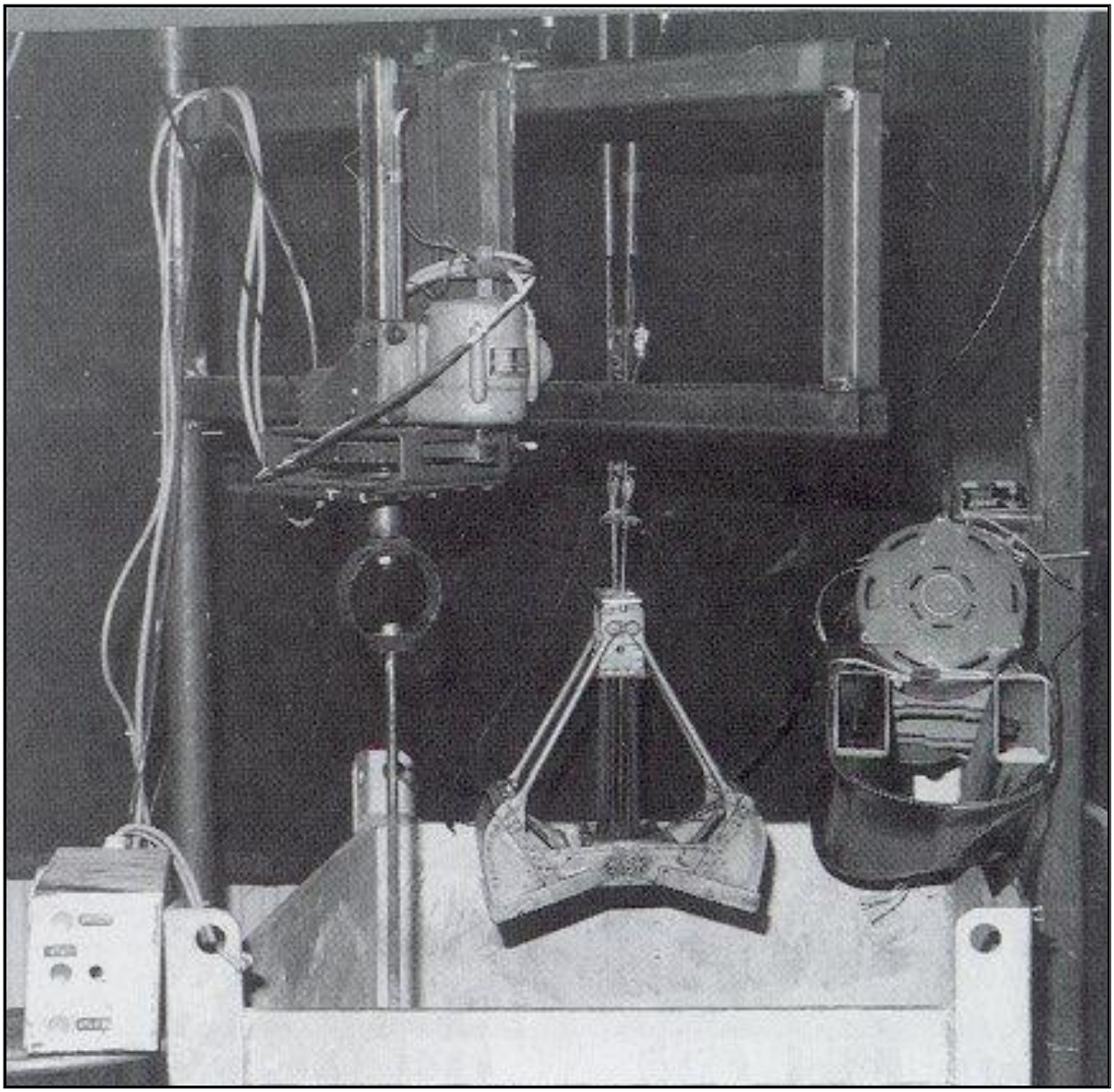

Figure 12-23: The test rig with the model clamshell grab, a vibration device and a cone penetrometer.

In the 90's a separate version of the CLAMSHELL program has been developed in cooperation with Boskalis called HYCLAM. This program is capable of simulating and prediction the closing behavior of hydraulic clamshells.

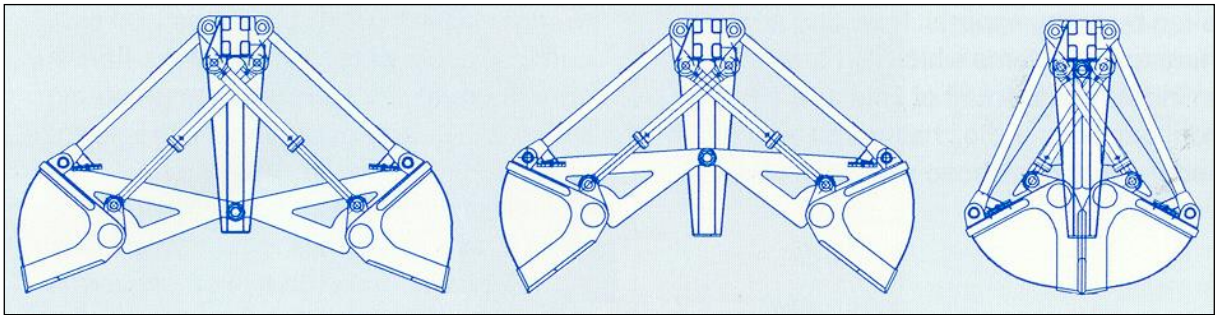

Figure 12-24: Horizontal closing hydraulic grab (Boskalis).

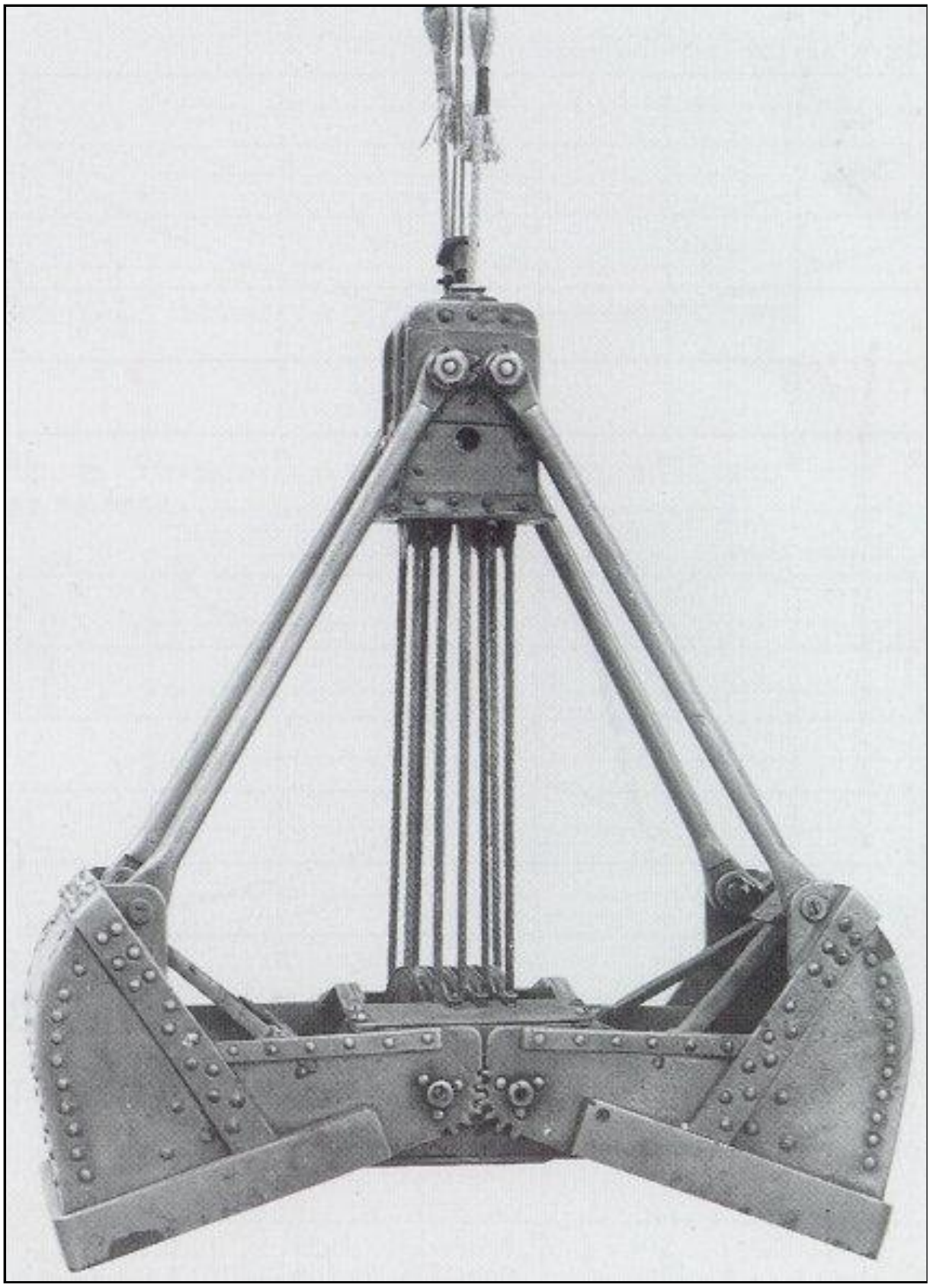

Figure 12-25: Close up of the clamshell model.

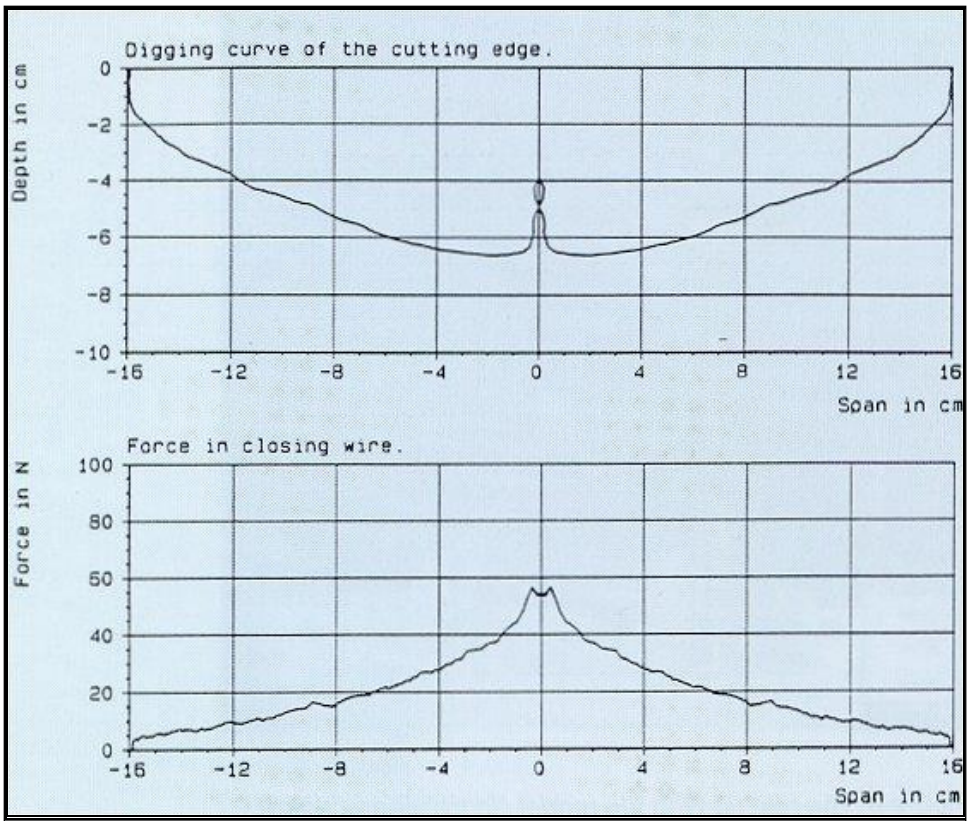

Figure 12-26: Result of a cutting test in dry sand.

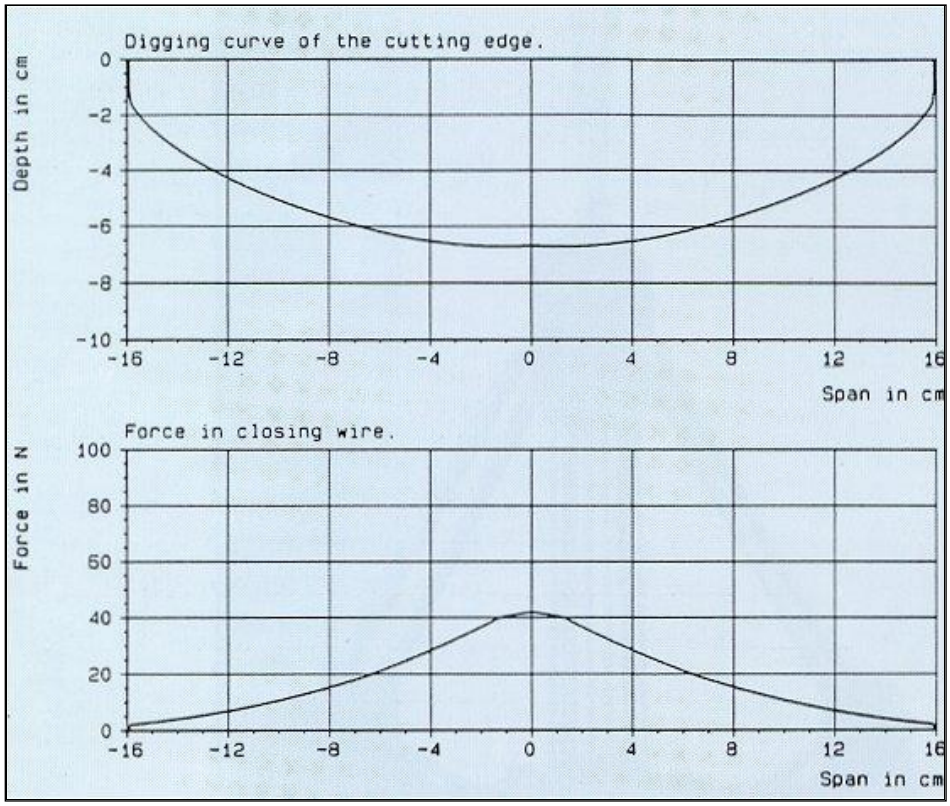

Figure 12-27: Result of a simulation in dry sand.

12.10. Conclusions.

As a result of analyzing the closing process of a clamshell from the point of view of a mechanical engineer and of a civil engineer, a numerical method of calculation has been developed that simulates the closing process very well. The laboratory research carried out has been a great help in adjusting and tuning the computer program CLAMSHELL. The correlation between the test results and the results of the simulations was good. With respect to the mathematical modeling it appears that the forces on the side edges of the buckets are of the same magnitude as the real cutting forces and can certainly not be neglected. With respect to the use of the CLAMSHELL program it can be stated that the program has already been very useful for the prediction of the production of a clamshell used in dredging operations, moreover the program can also be of great help in designing improved clamshells as well. Studies have already been carried out by Great Lakes, to find optimum clamshell kinematics and mass distribution. A next step in this research will be, the verification and validation of clay cutting with clamshell grabs.

12.11. Developments.

When cutting water saturated sand, as is done in dredging, agriculture and soil movement in general, the process is dominated by the phenomenon of dilatancy. Based on pore pressure calculations and the equilibrium of horizontal and vertical forces, equations can be derived to predict the cutting forces. The derivation of this model has been described extensively in previous papers by Miedema et al. (1987), (1993) and (2005). In the equations derived, the denominator contains the sine of the sum of the 4 angles involved, the cutting angle α, the shear angle β, the angle of internal friction φ and the soil interface friction angle δ. So, when the sum of these 4 angles approaches 180° the sine will become zero and the cutting forces become infinite. When the sum of these 4 angles is greater than 180° the sine becomes negative and so do the cutting forces. Since this does not occur in reality, nature must have chosen a different mechanism for the case where the sum of these 4 angles approaches 180°.
Hettiaratchi and Reece (1975) found a mechanism which they called boundary wedges for dry soil. At large cutting angles, a triangular wedge will exist in front of the blade, not moving relative to the blade. This wedge acts as a blade with a smaller blade angle. In fact, this reduces the sum of the 4 angles involved to a value much smaller than 180°. The existence of a dead zone (wedge) in front of the blade when cutting at large cutting angles will affect the value and distribution of vacuum water pressure on the interface. He and Vlasblom (1998), proved experimentally that also in water saturated sand at large cutting angles a wedge will occur.
The wedge occurs at blade angles larger than 70º and thus has a significant effect on the initial part of the closing process of clamshells. In following publications, the effect of this wedge on the closing process of clamshell's will be described, Miedema (2005).

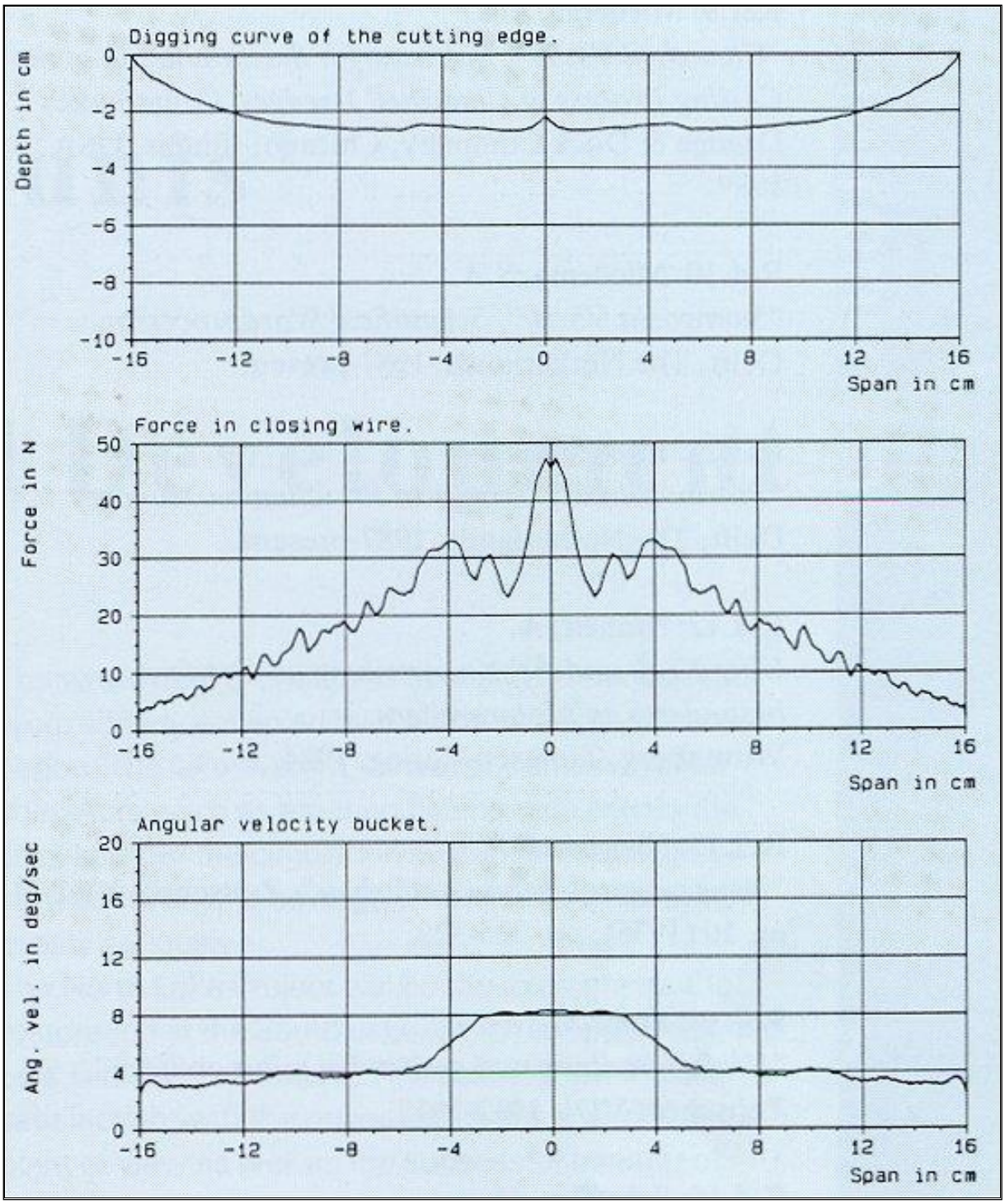

Figure 12-28: Result of a cutting test in saturated sand.

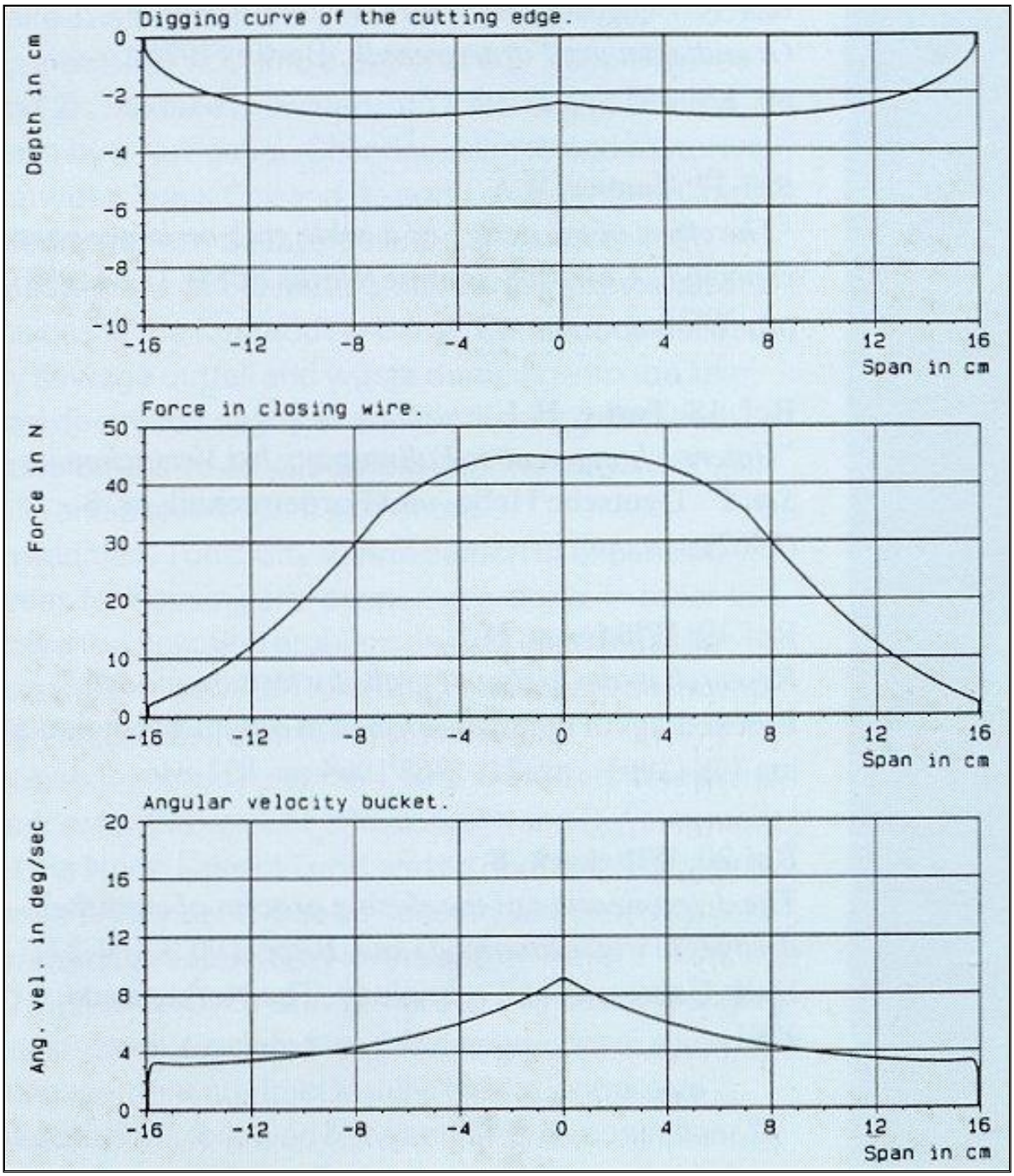

Figure 12-29: Result of a simulation in saturated sand.

12.12. Nomenclature.

ab	Distance between cutting edge and bucket bearing	**m**
A_e	Surface of side edges (thickness*length)	**m^2**
b	Width of the buckets	**m**
bc	Distance between bucket bearing and arm bearing	**m**
bg	Distance between bucket bearing and center of gravity	**m**
B	Width of grab	**m**
c	Cohesion	**Pa**
c_1	Proportionality coefficient non-cavitating cutting forces	**-**
c_2	Proportionality coefficient non-cavitating cutting forces	**-**
d_1	Proportionality coefficient cavitating cutting forces	**-**

d_2	Proportionality coefficient cavitating cutting forces	-
dc	Length of arm	m
d_m	Average grain diameter	µm
e	Volume fraction of dilatational expansion	-
e_1	Eccentricity arm bearing upper sheave block	m
e_2	Eccentricity bucket bearing lower sheave block	m
F_a	Force in one arm	N
F_{ch}	Horizontal force on the cutting edge	N
F_{cv}	Vertical force on the cutting edge	N
F_e	Force on side edges	N
F_{ev}	Vertical force on the side edges	N
F_r	Force in the closing rope (wire)	N
g	Gravitational constant (9.81)	m/s^2
h_i	Thickness of layer cut	m
h	The initial penetration	m
i	Number of parts of line	-
I_b	Mass moment of inertia of bucket	$kg \cdot m^2$
k_m	Average permeability	m/s
K_f	The grain shape factor	-
l	Rope length	m
L	Length of fully opened grab	m
m_b	Mass + added mass of bucket	N
m_l	Mass + added mass of lower sheave block	kg
m_u	Mass + added mass of upper sheave block and arms	kg
M_{bucket}	Mass of grab	kg
M_f	Mass of grab fill	kg
M_e	Moment of side edge forces around bucket bearing	Nm
N_c	Terzaghi coefficient	-
$N_{\square}$	Terzaghi coefficient	-
N_q	Terzaghi coefficient	-
p	Pressure	Pa
v_c	Cutting velocity	m/s
W_b	Underwater weight of bucket	N
W_l	Underwater weight of lower sheave block	N
W_u	Underwater weight of upper sheave block and arms	N
y_b	Vertical position of bucket center of gravity	m
y_l	Vertical position of lower sheave block	m
y_u	Vertical position of upper sheave block	m
z	Water depth	m
α	Angle of arm with vertical	rad
β	Angle between cutting edge, bucket bearing and bucket centre of gravity	rad
φ	Closing (opening) angle of bucket with vertical	rad
θ	Angle between cutting edge, bucket and arm bearings	rad
η(φ)	Function	m
ρ_w	Density water	kg/m^3
γ_w	Specific weight of water	N/m^3
ρ_s	The situ density of material to be dredged	kg/m^3
γ_s	Specific weight of sand under water	N/m^3
δ	Thickness of side edges	m

Chapter 13: Notes.

Chapter 14: References.

(WIHEE), W. I. (1960). River Mechanics (In Chinese). *Industry Press, China*, 44-60.

Abelev, A., & Valent, P. (2010). *Strain rate dependency of strength of soft marine deposits of the Gulf of Mexico.* Stennis Space Center, MS 39529, USA.: Naval Research Laboratory.

Abulnaga, B. E. (2002). *Slurry Systems Handbook.* USA: McGraw Hill.

Azamathulla, H. M., & Ahmad, Z. (2013). Estimation of critical velocity for slurry transport through pipeline using adaptive neuro-fuzzy interference system and gene-expression programming. *Journal of Pipeline Systems Engineering and Practice.*, 131-137.

Babcock, H. A. (1970). The sliding bed flow regime. *Hydrotransport 1* (pp. H1-1 - H1-16). Bedford, England: BHRA.

Bagnold, R. A. (1954). Experiments on a gravity free dispersion of large solid spheres in a Newtonian fluid under shear. *Proceedings Royal Society, Vol. A225.*, 49-63.

Bagnold, R. A. (1957). The flow of cohesionless grains in fluids. *Phil. Trans. Royal Society, Vol. A249*, 235-297.

Bagnold, R. A. (1966). An approach to the sediment transport problem from general physics. *Physiographic & Hydraulic Studies of Rivers.*, I1-I37.

Bain, A. G., & Bonnington, S. T. (1970). *The hydraulic transport of solids by pipeline.* Pergamon Press.

Barker, A., Sayed, M., & Carrieres, M. (2004). Determination of iceberg draft, mass and cross sectional areas. *14th international offshore and polar engineering conference.* Toulon, France.

Barrette, P. (2011). Offshore pipeline protection against seabed scouring, an overview. *Cold Regions Science Technology, Vol. 69.*, 3-20.

Barry, K. (2003). *The effect of clay particles in pore water on the critical shear stress of sand. (PhD thesis).* Gainesville: University of Florida.

Barry, K., Thieke, R., & Mehta, A. (2006). Quasi-hydrodynamic lubrication effect of clay particles on sand grain erosion. *Estuarine, Coastal and Shelf Science (67)*, 161-169.

Bauerslag, D. (1979). *Untersuchungen zum Fullverhalten von Motorgreifern. PhD Thesis.* Hannover, Germany: Universitat Hannover.

Becker, S., Miedema, S., Jong, P., & Wittekoek, S. (1992). On the Closing Process of Clamshell Dredges in Water Saturated Sand. *WODCON XIII* (p. 22 pages). Bombay, India: WODA.

Becker, S., Miedema, S., Jong, P., & Wittekoek, S. (1992, September). The Closing Process of Clamshell Dredges in Water Saturated Sand. *Terra et Aqua, No. 49*, 22 pages.

Berg, C. H. (1998). *Pipelines as Transportation Systems.* Kinderdijk, the Netherlands: European Mining Course Proceedings, IHC-MTI.

Berg, C. v. (2013). *IHC Merwede Handbook for Centrifugal Pumps & Slurry Transportation.* Kinderdijk, Netherlands: IHC Merwede.

Berman, V. P. (1994). *Gidro i aerodinamiceskie osnovy rascota truboprovodnych sistem gidrokontejnernogo i vysokonapornogo pnevmaticeskogo transporta.* Lugansk: East Ukrainian State University.

Biot, M. (1941). General theory of three dimensional consolidation. *Journal of Applied Physics, vol. 12.*, 155-164.

Bishop, A. (1966). The strength of soils as engineering materials. *Geotechnique, vol. 16, no. 2.*, 91-128.

Bisschop, F., Miedema, S. A., Rhee, C. v., & Visser, P. J. (2014). Erosion experiments on sand at high velocities. *To be submitted to the Journal of Hydraulic Engineering*, 28.

Blasco, S. M., Shearer, J. M., & Myers, R. (1998). Seabed scouring by sea ice: scouring process and impact rates. *1st ice scour and arctic marine pipelines workshop, 13th international symposium on Okhotsk Sea and Sea Ice.*, (pp. 53-58). Mombetsu, Hokkaido, Japan.

Blatch, N. S. (1906). Discussion of Works for the purification of the water supply of Washington D.C. *Transactions ASCE 57.*, 400-409.

Blythe, C., & Czarnotta, Z. (1995). Determination of hydraulic gradient for sand slurries. *8th International Freight Pipeline Society Symposium*, (pp. 125-130). Pittsburg, USA.

Bobertz, B., Harff, J., & Bohling, B. (2009). Parameterisation of clastic sediments including benthis structures. *Journal of Marine Systems (75)*, 371-381.

Bohling, B. (2009). Measurements of threshold values for incipient motion of sediment particles with two different erosion devices. *Journal of Marine Systems (75)*, 330-335.

Bonneville, R. (1963). *essais de synthese des lois debut d'entrainment des sediment sous l'action d'un courant en regime uniform.* Chatou: Bulletin Du CREC, No. 5.

Bonnington, S. T. (1961). *Estimation of Pipe Friction Involved in Pumping Solid Material.* BHRA, TN 708 (December 1961).

Boothroyde, J., Jacobs, B. E., & Jenkins, P. (1979). Coarse particle hydraulic transport. *Hydrotransport 6: 6th International Conference on the Hydraulic Transport of Solids in Pipes.* (p. Paper E1). BHRA.

Bos, C. G. (1987). *Weerstand van grijpermessen in stortgoed. MSc Thesis.* Delft, The Netherlands: Delft University of Technology.

Bourbonnair, J., & Lananyi, B. (1985). The mechanical behaviour of a frozen clay down to cryogenic temperatures. *4th symposium on ground freezing.*, (pp. 237-244). Sapporo, Japan.
Braaksma, J., Klaassens, J., Babuska, R., & Keizer, C. d. (2007). A computationally efficient model for predicting overflow mixture density in a hopper dredger. *Terra et Aqua, 106(16)*, 16-25.
Brakel, J. (1981). *Mathematisch model voor de krachten op een roterende snijkop van een in zeegang werkende snijkopzuiger.* Delft, Netherlands: Delft University of Technology - ScO/80/96.
Brauer, H. (1971). *Grundlagen der einphasen- und mehrphasenstromungen.* Verslag Sauerlander.
Bree, S. E. (1977). Centrifugal DredgePumps. *Ports & Dredging (10 issues, IHC Holland).*
Brooks, F. A., & Berggren, W. (1944). Remarks on turbulent transfer across planes of zero momentum exchange. *Transactions of the American Geophysics Union, Pt. VI.*, 889-896.
Brownlie, W. (1981). *Compilation of alluvial channel data: laboratory and field, Technical Report KH-R-43B.* Pasadena, California, USA: California Institute of Technology.
Buffington, J. M. (1999). The legend of A.F. Shields. *Journal of Hydraulic Engineering, 125*, 376–387.
Buffington, J. M., & Montgomery, D. R. (1997). A systematic analysis of eight decades of incipient motion studies, with special reference to gravel-bedded rivers. *Water Resources Research, 33*, 1993-2029.
Burger, M. (2001). Influence of ladder inclination angle and particle size on cutterhead production. *WODCON XVI.* Kuala Lumpur, Malaysia: WODA.
Burger, M. (2003). *Mixture forming processes in dredge cutter heads. PhD Thesis.* Delft, Netherlands: Delft University of Technology.
Burger, M. d., & Talmon, A. M. (2001). Mechanical transportation of particles induced by cutterblade geometry. *CEDA Dredging Days 2001.* Amsterdam, the Netherlands: CEDA.
Burger, M. d., & Talmon, A. M. (2002). Particle trajectories along a cutter blade, using the results of a CFD model for the flow. *Dredging 02 Key Technologies for Global Prosperity.* Orlando, Florida, USA: ASCE.
Burger, M. d., Vlasblom, W. J., & Talmon, A. M. (1999). Influence of operational parameters on dredge cutterhead spillage. *CEDA DRedging Days 1999.* Amsterdam, the Netherlands: CEDA.
Burger, M. d., Vlasblom, W. J., & Talmon, A. M. (2005). Design aspects for cutter heads related to the mixture forming process when cutting coarse materials. *Terra et Aqua 98*, 12-18.
Butterfield, R., & Andrawes, K. (1972). On the angles of friction between sand and plane surfaces. *Journal of Terramechanics, vol. 8, no. 4.*, 15-23.
Camenen, B., & Larson, M. (2013). Accuracy of Equivalent Roughness Height Formulas in Practical Applications. *Journal of Hydraulic Engineering.*, 331-335.
Camenen, B., Bayram, A. M., & Larson, M. (2006). Equivalent roughness height for plane bed under steady flow. *Journal of Hydraulic Engineering*, 1146-1158.
Camp, T. (1936). Study of rational design of settling tanks. *Sewage Works Journal 8-5.*, 742-758.
Camp, T. (1946). Sedimentation and the design of settling tanks. *ASCE Transactions*, 895-936.
Camp, T. (1953). Studies of sedimentation design. *Sewage & Industrial Wastes 25*, 1-14.
Cao, Z. (1997). Turbulent Bursting Based Sediment Entrainment Function. *Journal of Hydraulic Engineering, Vol. 123(3)*.
Carman, P. (1937). Fluid flow through granular beds. *Transactions Institute Chemical Engineering, 15, 150.*
Carman, P. (1956). *Flow of gases through porous media.* London: Butterworths Scientific Publications.
Charles, M. E. (1970). Transport of solids by pipeline. *Hydrotransport 1.* Cranfield: BHRA.
Charru, F., Mouilleron, H., & Eiff, O. (2004). Erosion and deposition of particles on a bed sheared by a viscous flow. *Journal of fluid mechanics, Vol. 519.*, 55-80.
Chaskelberg, K., & Karlin. (1976). *Rascot gidrotransporta pesanych materialov.* Moskov: Gidromechanizacija.
Chen, X., & Miedema, S. A. (2014). NUMERICAL METHODS FOR MODELING THE ROCK CUTTING PROCESS IN DEEP SEA MINING. *OMAE 2014* (p. 10). San Francisco, USA: ASME.
Chepil, W. (1958). The use of evenly spaced hemispheres to evaluate aerodynamic force on a soil failure. *Transaction of the American Geophysics Union, Vol. 39(3)*, 397-404.
Chepil, W. (1959). Equilibrium of soil grains at the threshold of movement by wind. *Soil Science Society of America Proceedings 23*, (pp. 422-428).
Chien, N., & Wan, Z. (1999). Mechanics of sediment transport. *ASCE.* Reston, Va, USA: ASCE.
Chin, C. O., & Chiew, Y. M. (1993). Effect of bed surface structure on spherical particle stability. *Journal of Waterway, Port, Coastal and Ocean Engineering, 119(3)*, 231–242.
Clift, R., Wilson, K. C., Addie, G. R., & Carstens, M. R. (1982). A mechanistically based method for scaling pipeline tests for settling slurries. *Hydrotransport 8* (pp. 91-101). Cranfield, UK.: BHRA Fluid Engineering.
Clift, R., Wilson, K., Addie, G., & Carstens, M. (1982). A mechanistically based method for scaling pipeline tests for settling slurries. *Hydrotransport 8* (pp. 91-101). Cranfield, UK.: BHRA.

References.

Colebrook, C. F., & White, C. M. (1937). Experiments with Fluid Friction in Roughened Pipes. *Proceedings of the Royal Society of London. Series A, Mathematical and Physical Sciences 161 (906).* (pp. 367-381). London: Royal Society of London.

Coleman, N. L. (1967). A theoretical and experimental study of drag and lift forces acting on a sphere resting on a hypothetical stream bed. *International Association for Hydraulic Research,12th Congress, 3*, pp. 185-192.

Coleman, N. L., & Ellis, W. M. (1976). Model study of the drag coefficient of a streambed particle. *Federal Interagency Sedimentation Conference*, (pp. 4-12). Denver, Colorado.

Condolios, E., & Chapus, E. E. (1963A). Transporting Solid Materials in Pipelines, Part I. *Journal of Chemical Engineering, Vol. 70(13).*, 93-98.

Condolios, E., & Chapus, E. E. (1963B). Designing Solids Handling Pipelines Part II. *Journal of Chemical Engineering, Vol. 70(14).*, 131-138.

Condolios, E., & Chapus, E. E. (1963C). Operating solids pipelines, Part III. *Journal of Chemical Engineering, Vol. 70(15).*, 145-150.

Coulomb, C. (1776). Essai sur une application des regles des maximis et minimis a quelques problemes de statique relatifs a l'architecture. *Academie royale des sciences, Paris, Memoires de mathematique et de physique, vol. 7.*, 343-382.

Cox, C. M., Eygenraam, J. A., Granneman, C. C., & Njoo, M. (1995). A Training Si,ulator for Cutter Suction Dredgers: Bridging the Gap between Theory and Practice. *WODCON XIV* (p. 10). Amsterdam, The Netherlands.: WODA.

Crowe, C. T. (2006). *MultiPhase Flow Handbook.* Boca Raton, Florida, USA: Taylor & Francis Group.

Dade, W., Nowell, A., & Jumars, P. (1992). Predicting erosion resistance of muds. *Marine Geology, 105*, 285-297.

Davies, J. T. (1987). Calculation of critical velocities to maintain solids in suspension in horizontal pipes. *Chemical Engineering Science, Vol. 42(7).*, 1667-1670.

Dekker, M. A., Kruyt, N. P., Burger, M. d., & Vlasblom, W. J. (2003). Experimental and numerical investigation of cutter head dredging flows. *Journal of Waterways, Port, Coastal and Ocean Engineering, Vol. (129 (5).*, 203-209.

Dekker, M. A., Vlasblom, W. J., & Kruyt, N. P. (1999). Measuring water velocities round a cutterhead. *CEDA Dredging Days 1999.* Amsterdam, the Netherlands: CEDA.

Detournay, E., & Atkinson, C. (2000). Influence of pore pressure on the drilling response in low permeability shear dilatant rocks. *International Journal of Rock Mechanics & Mining Sciences, vol. 37.*, 1091-1101.

Dey, S. (1999). Sediment threshold. *Applied Mathematical Modelling*, 399-417.

Dey, S. (2003). Incipient motion of bivalve shells on sand beds under flowing water. *Journal of Hydraulic Engineering*, 232-240.

Dey, S. (2014). *Fluvial Hydrodynamics.* Kharagpur, India: Springer, GeoPlanet: Earth and Planetary Sciences.

Dey, S., & Raikar, R. (2007). Characteristics of loose rough boundary streams at near threshold. *Journal of Hydraulic Engineering, ASCE.*, 288-304.

DHL. (1972). *Systematic Investigation of Two Dimensional and Three Dimensional Scour, Report M648/M863.* Delft, Netherlands: Delft Hydraulics Laboratory.

Di Filice, R. (1999). The sedimentation velocity of dilute suspensions of nearly monosized spheres. *International Journal of Multiphase Flows 25*, 559-574.

Dietrich, G. (1968). *Einfluss der Korngrosse des Schuttgutes auf die Fullmasse von zwei Schalengreifern. PhD Thesis.* Dresden, Germany: Technische Universitat Dresden.

Dittrich, A., Nestmann, F., & Ergenzinger, P. (1996). Ratio of lift and shear forces over rough surfaces. *Coherent flow structures in open channels.*, 126-146.

Dobbins, W. (1944). Effect of Turbulence on Sedimentation. *ASCE Transactions Vol. 109, No. 2218*, 629-656.

Doron, P., & Barnea, D. (1993). A three layer model for solid liquid flow in horizontal pipes. *International Journal of Multiphase Flow, Vol. 19, No.6.*, 1029-1043.

Doron, P., & Barnea, D. (1995). Pressure drop and limit deposit velocity for solid liquid flow in pipes. *Chemical Engineering Science, Vol. 50, No. 10.*, 1595-1604.

Doron, P., & Barnea, D. (1996). Flow pattern maps for solid liquid flow in pipes. *International Journal of Multiphase Flow, Vol. 22, No. 2.*, 273-283.

Doron, P., Granica, D., & Barnea, D. (1987). Slurry flow in horizontal pipes, experimental and modeling. *International Journal of Multiphase Flow, Vol. 13, No. 4.*, 535-547.

Doron, P., Simkhis, M., & Barnea, D. (1997). Flow of solid liquid mixtures in inclined pipes. *International Journal of Multiphase Flow, Vol. 23, No. 2.*, 313-323.

Dou, G. (1962). theorie de l'entrainement des particeles sedimentaires. *Scienta Sinica, vol. XI, Nr. 7, Trad. 1314 CREC, 1962.*

Dou, G. (1964). On threshold velocity of sediment particle. *Journal of Hydraulic Engineering (in Chinese)*, 22-31.

Dou, G. (2000). Incipient motion of sediment under currents. *China Ocean Engineering (4, in Chinese).*, 391.

Dou, G. (2001). Incipient motion of sediment by waves. *Science in China (44-3)*, 309-318.

Duckworth, & Argyros. (1972). Influence of density ratio on the pressure gradient in pipes conveying suspensions of solids in liquids. *Hydrotransport 2.* Coventry: BHRA.

Durand, R. (1953). Basic Relationships of the Transportation of Solids in Pipes - Experimental Research. *Proceedings of the International Association of Hydraulic Research.* Minneapolis.

Durand, R., & Condolios, E. (1952). Etude experimentale du refoulement des materieaux en conduites en particulier des produits de dragage et des schlamms. *Deuxiemes Journees de l'Hydraulique.*, 27-55.

Durand, R., & Condolios, E. (1952). Etude experimentale du refoulement des materieaux en conduites en particulier des produits de dragage et des schlamms. (Experimental study of the discharge pipes materieaux especially products of dredging and slurries). *Deuxiemes Journees de l'Hydraulique.*, 27-55.

Durand, R., & Condolios, E. (1956). Donnees techniques sur le refoulement des mixture en conduites. *Revue de lÍndustriele Minerale, no. 22F*, 460-481.

Durand, R., & Condolios, E. (1956). *Technical data on hydraulic transport of solid materials in conduits.* Revue de L'Industrie Minerale, Numero Special 1F.

Durepaire, M. P. (1939). Contribution a létude du dragage et du refoulement des deblais a état de mixtures. *Annales des ponts et chaussees, Memoires I.*, 165-254.

Egiazarof, I. (1965). Calculation of non-uniform sediment concentrations. *Journal of the Hydraulic Division, ASCE, 91(HY4)*, 225-247.

Einstein, A. (1905). On the motion of small particles suspended in liquids at rest required by the molecular kinetic theory of heat. *Annalen der Physik Vol.17.*, 549-560.

Ellis, H. S., & Round, G. F. (1963). Laboratory studies on the flow of Nickel-Water suspensions. *Canadian Journal on Minerals & Mettalurgy, Bull. 56.*

Engelund, F., & Hansen, E. (1967). A monograph on sediment transport to alluvial streams. *Copenhagen: Technik Vorlag*.

Evans, I. (1962). A theory on basic mechanics of coal ploughing. *International symposium on mining research.*, (pp. 761-798).

Evans, I. (1964). The force required to cut coal with blunt wedges. *Mining Research Establishment Isleworth*.

Evans, I. (1965). The force required to cut coal with blunt wedges. *International journal of rock mechanics and mining science.*, 1-12.

Evans, I., & Pomeroy, C. (1966). *The strength, fracture and workability of coal.* Pergamon Press.

Everts, C. (1973). Particle overpassing on flat granular boundaries. *Journal of Waterways, Harbors, & Coastal Engineering, ASCE Vol. 99(WW4).*, 425-438.

Fairhurst, C. (1964). On the validity of the Brazilian test for brittle materials. *International Journal of Rock Mechanics & Mining Sciences, vol. 1.*, 535-546.

Feiler, A., Bergstrom, L., & Rutland, M. (2008). Superlubricity using repulsive van der Waals forces. *Langmuir (24)*, 2274-2276.

Fenton, J. D., & Abbott, J. E. (1977). Initial movement of grains on a stream bed: The effect of relative protrusion. *Proceedings of Royal Society, 352(A)*, pp. 523–537. London.

Fernandez-Luque. (1974). *Erosion and Transport of Bed-Load Sediment. PhD Thesis.* Meppel, The Netherlands: Krips Repro B.V.

Fitton, T. G. (2015). A deposit velocity equation for open channels and pipes. *17th International Conference on Transport & Sedimentatin of Solid Particles.* (pp. 69-77). Delft, The Netherlands: Delft University of Technology.

Fowkes, R. S., & Wancheck, G. A. (1969). *Materials handling research: Hydraulic transportation of coarse solids.* U.S. Department of the interior, Bureau of Mines, Report 7283.

Franzi, G. (1941). *Sul moto dei liquidi con materie solide in suspensione.* Milano, Italy: Instituto di idraulica e costrusioni idrauliche dei politechnico di Milano, No. 47.

Fuhrboter, A. (1961). *Über die Förderung von Sand-Wasser-Gemischen in Rohrleitungen.* Mitteilungen des Franzius-Instituts, H. 19.

Fuhrboter, A. (1961). *Über die Förderung von Sand-Wasser-Gemischen in Rohrleitungen. (On the advances of sand -water mixtures in pipelines).* Mitteilungen des Franzius-Instituts, H. 19.

Gandhi, R. (2015, February). Personal communication.

Garcia, M. H. (2008). *Sedimentation Engineering* (Vol. 110). ASCE Manuals & Reports on Engineering Practise No. 110.

Garside, J., & Al-Dibouni, M. (1977). Velocity-Voidage Relationships for Fluidization and Sedimentation in Solid-Liquid Systems. *2nd Eng. Chem. Process Des. Dev., 16, 206*.

Gebhardt, R. (1972). Eindringwiederstande korniger haufwerke. *Hebezuege und Fordermittel 12.*, 241-247.

Gehking, K. (1987). *Rock Testing Procedures at VA's Geotechnical Laboratory in Zeltweg.* Zeltweg, Austria.: Voest Alphine, International Report TZU 48.

Gibert, R. (1960). Transport hydraulique et refoulement des mixtures en conduites. *Annales des Ponts et Chausees.*, 130(3), 307-74, 130(4), 437-94.

Gibert, R. (1960). Transport hydraulique et refoulement des mixtures en conduites. (Hydraulic transport and discharge pipes of mixtures). *Annales des Ponts et Chausees.*, 130(3), 307-74, 130(4), 437-94.

Gillies, D. P. (2013). *Particle contributions to kinematic friction in slurry pipeline flow, MSc Thesis.* University of Alberta, Department of Chemical Engineering.

Gillies, R. G. (1993). *Pipeline flow of coarse particles, PhD Thesis.* Saskatoon: University of Saskatchewan.

Gillies, R. G. (2015). Personal communication.

Gillies, R. G., & Shook, C. A. (1994). Concentration distributions of sand slurries in horizontal pipe flow. *Particulate Science and Technology, Vol. 12.*, 45-69.

Gillies, R. G., & Shook, C. A. (2000A). Modeling high concentration settling slurry flows. *Canadian Journal of Chemical Engineering, Vol. 78.*, 709-716.

Gillies, R. G., Schaan, J., Sumner, R. J., McKibben, M. J., & Shook, C. A. (2000B). Deposition velocities for Newtonian slurries in turbulent flow. *Canadian Journal of Chemical Engineering, Vol. 78.*, 704-708.

Gillies, R. G., Shook, C. A., & Wilson, K. C. (1991). An improved two layer model for horizontal slurry pipeline flow. *Canadian Journal of Chemical Engineering, Vol. 69.*, 173-178.

Gillies, R. G., Shook, C. A., & Xu, J. (2004). Modelling heterogeneous slurry flows at high velocities. *The Canadian Journal of Chemical Engineering, Vol. 82.*, 1060-1065.

Glasstone, S., Laidler, K., & Eyring, H. (1941). *The theory of rate processes.* New York: McGraw Hill.

Goedde, E. (1978). To the critical velocity of heterogeneous hydraulic transport. *Hydrotransport 5* (pp. B4-81-B4-98). Cranfield, Bedford, England: BHRA.

Gogus, M., & Kokpinar, M. A. (1993). Determination of critical flow velocity in slurry transporting pipeline systems. *Proceeding of the 12th International Conference on Slurry Handling and Pipeline Transport.* (pp. 743-757). Bedfordshire, UK.: British Hydraulic Research Group.

Govers, G. (1987). Initiation of motion in overland flow. *Sedimentology (34)*, 1157-1164.

Govier, G. W., & Aziz, K. (1972). *The Flow of Complex Mixtures in Pipes.* New York: University of Calgary, Alberta, Canada.

Grace, J. (1986). Contacting modes and behaviour classification of gas-solid and other two-phase suspensions. *Canadian Journal of Chemical Engineering, vol. 64.*, 353-363.

Graf, W. H., & Pazis, G. C. (1977). Les phenomenes de deposition et d'erosion dans un canal alluvionnaire. *Journal of Hydraulic Research, 15*, 151-165.

Graf, W. H., Robinson, M. P., & Yucel, O. (1970). *Critical velocity for solid liquid mixtures.* Bethlehem, Pensylvania, USA.: Fritz Laboratory Reports, Paper 386. Lehigh University.

Graf, W. H., Robinson, M., & Yucel, O. (1970). The critical deposit velocity for solid-liquid mixtures. *Hydrotransport 1* (pp. H5-77-H5-88). Cranfield, UK: BHRA.

Grant, W. D., & Madsen, O. S. (1982). Movable bed roughness in unsteady oscillatory flow. *Journal Geophysics Resources*, 469-481.

Grass, A. J. (1970). The initial instability of fine bed sand. *Journal of Hydraulic Division, ASCE, 96(3)*, 619-632.

Groot, J. (1981). *Rapport Beunbezinking (in Dutch).* Papendrecht: Royal Boskalis Westminster.

Grunsven, F. v. (2012). *Measuring the slip factor for various slurry flows using temperature calibrated Electrical Resistance Tomography.* Delft, The Netherlands.: Delft University of Technology.

Hansen, B. (1958). Line ruptures regarded as narrow rupture zones. *Earth Pressure Problems*, (pp. 39-48). Brussels.

Harada, E., Kuriyama, M., & Konno, H. (1989). Heat transfer with a solid liquid suspension flowing through a horizontal rectangular duct. *Heat Transfer Jap. Res. Vol. 18.*, 79-94.

Hatamura, Y., & Chijiiwa, K. (1975). Analyses of the mechanism of soil cutting, 1st report. *Bulletin of JSME, vol. 18, no. 120*, 619-626.

Hatamura, Y., & Chijiiwa, K. (1976A). Analyses of the mechanism of soil cutting, 2nd report. *Bulletin of the JSME, vol. 19, no. 131.*, 555-563.

Hatamura, Y., & Chijiiwa, K. (1976B). Analyses of the mechanism of soil cutting, 3rd report. *Bulletin of the JSME, vol. 19, no. 139.*, 1376-1384.

Hatamura, Y., & Chijiiwa, K. (1977A). Analyses of the mechanism of soil cutting, 4th report. *Bulletin of the JSME, vol. 20, no. 139.*, 130-137.

Hatamura, Y., & Chijiiwa, K. (1977B). Analyses of the mechanism of soil cutting, 5th report. *Bulletin of the JSME, vol. 20, no. 141.*, 388-395.

Hazen, A. (1982). Some physical properties of sands and gravels with special reference to their use in filtration. *24th Annual Report, Massachusetts State Board of Health, Pub. Doc. No. 34.*, 539-556.

He, J., & Vlasblom, W. (1998). Modelling of saturated sand cutting with large rake angles. *WODCON XV*. Las Vegas, USA: WODA.
He, J., Miedema, S., & Vlasblom, W. (2005). FEM Analyses Of Cutting Of Anisotropic Densely Compacted and Saturated Sand. *WEDAXXV/TAMU37*. New Orleans, Louisiana, USA: WEDA/TAMU.
Helmons, R. L., Miedema, S. A., & Rhee, C. v. (2014). A NEW APPROACH TO MODEL HYPERBARIC ROCK CUTTING PROCESSES. *OMAE 2014* (p. 9). San Francisco, USA: ASME.
Hepy, F. M., Ahmad, Z., & Kansal, M. L. (2008). Critical velocity for slurry transport through pipeline. *Dam Engineering, Vol. XIX(3).*, 169-184.
Hettiaratchi, D. (1967A). The mechanics of soil cultivation. *AES, no. 3/245/C/28.*
Hettiaratchi, D., & Reece, A. (1967B). Symmetrical three-dimensional soil failure. *Journal of Terramechanics 4 (3).*, 45-67.
Hettiaratchi, D., & Reece, A. (1974). The calculation of passive soil resistance. *Geotechnique 24, no. 3.*, 289-310.
Hettiaratchi, D., & Reece, A. (1975). Boundary wedges in two dimensional passive soil failure. *Geotechnique 25, no. 2.*, 197-220.
Hettiaratchi, D., Witney, B., & Reece, A. (1966). The calculation of passive pressure in two dimensional soil failure. *Journal of Agriculture Engineering Resources 11 (2)*, 89-107.
Hinze, J. (1975). *Turbulence.* McGraw Hill Book company.
Hjulstrøm, F. (1935). Studies of the morphological activity of rivers as illustrated by the River Fyris. *Bulletin of the Geological Institute, 25*, 221–527. University of Uppsala.
Hjulstrøm, F. (1939). Transportation of debris by moving water, in Trask, P.D., ed., Recent Marine Sediments. *A Symposium: Tulsa, Oklahoma, American Association of Petroleum Geologists*, (pp. 5-31). Tulsa, Oklahoma.
Hoek, E., & Brown, E. T. (1988). The Hoek-Brown Failure Criterion - a 1988 Update. *15th Canadian Rock Mechanics Symposium.*, (pp. 31-38).
Hofland, B. (2005). *Rock & Roll.* Delft, The Netherlands: PhD Thesis, Delft University of Technology.
Howard, G. W. (1938). Transportation of Sand and Gravel in a 4 Inch Pipe. *Transactions ASCE Vol. 104., No. 2039.*, 1334-1348.
Howard, G. W. (1939). Discussion on: Transportation of sand and gravel in a four inch pipe. *Transactions ASCE Vol. 104.*, 157, 316, 460, 1011.
Hsu. (1986). *Flow of non-colloidal slurries in pipeline.* PhD Thesis, University of Illinois.
Huisman, L. (1973-1995). *Sedimentation & Flotation 1973-1995.* Delft, Netherlands: Delft University of Technology.
Huisman, L. (1980). *Theory of settling tanks.* Delft, Netherlands: Delft University of Technology.
Hunerjager, H. (1957). *Kenngrossen fur das Forderverhalten von Schuttgutern. PhD Thesis.* Hannover, Germany: Technische Universitat Hannover.
Hunt, J. N. (1954). The turbulent transport of suspended sediment in open channels. *Royal Society of London, Proc. Series A, Vol. 224(1158).*, 322-335.
Hupe, W., & Schuszter, M. (1965). Verbesserte Motorgreifer als Beitrag zur allgemeinen Verbesserung des Greifernumschlages. *Hebezeuge und Fordermittel 1*, 6-9.
Huygens, M., & Verhofen, R. (1996). Some fundamental particularities on partly cohesive sediment transport in a circular test flume. *Advances in Fluid Mechanics (9)*, 11-20.
Ikeda, S. (1982). Incipient motion of sand particles on side slopes. *Journal of the Hydraulic division, ASCE, 108*(No. HY1).
Ismail, H. M. (1952). Turbulent transfer mechanism and suspended sediment in closed channels. *Transactions of ASCE, Vol. 117.*, 409-446.
Israelachvili, J. (1985). *Intermolecular and Surface Forces.* New York: Elsevier.
Iwagaki, Y. (1956). Fundamental study on critical tractive force. *Transactions of the Japanese Society of Civil Engineers, Vol. 41*, 1-21.
Jin, L., McNeil, J., Lick, W., & Gailani, J. (2002). *Effects of bentonite on the erosion rates of quartz particles.* Santa Barbara, California: Mechanics & Environmental Engineers, University of California.
Joanknecht, L. (1973). *Mechanisch graaf onderzoek onder water.* Delft, Netherlands: Delft University of Technology.
Joanknecht, L. (1974). *Cutting forces in submerged soils.* Delft, Netherlands: Delft University of Technology.
Jong, P. (1987). *Onderzoek naar de mogelijkheid van gecombineerd snijden en spuiten in zand, report: 87.3.GV.2311.* Delft, Netherlands: Delft University of Technology.
Jong, P. (1988A). *De uitvoering van een laboratorium onderzoek naar de mogelijkheden van gecombineerd snijden en spuiten in zand, report: 88.3.GV.2365.* Delft, Netherlands: Delft University of Technology.
Jong, P. (1988B). *Een productie optimalisatie van het gebruik van spuiters op de sleephopperzuiger Volvox Delta, report: 88.3.GV.2438.* Delft, Netherlands: Delft University of Technology.

References.

Jonge, K. (2017). *A trailing suction hopper dredge draghead production model, Masters Thesis.* Delft, Netherlands: Delft University of Technology.

Josselin de Jong, G. (1976). Rowe's stress dilatancy relation based on friction. *Geotechnique 26, no. 3*, 527-534.

Jufin, A. P. (1965). *Gidromechanizacija.* Moskau.

Jufin, A. P., & Lopatin, N. A. (1966). O projekte TUiN na gidrotransport zernistych materialov po stalnym truboprovodam. *Gidrotechniceskoe Strojitelstvo, 9.*, 49-52.

Jukes, P., Kenny, S., Panapitiya, U., Jafri, S., & Eltaher, A. (2011). Arctic and harsh environment pipeline trenching technologies and challenges. *OTC.* Houston: OTC.

Julien, P. (1995). Erosion and sedimentation. *Cambridge University Press.*

Kaitkay, P., & Lei, S. (2005). Experimental study of rock cutting under external hydrostatic pressure. *Journal of Materials Processing Technology, vol. 159.*, 206-213.

Karabelas, A. J. (1977). Vertical Distribution of Dilute Suspensins in Turbulent Pipe Flow. *AIChE Journal, Vol. 23(4).*, 426-434.

Karasik, U. A. (1973). Hydraulische Forderung von feinkorniqen Suspensionen (in russisch). *Gidromechanika, S.BO ff, Vol. 25. Kiew.*

Kaushal, D. R. (1995). *Prediction of particle distribution in the flow of multisized particulate slurries through closed ducts and open channels.* Delhi, India: I.I.T.. Department of Applied Mechanics, PhD Thesis.

Kaushal, D. R., & Tomita, Y. (2002B). Solids concentration profiles and pressure drop in pipeline flow of multisized particulate slurries. *International Journal of Multiphase Flow, Vol. 28.*, 1697-1717.

Kaushal, D. R., & Tomita, Y. (2002C). An improved method for predicting pressure drop along slurry pipeline. *Particulate Science and Technology: An International Journal, Vol. 20(4).*, 305-324.

Kaushal, D. R., & Tomita, Y. (2003B). Comparative study of pressure drop in multisized particulate slurry flow through pipe and rectangular duct. *International Journal of Multiphase Flow, Vol. 29.*, 1473-1487.

Kaushal, D. R., & Tomita, Y. (2013). Prediction of concentration distribution in pipeline flow of highly concentrated slurry. *Particulate Science and Technology: An International Journal, Vol. 31(1).*, 28-34.

Kaushal, D. R., Sato, K., Toyota, T., Funatsu, K., & Tomita, Y. (2005). Effect of particle size distribution on pressure drop and concentration profile in pipeline flow of highly concentrated slurry. *International Journal of Multiphase Flow, Vol. 31.*, 809-823.

Kaushal, D. R., Seshadri, V., & Singh, S. N. (2002D). Prediction of concentration and particle size distribution in the flow of multi-sized particulate slurry through rectangular duct. *Applied Mathematical Modelling, Vol. 26.*, 941-952.

Kaushal, D. R., Seshadri, V., & Singh, S. N. (2003A). Concentration and particle size distribution in the flow of multi-sized particulate slurry through rectangular duct. *Journal of Hydrology & Hydromechanics*, 114-121.

Kaushal, D. R., Tomita, Y., & Dighade, R. R. (2002A). Concentration at the pipe bottom at deposition velocity for transportation of commercial slurries through pipeline. *Powder Technology Vol. 125.*, 89-101.

Kazanskij, I. (1967). *Vyzkum proudeni hydrosmesi voda-pisek (untersuchung uber sans-wasser stromungen).* Mitteilungen des Franzius Instituts, Heft 33.

Kazanskij, I. (1972). *Berechnungsverfahren fur die Forderung von Sand-Wasser Gemischen in Rohrleitungen.* Hannover: Franzius Institut, Heft 33.

Kazanskij, I. (1978). Scale-up effects in hydraulic transport theory and practice. *Hydrotransport 5* (pp. B3: 47-74). Cranfield, UK: BHRA Fluid Engineering.

Kazanskij, I. (1980). Vergleich verschiedener Rohrmaterialen in Bezug auf Verschleiss und Energieverbrauch beim Hydrotransport in Rohrleitungen. *VDI Berichte Nr. 371*, pp. 51-58.

Kelessidis, V., & Maglione, R. (2008). Yield stress of water bentonite dispersions. *Colloids and Surfaces A: Physicochemical Engineering Aspects 318.*, 217-226.

Kelessidis, V., Tsamantaki, C., & Dalamarinis, P. (2007). Effect of pH and electrolyte on the rheology of aqueous Wyoming bentonite dispersions. *Applied Clay Science 38.*, 86-96.

Kesteren, W. G. (1995). Numerical simulations of crack bifurcation in the chip forming cutting process in rock. In G. B. Karihaloo (Ed.), *Fracture of brittle disordered materials: concrete, rock and ceramics.* (pp. 505-524). London, UK.: E&FN Spon.

Kim, J., Moin, P., & Moser, R. (1987). Turbulence statistics in fully developed channel flow at low Reynolds number. *Journal of Fluid Mechanics, 177*, 133-166.

King, R. P. (2002). *Introduction to Practical Fluid Flow.* University of Utah.: Butterworth Heineman.

Kirkby, M., & Statham, I. (1975). Surface stone movement and scree formation. *Journal of Geology, Vol. 83.*, 349-362.

Kokpinar, M. A., & Gogus, M. (2001). Critical velocity in slurry transport in horizontal pipelines. *Journal of Hydraulic Engineering, Vol. 127(9).*, 763-771.

Koning, J. d. (1977). Constant Tonnage Loading System of Trailing Suction Hopper Dredges. *International Course on Modern Dredging* (p. D6). The Hague, The Netherlands: Delft University of Technology & KIVI.

Koning, J. d., Miedema, S., & Zwartbol, A. (1983). Soil/Cutterhead Interaction under Wave Conditions. *WODCON X*. Singapore: WODA.

Korreman, S., & Posselt, D. (2001). Modification of anomalous swelling in multilamellar vesicles induced by alkali halide salts. *Euro Biophysics Journal (30)*, 121-128.

Korzajev, M. (1964). Metod rascota parametrov gidrotransporta gruntov. *Gidromechanizacija, Moskau*.

Kozeny, J. (1927). *Uber kapillare leitung des wassers in boden.* Wien: Sitzungsber. Akad. Wiss. Wien, Math. Naturwiss. Kl. Abt. 2a, 136, 271-306.

Kramer, H. (1935). Sand mixtures and sand movement in fluvial levels. *Transaction of ASCE 100.*, 798-838.

Kril, S. I. (1990). *Nopernye vzvesenesuscie potoki (pressurised slurry flows).* Kiev: Naukova Dumka.

Krivenko. (1970). Energieverlust in zwei phasen stromungen in hochkonzentrierten grobdispersionen. *Gidromechanica, Kiev.*

Krone, R. (1986). The significance of aggregate properties to transport processes. *Workshop on Cohesive Sediment Dynamics with Special Reference to Physical Processes in Estuaries.* (pp. 66-84). Tampa Florida: Springer Verlag.

Kumar, U., Mishra, R., Singh, S. N., & Seshadri, V. (2003). Effect of particle gradation on flow characteristics of ash disposal pipelines. *Powder Technology Vol. 132.*, 39-51.

Kumar, U., Singh, S. N., & Seshadri, V. (2008). Prediction of flow characteristics of bimodal slurry in horizontal pipe flow. *Particulate Science and Technology, Vol. 26.*, 361-379.

Kurihara, M. (1948). On the critical tractive force. *Research Institute for Hydraulic Engineering*, Report No. 3, Vol. 4.

Lahiri, S. K. (2009). *Study on slurry flow modelling in pipeline.* Durgapur, India: National Institute of Technology, Durgapur, India.

Lambe, T., & Whitman, R. (1969). *Soil Mechanics.* John Wiley & Sons.

Lambe, T., & Whitman, R. (1979). *Soil mechanics, SI version.* New York: John Wiley & Sons.

Lane, E. W., & Kalinske, A. A. (1941). Engineering calculations of suspended sediment. *Trans. Am. Geophysics Union, Vol. 20(3).*, 603-607.

Laribi, S., Fleureau, J., Grossiord, J., & Ariguib, N. (2005). Comparative yield stress determination for pure and interstratified smectite clays. *Rhology Acta (44).*, 262-269.

Leussen, W. v., & Os, A. v. (1987 December). Basic research on cutting forces in saturated sand. *Journal of Geotechnical Engineering, vol. 113, no. 12.*, 1501-1516.

Leussen, W., & Nieuwenhuis, J. (1984). Soil mechanics aspects of dredging. *Geotechnique 34, no. 3.*, 359-381.

Lick, W., Jin, L., & Gailani, J. (2004). Initiation of movement of quartz particles. *Journal of Hydraulic Engineering*, 755-761.

Liefferink, D. M., Alvarez Grima, M., Miedema, S. A., Plat, R., & Rhee, C. v. (2014). Failure mechanism of cutting submerged frozen clay in an arctic trenching process. *OTC 2014.* Houston, Texas, USA.: OTC.

Liu, H. (1957). Mechanics of sediment ripple formation. *Journal of the Hydraulics Division, Vol. 83, No. 2, March/April.*, 1-23.

Liu, Z. (2001). *Sediment Transport.* Aalborg, Denmark: Aalborg University.

Lobanov, V., & Joanknecht, L. (1980). The cutting of soil under hydrostatic pressure. *WODCON IX.* Vancouver, Canada: WODA.

Lodge, P. (2006). *Effects of surface slope on erosion rates of quartz particles. (MSc thesis Wilbert Lick).* Santa Barbara: University of California.

Loiseleux, T., Gondret, P., Rabaud, M., & Doppler, D. (2005). Onset of erosion and avalanche for an inclined granular bed sheared by a continuous laminar flow. *Physics of fluids, Vol. 17*, 1-9.

Longwell, P. A. (1977). *Mechanics of Fluid Flow.* New York: McGraw Hill.

Louis, A. A. (2017). *Cutter Suction Spillage.* Delft, the Netherlands: Delft University of Technology.

Luckner, T. (2002). Zum Bewegungsbeginn von Sedimenten. *Dissertation.* Darmstadt, Germany: Technische Universitat Darmstadt.

Luckner, T., & Zanke, U. (2007). An analytical solution for calculating the initiation of sediment motion. *International Journal of sediment Research, Vol. 22, No. 2.*, 87-102.

Ma, Y. (2001). *Mathematical model analysis for the saturated sand cutting with large cutting angles in the non-vavitation situation.* Delft, Netherlands: Delft University of Technology, Report: 2001.BT.5581.

Ma, Y., Ni, F., & Miedema, S. (2006A). Calculation of the Blade Cutting Force for small Cutting Angles based on MATLAB. *The 2nd China Dredging Association International Conference & Exhibition, themed Dredging and Sustainable Development.* Guangzhou, China: CHIDA.

Ma, Y., Ni, F., & Miedema, S. (2006B). Mechanical Model of Water Saturated Sand Cutting at Blade Large Cutting Angles. *Journal of Hohai University, ISSN 1009-1130, CN 32-1591*.

Madsen, O. S., Wright, L. D., Boon, J. D., & Chrisholm, T. A. (1993). *Wind stress, bed roughness and sediment suspension on the inner shelf during an extreme storm event.* Continental Shelf Research 13, 1303-1324.

References.

Madsen, O., & Grant, W. (1976). *Sediment transport in the coastal environment.* Cambridge, Massachusetts, USA: Technical report 209, M.I.T.

Mantz, P. A. (1977). Incipient transport of fine grains and flakes by fluids—Extended Shields diagram. *Journal of Hydraulic Division, ASCE, 103(6)*, 601-615.

Marsh, N. A., Western, A. W., & Grayson, R. B. (2004, July 1). Comparison of Methods for Predicting Incipient Motion for Sand Beds. *Journal of Hydraulic Engineering, 130*(No. 7, July 1, 2004)).

Matousek, V. (1996). Solids Transportation in a Long Pipeline Connected with a Dredge. *Terra et Aqua 62.*, 3-11.

Matousek, V. (1997). *Flow Mechanism of Sand/Water Mixtures in Pipelines, PhD Thesis.* Delft, Netherlands: Delft University of Technology.

Matousek, V. (2001). On the Amplification of Density Waves in Long Pipelines Connected with a Dredge. *World Dredging Conference 16.* Kuala Lumpur, Malaysia: WODA.

Matousek, V. (2004). *Dredge Pumps & Slurry Transport, Lecture Notes.* Delft: Delft University of Technology.

Matousek, V. (2007). Interaction of slurry pipe flow with a stationary bed. *Journal of the South African Institute of Mining and Metallurgy, 107(6).*, 367-374.

Matousek, V. (2009). Concentration profiles and solids transport above stationary deposit in enclosed conduit. *Journal of Hydraulic Engineering, Vol. 135*, 1101-1106.

Matousek, V. (2009). Predictive model for frictional pressure drop in settling-slurry pipe with stationar deposit. *Powder Technology*, 367-374.

Matousek, V. (2011). Solids Transport Formula in Predictive Model for Pipe Flow of Slurry above Deposit. *Particulate Science and Technology, Vol. 29(1).*, 89-106.

Matousek, V., & Krupicka, J. (2009). On equivalent roughness of mobile bed at high shear stress. *Journal of Hydrology & Hydromechanics, Vol. 57-3.*, 191-199.

Matousek, V., & Krupicka, J. (2010). Modeling of settling slurry flow around deposition limit velocity. *Hydrotransport 18* (p. 12). Rio de Janeiro, Brazil: BHR Group.

Matousek, V., & Krupicka, J. (2010). Semi empirical formulae for upper plane bed friction. *Hydrotransport 18* (pp. 95-103). BHRA.

Matousek, V., & Krupicka, J. (2011). Unified model for coarse slurry flow with stationary and sliding bed. *15th International Conference on Transport & Sedimentation of Solid Particles.*, (p. 8). Wroclaw, Poland.

Matousek, V., & Krupicka, J. (2011). Unified model for coarse slurry flow with stationary and sliding bed. *Transport and Sedimentation of Solid Particles, 15th*, (p. 9). Wroclav, Poland.

Matousek, V., & Krupicka, J. (2014). Interfacial friction and transport in stratified flows. *Maritime Engineering, Vol. 167(MA3)*, 125-134.

Matousek, V., & Krupicka, J. (2014). One dimensional modelling of concentration distribution in pipe flow of combined load slurry. *Powder Technology, Vol. 260.*, 42-51.

Matousek, V., Krupicka, J., & Penik, V. (2014). Distribution of medium to coarse glass beads in slurry pipe flow: Evaluation of measured concentration profiles. *Particulate Science and Technology, Vol. 32*, 186-196.

Matousek, V., Krupicka, J., & Picek, T. (2013). Validation of transport and friction formulae for upper plane bed by experiments in rectangular pipe. *Journal of Hydrology and Hydromechanics.*, 120-125.

Mavis, F., & Laushey, L. (1948). A Re-appraisal of the Beginning of Bed Movement Competent Velocity. *IAHR.* Stockholm.

Mehta, A., & Lee, S. (1994). Problems in linking the threshold condition for the transport of cohesionless and cohesive sediment grain. *Journal of Coastal Research 10*, 170-177.

Meijer, K. (1981). *Berekening van spanningen en deformaties in verzadigde grond.* Delft, Netherlands: Delft Hydraulics Laboratory, Report R914 part 1.

Meijer, K. (1985). *Computation of stresses and strains in saturated soil, PhD Thesis.* Delft, Netherlands: Delft University of Technology.

Meijer, K., & Os, A. (1976). Pore pressures near a moving under water slope. *Geotechnical Engineering Division ASCE 102, no. GT4.*, 361-372.

Merchant, M. (1944). Basic mechanics of the metal cutting process. *Journal of Applied Mechanics, vol. 11A.*, 168-175.

Merchant, M. (1945A). Mechanics of metal cutting process, orthogonal cutting and a type 2 chip. *Journal of Applied Physics, vol. 16, no. 5.*, 267-275.

Merchant, M. (1945B). Mechanics of metal cutting, plasticity conditions in orthogonal cutting. *Journal of Applied Physics, vol. 16, no. 6.*, 318-324.

Meyer-Peter, E., & Muller, R. (1948). Formulas for bed load transport. *2nd Meeting of the International Association for Hydraulic Structures Research.*, (pp. 39-64).

Miedema, S. (1981). *The flow of dredged slurry in and out hoppers and the settlement process in hoppers.* Delft, The Netherlands: Delft University of Technology, ScO/81/105, 147 pages.

Miedema, S. (1995). Production Estimation Based on Cutting Theories for Cutting Water Saturated Sand. *WODCON IV* (p. 30 pages). Amsterdam, The Netherlands: WODA.

Miedema, S. (2008A). An Analytical Approach to the Sedimentation Process in Trailing Suction Hopper Dredges. *Terra et Aqua 112*, 15-25.
Miedema, S. (2008B). An analytical method to determine scour. *WEDA XXVIII & Texas A&M 39.* St. Louis, USA: Western Dredging Association (WEDA).
Miedema, S. (2009A). The effect of the bed rise velocity on the sedimentation process in hopper dredges. *Journal of Dredging Engineering, Vol. 10, No. 1*, 10-31.
Miedema, S. (2009B). A sensitivity analysis of the scaling of TSHD's. *WEDA 29 & TAMU 40 Conference.* Phoenix, Arizona, USA: WEDA.
Miedema, S. (2010). Constructing the Shields curve, a new theoretical approach and its applications. *WODCON XIX* (p. 22 pages). Beijing, September 2010: WODA.
Miedema, S. (2010A). Constructing the Shields Curve: Part A Fundamentals of the Sliding, Rolling and Lifting Mechanisms for the Entrainment of Particles. *Submitted to the Journal of Hydraulic Engineering*.
Miedema, S. (2010B). Constructing the Shields Curve: Part B Sensitivity Analysis, Exposure & Protrusion Levels, Settling Velocity, Shear Stress & Friction Velocity, Erosion Flux and Laminar Main Flow. *Submitted to the Journal of Hydraulic Engineering*.
Miedema, S. (2010D). Constructing the Shields Curve: Part D Cohesion by Clay. *Submitted to the Journal of Hydraulic Engineering*.
Miedema, S. A. (1981). *The soil reaction forces on a crown cutterhead on a swell compensated ladder.* Delft, The Netherlands: Delft University of Technology.
Miedema, S. A. (1982). The Interaction between Cutterhead and Soil at Sea. *Dredging Day November 19th* (p. 25 pages in Dutch). Delft, The Netherlands: Delft University of Technology.
Miedema, S. A. (1982). *The mathematical modeling of the soil reaction forces on a cutterhead and the development of the computer program DREDMO.* Delft, The Netherlands: Delft University of Technology.
Miedema, S. A. (1984A). *Mathematical Modeling of a Seagoing Cutter Suction Dredge.* Delft, The Netherlands: Delft University of Technology/KIVI.
Miedema, S. A. (1984B, October). The Cutting of Densely Compacted Sand under Water. *Terra et Aqua, No. 28*, 4-10.
Miedema, S. A. (1985A, September). Derivation of the Differential Equation for Sand Pore Pressures. *Dredging and Port Construction*, 35.
Miedema, S. A. (1985B, July). Mathematical Modeling of the Cutting of Densely Compacted Sand Under Water. *Dredging and Port Construction*, 22-26.
Miedema, S. A. (1986A). The Application of a Cutting Theory on a Dredging Wheel. *WODCON XI* (p. 14 pages). Brighton, UK: WODA.
Miedema, S. A. (1986B, June). Underwater Soil Cutting: a Study in Continuity. *Dredging and Port Construction*, 47-53.
Miedema, S. A. (1987 September). *The Calculation of the Cutting Forces when Cutting Water Saturated Sand, PhD Thesis.* Delft: Delft University of Technology.
Miedema, S. A. (1987). *The Calculation of the Cutting Forces when Cutting Water Saturated Sand, PhD Thesis.* Delft: Delft University of Technology.
Miedema, S. A. (1987). *The Calculation of the Cutting Forces when Cutting Water Saturated Sand, PhD Thesis.* Delft: Delft University of Technology.
Miedema, S. A. (1989). Clamshell V1.50. *Software for the simulation of the closing process of clamshell dredges.* Chicago, USA: Great Lakes Dredge & Dock Company.
Miedema, S. A. (1989). On the Cutting Forces in Saturated Sand of a Seagoing Cutter Suction Dredge. *WODCON XII* (p. 27 pages). Orlando, Florida, USA: WODA.
Miedema, S. A. (1989, December). On the Cutting Forces in Saturated Sand of a Seagoing Cutter Suction Dredge. *Terra et Aqua, No. 41*, 27 pages.
Miedema, S. A. (1992). New developments of cutting theories with respect to dredging, the cutting of clay. *WODCON XIII.* Bombay, India: World Dredging Association (WODA).
Miedema, S. A. (1994). On the Snow-Plough Effect when Cutting Water Saturated Sand with Inclined Straight Blades. *ASCE Dredging 94* (p. 24 pages). Orlando, Florida, USA: ASCE.
Miedema, S. A. (1995). Dynamic Pump/Pipeline Behavior Windows. *Software*. Delft, The Netherlands: SAM-Consult.
Miedema, S. A. (1995). Production Estimation Based on Cutting Theories for Cutting Water Saturated Sand. *WODCON IV* (p. 30 pages). Amsterdam, The Netherlands: WODA.
Miedema, S. A. (1996). Modeling and Simulation of the Dynamic Behavior of a Pump/Pipeline System. *17th Annual Meeting & Technical Conference of WEDA.* (p. 10). New Orleans, USA.: WEDA.
Miedema, S. A. (1999). Considerations in Building and using Dredge Simulators. *WEDA XIX & TAMU 31* (p. 10). Louisville, Kentucky, USA: WEDA.

References.

Miedema, S. A. (1999). Considerations on limits of dredging processes. *19th Annual Meeting & Technical Conference of the Western Dredging Association.* Louisville, Kentucky, USA: WEDA/TAMU.

Miedema, S. A. (2000). The modelling of the swing winches of a cutter dredge in relation with simulators. *Texas A/M 32nd Annual Dredging Seminar*. Warwick, Rhode Island, USA: WEDA/TAMU.

Miedema, S. A. (2003). The Existence of Kinematic Wedges at Large Cutting Angles. *CHIDA Dredging Days.* Shanghai, China: CHIDA.

Miedema, S. A. (2004). The Cutting Mechanisms of Water Saturated Sand at Small and Large Cutting Angles. *International Conference on Coastal Infrastructure Development - Challenges in the 21st Century*. Hongkong: ICCD.

Miedema, S. A. (2005). The Cutting of Water Saturated Sand, the FINAL Solution. *WEDAXXV/TAMU37*. New Orleans, Louisiana, USA: WEDA/TAMU.

Miedema, S. A. (2006A). The Cutting of Water Saturated Sand, the Solution. *CEDA African Section: Dredging Days.* Tangiers, Morocco: CEDA.

Miedema, S. A. (2006B). The Cutting of Water Saturated Sand, the Solution. *The 2nd China Dredging Association International Conference & Exhibition, themed Dredging and Sustainable Development.* Guangzhou, China: CHIDA.

Miedema, S. A. (2009). New Developments Of Cutting Theories With Respect To Dredging, The Cutting Of Clay And Rock. *WEDA XXIX/Texas A/M 40.* Phoenix, Arizona, USA: WEDA/TAMU.

Miedema, S. A. (2010). New Developments of Cutting Theories with respect to Offshore Applications. *ISOPE* (p. 8). Beijing, China.: ISOPE.

Miedema, S. A. (2012A). Constructing the Shields Curve: Part A Fundamentals of the Sliding, Rolling and Lifting Mechanisms for the Entrainment of Particles. *Journal of Dredging Engineering, Vol. 12.*, 1-49.

Miedema, S. A. (2012A). Constructing the Shields Curve: Part A Fundamentals of the Sliding, Rolling and Lifting Mechanisms for the Entrainment of Particles. *Journal of Dredging Engineering*.

Miedema, S. A. (2012B). Constructing the Shields Curve: Part B Sensitivity Analysis, Exposure & Protrusion Levels, Settling Velocity, Shear Stress & Friction Velocity, Erosion Flux and Laminar Main Flow. *Journal of Dredging Engineering, Vol. 12.*, 50-92.

Miedema, S. A. (2012B). Constructing the Shields Curve: Part B Sensitivity Analysis, Exposure & Protrusion Levels, Settling Velocity, Shear Stress & Friction Velocity, Erosion Flux and Laminar Main Flow. *Journal of Dredging Engineering*.

Miedema, S. A. (2013). An overview of theories describing head losses in slurry transport. A tribute to some of the early researchers. *OMAE 2013, 32nd International Conference on Ocean, Offshore and Arctic Engineering.* (p. 18). Nantes, France: ASME.

Miedema, S. A. (2013). Constructing the Shields Curve: Part C Cohesion by Silt, Hjulstrom, Sundborg. *OMAE* (p. 22). Nantes: ASME.

Miedema, S. A. (2013D). Constructing the Shields Curve: Part D Cohesion by Clay. *Not yet submitted*.

Miedema, S. A. (2013S). *Software MS Excel 2LM & 3LM.* Retrieved from The Delft Head Loss & Limit Deposit Velocity Model: www.dhlldv.com

Miedema, S. A. (2014). An analytical approach to explain the Fuhrboter equation. *Maritime Engineering, Vol. 167, Issue 2.*, 68-81.

Miedema, S. A. (2014). *Dredging Processes Hydraulic Transport.* Delft, Netherlands: Delft University of Technology.

Miedema, S. A. (2014). *The Delft Sand, Clay & Rock Cutting Model.* (1st ed.). Delft: IOS Press, Delft University Press. doi:10.3233/978-1-61499-454-1-i

Miedema, S. A. (2014A). An overview of theories describing head losses in slurry transport - A tribute to some of the early researchers. *Journal of Dredging Engineering, Vol. 14(1)*, 1-25.

Miedema, S. A. (2014B). An analysis of slurry transport at low line speeds. *ASME 2014 33rd International Conference on Ocean, Offshore and Arctic Engineering, OMAE.* (p. 11). San Francisco, USA.: ASME.

Miedema, S. A. (2014C). An analytical approach to explain the Fuhrboter equation. *Maritime Engineering, Vol. 167(2).*, 1-14.

Miedema, S. A. (2014W). *DHLLDV/Experiments*. Retrieved from The Delft Head Loss & Limit Deposit Velocity Model.: www.dhlldv.com

Miedema, S. A. (2015). A head loss model for homogeneous slurry transport. *Journal of Hydrology & Hydrodynamics, Vol. 63(1).*, 1-12.

Miedema, S. A. (2015). Head Loss Model for Slurry Transport in the Heterogeneous Regime. *Submitted to the Journal of Ocean Engineering.*

Miedema, S. A. (2015A). A head loss model for homogeneous slurry transport. *Journal of Hydrology & Hydrodynamics, Vol. 1.*, 14 pages.

Miedema, S. A. (2015B). Head Loss Model for Slurry Transport in the Heterogeneous Regime. *Journal of Ocean Engineering. Accepted.*

Miedema, S. A. (2015B). THE SLIP RATIO OR HOLDUP FUNCTION IN SLURRY TRANSPORT. *Dredging Summit and Expo 2015.* (p. 12). Houston, Texas, USA.: WEDA.
Miedema, S. A. (2015C). Head Loss Model for Slurry Transport in the Heterogeneous Regime. *Journal of Ocean Engineering.*
Miedema, S. A. (2015D). A method to compare slurry transport models. *17th International Conference on Transport & Sedimentation of Solid Particles.* (p. 8). Delft, The Netherlands, September 2015.: T&S17.
Miedema, S. A. (2016). *OE4607 Introduction Dredging Engineering* (2nd Edition ed.). Delft, The Netherlands: Delft University of Technology.
Miedema, S. A. (2016). The heterogeneous to homogeneous transition for slurry flow in pipes. *Ocean Engineering, Vol. 123.*, 422-431.
Miedema, S. A. (2017A). A new approach to determine the concentration distribution in slurry transport. *Dredging Summit & Expo* (p. 16). Vancouver, Canada: WEDA.
Miedema, S. A. (2017B). The influence of local hindered settling on the concentration distribution in slurry transport. *Transport & Sedimentation of Solid Particles* (p. 8). Prague, Czech Republic: T&S17.
Miedema, S. A. (2017C). Slurry transport in inclined pipes. *Dredging Summit & Expo* (p. 15). Vancouver, Canada: WEDA.
Miedema, S. A. (2017D). A comparison of graded PSD methods in slurry transport. *20th International Conference on Hydrotransport.* (p. 15). Melbourne, Australia.: BHR.
Miedema, S. A. (2017E). Slurry transport of very large particles at high line speeds. *20th International Conference on Hydrotransport.* (p. 15). Melbourne, Australia.: BHR.
Miedema, S. A. (2018). *Spillage models for a cutter head in dredging sand or gravel.* Delft, The Netherlands: Delft University of Technology.
Miedema, S. A. (2018A). Slurry transport, fully stratified flow in the sliding flow regime. *Dredging Summit & Expo* (p. 15). Norfolk, Virginia, USA.: WEDA.
Miedema, S. A. (2018B). Which slurry transport regime should be used and why? *Terra et Aqua 152*, 7-17.
Miedema, S. A. (2019). Production Estimation of Waterjets in Drag Heads. *Proceedings of the Twenty- Second World Dredging Congress, WODCON XXII* (p. 17). Shanghai, China: CHIDA, EADA, WODA.
Miedema, S. A. (June 2016). *Slurry Transport: Fundamentals, A Historical Overview & The Delft Head Loss & Limit Deposit Velocity Framework.* (1st Edition ed.). (R. C. Ramsdell, Ed.) Miami, Florida, USA: Delft University of Technology.
Miedema, S. A. (June 2017). *Slurry Transport: Fundamentals, A Historical Overview & The Delft Head Loss & Limit Deposit Velocity Framework.* (2nd Edition ed.). (R. C. Ramsdell, Ed.) Delft, Netherlands: Delft University of Technology.
Miedema, S. A. (September 2015). *OE4607 Introduction Dredging Engineering* (1st Edition ed.). Delft, The Netherlands: Delft University of Technology.
Miedema, S. A., & Becker, S. (1993). The Use of Modeling and Simulation in the Dredging Industry, in Particular the Closing Process of Clamshell Dredges. *CEDA Dredging Days* (p. 26 pages). Amsterdam, The Netherlands: CEDA.
Miedema, S. A., & Chen, X. (2018). Criterion for the transition of heterogeneous flow to fully stratified flow in slurry transport. *Proceedings of The 1st International Water Environment Ecological Construction Development Conference.* (p. 9). Wuhan, China: CHIDA.
Miedema, S. A., & Frijters, D. (2003). The Mechanism of Kinematic Wedges at Large Cutting Angles - Velocity and Friction Measurements. *23rd WEDA Technical Conference/35th TAMU Dredging Seminar* (p. 14 pages). Chicago, Illinois, USA: WEDA/TAMU.
Miedema, S. A., & Frijters, D. (2004). The wedge mechanism for cutting of water saturated sand at large cutting angles. *WODCON XVII.* Hamburg, Germany: WODA.
Miedema, S. A., & He, J. (2002B). The Existance of Kinematic Wedges at Large Cutting Angles. *WEDA XXII Technical Conference/34th Texas A/M Dredging Seminar* (p. 20 pages). Denver, Colorado, USA: WEDA/TAMU.
Miedema, S. A., & Ma, Y. (2002A). The Cutting of Water Saturated Sand at Large Cutting Angles. *ASCE Dredging 02* (p. 16 pages). Orlando, Florida, USA: ASCE.
Miedema, S. A., & Matousek, V. (2014). An explicit formulation of bed friction factor for sheet flow. *International Freight Pipeline Society Symposium, 15th.* (p. 17 pages). Prague, Czech Republic: IFPS.
Miedema, S. A., & Nieuwboer, B. J. (2019). Cutter head spillage when dredging sand or gravel. *Dredging Summit & Expo 2019* (p. 20). Chicago, USA: WEDA.
Miedema, S. A., & Ramsdell, R. C. (2011). Hydraulic transport of sand/shell mixtures in relation with the critical velocity. *Terra et Aqua, Vol. 122.*
Miedema, S. A., & Ramsdell, R. C. (2013). A head loss model for slurry transport based on energy considerations. *World Dredging Conference XX* (p. 14). Brussels, Belgium: WODA.

References.

Miedema, S. A., & Ramsdell, R. C. (2014). An Analysis of the Hydrostatic Approach of Wilson for the Friction of a Sliding Bed. *WEDA/TAMU* (p. 21). Toronto, Canada: WEDA.

Miedema, S. A., & Ramsdell, R. C. (2014A). The Delft Head Loss & Limit Deposit Velocity Model. *Hydrotransport* (p. 15). Denver, USA.: BHR Group.

Miedema, S. A., & Ramsdell, R. C. (2014B). An Analysis of the Hydrostatic Approach of Wilson for the Friction of a Sliding Bed. *WEDA/TAMU* (p. 21). Toronto, Canada: WEDA.

Miedema, S. A., & Ramsdell, R. C. (2015, May). *Pages from The Delft Head Loss & Limit Deposit Velocity Framework: Wilson.* Retrieved from ResearchGate: https://www.researchgate.net/publication/277340666_Pages_from_The_Delft_Head_Loss_Limit_Deposit_Velocity_Framework_Wilson

Miedema, S. A., & Ramsdell, R. C. (2015). The Limit Deposit Velocity Model, a New Approach. *Journal of Hydrology & Hydromechanics, submitted.*, 15.

Miedema, S. A., & Ramsdell, R. C. (2015B). The Delft Head Loss & Limit Deposit Velocity Framework. *Journal of Dredging Engineering, Vol. 15(2).*, pp. 28.

Miedema, S. A., & Ramsdell, R. C. (2016). The Delft Head Loss & Limit Deposit Velocity Framework. *Journal of Dredging Engineering, Vol. 15(2).*, 3-33.

Miedema, S. A., & Ramsdell, R. C. (2017F). A head loss & limit deposit velocity framework. *Journal of Marine & Environmental Engineering, Vol10(1).*, 45-69.

Miedema, S. A., & Vlasblom, W. J. (1996). Theory for Hopper Sedimentation. *29th Annual Texas A&M Dredging Seminar & WEDA Conference.* (p. 10). New Orleans, USA.: WEDA.

Miedema, S. A., & Yi, Z. (2001). An Analytical Method of Pore Pressure Calculations when Cutting Water Saturated Sand. *Texas A/M 33nd Annual Dredging Seminar* (p. 18 pages). Houston, USA: WEDA/TAMU.

Miedema, S. A., & Zijsling, D. (2012). Hyperbaric rock cutting. *OMAE International Conference on Ocean, Offshore and Arctic Engineering* (p. 14). Rio de Janeiro, Brazil: ASME.

Miedema, S. A., Riet, E. J., & Matousek, V. (2002). Theoretical Description And Numerical Sensitivity Analysis On Wilson Model For Hydraulic Transport Of Solids In Pipelines. *WEDA Journal of Dredging Engineering.*

Miedema, S. A., Talmon, A. M., & Nieuwboer, B. J. (2019). Scaling laws for spillage in cutterheads in dredging. *19th International Conference on Transport & Sedimentation of Solid Particles* (p. 8). Cape Town, South Africa: Cape Peninsula University of Technology, Flow Process and Rheology Centre.

Miedema, S., & Rhee, C. v. (2007). A sensitivity analysis on the effects of dimensions and geometry of Trailing Suction Hopper Dredges. *WODCON*. Orlando, Florida, USA: WODA.

Miedema, S., & Vlasblom, W. (1996). Theory of Hopper Sedimentation. *29th Annual Texas A&M Dredging Seminar*. New Orleans: WEDA/TAMU.

Migniot, C. (1968). Etude des propriete physiques des differents sediments tres fins et de leur comportement sous des actions hydrodynamiques. *Houille Blanche 7*, 591-620.

Miller, D., & Bruggers, D. (1980). Soil and permafrost conditions in the Alaskan Beaufort Sea. *OTC 1980*. Houston, Texas, USA.: OTC.

Miller, M., McCave, I., & Komar, P. (1977). Threshold of sediment motion under unidirectional currents. *Sedimentology, Vol. 24.*, 507-527.

Miltenburg, C. J. (1982). *Stroming en mengselvorming in grote snijkoppen. LaO/82/101*. Delft, the Netherlands: Delft University of Technology.

Ming, G., Ruixiang, L., Ni, F., & Liqun, X. (2007). Hydraulic transport of coarse gravel. *WODCON XVIII*. Orlando, Florida, USA: WODA.

Mitchell, J. (1976). *Fundamentals of soil behavior*. John Wiley & Sons, Inc.

Mitchell, J., Campanella, R., & Singh, A. (1968). Soil creep as a rate process. *Journal SMFD, vol. 94, no. 1, ASCE.*

Mitchener, H., & Torfs, H. (1996). Erosion of mud/sand mixtures. *Coastal Engineering*, 1-25.

Mogi, K. (1966). Pressure dependence of rock strength and transition from brittle fracture to ductile flow. *Bulletin Earthquake Res. Inst. Japan, Vol. 44.*, 215-232.

Mol, A. (1977A). *Stroombeeld rond en in cutter deel II: Vrij in water draaiend; Injecties met kleurstof. BAGT 236.* Delft, the Netherlands: Delft Hydraulics.

Mol, A. (1977B). *Stroombeeld rond en in cutter deel III: Stroombeeld in cutter bij kunstmatige taluds; Injecties met stukjes plastic. BAGT 237.* Delft, the Netherlands: Delft Hydraulics.

Moody, L. F. (1944). Friction Factors for Pipe Flow. *Transactions of the ASME 66 (8).*, 671-684.

Moret, G. E. (1977A). *Stroombeeld rond en in cutter deel I: Stroombeeld rondom cutter bij kunstmatige taluds.* Delft, the Netherlands: Delft Hydraulics, BAGT 235.

Moret, G. E. (1977B). *Stroombeeld rond en in cutter deel IV: Stroombeeld bij kunstmatige taluds.* Delft, the Netherlands: Delft Hydraulics, BAGT 238.

Morsi, S., & Alexander, A. (1972). An investigation of particle trajectories in two-phase flow systems. *Journal of Fluid Mechanics, Vol. 55*, 193-208.
Mukhtar, A. (1991). *Investigations of the flow of multisized heterogeneous slurries in straight pipe and pipe bends.* Delhi, India: PhD Thesis, IIT.
Naden, P. (1987). An erosion criterion for gravel bed rivers. *Earth Surface and Landforms, Vol. 12.*, 83-93.
Nakagawa, H., & Nezu, I. (1977). Prediction of the contribution to the Reynolds stress from the bursting events in open-channel flows. *Journal of Fluid Mechanics, 80*, 99–128.
Neil, C. (1967). Mean velocity criterion for scour of coarse uniform bed material. *Proceedings of the twelfth I.H.A.R. Congress.*, (pp. 46-54).
Newitt, D. M., Richardson, J. F., & Gliddon, B. J. (1961). Hydraulic conveying of solids in vertical pipes. *Transactions Institute of Chemical Engineers, Vol. 39.*, 93-100.
Newitt, D. M., Richardson, J. F., Abbott, M., & Turtle, R. B. (1955). Hydraulic conveying of solids in horizontal pipes. *Transactions of the Institution of Chemical Engineers Vo.l 33.*, 93-110.
Newitt, D. M., Richardson, M. C., Abbott, M., & Turtle, R. B. (1955). Hydraulic conveying of solids in horizontal pipes. *Transactions of the Institution of Chemical Engineers Vo.l 33.*, 93-110.
Nezu, I., & Nakagawa, H. (1993). *Turbulence in Open Channel Flows.* A. A. Balkema.
Nezu, I., & Rodi, W. (1986). Open-channel flow measurements with a laser Doppler anemometer. *Journal of Hydraulic Engineering . ASCE, 112*, 335–355.
Ni, F., Zhao, L., Matousek, V., Vlasblom, W. J., & Zwartbol, A. (2004). Two phase flow of highly concentrated slurry in a pipeline. *Journal of Hydrodynamics, Series B, Vol. 16, No. 3.*, 325-331.
Ni, F., Zhao, L., Xu, L., & Vlasblom, W. J. (2008). A model calculation for flow resistance in the hydraulic transport of sand. *WODCON 18* (pp. 1377-1384). Orlando, Florida, USA: WODA.
Nielsen, P. (1981). Dynamics and geometry of wave generated ripples. *Journal of Geophysics Research, Vol. 86.*, 6467-6472.
Nieman, G. (1935). Neue erkentnisse im Greiferbau. *Zeitschrift VDI 79, Nr. 10, ,* 325-328.
Nikuradse, J. (1933, July/August). Stromungsgesetze in rauen Rohren. *VDI Forschungsheft 361, Beilage zo "Forschung auf dem Gebiete des Ingenieurwesens", Ausgabe B, Band 4.*
Ninnelt, A. (1924). *Uber Kraft und Arbeitsverteilung and Greifern besonderes an Motorgreifern.* Wittenberg Ziemsen Verlag.
Nino, Y., Lopez, F., & Garcia, M. (2003). Threshold of particle entrainment into suspension. *Sedimentology, Vol. 50.*, 247-263.
Nishimatsu, Y. (1972). The mechanics of rock cutting. *International Journal of Rock Mechanics & Mining Science, vol. 9.*, 261-270.
Nnadi, F. N., & Wilson, K. C. (1992). Motion of contact load particles at high shear stress. *Journal of Hydraulic Engineering, Vol. 118.*, 1670-1684.
Nnadi, F. N., & Wilson, K. C. (1995). Bed Load Motion at High Shear Stress: Dune Washout and Plane Bed Flow. *Journal of Hydraulic Engineering, Vol. 121.*, 267-273.
O'Brien, M. P. (1933). Review of the theory of turbulent flow and its relations to sediment transportation. *Transactions of the American Geophysics Union, Vol. 14.*, 487-491.
O'Brien, M. P., & Folsom, R. G. (1939). The transportation of sand in pipelines. *Vol. 3,No. 7 of University of California publications in engineering.*
Ofei, T. N., & Ismail, A. Y. (August 2016). Eulerian-Eulerian simulation of particle liquid slurry flow in horizontal pipe. *Journal of Petroleum Engineering.*, 18.
Ooijens, S. (1999). Adding Dynamics to the Camp Model for the Calculation of Overflow Losses. *Terra et Aqua 76*, 12-21.
Ooijens, S., Gruijter, A. d., Nieuwenhuizen, A., & Vandycke, S. (2001). Research on Hopper Settlement Using Large Scale Modeling. *CEDA Dredging Days 2001* (pp. 1-11). Rotterdam: CEDA.
Oroskar, A. R., & Turian, R. M. (1980). The hold up in pipeline flow of slurries. *AIChE, Vol. 26.*, 550-558.
Os, A. G. (1976). Snelle deformatie van korrelvormig materiaal onder water. *PT-P31, no. 12*, 735-741.
Os, A. G. (1977A). Behavior of soil when excavated under water. In *International course on modern dredging.* The Hague, Netherlands.
Os, A. G. (1977B). Snelle deformatie van korrelvormig materiaal onder water. *PT-B32, no. 8.*, 461-467.
Osman, M. (1964). The mechanics of soil cutting blades. *J.A.E.R. 9 (4)*, 313-328.
Osterkamp, T. (2001). *Sub-Sea Permafrost, Encyclopaedia of Ocean Sciences (2902-2912).*
Ourimi, M., Aussillous, P., Medale, M., Peysson, Y., & Guazzelli, E. (2007). Determination of the critical Shields number for particle erosion in laminar flow. *Physics of fluids, Vol. 19.*, 1-4.
Paintal, A. S. (1971). Concept of critical shear stress in loose boundary open channels. *Journal of Hydraulic Research, 8*(1), 91-109.
Palmer, A. (1999). Speed effects in cutting and ploughing. *Geotechnique 49, no. 3.*, 285-294.

Panagiotopoulos, I., Voulgaris, G., & Collins, M. (1997). The influence of clay on the threshold of movement of fine sandy beds. *Coastal Engineering (32)*, 19-43.

Paphitis, D. (2001). Sediment movement under unidirectional flows: an assesment of empirical threshold curves. *Coastal Engineering*, 227-245.

Parchure, T., & Mehta, A. (1985). Erosion of soft cohesive sediment deposits. *Journal of Hydraulic Engineering 111 (10).*, 1308-1326.

Parzonka, W., Kenchington, J. M., & Charles, M. E. (1981). Hydrotransport of solids in horizontal pipes: Effects of solids concentration and particle size on the deposit velocity. *Canadian Journal of Chemical Engineering, Vol. 59.*, 291-296.

Patankar, S. (1980). *Numerical heat transfer and fluid flow.* New York, USA: McGraw-Hill.

Peker, S. M., & Helvaci, S. S. (2008). *Solid-Liquid Two Phase Flow.* Amsterdam, The Netherlands: Elsevier.

Petrache, H., Zemb, T., Belloni, L., & Parsegian, V. (2006). Salt screening and specific ion adsorption determine neutral-lipid membrane interactions. *National Academy of Sciences of the USA No. 21.*, 7982-7987.

Pfahl, G. (1912). Kraftverteilung und greifen bei selbst greifern. *VDI 1912-1913*.

Pilotti, M., & Menduni, G. (2001). Beginning of sediment transport of incoherent grains in shallow shear flows. *Journal of Hydraulic Research, Vol. 39, No. 2.*, 115-124.

Poloski, A. P., Etchells, A. W., Chun, J., Adkins, H. E., Casella, A. M., Minette, M. J., & Yokuda, S. (2010). A pipeline transport correlation for slurries with small but dense particles. *Canadian Journal of Chemical Engineering, Vol. 88.*, 182-189.

Postma, H. (1967). Sediment transport and sedimentation in the estuarine environment. *Estuaries, AAAS, Washington D.C. Publ. 83.*, 158-179.

Prager, E., Southard, J., & Vivoni-Gallart, E. (1996). Experiments on the entrainment threshold of well-sorted and poorly sorted carbonate sands. *Sedimentology, Vol. 43.*, 33-40.

Prandl, L. (1925). Z. angew. *Math. Mech. 5 (1)*, 136-139.

Pugh, F. J., & Wilson, K. C. (1999). Role of the interface in stratified slurry flow. *Powder Technology, Vol. 104.*, 221-226.

Pugh, F. J., & Wilson, K. C. (1999). Velocity and concentration distribution in sheet flow above plane beds. *Journal of Hydraulic Engineering*, 117-125.

Raalte, G., & Zwartbol, A. (1986). Disc bottom cutterhead, a report on laboratory and field tests. *WODCON XI.* Brighton, UK: WODA.

Rafatian, N., Miska, S., Ledgerwood III, L., Hughes, B., Ahmed, R., Yu, M., & Takach, N. (2009). Experimental study of MSE of a single PDC cutter under simulated pressurized conditions. *SPE/IADC 119302 Drilling Conference & Exhibition.* Amsterdam, Netherlands: SPE International.

Ramsdell, R. C., & Miedema, S. A. (2010). Hydraulic transport of sand/shell mixtures. *WODCON XIX*. Beijing, China.: WODA.

Ramsdell, R. C., & Miedema, S. A. (2013). An overview of flow regimes describing slurry transport. *WODCON XX* (p. 15). Brussels, Belgium.: WODA.

Ramsdell, R. C., Miedema, S. A., & Talmon, A. (2011). Hydraulic transport of sand/shell mixtures. *OMAE 2011*. Rotterdam, Netherlands.: ASME.

Randal, R. E., Jong, P. S., & Miedema, S. A. (2000). Experiences with Cutter Suction Dredge Simulator Training. *WEDA/TAMU* (p. 10). Rhode Island, USA: WEDA.

Raudviki, A. J. (1990). *Loose Boundary Hydraulics.* University of Auckland: Pergamon Press.

Ravelet, F., Bakir, F., Khelladi, S., & Rey, R. (2012). Experimental study of hydraulic transport of large particles in horizontal pipes. *Experimental Thermal and Fluid Science*, 13.

Reece, A. (1965). The fundamental equation of earth moving machinery. *Symposium Earth Moving Machinery.* London: Institute of Mechanical Engineering.

Reichardt, H. (1951). Vollstandige Darstellung der Turbulenten Geswindigkeitsverteilung in Glatten Leitungen. *Zum Angew. Math. Mech., 3(7)*, 208-219.

Rhee, C. (1986). *De invloed van een waterstraal op een zandpakket, U12-1*. Delft, Netherlands: Waterloopkundig Laboratorium.

Rhee, C. (1987A). *Orienterende jetproeven op 190 mum zand met middelvaste pakking, U49-01*. Delft, Netherlands: Waterloopkundig Laboratorium.

Rhee, C. (1987B). *Orienterende jetproeven op 190 mum zand met vaste en zeer losse pakking, U10-1*. Delft, Netherlands: Waterloopkundig Laboratorium.

Rhee, C. (2015). Slope failure by unstable breaching. *Maritime Engineering ICE Vol. 168(2)*, 84-92.

Rhee, C. v. (2002A). The influence of the bottom shear stress on the sedimentation of sand. *11th International Symposium on Transport and Sedimentation of Solid Particles.* Ghent, Belgium.

Rhee, C. v. (2002B). Numerical modeling of the flow and settling in a Trailing Suction Hopper Dredge. *15th International Conference on Hydrotransport.* Banff, Canada.

Rhee, C. v. (2002C). *On the sedimentation process in a Trailing Suction Hopper Dredger.* Delft, Netherlands: Delft University of Technology, PhD Thesis.

Rhee, C. v., & Talmon, A. M. (2000). Entrainment of Sediment. *10th International Conference on Transport and Sedimentation of Solid Particles.* (pp. 251-262). Wroclaw, Poland.: T&S.

Rhee, C., & Steeghs, H. (1991 June). Multi blade ploughs in saturated sand, model cutting tests. *Dredging & Port Construction*.

Richardson, J. F., & Zaki, W. N. (1954). Sedimentation & Fluidization: Part I. *Transactions of the Institution of Chemical Engineering 32*, 35-53.

Richardson, J., & Zaki, W. (1954). Sedimentation & Fluidization: Part I. *Transactions of the Institution of Chemical Engineering 32*, 35-53.

Ridder, J. K. (2018). *Horizontal slurry transport on a large laboratory scale.* Delft, the Netherlands: Delft University of Technology.

Ridder, J. K., Vreede, M. A., Wang, F., Talmon, A. M., & Chen, X. (2017). Preliminary results on the behavior of hydraulic transported solids through a horizontal pipeline in a large laboratory test setup. *5th International Dredging Technology Development Conference of China.* Beijing, China: CHIDA.

Riet, E. J., Matousek, V., & Miedema, S. A. (1995). A Reconstruction of and Sensitivity Analysis on the Wilson Model for Hydraulic Particle Transport. *Proc. 8th Int. Conf. on Transport and Sedimentation of Solid Particles.* Prague, Czech Republic.

Riet, E. J., Matousek, V., & Miedema, S. A. (1996). A Theoretical Description and Numerical Sensitivity Analysis on Wilson's Model for Hydraulic Transport in Pipelines. *Journal of Hydrology & Hydromechanics*.

Rijn, L. v. (1984). Sediment transport: Part I: Bed load transport. *Journal of Hydraulic Engineering, Vol. 110(10)*, 1431-1456.

Rijn, L. v. (1993). *Principles of sediment transport in rivers, estuaries and coastal seas.* Utrecht & Delft: Aqua Publications, The Netherlands.

Rijn, L. v. (1993). *Principles of Sediment Transport, Part 1.* . Blokzijl: Aqua Publications.

Rijn, L. v. (2006). *Principles of sediment transport in rivers, estuaries and coastal areas, Part II: Supplement 2006.* Utrecht & Delft: Aqua Publications, The Netherlands.

Roberts, J., Jepsen, R., Gotthard, D., & Lick, W. (1998). Effects of particle size and bulk density on erosion of quartz particles. *Journal of Hydraulic Engineering*, 1261-1267.

Robinson, M. P. (1971). *Critical deposit velocities for low concentration solid-liquid mixtures. MSc Thesis.* Lehigh University, Fritz Laboratory.

Robinson, M. P., & Graf, W. H. (1972). *Critical deposit velocities for low concentration sand water mixtures. ASCE National Water Resources EnVg Meeting Preprint 1637, January 1972. Paper 1982.* Atlanta, Georgia, USA.: Lehigh University, Fritz Laboratory.

Roco, M. C., & Shook, C. A. (1983). Modeling of Slurry Flow: The effect of particle size. *The Canadian Journal of Chemical Engineering, Vol. 61.*, 494-503.

Rodi, W. (1993). *Turbulence models and their application in hydraulics, a state of the art review.* IAHR, Third Edition.

Rouse, H. (1937). Modern conceptions of the mechanics of fluid turbulence. *Transactions of the American Society of Cicil Engineers, Vol. 102*, 463-505, Discussion 506-543.

Rowe, P. (1962). The stress dilatancy relation for static equilibrium of an assembly of particles in contact. *Proceedings Royal Society A269.* (pp. 500-527). Royal Society.

Rowe, P. (1987). A convinient empirical equation for estimation of the Richardson-Zaki exponent. *Chemical Engineering Science Vol. 42, no. 11*, 2795-2796.

Rowe, P. N. (1987). A convinient empirical equation for estimation of the Richardson-Zaki exponent. *Chemical Engineering Science Vol. 42, no. 11*, 2795-2796.

Roxborough, F. (1987). The role of some basic rock properties in assessing cuttability. *Seminar on Tunnels - Wholly Engineered Structures* (pp. 1-21). Canberra, Australia: AFCC.

Saffman, P. G. (1965). The lift on small sphere in a slow shear low. *Journal of Fluid Mechanics, 22*, 385-400.

Sanders, R. S., Sun, R., Gillies, R. G., McKibben, M., Litzenberger, C., & Shook, C. A. (2004). Deposition Velocities for Particles of Intermediate Size in Turbulent Flows. *Hydrotransport 16* (pp. 429-442). Santiago, Chile.: BHR Group.

Schaan, J., & Shook, C. A. (2000). Anomalous friction in slurry flows. *Canadian Journal of Chemical Engineering, Vol. 78.*, 726-730.

Scheffler, M. (1972). Neue Erkentnisse uber die Auslegung von Zweischalen Schuttgutgreifern. *Deutsche Hebe und Fordermittel Nr. 12*.

Scheffler, M., Pajer, G., & Kurth, F. (1976). Grundlagen der Fordertechnik. *Grondlagen der Fordertechnik*, 134-145.

Scheurel, H. G. (1985). *Rohrverschleiss beim hydraulischen feststoffentransport.* Karlsruhe: Universitat Karlsruhe.

References.

Schiller, R. E., & Herbich, J. B. (1991). *Sediment transport in pipes. Handbook of dredging.* New York: McGraw-Hill.

Schlichting, H. (1968). *Boundary layer theory.* 6th ed. New York: McGraw-Hill.

Schrieck, G. (1996). *Introduction to Dredging Engineering.* Delft, the Netherlands: Delft University of Technology.

Segal, G. (2001). *Sepra analysis programmers guide, standard problems and users manual.* Leidschendam, Netherlands: Ingenieursbureau Sepra.

Sellgren, A., & Wilson, K. (2007). Validation of a four-component pipeline friction-loss model. *Hydrotransport 17* (pp. 193-204). BHR Group.

Sellgren, A., Visintainer, R., Furlan, J., & Matousek, V. (2014). Pump and pipeline performance when pumping slurries with different particle gradings. *Hydrotransport 19* (pp. 131-143). Denver, Colorado, USA.: BHR Group.

Sellgren, A., Visintainer, R., Furlan, J., & Matousek, V. (2016). Pump and pipeline performance when pumping slurries with different particle gradings. *The Canadian Journal of Chemical Engineering, Vol. 94(6)*, 1025-1031.

Seshadri, V., Singh, S. N., & Kaushal, D. R. (2006). A model for the prediction of concentration and particle size distribution for the flow of multisized particulate suspensions through closed ducts and open channels. *Particulate Science and Technology: An International Journal.*, 239-258.

Sha, Y. (1965). Elementary sediment mechanics. *Industry Press, China 302 (in Chinese).*

Sharif, A. (2002). *Critical shear stress and erosion of cohesive soils.* Buffalo, New York: SUNY Buffalo, NY.

Shields, A. (1936). Anwendung der Aehnlichkeitsmechanik und der Turbulenzforschung auf die Geschiebebewegung. *Mitteilung der Preussischen Versuchsanstalt fur Wasserbau und Schiffbau, Heft 26, Berlin.* Belin.

Shook, C. A., Geller, L., Gillies, R. G., Husband, W. H., & Small, M. (1986). Experiments with coarse particles in a 250 mm pipeline. *10th International Conference on the Hydraulic Transport of Solids in Pipelines (Hydrotransport 10).* (pp. 219-227). Cranfield, UK.: BHRA Fluid Eng.

Shook, C. A., Gillies, R. G., & Sanders, R. S. (2002). *Pipeline Hydrotransport with Application in the Oil Sand Industry.* Saskatoon, Canada: Saskatchewan Research Council, SRC Publication 11508-1E02.

Shook, C., & Roco, M. (1991). *Slurry Flow, Principles & Practice.* Boston: Butterworth Heineman.

Silin, M. O., Kobernik, S. G., & Asaulenko, I. A. (1958). *Druckhohenverluste von Wasser und Wasser-Boden-Gemischen in Rohrleitungen grossen Durchmessers.* Ukrain: Dopovidi Akad. Nauk. Ukrain RSR.

Silin, N. A., & Kobernik, S. G. (1962). Rezimy raboty zemlijesosnych snarjadov, Kijev.

Simons, D. (1957). *Theory and design of stable channels in alluvial material.* PhD thesis: Colorado State University.

Sinclair, C. G. (1962). The limit deposit velocity of heterogeneous suspensions. *Proceedings Symposium on the Interaction Btween Fluids and Particles.* Institute of Chemical Engineers.

Smoldyrev. (1970). *Truboprowodnyi transport(rohrleitungstransport).* Moskau.

Sobota, J., & Kril, S. I. (1992). Liquid and solid velocity during mixture flow. *Proceedings 10th International Colloquium Massenguttransport durch Rohrleitungen.*, (p. K). Meschede, Germany.

Sohne, W. (1956). Some basic considerations of soil mechanics as applied to agricultural engineering. *Grundlagen der landtechnik (7).*, 11-27.

Soleil, G., & Ballade, P. (1952). Le transport hydraulique des materiaux dans les travaux publics, observations des resultats d'essais en grandeur nature. *Deuxiemes Journees de l'Hydraulique*, 9-26.

Soulsby, R., & Whitehouse, R. (1997). Threshold of sediment motion in coastal environment. *Proceedings Pacific Coasts and Ports.* (pp. 149-154). Christchurch, New Zealand: University of Canterbury.

Souza Pinto, T. C., Moraes Junior, D., Slatter, P. T., & Leal Filho, L. S. (2014). Modelling the critical velocity for heterogeneous flow of mineral slurries. *International Journal of Multiphase Flow, 65.*, 31-37.

Soydemir, C. (1977). Potential models for shear strength generation in soft marine clays. *International Symposium on Soft Clay.* Bangkok, Thailand.

Spelay, R., Hashemi, S. A., Gillies, R. G., Hegde, R., Sanders, R. S., & Gillies, D. G. (2013). Governing friction loss mechanisms and the importance of offline characterization tests in the pipeline transport of dense coarse particle slurries. *Proceedings of the ASME 2013 Fluids Engineering Division Summer Meeting.* (pp. 1-7). Incline Village, Nevada, USA.: FEDSM2013.

Stam, P. (1983). *Analyse ten behoeve van het ontwerp van een klei snijdende sleepkop, CO/82/129.* Delft, Netherlands: Delft University of Technology.

Stansby, P. (1997). Semi-implicit finite shallow-water flow and solute transport solver with k-epsilon turbulence model. *International Journal for Numerical Methods in Fluids, vol. 25.*, 285-313.

Steeghs, H. (1985A). Snijden van zand onder water, part I. *Ports & Dredging no. 121*.

Steeghs, H. (1985B). Snijden van zand onder water, part II. *Ports & Dredging no. 123.*

Steinbusch, P. J., Vlasblom, W. J., & Burger, M. d. (1999). Numerical simulation of the flow generated by cutter heads. *Hydrotransport 14* (pp. 435-443). Cranfield, UK: BHRG.

Stelling, G., & Kester, J. (1994). On the approximation of horizontal gradients in sigma coordinates for bathymetry with steep bottom slopes. *International Journal for Numerical Methods in Fluids, vol. 18*, 915-935.

Stevenson, P., Cabrejos, F. J., & Thorpe, R. B. (2002). Incipient motion of particles on a bed of like particles in hydraulic and pneumatic conveying. *Fourth World Congress of Particle Technology, Sydney, 21st–25th July (paper 400).* Sydney.

Stevenson, P., Thorpe, R. B., & Davidson, J. F. (2002). Incipient motion of a small particle in the viscous boundary-layer at a pipe wall. *Chemical Engineering Science, 57*, 4505–4520.

Sundborg, A. (1956). The River Klarålven: Chapter 2. The morphological activity of flowing water erosion of the stream bed. *Geografiska Annaler, 38*, 165-221.

Swamee, P. K. (1993). Critical depth equations for irrigation canals. *Journal of Irrigation and Drainage Engineering, ASCE.*, 400-409.

Swamee, S. E., & Jain, K. A. (1976). Explicit equations for pipe-flow problems. *Journal of the Hydraulics Division (ASCE) 102 (5).*, 657-664.

Talmon, A. (2013). Analytical model for pipe wall friction of pseudo homogeneous sand slurries. *Particulate Science & technology: An International Journal*, 264-270.

Talmon, A. M. (1999). Mathematical Analysis of the Amplification of Density Variations in Long Distance Sand Transport Pipelines. *Hydrotransport 14* (pp. 3-20). Maastricht, The Netherlands: BHRA.

Talmon, A. M. (2011). Hydraulic Resistance of Sand-Water Mixture Flow in Vertical Pipes. *T&S, Transport and Sedimentation of Solid Particles* (pp. 137-147). Wroclaw, Poland: T&S.

Talmon, A. M. (2013). Analytical model for pipe wall friction of pseudo homogeneous sand slurries. *Particulate Science & technology: An International Journal*, 264-270.

Talmon, A. M., Vlasblom, W. J., & Burger, M. d. (2010). Cutter production and kinematics of mixture forming. *WODCON XIX* (pp. 838-847). Beijing, China: WODA.

Talmon, A., & Huisman, M. (2005). Fall velocity of particles in shear flow of drilling fluids. *Tunneling and Underground Space Technology (20).*, 193-201.

Tang, C. (1964). Law of sediment threshold. *Journal of Hydraulic Engineering (in Chinese)*.

Tauber, B. A. (1958). The effect of the design of a cable grab on its scooping capacity. *Collection of Scientific Works of MLTI 8*, 30-34.

Televantos, Y., Shook, C. A., Carleton, A., & Street, M. (1979). Flow of slurries of coarse particles at high solids concentrations. *Canadian Journal of Chemical Engineering, Vol. 57.*, 255-262.

Ternat, F. (2007). *Erosion des Sediments Cohesifs en Auto Consolidation (PhD thesis in French).* Marseille: Universite de la Medirerranee.

Ternat, F., Boyer, P., Anselmet, F., & Amielh, M. (2008). erosion threshold of saturated natural cohesive sediments: Modeling and experiments. *water Resources Research, Vol. 44, W11434*, 1-18.

Terzaghi, K., & Peck, R. (1964). *Soil mechanics in engineering practise.* New York: John Wiley & Sons.

Thomas, A. (1976). SCALE-UP METHODS FOR PIPELINE TRANSPORT OF SLURRIES. *International Journal of Mineral Processing, Vol. 3.*, 51-69.

Thomas, A. D. (1979). Predicting the deposit velocity for horizontal turbulent pipe flow of slurries. *International Journal of Multiphase Flow, Vol. 5.*, 113-129.

Thomas, A. D. (2014). Slurries of most interest to the mining industry flow homogeneously and the deposit velocity is the key parameter. *HydroTransport 19.* (pp. 239-252). Denver, Colorado, USA.: BHR Group.

Thomas, A. D. (2015). A modification of the Wilson & Judge deposit velocity, extending its application to finer particles and larger pipe sizes. *17th International Conference on Transport & Sedimentation of Solid Particles.* (pp. 335-344). Delft, The Netherlands: Delft Univesity of Technology.

Thomas, D. G. (1962). Transport Characteristics of Suspensions: Part VI. Minimum velocity for large particle size suspensions in round horizontal pipes. *A.I.Ch.E. Journal, Vol.8(3).*, 373-378.

Thomas, D. G. (1965). Transport characteristics of suspensions: VIII. A note on the viscosity of Newtonian suspensions of uniform spherical particles. *Journal Of Colloidal Sciences, Vol. 20.*, 267-277.

Tison, L. (1953). Studies of the critical tractive force of entrainment of bed materials. *Proceedings of the fifth I.A.H.R. Congress.*, (pp. 21-35).

Torfs, H. (1995). *Erosion of mud/sand mixtures. (PhD thesis).* Leuven: Katholieke Universiteit Leuven.

Torfs, H., Jiang, J., & Mehta, A. (2001). Assesment of the erodibility of fine/coarse sediment mixtures. *Coastal and Estuarine Fine Sediment Processes (McAnnally, W.H. & Mehta, A.J. Editors)* (pp. 109-123). Amsterdam: Elsevier.

Torke, H. J. (1962). Untersuchungen uber Fullvorgang bei Versuchen im Sand. *Deutsche Hebe und Fordertechnik Nr. 8*.

Turian, R. M., & Yuan, T. F. (1977). Flow of slurries in pipelines. *AIChE Journal, Vol. 23.*, 232-243.

Turian, R. M., Hsu, F. L., & Ma, T. W. (1987). Estimation of the critical velocity in pipeline flow of slurries. *Powder Technology, Vol. 51.*, 35-47.

Turnage, G., & Freitag, D. (1970). Effects of cone velocity and size on soil penetration resistance. *ASEA 69-670.*

Turner, T. (1996). *Fundamentals of Hydraulic Dredging.* New York: ASCE.

Turton, R., & Levenspiel, O. (1986). A short note on the drag correlation for spheres. *Powder technology Vol. 47*, 83-85.

Unsold, G. (1984). *Der Transportbeginn rolligen Sohlmaterials in gleichformigen turbulenten Stromungen, Eine kritische Uberprufung der Shields Function und ihre experimentelle Erweiterung auf feinkornige, nichtbindige Sedimente.* Kiel, Germany: Dissertation Universitat Kiel Deutschland.

USWES. (1936). *Flume tests made to develop a synthetic sand which will not form ripples when used in movable bed models.* Vicksburg, Mississippi, USA: United States Waterways Experiment Station, tech. Memo 99-1.

Vanoni, V. A. (1975). *Sedimentation Engineering: American Society of Civil Engineers, Manuals and Reports on Engineering Practice. No. 54. P.745.*

Verdoodt, L. L., & Burger, M. d. (2001). Measurements of the flow generated by a cutter head. *WODCON XVI.* Kuala Lumpur, Malaysia: WODA.

Verhoef, P. (1997). *Wear of rock cutting tools: Implications for site investigation of rock dredging projects.* Delft, Netherlands: Balkema Rotterdam.

Verruijt, A. (1983). *Soil Mechanics.* Delft: DUM, Netherlands.

Vlasak, P. (2008). *Laminar, transitional and turbulent flow of fine grained slurries in pipelines.* Prague.: Czech Technical University in Prague, Fakulty of Civil Engineering.

Vlasak, P., Chara, Z., Krupicka, J., & Konfrst, J. (2014). Experimental investigation of coarse particles water mixture flow in horizontal and inclined pipes. *Journal of Hydrology & Hydromechanics, Vol. 62(3).*, 241-247.

Vlasak, P., Kysela, B., & Chara, Z. (2012). FLOW STRUCTURE OF COARSE-GRAINED SLURRY IN A HORIZONTAL PIPE. *Journal of Hydrology & Hydromechanics, Vol. 60.*, 115-124.

Vlasblom, W. (2003-2007). *Rock Cutting, Lecture Notes.* Delft, Netherlands: Delft University of Technology.

Vlasblom, W. J. (2003-2007). *Designing dredging equipment, lecture notes.* Delft, Netherlands: Delft University of Technology.

Vlasblom, W. J., & Talmon, A. M. (2006). Spillage problem of cutter suction dredgers. *2nd Chinese International Dredging Congress.* Guangzhou, China: CHIDA.

Vlasblom, W., & Miedema, S. (1995). A Theory for Determining Sedimentation and Overflow Losses in Hoppers. *WODCON IV.* Amsterdam, Netherlands: WODA.

Vocadlo, J. J. (1972). Prediction of pressure gradient for the horizontal turbulent flow of slurries. *Hydrotransport 2.* Coventry: BHRA.

Vocadlo, J. J., & E., C. M. (1972). Prediction of pressure gradient for the horizontal turbulent flow of slurries. *Conference on the Hydraulic Transport of Solids in Pipes.* Warwick, England: British Hydromechanics Research Association.

Vreede, M. d. (2018). *Hydraulic transport in inclined large diameter pipelines.* Delft, the Netherlands: Delft University of Technology.

Vukovic, M., & Soro, A. (1992). Determination of hydraulic conductivity of porous media from grain size composition. *Water Resources Publications, Littleton, Colorado.*

Wallis, G. (1969). *One Dimensional Two Phase Flow.* McGraw Hill.

Wasp, E. J. (1963). Cross country coal pipeline hydraulics. *Pipeline News.*, 20-28.

Wasp, E. J., & Slatter, P. T. (2004). Deposition velocities for small particles in large pipes. *12th International Conference on Transport & Sedimentation of Solid Particles*, (pp. 20-24). Prague, Czech Republic.

Wasp, E. J., Kenny, J. P., & Gandhi, R. L. (1977). Solid liquid flow slurry pipeline transportation. *Transactions Technical Publications.*

Wasp, E. J., Kenny, J. P., Aude, T. C., Seiter, R. H., & Jacques, R. B. (1970). Deposition velocities transition velocities and spatial distribution of solids in slurry pipelines. *Hydro Transport 1, paper H42.* (pp. 53-76). Coventry: BHRA Fluid Engineering.

Weegenaar, R. A., Keetels, G. H., Winkelman, M. O., & Rhee, C. v. (2015). Sand erosion with a traversing circular jet. *Maritime Engineering ICE Vol. 168(MA2).*, 76-83.

Weibull, W. (1939). A statistical theory of the strength of materials. *Royal Swedish Institute of Engineers, 151:1.*

Weijermars, R. (1997-2011). *Principles of rock mechanics.* Delft, Netherlands: Alboran Science Publishing.

Welte, A. (1971). Grundlagen der Berechnung der Rohrleitungsdruckverluste. *Konstruction 23, Heft 5 & 6.*

Werkhoven, J. J., Nieuwboer, B. J., Louis, A. A., Ramsdell, R. C., & Miedema, S. A. (2018). A pseudo analytical model for CSD spillage due to rotational velocity induced flow. *Dredging Summit & Expo 18* (p. 18). Norfolk, Virginia, USA: WEDA.

Werkhoven, J. J., Nieuwboer, B. J., Louis, A. A., Ramsdell, R. C., & Miedema, S. A. (2019A). Modelling a Rotating Cutterhead's Spillage with more Accuracy. *Terra et Aqua 153*, 15.

Werkhoven, J. J., Nieuwboer, B. J., Ramsdell, R. C., & Miedema, S. A. (2019). CSD Spillage Model for Sand and Rock. *World Dredging Conference* (p. 17). Shanghai, China: CHIDA, EADA, WODA.

Westendorp, J. H. (1948). *Verslag literatuurstudie over persen van zand M.276.* Delft, Netherlands: Delft Hydraulics Laboratory.

White, C. M. (1940). The equilibrium of grains on the bed of a stream. *Proceedings Royal Society of London, A174*, pp. 322-338.

White, S. (1970). Plane bed thresholds of fine grained sediments. *Nature Vol. 228.*, 152-153.

Whitehouse, R., Soulsby, R., Roberts, R., & Mitchener, H. (2000). *Dynamics of estuarine muds: A manual for practical applications.* London: Thomas Telford Publications.

Whitlock, L., Wilson, K. C., & Sellgren, A. (2004). Effect of near-wall lift on frictional characteristics of sand slurries. *Hydrotransport 16* (pp. 443-454). Cranfield, UK.: BHR Group.

Wiberg, P. L., & Smith, J. D. (1987A). Calculations of the critical shear stress for motion of uniform and heterogeneous sediments. *Water Resources Research, 23*(8), 1471–1480.

Wiberg, P., & Smith, J. (1987B). Initial motion of coarse sediment in streams of high gradient. *Proceedings of the Corvallis Symposium.* IAHS Publication No. 165.

Wiedenroth, W. (1967). *Untersuchungen uber die forderung von sand wasser gemischen durch rohrleitungen und kreiselpumpen.* Hannover: PhD Thesis, Technische Hochschule Hannover.

Wikipedia. (n.d.). Retrieved from Wikipedia: http://en.wikipedia.org/wiki/Erosion

Wikramanayake, P. N., & Madsen, O. S. (1991). *Calculation of movable bed friction factors.* Vicksburg, Mississippi.: Tech. Rep. DACW-39-88-K-0047, 105 pp., Coastal Eng. Res. Cent.,.

Wilkinson, H. N. (1963). Research in the design of grabs by tests on models. *Proceeding Institution of Mechanical Engineering Nr. 31*, (pp. 831-846).

Wilson, K. C. (1965). *Application of the minimum entropy production principle to problems in two-phase flow, PhD Thesis.* Kingston, Ontario, Canada.: Queens University.

Wilson, K. C. (1966). Bed Load Transport at High Shear Stress. *Journal of the Hydraulics Division*, 49-59.

Wilson, K. C. (1970). Slip point of beds in solid liquid pipeline flow. *Journal of Hydraulic Division, Vol 96(HY1)*, 1-12.

Wilson, K. C. (1970). Slip point of beds in solid-liquid pipeline flow. *Proceedings American Society of Civil Engineers, Vol. 96, HY1.*

Wilson, K. C. (1972). A Formula for the Velocity Required to Initiate Particle Suspension in Pipeline Flow. *Hydrotransport 2* (pp. E2 23-36). Warwick, UK.: BHRA Fluid Engineering.

Wilson, K. C. (1974). Coordinates for the Limit of Deposition in Pipeline Flow. *Hydrotransport 3* (pp. E1 1-13). Colorado School of Mines, Colorado, USA.: BHRA Fluid Engineering.

Wilson, K. C. (1975). Stationary Deposits and Sliding Beds in Pipes Transporting Solids. *Dredging Technology* (pp. C3 29-40). College Station, Texas, USA.: BHRA Fluid Engineering.

Wilson, K. C. (1976). A Unified Physically based Analysis of Solid-Liquid Pipeline Flow. *Hydrotransport 4* (pp. A1 1-16). Banff, Alberta, Canada: BHRA Fluid Engineering.

Wilson, K. C. (1979). Deposition limit nomograms for particles of various densities in pipeline flow. *Hydrotransport 6* (p. 12). Canterbury, UK: BHRA Fluid Engineering.

Wilson, K. C. (1980). Analysis of Slurry Flows with a Free Surface. *Hydrotransport 7* (pp. 123-132). Sendai, Japan: BHRA Fluid Engineering.

Wilson, K. C. (1984). Analysis of Contact Load Distribution and Application to Deposition Limit in Horizontal Pipes. *Journal of Pipelines, Vol. 4.*, 171-176.

Wilson, K. C. (1986). Effect of Solids Concentration on Deposit Velocity. *Journal of Pipelines, Vol. 5.*, 251-257.

Wilson, K. C. (1987). Analysis of Bed Load Motion at High Shear Stress. *Journal of Hydraulic Engineering, Vol. 113.*, 97-103.

Wilson, K. C. (1988). Evaluation of interfacial friction for pipeline transport models. *Hydrotransport 11* (p. B4). BHRA Fluid Engineering.

Wilson, K. C. (1989). Mobile Bed Friction at High Shear Stress. *Journal of Hydraulic Engineering, Vol. 115.*, 825-830.

Wilson, K. C., & Addie, G. R. (1997). Coarse particle pipeline transport: effect of particle degradation on friction. *Powder Technology, Vol. 94.*, 235-238.

Wilson, K. C., & Brown, N. P. (1982). Analysis of Fluid Friction in dense Phase Pipeline Flow. *The Canadian Journal of Chemical Engineering, Vol. 60.*, 83-86.

Wilson, K. C., & Judge, D. G. (1976). New Techniques for the Scale-Up of Pilot Plant Results to Coal Slurry Pipelines. *Proceedings International Symposium on Freight Pipelines.* (pp. 1-29). Washington DC, USA: University of Pensylvania.

References.

Wilson, K. C., & Judge, D. G. (1977). Application of Analytical Model to Stationary Deposit Limit in Sand Water Slurries. *Dredging Technology* (pp. J1 1-12). College Station, Texas, USA.: BHRA Fluid Engineering.

Wilson, K. C., & Judge, D. G. (1978). Analytically based Nomographic Charts for Sand-Water Flow. *Hydrotransport 5* (pp. A1 1-12). Hannover, Germany: BHRA Fluid Engineering.

Wilson, K. C., & Judge, D. G. (1980). New Techniques for the Scale-up of Pilot Plant Results to Coal Slurry Pipelines. *Journal of Powder & Bulk Solids Technology.*, 15-22.

Wilson, K. C., & Nnadi, F. N. (1990). Behavior of Mobile Beds at High Shear Stress. *Proceedings Coastal Engineering 22.*, (pp. 2536-2541). Delft.

Wilson, K. C., & Pugh, F. J. (1988). Dispersive Force Basis for Concentration Profiles. *Journal of Hydraulic Engineering, Vol. 114, No. 7.*, 806-810.

Wilson, K. C., & Pugh, F. J. (1988). Dispersive Force Modelling of Turbulent Suspension in Heterogeneous Slurry Flow. *The Canadian Journal of Chemical Engineering, Vol. 66.*, 721-727.

Wilson, K. C., & Sellgren, A. (2001). *Hydraulic transport of solids, Pump Handbook, pp. 9.321-9.349.* McGraw-Hill.

Wilson, K. C., & Sellgren, A. (2003). Interaction of Particles and Near-Wall Lift in Slurry Pipelines. *Journal of Hydraulic Engineering, Vol. 129.*, 73-76.

Wilson, K. C., & Sellgren, A. (2010). Behavior of intermediate particle slurries in pipelines. *Hydrotransport 18* (pp. 117-128). Rio de Janeiro: BHR Group.

Wilson, K. C., & Sellgren, A. (2012). Revised Method for Calculating Stratification Ratios for Heterogeneous Flows. *14th International Conference on Transport & Sedimentation of Solid Particles.*, (pp. 334-340).

Wilson, K. C., & Watt, W. E. (1974). Influence of Particle Diameter on the Turbulent Support of Solids in Pipeline Flow. *Hydrotransport 3* (pp. D1 1-9). Colorado School of Mines, Colorado, USA.: BHRA Fluid Engineering.

Wilson, K. C., Addie, G. R., & Clift, R. (1992). *Slurry Transport using Centrifugal Pumps.* New York: Elsevier Applied Sciences.

Wilson, K. C., Addie, G. R., Clift, R., & Sellgren, A. (1997). *Slurry Transport using Centrifugal Pumps.* Glasgow, UK.: Chapman & Hall, Blackie Academic & Professional.

Wilson, K. C., Addie, G. R., Sellgren, A., & Clift, R. (2006). *Slurry transport using centrifugal pumps.* New York: Springer Science+Business Media Inc.

Wilson, K. C., Clift, R., & Sellgren, A. (2002). Operating points for pipelines carrying concentrated heterogeneous slurries. *Powder Technology, Vol. 123.*, 19-24.

Wilson, K. C., Clift, R., Addie, G. R., & Maffet, J. (1990). Effect of Broad Particle Grading on Slurry Stratification Ratio and Scale-up. *Powder Technology, 61.*, 165 - 172.

Wilson, K. C., Sanders, R. S., Gillies, R. G., & Shook, C. A. (2010). Verification of the near wall model for slurry flow. *Powder Technology, Vol. 197.*, 247-253.

Wilson, K. C., Sellgren, A., & Addie, G. R. (2000). Near-wall fluid lift of particles in slurry pipelines. *10th Conference on Transport and Sedimentation of Solid Particles.* Wroclav, Poland: T&S10.

Wilson, K. C., Streat, M., & Bantin, R. A. (1972). Slip model correlation of dense two phase flow. *Hydrotransport 2* (pp. B1 1-10). Warwick, UK: BHRA Fluid Engineering.

Wilson, W. E. (1942). Mechanics of flow with non colloidal inert solids. *Transactions ASCE Vol. 107.*, 1576-1594.

Winterwerp, J., & Kesteren, W. v. (2004). *Introduction to the physics of cohesive sediment in the marine environment.* Delft: Elsevier.

Wismer, R., & Luth, H. (1972A). Performance of Plane Soil Cutting Blades. *Transactions of ASEA.*

Wismer, R., & Luth, H. (1972B). Rate effects in soil cutting. *Journal of Terramechanics, vol. 8, no. 3.*, 11-21.

Wittekoek, S. (1991A). *The determination of the closing process of clamshell dredges in water saturated sand. MSc Thesis. 90.3.GV.2771.* Delft, The Netherlands: Delft University of Technology.

Wittekoek, S. (1991B). *The development of an improved clamshell. MSc Thesis 90.3.GV.2858.* Delft, The Netherlands: Delft University of Technology.

Wittekoek, S. (1991C). *The validation of a calculation method for the simulation of the closing process of clamshell grabs for dredging purposes. MSc Thesis 90.3.GV.2829.* Delft, The Netherlands: Delft University of Technology.

Wood, D. J. (1966). An explicit friction factor relationship. *Civil Engineering, Vol. 36, ASCE.*, 60-61.

Worster, R. C., & Denny, D. F. (1955). Hydraulic transport of solid materials in pipelines. *Institution of Mechanical Engineers (London)*, 563-586.

Wu, W., & Wang, S. (2006). Formulas for sediment porosity and settling velocity. *Journal of Hydraulic Engineering, 132(8)*, 858-862.

Xiong, T., Miedema, S. A., & Chen, X. (2018). Comparative Analysis between CFD Model and DHLLDV Model in Fully suspended Slurry Flow. *Submitted to: Ocean Engineering*, 16.

Yagi, T. (1970). Sedimentation effects of soil in hopper. *WODCON III* (pp. 1-22). Singapore: WODA.

Yagi, T., Okude, T., Miyazaki, S., & Koreishi, A. (1972). *An Analysis of the Hydraulic Transport of Solids in Horizontal Pipes.* Nagase, Yokosuka, Japan.: Report of the Port & Harbour Research Institute, Vol. 11, No. 3.

Yalin, M. S., & Karahan, E. (1979). Inception of sediment transport. *ASCE Journal of the Hydraulic Division, 105*, 1433–1443.

Yi, Z. (2000). *The FEM calculation of pore water pressure in sand cutting process by SEPRAN*. Delft, Netherlands: Delft University of Technology, Report: 2001.BT.5455.

Yi, Z., & Miedema, S. (2001). Finite Element Calculations To Determine The Pore Pressures When Cutting Water Saturated Sand At Large Cutting Angles. *CEDA Dredging Days* (p. 20 pages). Amsterdam, The Netherlands: CEDA.

Yi, Z., & Miedema, S. (2002). Finite Element Calculations To Determine The Pore Pressures When Cutting Water Saturated Sand At Large Cutting Angles. *CEDA Dredging Days* (p. 20 pages). Amsterdam, The Netherlands: CEDA.

You, Z. (2006). Discussion of "Initiation of Movement of Quartz Particles". *Journal of Hydraulic Engineering*, 111-112.

Youd, T. (1973). Factors controlling maximum and minimum densities of sands. *ASTM special technical publications, no 523.*, 98-112.

Zandi, I. (1971). Hydraulic transport of bulky materials. In I. Zandi, *Advances in Solid–Liquid Flow in Pipes and its Applications.* (pp. 1-38). Oxford: Pergamon Pres.

Zandi, I., & Govatos, G. (1967). Heterogeneous flow of solids in pipelines. *Proc. ACSE, J. Hydraul. Div.,, 93(HY3).*, 145-159.

Zanke, U. C. (1977). *Berechnung der Sinkgeschwindigkeiten von Sedimenten.* Hannover, Germany: Mitteilungen Des Francius Instituts for Wasserbau, Heft 46, seite 243, Technical University Hannover.

Zanke, U. C. (1977). *Neuer Ansatz zur Berechnung des Transportbeginns von Sedimenten unter Stromungseinfluss.* Hannover: Mitteilungen des Francius Instituts.

Zanke, U. C. (1982). *Grundlagen der Sedimentbewegung.* Berlin, Heidelberg, New York: Springer Verlag.

Zanke, U. C. (2001). *Zum Einfluss der Turbulenz auf den Beginn der Sedimentbewegung.* Darmstadt, Germany: Mitteilungen des Instituts fur Wasserbau und Wasserwirtschaft der TU Darmstadt, Heft 120.

Zanke, U. C. (2003). On the influence of turbulence on the initiation of sediment motion. *International Journal of Sediment Research*, *18*(1), 17–31.

Zeng, D., & Yao, Y. (1988). Investigation on the relationship between soil metal friction and sliding speed. *2nd Asian Pacific Conference of ISTVS.* Bangkok, Thailand.

Zeng, D., & Yao, Y. (1991). Investigation on the relationship between soil shear strength and shear rate. *Journal of Terramechanics, 28 (1).*

Ziervogel, K. (2003). *Aggregation and transport behavour of sediment surface particles in Mecklenburg Bight, south western Baltic Sea affected by biogenic stickiness.* Rostock: PhD Thesis, Universitat Rostock, Germany.

Ziervogel, K., & Bohling, B. (2003). Sedimentological parameters and erosion behaviour of submarine coastal sediments in the South-Western Baltic sea. *Geo-Marine Letters (23-1)*, 43-52.

Zijsling, D. (1987). Single cutter testing - a key for PDC bit development (SPE 16529). *Offshore Europe 87.* Aberdeen, Scotland.

Chapter 15: List of Figures.

List of Figures.

Chapter 16: List of Tables.

Dredging Engineering
Special Topics

Entrainment of Particles
Cutter Head Spillage
Centrifugal Pumps
Pump/Pipeline Dynamics
Swing Winches
Trailing Suction Hopper Sedimentation
TSHD Water Jets
Clamshell Dredging

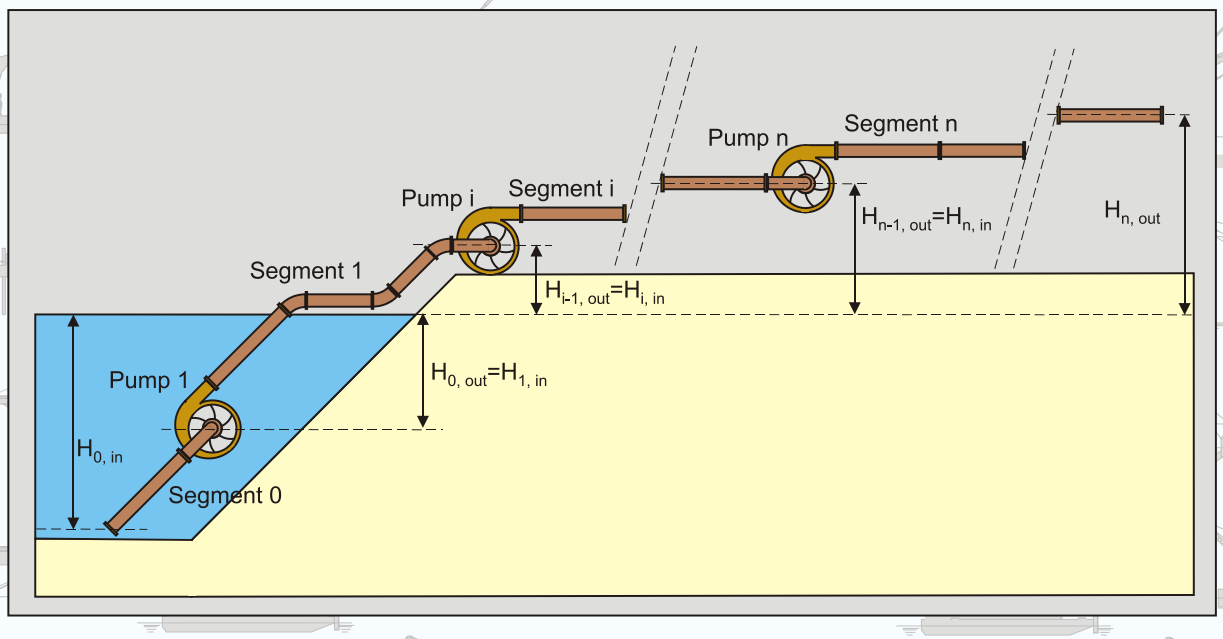

by
Dr.ir. Sape A. Miedema

Dredging Engineering Special Topics

Sape A. Miedema

In dredging, production estimating is carried out mainly with analytical physical models of the different dredging processes. Slurry transport of settling slurries and cutting processes in sand, clay and rock are already covered in two other books by the author. Other processes like hopper sedimentation and erosion, water jet fluidization, cutter head spillage, pump/pipeline dynamics and clamshell dredging are covered in this Special Topics Edition. New topics may be added in the near future.

Dr. ir. Sape A. Miedema
TU Delft | Martime and Transport Engineering

Dr.ir. S.A. Miedema teaches (or has taught) courses on soil mechanics and soil cutting, pumps and slurry transport, hopper sedimentation and erosion, mechatronics, applied thermodynamics related to energy, drive system design principles, mooring systems, hydromechanics and mathematics. He is (or has been) also teaching at Hohai University, Changzhou, China, at Cantho University, Cantho Vietnam, at Petrovietnam University, Baria, Vietnam and different dredging companies in the Netherlands and the USA.His research focuses on the mathematical modeling of dredging systems like, cutter suction dredges, hopper dredges, clamshell dredges, backhoe dredges and trenchers. The fundamental part of the research focuses on the cutting processes of sand, clay and rock, sedimentation processes in Trailing Suction Hopper Dredges and the associated erosion processes. Lately the research focuses on hyperbaric rock cutting in relation with deep sea mining and on hydraulic transport of solids/liquid settling slurries.

ISBN 978-94-6366-174-4
DOI https://doi.org/10.5074/t.2019.004

textbooks.open.tudelft.nl

Cover image: A cutter suction dredge and a trailing suction hopper dredge at a huge land reclamation work in Singapore 2001